LBL-6575
c.1



# NUCLEAR SCIENCE

## Annual Report
## 1976-1977



*Lawrence Berkeley Laboratory*
*University of California/Berkeley*

Prepared for the U.S. Energy Research and Development Administration under Contract W-7405-ENG-48

LBL-6575
c.1

## DISCLAIMER

LBL-6575
UC-34
Physics-General
TID 4500-R66

# NUCLEAR SCIENCE

## Annual Report
## for the period
## July 1, 1976 — June 30, 1977

B.G. HARVEY
*Director*

H.E. CONZETT
W.D. MYERS
L.S. SCHROEDER
*Editors*

*Lawrence Berkeley Laboratory*
*University of California/Berkeley*

## CONTENTS

## 2. Macroscopic

### 3. Relativistic



## B. Nuclear Structure



# III. APPARATUS

## A. Accelerator Operations and Development

I.

# EXPERIMENTAL RESEARCH

# A. NUCLEAR STRUCTURE

## $\beta^+$-DELAYED PROTON DECAY OF $^{29}$S†

D. J. Vieira, R. A. Gough, and Joseph Cerny

The nuclide $^{29}$S is a relatively uninvestigated member of the $T_z$ = - 3/2, A = 4n + 1 series of strong $\beta^+$-delayed proton precursors. The decay schemes of these nuclei are characterized by strong branching (12-100%) to unbound levels in the daughter nuclei which subsequently break up by emitting protons of discrete energies. By accurately measuring the energies and intensities of these delayed protons, it is possible to determine excitation energies of states in the daughter nucleus and further to determine the beta decay transition strengths feeding them. Such spectroscopic studies of the $\beta^+$-delayed proton decay of $^{29}$S are presented in this report.

The $^{28}$Si($^3$He,2n) reaction was used to produce $^{29}$S in irradiations of natural silicon targets with the 32 MeV $^3$He beam at the 88-inch cyclotron. High energy resolution, low background delayed proton spectra covering an energy region from 600 keV to 8 MeV have been obtained using counter telescopes and particle identification techniques in conjunction with a helium-jet transport system.

Two of the observed delayed proton spectra obtained from these $^3$He bombardments are shown in Figs. 1 and 2. Additional data, not shown here, were also acquired and incorporated into the following analysis and calculations.

All the proton groups labeled with numbers are attributed to delayed protons from $^{29}$S. More than fifteen previously unobserved delayed proton groups have been characterized, while other groups observed in the earlier works[1,2] have been resolved into multiple groups. All assigned peaks exhibit the same half-life to within their respective uncertainties, and after combining four independent measurements a half-life of 187 ± 6 ms was obtained for $^{29}$S. This agrees well with the previous measurements[1,2] of 195 ± 8 and 180 ± 10 ms. The weighted average of these determinations gives 188.0 ± 4.3 ms which has been adopted for all subsequent calculations and results reported here.

Two contaminant groups were also observed and are labeled with letters. Group A was observed only in the data shown in Fig. 1. No evidence for this group can be seen in Fig. 2 or in any of the other data that were obtained. The origin of this group is uncertain, but it definitely does not originate from the decay of $^{29}$S. Peak B is attributed to the decay of $^{25}$Si since its energy coincides with the energy of the strongest delayed

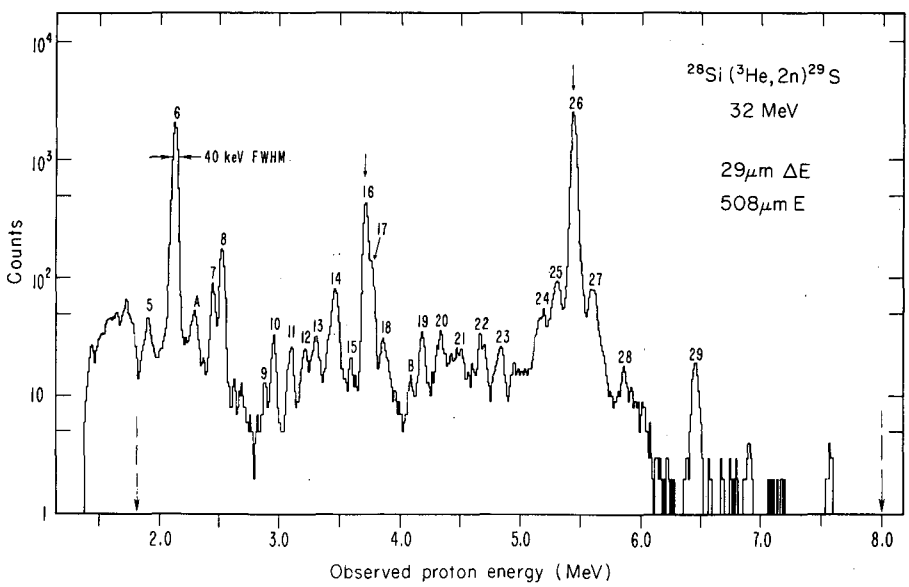


Fig. 1. The proton spectrum observed following the $\beta^+$-decay of $^{29}$S to unbound levels in $^{29}$P. All numbered peaks are identified with the decay of $^{29}$S (Groups A and B arise from contaminants). The dashed vertical arrows indicate the energy region over which protons could be reliably identified. (XBL 7610-4223A)

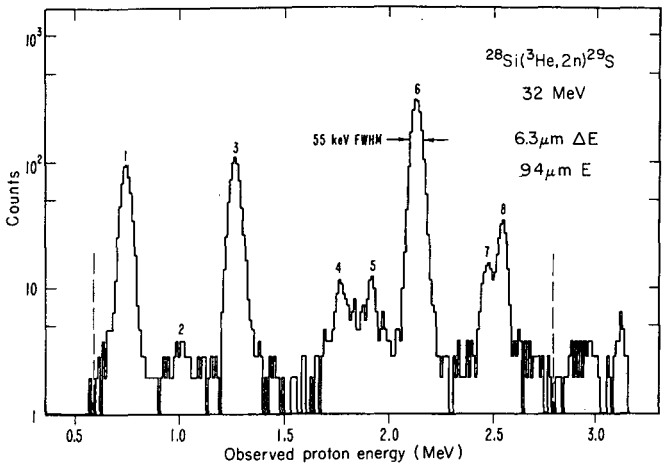


Fig. 2. Delayed protons from $^{29}S$ with energies less than 2.8 MeV. As in Fig. 1, the dashed vertical arrows indicate the energy region over which protons could be reliably identified. (XBL 7610-4224)

proton group of $^{25}Si$(ref. 3); the relative intensity of this group was observed to vary widely from target to target, which is consistent with its arising from the ($^{3}He$,2n) reaction on a small magnesium contamination (< 0.2%) in some of the silicon targets.

The center-of-mass energies for each observed proton group are listed in Table 1 together with their respective assignments to specific levels in $^{29}P$. Since states above 4.5 MeV in excitation energy can proton decay to either the ground state or first excited state of $^{28}Si$, these assignments have been made insofar as possible through correspondence to known levels of $^{29}P$. The ground state spin and parity of $^{29}S$ are assumed to be $5/2^+$ in agreement with $J^\pi = 5/2^+$ ground state[8] of its mirror, $^{29}Al$. Therefore allowed β-decay of $^{29}S$ would populate levels in $^{29}P$ which have spins and parities of $3/2^+$, $5/2^+$, or $7/2^+$.

Proton groups 12, 17, and 19 have been tentatively assigned to three previously unobserved states in $^{29}P$ through comparison with known[8]

Table 1. Observed proton energies from the decay of unbound levels in $^{29}P$ (fed by the $\beta^+$ decay of $^{29}S$ to various final states in $^{28}Si$, and a comparison of deduced level energies in $^{29}P$ with previous results. All entries are given in the c.m. system as MeV ± keV and are preceded by their peak number given in Fig. 1 and 2. Those spaces marked by ... represent proton groups predicted to be outside our range of observation, while those marked by X correspond to groups which could be detected, but which were not observed. Peaks in parentheses are assignments of new energy levels in $^{29}P$ deduced from the present work.

| Proton energies corresponding to decay to the following $^{28}Si$ states: | | | | | | Deduced excitation energies in $^{29}P$ | | |
|---|---|---|---|---|---|---|---|---|
| | g.s. | | 1.779 | | 4.618 | Present work[a] | Previous work[a] E,$J^\pi$ | Ref. | Average excitation energy |
| 6 | 2.2059[b] | | ... | | | - | 4.9541±0.5,$5/2^+$ | 4 | 4.9541±0.5 |
| 7 | 2.5448[b] | 1 | 0.7659[b] | | | - | 5.2930±0.5,7/2 | 4 | 5.2930±0.5 |
| 10 | 3.067±15 | 3 | 1.302±10 | | | 5.825±8 | 5.826±5 | 5 | 5.826±4 |
| 11 | 3.212±15 | | X | | | 5.960±15 | 5.967±3,$3/2^+$ | 6,7,8 | 5.967±3 |
| 12 | 3.326±15 | | X | | | (6.074±15) | [6.108,($3/2^+$,5/2)][c] | 8,9 | (6.074±15) |
| 14 | 3.579±15 | | X | | | 6.328±15 | 6.330±4,$3/2^+$ | 6,7,8 | 6.330±4 |
| | X | 4 | 1.829±15 | | | (6.356±15) | - | | (6.356±15) |
| | X | 5 | 1.978±15 | | | 6.505±15 | (6.49) | 8 | 6.505±15 |
| 17 | 3.905±15 | | X | | | (6.653±15) | [6.711,($3/2^+$,$5/2^+$)][c] | 8,9 | (6.653±15) |
| 19 | 4.335±20 | | X | | | (7.083±20) | [7.069,($3/2^+$,7/2)][c] | 8,9 | (7.083±20) |
| | | 8 | 2.621±10 | | | (7.148±10) | - | | (7.148±10) |
| 20 | 4.493±20 | | X | | | 7.241±20 | 7.25 | 8 | 7.241±20 |
| 21 | 4.640±25 | | X | | ... | 7.388±25 | 7.362±10 | 8 | 7.366±9 |
| | X | 9 | 2.986±15 | | ... | 7.513±15 | 7.527±5,($\leq 5/2^+$,$1/2^-$) | 6,7,8 | 7.526±5 |
| 23 | 5.008±20 | | X | | ... | 7.756±20 | 7.759±5,($3/2^+$) | 6,7,8 | 7.759±5 |
| 24 | 5.359±15 | | X | | X | 8.107±15 | 8.105±11,$5/2^+$ | 8 | 8.106±9 |
| 25 | 5.493±15 | 15 | 3.715±15 | | X | 8.242±11 | 8.221±11,($3/2^+$,$5/2^+$) | 8 | 8.231±11[d] |
| 26 | 5.6324[b] | 16 | 3.8535[b] | 2 | 1.042±25 | - | 8.3806±2.1,$5/2^+$,T=3/2 | 8,10 | 8.3806±2.1 |
| 27 | 5.784±20 | 18 | 4.008±20 | | X | 8.534±14 | 8.530±11,($3/2^+$,$5/2^+$) | 8 | 8.532±9 |
| 28 | 6.062±30 | | X | | X | 8.810±30 | 8.781±15 | 8 | 8.787±13 |
| 29 | 6.676±30 | 22 | 4.852±20 | | X | 9.392±21[d] | 9.389±15,($\leq 5/2^+$) | 8 | 9.390±12 |
| ... | Unassigned proton peak : ..... | | | | | | | | |
| | 13 | 3.414±15 | | | | | g.s. - 6.162±15<br>1x - 7.941±15 | | |

a) Excitation energies have been calculated from the present work or recalculated from previous works using a proton separation energy of 2.7482±0.0008 MeV[4].

b) These proton energies were used, in part, to determine the energy calibration.

c) Levels at this energy are known in the nucleus $^{29}Si$, mirror of $^{29}P$.

d) These errors have been increased by a scaling factor $S = [\chi^2/(n-1)]^{1/2}$.

levels of the appropriate spin and parity in the mirror nucleus in $^{29}$Si (see Table 1). Since there currently is level to level agreement between mirror states of $^{29}$P and $^{29}$Si up to an excitation energy of 5.5 MeV, the possibility of additional levels in this energy region is unlikely. With this noted, tentative assignment of groups 4 and 8 to states which predominately decay to the first excited state of $^{28}$Si rather than its ground state have been made. Group 13 has been left unassigned due to the lack of supplementary information needed to determine which final state in $^{28}$Si was populated. Though this group was not assigned a parent state in $^{29}$P, its intensity is included in subsequent branching-ratio determinations.

Of particular interest is the proton decay of the lowest T = 3/2 state in $^{29}$P at 8.380 MeV, the analog state of the ground state of $^{29}$S, which has been previously studied in isospin-forbidden proton resonance and γ-decay studies[8]. Strongly fed by superallowed $\beta^+$-decay, proton groups 26, 16, and 2 are attributed to break up at this state to the ground, first, and second excited states of $^{28}$Si, respectively.

Absolute branching ratios and log ft values for $\beta^+$-decay to unbound levels in $^{29}$P have been determined from the observed proton intensities, utilizing in addition the β-transition strength to the analog state. Assuming complete isospin purity the log ft for this superallowed branch is 3.29, as calculated in recent shell model calculations[11]. The resulting branching ratios are shown in the decay scheme displayed in Fig. 3.

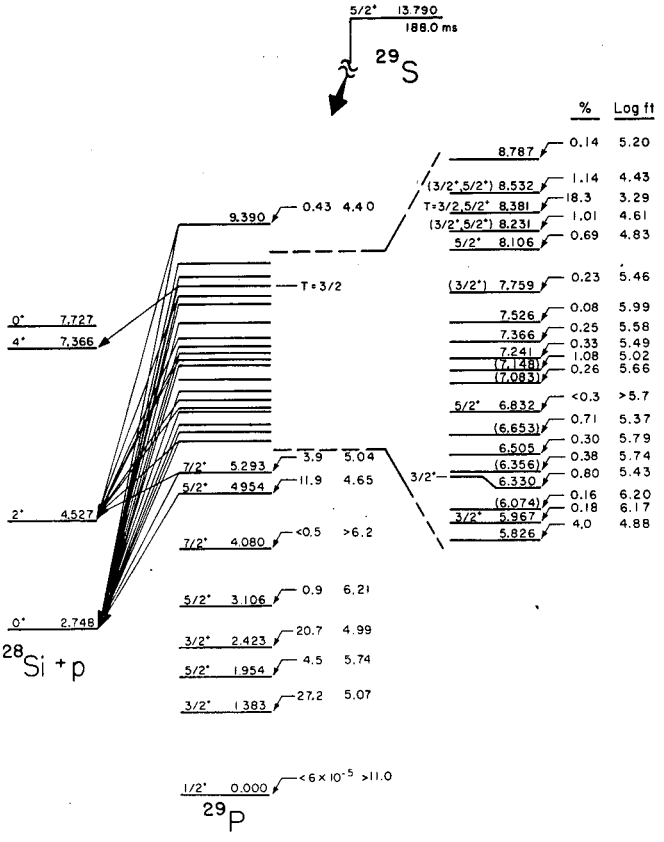


Fig. 3 Proposed decay scheme for $^{29}$S.
(XBL 778-1674A)

Branching ratios to the proton bound levels were calculated from the known mirror $^{29}$Al $\beta^-$ $^{29}$Si* log ft values[8] which were renormalized to account for the missing strength. This renormalization turned out to be small, $ft^+/ft^- = 1.04 \pm 0.07$, indicating good mirror symmetry between $\beta^+$ and $\beta^-$ decay transition rates.

The log ft values are shown in Fig. 4 in comparison to the shell model predictions of Chung and Wildenthal.[11] Good agreement between experiment and theory is observed for levels up to 6 MeV, above which no attempt has been made to correlate levels due to the rapid increase in level density and the lack of spin and parity information.

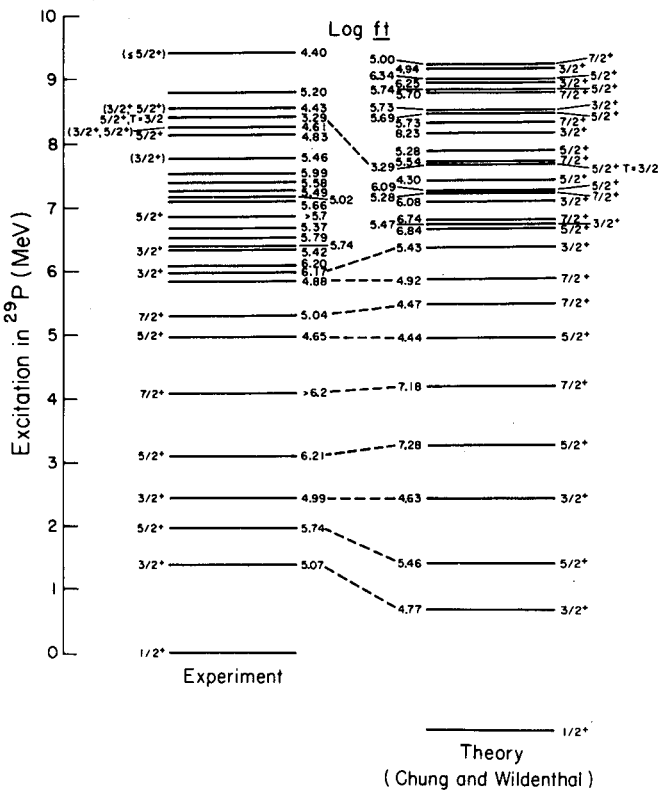


Fig. 4. Experimental and theoretical excitation energies $J^\pi$ and log ft values for states in $^{29}$P fed by allowed β+ decay of $^{29}$S. The theoretical energies have been normalized at the 4.954 MeV state.
(XBL 778-1675)

## Footnote and References

†Condensed from LBL 6556; submitted to Phys. Rev. C.

1. J. C. Hardy and R. I. Verrall, Phys. Lett. 13, 148 (1964); R. I. Verrall, McGill University, Ph.D. Thesis (1968), unpublished.

2. R. W. Fink, T. H. Braid, and A. M. Freidman, Ark. Fys. 36, 471 (1967).

3. R. G. Sextro, LBL-2360, Ph.D. Thesis (1973) unpublished.

4. T. Bryski, F. A. Beck, P. Englestein, M. Forterre, and A. Knipper, Nucl. Phys. A 223, 125 (1974).

5. N. A. Detorie, J. D. Goss, A. A. Rolefson, and C. P. Browne, Phys. Rev. C 10, 991 (1974).

6. N. Tsonpas, H. J. Hansman, N. L. Gearhart, and G. H. Terry, Phys. Rev. C 13, 510 (1976).

7. N. L. Gearhart, H. J. Ansman, J. F. Morgan, G. A. Norton, and N. Tsonpas, Phys. Rev. C 10, 1739 (1974).

8. P. M. Endt and C. Van der Leun, Nucl. Phys. A 214, 227 (1973); Nucl. Phys. A 105, 161 (1967), and references therein.

9. D. A. Vigars, P. A. Butler, P. E. Carr, L. L. Gadeken, L. L. Green, A. N. James, P. J. Nolan, and J. F. Sharpey-Schafer, J. Phys. A 7, 360 (1974).

10. R. A. Gough, R. G. Sextro, and J. Cerny, Phys. Lett. 43B 33 (1973), and references therein.

11. W. Chung and B. H. Wildenthal, private communication.

## COLLECTIVE EXCITATIONS IN $^{129,131}$Ce†

J. Gizon,* A. Gizon,* R. M. Diamond, and F. S. Stephens

The high-spin level structures of $^{129,131}$Ce have been studied in the reactions $^{116,118}$Sn($^{16}$O,3n) by means of in-beam γ-ray spectroscopy. The experiments were carried out at the Berkeley 88-in. and the Grenoble cyclotrons.

Two strongly populated band structures are observed, as shown in Fig. 1. The odd-parity levels constitute a system which has already been seen[1] in $^{133,135}$Ce and is explained, in the triaxial-rotor-plus-particle model,[2] as the result of the coupling of an $h_{11/2}$ neutron-hole to the triaxial core.

Besides the $h_{11/2}$ hole-system, another group of levels appears in the Ce nuclei with N < 73. The spin and parity of its basic state have not been directly determined in the Ce nuclei but, by analogy with $^{129}$Ba (N = 73) where they have been deduced from polarization measurements of γ rays,[3] we assign it as a $I^{\pi} = 7/2^+$ state. This band structure corresponds to collective excitations associated with a neutron hole in the $g_{7/2}$ shell, and is compared in the figure for the N = 71 and 73 Ba and Ce isotones.

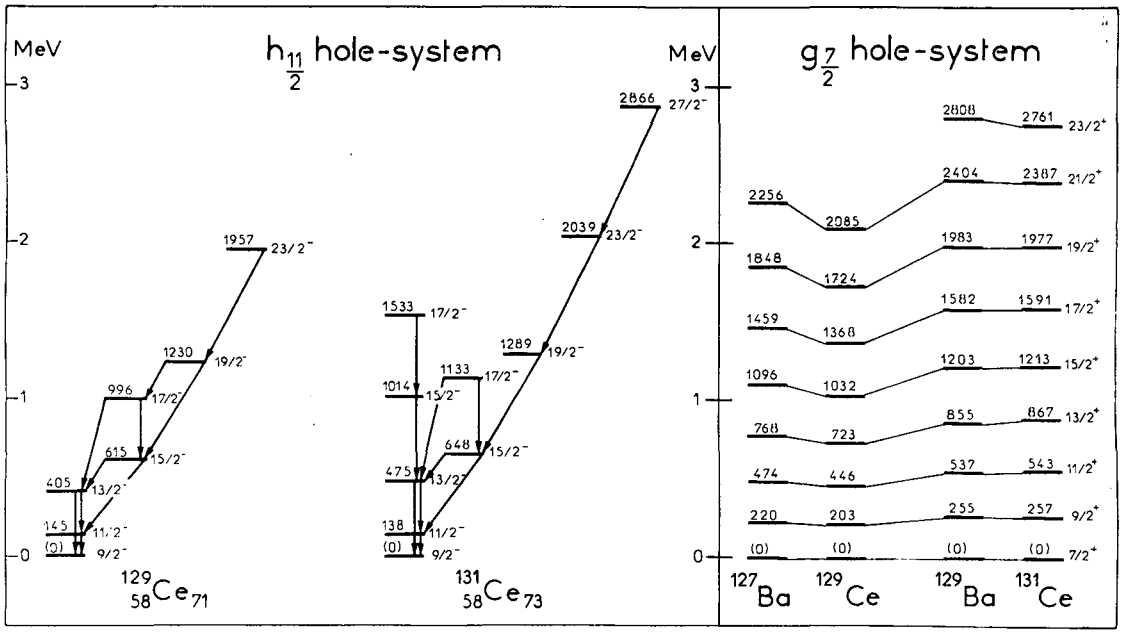


Fig. 1. The $h_{11/2}$ hole-system in $^{129,131}$Ce and comparison of the $g_{7/2}$ hole-system for N=71 and 73 Ba and Ce isotones. (XBL 778-1620)

Footnotes and References

†Condensed from report submitted to Nucl. Phys.

*Institut des Sciences Nucléaires, Grenoble, France

1. J. Gizon, A. Gizon, M. R. Maier, R. M. Diamond and F. S. Stephens, Nucl. Phys. A 222, 557 (1974).
2. J. Meyer-ter-Vehn, Nucl. Phys. A 249, 111 and 141 (1975).
3. Y. K. Lee, D. Elliott, A. Gizon and J. Gizon, to be published.


# DIFFERENT STRUCTURE COLLECTIVE BANDS IN THE N=87 NUCLEI $^{149}$Sm, $^{151}$Gd, and $^{153}$Dy†


P. Kleinheinz,* A. M. Stefanini,‡ M. R. Maier,§
R. K. Sheline, ‖ R. M. Diamond, F. S. Stephens


The $(\alpha,3n\gamma)$ reaction was used to study the N=87 isotones $^{149}$Sm, $^{151}$Gd, and $^{153}$Dy with 35 to 45 MeV alpha beams. The measurements included $\gamma$-ray singles excitation function, angular distribution, and linear polarization studies as well as $\gamma\gamma$-coincidence measurements. The high-spin level patterns are remarkably similar for the three isotones and are shown in Figs. 1,2, and 3. The predominant $\gamma$-decay proceeds via E2 transitions through several parallel $\Delta I = 2$ bands associated with the $i_{13/2}$, $h_{9/2}$ and $f_{7/2}$ intrinsic configurations. Also observed in each nucleus is a weakly populated $\Delta I = 1$ band, dominated by M1 radiation, built upon the $h_{11/2}$ intrinsic state. From the observed band structures we conclude that the $h_{11/2}$ configurations are strongly deformed, in contrast to the other intrinsic configurations.

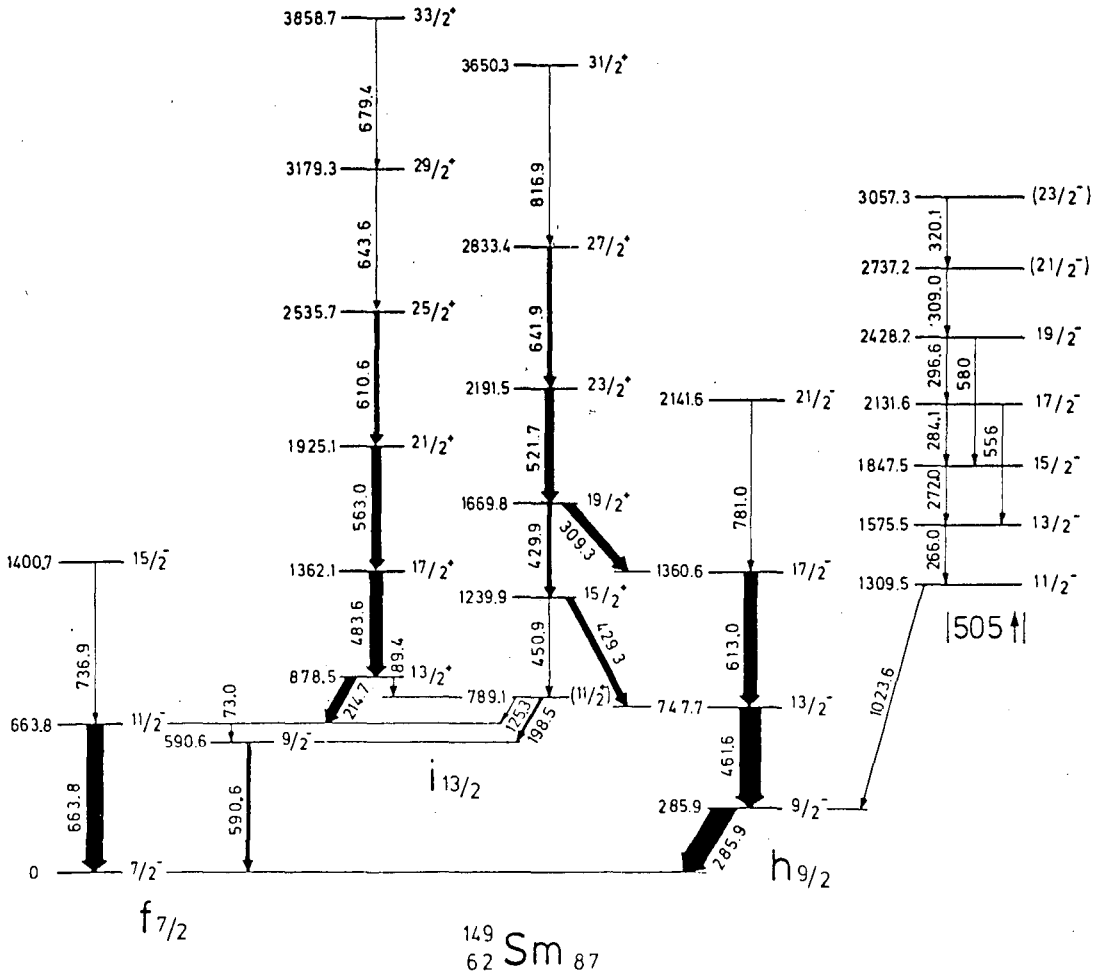


Fig. 1. Level scheme of $^{149}$Sm established from the present experiments. The widths of the arrows indicate $\gamma$-intensities. Transitions connecting different intrinsic configurations are shown slanted. (XBL 778-1621)

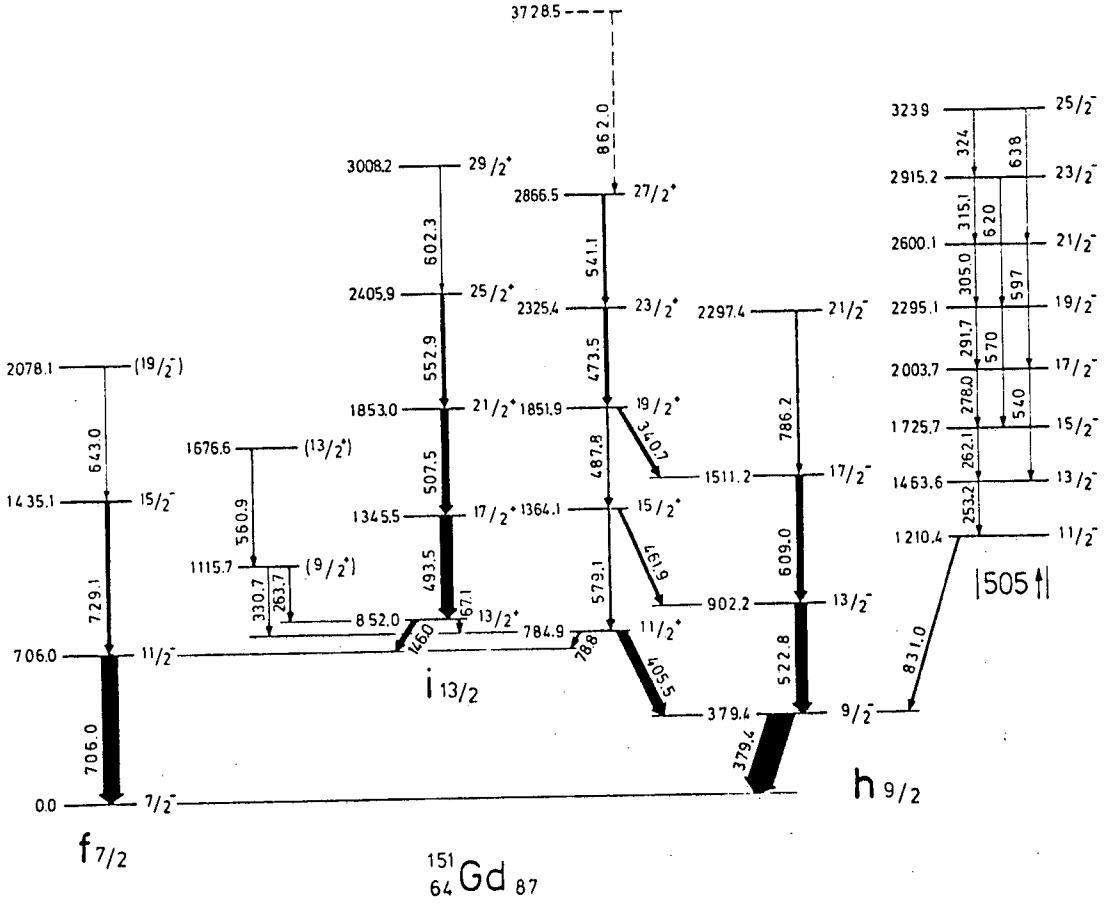


Fig. 2. Level scheme of $^{151}$Gd (cf. caption to Fig. 1). (XBL 778-1622)

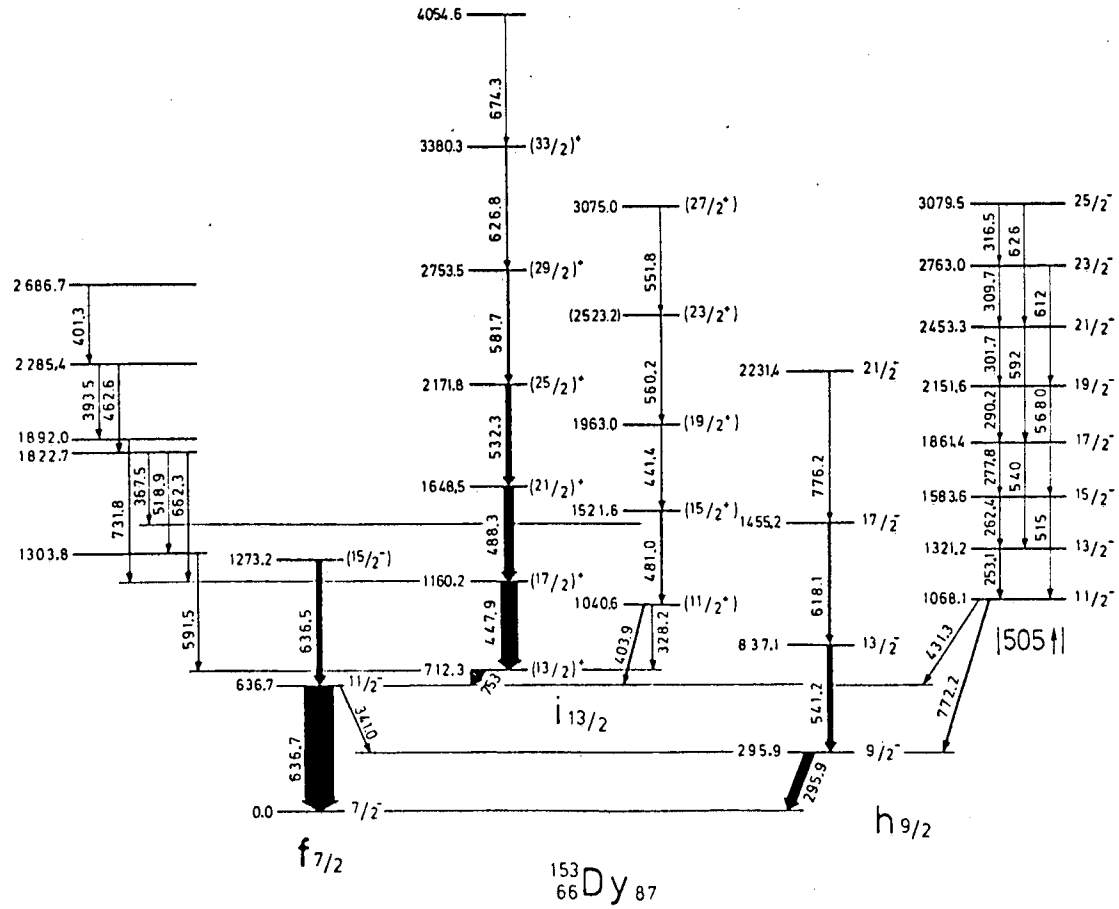


Fig. 3. Level scheme of $^{153}$Dy (cf. caption to Fig. 1). (XBL 778-1623)

Our present interpretation of the $i_{13/2}$ band structure is basically the same as the one previously[1] given for $^{151}$Gd except that the introduction of shape asymmetry required by the associated $11/2^+$ bands results in slightly larger deformation. However the $|505\uparrow|$ bands which now are identified in three isotones are considerably more deformed and therefore constitute strong evidence for shape co-existence in the N=87 nuclei.

The large deformation of the $11/2^-$ $|505\uparrow|$ excitations in the N=87 isotones can be understood by inspection of the Nilsson diagram in the region around N=82 shown in Fig. 4. The orbitals immediately above N=82 generally slope downwards and thus favor deformation whereas occupation of the $|505\uparrow|$ orbital with its strong upward slope will favor a spherical nuclear equilibrium shape. In their ground states the N=87 nuclei have two pairs and the odd neutron occupying the downsloping orbitals above N=82. Promotion of the odd neutron from the ground state orbital into a $i_{13/2}$ orbital represents a promotion from a moderately downsloping orbital to a similar downsloping orbital. Such a change in occupation should leave the nuclear deformation relatively unaffected.

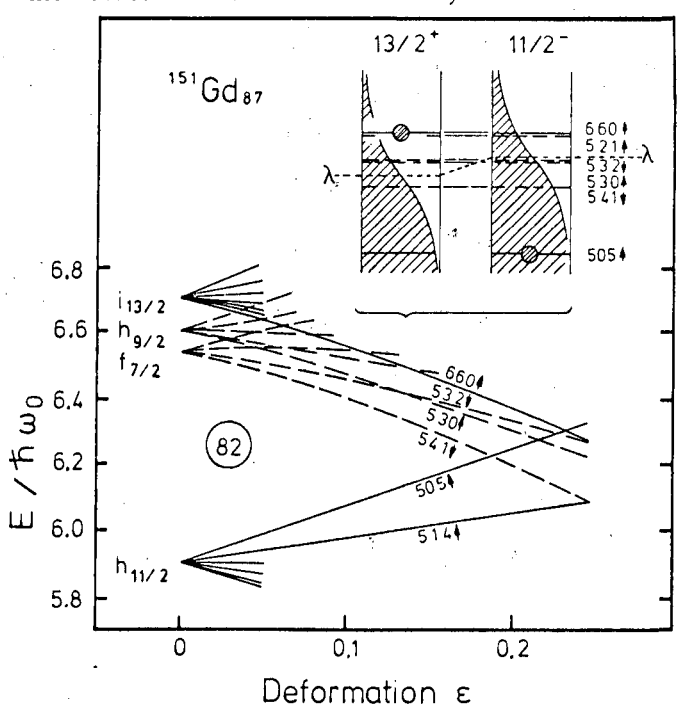


Fig. 4. Nilsson diagram for the N=82 region. The inserts present the $i_{13/2}$ and $h_{11/2}$ intrinsic configurations at small deformation. The pertinent Fermi energies and occupation probabilities for N=86 and N=88, respectively, are also shown.
(XBL 778-1624)

In the $11/2^-$ configuration, however, a neutron has been lifted above the N=82 gap. The nucleus now has three pairs in the downsloping orbitals, and the $|505\uparrow|$ orbital has become 50% unoccupied. Both consequences of this rearrangement produce a strong tendency towards deformation.

The considerable difference in ground state deformation of even-even nuclei observed as one goes from 88 to 90 neutrons was first theoretically interpreted by Mottelson and Nilsson[2] as a consequence of the similar rearrangement of a pair of neutrons from the $|505\uparrow|$ orbital to the downsloping orbitals above the 82 shell. One might speculate that the excited deformed $0^+$ states in the N=88 and 86 even nuclei observed in (p,t) studies[3,4] similarly involve the removal of a $|505\uparrow|$ neutron pair. However, this mechanism is complicated in the even nuclei by the pairing correlations which smear out the occupation probabilities. This uncertainty is removed in an odd-A nucleus, where the presence of an odd particle unambiguously determines a 50% occupation probability. Thus, whereas it is difficult to specify the configuration of the deformed $0^+$ states in the even-even nuclei, the connection of a specific orbital to the deformed shapes is clear in odd-A nuclei like the N=87 isotones.

## Footnotes and References

†Condensed from report submitted to Nuclear Physics.

*Permanent address: Institut für Kernphysik, KFA Jülich, D-5170 Jülich, F. R.-Germany; also supported by Florida State University.

‡Permanent address: Laboratori Nazionali di Legnaro, INFN and Istituto di Fisica dell' Università, I-35100 Padova, Italy.

§Permanent address: Physik-Department E12 der Technischen Universität München, D-8046 Garching, F.R.-Germany.

||Permanent address: Florida State University, Tallahassee, FL 32306.

1. P. Kleinheinz, R. K. Sheline, M. R. Maier, R-M. Diamond, and F. S. Stephens, Phys. Rev. Lett. 32, 68 (1974).

2. B. R. Mottelson and S. G. Nilsson, Phys. Rev. 99, 1615 (1955).

3. P. Debenham and N. M. Hintz, Nucl. Phys. A 195, 385 (1972).

4. D. G. Fleming, C. Günther, G. Hagemann, B. Herskind and P. O. Tjom, Phys. Rev. C 8, 806 (1973).

# COULOMB EXCITATION INTO THE BACKBEND REGION OF $^{164}$Er†

I. Y. Lee, D. Cline,* R. S. Simon,‡ P. A. Butler,§ P. Colombani,‖
M. W. Guidry, F. S. Stephens, R. M. Diamond, N. R. Johnson¶ and E. Eicler¶

Present experimental evidence[1,2] suggests that backbending is caused by the intersection of the ground-state rotational band with a second rotational band possessing an appreciably larger moment of inertia. Two possibilities have emerged for the most likely nature of this second band. The Coriolis antipairing[3] model considers it to be a band for which the pairing has collapsed while the rotation-alignment[4] model attributes the band to two quasi-particles which are aligned with the rotating core by the Coriolis force. Observation of additional levels and a determination of the interaction matrix elements between the intersecting bands can shed considerable light on the structure of the bands.

Previously, backbending has been studied exclusively using (HI,xn) reactions to populate highly excited high-spin states which subsequently de-exite by γ-ray cascades into the yrast sequence of states. In contrast, multiple Coulomb excitation specifically excites those collective bands which are strongly coupled to the ground state and thus is a complementary probe of the backbending phenomenon. In addition, Coulomb excitation can be used to study neutron-rich nuclei which cannot be reached by (HI,xn) reactions. The present paper describes the first case where states through a reasonably sharp backbend region have been Coulomb excited.

Beams of 612 MeV and 547 MeV $^{136}$Xe ions from the LBL SuperHILAC were used to bombard a 1.34 mg/cm$^2$ self-supporting metallic foil of $^{164}$Er. The isotopic enrichment was 73.6%. Three silicon detectors were used to detect scattered Xe ions at angles of 65°, 77° and 90° in coincidence with de-excitation γ-rays observed in a Ge(Li) detector located at -30° to the incident beam. The Ge(Li) detector was placed in the average recoil direction where the Doppler shift is a maximum 8% and the Doppler broadening is a minimum. A γ-ray energy resolution of ≤1% (FWHM) was achieved. Four 7.6 cm by 7.6 cm NaI detectors, serving as a multiplicity filter, were placed around the target. The number of NaI detectors in coincidence was used to determine the multiplicity of each γ-ray transition observed in the Ge(Li) spectrum in coincidence with the scattered ions. The dependence of the γ-ray yields on the multiplicity distribution, on the bombarding energy and on the projectile scattering angle provided three independent measures of the location of each de-excitation gamma transition in the nuclear decay scheme. A γ-ray spectrum is shown in the upper section of Fig. 1.

The $^{164}$Dy(α,4n) $^{164}$Er reaction was studied, in addition to the Coulomb excitation, to search for weak γ-gamma branching at the backbend. Two 50 cm$^3$ coaxial Ge(Li) detectors, with energy resolution of 2.3 keV FWHM at 1.1 MeV, were used and both singles and coincident γ-ray spectra were

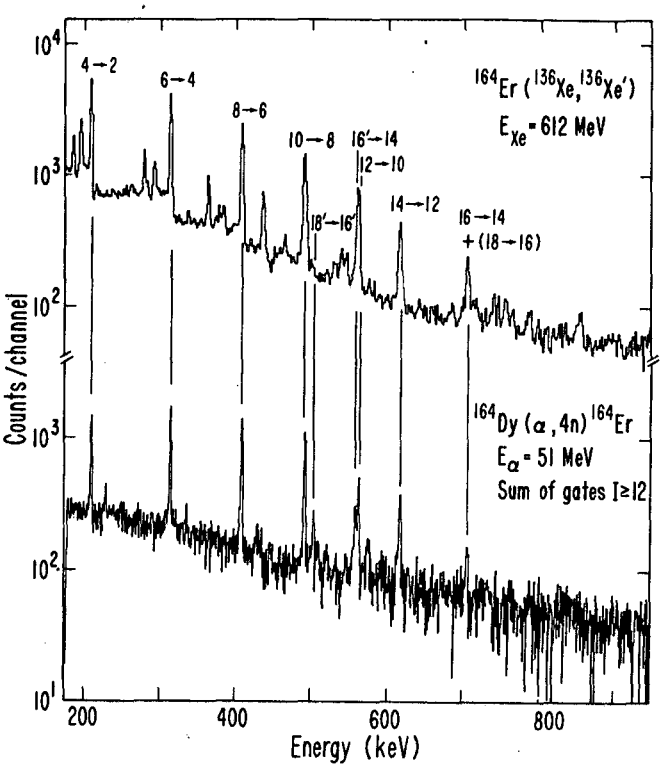


Fig. 1. Coincidence γ-ray spectra for $^{164}$Er. The upper spectrum is for the excitation of $^{164}$Er by $^{136}$Xe. The lower spectrum is for the sum of the coincidence spectra gated by the transitions from states with spin ≥12 fed by the $^{164}$Dy(α,4n) reaction. (XBL 763-2513A)

accumulated. The lower part of Fig. 1 shows the coincidence spectrum gated by transitions originating from states with I ≥ 12.

The decay scheme derived from the present work is shown in Fig. 2, and a conventional backbending plot of these results is shown in Fig. 3. The B(E2) values at the band intersection are sensitive to the band mixing. The Coulomb excitation and branching ratio data suggest band mixing corresponding to a 38 keV interaction strength at the intersection. The unperturbed ground band $14^+$ and $16^+$ state fall on an extension of the line through the lower spin states on a backbending plot, as indicated by the dashed line in Fig. 3, provided that the interaction matrix elements are taken to be 38 keV. The ground-band B(E2) values derived from the Coulomb excitation yields obey the rigid-rotor relation to ± 25% which is consistent with the above interaction strength. The γ-ray branching ratio at the backbend has been measured[5,6] in two other nuclei, the N=90 isotones $^{154}$Gd and $^{156}$Dy. A similar analysis

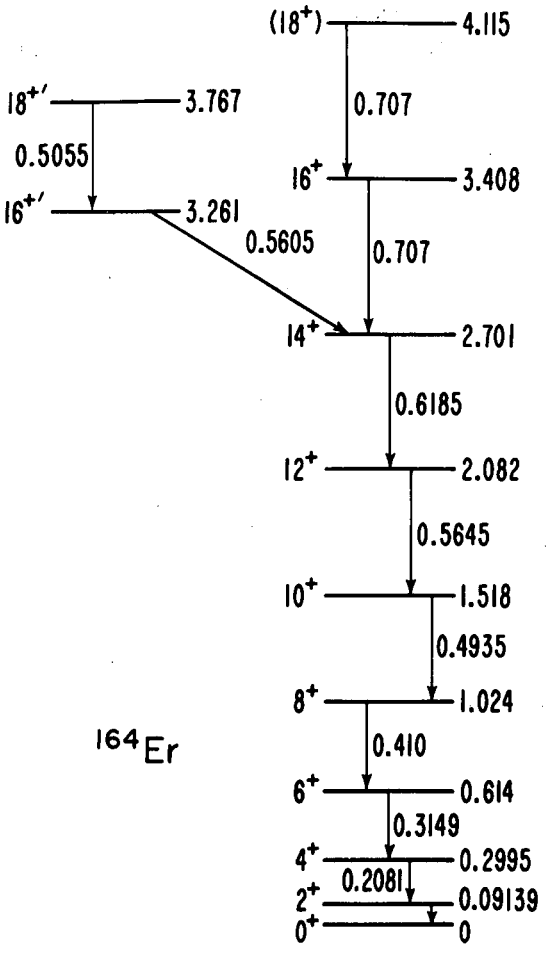


Fig. 2. Level scheme of $^{164}$Er. (XBL 763-2514A)

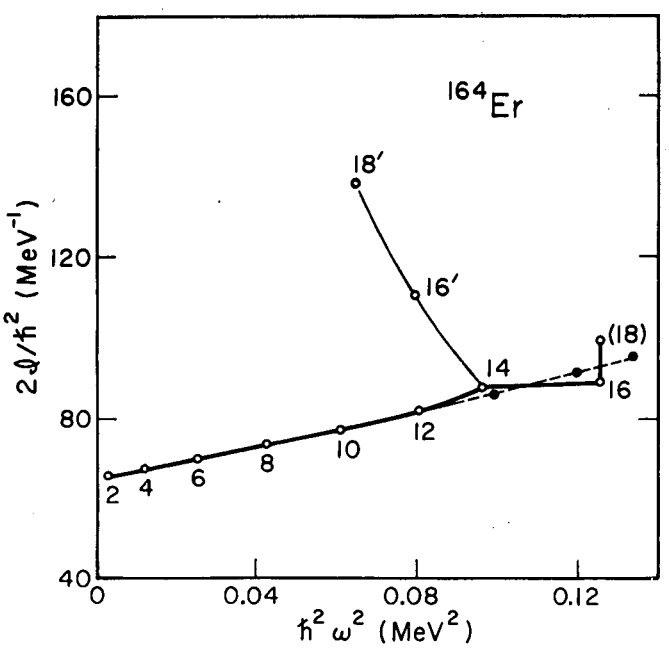


Fig. 3. Plot of the moment of inertia vs the square of the angular velocity for $^{164}$Er. The dashed line calculates a smooth extrapolation of the line through the lower spin states. (XBL 763-2515A)

gives an average interaction matrix element for the $16^+$ and $18^+$ states of 23.5±1.5 keV in $^{154}$Gd and 8.5±1.5 keV for the $16^+$ state in $^{156}$Dy.

Band interaction matrix elements of less than 40 keV at the backbend are remarkably small, i.e., they are nearly two orders of magnitude smaller than might be expected for Coriolis matrix elements at these spins. However, this behavior can be understood in the rotation-alignment model. Two calculations within this model[4,7] suggest that the interaction is $\leq$ 140 keV and is nearly constant for $10 < I < 22$.

This first example of Coulomb excitation through a known backbend illustrates the power of this technique which can be used on many nuclei that cannot be excited by (HI,xn) reactions. The ground-band B(E2) values have been measured in $^{164}$Er and follow the rigid-rotor relation to within ±25% throughout the backbend. The band intersecting the ground band in $^{164}$Er is closely similar to the bands seen in $^{154}$Ge and $^{156}$Dy which shows that this type of behavior is not peculiar to the 90 neutron region. The B(E2) data and the level energies in all three nuclei are consistent with a two-band mixing model having a remarkably weak interaction strength at the backbend, i.e., <40 keV. This behavior is reasonably well described by the rotation-alignment model.

## Footnotes and References

†Condensed from Phys. Rev. Lett. 37, 4 (1976).

*Partially supported by NSF. Permanent address: Nuclear Structure Research Laboratory, University of Rochester, Rochester, NY 14627.

‡On leave from Sektion Physik der Ludwig-Maximilians-Universität München, 8046 Garching, Germany; sponsored by the Bundesministerium für Forschung und Technologie.

§U.K.S.R.C./N.A.T.O. fellow.

‖Permanent address: Institut de Physique Nucléaire, 91406 Orsay, France.

¶Oak Ridge National Laboratory, Oak Ridge, TN.

1. R. A. Sorensen, Rev. Mod. Phys. 45, 353 (1973).

2. F. S. Stephens, Rev. Mod. Phys. 47, 43 (1975).

3. B. R. Mottelson and J. G. Valatin, Phys. Rev. Lett. 5, 511 (1960).

4. F. S. Stephens and R. S. Simon, Nucl. Phys. A 183, 257 (1972).

5. T. L. Khoo, F. M. Bernthal, J. S. Boyno, and R. A. Warner, Phys. Rev. Lett. 31, 1146 (1973).

6. H. R. Andrews, D. Ward, R. L. Graham, and J. S. Geiger, Nucl. Phys. A 217, 141 (1974).

7. C. Flaum and D. Cline, Proc. of the Symp. on High Spin States, Jülich 1975, Phys. Rev. C 14, 1224 (1976).

# DETERMINATION OF γ-SOFTNESS IN $^{192,194,196}$Pt FROM COULOMB EXCITATION WITH $^{136}$Xe PROJECTILES*

I. Y. Lee, D. Cline,† P. A. Butler, R. M. Diamond,
J. O. Newton,‡ R. S. Simon,§ and F. S. Stephens

The collective properties of nuclei in the Os, Pt and Hg region have been the subject of many recent experimental and theoretical studies. These nuclei are in the shape transitional region between the well-deformed rare earth nuclei and the double closed-shell $^{208}$Pb, and several different collective models have been used to account for the properties of their lowest-lying states. These models range from the triaxially deformed rigid rotor,[1] through various rotation-vibration models about triaxial or axial shapes to the γ-unstable (shape-unstable) model.[2] Collective model calculations with the complete Bohr Hamiltonian within the pairing plus quadrupole model predict a prolate to oblate shape transition in the Os-Pt region.[3] In addition, they predict shallow deformation potentials, especially soft to γ-vibrations.

The experimental evidence for non-axial collective motion in these nuclei is quite convincing.[4-6] Static electric quadrupole moments and energy level spectra strongly suggest that the average nuclear shape undergoes a gradual prolate to oblate shape transition, that is, from $\gamma=20°$ in $^{186}$Os to $\gamma\approx35°$ in $^{198}$Pt. The γ softness of the nuclear shape has not been measured previously. Level energies are rather insensitive to γ-softness whereas E2 matrix elements can be quite sensitive to γ-softness.[7] In particular, E2 transitions within the γ-band, between the ground and γ-bands and to the 0' double gamma vibrational state are sensitive to γ-softness. The goal of the present work was to determine the γ-softness of the Pt nuclei from measurement of these E2 transition strengths by heavy-ion Coulomb excitation.

The Pt isotopes were Coulomb excited using a $^{136}$Xe beam from the SuperHILAC of the Lawrence Berkeley Laboratory. The targets consist of ~1 mg/cm$^2$ self-supporting rolled metallic foils of isotopically enriched $^{192}$Pt(57.3%), $^{194}$Pt(97.4%), and $^{196}$Pt(94.5%). The experimental procedure is identical to that described in the preceding contribution on $^{164}$Er.

Members of both the ground band and gamma band were strongly populated as illustrated in Fig. 1. Since there are two coupled bands excited with comparable strength, a given level can be excited through several paths so that its yield will depend on many E2 matrix elements. This makes it difficult in most cases to extract the individual E2 matrix elements from the present Coulomb excitation data. Therefore we compare in Fig. 2 the experimental yields with the yields calculated using E2 matrix elements given by different collective models. We used matrix elements given by the rigid triaxial model[1] for $\gamma=30°$, the γ-unstable model[2] and two intermediate potentials[8] with holes 2 MeV (soft) and 5 MeV (stiff) deep at $\gamma=30°$. All models predict similar results for the ground band but show large differences for the gamma band and the $0^+$ state. The experimental ground-band yields fall below the calculated yields at high spin due to intersection with known two-quasi-particle bands. The experimental yields for the γ-band are in good agreement only with the rigid triaxial model. The weakness for exciting 0' states also argues rather strongly against γ-soft potentials. Sufficient data are available to determine some individual B(E2) values. These are compared with model predictions in Fig. 3. Overall, it seems clear that these B(E2) values follow the predictions of a rather rigid triaxial-rotor model, though some discrepancies remain.

These first measurements of γ-softness indicate that the $^{192,194,196}$Pt nuclei behave like rather rigid triaxial rotors. Although the

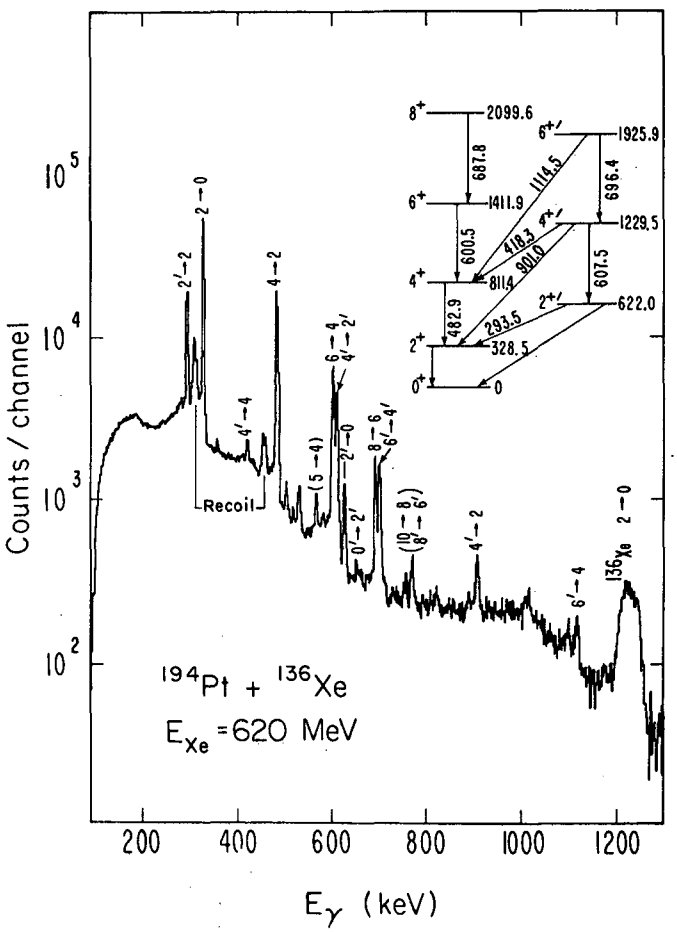


Fig. 1. Coincidence gamma-ray spectrum and partial level scheme for $^{194}$Pt. (XBL 771-154)

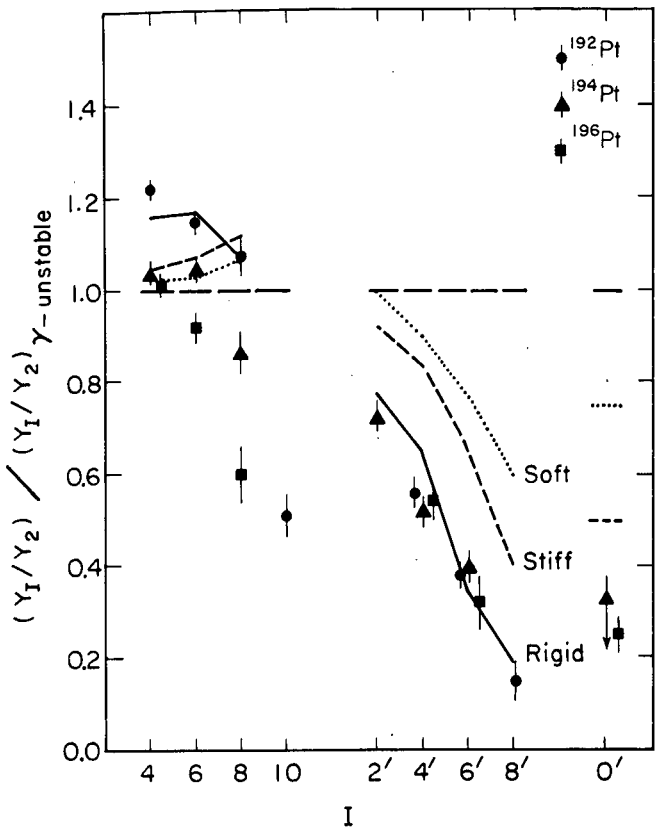


Fig. 2. Experimental and calculated relative yields for Pt isotopes. The yields are normalized to that of the $2^+$ state in order to eliminate the need for the absolute yields. The ratio to the calculated yield of the γ-unstable model is made to enable us to put the results for the different nuclei on the same graph. (XBL 776-1113)

analysis of the yields in Fig. 2 is model dependent, the few directly extracted B(E2) values shown in Fig. 3 clearly show the same qualitative features. These conclusions contradict current theories which predict γ-soft nuclear potential surfaces. It is not clear whether this disagreement reflects inadequacies in the microscopic calculations of the potential surface and inertial parameters of the Bohr collective Hamiltonian or whether this Hamiltonian gives an incomplete description for the structure of the low-lying states of the Pt nuclei.

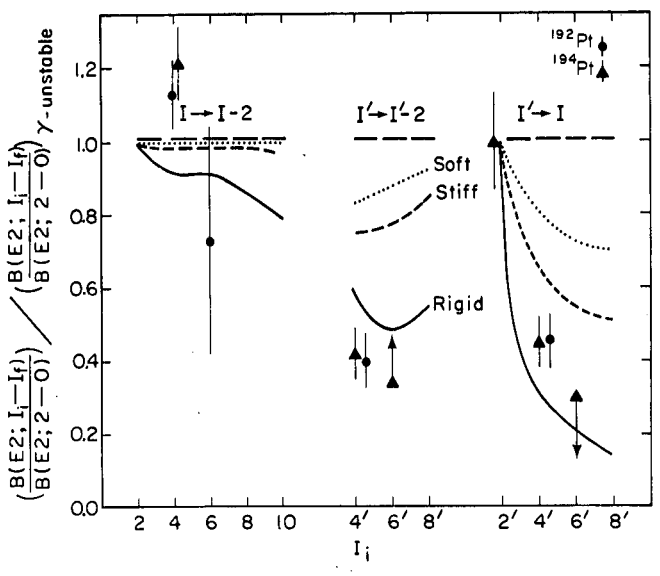


Fig. 3. Experimental and calculated relative B(E2) values (normalized to the calculated values of γ-unstable mode) for Pt isotopes. The experimental values for the ground band I → I - 2 transition are taken from Ref. 9. The E2/M1 mixing ratio for the 4' → 4 transition for $^{194}$Pt is assumed to be large as is measured in $^{192}$Pt. (XBL 776-1112)

## Footnotes and References

*Condensed from Phys. Rev. Lett. 39, 684 (1977).

†Partially supported by the National Science Foundation. Present address: Nuclear Structure Research Laboratory, Univeristy of Rochester, Rochester, NY 14627

‡Present address: The Australian National University, Canberra, A.C.T. 2600 Australia.

§Present address: Gesellschaft für Schwerionenforschung, Darmstadt, Germany.

1. A. S. Davydov and G. F. Filippov, Nucl. Phys. 8, 237 (1958).

2. L. Wilets and M. Jean, Phys. Rev. 102, 778 (1956).

3. K. Kumar and Baranger, Nucl. Phys. A 122, 273 (1968).

4. J. E. Glenn, R. J. Pryor and J. X. Saladin, Phys. Rev. 188, 1905 (1969).

5. S. A. Lane and J. X. Saladin, Phys. Rev. C 6, 613 (1972).

6. P. Russo, D. Cline, J. K. Sprinkle, R. P. Scharenberg and P. B. Vold, Bull. Am. Phys. Soc. II22, 545 (1977).

7. D. Cline, J. Phys. Soc. Japan 34 (1973), Suppl. 377.

8. G. Leander, Nucl. Phys. A 273, 286 (1976) and private communication, 1977.

9. N. R. Johnson, P. P. Hubert, E. Eichler, D. G. Sarantites, J. Urbon, S. W. Yates, and T. Lindblad, Phys. Rev. A 15, 1325 (1977).

# SUBCOULOMB FISSION INDUCED BY Xe AND Kr IONS*

P. Colombani,† P. A. Butler,‡ I. Y. Lee, D. Cline,§
R. M. Diamond, F. S. Stephens, and D. Ward||

Coulomb fission is one possible consequence of the excitation of nuclei by the Coulomb interaction between two very heavy ions. Observation of this phenomenon would be very interesting since it can provide information on the variation of the collective potential energy surface as a function of deformation up to the saddle point.

Most theoretical calculations[1-4] assume E2 excitation of low-lying β vibrational states, and indicate that Coulomb fission is likely to occur only when heavy projectiles (e.g., Xe) interact with easily fissionable targets. Predicted values of fission cross sections near the Coulomb barrier for Xe + U range from 0.1 to 100 mb/sr for backscattered projectiles. Previous attempts to observe Coulomb fission with Kr and lighter ions have failed.[5-7]

This work gives the results of a study of the fission of $^{238}U$ and $^{232}Th$ by Xe and Kr ions at incident energies close to the Coulomb barrier. At these energies processes acting through the tail of the nuclear force can supply enough excitation energy to induce fission. In order to differentiate Coulomb fission from these processes, we have compared the excitation functions of Xe- and Kr-induced reactions on $^{238}U$ and $^{232}Th$, since for incident energies below the Coulomb barrier the excitation functions are expected to be sensitive to the admixture of Coulomb fission. The Coulomb fission cross section is also expected to depend strongly on the fission barrier, and thus a comparison of these two targets with different barriers (e.g., the barrier height is ≈ 5.8 MeV for $^{238}U$, ≈ 6.0 MeV for $^{232}Th$ may give additional information.[8]

The experimental system was designed so that the two forward correlated fission fragments were detected in coincidence with the backscattered projectile. Assuming asymmetric fission and an isotropic angular distribution of the fragments, the overall fission detection efficiency was ≈ 5% for a Xe + U reaction, ≈8% for Kr + U. In this manner excitation functions were measured for all reactions at energies ranging from 90 to 105% of the Coulomb barrier $E_C$, calculated with an interaction radius $R_C = 1.16\ (A_1^{1/3} + A_2^{1/3} + 2)$ fm. The $^{238}U$ targets were 1.3 mg/cm$^2$ thick on a 0.6 mg/cm$^2$Al backing; the $^{232}Th$ targets were 2 mg/cm$^2$ thick, self-supporting.

Typical energy spectra of events observed in the fission counters, in coincidence with the opposite one and the backscatter detector, are shown on Fig. 1 for the reaction Xe + U at 750 MeV. (For comparison the singles spectrum of the forward scattered Xe ions is shown also in Fig. 1.) The following facts indicate that the observed events are due to fission: (1) the energy spectrum from each fission detector [(Figs. 1(a), (b)] is very broad; (2) the spectrum of the sum

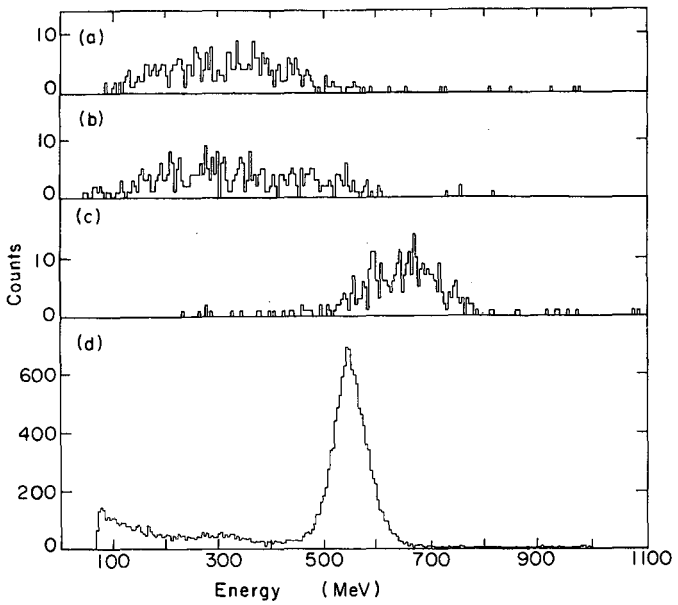


Fig. 1. Energy spectra in the forward fission detectors for the reaction $^{136}Xe + ^{238}U$ at 750 MeV. (a) Spectrum of events in a single detector in coincidence with the opposite detector and the backscatter detector. (b) The corresponding spectrum in the opposite detector. (c) Spectrum of the sum of the fission energies for correlated events. (d) Singles spectra showing the elastic peak from the forward scattered Xe ions. (XBL 767-3088)

of the energies for correlated events [(Fig. 1(c)] is much narrower, and the mean energy is consistent with the total energy expected from the fission of a heavy nucleus like $^{238}U$ after a quasi-elastic collision with a Xe ion; (3) almost all observed triple coincidences were detected in opposite detectors. Such triple coincidences were observed with both projectiles on $^{238}U$ and $^{232}Th$, with the same characteristic features of fission events.

The differential cross sections for the triple events were calculated assuming that the fission angular distribution is $1/\sin\theta$ with respect to the symmetry axis of the collision and assuming a mass asymmetry similar to the one observed for the fission of $^{238}U$ at low excitation energy. Corrections for the target thickness and the beam energy spread were made. The absolute cross sections were estimated by normalizing to the Rutherford scattering observed in the back-scattered detector at the lowest energy for each reaction, and then scaling to higher energies according to the integrated beam current collected during each experiment.

The excitation functions are presented together with the results from measurements on other targets ($^{244}$Pu and $^{248}$Cm) in a subsequent publication.

It is evident from these data that the cross sections obtained are due to fission following an almost elastic collision. These cross sections are of interest since they are at least a factor of five smaller than the most recent theoretical estimate,[4] which predicts $d\sigma/d\Omega$ (180°) ≈ 10 mb/sr for Xe + $^{238}$U at an incident energy of ≈ 670 MeV. The next step would be to prove beyond any doubt that these events do correspond to Coulomb induced fission. This might be done either by measuring the angular distribution of the fission fragments or by identifying the backscattered projectile (e.g., by observing a radiative transition in the projectile following Coulomb excitation). Such experiments are feasible despite the low observed cross sections.

Footnotes and References

*Published in Phys. Lett. 65B, 39 (1976).

†Permanent address: Institut de Physique Nucléaire,

‡UKSRC/NATO fellow.

§Permanent address: Nuclear Structure Research Laboratory, University of Rochester, Rochester, NY 14627. Partially supported by NSF.

‖Permanent address: Chalk River Nuclear Laboratory, Chalk River, Ontario, Canada.


1. E. Guth and L. Wilets, Phys. Rev. Lett. 16, 30 (1966).
2. L. Wilets, E. Guth, and J. S. Tenn, Phys. Rev. 156, 1349 (1967).
3. K. Beyer and A. Winther, Phys. Lett. B 30, 296 (1969).
4. H. Holm and W. Greiner, Nucl. Phys. A 195, 333 (1972).
5. Yu. P. Gangrsky, B. N. Markov, N. Khanh, Yu. Ts. Oganesyan, and P. Z. Khien, JINR Report P7-7022, Dubna, USSR, 1973.
6. C. Ngô, J. Peter, B. Tamain, Nucl. Phys. A 211, 37 (1974).
7. C. E. Bemis, Jr., F. Plasil, R. L. Ferguson, E. E. Gross, and A. Zucker, Phys. Rev. C 10, 1590 (1974).
8. R. Vandenbosch and J. R. Huizenga in Nuclear Fission (Academic Press, NY, 1973), p. 255.


# FISSION OF $^{232}$Th, $^{238}$U, $^{244}$Pu, $^{248}$Cm INDUCED BY Xe AND Kr IONS AT COULOMB BARRIER ENERGIES*


P. A. Butler, I. Y. Lee, J. O. Newton,† Y. El-Masri,‡ M. M. Aleonard,§
P. Colombani,‖ R. M. Diamond, F.S. Stephens, R. W. Lougheed,¶ and E.K. Hulet ¶


We have reported measurements of excitation functions for $^{86}$Kr(Z=36) and $^{136}$Xe(Z=54) induced fission of $^{232}$Th and $^{238}$U which showed that fission of the heavy targets could be induced at incident energies below the Coulomb barrier.[1] These data did not show unambiguously that there was any pure Coulomb fission although there were some positive indications. The present work was undertaken in an attempt to resolve this question.

In order to distinguish Coulomb fission from that caused by nuclear processes, we have studied the dependence of the fission cross sections on projectile Z at incident energies below the Coulomb barrier, where pure Coulomb effects are expected to increase relative to nuclear processes as the energy decreases. We have also studied the dependence of the cross sections on the fission barrier, to which Coulomb induced fission might be expected to be sensitive. In contrast, those nuclear processes which involve excitations comparable to or greater than the fission barrier, would be unlikely to be very sensitive to the barrier. In addition, we have measured angular distributions of the fission fragments. The angular distribution for Coulomb fission should peak at 90° to the beam axis for head-on collisions provided the fission takes place when the projectile is still very near the target. On the other hand, fission following direct nuclear processes, such as transfer reactions or deep-inelastic scattering, is more likely to peak forward and backward along the recoil direction.

In this work we report new measurements on the Kr and Xe induced fission of $^{232}$Th and $^{238}$U (barrier heights 6.0 and 5.8 MeV, respectively,[2] and results for fission of $^{244}$Pu (barrier height 5.4 MeV)[2] and $^{248}$Cm. Beam energies were measured by time-of-flight and, for the Kr runs, independently checked by magnetic analysis; the uncertainty was 0.5%. The rolled 2.0 mg/cm$^2$ $^{232}$Th target was self-supporting: the 0.64 mg/cm$^2$ $^{238}$U was evaporated on 0.5 mg/cm$^2$ Al. The 0.94 mg/cm$^2$ $^{248}$Cm, in the form of $CmF_3$, was evaporated onto a 1.2 mg/cm$^2$ Al backing, and the 0.30 mg/cm$^2$ $^{244}$Pu, in the form $PuO_2$, was electroplated on 1.2 mg/cm$^2$ Ni.

The detection system for the excitation function measurements is identical to that described before[1] and allows detection of coincident fission fragments in four 1.5 × 0.8 cm detectors (each subtending 70° in $\phi$ and about 10° in $\theta$), in (triple) coincidence with the backscattered projectile detected in an annular counter. The average c.m. scattering angle was about 164°.

In order to determine the differential fission cross sections with respect to the backscattered projectile, $d\sigma/d\Omega_p$, which are shown in Fig. 1, we have assumed that the collision is nearly elastic, that the fission fragment mass distribution is asymmetric, and that the fragment angular distribution has the limiting form $d\sigma/d\Omega_f \propto 1/\sin\theta_f$ in the c.m., where $\theta_f$ is measured from the direction of the recoiling heavy nucleus. It was estimated that the overall uncertainty in the measured cross sections from all sources, including the assumptions made, is about 50%. The relative uncertainty between the Kr and Xe excitation functions is better than 35%, whereas for the same projectile the uncertainty between runs at different bombarding energies and on different targets is no more than 20%. This last error is included together with the statistical errors in the values of $d\sigma/d\Omega_p$ shown in Fig. 1.

The fission-fragment angular distribution, $d^2\sigma/d\Omega_p d\Omega_f$, was measured with a single counter with solid angle ~ 0.05 sr, subtending about 5° in $\theta$. By requiring a coincidence with a backscattered particle, only those heavy fissioning nuclei which recoiled at about 10° to the beam axis were selected. The recoil direction was further restricted to ± 45° in $\phi$ by masking the annular backscatter counter. It was thus possible to measure the angular distribution as far forward as $\theta_f = 40°$ (c.m.) without placing the fission counter closer than 20° (lab) to the beam axis. The values of $d^2\sigma/d\Omega_p d\Omega_f$ shown in Fig. 2 include an uncertainty of 20% which is inherent in the estimated relative values of the c.m. solid angle of the fission counter.

The excitation functions for each target shown in Fig. 1 are quite similar, and the variation for different targets is small. The data reported previously have been included in Fig. 1. It is apparent that the Xe cross sections for $^{238}U$, $^{244}Pu$ and $^{248}Cm$ remain ~50% larger than those for Kr. The fission angular distribution measurements are shown in Fig. 2. They indicate $d^2\sigma/d\Omega_p d\Omega_f$ is larger at small $\theta_f$ than at $\theta_f = 90°$,

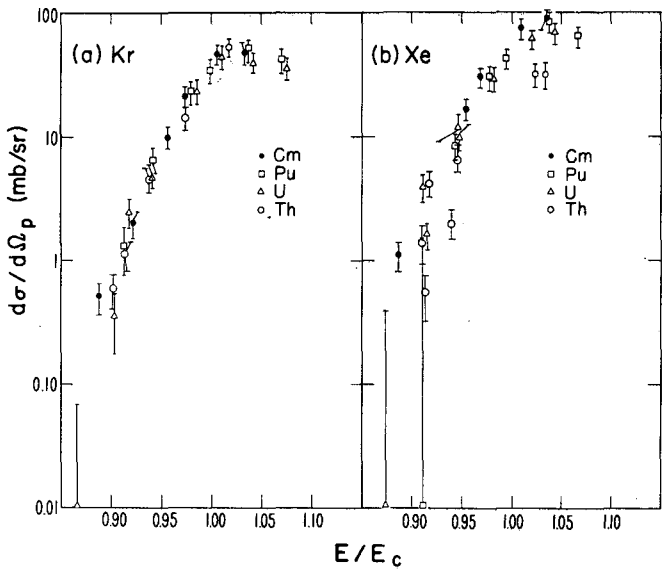


Fig. 1. Differential cross sections with respect to the backscattered projectile $d\sigma/d\Omega_p$ (in c.m.) at $\theta_p = 164°$ (c.m.) for (a) $^{86}Kr$ and (b) $^{136}Xe$ induced fission of $^{232}Th$, $^{238}U$, $^{244}Pu$, $^{248}Cm$ as a function of bombarding energy. The incident energy E is expressed as a fraction of the Coulomb barrier $E_c$ evaluated using an interaction radius $R = 1.16 (A_1^{1/3} + A_2^{1/3} + 2)$ fm. (XBL 7612-11145A)

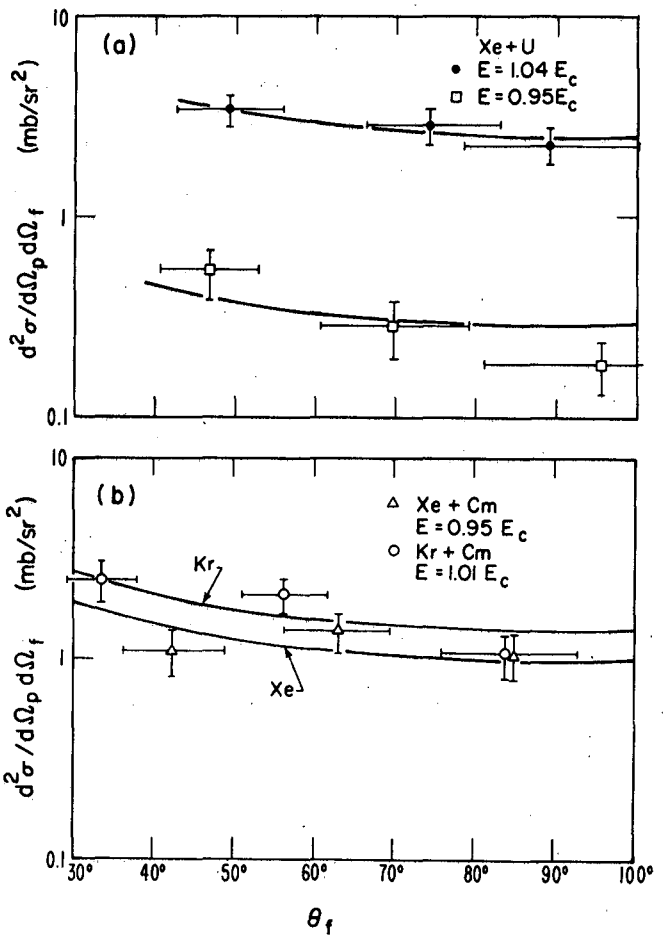


Fig. 2. Fission fragment angular distributions $d^2\sigma/d\Omega_p d\Omega_f$ at $\theta_p = 160°$ (c.m.) for (a) $^{136}Xe + ^{238}U$ ($E = 1.04\ E_c$ and $E = 0.95\ E_c$); and (b) $^{136}Xe + ^{248}Cm$ ($E = 0.95\ E_c$) and $^{86}Kr + ^{248}Cm$ ($E = 1.01\ E_c$). The horizontal bars reflect the range of $\theta_f$ seen in the fission detector caused by its finite solid angle. The best fit for a $1/\sin\theta$ distribution is indicated by the solid lines. (XBL 7612-11146)

though the data for two of the systems are consistent with isotropic emission of the fission fragments.

The fission events discussed here do not appear to be due to pure Coulomb fission because there is no large variation with projectile, target or fission fragment angle. However we cannot exclude the presence of some Coulomb fission since (1) the Xe cross sections are significantly higher than those for Kr for the U, Pu and Cm targets; (2) the dependence of the Coulomb fission process on the fission barrier is not reliably known; and (3) there is uncertainty as to the exact form of the angular distribution for both nuclear and pure Coulomb processes. It seems more likely that the observed events are due to a nuclear process such as transfer-induced fission. In this case the lack of sensitivity to the fission barrier probably indicates that the process involves excitation energies comparable to or greater than the fission barrier.

Footnotes and References

*Condensed from LBL-5854; Phys. Lett. 68B, 122 (1977).

†On leave from the Australian National University, Canberra, A.C.T. 2600 Australia

‡On leave from Institut de Physique Corpusculaire, B-1348 Louvain-la-Neuve, Belgium

§On leave from Centre d'Etudes Nucleaires de Bordeaux-Gradignan, Domaine du Haut-Vigneau, 33170 Gradignan, France

‖Present address: Institut de Physique Nucleaire, 91406 Orsay, France

¶Lawrence Livermore Laboratory

1. P. Colombani, P. A. Butler, I. Y. Lee, D. Cline, R. M. Diamond, F. S. Stephens and D. Ward, Phys. Lett. 65B, 39 (1976).

2. R. Vandenbosch and J. R. Huizenga in Nuclear Fission (Academic Press, N.Y. 1973) p. 255.

## SECOND DISCONTINUITY IN THE YRAST LEVELS OF $^{158}$Er†

I. Y. Lee, M. M. Aleonard,* M. A. Deleplanque,‡ Y. El-Masri,§
J. O. Newton,‖ R. S. Simon,¶ R. M. Diamond, and F. S. Stephens

In some light rare earth nuclei, there is a discontinuity in the yrast level sequence around spin I ≈ 14 ħ so that the regular increase in the γ-ray transition energies with increasing spin is temporarily reversed. Since the discovery[1] of this "backbending" effect, a considerable amount of experimental data has been accumulated on the properties of collective states[2] with spins up to I ≈ 20 ħ from studies of HI,xn reactions and Coulomb excitation. In the present work we have combined several recently developed techniques to study the discrete transitions from states with I > 20 ħ.

We have studied the high-spin yrast levels of $^{158}$Er using the $^{122}$Sn ($^{40}$Ar,4n) reaction. This nucleus was studied previously[3-5] and a backbend was observed at I = 14 ħ. Using $^{40}$Ar as a projectile the compound nucleus can be formed with higher angular momentum, so that there is a larger population for the higher spin states. The experiments were performed using a self-supporting enriched $^{122}$Sn foil of 1 mg/cm$^2$ thickness. The thin target allows the compound nuclei to recoil out of the target and decay in flight, thus avoiding the Doppler broadening from the slowing down in the thick target. A multiplicity filter consisting of six 7.5 cm x 7.5 cm NaI detectors was used, and the number of NaI detectors firing in coincidence with each event (singles or coincidence) observed in the Ge(Li) detectors was recorded. The 166 MeV beam energy was carefully chosen so that the 4n channel had the highest multiplicity among all the xn channels. Therefore by selecting the events with more NaI coincidences, the γ-rays from the low-multiplicity channels (e.g., 5n) could be progressively filtered out, even though they were nearly as large as those from the 4n channel in total cross section.

Figure 1 shows some of the γ-γ coincidence spectra where one or more NaI detectors fired (≥ 1-fold coincidence spectra). The yields of these γ-rays were measured at 0° and 90° from ≥ 1-fold singles spectra. These 0°/90° intensity ratios were found to be consistent with stretched

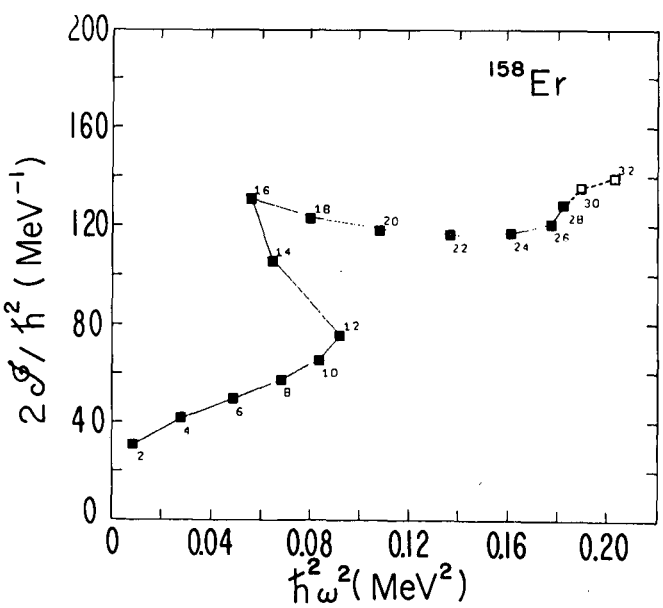


Fig. 1. Coincidence γ-ray spectra from $^{122}$Sn($^{40}$Ar, 4n)$^{158}$Er reaction. (XBL 774-865)

E2 decays. From these (and other) data the yrast level sequence can be established with reasonable certainty up to I = 28 ħ and tentatively on to I = 32 ħ. A second discontinuity in the yrast level sequence at I = 28 ħ is evident from the close spacing of the $26^+ \rightarrow 24^+$, $28^+ \rightarrow 26^+$ and $30^+ \rightarrow 28^+$ transitions. Even without considering the tentatively assigned $30^+ \rightarrow 28^+$ transition, the existence of this discontinuity is clear. Figure 2 shows a plot of the moment of inertia vs the square of the rotational frequency for this level sequence, and in this plot the second discontinuity shows up as a rapid increase of the moment of inertia of the states with spin larger than $26^+$. (If the 843 and 855 keV transitions were reversed in order, there would be a small backbend at this point rather than this increase in moment of inertia.)

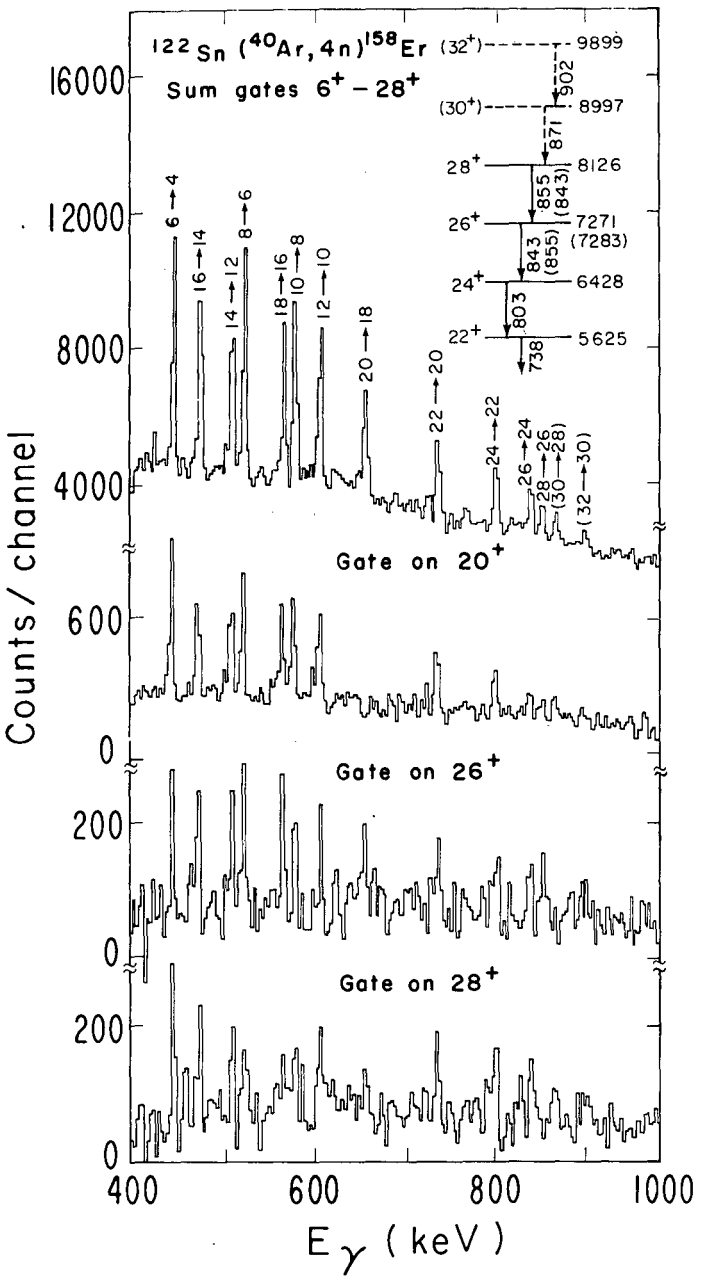


Fig. 2. Plot of the moment of inertia vs the square of the angular velocity for $^{158}$Er. (XBL 774-804)

Backbending has been shown in several cases to be due to the crossing of a second band below the ground-state rotational band. Three possible explanations have been given for the nature of this second band. They are (1) a shape change of the nucleus,[6] (2) a collapse of the pairing correlation,[7] (3) an alignment of the angular momentum of two high-j nucleons with the rotational angular momentum.[8] It has been shown[9] that the first backbending of the light rare earth nuclei is probably due to the alignment of a pair of $i_{13/2}$ neutrons. At higher spins additional pairs of high-j nucleons will tend to be aligned and this might well cause additional discontinuities in the level sequence. For $^{158}$Er this second pair would probably be either additional $i_{13/2}$ neutrons or $h_{11/2}$ protons. Since the first backbending is due to alignment it seems most likely to us that the second discontinuity is also due to this effect.

The alignment of particles breaks the axial symmetry of these prolate-shaped nuclei. It has been pointed out that the liquid-drop model of the nucleus predicts that the shape at higher spin values will be oblate,[10] with all the angular momentum carried by aligned particles. The first backbend seems to be a step directly toward this situation, and if the alignment explanation is correct, the second discontinuity observed here would indicate a second step in this direction. It would be interesting to find out whether this trend continues at still higher spins.

## Footnotes and References

*Condensed from LBL-6559; Phys. Rev. Lett. 38, 1454 (1977).

†On leave from Centre d'Etudes Nucleaires de Bordeaux-Gradignan, Domaine du Haut-Vigneau, 33170 Gradignan, France.

‡On leave from Institut de Physique Nucleaire, 91406 Orsay, France; supported by Centre National de la Recherche Scientifique and NSF.

§On leave from Institut de Physique Corpusculaire, B-1348 Louvain-la-Neuve, Belgium.

‖Present address: Australian National University, Canberra, A.C.T. 2600 Australia.

¶Present address: Gesellschaft für Schwerionenforschung, Darmstadt, Germany.

1. A. Johnson, H. Ryde and J. Sztarkier, Phys. Lett. 34, 605 (1971).

2. R. O. Sayer, J. S. Smith III and W. T. Milner, Atomic Data and Nuclear Data Tables 15, 85 (1975).

3. R. M. Lieder, H. Beuscher, W. F. Davidson, P. Jahn, H. J. Probst and C. Mayer-Boericke, Z. Physik 257, 147 (1972).

4. D. Ward, H. R. Andrews, J. S. Geiger, R. L. Graham and J. F. Sharpey-Schafer, Phys. Rev. Lett. 30, 493 (1973).

5. A. Johnson, Lectures of International Extended Seminar on Heavy Ion, High-Spin States and Nuclear Structure, Trieste 1973 (IAEA, Vienna, 1975, Vol. 1, p. 517.

6. P. Thieberger, Phys. Lett. 45 B, 417 (1973).

7. B. R. Mottelson and J. B. Valatin, Phys. Rev. Lett. 5, 511 (1960).

8. F. S. Stephens, Rev. Mod. Phys. 47, 43 (1975).

9. E. Grosse, F. S. Stephens and R. M. Diamond, Phys. Rev. Lett. 31, 840 (1973); Phys. Rev. Lett. 32, 74 (1974).

10. S. Cohen, F. Plasil and W. J. Swiatecki, Ann. of Phys. (New York) 84, 1 (1974).

# ENERGY-DEPENDENT MULTIPLICITIES OF CONTINUUM GAMMA RAYS*

J. O. Newton,† I. Y. Lee, R. S. Simon,‡ M. M. Aleonard,§
Y. El-Masri,|| F. S. Stephens, and R. M. Diamond

Information about states of very high angular momentum can be obtained from the continuum $\gamma$-rays following (HI, xn) reactions. We have measured the multiplicities as a function of $\gamma$-ray energy $E_\gamma$ and show that, for a wide range of final nuclei, there exist energy regions with high multiplicity.

Targets of $^{12}C$, $^{27}Al$, KCl, Ti, Fe, $^{68}Zn$, $^{82}Se$, $^{126}Te$, and $^{130}Te$, 0.5-1.2 mg cm$^{-2}$ thick, deposited on 0.02 mm Pb backings, were bombarded with $^{40}Ar$ ions from the 88-in. cyclotron; the energy ranged between 119 and 185 MeV. A "multiplicity filter" was used consisting of six 7.5 cm x 7.5 cm NaI(Tl) detectors placed symmetrically around the beam axis. The number of NaI detectors firing in coincidence with events in a 50 cm$^3$ Ge(Li) detector, placed at an angle of 45° to the beam direction and 7.5 cm from the target, or in a 7.5 cm × 7.5 cm NaI detector at -45° and 60 cm was recorded. Neutron events in this NaI detector were excluded by time-of-flight. From the probabilities that various numbers of the NaI dectors fired, one can calculate the multiplicity for any selected gating events.† The data from the Ge(Li) detector gave multiplicities for individual $\gamma$-lines, and hence individual reaction channels, while the NaI data gave the multiplicity as a function of $E_\gamma$, irrespective of reaction channel.

Some of these multiplicity distributions for the NaI pulse-height spectra are shown in Fig. 1(a), (b), (c). The characteristic feature is a peak at an energy somewhere between 1 and 3 MeV. The energy region above this peak arises from the statistical emission of $\gamma$-rays which occurs irrespective of the angular momentum of the system. It would therefore be expected to have about the average multiplicity of all reaction channels. From this average multiplicity one can estimate the maximum multiplicity and hence the maximum spin, I(max), involved. The peak itself arises from the cascade of $\gamma$-rays parallel to the yrast line. If some type of rotational motion is involved, the highest $\gamma$-ray energy in the yrast cascade, $E_\gamma$(max), will correspond generally to the highest initial angular momentum and hence the highest multiplicity.

The angular momentum reaching the yrast region could be limited by (1) the maximum angular momentum involved in complete fusion, (2) fission of the compound system, and (3) particle emission competing with $\gamma$-emission in the yrast region. For the highest bombarding energies used here, (1) is expected to be well above that observed. We have made estimates for the limiting angular momenta I(max) and for the corresponding end-point $\gamma$-ray energies $E_\gamma$(max) for (2) and (3). Those from fission were obtained from the liquid-drop model following the method of Cohen, Plasil, and Swiatecki.[1] (We assumed a fission barrier of 10 MeV, taken to be an effective particle binding energy.) It is easy to show that $\alpha$-particles set the lowest angular momentum limit for any type of particle evaporation, and this limit has been estimated in the full report of this work.

The results for I(max) and $E_\gamma$(max) are shown in Fig. 2, and there is reasonably good agreement with the experimental data. The limiting angular momenta are low for the lower Z values, which results in smaller peaks since the number of $\gamma$-rays decreases and $E_\gamma$(max) increases. Figure 1(b) shows that peaks cannot be observed clearly below the Ti + Ar system (Z = 40).

It should be pointed out that variations from the rather smooth behavior of the lines in Fig. 2 will occur since both the B($\alpha$) and the fission limits change appreciably for a change in neutron number for fixed Z. Also, theoretical calculations[2] indicate that shell effects should not be completely absent at high angular momenta, and may show up as local variations in the moment of inertia. If these shell effects are large, then the estimate for $E_\gamma$(max) may be better than that for I(max), since the energy available for $\alpha$-emission depends more on the local slopes of the yrast lines than on the value of I.

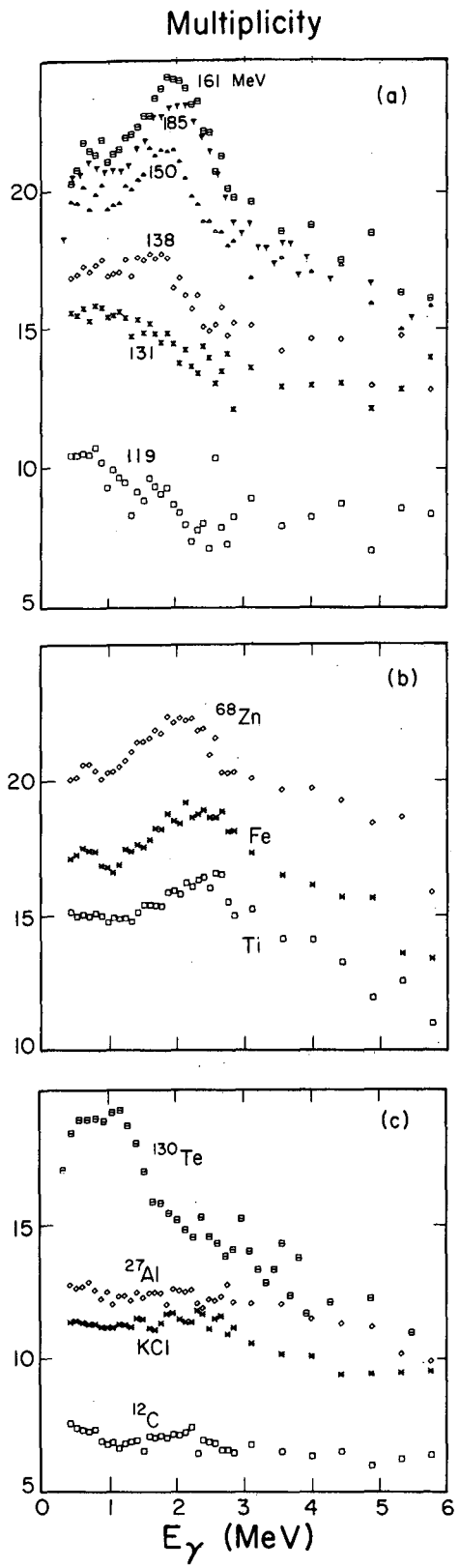


Fig. 1. Multiplicities as a function of γ-ray energy (NaI pulse height) for (a) $^{40}$Ar + $^{82}$Se at the indicated bombarding energies, and (b) and (c) targets bombarded by $^{40}$Ar ions of 161 MeV, except for $^{130}$Te (185 MeV) and $^{12}$C(131 MeV).

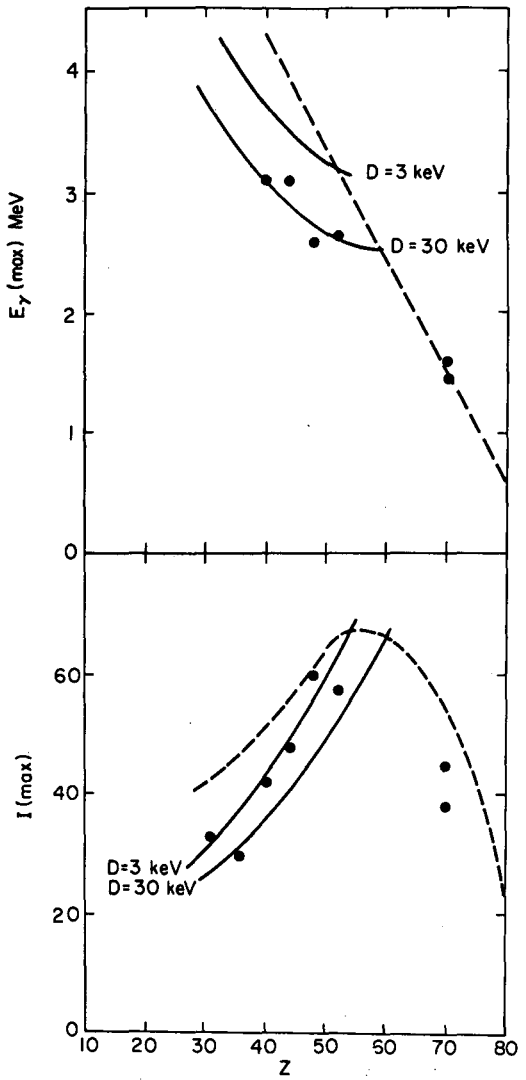


Fig. 2. The solid (dashed) lines show the calculated $E_\gamma$(max) and I(max) values given by α-particle emission (fission). The experimental points come from Fig. 1, where I(max) is twice the maximum multiplicity which in turn is estimated to be 3/2 of the average multiplicity. (XBL 771-49)

## Footnotes and References

*Condensed from LBL-5830, Phys. Rev. Lett. 38, 810 (1977).

†Nuclear Physics Department, The Australian National University, Canberra, A.C.T. 2600, Australia.

‡On leave from Sektion Physik der Ludwig-Maximilians-Universität München, 8046 Garching, Germany; sponsored by the Bundesministerium für Forschung und Technologie.

§On leave from Centre d'Etudes Nucléaires de Bordeaux-Gradignan, Domaine du Haut-Vigneau, 33170 Gradignan, France.

‖On leave from Institut de Physique Corpusculaire, B-1348 Louvain-la-Neuve, Belgium.

1. S. Cohen, F. Plasil, and W. J. Swiatecki, Annals of Physics 82, 557 (1974).

2. I. Ragnarsson and D. P. Soroka, private communication, June 1976.

# MULTIPLICITIES OF γ-RAYS OBSERVED IN $^{86}$Kr-INDUCED DEEP-INELASTIC PROCESS*

P. Glässel,† M. M. Aleonard,‡ G. Bizard,§ M. A. Deleplanque,‖ R. C. Jared,
L. G. Moretto, R. P. Schmitt, F. S. Stephens, G. J. Wozniak, and R. M. Diamond

Studies of deep inelastic reactions on a variety of nuclei have led to the concept of a short lived di-nuclear complex which separates into projectile-like and target-like fragments. Measurements of the γ-ray multiplicities observed give information on the angular momentum transfer. Such measurements were done for the systems $^{86}$Kr + $^{197}$Au (598 and 618 MeV), $^{86}$Kr + $^{165}$Ho, and $^{86}$Kr + $^{nat}$Ag (618 MeV). Although these data are still being analyzed, we present here some preliminary results for the Kr + Au system.

The Kr + Au study at 598 MeV utilized the same technique as in Ref. 1 and will not be elaborated on here. The γ-ray multiplicities $M_\gamma$ (see Ref. 1) were measured for the relaxed component as a function of the atomic number $Z_3$ of the light fragment which was detected in a ΔE-E telescope. Measurements were undertaken for several positions of this telescope (30 to 70°). In Fig. 1 the trends to be noticed are: (a) the absence of any pronounced structure in the multiplicity as a function of $Z_3$; (b) the evolution of the multiplicity with angle, increasing from backward angles (70°) to the forward angles (30°) with a slight maximum for 55° ($\theta_{graz}$ = 41°). This behavior is quite different from that observed for the $^{20}$Ne + Ag system (Ref. 1).

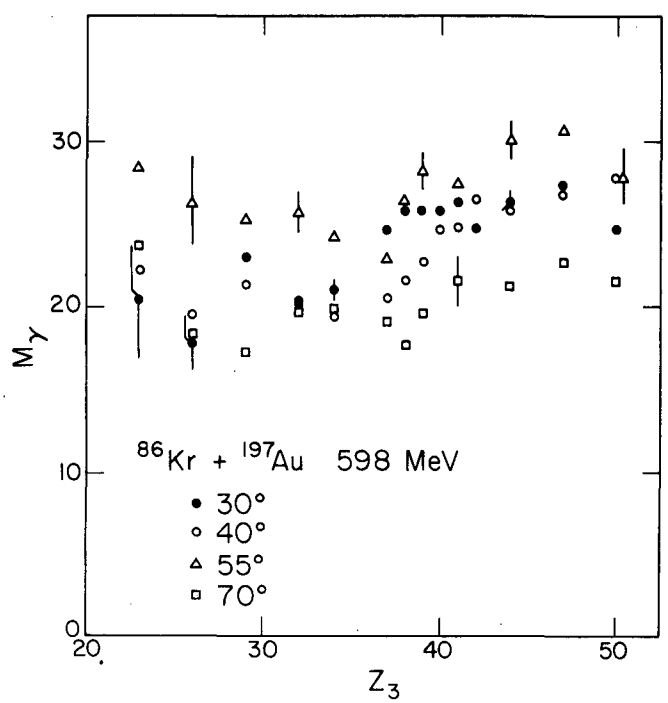


Fig. 1. Gamma multiplicity vs $Z_3$ for the relaxed component (lab angles). (XBL 778-1732)

In the heavier system Kr + Au the contribution of the fission channel (seen in other experiments with large probability)[2] could possibly explain this difference. In order to determine the effect of this channel on $M_\gamma$ a new set of experiments were undertaken at 618 MeV for the systems $^{86}$Kr + $^{197}$Au, $^{86}$Kr + $^{165}$Ho and $^{86}$Kr + $^{nat}$Ag. A triple coincidence between the γ rays and both the projectile-like and target-like fragments was required. Better efficiency was achieved for the γ-ray detectors, in that a γ-ray multiplicity filter (six 3 × 3" NaI detectors) was placed 5" about the target. The experimental setup consisted of a solid state E, gas ΔE counter[3] and an x-y position-sensitive telescope[4] (PSD) which were placed in the reaction plane on opposite sides of the beam axis. The number of NaI detectors involved in coincidence with a fragment in the telescope and the additional information on the correlated fragments both in the telescope and the PSD were recorded event-by-event. Measurements were performed for several sets of angles for the telescope (20 to 40°) and for the PSD (40 to 53°) to study the kinematically correlated fragments as a function of the energy damping and mass asymmetry of the intermediate complex. The multiplicity associated with each $Z_3$ and a fissioning or non fissioning $Z_4$ (selected by its energy) was deduced from the number of counts obtained in the different p-fold coincidences with the NaI detectors (p=1 to 6). The efficiency of the NaI detectors, measured with a $^{60}$Co source, was scaled to set the efficiency for the mean energy of the γ rays observed in the previous experiment at 598 MeV.

The preliminary results for the Kr + Au system at 618 MeV are shown in Fig. 2. Since within the statistical limits, we did not find any dependence of the multiplicity for different positions of the PSD, and since the previous data (Fig. 1) for the telescope at 30 or 40° were nearly the same, we present in Fig. 2 the

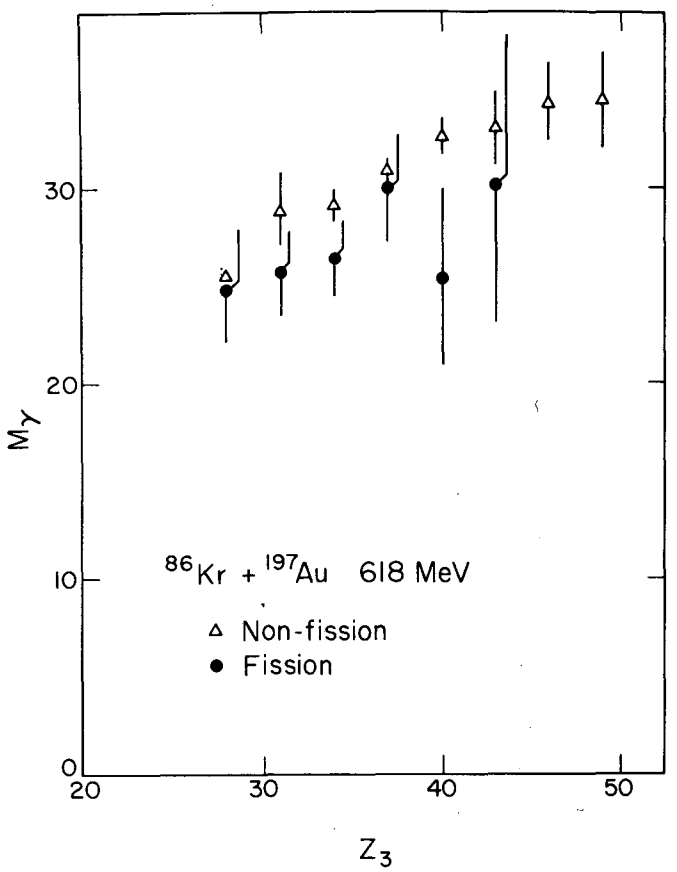


Fig. 2. Gamma multiplicity vs $Z_3$ in correlation with fissioning and nonfissioning $Z_4$-fragments. These values are from the sum of the information for the ΔE-E telescope at 30 and 40° and the X-Y position sensitive counter at 45 and 53°.
(XBL 778-1733)

multiplicity for the sum of all the data collected for the different positions of the detectors. As can be seen the multiplicity for fissioning and nonfissioning channels are comparable within statistical errors though the fissioning events may indicate a systematic smaller multiplicity. The interpretation of the multiplicity as a function of $Z_3$ is complicated by the fact that different mass asymmetries ($Z_3$) are likely to be populated by different ℓ-waves in the entrance channel. The data from the lighter systems Kr + $^{165}$Ho and Kr + $^{Nat}$Ag will hopefully help in understanding this ℓ dependence.

Footnotes and References

*Preliminary results

†Present address: Physikalisches Institut der Universität Heidelberg Philosophenweg 12, D-69, Heidelberg, W. Germany.

‡Nato Fellow

§Present address: Laboratoire de Physique Corpusculaire Université de Caen, 14000 Caen-France

‖Sponsored by NSF

1. P. Glässel, R. S. Simon, R. M. Diamond, R. C. Jared, I. Y. Lee, L. G. Moretto, J. O. Newton, R. Schmitt and F. S. Stephens, Phys. Rev. Lett. 38, 331 (1977).

2. G. J. Wozniak et al., Secondary Fission of Target-Like Nuclear Produced in Deep Inelastic Collisions, in this Annual Report.

3. M. M. Fowler and R. C. Jared, Nucl. Instrum. and Meth. 124, 341 (1975).

4. R. C. Jared, P. Glässel, J. B. Hunter, and L. G. Moretto, A Simple Position-Sensitive Parallel-Plate Avalanche Counter with Two-Dimensional Readout, in this Annual Report.

## EXPERIMENTAL STUDY OF Yb NUCLEI AT HIGH ANGULAR MOMENTUM*

R. S. Simon,† M. V. Banaschik,‡ R. M. Diamond, J. O. Newton,§ and F. S. Stephens

We have used bombardments of 88 MeV $^{16}$O on $^{150}$Sm, 161 MeV and 185 MeV $^{40}$Ar on $^{126,130}$Te and 309 MeV and 334 MeV $^{86}$Kr on $^{80,82}$Se to produce Yb nuclei in a broad range of angular momenta up to the limit which these nuclei can hold. The compound system most completely studied was $^{166}$Yb. Additional results were obtained for $^{168}$Yb via the $^{86}$Kr reaction on $^{82}$Se and for $^{170}$Yb via $^{40}$Ar bombarment of $^{130}$Te.

Our experimental arrangement to study the continuum γ rays from the evaporation residues is shown schematically in Fig. 1. The beam strikes a thin target on 0.025 mm lead backing. Target thicknesses are below 1 mg/cm$^2$ and introduce less than ±4 MeV spread around the average beam energy. (We will refer to these averages rather than the full incident beam energies. The lead backing stops recoils and projectiles without generating appreciable background radiation. The γ continuum is observed in three 7.5 × 7.5 cm NaI(Tℓ) detectors at 0°, 45°, and 90° with respect to the beam direction and 60 cm from the target. These detectors are gated by coincident pulses from a 10 cm$^3$ planar Ge detector at 225° and 5 cm from the target. The coincidence requirement with the Ge detector serves two purposes: (1) to obtain the continuum spectrum associated with an individual reaction channel by gating on the discrete γ lines from the corresponding evaporation residue, and (2) to provide a time signal to distinguish pulses in the NaI detectors due to γ rays from those due to neutrons on the basis of the longer neutron flight times.

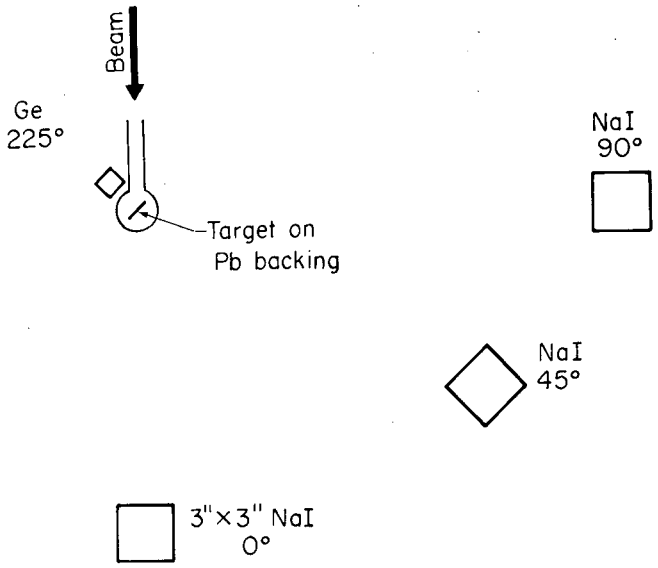


Fig. 1. Experimental arrangement to study continuum γ rays. (XBL 771-155)

The true energy distribution of the continuum γ radiation is obtained from the observed NaI pulse-height spectra by an "unfolding" procedure[1] which assumes a distribution of Compton and pair production events for each full-energy γ quantum detected. To allow computer analysis, the detector response to γ radiation is represented by a two-dimensional matrix of experimental pulse-height distributions vs γ-ray energies. Unfolding is achieved in successive steps: an initial guess of the true γ-ray energy distribution is multiplied by the response matrix to generate the corresponding pulse-height spectrum. This spectrum is compared to the experimental one and deviations between the two are used to improve the estimate for the next iteration.

For the reaction $^{126}Te(^{40}Ar, 4n)^{162}Yb$ at 181 MeV. The original "raw" pulse-height spectrum and the unfolded spectrum are shown in Fig. 2, as well as the ratio of events at 0° to those at 90°. To obtain $\bar{N}_\gamma$, we have summed the transitions in the unfolded spectrum above 0.34 MeV (the lowest energy coincident to be reliable) and then added two transitions to represent the 166 keV $2^+ \rightarrow 0^+$ and 320 keV $4^+ \rightarrow 2^+$ lines in $^{162}Yb$.

Absolute cross sections for the various xn reaction channels have been obtained from the Ge singles spectra in two ways. In the first method, the γ intensities of interest, corrected for pile-up, for the relative efficiency of the Ge detector, and for internal conversion, are compared to the corrected intensity of the 803 keV $2^+ \rightarrow 0^+$ transition in $^{206}Pb$ which is produced simultaneously by Coulomb excitation of the natural lead backing. The 803 keV γ-ray yield can be derived from semi-classically calculated populations[2,3] of the $2^+$ state, and the projectile stopping powers in lead, thus leading to an absolute normalization. The target thicknesses were determined by x-ray

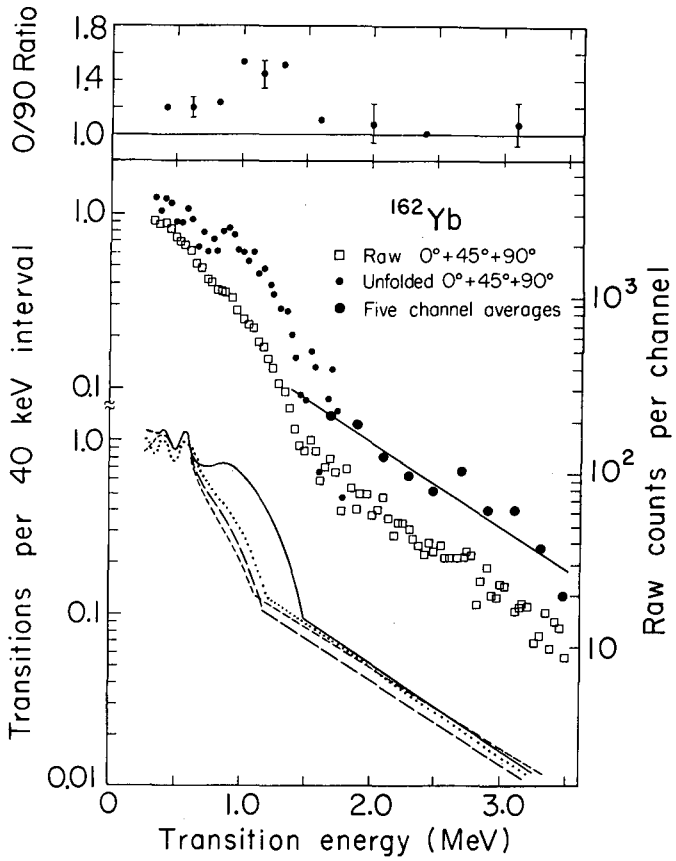


Fig. 2. Raw (□) and normalized unfolded (•) continuum γ spectrum from the reaction $^{126}Te(^{40}Ar,4n)^{162}Yb$ at 181 MeV. The larger dots represent 5-channel averages. Also shown is the 0/90 ratio for the true γ distribution. At the bottom are schematic spectra for this case (solid line) and for the reactions $^{80}Se(^{86}Kr,4n)^{162}Yb$ at 331 MeV (dotted line), $^{126}Te(^{40}Ar,4n)^{162}Yb$ at 157 MeV (longer-dashed line), and $^{150}Sm(^{16}O,4n)^{162}Yb$ at 87 MeV (shorter-dashed line). (XBL 771-162A)

fluorescence. The other method compares the corrected γ intensities with the $2^+ \rightarrow 0^+$ Coulomb excitation yield of the target measured at a safe bombarding energy below the barrier.

The unfolded spectra have a common general structure. Their intensity decreases nearly exponentially with energy at high γ energies, and somewhere below 1.5 MeV they show a rather pronounced "bump" of intensity rising from this exponential tail. This feature is clearly seen in the spectrum of $^{162}Yb$ from the $^{40}Ar$, 4n reaction at 181 MeV given in Fig. 2 and is present even in the original raw spectrum.

The exponential tail above 1.5 MeV seems to have no sharp high energy cut-off and has a slope which is consistent with estimates for a statistical cascade.[4] The nearly isotropic angular distribution in the tail region is also consistent

with this conclusion, as is the general similarity of this part of the spectrum in the various reactions studied. From this and from previous work,[5,6] it is very likely that these transitions do come, at least mainly, from the predicted statistical cascade.

Below about 1.5 MeV, in the bump region, the anisotropy suggests a dominance of stretched-E2 I → I-2 transitions. Here the spectrum does change with bombarding conditions. At the bottom of Fig. 2 the shape of the unfolded $^{162}$Yb spectrum from the $^{40}$Ar,4n reaction at 181 MeV (obtained from the spectrum above) is compared with that from the same 4n reaction channel at 157 MeV and with spectra from the $^{150}$Sm ($^{16}$O, 4n) and $^{80}$Se($^{86}$Kr,4n) reactions. The last three bombardments, though very different in their target-projectile combinations, generate almost identical spectra. Very clearly, the bump in the 181 MeV $^{40}$Ar spectrum is more developed and extends to higher energies. This seems to be an angular-momentum effect and suggests that the bump arises from the predicted collective transitions parallel to the yrast line. It is natural then to expect similar spectra from the $^{16}$O and the low-energy $^{40}$Ar and $^{86}$Kr reactions shown, since similar amounts of angular momentum are brought into the compound system in these cases. Increasing the angular-momentum input, as in the 181 MeV $^{40}$Ar reaction, extends the collective cascade to higher energies. The average values of the angular momenta for the individual channels derived from the cross sections are compared with the corresponding average γ-ray multiplicities in Fig. 3 after the odd-n channel multiplicities have been increased by 3 to treat them on the same footing as the even-n values (the prompt cascade down the decoupled $i_{13/2}$ band leaves the odd nuclei with 13/2 units of angular momentum which would correspond to about 3 more γ transitions).

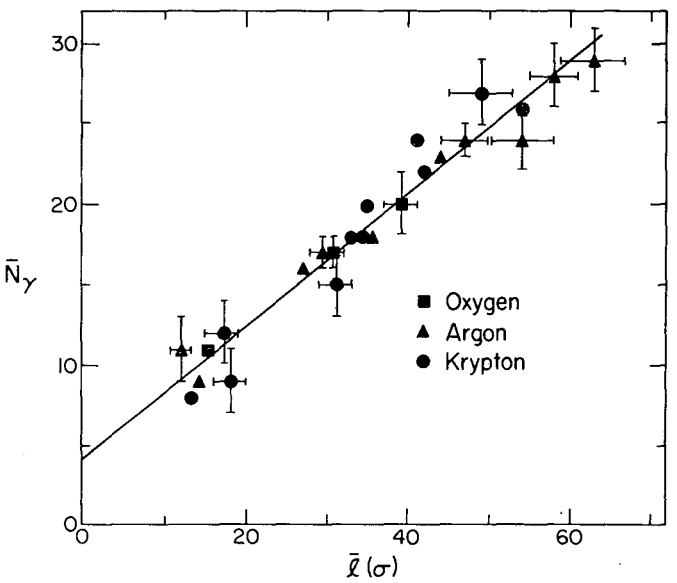


Fig. 3. This figure plots the observed average γ multiplicities. Diamonds (♦), triangles (▲) and dots (●) indicate O, Ar and Kr results. The straight line fitted to the data has a slope of 0.43.
(XBL 771-158A)

A relationship between the average γ-ray multiplicity $\bar{N}_\gamma$ and the average channel angular momentum $\bar{\ell}(\sigma)$ as derived from the cross sections is clearly established in Fig. 3. The average ratio of $\bar{\ell}(\sigma)/\bar{N}_\gamma$ is close to 2, very much in agreement with the E2-character of the bump. There are no obvious differences between the $^{16}$O, $^{40}$Ar and $^{86}$Kr points. Thus, the $\bar{N}_\gamma$ values observed seem to be generally consistent with a picture where the total angular momentum distribution is fractionated on the individual xn channels. The situation might be different for lighter ions, where less angular momentum is brought into the compound system, and the slope of the yrast line is correspondingly smaller.

In the ground-state rotational bands of these rare-earth nuclei moments of inertia $\mathscr{F}$ have been calculated using the approximate relation,

$$E_t = \frac{\hbar^2}{2\mathscr{F}}(4I-2), \qquad (1)$$

which connects an E2 transition energy $E_t$ with the spin I of the decaying state. In Fig. 4 we show

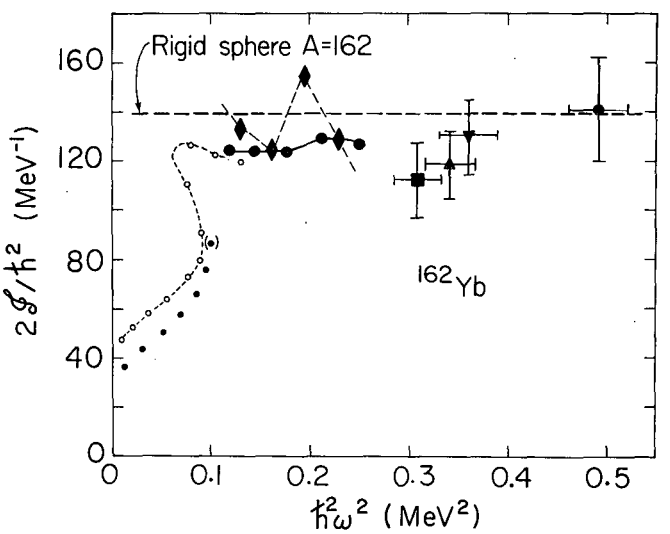


Fig. 4. Backbending plot for $^{162}$Yb. The small dots indicate the known low-spin states whereas the open circles are for the isotone $^{160}$Er. The large dots connected by a solid line correspond to $^{162}$Yb values derived by the integral method from the 181 MeV $^{40}$Ar spectrum between 0.7 and 1 MeV and the diamonds come from the differential method applied to the same data. The isolated square, triangles, and solid dot represent values from the top of the collective cascade as observed in the 87 MeV $^{16}$O, 157 MeV $^{40}$Ar, 331 MeV $^{86}$Kr, and 181 MeV $^{40}$Ar reactions. The horizontal dashed line corresponds to a rigid diffuse sphere with A = 162.
(XBL 771-161)

the usual backbending type of plot for $^{162}$Yb, where $2\mathcal{J}/\hbar^2$ is plotted against $(\hbar\omega)^2$, the square of the rotational frequency (which is very nearly $E_t^2/4$). Around spin 12 the moment of inertia rises sharply, suggesting that the curve will backbend as it does in the isotone $^{160}$Er. Equation (1) can also be applied to high-spin states in the collective cascade, if we confine ourselves to a region of the spectrum corresponding to I values below which there is no appreciable direct population into the channel of interest. This region is likely to be below I=35 for the 4n channel in the $^{126}$Te + $^{40}$Ar case at 181 MeV since most of the population with lower spins goes into the 5n or 6n channels, but it would be less than I=20 for the $^{16}$O and low energy Ar cases. Provided there is a monotonic increase of transition energy with spin (no additional backbending), a spin value for each transition energy can be obtained by summing all the transitions (less the estimated statistical-cascade background) up to that transition energy and multiplying by 2. This method is applicable between ~ 0.7 and 1.0 MeV in the spectrum and leads to the moments of inertia given by the dots connected by a solid line in Fig. 4.

Another place in the spectra where relation (1) may give moments of inertia is at the edge of the bump. From the bottom part of Fig. 2 the edge in the $^{40}$Ar spectrum at 181 MeV is clearly higher than in the other three cases where less angular momentum is brought into the system. This suggests that the energies of the edge can be associated with $\gamma$-transitions between the highest spin states in the collective cascade. On the basis of this assumption, four values for $2\mathcal{J}/\hbar^2$ can be obtained and are plotted in Fig. 4. As an estimate of the angular momentum at the top of the collective cascade we used the corresponding upper channel angular momentum as derived from the cross sections, but subtracted 15% to allow for the amount carried off by neutrons and the statistical cascade. During a backbend the edge of the bump and the top $\gamma$-transition energy in the cascade would not be identical and then moments of inertia would not be derivable in this manner.

The preceding method is an "integral" one and thus not very sensitive to local variations in the moment of inertia. There exists an alternative, a "differential" method, that can show such local variations. Each point on the unfolded spectrum of Fig. 1 gives the number of transitions per 0.04 MeV energy interval. The reciprocal of this $(0.04/\bar{N}_\gamma)$ is the difference between transition energies $\Delta E_t$ and can be related to the moment of inertia by differentiating expression (1) for $E_t$, yielding

$$\Delta E_t = \frac{8\hbar^2}{2\mathcal{J}} - \frac{2E_t \, d\ell n}{dI} \quad . \qquad (2)$$

This method also requires the full population in the channel, and thus again can only be applied quantitatively below I = 35 in the 181 MeV $^{40}$Ar case. For the region between 0.7 and 1.0 MeV, $\mathcal{J}$ is nearly constant so that the last term of Eq. (2) can be neglected, giving $2\mathcal{J}/\hbar^2 \approx 8/\Delta E_t$. This procedure leads to the diamonds connected by the dashed line in Fig. 4. The results are in good agreement with those from the integral method and this agreement suggests that the various approximations used are reasonable. The power of the differential method is that changes in the moment of inertia can be recognized directly from irregularities in the spectrum, thereby providing a simple means to pick out regions of particular interest, namely, regions showing some type of structure.

## Footnotes and References

*Condensed from LBL-5827 and Nucl. Phys.

†Present address, Gesellschaft für Schwerionenforschung, Darmstadt, Germany.

‡Present address: Gesellschaft für Reaktorsicherheit, Köln, Glokengasse 2, Germany.

§Present address: The Australian National University, Canberra, A.C.T. 2600 Australia.

1. J. F. Mollenauer, Phys. Rev. 127, 867 (1962).

2. A. Winther and J. de Boer, California Institute of Technology Report, Nov. 18, 1965.

3. J. L. Quebert, K. Nakai, R. M. Diamond, and F. S. Stephens, Nucl. Phys. A 150, 68 (1970).

4. J. R. Grover and J. Gilat, Phys. Rev. 157, 814 (1967).

5. J. O. Newton, J. C. Lisle, G. D. Dracoulis, J. R. Leigh, and D. C. Weisser, Phys. Rev. Lett. 34, 99 (1975).

6. M. V. Banaschik, R. S. Simon, P. Colombani, D. P. Soroka, F. S. Stephens, and R. M. Diamond, Phys. Rev. Lett. 34, 892 (1975).

# NUCLEAR STRUCTURE AT HIGH ANGULAR MOMENTUM*

F. S. Stephens

There has been considerable progress recently in understanding the effects of high angular momentum on nuclei. The interest in this subject increased sharply in 1971 with the discovery[1] of a pronounced irregularity called "backbending" in the rotational energies of some rare earth nuclei. The theoretical study of this process constituted the first general consideration of the effects of angular momentum on nuclear structure, and a number of interesting aspects emerged. In one direction, a connection was made between the behavior of strongly deformed nuclei at high spin values and that of weakly deformed nuclei at moderately low spin values, which correspond, nevertheless, to similar rotational frequencies. This stimulated the study of these weakly deformed transitional (often called "vibrational") nuclei, and that subject constitutes one section of the present paper. The second section deals with the backbending phenomenon itself, and the present understanding of this process, which seems to be improving considerably. In another direction, the theoretical studies led to the prediction of profound structural changes in nuclei at much higher angular momenta (up to the limit of instability against fission or particle emission) and this has spurred the experimental study of this angular-momentum range. That area constitutes the last part of this paper. The order of these three parts has been chosen to correspond to increasing angular momentum, although it is not clear that this order reflects increasing complexity in the nuclear structure. More complete discussions of these topics are given in the full report of these lectures.

## 1. Transitional Nuclei

The level structure of nuclei in the vicinity of the ground state is reasonably well understood at closed shells, where the collective motion is not very important, and the independent-particle (shell) model accounts for the main features. In regions of well deformed nuclei the structure is also basically understood, and consists of a slow rotational motion of the system as a whole, superposed on a deformed shell-model level structure for the individual nucleons. The nuclei between these two regions have generally been more difficult to understand; however, considerable progress has been made recently in these transitional nuclei, due mostly to the systematic study of high-spin states following heavy-ion compound-nucleus reactions.

It is now clear that there are simple collective features involving the quadrupole deformation coordinates in the odd-mass transitional nuclei, the most obvious of which are decoupled and strongly coupled rotational bands. Such bands correspond to rotation around an axis either parallel to or perpendicular to the one to which the particle's angular momentum is coupled. These bands appear to follow in leading order from anharmonic oscillator models also, and more general solutions of Bohr's collective quadrupole Hamiltonian show that they develop for a wide variety of potential-energy surfaces. This is fortunate in that it makes these simple patterns easy to recognize in many nuclei, but it is unfortunate in that it makes it difficult to decide among various types of nuclear potential-energy surfaces. To make these distinctions the nuclear spectra must be studied carefully and compared in detail with the calculated ones. A number of such comparisons have now been made which give excellent fits for many levels, but these fits require more $\gamma$ dependence in the potential energy than is presently obtained from the Strutinsky-type calculations. In some cases the spectra seem to require stable triaxial shapes which are not given by the calculations. Whether this reflects a problem in interpreting the experimental spectra, or a problem in the Strutinsky-type calculations is an open question at the present time.

## 2. Backbending

In 1971 Johnson, Ryde, and Sztarkier[1] found a distinct anomaly around spin 16 in the rotational energy-level spacings of several rare-earth nuclei. This behavior was called backbending and there was considerable interest about its cause. During the intervening years there has been a rather large theoretical effort to try to understand how nuclei behave at high angular momentum, and there has also been a strong experimental program to find out more about backbending and other similar phenomena. We now have a reasonably clear idea what causes the backbending first observed in 1971, and we also know about several other similar processes.

All of the three proposed causes for backbending (shape change, pairing collapse and alignment) have been found to give rise to important effects as the angular momentum in nuclei increases. Shape changes occur for the weakly deformed nuclei ($\beta < 0.3$), and in such regions these changes can occasionally produce sudden effects which give rise to backbending behavior. The pairing correlations seem to be steadily decreasing in most nuclei as the angular momentum increases, but no sudden changes clearly due to this effect have yet been observed. The main cause for most backbending seems to be the alignment of the angular momentum of two high-j nucleons, $i_{13/2}$ neutrons in the light rare-earth region. This alignment, in addition, is a step toward lower pairing, since a pair is broken, but it is not generally a pair just at the Fermi level which would be the most effective in reducing the pairing. The alignment also corresponds to a small shape change since the orbit of an aligned particle represents a triaxial bulge. However, the main effect is the addition of angular momentum (12 $\hbar$ for two $i_{13/2}$ neutrons)

along the rotation axis. In the cases where sufficient information exists, the backbending has so far always involved the crossing of two bands -- this is the mechanism for the sudden change. The study of this band crossing and the mixing which occurs at that point is now of considerable interest, and Coulomb excitation with the recently available very heavy ions seems to be a promising tool for this study.

3. Very High Angular Momentum

The interest generated in understanding the processes involved in backbending has carried over into the regions of higher angular momemtum, and a large effort is now being made there, both theoretically and experimentally. On the theoretical side, the liquid-drop model provided the basic outline of what might be expected, and the effects of the shell structure have been added onto this basis, first qualitatively and more recently with detailed microscopic calculations. The prospects envisioned have spurred the experimental program, and some real progress has been made recently, though there are still many problems in extracting information about nuclear structure for states with spins much above 20 ħ.

These very high spin states can be studied experimentally so far only through the "continuum" gamma-ray spectra following heavy-ion reactions. In this way, moments of inertia for states up to 50 ħ have been obtained and more recently, structure has been identified in the spectra of $^{118}$Te which can tentatively be related back to the calculated shell effects. These are important steps which show that the full range of angular momenta ($\lesssim$ 70 ħ) is open to study for nuclei stable against fission and particle evaporation. However such studies involving unresolved continuum spectra are difficult and represent a challenge to the experimental techniques. This is an area we are only beginning to explore, but one with much promise.

Footnote and Reference

*Condensed from LBL-5041, lectures presented at the International School of Physics, Varenna, Italy, July 1976; to be published in Nuovo Cimento.

1. A. Johnson, H. Ryde, and J. Sztarkier, Phys. Lett. B 34, 605 (1971).

# VERY HIGH-SPIN STATES IN NUCLEI*

Richard M. Diamond

Today it is possible to obtain information on nuclei at very high spins, and to determine whether there are differences in behavior from nuclei at low spins. When 100 units of angular momenta are added to a nucleus, we enter a new nuclear regime in which the rotational energy approaches the order of magnitude of the Coulomb and surface energies, and is much larger than pairing and shell effects. As a result, effects on the nuclear shape, on the moments of inertia, even on the modes of decay, might be expected, and there will be an interplay between the single-particle and collective motions to most efficiently carry the angular momentum.

The use of heavy ions has made possible the investigation of high-spin states, and there have been three principal classes of studies:

1) Heavy-ion Coulomb excitation

2) (Heavy-ion,xnγ) reactions to study the discrete states up to spin 24-28 ħ.

3) (Heavy-ion,xnγ) reactions to study the yrast region up to spin 60 ħ via continuum γ-rays.

It is the third type of study that will be considered, involving the properties and behavior of nuclei with spins $\geq$ 30 ħ.

Our studies of these continuum gamma rays over the past several years have resulted in the following conclusions, which are discussed more fully in the complete report of this lecture.

1) Continuum spectra have a gross structure; they usually consist of an "yrast bump" and a "statistical" tail.

2) For medium to heavy nuclei, the yrast bump contains most of the γ-rays, and they are stretched E2 transitions. An approximate value for the angular momentum carried by the γ-cascade is $2\bar{N}_\gamma$.

3) There is evidence for fractionation of the reaction products with the angular momentum of the initial compound nuclei. The difference in angular momentum per neutron emitted is $\sim$ 12h with the heavy-ion projectiles used.

4) Under favorable conditions, effective moments of inertia can be determined up to I(max), 50-60ħ for the Te and Yb nuclei studied.

5) Continuum γ-ray spectra may show finer details of nuclear structure, e.g., backbends.

6) The maximum angular momentum in yrast cascades is probably limited by fission for A > 150 and by α-emission along the yrast region for A < 150.

Footnote

*Condensed from LBL-6505, lecture presented at the Physics Summer School Meeting, Jindabyne, Australia, Feb. 1977; to be published in the Australian Journal of Physics.

# A STUDY OF $\beta^-$-EMITTING ACTINIDES PRODUCED IN HEAVY-ION REACTIONS

K. E. Thomas and G. T. Seaborg

Our overall program is aimed at the determination of cross sections for the production of transuranium elements in the bombardment of uranium and transuranium targets with heavy ions. We hope to observe trends in the production of these elements which might be applied to the heaviest targets in order to produce superheavy elements. As a part of this program we are determining the yields of $\beta^-$-emitting actinides and investigating the possibility of producing new neutron-excess isotopes of the actinide elements. Results from the observation of light fragments from heavy-ion reactions suggest the possibility of producing these very heavy nuclides through a deep-inelastic process.[1] This investigation involves isolating chemically pure samples of the elements of interest for $\beta^-$-counting in gas-flow proportional counters. The decay curves are followed for periods of up to two months and are then resolved into the individual components. Identification is by chemical fraction and half-life.

To date we have had two $^{18}O$ (112 MeV) bombardments, two $^{86}Kr$ (731 MeV) bombardments, and two $^{136}Xe$ (1150 MeV) bombardments of uranium. In all bombardments, neptunium and plutonium fractions were isolated. Also, in one bombardment with each ion, a thorium fraction was obtained. These fractions were isolated by first dissolving the thick, metallic uranium target and then performing a lanthanum floride precipitation. The precipitate was then dissolved in boric acid and nitric acid and loaded onto an anion exchange column (1 mm × 2 cm, Dowex 1 × 8, 325-400 mesh). The column was first washed with 8 M $HNO_3$ to remove +3 actinides and lanthanides followed by desorption of the thorium using 12M HCl. Plutonium was then removed by elution with 0.2 M HI/12M HCl. Finally, neptunium was removed from the column with 0.1 M HF/4M HCl. The samples were then evaporated onto stainless steel disks for $\beta^-$-counting. Chemical yields are determined by use of α-emitting tracers.

Data from the $^{18}O$ and $^{86}Kr$ bombardments are currently being analyzed. Approximate cross sections have been determined; however, more precise values will be calculated when chemical yields and detection efficiencies have been more accurately determined. Listed in Table 1 are the activities that have been observed in the $^{86}Kr$ bombardments and their production cross sections. It should be noted that it is more meaningful to compare cross sections from the same chemical fraction due to estimates of chemical yields and efficiencies used in calculations. Preliminary analysis of the $^{18}O$ data indicates the production of $^{234}Pu$, $^{245}Pu$, $^{240}Np$, $^{238}Np$, and $^{239}Np$. Also, there is some evidence in the plutonium fraction of an unidentified activity with a half-life of approximately 15 min. Data are presently being collected from the two $^{136}Xe$ experiments. The new activities may be new isotopes or isomers of plutonium and thorium.

Table 1. Thick target cross sections from $^{86}Kr$ + U

| Chemical fraction | Half-life | Nuclide | Cross section |
|---|---|---|---|
| Pu | 4.9 hr | $^{243}Pu$ | 8 μbarn |
| | 10.5 hr | $^{245}Pu$ | 10 μbarn |
| | 10.9 day | $^{246}Pu$ | 8 μbarn(a) |
| | 10-15 min | new activity | 12 μbarn |
| | 40 min | new activity | 20 μbarn |
| Np | 7 min | $^{240m}NP$ | 20 mbarn |
| | 65 min | $^{240}Np$ | 0.5 mbarn |
| | 2.3 day | $^{238}Np$(b) | 0.2 mbarn |
| | | $^{239}Np$(b) | 10 mbarn |
| Th | 29 min | $^{233,235,236}Th$ | 1 mbarn(c) |
| | 26 hr | $^{231}Th$ | 0.6 mbarn |
| | 24 day | $^{234}Th$ | (d) |
| | 2.4 hr | new activity | 0.7 mbarn |

(a) Upper limit.

(b) γ-ray analysis used to distinguish these.

(c) Total cross section.

(d) Large contribution from daughter of $^{238}U$ target material.

Further work will involve characterization of the activities by use of x-ray and γ-ray analysis as well as by further chemical and $\beta^-$-counting studies. Also, the searches will be extended to americium, curium, berkelium, and transberkelium samples in order to map out the yields of heavy isotopes in this region as well as to look for new activities.

Reference

1. A. G. Artyukh, V. V. Volkov, G. F. Gridnev, A. S. Il'inov and V. L. Mikheev, Yad Fiz. 19 (1974).

## NEW ISOMERS IN BISMUTH

P. A. Baisden, R. E. Leber, J. M. Nitschke,
M. Nurmia, and A. Ghiorso

During a search for superheavy elements via the reaction of $^{48}Ca$ with $^{248}Cm$, an alpha activity characterized by a series of high energy alpha lines centered around 10.2 MeV was observed. In addition a less intense line was found at 11.6 MeV. Although the energy of this less abundant line was suggestive of $^{212m}Po$, the activity was observed to decay with a half-life much longer than the characteristic 46s decay of $^{212m}Po$. Shortly after their discovery the possibility of these activities being superheavy elements was ruled out when the same alpha lines appeared in the reaction of $^{40}Ar$ with $^{208}Pb$.

From the information gained in various cross bombardments at the SuperHILAC and taking into account the high energy associated with their decay, these activities were presumed to be nuclides in the lead region. This initial assumption was confirmed chemically in that both the 10.2 and 11.6 MeV activities were co-precipitated with CuS from an acidic solution.

Using the vertical wheel technique[1] excitation functions were measured in the reaction of $^{40}Ar$ with $^{238}U$ for the 10.2 MeV alpha activity and $^{212m}Po$ and are shown in Fig. 1. Although the yield of $^{212m}Po$ was two orders of magnitude larger, the rate of increase of the cross section with energy was not as rapid as that found for the 10.2 MeV alpha group. At the higher energies the production of the 10.2 MeV activity falls off sharply as compared to $^{212m}Po$, which would indicate a difference in the reaction mechanism for the production of the two activities.

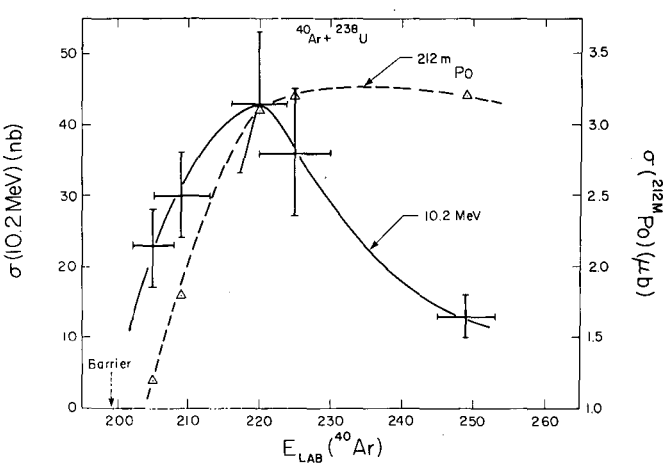


Fig. 1. Excitation functions for the 10.3 MeV alpha activity and $^{212m}Po$ in the reaction $^{40}Ar$ + $^{238}U$. (XBL 778-1655)

Subsequent studies were carried out at the 88-in. cyclotron with 224 MeV $^{40}Ar$ on 2 mil $^{238}U$ targets. The following radiochemical separation procedures designed for elemental differentation of Pb, Bi, Po, and At were performed on the irradiated targets.

After dissolution of the target using a mixture of nitric and hydrochloric acids, the solution was heated to remove the nitric as nitrous oxide. Using a pH-meter the pH was adjusted to 2.5±0.5 with ammonium hydroxide. To his solution 0.5 ml of a 0.1% solution of diphenylthiocarbazone (DTZ) in $CCl_4$ was added. The phases were equilibrated for 1 to 2 min using a vortex mixer. Under these conditions bismuth and polonium were separated from 85 to 90% of the lead by extraction into the organic phase. Astatine was also found in this phase. Although no chemical reagents were introduced to specifically reduce At to the zero-valent state, it is believed that its presence was the result of the interaction of the $At^\circ$ or $At_2$ species with the nonpolar solvent, $CCl_4$. After evaporating the DTZ solution onto a platinum disk, the sample was flamed at about 600°C to remove organic residues.

A typical spectrum obtained from this sample is shown in Fig. 2. With a rather intense, unidentified peak at 6.28 MeV the possibility that the 6.28 MeV line could be associated with the decay of $^{211}Bi$ fed by 36m $^{211}Pb$ was investigated. When the conditions for the extraction step were changed to afford a greater then 99% decontamination from lead this possibility, however, was ruled out. Decay curve analysis yielded within experimental errors the same half-life, 25 ± 2m, for both the 6.28 and 10 MeV alpha activities and a half-life of 5 ± 2m for the 11.6 MeV line.

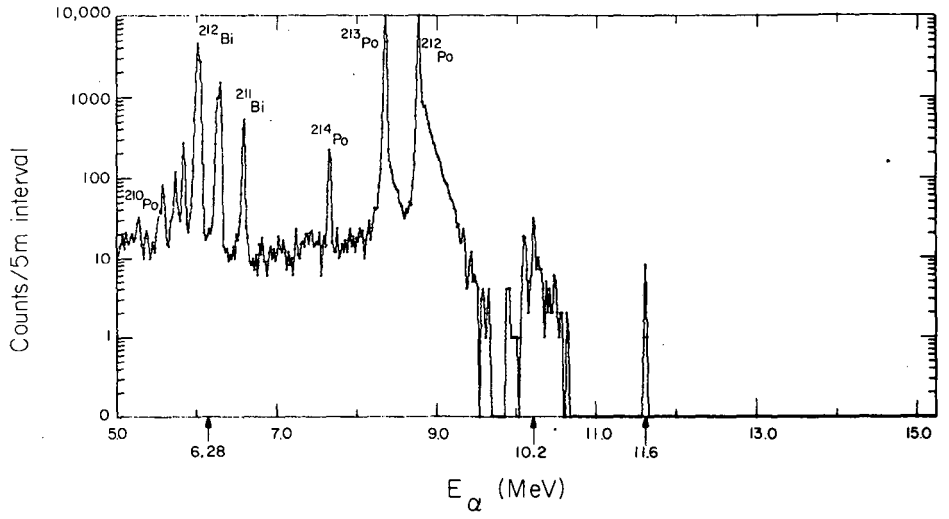


Fig. 2. Alpha spectrum of flamed DTZ sample. (XBL 778-1656)

The chemical identification of the 25m activities was achieved through the technique of residue adsorption or chemisorption.[2] This technique is based on the self-deposition of certain elements onto noble metals followed by separation through selective desorption with an appropriate solvent. This technique proved unambiguously that the 6.28 and 10.3 MeV activities are associated with a bismuth isotope. Due to the fact that the chemistry required 50m, the identity of the 5m 11.6 MeV activity has not yet been determined. Further experiments will be carried out to determine the mass numbers through the decay of the daughter, thallium isotopes.

Since the production of these activities has not been reported in reactions of light heavy ions with lead or bismuth, we believe these activities to be relatively neutron rich. This is further supported by the fact that these activities were produced in higher yields in cross bombardment studies with the more neutron rich target-projectile combinations. The presence of unpaired nucleons ($g_{9/2}$ neutrons and $h_{9/2}$ protons) and the prospect of recoupling correlated neutron pairs outside the $^{208}Pb$ core, suggest that isomeric states would more likely be found in even-mass isotopes of Bi. The energy equivalence of the 11.6 MeV activity with the unique transition in $^{212m}Po$ further suggests that the 5m 11.6 MeV activity results from the beta decay of an isomeric state in $^{212}Bi$ to the known level responsible for $^{212m}Po$. It may be argued that a 25m isomer in $^{214}Bi$ which beta decays to an excited state(s) in $^{214}Po$ gives rise to the 10.2 MeV alpha group. This possibility is supported by the similarity between the line separations in the 10.2 MeV multiplex and the known level spacings in $^{210}Pb$.

In addition to the experiments to determine the mass numbers other studies such as a alpha-gamma coincidence spectroscopy are planned.

## References

1. A. Ghiorso, J. M. Nitschke, J. R. Alonso, C. T. Alonso, M. Nurmia, G. T. Seaborg, E. K. Hulet, and R. W. Lougheed, Phys. Rev. Lett. 33, 1490 (1974).

2. H. W. Kirby, J. Inorg. Nucl. Chem. 35, 2043 (1973).

## BRANCHING DECAYS IN $^{259}$No AND THE NEW NUCLIDE, $^{259}$Md

J. F. Wild,* E. F. Hulet,* R. W. Lougheed,*
J. H. Langrum,* J. M. Nitschke, and A. Ghiorso

The nuclide, $^{259}$No, was discovered some years ago in a joint effort by ORNL and LBL collaborators[1] and found to decay principally by alpha particle emission with a half-life of about one hour. Spontaneous fission was also observed in the chemically spearated nobelium fraction and it was assumed that it was due to a 20% fission branch decay of $^{259}$No.

We have recently bombarded a $^{248}$Cm target with 100 MeV $^{18}$O ions at the 88-in. cyclotron to explore this matter further. In this case we used the recoil technique rather than dissolve the target as was done before to reduce the time for chemical purification. We found that a pure $^{259}$No sample does not exhibit spontaneous fission activity immediately after separation from other actinide elements; however, such activity does grow into the nobelium fraction slowly with a half-life in the hour region. Further experiments showed that mendelevium S.F. activity with a half-life of 95 min could be chemically milked from $^{259}$No samples. We conclude that $^{259}$No does not undergo spontaneous fission to any appreciable extent (< 2%) but that it does branch decay (22%) by electron-capture to $^{259}$Md, which in turn decays principally by spontaneous fission.

Preliminary measurements of coincident fission fragments from $^{259}$Md indicate a spectrum much like that of $^{258}$Fm (which also has 158 neutrons) in that there seems to be a strong symmetric component along with considerable asymmetric fission. Further experiments will be carried out.

### Footnote and Reference

* Lawrence Livermore Laboratory

1. R. J. Silva, P. F. Dittner, M. L. Mallory, O. L. Keller, K. Eskola, P. Eskola, M. J. Nurmia, and A. Ghiorso, Nucl. Phys. A 216, 97 (1973).

## OBSERVATIONS IN THE REACTION OF TWO DOUBLY-MAGIC NUCLEI: $^{208}$Pb AND $^{48}$Ca†

J. M. Nitschke, R. E. Leber, M. J. Nurmia, and A. Ghiorso

All attempts to synthesize superheavy elements via nuclear reactions have failed thus far despite efforts to come as close as possible to the predicted island of stability by using for instance the neutron-rich projectile $^{48}$Ca to bombard the neutron-rich target $^{248}$Cm. Since it is of utmost importance to form superheavy nuclei with as little excitation energy as possible, we have studied a "stand-in reaction" which leads to the formation of a compound nucleus product with well-known properties: $^{208}$Pb($^{48}$Ca, Xn)$^{256-x}$No. The minimum excitation energy is 26.1 MeV. To evaluate the effect of slightly higher excitation energies a very similar system $^{208}$Pb($^{40}$Ar, xn) $^{248-x}$Fm with a minimum excitation energy of 36.4 MeV was studied and compared to the $^{48}$Ca reaction.

The experimental technique consisted of transporting nuclei in a stream of helium seeded with sodium chloride aerosols through a teflon capillary to the surface of a magnesium wheel which is stepped at a predetermined rate to position the activity spots in front of seven surface barrier detectors.

Excitation functions for the $^{208}$Pb(HI,xn) reactions and for transfer products in the Bi-Po region were measured and are shown in Fig. 1. The same figure shows the calculated cross sections for the xn exit channels. The $^{48}$Ca reaction displays two unexpected effects.

1) The onset of the production of the transfer reaction nuclides $^{211}$Bi, $^{211m}$Po, and $^{212m}$Po begins at the same energy as for the compound-nucleus product, $^{254}$No, in sharp contrast to the $^{40}$Ar case where their production begins at an energy 10-15 MeV lower than that of the compound-nucleus product, $^{245}$Fm.

2) The 3n evaporation product $^{253}$No which was calculated to be produced with a cross section of 6μb is not observed above a detection limit of 20nb. The 2n evaporation residue $^{254}$No is seen with a maximum cross section of 3.4 ± 0.4 μb at 227 MeV bombarding energy. Further, the width of the 2n distribution is wider than expected from calculations.

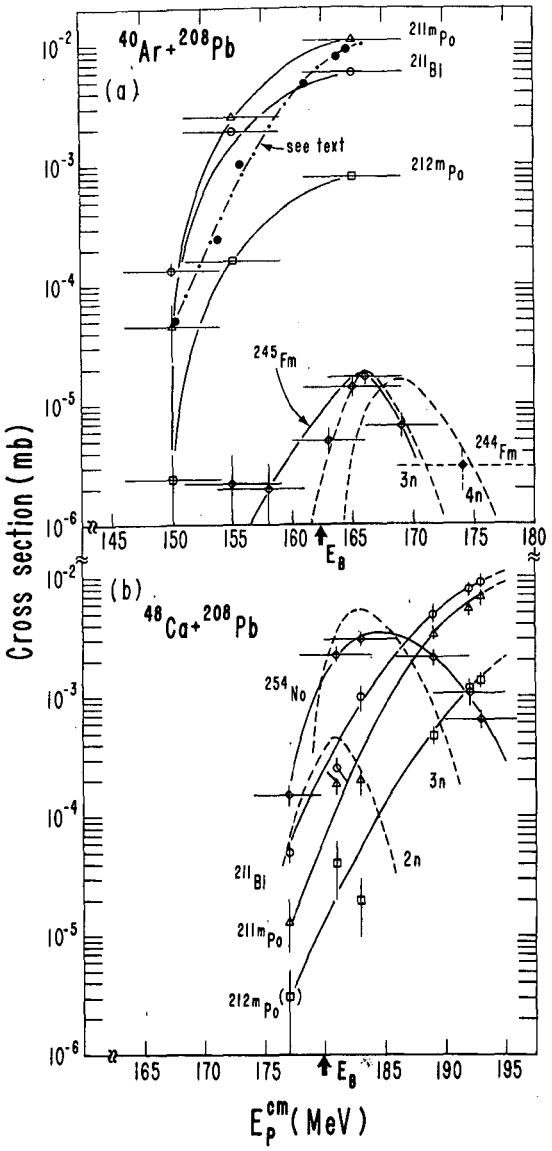


Fig. 1. XBL 776-1085

Our understanding of the displacement of the transfer reaction is based on the observation that the same cluster of transferred nucleons is more strongly bound in $^{48}Ca$ than in $^{40}Ar$. A smaller distance between $^{48}Ca$ and the $^{208}Pb$ nucleus is therefore necessary in order to obtain the same transfer probability.

Taking the reaction $^{208}Pb + 2np \rightarrow {}^{211}Bi$ as a representative case, we calculate from experimental masses that the binding energy for the (2np) cluster in $^{48}Ca$ is 32.23 MeV and in $^{40}Ar$ 28.67 MeV.

Employing a suitably chosen interaction potential we have shown, that in order to obtain the same probability for the transfer of the 2np cluster from the $^{48}Ca$ to the $^{208}Pb$ nucleus as in the $^{40}Ar$ case, the $^{48}Ca$ has to be 0.18 fm closer to the surface of the $^{208}Pb$ nucleus. This can be achieved when the two nuclei have an angular momentum of about 53 ħ and a 10.4 MeV higher center-of-mass energy. To indicate the usefulness of this simple model, the solid dots in Fig. 1(a) indicate the position of $^{211}Bi$ from the $^{48}Ca$ (!) on $^{208}Pb$ reaction transformed into the $^{40}Ar$ - $^{208}Pb$ system and neglecting the additional binding energy of the 2np cluster in the $^{48}Ca$ nucleus.

The fact that the 3n reaction product is not observed in the $^{48}Ca$ on $^{208}Pb$ bombardment contrary to the $^{40}Ar$ on $^{208}Pb$ case is related to the low excitation energy and the higher angular momentum brought in by the $^{48}Ca$ projectile. The maximum angular momentum varies from 30 to 83 ħ over the measured range of the excitation function. The energy difference between the available excitation energy and the lowest yrast state is too small to allow the evaporation of more than 2 neutrons. In the $^{40}Ar$ on $^{208}Pb$ case the evaporation of 3 neutrons becomes possible because of the 10 MeV higher excitation energy in agreement with the experiment.

Footnote

†Condensed from LBL-6534.

## ESTIMATES OF SUPERHEAVY ELEMENT PRODUCTION CROSS SECTION FOR THE REACTION OF $^{48}Ca$ WITH $^{248}Cm$

D. J. Morrissey, W. Loveland,† R. J. Otto, and G. T. Seaborg

In connection with our superheavy element (SHE) research program, our ultimate aim is to evaluate the evaporation residue cross sections for $^{48}Ca$ induced reactions with heavy element targets such as $^{248}Cm$ and $^{238}U$. We have recently completed a search for SHE reaction products produced by the bombardment of $^{248}Cm$ with $^{48}Ca$. No such SHE were observed and upper limit cross sections for their production have been reported.[1,2] As an initial attempt to predict and understand these cross section limits we have used the results of our mass distribution study of the reaction $^{48}Ca + 208_{Pb}$ and the studies of evaporation residue products by Nitschke et al.[3] from the reactions of $^{48}Ca$ and $^{40}Ar$ with $^{208}Pb$.

Nitschke et al. have found that the peak cross section for the neutron evaporation residue, $\sigma_{ER}$, for the reaction $^{208}Pb(^{48}Ca,2n)$ is ∿3 μb, whereas the peak cross section for the reaction $^{208}Pb$

($^{40}$Ar,3n) is 15 nb. Using a modified version of the statistical evaporation code OVERLAID ALICE[4] with the inclusion of realistic fission barriers[5] and a fitted level density parameter ratio $a_f/a_n$ value of 1.1 we are able to reproduce the measured $\sigma_{ER}/\sigma_{CF}$ ratio and to understand these results in terms of the differences in the fission barriers and excitation energies of the nuclei produced. This encouraged us to extend these calculations with these "calibrated" input parameters to the $^{48}$Ca + $^{248}$Cm system. Such an application yields a value of $\sigma_{ER}$ as large as $\sim 10^{-32}$ cm$^2$ at $E_{lab}$ = 240 MeV and $\sigma_{ER}$ $\sim 10^{-36}$ cm$^2$ at $E_{lab}$ = 255 MeV for the $^{248}$Cm($^{48}$Ca,xn) reaction with the predicted element 116 ground state fission barriers.[5] The $^{248}$Cm reaction[1,2] was performed at an average laboratory bombarding energy of 255 MeV and set upper limits on the production cross section for SHE's at $\sim 10^{-35}$ cm$^2$. This result is consistent with our calculation. Although the estimated $\sigma_{ER}$ $\sim 10^{-32}$ cm$^2$ may well be over optimistic, it does give us some hope for further attempts to synthesize SHE with low energy (E~240 MeV) $^{48}$Ca bombardments of $^{248}$Cm, assuming the complete fusion cross section does not become vanishingly small at this near barrier energy.[6]

Footnote and References

†Permanent address: Department of Chemistry, Oregon State University, Corvallis, OR 97331.


1. E. K. Hulet et al., UCRL-79441, Phys. Rev. Lett. 39, 385 (1977).

2. R. J. Otto et al., LBL-6509, to be published in J. Inorg. Nucl. Chem.; see also R. J. Otto et al., A Search for Superheavy Elements with Half-Lives Between a Few Minutes and Several Hundred Days, Produced in the $^{48}$Ca + $^{248}$Cm Reaction, in this Annual Report.

3. J. M. Nitschke, R. E. Leber, M. J. Nurmia and A. Ghiorso, LBL-6534.

4. F. Plasil and M. Blann, Phys. Rev. C 11, 508 (1975).

5. W. D. Myers and W. J. Swiatecki, private communication, 1976.

6. C. F. Tsang, LBL-2366 (1974), p. 146.


## A SEARCH FOR SUPERHEAVY ELEMENTS WITH HALF-LIVES BETWEEN A FEW MINUTES AND SEVERAL HUNDRED DAYS, PRODUCED IN THE $^{48}$Ca + $^{248}$Cm REACTION*


R. J. Otto, D. J. Morrissey, D. Lee, A. Ghiorso, J. M. Nitschke,
G. T. Seaborg, M. M. Fowler,† and R. J. Silva‡


The results of recent unsuccessful attempts to synthesize and identify superheavy elements at the Lawrence Berkeley Laboratory SuperHILAC are described. A thin $^{248}$Cm target was irradiated with $^{48}$Ca ions at an average energy in the target of 255 MeV. Direct counting of thin recoil foils for short-lived spontaneous fission (SF) activity was done. Two long irradiations were also made and radiochemical group separations for the superheavy elements were carried out.

In the first radiochemical experiment (Scheme I), a thin superheavy element sample was prepared and has been continuously counted for spontaneous fission events in a dual surface barrier coincidence counter. In the second experiment (Scheme II), two superheavy element fractions were obtained and were counted for spontaneous fission events; the two fractions contained those elements that co-precipitated with copper sulfide from either an acid or basic solution.

The nonvolatile superheavy element fraction from chemistry Scheme I has been counted for over 230 days. Only one coincidence SF event was observed on the 60th day of counting. The total kinetic energy (TKE) of this event is 215 MeV ($E_1$ = 138 MeV, $E_2$ = 77 MeV) which, although significantly larger than the most probable TKE for SF of $^{248}$Cm, cannot be excluded from the energy distribution of fragments from the SF of an actinide element (see Fig. 1). Four other non-coincident events were also observed. Three of these events have energies between 50 and 60 MeV and one has an energy of 138 MeV. There has been no indication of any decay associated with these events. A CuS-acid sample and CuS-base sample from Scheme II have shown no fission counts over the period these samples have been counted (60 and 90 days).

In a separate experiment in which recoils were collected on Al foils (SF4) three coincident and one non-coincident fission event have been seen. These three events have an average measured TKE of 161 MeV. The average measured TKE for the SF of $^{248}$Cm under identical conditions is 158 MeV. Thus the four events observed in this experiment could very well be due to actinide element SF decay.

As a summary of our results, Fig. 2 shows the upper limit cross sections for the formation of SHE's 108-116 plotted as a function of the assumed half-life of the SHE's. The variation in cross sections is a result of bombardment saturation effects for the short half-lives and

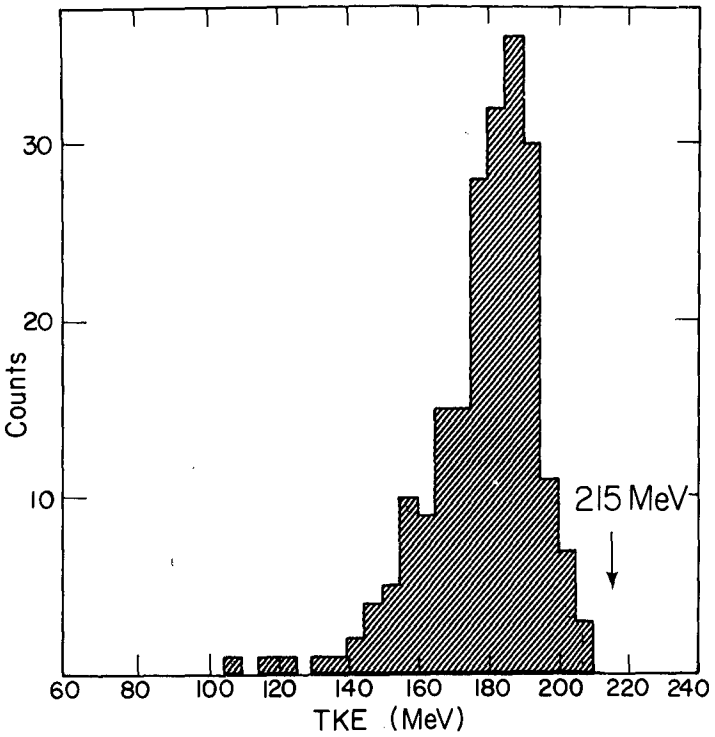


Fig. 1. TKE spectrum from the $^{252}Cf$ calibration. Also shown is the position of the 215 MeV TKE event seen in the first radiochemistry experiment (Scheme I). (XBL 775-1029)

incomplete decay for the half-lives comparable in length to the total counting time.

It is apparent that the small number of SF counts observed in our SHE chemical fractions could be accounted for by the presence of extremely small quantities of actinide isotopes in these chemical fractions or by background SF counts. Thus our results indicate the absence of SHE of half-lives and production cross sections that would be detectable under the conditions of our experiments. A possible exception to this interpretation is the SF event observed with TKE 215 MeV because such a large energy with the asymmetry measured would be observed in less than 0.1% of

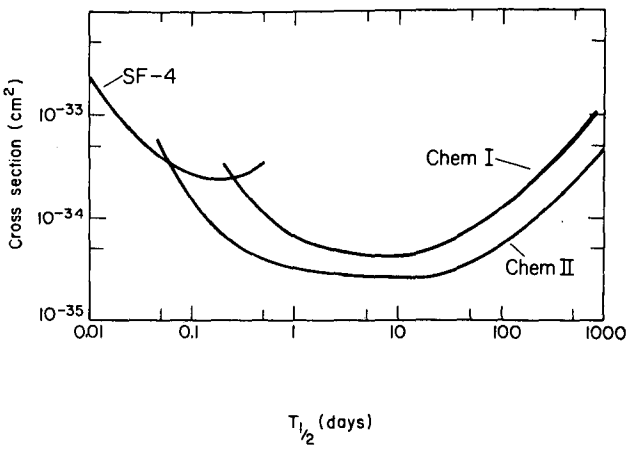


Fig. 2. Upper limit cross sections for SHE's 108-116 plotted vs half-life from this work. The curve labeled SF4 is based on the direct counting experiments. Curves labeled Chem I and Chem II are based on the result of the radiochemistry Schemes I and II respectively. (XBL 775-1033)

the events that might arise from the SF decay due to any known actinide nuclide (see Fig. 1).

Most likely explanations for negative results include: (1) the half-lives may be too short or too long to have been detected; (2) the production cross sections are actually below the limits set by our experiments; and (3) less likely, the actual chemical properties of the SHE's are very different than the predicted properties.

## Footnotes

*Condensed from LBL-6509, to be published in J. Inorg. Nucl. Chem. (1977).

†Permanent address: Los Alamos Scientific Laboratory, Los Alamos, NM 87545

‡Permanent address: Oak Ridge National Laboratory, Oak Ridge, TN 37830

# SEARCHING FOR VOLATILE SUPERHEAVY ELEMENTS*

S. Yashita and R. E. Leber

There have been predictions[1] that through enhanced binding of valence electrons some of the superheavy elements (for example, 112, 114 and 118) may be chemically inert and volatile. Considerations of the finite size of the nucleus, the orbital velocities and the angular momenta of electrons in these high-Z atoms indicate that relativistic effects may significantly influence electron energy and spatial distributions, thereby potentially modifying chemical behavior.

Splitting of the p, d, and f shells into subshells: $j = \ell + 1/2$ and $j = \ell - 1/2$ may stabilize, say, elements 112 and 114 to the extent that their respective $7s^2$ and $7p_{1/2}^2$ configurations will represent shell closures. Thus, both the binding and promotion energies of the valence electrons in these elements would be increased. Radial contraction of low-momentum ($\ell - 1/2$) electrons due to relativistic terms could change the degree of screening of the nuclear charge as well as the "softness" and angular distribution of the electron cloud and thus alter the chemistry of these elements. Evidence in support of predictions of an increase in chemical inertness and volatility of the superheavy elements over their lighter homologs may be obtained by extrapolating the properties of known elements.

Reduced chemical reactivity in the IIB elements is indicated in Fig. 1 by the heat-of-formation curves for the aqueous halides. Of the dihalides, only the fluorides are likely to be stable. The free energies of formation of the element 112 salts will exceed by about 70 kcal/mole, those of the corresponding mercury compounds. Accordingly, only the formation of $(E112)F_2$ will proceed exothermically. (The anionic halide complexes $MCl_4^{2,-3}$ and $MBr_4^{2,-3}$ are predicted to be stable, however.) Empirical data clearly show the increasing endothermicity of reactions with the heavier IIB elements. Hence, unless element 112 (eka-mercury) was to be stabilized as the fluoride or through hybrid bonding strong enough to offset spin-orbit splitting, we would expect it to be relatively inert and volatile. Moreover, depending on the number and binding energy of their valence electrons, other superheavy elements may show similar behavior. Elements with these properties could readily escape from conventional chemistry, so a system to trap and analyze evolved radionuclides has been designed.

Volatile radioactivities have been handled and counted with the apparatus shown in Fig. 2. The gases evolving from target (targets used in these experiments were typically 10-mil uranium collimators) dissolution are trapped on and subsequently desorbed from activiated charcoal. Alpha and fission spectroscopy is performed at high geometry by condensing the gases on a liquid-nitrogen cooled mica disk situated beneath a solid state detector. Prior to its registration in multichannel analysers and scalers, an event is subject to pile-up and noise rejection.

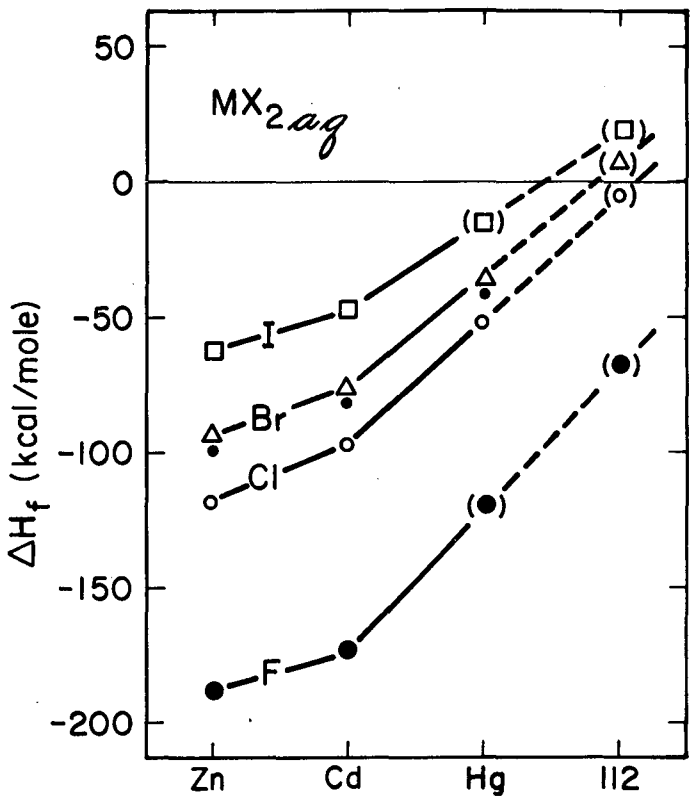


Fig. 1. Systematics of heat of formation for IIB aqueous halides. The unconnected dots represent the free energy of formation for aqueous chlorides. (XBL 774-803)

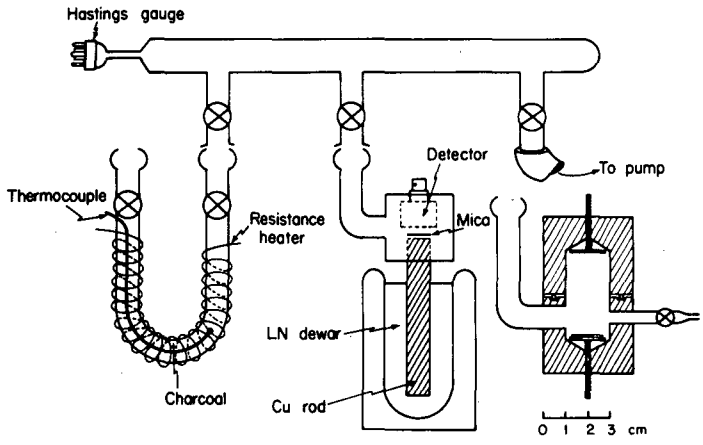


Fig. 2. Line drawing of gas-handling apparatus. (XBL 773-598)

While we cannot establish the production of superheavy elements from these experiments (see Table 1), we did observe a good yield of volatile alpha activity which we have assigned to radon isotopes. Produced in the bombardments of natural uranium with $^{40}Ar$, $^{48}Ca$, $^{86}Kr$, and $^{136}Xe$, radon isotopes 207 through 212 inclusive were identified by the alpha decay and half-lives of their respective astatine electron-capture daughters. The 0.7 ± 0.2 mb production cross section of $^{211}Rn$ estimated for reactions of $^{nat}U$ with full-energy (8.5 MeV/A) $^{136}Xe$ is consistent with mass yields found by Otto, et al.[2] These nuclides result from the exchange of nuclear material between target and projectile nuclei in quasi-fission or deep-inelastic scattering.

These observations cannot be unequivocally attributed either to contaminants or electrical artifacts or to produced radioactivity. If these events are not due to accidental counts, excited states in $^{212}Rn$ or heavy elements--possibly SHE--may be considered as explanations for the data.

Coupling of high-spin particle and hole states outside the $^{208}Pb$ core may yield isomers in $^{212}Rn$ with spins of 20 or more. Placement of these levels at about 8 MeV excitation would indicate the presence of high-energy (roughly 15 MeV) alpha decay to $^{208}Pb$ as well as a virtual fission barrier of only 4 or 5 MeV. In these studies, we have seen--in addition to fission events--evidence for high-energy alpha decay.

Volatile superheavy elements would be produced in these experiments as deep-inelastic transfer products. If the intermediate complex in the $^{136}Xe$ + $^{238}U$ reactions becomes mass equilibrated, the derived charge-to-mass ratio (0.39) would give 302 as the most probable mass for element 118 (eka-radon). The most probable isotope would thus have N = 184, which is expected to be a magic number.

Footnote and References

*Condensed from LBL-6547

1. K. S. Pitzer, J. Chem. Phys. 63, 1032 (1975).

2. R. J. Otto, M. M. Fowler, D. Lee, and G. T. Seaborg, Phys. Rev. Lett. 36, 135 (1976).

## STUDIES OF NEUTRON-DEFICIENT BERKELIUM ISOTOPES

K. E. Williams and G. T. Seaborg

As part of our continuing program concerning the isolation and identification of new actinide isotopes, efforts are being made to identify the neutron-deficient berkelium isotopes-242, 241, 240. Few studies have been made of light berkelium isotopes since those of Chetham-Strode[1] in 1956. In fact, the first berkelium isotope identified[2] is still the lightest berkelium known. By characterizing these lighter berkelium isotopes, we hope to provide further insights into the structure and behavior of neutron-deficient actinides.

The experiments are being performed at the 88-inch cyclotron, making use of the high intensity (several μA) boron beams and the ready availability of uranium isotopes as target material. Recoil nuclei are trapped either on a thin aluminum catcher foil or in a helium-jet system. The chemistry, which is essentially that of Moore,[3] consists of oxidation of Bk(III) to Bk(IV) with dichromate ion followed by a thenoyltrifluoracetone (TTA) extraction of Bk(IV). This procedure provides excellent separation of berkelium from other actinides and lanthanides with the exception of cerium whose oxidation potential is very close to that of berkelium. Other chemistries employed include extraction of Bk(IV) with HDEHP and anion exchange chromatography. The time from the end of bombardment to the detector is less than 30 minutes and should be cut in half in future experiments. The berkelium samples are mounted on standard aluminum cards and are then examined for x-ray and γ-ray emission.

At present, only natural uranium targets have been bombarded. Attention was focused on the production of the known isotopes $^{243,244}Bk$ in order to test the experimental procedure. The combined cross section for $^{238}U(^{10}B, 5/4n)$ $^{243/244}Bk$ was found to be approximately 14 μb at a lab bombarding energy of 60 MeV. Only a combined cross section was obtained since the half-lives of $^{243}Bk$ and $^{244}Bk$ are very close. A preliminary experiment performed at a lab energy of 67 MeV to investigate the $^{238}U(^{10}B,6n)$ reaction failed to produce any detectable amount (<10 μb cross section for half-lives greater than 5 min) of $^{242}Bk$ as determined by the absence of curium x rays in the Bk fraction. A cross section of about 25 μb was expected.

The next experiments will use a $^{235}U$ target and a $^{11}B$ beam. The energy will be optimized for the 4n reaction to produce $^{242}Bk$. This isotope

is predicted to decay by electron capture with a half-life of ~5 to 20 minutes. The berkelium fractions will be examined for both x-ray and γ-ray emission to look for short-lived components in the curium x-ray and in the γ-ray decay. A reasonable cross section for this reaction would be ~50 μb.

References


1. A. Chetham-Strode, Jr., UCRL-3322 (1956).
2. S. G. Thompson, A. Ghiorso, G. T. Seaborg, Phys. Rev. 80, 781 (1950).
3. F. L. Moore, Anal. Chem. 38, 1872 (1966).


# THE PRODUCTION OF TRANSPLUTONIUM ELEMENTS IN THE REACTION OF $^{40}Ar$ WITH $^{238}U$

P. A. Baisden, K. E. Thomas, and G. T. Seaborg

The possibility of synthesis of very heavy elements in heavy ion reactions with heavy targets has received much attention in the past few years particularly with regard to predictions of the existence of an island of stability for nuclei in the region Z=114 and N=184.[1] One of the important results of the search for these heavy elements by means of heavy ions has been the observation of a new reaction mechanism. This new reaction channel, termed multinucleon or deep inelastic transfer, has been found to contribute more significantly to the total cross section than complete fusion in reactions induced by very heavy projectiles such as krypton and xenon.[2]

Much of the information concerning the deep inelastic transfer process has been gained through ΔE/E counter telescope studies of the light fragments formed in these reactions. Since this technique is limited to the study of fragments with $Z \leq 50$, no direct information is obtained about the complementary heavy fragment. Direct observation of these heavy fragments requires radiochemical or radioanalytical methods. The study of the target-like fragments becomes increasingly difficult when high Z targets are employed. For example when using uranium targets the yields of deep inelastic transfer products in this region are severely diminished because of their high fissility and the strong damping of the initial kinetic energy into internal excitation.

However, some estimates have been made for the production of transuranium elements in heavy ion reactions with thorium and uranium targets using experimental data on the light products associated with the multinucleon transfer process.[3] These estimates seem to indicate that this reaction channel may lead to the production of more neutron-rich isotopes of the transuranium elements than those found in light heavy-ion reactions where the complete fusion mechanism predominates.

In order to compliment the over growing amount of kinematic data and to investigate the effect of fission competition with respect to the survival of target-like products formed via deep inelastic collisions, we have begun a systematic study of the production of the transplutonium elements. In this paper we report the results of a radiochemical study of alpha emitting isotopes in this region in the reaction of 340 MeV $^{40}Ar$ ions with $^{238}U$.

Shown in Fig. 1 is the chemical separation procedure used in this work. The separation scheme was designed primarily for rapidly obtaining a pure transplutonium(III) fraction in a form suitable for alpha counting. Since other elements in the vicinity of the target material such as thorium, actinium, and radium are made in very high yields compared to the elements of interest, several chemical steps are required for their removal. Failure to remove these

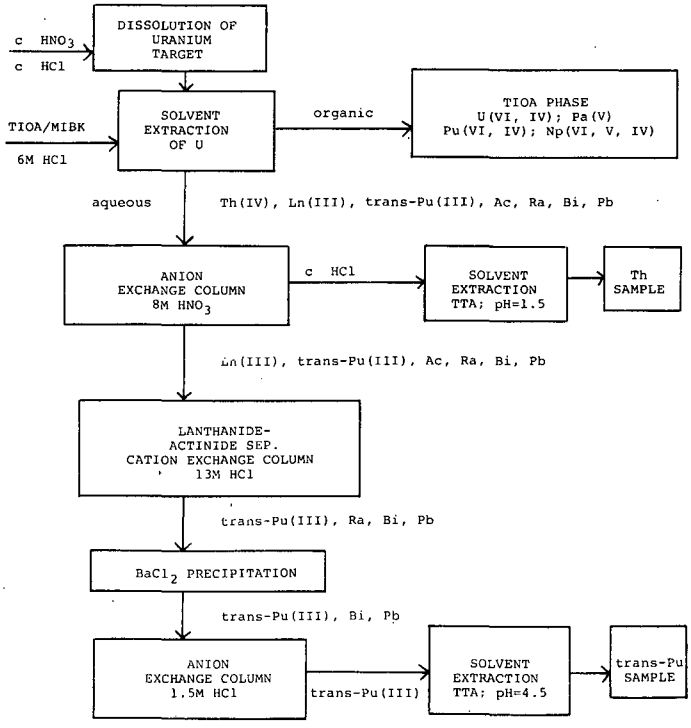


Fig. 1. Radiochemical procedure. (XBL 778-1804)

elements and elements such as lead and bismuth which are either made directly or are present via decay chains, result in very complex alpha spectra. The data analysis then requires deconvolution of complicated decay curves. Thus the design for this work was constrained to rather rapid procedures involving separation factors as large as $10^6$-$10^7$.

The target used was a depleted uranium foil approximately ten mils thick. After receiving a total of $3.4 \times 10^{15}$ particles in slightly over a two hour bombardment in the SuperHILAC the irradiated surface was etched with hydrochloric acid and a small portion of nitric acid. The bulk of the uranium was removed from the acidic chloride solution by extraction into a 20% solution of triisoctylamine (TIOA) in methylisobutyl ketone (MIBK). Due to the fact that thorium does not form polyanionic chloride complexes, it was not removed in this step. Instead thorium was removed by adsorption on an-anion exchange column, (2.5 mm × 2.5 cm Dowex 1 × 8, 325-400 mesh) from a solution of 8M $HNO_3$. The next step in the procedure was a group separation of the lanthanides(III) from the actinides(III) on a cation exchange column using freshly saturated HCl. A 2.5 mm × 2.5 cm column employing a macroporous resin, Bio-Rad MP-50, was used. Under these conditions the order of elution was that of the actinides(III) then the lanthanides(III). Within a given group the heavier elements eluted first. Actinium was sufficiently retained on the column that a separation factor of $10^3$ or greater was obtained for this element with respect to the transplutonium elements. To the solution of 13M HCl from the cation column containing the actinides(III) 1 mg of $BaNO_3$ was added. Upon cooling $BaCl_2$ precipitated carrying with it most of the radium. The precipitation was repeated once. The remaining contaminants, Pb and Bi, were eliminated by adsorption on another anion column (2 mm × 1.7 cm) from 1.5M HCl. After evaporating the transplutonium fraction, the activity was dissolved in a pH=4.5 acetate buffer and extracted into a 0.2M TTA (thenoyltrifluoro-acetone) in benzene. This step offered further decontamination from radium in that radium is not extracted into TTA/benzene under any conditions. Preparation of a weightless alpha source was accomplished by evaporating the TTA/benzene solution onto a platinum disk and flaming to red hot to remove the residue. In addition to the transplutonium sample a thorium sample was also prepared. Thorium was desorbed from the anion column using concentrated HCl and taken to dryness. The source was prepared in an analogous fashion to the actinide(III) sample except that the extraction into the organic TTA phase was from a pH=1.5 aqueous phase. The pulse-height spectra for both chemical fractions were obtained from 300 $mm^2$ silicon barrier detectors.

The isotopes observed and their cross section are given in Table 1. An effective target thickness of 28.5 $mg/cm^2$ was used for the calculation of the cross sections. The results of Wolf et al. for some of these isotopes in the reaction of 288 MeV $^{40}Ar$ with $^{238}U$ are shown for comparison.[4]

Table 1. Thick target cross sections.

| Isotope | $T_{1/2}$ | $\sigma(cm^2)$ 340 MeV | Wolf et al.[4] $\sigma(cm^2)$ 288 MeV |
|---|---|---|---|
| $^{240}Cm$ | 27d | $5.1 \times 10^{-31}$ | $5.9 \times 10^{-31}$ |
| $^{242}Cm$ | 163d | $1.9 \times 10^{-29}$ | $2.8 \times 10^{-29}$ |
| $^{243}Cm$ | 23y | $2.55 \times 10^{-29}$ | $<1.5 \times 10^{-29}$ |
| $^{244}Cm$ | | | |
| $^{245}Cf$ | 44m | $<2.0 \times 10^{-33}$ | -- |
| $^{246}Cf$ | 35.7h | $1.8 \times 10^{-32}$ | $1.4 \times 10^{-31}$ |
| $^{248}Cf$ | 333d | $<3 \times 10^{-35}$ | $<2 \times 10^{-32}$ |
| $^{253}Es$ | 20.5d | $<3 \times 10^{-35}$ | -- |
| $^{254m}Es$ | 39.3h | $<3 \times 10^{-35}$ | -- |
| $^{255}Es$ | 39.8d | $<3 \times 10^{-35}$ | -- |
| $^{256}Es$ | 7.6h | $<5 \times 10^{-35}$ | -- |
| $^{252}Fm$ | 22.8h | $<3 \times 10^{-35}$ | -- |
| $^{254}Fm$ | 3.24h | $<4 \times 10^{-35}$ | -- |
| $^{255}Fm$ | 20.1h | $<3 \times 10^{-35}$ | -- |
| $^{256}Fm$ | 2.63h | $<5 \times 10^{-35}$ | -- |
| $^{226}Th$ | 31m | $4.3 \times 10^{-29}$ | -- |
| $^{227}Th$ | 18.7d | $3.9 \times 10^{-29}$ | -- |
| $^{228}Th$ | 1.9y | $7.3 \times 10^{-29}$ | -- |

The cross sections for the curium isotopes are comparable at the two energies. Possibly the more neutron-rich isotopes are formed in higher yield at the higher energy; here a greater probability for nucleon pickup may outweigh a greater probability for fission. The yield for $^{246}Cf$ appears to be lower at the higher energy which may be due to the predominance of increased fission competition. It should be noted that a direct comparison of thick target cross sections at different energies may be quite misleading, since the energy dependence of the cross sections are not known. No evidence was found for the production of elements heavier than californium. Upper limits for the detection of some of these higher Z elements are also presented in Table 1.

The yields of actinides are being measured in the reactions of $^{86}Kr$ and $^{136}Xe$ with $^{238}U$. An expanded procedure will be employed to include detection of neutron deficient and neutron-rich nuclides by x ray and beta counting, respectively. In this way we hope to find some systematic trends which might enable us to understand more fully the deep inelastic process and the loss of products due to competition with fission.

References

1. C. E. Bemis, Jr., and J. R. Nix, Nucl. Part. Phys. in press (1977).

2. M. Lefort, Y. Le Beyec, and J. Peter, Proc. Int. Conf. on Reactions Between Complex Nuclei, Nashville, TN, June 1974 (North-Holland, Amsterdam, 1974), Vol. II, p.81.

3. A. G. Artyukh, V. V. Volkov, G. F. Gridnev, A. S. Il'inov, and V. L. Mikheev, Yad Fiz. 19, 54 (1974).

4. K. L. Wolf, J. P. Unik, E. P. Horwitz, C. A. A. Bloomquist and W. Delphin, The Production of Trans-Plutonium Nuclides by Bombardment of $^{238}U$ with $^{40}Ar$, $^{84}Kr$, and $^{136}Xe$ Ions, Bull. Am. Phys. Soc. 22(1), 67 (1977).

# A 2.6-MINUTE SPONTANEOUS FISSION ACTIVITY IN THE REACTION $^{10}B + ^{233}U$

L. P. Somerville, A. Ghiorso, M. T. Nurmia, and G. T. Seaborg

The 2.6 min spontaneous fission activity first produced by Dubna experimenters Kuznetsov et al.[1,2] in the reactions $^{11,10}B + ^{233}U$ and $^{10}B + ^{230}Th$ has been verified at the 88-inch cyclotron. In our first experiment 60.2 MeV $^{10}B^{+3}$ ions were incident on a 378 μg/cm$^2$ $^{233}U_3O_8$ target. Recoils from the target were caught on a drum rotating with a speed of 611.3 ± 0.3 sec per revolution. 3.1 cm wide fixed mica track detectors registered the spontaneous fissions about a millimeter from the surface of the rotating drum (see Fig. 1). A total of 416 tracks were observed with 25.1 μA hr of $^{10}B^{+3}$ ions. Figure 1 also includes the decay curve for the spontaneous fission activity. A least squares fit to these data points gave a half-life of 2.6 ± 0.2 min with no background subtracted, in good agreement with the results of Kuznetsov et al.[1] The spontaneous fission tracks were enlarged to a few microns in size by chemical etching in 48% hydrofluoric acid for about 1 hr at 60°C. The mica sheets were scanned by microscope for fission tracks using a x100 power magnification with ~78% measured efficiency. The beam intensity was measured using the rotating drum and target as a Faraday cup. Care was taken to make sure the $^{10}B^{+3}$ beam was properly collimated before reaching the target foil so that the target and drum could be electrically tied together to eliminate any secondary electron effects during beam intensity measurements. A ~33 μg/cm$^2$ aluminum foil was positioned just downstream from the target to stop $^{233}U$ target atoms from being knocked over to the drum where they could contribute background by fissioning under the intense neutron flux generated by the $^{10}B$ beam.

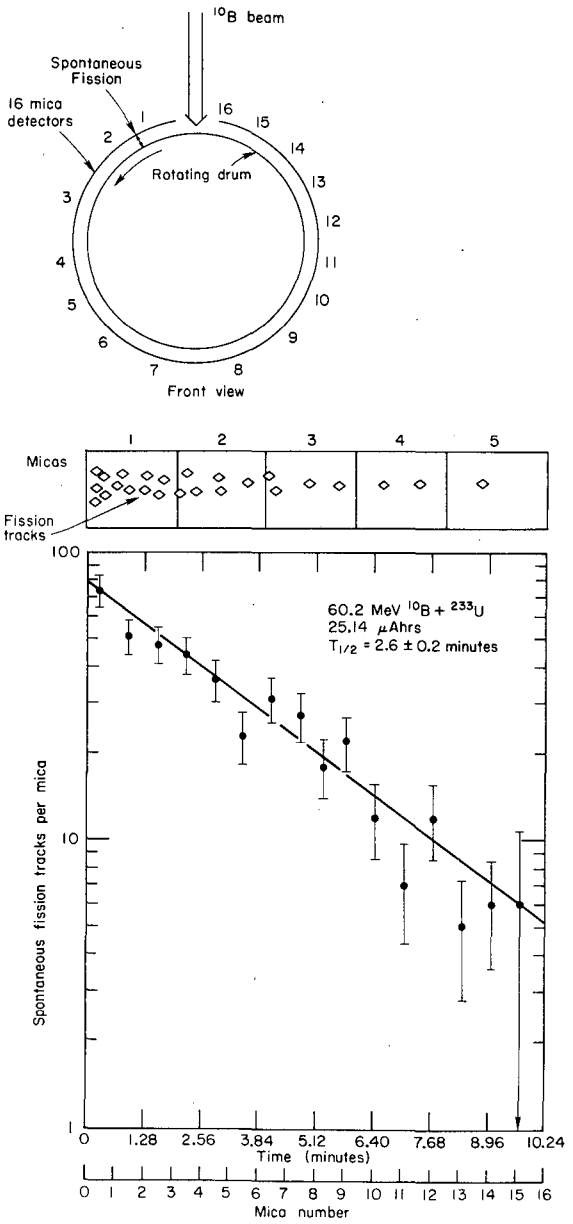


Fig. 1. Rotating drum assembly and decay curve of the spontaneous fissions detected with this assembly in the reaction $^{10}B + ^{233}U$. (XBL 778-1633)

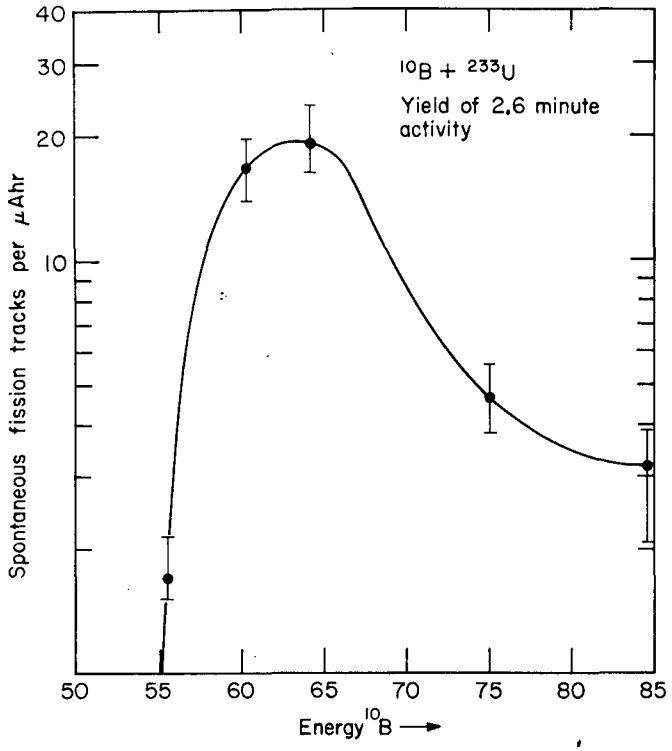


Fig. 2. Yield vs $^{10}B$ energy of the 2.6 minute activity from the reaction $^{10}B + ^{233}U$. (XBL 778-1634)

The yield of tracks/μAhr was measured at several different bombarding energies (55.5-84.6 MeV $^{10}B^{+3}$) for the first time for the reaction $^{10}B + ^{233}U$ (Fig. 2). The cross section to make the 2.6 minute spontaneous fission activity is uncertain due to uncertainty in the recoil range. But in a separate experiment using 64.2 MeV $^{10}B$ with a 177.5 μg/cm$^2$ $^{233}U_3O_8$ target a yield of 18.3 tracks/μA hr was obtained, within 5% of the 19.2 tracks/μA hr produced with a 378 μg/cm$^2$ $^{233}U_3O_8$ target at the same energy. In both cases the ~33 μg/cm$^2$ aluminum foil was placed after the target. Evidently the recoil range is much less than the thickness of the $^{233}U_3O_8$ target (378 μg/cm$^2$) used for the determination of the yield curve of Fig. 2. These two measurements alone indicate that the recoil range must be less than or equal to 284 μg/cm$^2$ $^{233}U_3O_8$. This means that the yield at the peak of the yield curve (Fig. 2) must be at least 9.8 nanobarns. This value is considerably higher than the ~2 nanobarns reported by Kuznetsov et al.[1]

The "5±1 second activity" observed by Kuznetsov et al.[1] in the reaction $^{11}B + ^{233}U$ for $^{11}B$ energies of 75 MeV or more is not observed in any of our recoil $^{10}B + ^{233}U$ experiments at the 88-inch cyclotron. We consider the 5 sec activity to be more likely due to delayed neutron fission of the $^{233}U$ target induced by delayed neutron emitters such as $^{89}Br$ produced by prompt fission of the $^{233}U$ target.

The angular distribution of the 2.6 min activity was measured in a separate experiment using a drum for catching the recoils which was rotated by 24° every 60 sec. This meant that the spontaneous fissions from the drum were concentrated in spots characteristic of the angular distribution in which the recoils were caught on the drum. Unfortunately the substantial broadening of the angular distribution caused by the 3/16-in. target width does not allow us to distinguish between compound nucleus and transfer type reaction mechanisms.

Since we do not make measurements of the spontaneous fission on the $^{233}U$ target directly as Kuznetsov et al. have done,[1] but instead register the decays of recoil atoms only, we can say with confidence that the 2.6-min half-life for decay is not due to fission induced by delayed neutrons in the $^{233}U$ target. Kuznetsov et al.[1] presumed this activity to be due to $^{234}Am$, based on the production of this activity from the reactions $^{10}B + ^{230}Th$ and $^{10,11}B + ^{233}U$. Under the delayed fission hypothesis proposed by Kuznetsov et al.,[1] the $^{234}Am$ nucleus undergoes electron capture decay with a 2.6-min half-life to a short lived fissioning isomeric state of $^{234}Pu$. It is also possible that the 2.6-min activity is due to a 2.6-min fission isomer of $^{234}Am$, although the longest lived fission isomer to date $^{242m}Am$ has a half-life of only 14 msec. Using the predicted Q value[3] for electron capture for $^{234}Am$ and extrapolating the log ft values for electron capture decay of odd-odd Am isotopes[4] gives 3 min for a first approximation for the electron capture half-life of $^{234}Am$. Direct production of $^{234}Pu$ will be attempted in order to establish whether it has a short-lived isomeric state that decays by spontaneous fission. In a future experiment we hope to check the delayed fission hypothesis by looking for Pu K x rays from the electron capture of $^{234}Am$ in coincidence with the fission of $^{234}Pu$.

## References

1. V. I. Kuznetsov, N. K. Skobelev, and G. N. Flerov, J. Nucl. Phys. (USSR) 4, 99 (July 1966).

2. V. I. Kuznetsov, N. K. Skobelev, and G. N. Flerov, J. Nucl. Phys. (USSR) 5, 271 (Feb. 1967).

3. V. E. Viola, Jr. and G. T. Seaborg, J. Inorg. Nucl. Chem. 28, 697 (1966).

4. C. M. Lederer, J. M. Hollander and I. Perlman, Table of Isotopes, Sixth Edition, New York, John Wiley & Sons, Inc., 1967.

# MEASUREMENT OF THE MASSES OF THE UNBOUND NUCLEI $^{16}$Ne, $^{15}$F, AND $^{12}$O*

G. J. Kekelis,† M. S. Zisman, D. K. Scott, R. Jahn,
D. J. Vieira, Joseph Cerny, and F. Ajzenberg-Selove‡

We have been devoting considerable effort to the task of producing, identifying, and measuring the masses of neutron deficient nuclei which are far from the valley of stability.[1] We report on investigations designed to measure the masses of $^{16}$Ne, $^{15}$F, and $^{12}$O via the $^{20}$Ne($^{4}$He,$^{8}$He)$^{16}$Ne, $^{20}$Ne($^{3}$He,$^{8}$Li)$^{15}$F, and $^{16}$O($^{4}$He,$^{8}$He)$^{12}$O reactions. The masses of $^{16}$Ne and $^{12}$O are of particular interest since they have long been postulated to be nuclei which decay by prompt diproton emission.[2] An evaluation of the masses and ground state widths of these nuclei would permit an evaluation of their diproton decay widths.

Beams of 87 and 75 MeV $^{3}$He$^{+2}$ and 117 MeV $^{4}$He$^{+2}$ particles were obtained from the 88-inch cyclotron. After energy analysis, the beam entered a 24 in. scattering chamber, passed through a gas target and was stopped in a split Faraday cup. In order to enhance our ability to measure the expected small differential cross sections for these exotic reactions, it is important to take data at a small angle. Therefore, a special small-angle gas target and associated slit system were designed to operate at angles less than 10°.

Emitted reaction products were collimated, passed through a light-ion parallel plate gas detector[3] (to obtain a time-of-flight signal), and entered the 2 msr solid angle of a Quadrupole-Sextupole-Dipole spectrometer. Particle identification was performed on those particles reaching the focal plane of the spectrometer.[4] Double position measurements were performed in two Borkowski-Kopp proportional counters and differential energy loss information was obtained both from an ion chamber and from the first proportional counter. The residual energy was measured using a plastic scintillator coupled to a photomultiplier tube, (whose anode was used to provide a time-of-flight signal). By combining the two position measurements to obtain trajectory information and gating on all of the above parameters, the system was easily capable of identifying one $^{8}$He particle from more than $10^{7}$ charged particles incident on the detector.

The unknown masses were determined by comparing the rigidities of the emitted $^{8}$He or $^{8}$Li particles to the known rigidities of particles produced in other reactions. Numerous independent measurements were performed to determine the target and time-zero detector thicknesses accurately, since uncertainties in the energy loss of the different charged particles were potentially the largest source of error in these mass measurements.

$^{8}$He energy spectra produced in the $^{20}$Ne($^{4}$He,$^{8}$He)$^{16}$Ne reaction are shown in Fig. 1. The spectrum in Fig. 1c is the kinematically corrected sum of two spectra (Figs. 1a and 1b) which were taken at 117.7 and 117.4 MeV and $\Theta_L = 8°$.

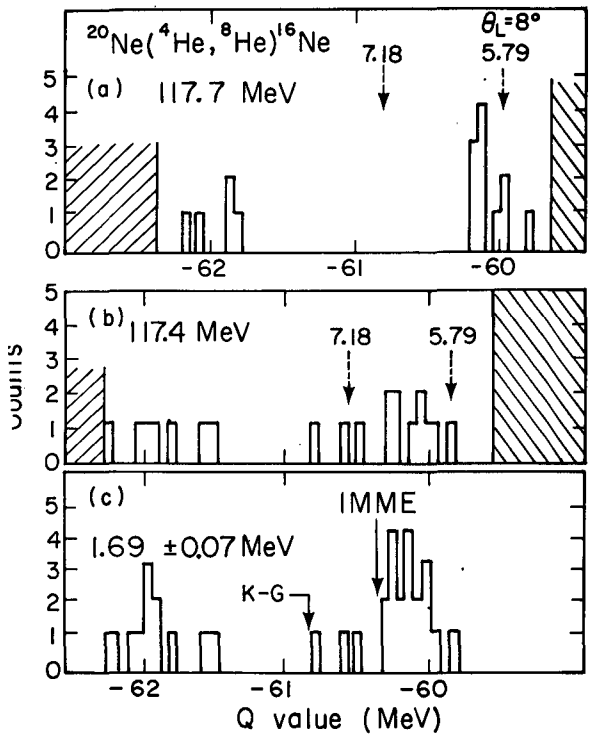


Fig. 1. (a) $^{8}$He-gated position spectrum obtained for the $^{20}$Ne($^{4}$He,$^{8}$He)$^{16}$Ne reaction at 117.7 MeV incident energy. Cross-hatched regions indicate the limits of the detector. The dashed arrows indicate the position of strong $^{20}$Ne inelastic states. (b) As in (a), but at 117.4 MeV. (c) Kinematically corrected sum of (a) and (b). (XBL 776-1454)

The ground state differential cross section is 5±3 nb/sr with $\Gamma_{c.m.}$ = 200 ± 100 keV. The measured reaction Q-value is -60.15±0.08 MeV, which corresponds to a $^{16}$Ne mass excess of 23.92±0.08 MeV. The first excited state at 1.69±0.07 MeV serves to confirm the mass assignment since it agrees well with the energy of the first excited state (1.75 MeV) in the mirror nucleus $^{16}$C.

Figure 2 shows $^{8}$Li energy spectra produced from the $^{20}$Ne($^{3}$He,$^{8}$Li)$^{15}$F reaction at 87.8 and 75.4 MeV. The laboratory differential cross section for the ground state is 8±4 nb/sr and its width is $\Gamma_{c.m.}$ = 0.8±0.3 MeV. The resulting $^{15}$F mass excess is 16.67±0.18 MeV. A Thomas-Ehrman shift of the probable 1/2+ ground state of $^{15}$F could account for the first excited state lying at 1.3±0.1 MeV compared to an excitation of 0.74 MeV in $^{15}$C.[5]

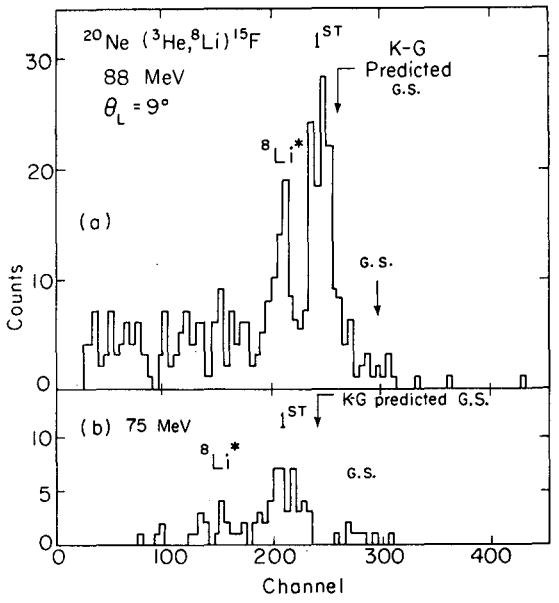


Fig. 2. (a) $^{8}$Li-gated position spectrum obtained for the $^{20}$Ne($^{3}$He,$^{8}$Li)$^{15}$F reaction at 87.8 MeV. The continuum below the $^{8}$Li* peak is due to three-body breakup. (b) As in (a), but at 75.4 MeV incident energy. (XBL 776-1455)

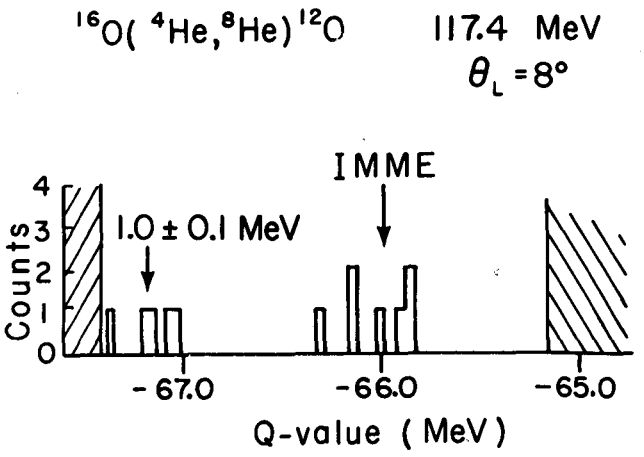


Fig. 3. $^{8}$He-gated position spectrum obtained for the $^{16}$O($^{4}$He,$^{8}$He)$^{12}$O reaction at 117.4 MeV incident energy. Cross hatched regions indicate the limits of the detector. (XBL 776-1456)

Finally, in Fig. 3 we have observed 7 counts attributable to the production of $^{12}$O via the $^{16}$O($^{4}$He,$^{8}$He)$^{12}$O reaction. These correspond to a cross section of 2±1 nb/sr with $\Gamma_{c.m.}$ = 0.40±0.25 MeV. Based on a measured Q-value of -66.02±0.12 MeV, the inferred $^{12}$O mass excess is 32.10±0.12 MeV. Counts perhaps attributable to a first excited state transition at 1.04±0.09 MeV lie at the detector edge. Although $^{12}$O has never been observed prior to this measurement, a first excited state in its mirror nucleus, $^{12}$Be, has been reported at 0.8 MeV by means of the $^{7}$Li($^{7}$Li,$^{2}$p)$^{12}$Be reaction.[6] However, two other reactions, $^{14}$C($^{18}$O,$^{12}$Be) (Ref. 7) and $^{10}$Be(t,p)$^{12}$Be (Ref. 8), report no evidence of a state near 1 MeV and raise doubts as to the location of the first excited state in both $^{12}$O and $^{12}$Be.

As is common for neutron deficient light nuclei, the above mass excesses were found to be smaller than the Kelson-Garvey predictions by 0.7 to 1.0 MeV as shown in Table 1.[9] In contrast the Isobaric Multiplet Mass Equation,[10] which predicts that the masses of an isobaric multiplet should be described by the quadratic equation $M(A,T_z) = a + bT_z + cT_z^2$, provides a reasonably good description of the mass 12 and 16 multiplets even though $^{12}$O and $^{16}$Ne are unbound to prompt proton decay. However, if one continues this perturbation expansion to second order, obtaining a term $dT_z^3$, then the nonzero d-coefficient so obtained has a value of 7±4 keV for mass 16. In this respect mass 16 is similar to mass 8 which also requires a nonzero d-coefficient (d = 6±2 keV).[11] The implications of a nonzero d-coefficient are discussed elsewhere.[10-12]

Finally, the diproton branching ratios for $^{16}$Ne and $^{12}$O were evaluated by calculating the relative penetrabilities of a proton and diproton (the only energetically allowed decays) and assuming the Wigner limit for the reduced width of a proton and diproton. The resulting diproton branching ratios for prompt decay are ~20% and ~40% for $^{16}$Ne and $^{12}$O, respectively. A more realistic estimate for the diproton reduced width, obtained by projecting out (via Moshinsky brackets) a diproton cluster assuming a simple $(1d_{5/2})^2_{0^+}$ configuration for $^{16}$Ne and a $(1p_{1/2})^2_{0^+}$ configuration for $^{12}$O, leads to branching ratios of 3% and 6% for the diproton decays of $^{16}$Ne and $^{12}$O, respectively. These results appear to confirm early predictions of the unique prompt diproton decay in these nuclei.

Table 1.

| Nuclide | Experimental Mass Excess (keV) | Kelson Garvey Prediction (keV) | 1p Binding Energy (keV) | 2p Binding Energy (keV) | $\Gamma_{c.m.}$ (g.s.) (keV) | d[a] (keV) |
|---|---|---|---|---|---|---|
| | | | $T_z$ = -2 Nuclei | | | |
| $^{8}C$ | 35100 ± 30[b] | 35770 | 130±110 | -2150 ± 30 | 230 ± 50[b] | 6.5±2.2 |
| $^{12}O$ | 32100±120 | 33050 | 100±180 | -1820±120 | 400±250[c] | 0±11 |
| $^{16}Ne$ | 23920 ± 80 | 24668 | 40±200 | -1330 ± 80 | 200±100 | 8±5 |
| $^{20}Mg$ | 17570 ± 30 | 17400 | 2650 ± 30 | 2330 ± 30 | - | -2.3±1.8 |
| | | | $T_z$ = -3/2 Nuclei | | | |
| $^{11}N$ | (24920±110[d]) | 25450 | (-1930±110) | (2070±110) | (1500±700)[d] | - |
| $^{13}O$ | 23105 ± 10 | 23520 | 1522 ± 10 | 2123 ± 10 | - | -0.5±2.3 |
| $^{15}F$ | 16670±180 | 17610 | -1370±180 | 3250±180 | 800±300 | - |
| $^{17}Ne$ | 16480 ± 30 | 16630 | 1500 ± 30 | 950 ± 30 | - | 4.8±5.6 |

[a]The d-coefficients for $T_z$=-2 nuclei were calculated using the mass excesses of the $0^+$, T=2 states in the $T_z$=-2,0,1, and 2 nuclei.

[b]Mass excess and natural width of $^{8}C$ are weighted averages of published results.

[c]Because of the poor statistics in the $^{12}O$ ground state the width is only an estimate.

[d]"Experimental" mass excess of $^{11}N$ is an IMME prediction using the $1/2^+$, T=3/2 states in $T_z$=-1/2,1/2, and 3/2 nuclei. The width is estimated relative to that for the known $^{11}N$ first-excited state.

## Footnotes and References

*Condensed from LBL-6557.

†Present address: Williams College, Williamstown, MA 01267.

‡Permanent address: Dept. of Physics, Univ. of Pennsylvania, Philadelphia, PA 19174.


1. See Nuclear Science Annual Report, 1975 (LBL-5075) pp. 81,88,89.
2. V. I. Goldanski, Nucl. Phys. 19, 482 (1960).
3. G. KeKelis and G. Gabor, Nuclear Science Annual Report, 1975 (LBL-5075) p. 352.
4. B. G. Harvey, J. Mahoney, and R. F. Burton, Nuclear Science Annual Report, 1975 (LBL-5075) p. 354.
5. A. M. Lane and R. G. Thomas, Rev. Mod. Phys. 30, 257 (1958).
6. H. H. Howard, R. H. Stokes, and B. H. Erkkila, Phys. Rev. Letts. 27, 1086 (1971).
7. G. C. Ball, J. G. Costa, W. G. Davies, J. S. Forster, J. C. Hardy, and A. B. McDonald, Phys. Letts. 49B, 33 (1974).
8. D. E. Alburger, D. P. Balamuth, J. M. Lind, L. Mulligan, K. C. Young, R. W. Zurmühle, and R. Middleton, unpublished abstract.
9. I. Kelson and G. T. Garvey, Phys. Letts. 23, 689 (1966).
10. E. P. Wigner, in Proceedings of Robert A. Welch Foundation Conferences of Chemical Research, edited by W. D. Milligan (Robert A. Welch Foundation, Houston, Texas, 1957) p. 67.
11. R. E. Tribble, R. A. Kenefick, and R. L. Spross, Phys. Rev. C 13, 50 (1976).
12. D. H. Wilkinson, Phys. Rev. Letts. 13, 571 (1964).

# OBSERVATION OF THE NEW NUCLIDES $^{27}$Ne, $^{31}$Mg, $^{32}$Mg, $^{34}$Al, AND $^{39}$P*

G. W. Butler,† D. G. Perry,† L. P. Remsberg,‡
A. M. Poskanzer, J. B. Natowitz,§ and F. Plasil||

We report the observation of five new neutron-rich nuclides, $^{27}$Ne, $^{31}$Mg, $^{32}$Mg, $^{34}$Al, and $^{39}$P, among the fragments produced by the interaction of the LAMPF 800-MeV proton beam with a uranium target. The fragment Z was identified with a silicon ΔE-E detector telescope, and the mass number was determined by a time-of-flight method which utilizes the rf microstructure (~0.5 nsec wide pulses at a frequency of 201.25 MHz) of the primary beam to provide one of the two timing signals. The high beam current (35 μa at the time of this experiment) made it practical to use a very long flight path (4.3 m) to achieve excellent fragment mass resolution. Because the fragment flight times are much longer than the rf period, they are uncertain by an unknown multiple of this period. Thus, an essential component of this method is the simultaneous time-of-flight measurement over a short flight path between the ΔE and E detectors to obtain the fragment velocity with sufficient accuracy to determine the number of rf periods in the flight time over the long flight path. This new technique extends the ΔE-E, time-of-flight method of nuclide identification[1,2] up to a mass number of ~40.

The experiment was carried out in the thin target area at LAMPF. The 800-MeV proton beam passed through a 3.5 mg/cm$^2$ uranium target mounted in a scattering chamber which is about 12 m upstream of the first pion production target. The ΔE and E detectors were in a detector box at the end of a 4 m flight tube which was connected to the scattering chamber at an angle of 45°. A 1-m thick concrete shield separates the room containing the detector box from the scattering chamber and the primary proton beam line. The long flight path from the target to the ΔE detector was 433 cm, and the short flight path between the ΔE and E detectors was 39 cm. The short flight path distance was chosen to insure a total lack of ambiguity in the calculation of the long flight path flight time while minimizing the loss of events due to multiple coulomb scattering in the ΔE detector. The aluminum target ladder, which was insulated from the scattering chamber, was used as a beam pickoff. The zero-crossing point of the output of a fast, bipolar amplifier which was DC coupled to the ladder was used to derive the beam pickoff signal. The time measured was the interval between the ΔE fast timing signal and the next following beam pickoff signal. About 350,000 events of the elements B through Ar were collected during a 5-day period. Events for which the residual fragment energy E was between 15 and 60 MeV were selected for analysis. A time resolution of 150 psec (FWHM) was achieved for the short flight path, and the time resolution for the long flight path was 0.5 nsec.

The results are shown in the form of a scatter plot in Z and A in Fig. 1. The good

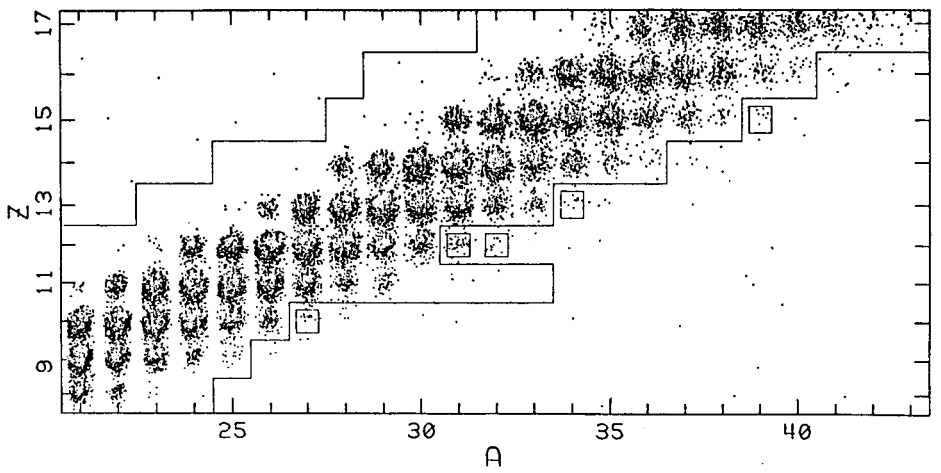


Fig. 1. Distribution in Z and A of fragments detected. Each dot represents one event. The boxes outline the regions of the nuclides $^{27}$Ne, $^{31}$Mg, $^{32}$Mg, $^{34}$Al, and $^{39}$P. The solid lines enclose the region of previously known nuclei (Ref. 3).
(XBL 777-9537)

resolution in both parameters is clear, and, more importantly, it can be seen that there is no tailing, in any direction, from an abundant peak into the region of a lightly populated one. All of the stable and known[3] neutron-rich nuclides (except for $^{24}O$ and the more neutron-rich Na isotopes) are seen. The five previously unobserved neutron-rich nuclides $^{27}Ne$, $^{31}Mg$, $^{32}Mg$, $^{34}Al$, and $^{39}P$ are clearly evident; each of these peaks contains 10 or more events. There are five additional nuclides whose existence is suggested by from 3 to 6 events each, but we do not consider this evidence to be conclusive. Elemental mass spectra, cuts through Fig. 1 with windows on the Z peaks, are shown in Fig. 2 for the elements Ne, Mg, Al, and P. The five new nuclides appear as peaks, and it can be seen that the yields of these nuclides follow systematic trends from the yields of the known nuclides. The energy spectra of these nuclides were found to be consistent with those of the adjacent known nuclides.

All of these new nuclides have been predicted to be particle stable.[4] Because of the pairing energy effect, the particle stability of $^{27}Ne$ and $^{34}Al$ strongly implies that $^{28}Ne$ and $^{35}Al$ should also be particle stable. The nuclide $^{33}Mg$ is predicted to be bound by only 0.48 MeV,[4] a value which is close to the expected uncertainty of the predictions, and it would thus be of interest, with an order of magnitude more data, to see if it can be observed.

The yields shown in Fig. 2 cannot be considered as relative cross sections because of energy windows, multiple scattering losses, etc., but they are likely to be correct to within a factor of two. The yield distribution of Na isotopes as far as was measured in this work agreed within a factor of two with the cross-section distribution of Na isotopes produced by the irradiation of uranium by 24-GeV protons,[5] although the absolute values of the cross sections are considerably lower at 800 MeV. This suggests that at least some aspects of the mechanisms of the production of these light fragments from the proton bombardment of heavy element targets do not change over this range of proton energies. It also shows that the irradiation of uranium by a very intense 800-MeV proton beam is a good method for the production of light, highly neutron-rich nuclides.

We thank the staff at LAMPF for major support in installing this experiment and Don Landis for extensive help with the electronics.

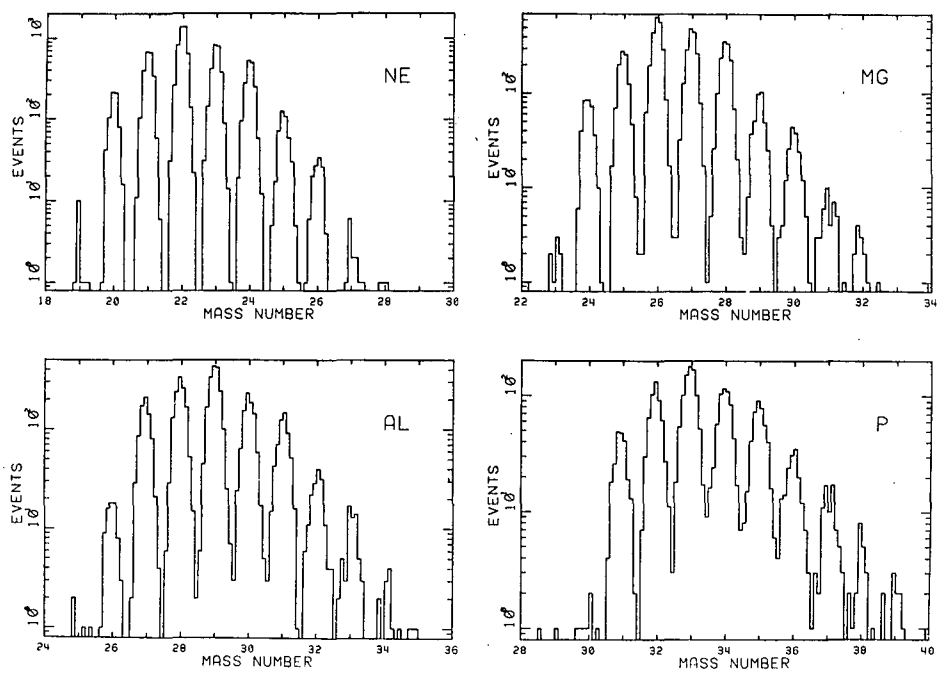


Fig. 2. Mass spectra for the elements Ne, Mg, Al, and P.
(XBL 777-9538)

## Footnotes and References

*Condensed from Phys. Rev. Lett. 38, 1380 (1977).

†Los Alamos Scientific Laboratory, Los Alamos, NM 87545

‡Brookhaven National Laboratory, Upton, NY 11973

§Texas A & M University, College Station, TX 77843

‖Oak Ridge National Laboratory, Oak Ridge, TN 37830

1. G. W. Butler, A. M. Poskanzer, and D. A. Landis, Nucl. Instrum. Meth. 89, 189 (1970).

2. J. D. Bowman, A. M. Poskanzer, R. G. Korteling, and G. W. Butler, Phys. Rev. C 9, 836 (1974).

3. Studies of Exotic Light Nuclei, J. Cerny, Proceedings of the 3rd International Conference on Nuclei Far from Stability, CERN Report 76-13, p. 225 (1976).

4. C. Thibault and R. Klapisch, Phys. Rev. C 9, 793 (1974).

5. R. Klapisch, C. Thibault, A. M. Poskanzer, R. Prieels, C. Rigaud, and E. Roeckl, Phys. Rev. Lett. 29, 1254 (1972).

# B. NUCLEAR REACTIONS AND SCATTERING

## 1. Microscopic

### POLARIZATION IN PROTON-DEUTERON SCATTERING AT 50 MeV*

N. S. P. King,† J. L. Romero, ‡ and J. Ullmann‡
H. E. Conzett, R. M. Larimer, and R. Roy§

Although considerable progress in three-nucleon calculations has been made, a successful detailed reproduction of the experimental nucleon analyzing powers in N-d elastic scattering has not been made. At proton energies above 35 MeV the experimental uncertainties in the existing $\vec{p}$-d analyzing powers are such that the steadily improving quality of the predictions may soon require more precise data to test various theoretical assumptions. In particular, at 50 MeV[1] uncertainties of ∿20% in the analyzing power occur near the negative maximum at $\theta_{c.m.} = 120°$, where calculations of both cross sections and analyzing powers are sensitive to the details of the two-nucleon $^3S_1$-$^3D_1$ tensor interaction.[2,3]

Also, since charge symmetry of nuclear forces implies equality between the nucleon analyzing powers in $\vec{p}$-d and $\vec{n}$-d scattering except for Coulomb contributions, several experimental comparisons of these analyzing powers have been made at lower energies. Earlier differences between those measurements near 17 and 22 MeV have been resolved, and the only remaining discrepancy between p-d and n-d measurements exists at 35 MeV. A detailed comparison of these analyzing powers is now being undertaken[4] at 50 MeV in which the absolute uncertainties in the neutron data are ±0.07 and below. Thus, for this comparison, we have measured the $\vec{p}$-d analyzing power near 50 MeV with the considerably improved accuracy that is possible with the presently available polarized beam intensities.

In brief, a 49.5 polarized proton beam from the Berkeley 88-inch cyclotron was transported to a 36-in scattering chamber and focused onto a deuterium gas target cell with 0.001-in Havar windows. The target gas and foil degraded the beam energy to 49.3 MeV at the center of the gas cell. Beam alignment in the chamber was maintained by a series of rectangular slits upstream from the chamber, immediately in front of the target, and at the exit port. Silicon charged-particle detectors were placed at equal angles on opposite sides of the beam, two on each side. Particle identification was utilized to obtain both proton and deuteron data. A double slit system limited the angular acceptance of the detectors to ±0.25° resulting in negligible finite angular corrections. Detector angles were accurate to 0.1°. A helium gas cell along with a pair of silicon detectors at equal left and right scattering angles were located in a smaller scattering chamber downstream from the main chamber to provide a continuous monitoring of the beam polarization. A 479.9 mg/cm$^2$ aluminum beam degrader was placed between the two chambers resulting in a 44.1 MeV beam at the polarimeter scattering center. At the polarimeter scattering angle of $\theta_L = 130°$, the p-$^4$He analyzing power was taken to be 0.87±0.02, the value calculated from p-$^4$He phase shifts interpolated between 40 MeV[5] and 48 MeV[6]. This value is 5% lower than that given by an interpolation between the experimental values at 39.8 and 45.0 MeV.[7] An examination of those data revealed that the 45.0 MeV, $\theta_L = 130°$ point was not consistent with a smooth variation of the analyzing power as a function of angle and energy. Since the 44.1 MeV calculated value at that particular angle is quite insensitive to allowable small changes in some of the phase shifts, we take it to be the more reliable result. Typical beam polarizations were 0.80 throughout the experiment.

The analyzing power is plotted in Fig. 1. Quoted uncertainties are based on statistics and

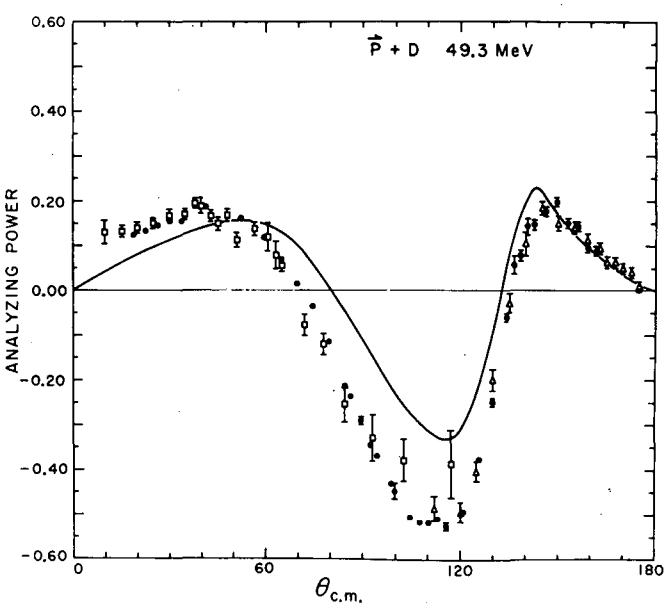


Fig. 1. The $\vec{p}$ + d analyzing power at 49.3 MeV. Solid circles are the present work. The open triangles and squares are data from Ref. 6. The calculated curve is from Ref. 3. (XBL 778-9849)

do not include uncertainties associated with the p-$^4$He analyzing power. Reasonable agreement with previous results occurs for most angles except at far forward angles where a trend to lower analyzing powers occurs and in the negative maximum where larger values are obtained. The smooth curve is a theoretical prediction from Ref. 3 at 46 MeV utilizing the Reid soft core nucleon-nucleon interaction.

Footnotes and References

*Condensed from LBL-5849, submitted to Phys. Lett.

†Present address: Los Alamos Scientific Laboratory, Los Alamos, New Mexico.

‡Physics Department, University of California, Davis, California.

§Present address: Physics Department, Laval University, Quebec, Canada.

1. A. R. Johnston, W. R. Gibson, E. A. McClatchie, J. N. P. C. Megaw, and R. J. Griffiths, Phys. Lett. 21, 309 (1966).

2. P. Doleschall, Nucl. Phys. A 220, 491 (1974).

3. C. Stolk and J. A. Tjon, Phys. Rev. Lett. 35, 985 (1975).

4. N. S. P. King et al., to be published.

5. G. R. Plattner, A. D. Bacher, and H. E. Conzett, Phys. Rev. C 5, 1158 (1972).

6. B. W. Davies, M. K. Craddock, R. C. Hanna, Z. J. Moroz, and L. P. Robertson, Nuclear Physics A 97, 241 (1967).

7. A. D. Bacher, G. R. Plattner, H. E. Conzett, D. J. Clark, H. Grunder, and W. F. Tivol, Phys. Rev. C 5, 1147 (1972).

## TENSOR ANALYZING POWER IN $\vec{d}$-p SCATTERING AT 45.4 MeV*

R. Roy,† H. E. Conzett, B. T. Leemann, F. N. Rad,‡ and E. J. Stephenson

A primary goal of the three-body theory has certainly been to reproduce the three-nucleon experimental data from exact calculations (via the Faddeev equations) that use the known two-nucleon forces. During the past few years, considerable success has been achieved in fitting the cross-section and polarization data in nucleon-deuteron elastic scattering.[1] The principal remaining discrepancy is the failure to provide a quantitative fit to both the nucleon and deuteron vector analyzing powers at scattering angles forward of $\theta_{cm} = 120°$[2,3]. Doleschall's calculation[2] shows that the vector analyzing powers are quite sensitive to the details of the input nucleon-nucleon ($^3S_1$-$^3D_1$) tensor interaction; thus it seems likely that this discrepancy is coupled to the difficulty in providing a separable tensor interaction which simultaneously reproduces the $^3S_1$,$^3D_1$ phase shifts and the corresponding mixing parameter $\varepsilon_1$.[2]

Since the calculations at $E_N = 22.7$ MeV also show a significant sensitivity of the deuteron tensor polarizations to changes in the nucleon-nucleon tensor interaction, we have made measurements of the tensor analyzing powers $T_{20}$ and $T_{22}$ in $\vec{d}$-p scattering at $E_{\vec{d}} = 45.4$ MeV for direct comparison with the calculated results at the equivalent nucleon energy of 22.7 MeV. Figs. 1 and 2 show our experimental results along with the calculated predictions[2] for three different tensor forces, all of which assumed a deuteron D-state probability of 4%. The solid curves were obtained with the Yamaguchi tensor force (YY4), which fit only the $^3S_1$ nucleon-nucleon phase shifts; the dotted curves, with a force (T4M) which fit the $^3S_1$ phase shifts and $\varepsilon_1$ but not the $^3D_1$ phase shifts. Although the shapes of the calculated curves are in good accord with the data, it is clear that quantitative agreement is lacking.

Although the T4D force fits the $T_{20}$ data very well except near $\theta_{cm} = 120°$, neither the T4D nor the T4M force provides a very good fit to the $T_{22}$ data. Doleschall[4] has very recently constructed a

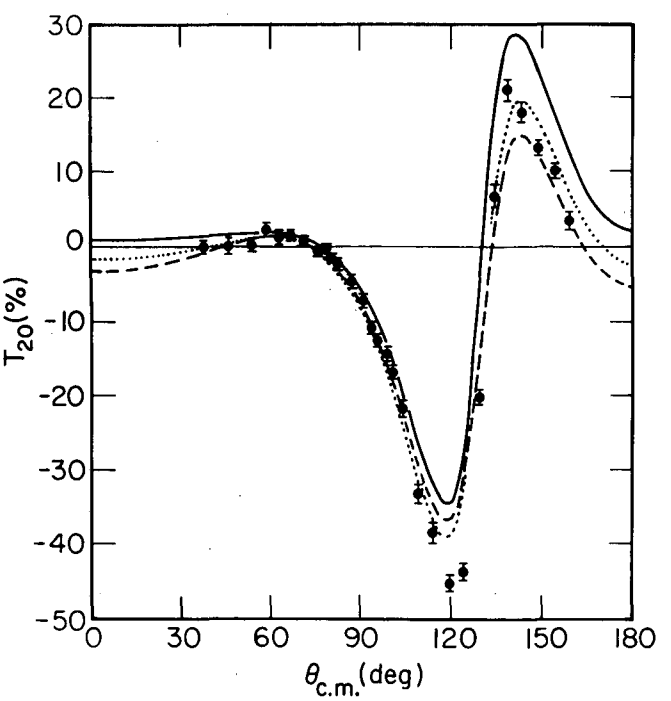


Fig. 1. The deuteron tensor analyzing power $T_{20}$ in $\vec{d}$-p elastic scattering at 45.4 MeV. The curves are calculated results from Ref. 2. As explained in the text, they correspond to different forms of the input two-nucleon tensor interaction.

(XBL 764-2770)

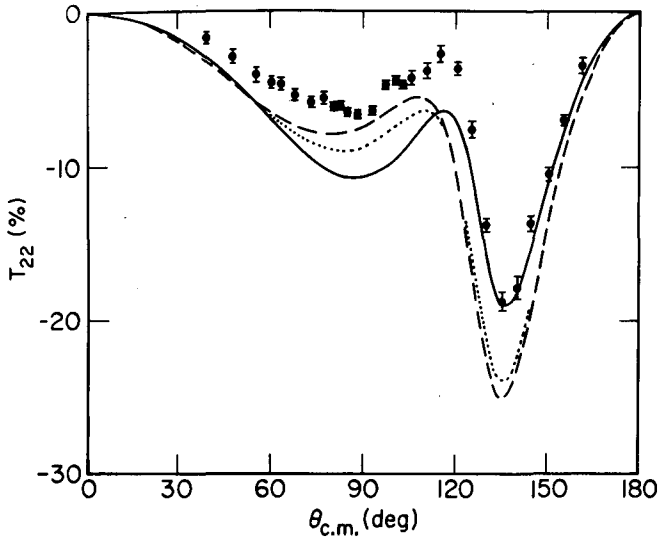


Fig. 2. The deuteron tensor analyzing power $T_{22}$ in $\vec{d}$-p elastic scattering at 45.4 MeV. The curves are as in Fig. 1.
(XBL 764-2771)

separable tensor potential which provides agreement with both the $^3S_1$, $^3D_1$ phase shifts and $\varepsilon_1$, so it will be most interesting to see if the forthcoming results calculated with this potential are in improved agreement with the several experimental observables that have now been measured in $\vec{p}$-d elastic scattering.

Footnotes and References

*Presented at the International Conference on Nuclear Structure, Tokyo, September 5-10, 1977.

†Physics Department, Laval University, Quebec, Canada.

‡Laboratory of Nuclear Science, MIT, Cambridge, Massachusetts.

1. H. E. Conzett, Few Body Problems in Nuclear and Particle Physics, ed. R. J. Slobodrian et al. (Laval University Press, Quebec, 1975, p. 566.

2. P. Doleschall, Nucl. Phys. A220, 491 (1974).

3. F. N. Rad et al., Phys. Rev. Lett. 20, 1227 (1974).

4. P. Doleschall, private communication.

## GIANT DIPOLE RESONANCE EFFECTS IN THE ELASTIC SCATTERING OF POLARIZED PROTONS FROM $^{24}$Mg, $^{27}$Al, AND $^{32}$S*

R. Roy,† C. R. Lamontagne,† R. J. Slobodrian,† J. Arvieux,‡ J. Birchall,§ R. M. Larimer, and H. E. Conzett

Proton elastic cross section and asymmetries have been measured from $^{24}$Mg, $^{27}$Al, and $^{32}$S nuclei between 13 and 27 MeV in 2 MeV steps with the polarized proton beam of the Berkeley 88-in cyclotron. The experimental facility and methods have been described elsewhere.[1,2] For each nucleus, an optical model (OM) analysis using the code MAGALI[3] has been performed on the cross section and analyzing power data simultaneously. As done previously[2] on $^{28}$Si, only the forward angle data have been used in the OM analysis in an attempt to determine unambiguously the spin-orbit (SO) interaction.[4] The final sets of parameters were obtained by minimizing the total $\chi^2$ searching on potential values and keeping fixed the geometry parameters throughout the energy range for a given nucleus. Fig. 1 shows the variation of the SO potential for each nucleus. For comparison, the values[2] for $^{28}$Si are plotted. In each case, the maximum corresponds in energy to the expected location of the giant dipole resonance of the target nucleus plus a proton. The complete angular distributions are in general well represented by the sets of parameters obtained as described above. Similar effects have been observed both up and down in the nuclide chart by other experiments,[5] and it seems then to be of general nature.

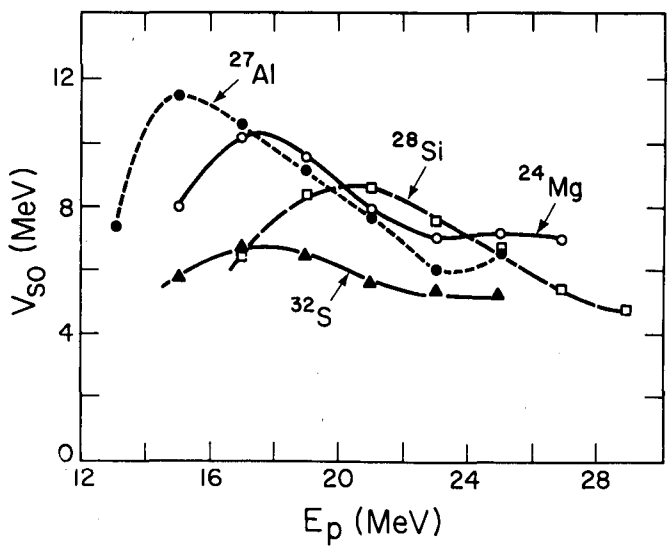


Fig. 1. Energy variation of the proton spin-orbit potentials, $V_{SO}$, for $^{24}$Mg, $^{27}$Al, $^{28}$Si, and $^{32}$S. The curves serve only to guide the eye. (XBL 778-1609)

Footnotes and References

*Submitted to the International Conference on Nuclear Structure, Tokyo, September 5-10, 1977.

†Physics Department, Laval University, Quebec, Canada.

‡Institute of Nuclear Sciences, University of Grenoble, France.

§Physics Department, University of Manitoba, Winnipeg, Manitoba, Canada.

1. A. D. Bacher et al., Phys. Rev. C 5, 1147 (1972).

2. C. R. Lamontagne et al., Phys. Lett. 45B, 465 (1973).

3. J. Raynal, 1969 D. Ph. T/69, 42 (CEN Saclay).

4. G. R. Satchler, Nucl. Phys. A 92, 273 (1967).

5. H. R. Weller et al., Phys. Rev. C 13, 1055 (1976) and references therein.

# TENSOR ANALYZING POWERS IN $^{58}$Ni(d,d)$^{58}$Ni ELASTIC SCATTERING AT 45 MeV*

E. J. Stephenson, H. E. Conzett, G. Delic,† B. T. Leemann, and B. A. Robson‡

Recently, Ioanides and Johnson[1] and Austern[2] have investigated the changes in deuteron internal structure that occur as the deuteron penetrates the nucleus. They found significant changes inside nuclear matter due to Pauli exclusion for deuteron energies near 100 MeV. In addition, they found that these changes could be represented by a tensor term in the optical potential whose spin dependence is given by

$$T_p = (\vec{S}\cdot\vec{P})^2 - \frac{2}{3}P^2 \quad , \qquad (1)$$

where $\vec{S}$ is the deuteron spin and $\vec{P}$ is the motion of its center of mass. Such tensor terms may be investigated[3] through the measurement of tensor analyzing powers, i.e., the fractional change in the scattering cross section that occurs when the beam is tensor polarized or aligned. In addition, Goddard[4] has recently completed work on an optical model program that includes the Tp potential, thus making theoretical calculations possible for such an experiment.

Several previous measurements[5] have been made of deuteron elastic scattering tensor analyzing powers at lower energies, but the investigations which followed have focused on the effects of the $T_R$ potential. This potential, which arises from the influence of the deuteron D-state on elastic scattering, depends on deuteron spin according to

$$T_R = (\vec{S}\cdot\hat{r})^2 - \frac{2}{3} \quad , \qquad (2)$$

where $\hat{r}$ is the nucleus-deuteron radius vector. In only a limited number of cases[5] has the use of this potential led to a successful model for the tensor analyzing power measurements. Thus it seems appropriate to investigate whether the inclusion of the momentum-dependent Tp potential would lead to a more successful interpretation of such measurements. It was felt that new measurements were needed at higher energies where the Tp interaction was expected to be more important.

We chose to measure the elastic scattering tensor analyzing powers at 45 MeV to look for evidence of deuteron-nucleus tensor forces, with particular emphasis upon the momentum-dependent term. Cross section and vector analyzing power were also measured to assist in the selection of optical model parameters for the central and spin-orbit potential terms.

At the Berkeley 88-in. cyclotron, the quantization axis of the polarized beam is perpendicular to the beam direction. By rotating the plane of the scattering chamber about the beam line, measurements were made of the two tensor analyzing powers, $A_{xx}$ and $A_{yy}$. Linear combinations of these analyzing powers give the spherical tensor analyzing powers $T_{20}$ and $T_{22}$[b]. The tensor polarized beam also carries a vector polarized component, so the vector analyzing power $A_y$ (or $2iT_{11}/\sqrt{3}$) was measured at the same time as $A_{yy}$.

The cross section was measured simultaneously to the left and right of the beam by silicon detector telescopes. The analyzing powers were measured by comparing the cross sections observed with the beam polarization on and off, using the equations of Ref. 6. The beam polarization was measured by observing deuterons elastically scattered from $^4$He in a second scattering chamber immediately behind the first. Background in the silicon detector telescopes was reduced through the use of on-line analog particle identification circuits.

The optical-model investigation was initiated using a program written by two of us (GD and BAR). This program was used to adjust the parameters of the central and spin-orbit potentials to obtain the best agreement with the measured cross section and vector analyzing power. As shown in Fig. 1, the calculation reproduces the general features of the measurements, and agrees best at forward angles. This calculation required a spin-orbit potential whose radius and diffuseness parameters are somewhat smaller than usually encountered in the literature.[5]

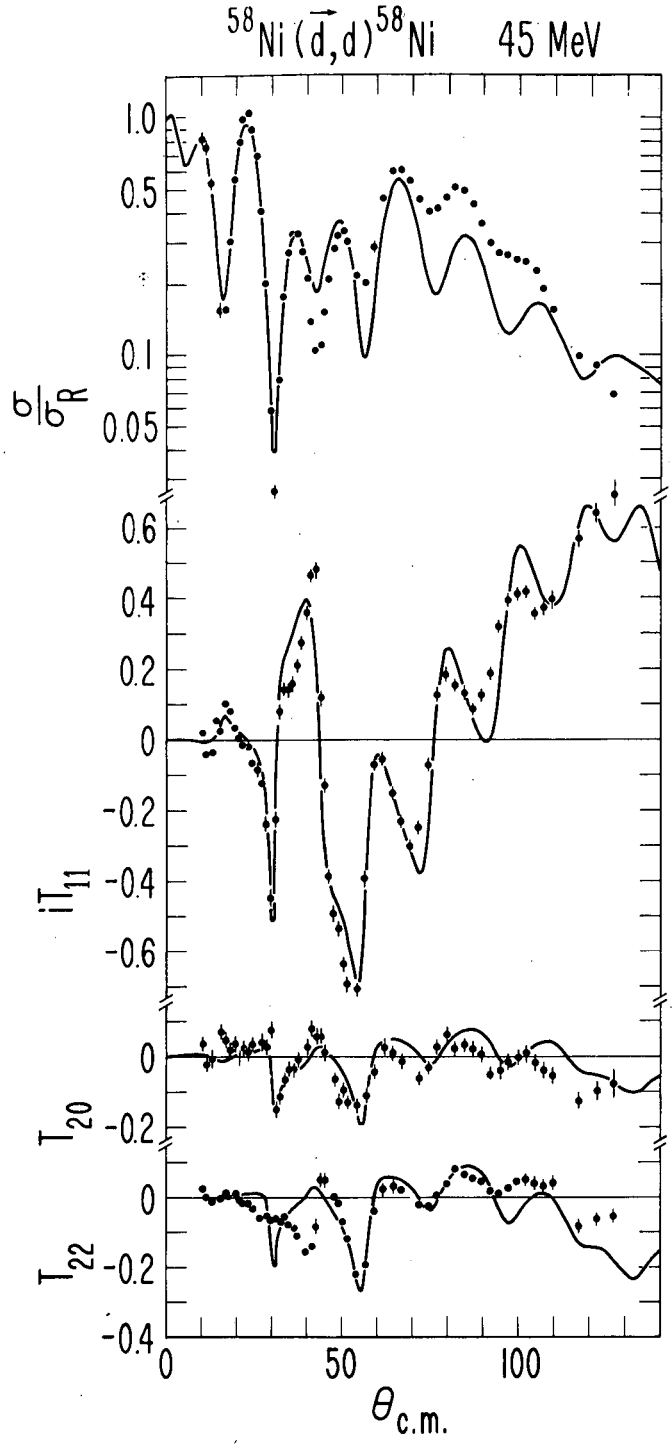


Fig. 1. Measurements of cross section (ratio to Rutherford), vector and tensor analyzing powers for elastic scattering of 45 MeV deuterons from $^{58}$Ni. Curves are optical model calculations including only central and spin-orbit terms. (XBL 778-1614)

Fig. 1 also shows measurements of $T_{20}$ and $T_{22}$. Even though the calculation includes only central and spin-orbit potentials, it gives a good representation of $T_{20}$. The only significant discrepancies occur for $T_{22}$ at forward angles. In general, the spin-orbit potential alone seems to account quite well for the observed tensor analyzing powers. A coupled-channel calculation including the first $2^+$ state in $^{58}$Ni has indicated that coupling changes the calculated tensor analyzing powers by less than 0.02, so this effect will be neglected in this analysis.

Next the optical model calculation was repeated, including the $T_R$ and Tp potential terms. The radial dependence and strength of the tensor potentials are predicted by various models.[1,7] The complex $T_R$ potential has a part which varies roughly as the second derivative of the real and imaginary central potentials. The Tp potential varies approximately as the nuclear density. The inclusion of these potentials in an optical model calculation has little effect on the cross section and vector analyzing power.

The calculations with only spin-orbit potential for the two tensor analyzing powers are quite similar. This is a property of the spin-orbit potential that is not shared by the tensor potentials.[3] To first order, the spin-orbit contributions may be eliminated by considering instead the difference between the two analyzing powers. Since this difference depends primarily on the tensor interaction,[3] it is particularly useful in investigating the effects of tensor forces.

That difference, plotted in Fig. 2, is most significant at forward angles. The remaining spin-orbit contribution is small and is shown by the dotted line. The spin-orbit potential alone cannot explain the magnitude of the difference observed here. The dashed curve includes the effect of just the $T_R$ term, and immediately reproduces the general features of the analyzing power. When these calculations are compared with $T_{20}$ and $T_{22}$ separately, the agreement is better except for the minimum in $T_{22}$ near 30°. Including the momentum-dependent term $T_P$ as well produces the

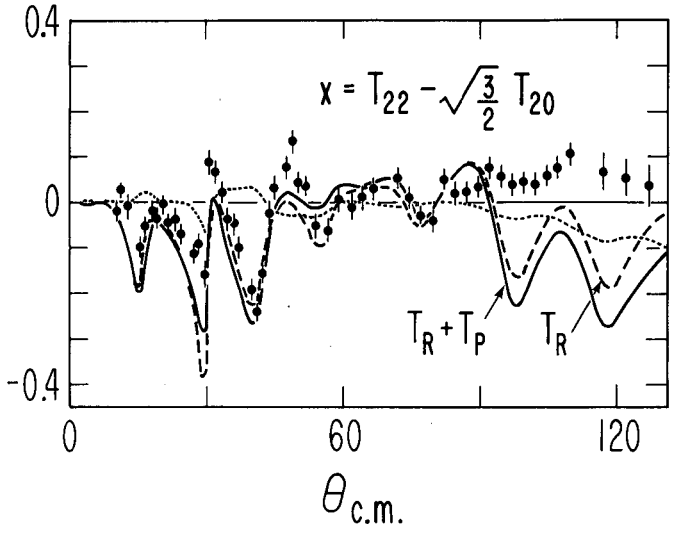


Fig. 2. Measurements of the quantity X = $T_{22} - \sqrt{3}\,T_{20}/\sqrt{2}$. Curves are optical model calculations with no tensor potential (dotted), $T_R$ potential alone (dashed), and both $T_R$ and Tp potentials (solid). (XBL 778-1615)

solid curve. The effect of the Tp potential at 45 MeV seems to be small. Given the uncertainties in the calculation, it will be quite difficult to distinguish the effects of the Tp potential, even though those effects appear to be different in kind from the effects of the $T_R$ alone. In general, the calculation with tensor potentials is too negative. This suggests that the strength of the $T_R$ term should be smaller, a conclusion that is consistent with what has been observed at other energies.[5]

Footnotes and References

*Condensed from LBL-5835 Abstract.

†Present address: Institut fur Kernphysik, Technische Hochschule, 61 Darmstadt, West Germany.

‡Permanent address: Dept. of Theoretical Physics, Australian National University, P. O. Box 4, Canberra A.C.T. 2600, Australia.


1. A. A. Ioanides and R. C. Johnson, Phys. Lett. 61B, 4 (1976).

2. N. Austern, Phys. Lett. 61B, 7 (1976).

3. R. C. Johnson, Nucl. Phys. A 90, 289 (1967).

4. R. P. Goddard, to be published.

5. G. Perrin, Nguyen van Sen, J. Arvieux, R. Darves-Blanc, J. L. Durand, A. Fiore, J. C. Gondrand, F. Merchaz, and C. Perrin, Nucl. Phys. A 282, 221 (1977).

6. The Madison Convention, Third Int. Conf. on Polarization Phenomena in Nuclear Reactions, eds. H. H. Barschall and W. Haeberli (Univ. of Wisconsin Press, Madison, 1971) p. xxv.

7. P. W. Keaton, Jr. and D. D. Armstrong, Phys. Rev. C 8, 1692 (1973).


## EXTREME VALUES OF SPIN-POLARIZATION ANALYZING POWERS IN NUCLEAR FRACTIONS: M-MATRIX CONDITIONS*

H. E. Conzett and F. Seiler†

In nuclear scattering and reactions, points in energy and angle $(E_0,\theta_0)$ at which a component of the analyzing power for spin-polarization reaches its theoretical maximum are of particular interest and importance. Experimentally, they provide valuable absolute calibrations. Theoretically, there exist at such points important conditions on, or relations among, the elements of the transition matrix $\underline{M}$ which connects the initial and final states, $\chi_f = \underline{M}\chi_i$. As a consequence, other polarization observables are determined, and in reactions with a particularly simple spin structure it is possible that all such observables are determined.

The simplest case is that with the spin structure $1/2 + 0 \rightarrow 1/2 + 0$. Here it has been shown that points exist where the analyzing power $A_y(E_0,\theta_0) = \pm 1$ in N-$^4$He, $^3$He-$^4$He, and $^3$H-$^4$He elastic scattering.[1,2] The resulting condition on the two independent M-matrix elements $M_{f,i}$ is

$$M_{1/2,1/2} = \pm i\, M_{1/2,-1/2}\ , \qquad (1)$$

and the other polarization observable, the spin rotation angle, is determined.

Similar investigations involving spin-1 projectiles have now been made. Studies of d-$^4$He elastic scattering[3] $(1+0 \rightarrow 1+0)$ have led to the identification of points at which the tensor analyzing-power component $A_{yy}$ is equal to its maximum value of unity. The possibility of an extreme value $A_{yy}$ point in a nuclear reaction, as opposed to elastic scattering, was first proposed by Seiler[4] in the $^3$He(d,p)$^4$He reaction $(1+1/2 \rightarrow 1/2+0)$. Subsequent measurements by Grüebler et al.[5] confirmed that $A_{yy}$ does reach the value of unity, within experimental error, near the energy and angle suggested. Finally, two extreme points of $A_{yy}$ have been proposed[6] in the $^6$Li(d,$\alpha$)$^4$He reaction $(1+1 \rightarrow 0+0)$ near 6 and 8 MeV, respectively.

In addition, the corresponding linear relations among the M-matrix amplitudes, analogous to Eq. (1), at points $A_{yy} = 1$ and $A_y = \pm 1$ have been given for processes having these particular spin structures.[3,4,6,7] In the d-$^4$He study it was seen[3] that at a point of maximum vector analyzing power, $A_y = \pm 1$, three equations must be satisfied among the M-matrix elements, with the important consequence that all the remaining analyzing powers were then determined:

$$A_{yy} = 1,\ A_{xx} = A_{zz} = -1/2,\ \ A_{xz} = 0\ . \qquad (2)$$

These necessary conditions for the existence of an $A_y = \pm 1$ point have been shown to be valid in general; that is, they are valid for all reactions with the spin structure $1 + b \rightarrow c + d$, where b, c, and d are arbitrary spins.[8] This result follows from the requirement that the spin-1 density matrix be positive semidefinite. Correspondingly, it is of considerable interest to establish, for this general case, the conditions among the M-matrix elements that result whenever an extreme value of an analyzing-power component is reached.

If an analyzing-power, $A_a$, for the spin-a particle reaches an extreme value Q,

$$A_a = \mathrm{tr}(\underset{\sim}{M}\underset{\sim}{P}\underset{\sim}{M}^{\dagger})/\mathrm{tr}(\underset{\sim}{M}\underset{\sim}{M}^{\dagger}) = Q \quad . \tag{3}$$

The corresponding operator is $\underset{\sim}{P} = P_{\underset{\sim}{a}} \otimes I_{2b+1}$ where $I_{2b+1}$ is the unit matrix of order (2b+1), and the operator matrix $P_{\underset{\sim}{a}} \equiv [P_{\alpha\alpha'}]$ is of order (2a+1). In order to reduce the number of terms in writing out the traces in Eq. (3), it is convenient to partition the matrices $\underset{\sim}{M}$ and $\underset{\sim}{P}$ as follows:

$$\underset{\sim}{M} \equiv [M_{\gamma,\alpha}] \tag{4}$$

of dimensions (2c+1) by (2a+1), with the (2d+1) by (2b+1) submatrices

$$M_{\gamma,\alpha} \equiv [M_{\gamma\delta,\alpha\beta}], \tag{5}$$

and

$$\underset{\sim}{P} \equiv [p_{\alpha\alpha'}] \ , \text{ with } p_{\alpha\alpha'} \equiv [P_{\alpha\alpha'}, I_{\beta\beta}]. \tag{6}$$

Using Eqs. (4) and (6), Eq. (3) becomes

$$\sum_{\gamma=a}^{c} \sum_{\alpha=a}^{a} \sum_{\alpha'=a}^{a} M_{\gamma,\alpha} P_{\alpha,\alpha'} M^{*}_{\gamma,\alpha'} - \underset{\sim}{Q} M_{\gamma,\alpha} M_{\gamma,\alpha} = 0 \tag{7}$$

and this is the general equation to be satisfied by the M-matrix elements whenever a component of the analyzing power for the spin-a particle reaches its extreme value Q.

For a polarized particle with spin a=1, two observables are of immediate interest, since extreme values $A_{yy}$=1 and $A_y$=±1 have been observed or proposed.

At a point $A_{yy}$=+1, Eq. (7) yields

$$\sum_{\gamma=c}^{c} |M_{\gamma,1} + M_{\gamma,-1}|^2 = 0 \quad . \tag{8}$$

Then with the definition in Eq. (5), Eq. (8) gives the set of conditions

$$M_{\gamma\delta,1\beta} + M_{\gamma\delta,-1\beta} = 0 \tag{9}$$

for all independent combinations of β,γ and δ.

In the same manner, for the extreme value Ay=±1, Eq. (8) yields

$$\sum_{\gamma=c}^{c} |\sqrt{2}\, M_{\gamma,1} \mp i\, M_{\gamma,0}|^2 + |\sqrt{2}\, M_{\gamma,-1} \pm i\, M_{\gamma,0}|^2 = 0 \ , \tag{10}$$

from which one obtains

$$M_{\gamma\delta,0\beta} \pm i\sqrt{2}\, M_{\gamma\delta,1\beta} = 0 \tag{11a}$$

and

$$M_{\gamma\delta,1\beta} + M_{\gamma\delta,-1\beta} = 0 \tag{11b}$$

Note that Eqs. (11) include the necessary and sufficient conditions in Eq. (9) for the existence of the point $A_{yy}$=+1, a requirement that was previously established from the positivity requirement of the density matrix.[8]

We have derived the sets of linear relations among the M-matrix amplitudes in Eq. (5) that correspond to the existence of extreme values of spin-1 and spin-1/2 analyzing powers. These conditions, given by Eqs. (9) and (11) are similar in form to those imposed by parity conservation. However, unlike the latter, which are universally valid, these hold only at points $(E_0,\theta_0)$ where a particular analyzing-power component reaches its extreme value. Thus, it is clear that at or near such points, considerably more information is available for the determination of these amplitudes and, consequently, the other observables. Discussions of such determinations, for several specific cases in which such points have been proposed and have been located, are contained in a forthcoming paper.[9]

## Footnotes and References

*Condensed from LBL-5850, submitted to Nucl. Phys.

†Physics Department, University of Basel, Basel, Switzerland.

1. G. R. Plattner and A. D. Bacher, Phys. Lett. 36B, 211 (1971).

2. R. A. Hardekopf, G. G. Ohlsen, R. V. Poore, and Nelson Jarmie, Phys. Rev. C 13, 2127 (1976).

3. W. Grüebler, P. A. Schmelzbach, V. König, B. Jenny, and D. Boerma, Nucl. Phys. A 242, 285 (1975).

4. F. Seiler, Phys. Lett. 61B, 144 (1976).

5. W. Grüebler, P. A. Schmelzbach, V. König, B. Jenny, R. Risler, H. R. Bürgi, and J. Nurzynski, Phys. Lett. 63B, 273 (1976); Nucl. Phys. A 271, 29 (1976).

6. F. Seiler, F. N. Rad, H. E. Conzett, and R. Roy, Proc. Fourth Int. Symposium on Polarization Phenomena in Nuclear Reactions, W. Grüebler and V. König, eds. (Birkhäuser Verlag, Basel, 1976), p. 587.

7. F. Seiler, R. Roy, H. E. Conzett, and F. N. Rad, Ibid 6, p. 550.

8. F. Seiler, F. N. Rad, and H. E. Conzett, Ibid 6, p. 897.

9. F. Seiler, F. N. Rad, H. E. Conzett, and R. Roy, LBL-5851, submitted to Nucl. Phys.

# STATES OF MAXIMUM POLARIZATION IN NUCLEAR REACTIONS*

F. Seiler,† F. N. Rad,‡ H. E. Conzett, and R. Roy§

In a recent paper,[1] an enumeration has been made of the studies that have been concerned with the identification of points of maximum polarization efficiency (analyzing-power) for spin-1/2 and spin-1 particles in nuclear scattering and reactions. Also, for the general four-particle reaction A + B → C + D with the spin structure a + b → c + d, sets of linear relations among the transition-matrix (M) elements at such points were derived for the cases a = 1/2 and a = 1. In instances of the particularly simple spin structure 1/2 + 0 → 1/2 + 0 and 1 + 0 → 1 + 0, at points of $A_y = \pm 1$ and $A_{yy} = +1$, respectively, a single equation connecting two M-matrix amplitudes is satisfied. This has made it possible, in several cases of elastic scattering, to locate points of $A_y = \pm 1$ (spin-1/2) and $A_{yy} = 1$ from determinations of the two amplitudes through phase-shift or R-matrix analyses of the available data.

For processes with a more complex spin structure, the corresponding increase in the number of relations among the M-matrix amplitudes makes such a procedure inapplicable. However, experimental criteria, in the form of required values of other polarization observables, can still be given for such extreme-value points. Several contributions to the Fourth Polarization Symposium[2] at Zurich discussed such criteria for several reactions.

In this paper, we provide a more general discussion of extreme values of analyzing powers. States of maximum polarization (analyzing power) are described, and we discuss their usefulness in the calibration of polarization measurements and in the analysis of data for the determination of the M-matrix amplitudes. Known and proposed points of extreme values in elastic scattering and reactions are reviewed, and the corresponding required values of the other polarization observables are listed.

The specific results discussed in this paper are the following:

1) description of spin-1 polarization.

2) limits imposed on the spin-1 analyzing powers.

3) M-matrix conditions at points of maximum analyzing power.

4) value of points of maximum analyzing power to polarization calibrations and to analysis of data.

5) review of conditions associated with points of extreme analyzing power for reactions of specific spin structure,

$$
\begin{aligned}
1/2 + 0 &\rightarrow 1/2 + 0 \quad ; \quad {}^4\mathrm{He}(\vec{p},p){}^4\mathrm{He} \\
1 + 0 &\rightarrow 1 + 0 \quad ; \quad {}^4\mathrm{He}(\vec{d},d){}^4\mathrm{He} \\
1 + 0 &\rightarrow 1 + 0 \quad ; \quad {}^{16}\mathrm{O}(\vec{d},\alpha_1){}^{14}\mathrm{N}^*(0^+) \\
1 + 1/2 &\rightarrow 1/2 + 0 \quad ; \quad {}^3\mathrm{He}(\vec{d},p){}^4\mathrm{He} \\
1 + 1 &\rightarrow 0 + 0 \quad ; \quad {}^6\mathrm{Li}(\vec{d},\alpha){}^4\mathrm{He} \quad .
\end{aligned}
$$

Footnotes and References

*Abstracted from LBL-5851, submitted to Nucl. Phys.

†Physics Department, University of Basel, Basel, Switzerland.

‡Laboratory for Nuclear Science, MIT, Cambridge, Mass.

§Physics Department, Laval University, Quebec, Canada.

1. H. E. Conzett and F. Seiler, Nucl. Phys.

2. Proc. Fourth Int. Symposium on Polarization Phenomena in Nuclear Reactions, W. Grüebler and V. Konig, eds. (Birkhäuser Verlag, Basel, 1976).

# STUDY OF THE (d,$^2$He) REACTION*

R. Jahn,† D. P. Stahel, G. J. Wozniak, and Joseph Cerny

Recently, the feasibility of detecting the unbound $^2$He system as a nuclear reaction product has been demonstrated in a study of the ($\alpha$,$^2$He) reaction on several light nuclei.[1] This large solid angle detection system opens up a wide range of new nuclear reactions which can be used for the study of nuclear structure and reaction mechanisms. Among these reactions, that of charge-exchange via (d,$^2$He) is of particular interest because it should be a useful complement to other charge-exchange reactions such as (n,p), (t,$^3$He) and heavy-ion induced reactions, many of which have experimental problems associated with their general application. For example, neutron beams have poor energy resolution and low intensities whereas triton beams are currently

only available at fairly low energies (≤25 MeV). Though heavy-ion reactions [e.g., ($^7$Li,$^7$Be)] are being increasingly employed, the presence of bound excited states of the ejectile frequently complicates the interpretation of the spectra. Since intense high energy deuteron beams are readily available and there are no bound states in $^2$He, the (d,$^2$He) reaction is likely to be a promising tool for studying neutron-rich nuclei such as $^{18}$N via the $^{18}$O(d,$^2$He)$^{18}$N reaction.

To investigate the feasibility of the (d,$^2$He) reaction, the $T_z$ = 0 targets $^6$Li, $^{10}$B, and $^{12}$C were bombarded with 55 MeV deuterons from the 88-in. cyclotron. The same $^2$He detection system as described in detail in Ref. 1 has been used. Figure 1 shows a typical spectrum from the $^{12}$C (d,$^2$He)$^{12}$B reaction at 50° in the laboratory. Transitions are observed to the known 1$^+$, ground and 4$^-$, 4.52 MeV states and to a previously unknown state at 8.35 ± 0.1 MeV. No evidence for transitions to the 2$^+$,0.95 MeV state is seen at this angle, although it was observed with moderate strength at forward angles. This preferential population of the 1$^+$ ground state of $^{12}$B and the 4$^-$ state at 4.52 MeV, as well as the moderate population of the state at 8.35 MeV at backward angles, is similar to the results observed in a study of the $^{12}$C(n,p)$^{12}$B reaction at 56 MeV,[2] where strong transitions to states at 0.0, 4.4, and 7.8 MeV have been reported. The latter experiment had very poor energy resolution and therefore we assume that the states reported at 4.4 MeV and 7.8 MeV correspond to these levels observed at 4.52 MeV and 8.35 MeV in the present results. This indicates that the (d,$^2$He) reaction, at comparable beam energies, preferentially populates the same states as does the (n,p) reaction, even though the (d,$^2$He) reaction is restricted to spin-flip(ΔS=1) transitions, whereas in the (n,p) reaction both ΔS=0 and ΔS=1 transitions are allowed.

In order to understand the mechanism of the (d,$^2$He) reaction, simple microscopic calculations have been performed. Since the (d,$^2$He) reaction introduces both spin and isospin flip (ΔS=ΔT=1), only the spin-isospin dependent part of the nucleon-nucleon interaction can contribute. Thus the following form was assumed:

$$V(r_i-r_j) = V_{11}\sigma_i\sigma_j\tau_i\tau_j g(r_i-r_j).$$

For the radial dependence g(r) a Yukawa form with a range of 1 fm$^{-1}$ was used. The calculations have been carried out with the code DWUCK IV. The projectile and target nucleus spectroscopic amplitudes have been calculated using the formalism developed by Madsen[3]. For the single particle transitions to p-shell states the intermediate coupling wavefunction of Cohen and Kurath[4] have been used, whereas for transitions to d-shell states pure jj-coupling wavefunctions were assumed. The deuteron optical potentials were obtained from Ref. 5. They have also been used to describe the $^2$He channels.

The experimental and calculated angular distributions for the reaction $^{12}$C(d,$^2$He)$^{12}$B are shown in Fig. 2. As can be seen, the shape of the angular distributions is remarkably well described by the calculations. The obtained average nucleon nucleon interaction is $V_{11}$=10.5 MeV for this reaction, which compares quite well with the result $V_{11}$=16.5 MeV that was obtained for the average nucleon-nucleon interaction in an extensive study of the ($^3$He,t) reaction on various p-shell nuclei.[6]

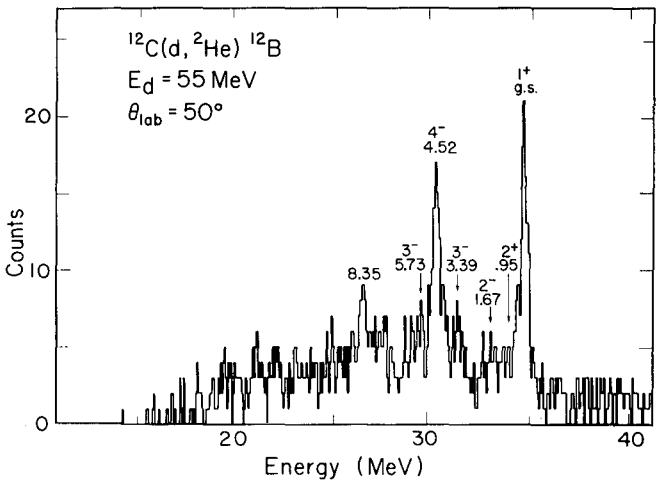


Fig. 1. $^2$He energy spectrum obtained from the reaction $^{12}$C(d,$^2$He)$^{12}$B at 50° lab. angle. (XBL 774-3260)

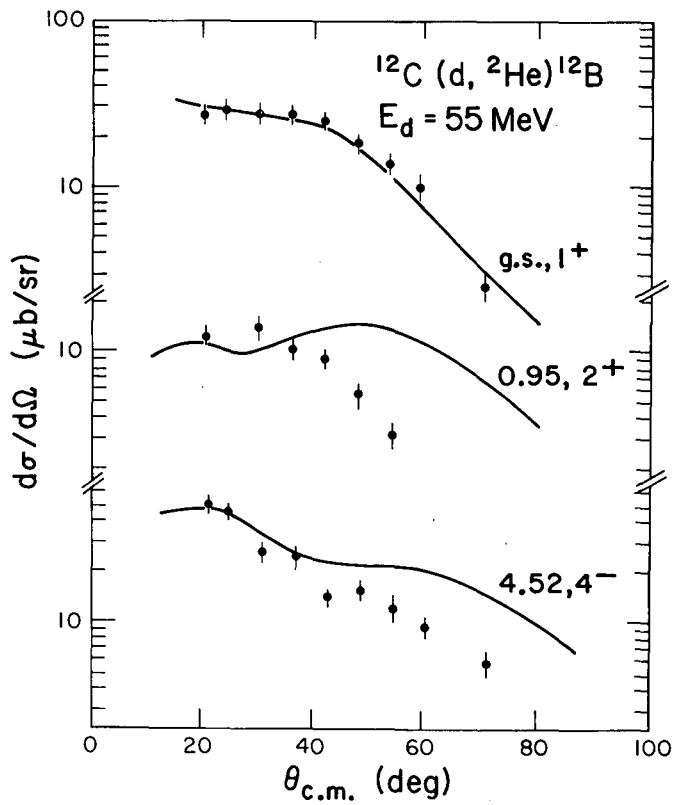


Fig. 2. Absolute differential cross sections for the reaction $^{12}$C(d,$^2$He)$^{12}$B at 65 MeV. Statistical error bars are shown. The solid lines represent microscopic DWBA calculations. (XBL 774-3259)

This good agreement of the zero-range DWBA calculations with experiment indicates that the (d,$^2$He) reaction is direct, and furthermore it confirms the assumption that the correlated two proton system can be well described as an unbound $^2$He particle.

Footnotes and References

*Condensed from LBL-6589

†On leave from ISKP Bonn, Germany; supported by Deutscher Akademischer Austauschdienst.

1. R. Jahn, D. P. Stahel, G. J. Wozniak, and J. Cerny, Phys. Rev. Lett. 37, 812 (1976).

2. M. W. McNaughton et al., Nucl. Instrum. and Meth. 129, 241 (1975).

3. V. A. Madsen, Nucl. Phys. 80, 177 (1966).

4. S. Cohen and D. Kurath, Nucl. Phys. A 101, 1 (1967).

5. F. Hinterberger et al., Nucl. Phys. A 111, 265 (1968).

6. G. Ball and J. Cerny, Phys. Rev. 177, 1466 (1969).

## DWBA ANALYSIS OF THE ($^3$He, $^2$He) REACTION

D. P. Stahel, R. Jahn, G. J. Wozniak, and Joseph Cerny

The feasibility of detecting two protons correlated by their final state interaction ($^2$He) as an outgoing particle in direct nuclear reactions with a moderate solid angle has been demonstrated in a study of the ($\alpha$,$^2$He) reaction.[1] An identical detection system has been employed in the present investigation of the ($^3$He,$^2$He) reaction at 60 MeV on several light targets. Since this is the simplest reaction that produces $^2$He as an outgoing particle in a stripping process, it is well suited for studies of the dynamics of reactions involving $^2$He. It is of particular interest to determine whether the neutron transfer can be described with the distorted-wave Born-approximation (DWBA) under the assumption of a $^2$He particle consisting of two protons with no internal energy.

In the present experiment, the unbound $^2$He system was detected by means of a coincidence measurement using two $\Delta$E-E counter telescopes arranged symmetrically above and below the reaction plane. To assure good detection efficiency, the geometry was chosen such that the two protons from $^2$He with a breakup angle between 5 and 15° could be detected, whereas energy resolution considerations mandated a limitation of the horizontal $^2$He acceptance angle to 4°.

In order to obtain absolute experimental cross sections, the $^2$He detection efficiency must be calculated. For a given geometry and $^2$He lab energy this efficiency depends critically on the relative energy $\varepsilon$ of the two protons in the $^2$He c.m. system. Unfortunately, $\varepsilon$ has no sharp value; its probability distribution P($\varepsilon$) peaks around $\varepsilon$ = 400 keV and falls off at larger values as approximately $1/\varepsilon$. Taking into account P($\varepsilon$), the $^2$He detection efficiency $F_{^2He}$ is given by

$$F_{^2He} = \frac{\int_0^\infty P(\varepsilon)\, F(\varepsilon)\, d\varepsilon}{\int_0^\infty P(\varepsilon)\, d\varepsilon} \qquad (1)$$

The exact shape of P($\varepsilon$) is not known. Therefore, an experimental distribution was taken from a study[2] of the $^2$H($^3$He,t)$^2$He reaction. The upper limit to the integration was set at $\varepsilon$ = 3 MeV, since for larger values of $\varepsilon$,P($\varepsilon$) is small and therefore only a small fraction of $^2$He lies in this region. The uncertainty of the shape of P($\varepsilon$) and the upper cut-off in the integration introduces a potentially large error in the absolute efficiency calculations. As a result, the absolute cross section can only be determined to approximately ± 40% even though the relative ones are estimated to be accurate to about ± 5%.

$^2$He energy spectra were measured for the ($^3$He,$^2$He) reaction on targets of $^6$Li, $^7$Li, $^9$Be, $^{12}$C and $^{13}$C. The same states in the final nuclei were observed in these spectra as in other light-ion single-neutron transfer reactions, such as (d,p). The ($^3$He,$^2$He) reaction, however, can populate states that are not allowed in (d,p) reactions, namely those that involve transitions in which an isospin transfer $\Delta$T = 1 takes place. Because such transitions involve target core excitation, their probability is substantially reduced. In fact, no evidence for such transitions was observed within the limited statistics of this experiment.

Angular distributions were measured for reactions on the $^{12}$C and $^{13}$C targets. Those for the $^{13}$C($^3$He,$^2$He)$^{14}$C reaction leading to the g.s., $0^+$ and 6.73 MeV, $3^-$ state in $^{14}$C are shown in Fig. 1. The solid lines represent results of DWBA calculations. For the stripping reaction A(a,b)B, the differential cross section for a given orbital angular momentum transfer $\ell$ and total angular momentum transfer j is calculated in the zero-range DWBA as

$$\sigma^{\ell}(\Theta) = \frac{2J_B+1}{2J_A+1} \; N \; S_{B\to A+x} \; \frac{\sigma^{\ell}_{DW}(\Theta)}{2j+1} \qquad (2)$$

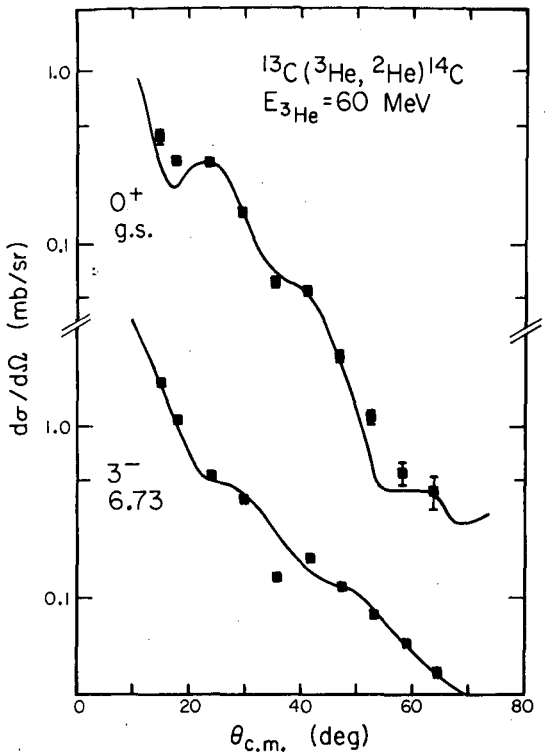


Fig. 1. Angular distributions for the $^{13}C(^3He, ^2He)^{14}C$ reaction. The solid lines represent zero-range DWBA calculations. (XBL 7612-11113)

$\sigma_{DW}$, which represents the kinematical part of the cross sections, describes the shape of the distribution and was calculated using the program DWUCK 4. The optical model potential parameters utilized in these calculations were taken from the literature[3]. For the exit channel, the $^2He$ potentials were approximated by using parameters from deuteron potentials. For the spectroscopic factors S, the theoretical values of Cohen and Kurath[4] were taken for p-shell configurations and for sd-shell configurations they were assumed to be unity. The normalizing factor N is defined as

$$N = S_{a\to b+x} \frac{D_o^2}{10^4} \qquad (3)$$

where

$$D_o = \int_o^\infty \varphi_{bx}(\vec{r})\, V_{bx}(\vec{r})\, d\vec{r}\,.$$

$\varphi_{bx}(\vec{r})$ is the wave function for the relative motion of b and x within the projectile a, and $V_{bx}(\vec{r})$ the interaction potential between b and x at the distance $\vec{r}$. N depends on the projectile and outgoing particle system only and should be independent of target and incident energy. For the $(^3He, ^2He)$ reaction, for which N is not known, experimental values were determined by normalizing the calculated to the experimental cross sections for four transitions. An average value of N = 0.8 was obtained. In order to compare the experimental normalization with theoretical estimates, N must be calculated from Eq. (3). Assuming $S_{^3He\to ^2He+n} = 1$ the calculation of N reduces to the evaluation of the overlap integral $D_o$ (Eq. (4)). If one chooses for $\varphi_{bx}$ and $V_{bx}$ a Hulthen-type wavefunction and interaction potential, the volume integral can be solved analytically.[5] With a short-range parameter $\beta = 1.36 fm^{-1}$ and long-range parameter $\alpha$ which is proportional to the one-neturon binding energy of $^3He$ one finds $D_o = -177$ MeV $fm^{3/2}$ and N = 3.13.

Although the shapes of the angular distributions are well reproduced by the DWBA theory, which indicates that the reaction dynamics can be well understood by treating the two correlated protons as $^2He$ particle, the normalization factor N was found to be smaller than the theoretical estimate by a factor of about 4. This could imply that the actual overlap between the $^3He$ and $^2He$ wavefunctions is smaller than what is expected based on our simple evaluation of $D_o$; more detailed calculations that take into account the effects of the final-state interaction may be required.

## References

1. R. Jahn, G. J. Wozniak, D. P. Stahel and J. Cerny, Phys. Rev. Lett. 37, 812 (1976).

2. B. J. Morton et al., Phys. Rev. 169, 825 (1968).

3. G. C. Ball and J. Cerny, Phys. Rev. 177, 1466 (1969).
F. Hinterberger et al., Nucl. Phys. A 111, 265 (1968).

4. S. Cohen and D. Kurath, Nucl. Phys. A 101, 1 (1967).

5. W. J. Thompson and W. R. Hering, Phys. Rev. Lett. 24, 272 (1970).

# SEARCH FOR TWO-NEUTRON STATES OF $(f_{7/2})^2_{6+}$ CHARACTER IN sd-SHELL NUCLEI

R. Jahn,* D. P. Stahel, G. J. Wozniak, and Joseph Cerny

Recently, in a study of the $(\alpha,{}^2He)$ reaction on several p-shell nuclei,[1] selective population of 2n states of $(d_{5/2})^2_{4+}$ character has been reported. This reaction is similar to the well studied $(\alpha,d)$ reaction, which favors transitions in which a np pair can be simply captured in a relative triplet state about the undisturbed target core, in that the $(\alpha,{}^2He)$ reaction selectively populates states in which a nn pair is captured in a relative singlet state. In the present experiment, the $(\alpha,{}^2He)$ reaction has been studied on the targets $^{24}Mg$, $^{28}Si$, $^{32}S$, $^{36}Ar$, and $^{40}Ca$ with 55 to 65 MeV $\alpha$-beams of the 88-in. cyclotron. At this beam energy, the $(\alpha,{}^2He)$ reaction kinematically favors $\ell = 6$ transitions, thus making it a potentially useful tool for locating 2n states of $(f_{7/2})^2_{6+}$ character.

Since $^2He$ is unbound, it has to be detected by means of a coincidence measurement of its two breakup protons. The detection system consisted of two large solid-angle counter telescopes collimated by 8-mm wide and 10-mm high slits which were separated by a 10-mm high central post. At 11-cm distance from the target, this system subtended a 15° vertical and a 4° horizontal acceptance angle. The ΔE counters were phosphorus diffused silicon, 380 μm thick, and the E detectors were Si(Li), 5 mm thick all having the same area of $1 \times 1.4$ cm$^2$. In addition, two 5-mm thick counters were mounted behind the E detectors in order to reject events that traversed the ΔE-E system.

To characterize $^2He$ events, a subnanosecond fast coincidence between the two ΔE counters and particle identification of the protons in each telescope was required. An electronic time resolution of ∿ 200 ps (FWHM) was measured for simulated $^2He$ events by utilizing a fast risetime pulser and fast/slow preamplifiers. To minimize the charge collection time in the ΔE counters, a high bias voltage (2V/μm) was maintained. The time-of-flight difference (ΔTOF) spectra of the two protons had a half-width at half-maximum of about 500 ps, which is in good agreement with calculated values. Since the width of a single beam burst was 6 ns, random coincidences were drastically reduced by setting a 1 ns wide window around the $^2He$ peak in the ΔTOF spectrum. Furthermore, a fast pileup rejection system was utilized which permitted a high count rate (32,000 s$^{-1}$) in each ΔE counter, with an associated system dead time of about 20%. The detection efficiency was about 1% for 20 to 55 MeV $^2He$ events.

A spectrum of the $(\alpha,{}^2He)$ reaction on a $^{40}Ca$ target is shown in Fig. 1. The extreme selectivity of this two-neutron transfer reaction is well demonstrated in this spectrum. In $^{42}Ca$, only the state at 3.19 MeV is strongly populated which is known to be of $(f_{7/2})^2_{6+}$ character.[2] Figure 2 shows a plot of the Q-values of the transitions to

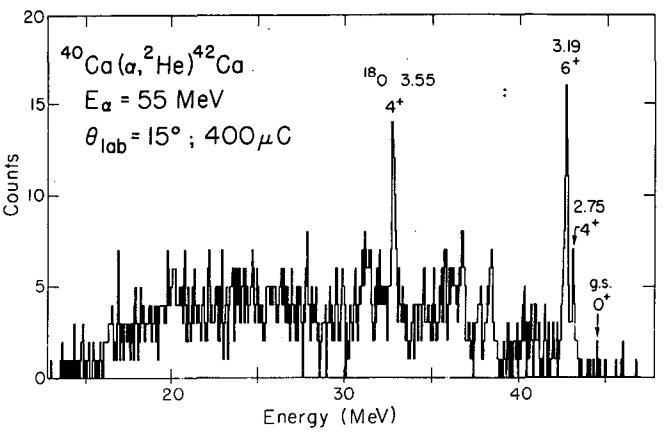


Fig. 1. Energy spectrum from the reaction $^{40}Ca(\alpha,{}^2He)^{42}Ca$. (XBL 764-2749)

the tentatively assigned $(f_{7/2})^2_{6+}$ states vs the atomic mass number of the final nuclei. It can be seen that the Q-values depend linearly on the mass number. These Q-values of the $(\alpha,{}^2He)$ reaction are related to the binding energy $B_{2n}$ of the two neutrons relative to the target core by $B_{2n} = Q(\alpha,{}^2He) + 28.30$ [MeV]. This systematic behavior of the binding energy of the two stripped particles

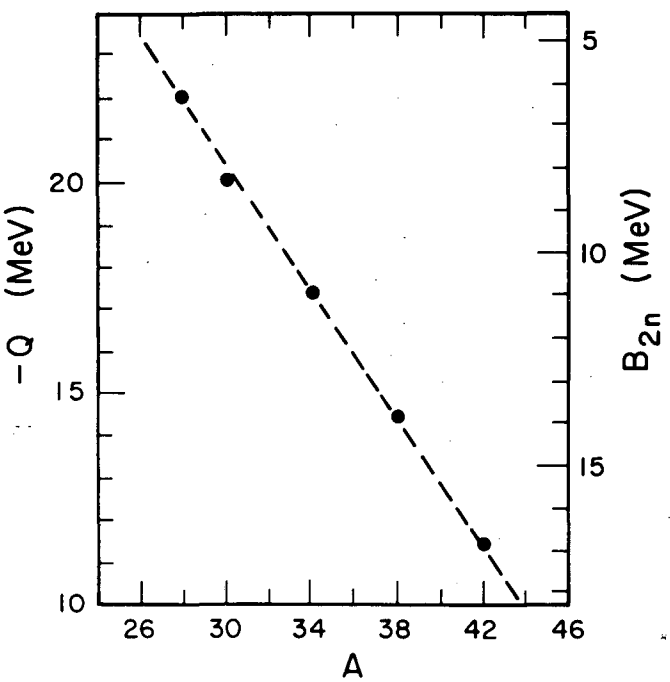


Fig. 2. Dependence of the reaction Q-values for transitions to $6^+$ states vs the atomic mass number. The corresponding 2n binding energy $B_{2n}$ is also listed. (XBL 778-1792)

is well known from studies of the (α,d) reaction on p- and sd- shell targets[3,4] and provides a convenient way of identifying states of predominant $(f_{7/2})^2$ configuration in the final nuclei.

Table 1. Excitation energies of the $(f_{7/2})^2 6^+$ states.

| | $E_x$ [MeV] |
|---|---|
| $^{26}$Mg | 11.23 ± 0.07 |
| $^{30}$Si | 9.02 ± 0.07 |
| $^{34}$S | 8.45 ± 0.07 |
| $^{38}$Ar | 6.41 |
| $^{42}$Ca | 3.19 |

The excitation energies of the $(f_{7/2})^2 6^+$ states observed in the present study are listed in Table 1. Except for the 6.41 MeV state in $^{38}$Ar and the 3.19 MeV state in $^{42}$Ca, all identified $6^+$ states were previously unknown.

Footnotes and References

*On leave from ISKP Bonn, Germany; supported by Deutscher Akademischer Austauschdienst.

1. R. Jahn, G. J. Wozniak, D. P. Stahel, and J. Cerny, Phys. Rev. Lett. 37, 812 (1976).

2. I. Kanestrøm and H. Koren, Nucl. Phys. A 130, 527 (1969).

3. E. Rivet, R. H. Pehl, J. Cerny, and B. G. Harvey, Phys. Rev. 141, 1021 (1966).

4. R. Sherr, R. Kouzes, and R. DelVecchio, Phys. Lett. 52B, 401 (1974).

## MONOPOLE EXCITATION OF $^4$He IN α-PARTICLE SCATTERING FROM $^{12}$C, $^{13}$C, and $^{16}$O*

R. Jahn,† D. P. Stahel, G. J. Wozniak, Joseph Cerny, and H. P. Morsch‡

Monopole excitations of nuclei are of considerable interest. One of the simplest examples of a monopole state is the first excited state of $^4$He, which in the shell model is largely described by a $(1s_{1/2}^{-1}\ 2s_{1/2})$ particle-hole excitation.[1] This unbound state at 20.1 MeV excitation energy ($\alpha^*$, $\Gamma$ = 0.27 MeV) lies 0.3 MeV above the t+p breakup threshold of the α-particle and decays entirely via this channel.[2,3] An experimental system has been developed which is capable of selectively detecting an α-particle excited to this $\alpha^*$ state by measuring its correlated decay products in coincidence and identifying them as a proton and a triton.

Figure 1(a) shows the $\alpha^*$ detection system. Standard particle identification techniques were used to identify the $\alpha^*$ events. In order to reduce random events, a subnanosecond fast coincidence was required (the FWHM of the observed differential time of flight (Δ TOF) peak was 850 ps as expected from the $\alpha^*$ decay characteristics under our experimental conditions).

Figure 1(b) shows a spectrum of the $(\alpha,\alpha^*)$ reaction on $^{12}$C at 20° lab angle using a 65 MeV beam from the 88-in. cyclotron. The observed energy resolution of 450 keV was primarily determined by kinematic broadening due to the 4° acceptance angle. This spectrum shows appreciable transitions to the ground state, the $2^+$ state at 4.44 MeV, and to the $3^-$ state at 9.64 MeV and a weak transition to the first excited $0^+$ state of $^{12}$C at 7.66 MeV; the latter is particularly interesting insofar as it represents a double monopole (target + ejectile) excitation.

Microscopic calculations for $\alpha^*$ transitions, which left the several targets undisturbed, were performed in which a target nucleus-nucleon interaction was obtained by folding a nucleon-nucleon force into a target nucleus density distribution. A simple Wigner force of Gaussian form with a range of 1.6 fm and a volume integral of 446 MeV fm$^3$ was used. For the monopole transition of $^4$He, transition densities from both a microscopic model and a collective model were used. A microscopic $(1s_{1/2}^{-1}\ 2s_{1/2})$ transition density was calculated using radial wavefunctions generated in Woods-Saxon potentials. The collective model transition density was obtained from derivatives of the ground state density. Optical potentials were used which were obtained from a best fit description of 65 MeV elastic α-scattering data.[4]

The calculated and experimental angular distributions for $(\alpha,\alpha^*)$ transitions to the ground states of $^{12}$C, $^{13}$C, and $^{16}$O are shown in Fig. 2.

The magnitudes of the calculated absolute cross sections at forward angles are in good agreement with the measured data. (Note that in this description there is no free parameter with which to adjust theory to experiment.) On the other hand the experimental angular distributions do not show the structure predicted by theory,

although similar pronounced structure is observed in monopole target excitations of light nuclei.[5] [It is important to observe that, in the same $\alpha + {}^{12}C$ system studied here, the angular distribution of the monopole excitation of the $^{12}C$ target ($0^+$, 7.66 MeV) is remarkably well reproduced by a similar microscopic calculation.][6] Even using different optical potentials for the exit channel, e.g., from fitting 42 MeV α scattering data, results in no improved agreement of this calculation with experiment. This failure of a one-step DWBA approach to describe the experimental angular distributions may be indicative of higher order effects in the projectile excitation.

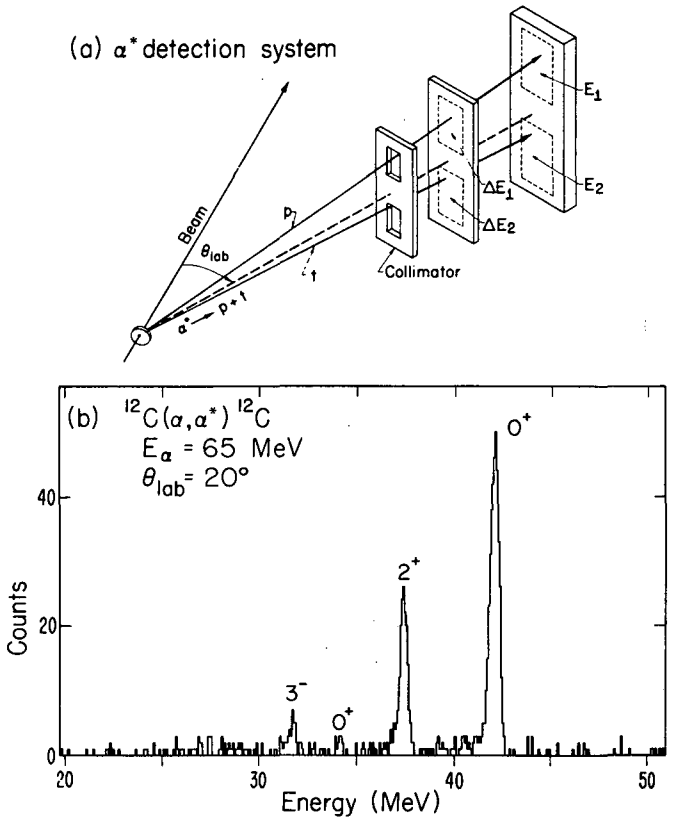


Fig. 1. (a) Schematic diagram of the $\alpha^*$ detection system (see text). (b) Energy spectrum of the reaction $^{12}C(\alpha,\alpha^*)^{12}C$ at an α-particle energy of 65 MeV at 20° laboratory angle. (XBL 768-3896)

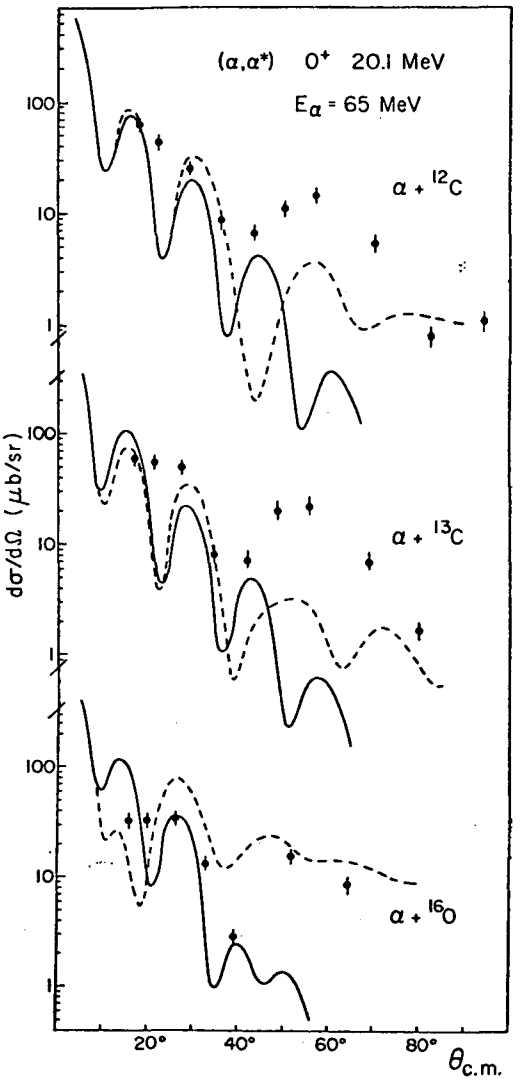


Fig. 2. Experimental and theoretical angular distributions of the ground state transitions for the $(\alpha,\alpha^*)$ reaction on $^{12}C$, $^{13}C$ and $^{16}O$ at 65 MeV beam energy. The curves correspond to microscopic calculations using 1p-1h (solid lines) and collective model (dashed lines) transition densities. XBL 769-10682)

Footnotes and References

*Condensed from Phys. Lett. 65B, 339 (1976).

†On leave from Institut für Strahlen- und Kernphysik der Universität Bonn, Germany, supported by Deutscher Akademischer Austauschdienst.

‡Cyclotron Laboratory, Michigan State University, East Lansing, MI 48824; Present address: Institut für Kernphysik, KFA Jülich, 5170 Jülich, Germany.

1. P. P. Szydlik, Phys. Rev. C 1, 146 (1970).

2. S. Fiarman and W. E. Meyerhof, Nucl. Phys. A 206, 1 (1973).

3. D. Robson, Nucl. Phys. A 204, 523 (1973).

4. B. G. Harvey, et al., Nucl. Phys. 52, 465 (1964).

5. H. P. Morsch, Nucl. Phys. A 226, 1527 (1975) and 35, 192 (1975).

6. H. P. Morsch, P. Decowski and H. B. Wildenthal, to be published.

# MECHANISM AND STRUCTURE STUDIES WITH THE ($^3$He, $\alpha^*$) REACTION

D. P. Stahel, R. Jahn, G. J. Wozniak, and Joseph Cerny

An investigation of the ($^3$He, $\alpha^*$ (20.1 MeV, $0^+$)) reaction has two aspects. It is interesting for reaction mechanism studies and at the same time it can provide valuable information on the structure of the $\alpha^*$ state. As for the reaction mechanism, a comparison between the ($^3$He, $\alpha$) and the ($^3$He, $\alpha^*$) reactions is particularly worthwhile since the $\alpha$, g.s. and $\alpha^*$ 20.1 MeV state have the same quantum numbers T=0 and $J^\pi = 0^+$. Therefore the same selection rules apply to both reactions and the same final states in the residual nuclei should be populated with relative yields that are affected by the difference in the reaction Q-value of 20.1 MeV. If the Q-value dependence of the yield can be accounted for by the distorted-wave Born-approximation (DWBA), then the remaining difference in cross section is due to the structural difference between the $\alpha$ and the $\alpha^*$ states.

In this work the ($^3$He, $\alpha$) and ($^3$He, $\alpha^*$) reactions were measured on $^6$Li, $^9$Be, $^{12}$C, and $^{13}$C targets at an incident energy of 60 MeV. The experimental set-up[1] consisted of an $\alpha^*$ detector system which was made up of two silicon $\Delta$E-E counter telescopes in a vertical arrangement capable of detecting in coincidence the decay products p and t from the breakup of the particle-unstable $\alpha^*$ state. The geometry was designed such that p and t with a breakup angle between 5 and 16° could be detected. To measure the ($^3$He, $\alpha$) reaction, a standard $\Delta$E-E silicon counter telescope was employed and was mounted on the opposite side of the beam.

Fig. 1 shows spectra from the ($^3$He, $\alpha$) and ($^3$He, $\alpha^*$) reactions on a $^{13}$C target. As expected, the same final states were populated in both reactions. Whereas in the ($^3$He, $\alpha$) reaction preferential transitions to excited states were observed, the ($^3$He, $\alpha^*$) reaction populated the states near the g.s. more strongly than the excited states. This difference in the relative strengths can be explained by the difference in the Q-values. Due to the large binding energy of the $\alpha$-particle, the Q-values for the ($^3$He, $\alpha$) reactions are quite positive giving rise to a severe angular momentum mismatch and thus small cross sections for transitions to low lying states. Optimum matching is achieved for transitions with $Q \approx 0$. In the ($^3$He, $\alpha^*$) reaction, this condition is met for transitions near the g.s., while the transitions to the excited states are mismatched, since $Q << 0$, and thus reduced in cross section.

Angular distributions from the ($^3$He, $\alpha$) and ($^3$He, $\alpha^*$) reactions on $^{13}$C were measured and are presented in Fig. 2 along with results of DWBA calculations. In the zero-range DWBA, the cross section for the pickup reaction B(b,a) A is given by

$$\sigma^{\ell}(\vartheta) = N\, S_{B\to A+x}\, \frac{\sigma^{\ell}_{DW}(\vartheta)}{2j+1} \qquad (1)$$

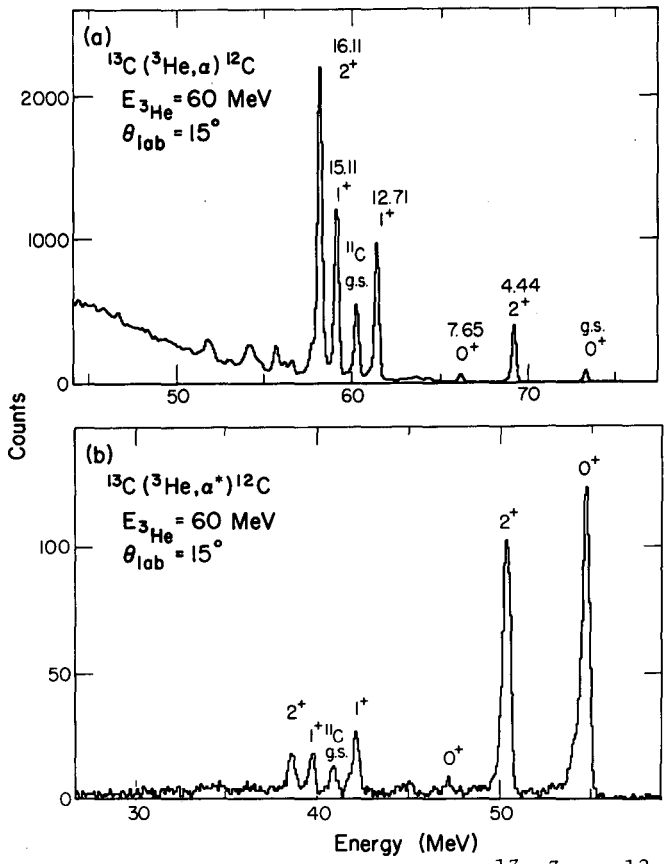


Fig. 1. Energy spectra from (a) the $^{13}$C($^3$He,$\alpha$)$^{12}$C and (b) $^{13}$C($^3$He, $\alpha^*$) $^{12}$C reactions. (XBL 7610-4152)

The kinematical part, $\sigma_{DW}$, was calculated with the computer program DWUCK 4 using optical potentials taken from the literature.[2] Since $\sigma_{DW}$ is quite sensitive to variations of the optical potentials, especially for the momentum mismatched transitions, the same set of parameters was used for the ($^3$He, $\alpha$) and ($^3$He, $\alpha^*$) reactions. For the spectroscopic factors $S_B$, the theoretical values of Cohen and Kurath[3] were taken.

The normalizing factor N is defined for pickup reactions as

$$N = \frac{2s_a + 1}{2s_b + 1}\, S_{a\to b+x}\, \frac{Do^2}{10^4}\ , \qquad (2)$$

where

$$D_o = \int_0^\infty \varphi_{bx}(\vec{r})\, V_{bx}(\vec{r})\, d\vec{r}\ . \qquad (3)$$

Denoting the normalization factor for the ($^3$He, $\alpha$) and ($^3$He, $\alpha^*$) reaction as $N_\alpha$ and $N_{\alpha^*}$ respectively,

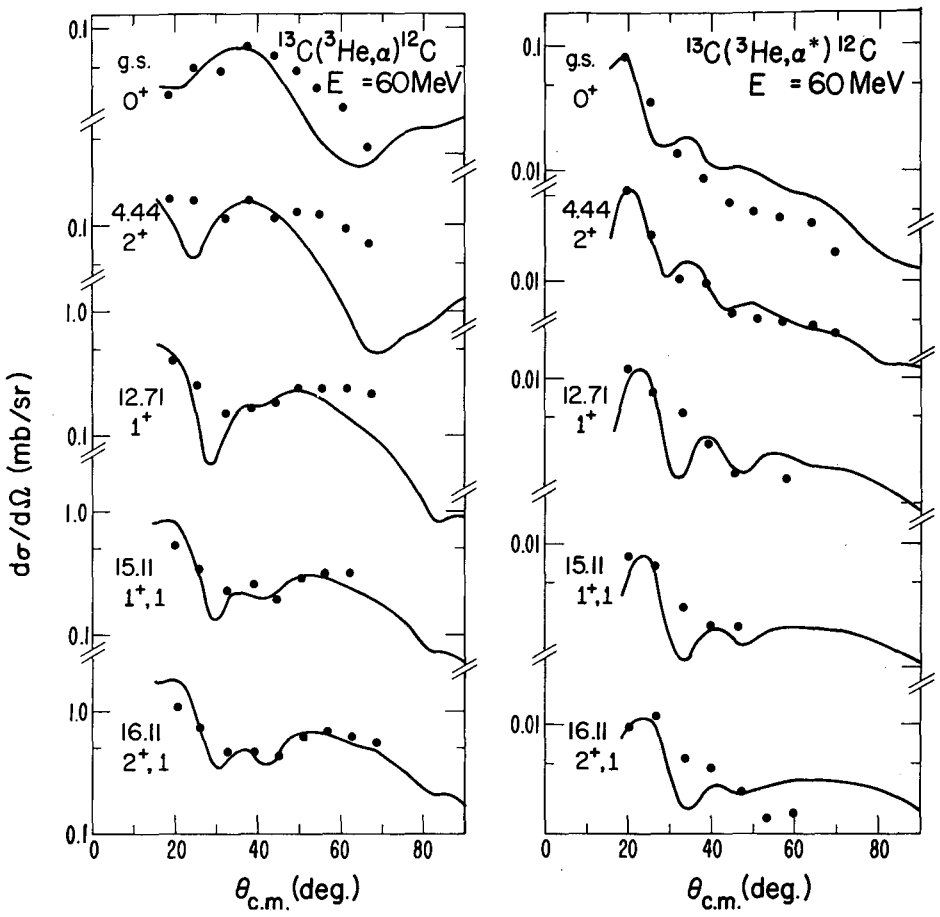


Fig. 2. Angular distributions for the $^{13}C(^3He,\alpha)^{12}C$ and $^{13}C(^3He,\alpha^*)^{12}C$ reactions. The solid lines are zero-range DWBA calculations. (XBL 7610-4158)

the theoretical ratio of $N_\alpha$ to $N_\alpha$* is given by

$$\frac{N_\alpha}{N_\alpha^*} = \frac{S_\alpha \; D_o^2(\alpha)}{S_\alpha^* \; D_o^2(\alpha^*)} \qquad (4)$$

If one chooses a Woods-Saxon type potential $V_{bx}$ with radius $R = 1.25 \times 4^{1/3}$ fm and diffuseness a = 0.65 fm and wavefunction $\varphi_{bx}$ that are determined by adjusting the well depth to reproduce the neutron separation energy of the α and α* states, respectively, $D_o$ can be evaluated by numerical integration[4] of Eq. (3). Setting $S_\alpha = 2$ and $S_\alpha^* = 0.5$ (assuming pure $(1s_{1/2}^{-1}\ 2s_{1/2})$ configuration) one finds $N_\alpha/N_\alpha^* = 76$. The experimental values of $N_\alpha$ and $N_\alpha^*$ were obtained by normalizing the calculated cross sections to the experimental ones for each transition. Using the average values of $N_\alpha$ and $N_\alpha^*$, the ratio $N_\alpha/N_\alpha^*$ was determined to be equal to 120 which is about two times larger than the theoretical prediction. This discrepancy could indicate $S_\alpha^* < 1$, which implies that the α* state does not have a pure $(1s_{1/2}^{-1}\ 2s_{1/2})$ configuration and that other configurations such as 2 particle-2 hole admixtures could be important.

## References

1. R. Jahn, D. P. Stahel, G. J. Wozniak, J. Cerny and H. P. Morsch, Phys. Lett. 65B, 339 (1976).

2. G. C. Ball and J. Cerny, Phys. Rev. 177, 1466 (1969); P. Gaillard et al., Nucl. Phys. A 131, 353 (1969).

3. S. Cohen and D. Kurath, Nucl. Phys. A 101, 1 (1967).

4. R. M. DeVries, computer LOLA.

# THE ELASTIC SCATTERING OF $^{16}O$ + $^{208}Pb$ AND THE ENERGY DEPENDENCE OF THE INTERACTION RADIUS*

C. Olmer,† M. C. Mermaz,‡ M. Buenerd,§ C. K. Gelbke,|| D. L. Hendrie, J. Mahoney, and D. K. Scott

The study of elastic scattering over a wide range of incident energies may be able to provide information concerning the energy dependence of the interaction radius and whether, as naively expected, one is able to sample the field more deeply inside the target nucleus as the energy of the projectile is increased. We have measured the elastic scattering of 312.6 MeV $^{16}O$ by $^{208}Pb$, and have compared these data with those measured[1-5] at lower incident energies.

The $^{16}O$ + $^{208}Pb$ elastic scattering angular distribution measured at 312.6 MeV is displayed in Fig. 1. Several optical model descriptions of these data have been investigated using the program PTOLEMY.[6] In particular, several sets of energy-dependent and independent Woods-Saxon optical potentials which fit the elastic scattering data between 104 and 216.6 MeV have been recently derived.[1] The optical potential Q2 was obtained[1] from an eleven-parameter global fit to these low-energy data, allowing quadratic energy dependence in the geometrical parameters ($a$, $a_i$, $r_o$, $r_{oi}$), energy independence in the well depths ($V$,$W$), and equal real and imaginary radii. The resulting parameters were first extrapolated to 312.6 MeV and were then used as initial values in a least-squares fit to the elastic scattering data at 312.6 MeV, producing a final chi-square per point of 0.8 obtained for 5% error bars. The optical potential I2, on the other hand, was obtained by individual three-parameter fits to the low-energy data at each energy, requiring that the real and imaginary well depths, as well as the real and imaginary diffusivities, are equal, and that $V = W = 50$ MeV. The corresponding parameters for the potential I2 at 312.6 MeV were derived in a similar manner by a three-parameter ($r_o$, $r_{oi}$, $a$) fit to these data, and a similarly small final chi-square per point was obtained. Finally, the optical potential C1 was obtained[1] from a four-parameter, energy-independent global fit to the elastic scattering data between 104 and 216.6 MeV, requiring that $V = 100$ MeV and $W = 20$ MeV, and allowing the geometrical parameters ($r_o$, $r_{oi}$, $a$ $a_i$) to vary. The extracted parameters account reasonably well for the elastic scattering data at 312.6 MeV but, as discussed in Ref. 1, this (or any) energy-independent potential does not fit the lower energy data as well as do the energy-dependent potentials. The final parameters for optical potentials Q2, I2 and C1 at 312.6 MeV are presented to four significant figures in Table 1, and the fits to the 312.6 MeV elastic scattering data are displayed in Fig. 1.

For each of these potentials, the grazing angular momentum $\ell_{1/4}$ has been calculated according to the semiclassical quarter-point method

$$\ell_{1/4} + \frac{1}{2} = \eta \cot\left(\frac{1}{2}\Theta_{1/4}\right)$$

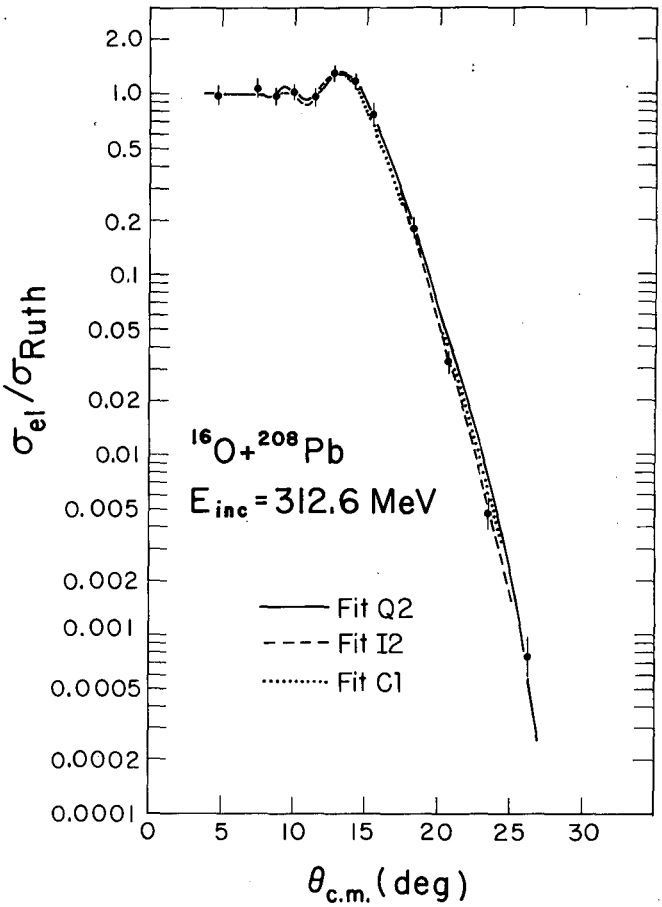


Fig. 1. Elastic scattering angular distribution for 312.6 MeV $^{16}O$ on $^{208}Pb$. The curves are optical model fits using the parameters listed in Table 1. (XBL 777-1358)

where $\eta = z_1 z_2 e^2/\hbar v$ is the Sommerfeld parameter and $\Theta_{1/4}$ is the center-of-mass angle at which the experimental elastic scattering cross section equals 1/4 of the Rutherford value. The corresponding strong absorption radius is then defined as the distance of closest approach for a Rutherford trajectory, and is given by

$$R_{1/4} = \frac{\eta}{k}\left[1 + \csc\left(\frac{1}{2}\Theta_{1/4}\right)\right] , \qquad (1)$$

where k is the entrance-channel wavenumber. The strong absorption radius can be defined in an alternative manner from the grazing angular momentum $\ell_{1/2}$ for which the optical potential transmission coefficient $T_\ell$ equals 0.5:

$$R_{1/2} = \frac{\eta}{k}\left\{1 + \left[\frac{\ell_{1/2}(\ell_{1/2}+1)}{\eta^2}\right]^{\frac{1}{2}}\right\}$$

Table 1. Interaction radii for $^{16}O + ^{208}Pb$ elastic scattering.

| Potential | $E_{lab}$ (MeV) | V (MeV) | W (MeV) | $r_o$ (fm) | $r_{oi}$ (fm) | a (fm) | $a_i$ (fm) | $r_e$ (fm) | $r_{1/4}$ (fm) | $r_{1/a}$ (fm) | $r_s$ (fm) |
|---|---|---|---|---|---|---|---|---|---|---|---|
| Q2 | 312.6 | 51.09 | 51.46 | 1.114 | 1.114 | .7964 | .7410 | 1.3 | 1.431 | 1.420 | -- |
| I2 | 312.6 | 50.00 | 50.00 | 1.181 | 1.145 | .6820 | .6820 | 1.3 | 1.431 | 1.416 | -- |
| C1 | 312.6 | 100.0 | 20.00 | 1.090 | 1.273 | .7770 | .5970 | 1.3 | 1.431 | 1.440 | -- |

The strong absorption radii $R_{1/2}$, calculated with optical potential I2, and $R_{1/4}$ are listed in Table 1 and displayed in Fig. 2 for elastic scattering at the various incident energies. The indicated error bars were calculated assuming uncertainties of ± 0.5 ħ and ± 0.2° in the values of $\ell_{1/2}$ and $\Theta_{1/4}$, respectively. Over this range of incident energies, the strong absorption radii $R_{1/2}$ and $R_{1/4}$ are generally equivalent.

It has been recently noted[5,6] that for incident energies less than 216.6 MeV, $R_{1/2}$ decreases slowly as the incident energy is increased, whereas $R_{1/4}$ remains nearly constant. With the addition of the higher energy data, it is now apparent that both these radii show a systematic decrease for increasing incident energy, although the magnitude of this effect is rather small. Similarly small effects have also been observed in studies[7] of $^{16}O + ^{28}Si$ elastic scattering. Additional studies at still higher incident energies and for other nuclear systems are necessary for further investigation and verification of the observed energy dependence of the interaction radius.

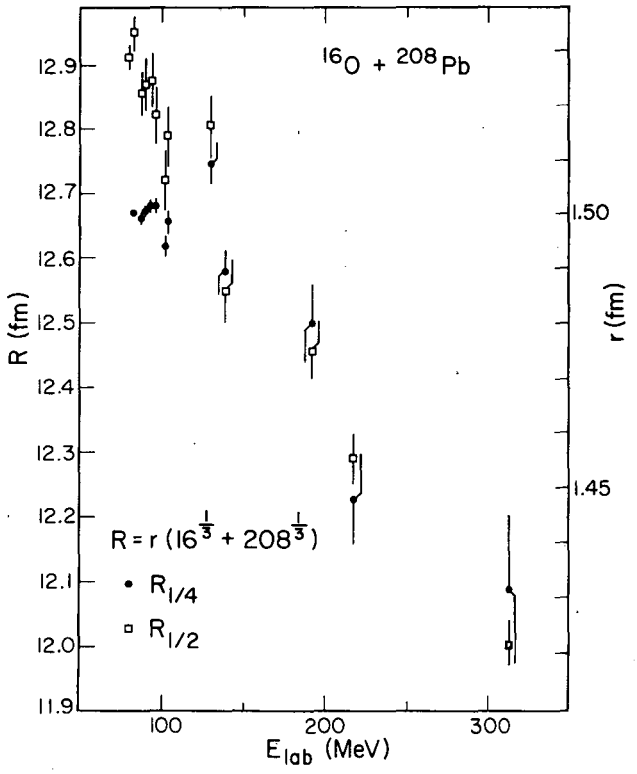


Fig. 2. The strong absorption radii $R_{1/4}$ (determined from the angle at which the experimental elastic scattering cross section equals 1/4 of the Rutherford value) and $R_{1/2}$ (determined from the angular momentum for which the transmission coefficient $T_\ell$ equals 0.5 for optical potential I2) as a function of the incident energy.
(XBL 778-1434)

Footnotes and References

*Condensed from LBL-6553.

†Present address: Physics Division, Argonne National Laboratory, Argonne, Illinois 60439.

‡Permanent address: Centre d'Etudes Nucleaires de Saclay, Gif-Sur-Yvette 91190, France.

§Permanent address: Institut des Science Nucleaires, Grenoble, France.

‖Present address: Department of Physics, Michigan State University, East Lansing, MI 48824.

1. S. C. Pieper, M. H. Macfarlane, D. G. Kovar, D. H. Glockner, F. D. Becchetti, B. G. Harvey, D. L. Hendrie, H. Homeyer, J. Mahoney, R. Puhlhofer, W. von Oertzen and M. Zisman, in preparation.

2. D. G. Kovar, B. G. Harvey, F. D. Becchetti, J. Mahoney, D. L. Hendrie, H. Homeyer, W. von Oertzen and M. A. Nagarajan, Phys. Rev. Lett. 30, 1075 (1973).

3. J. B. Ball, C. B. Fulmer, E. E. Gross, M. L. Halbert, D. C. Hensley, C. A. Ludemann, M. J. Saltmarsh and G. R. Satchler, Nucl. Phys. A 252, 208 (1975).

4. J. D. Garrett and S. C. Pieper, Private communication.

5. F. Videbaek, R. B. Goldstein, L. Grodzins, S. G. Steadman, T. A. Belote and J. D. Garrett, Phys. Rev. C 15, 954 (1977).

6. D. H. Glockner, M. H. Macfarlane and S. C. Pieper, Argonne National Laboratory, Report ANL-76-11 (1976).

7. J. G. Cramer and R. M. DeVries, in preparation; J. G. Cramer, Bull. Am. Phys. Soc.

# THE TRANSITION BETWEEN LIGHT- AND HEAVY-ION ELASTIC SCATTERING*

R. M. DeVries,† D. A. Goldberg,‡ J. W. Watson,§ M. S. Zisman, and J. G. Cramer||

Recently we showed[1] that high energy ($E_i$ = 215 MeV) $^{16}O$ + $^{28}Si$ elastic scattering exhibits angular distributions and resultant optical model parameters which are quite different from those observed for light ions. In particular, high energy light-ion angular distributions exhibit at angles beyond the diffraction oscillations a structureless fall-off characteristic of a nuclear rainbow.[2] These rainbow data not only allow the determination of the strength of the real part of the potential but also indicate that light-ion optical potentials have a central imaginary well depth 1/3 - 1/6 of the real depth. Furthermore, both the real and imaginary depths of light-ion potentials are energy dependent.[3] In contrast, our results for $^{16}O$ scattering[1] indicated (a) no evidence of rainbow scattering effects, (b) W/V $\geq$ 1 in the nuclear surface, and (c) good fits with an energy-independent potential.

The purpose of the present study was to explore what happens with projectiles of masses intermediate to light (d, $^3$He, $\alpha$) and heavy ($^{16}O$) ions. Data were taken using $^6Li^{3+}$ (135.1 MeV) and $^{12}C^{4+}$ (186.4 MeV) beams from the 88-in. cyclotron. Most of the data were taken using the counter system described in Ref. 1; a portion of the $^6Li$ data was acquired using the LBL QSD spectrometer. An additional experimental refinement consisted of correcting for the zero-angle drift in the beam by monitoring the ground state/2+ (1.78 MeV) intensity ratio as recorded by a counter placed at a fixed angle. The error bars in the data include the ± 0.1° uncertainty associated with these corrections. Existing $^6Li$ data at 13 MeV[4] and $^{12}C$ data at 24 MeV[5] and 49.3 MeV[6] are shown in Fig. 1 along with the new data. The difference in the shapes of the two high energy data sets is striking. Specifically, $^6Li$ + $^{28}Si$ displays at large angles the characteristic structureless fall-off of nuclear rainbow scattering typical of light-ion projectiles while $^{12}C$ + $^{28}Si$ displays instead a diffractive, oscillatory angular distribution very similar to $^{16}O$ scattering.

Optical model analyses of the data sets yield equally distinctive results. The $^{12}C$ data have been analyzed in a manner similar to that employed with the $^{16}O$ data[1]; i.e., searches were performed (with the code GENOA)[7] on the 24 and 186.4 MeV data simultaneously. The potentials which result from such an energy-independent assumption provide a convenient characterization of the data and permit comparison with $^{16}O$ potentials derived in an identical manner. Two real well depths were chosen ($V_0$ = 10,100 MeV) while all other parameters were varied, resulting in the parameters shown in Table 1 and fits displayed in Fig. 1(a). The $V_0$ = 10 MeV potential (H 12) yields excellent fits with parameters very similar to those obtained from the $^{16}O$ analysis;[1] the $V_0$ = 100 MeV potential (L8) fails to give comparably good fits to the data, also in accord with our $^{16}O$ results. The 10 MeV potential (H12) also predicts correctly the overall behavior of the data of Kohno, et al.[6] at the intermediate energy of 49.3 MeV, although it fails to reproduce the oscillations appearing at larger angles [see Fig. 1(a)]. However, here again the situation parallels the $^{16}O$ case where similar structure is observed which cannot be fit by any potential resembling those capable of fitting either the high or low energy data.[8]

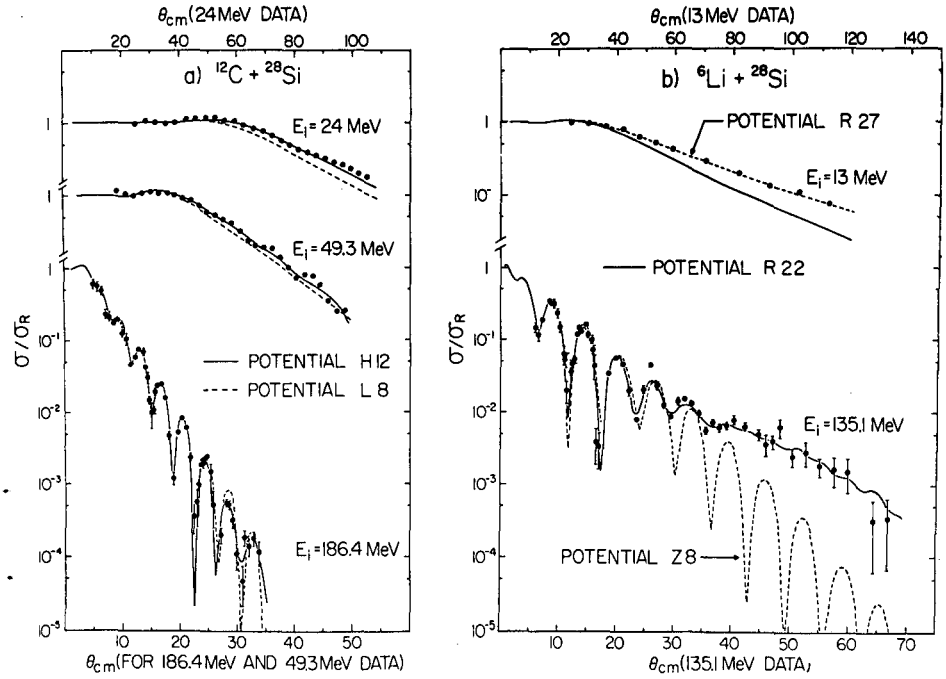


Fig. 1. Elastic scattering of $^{12}C$ and $^6Li$ from $^{28}Si$. Note that the high energy $^{12}C$ scattering is similar to $^{16}O$ scattering (Ref. 1) while the high energy $^6Li$ data is similar to light ion data (Ref. 2). (XBL 777-9736)

Table 1. $^{12}C + {}^{28}Si$ Woods-Saxon optical model potentials.

| Set | Parameters | | | | | | $\chi^2/F$ |
|---|---|---|---|---|---|---|---|
| | $V_0$(MeV) | $r_0$[a](fm) | $a_0$(fm) | $W_0$(MeV) | $r_I$[a](fm) | $a_I$(fm) | (186.4 MeV data) |
| H12 | 10. | 1.32 | 0.617 | 30.3 | 1.16 | 0.609 | 2.3 |
| L8 | 100. | 0.868 | 0.838 | 42.7 | 1.08 | 0.743 | 5.1 |

[a] $R = r(12^{1/3} + 28^{1/2})$.

In contrast, the optical model analysis (see Table 2) of the $^6Li$ data yields quite different results. As might be expected from the presence of the nuclear rainbow, a reasonable fit to the 135.1 MeV data cannot be obtained with a well depth shallower than ~ 100 MeV; as can be seen from Fig. 1(b), the "best-fit" 10 MeV potential (Z8) which is quite similar to E18 and H12, fails utterly to fit the data in the rainbow region. However, a potential with $V_0$ = 150 MeV (R22) or greater yields an excellent fit to the complete angular distribution. Moreover, it is not possible to fit both the 13 MeV and 135.1 MeV data sets with a single potential. The best simultaneous fit to the 135.1 MeV and 13 MeV data sets with $V_0$ = 150 MeV yields a $\chi^2/F$ for the 13 MeV data which is a factor of 15 greater than that of the best fit to those low energy data alone (potential R27). Therefore, in terms of both energy dependence and well strength, the $^6Li$ potential much more nearly resembles those for light ions than those for $^{12}C$ and $^{16}O$.

In summarizing our results, we have determined that there is a pronounced transition from light-ion to heavy-ion scattering, the most striking aspect of which is the rapidity with which it occurs. By A = 6 it appears to have only begun; by A = 12 it appears to be complete. While energy dependence of the potentials has been predicted[9] to decrease with increasing projectile mass (consistent with our data), we are unaware of any theoretical treatment which explains the abrupt change of the potential from moderately absorptive and refractive, to very strongly absorbing and diffracting. Clearly also, further high energy experiments in the A = 7 to 11 mass region are needed to elucidate the nature of this transition.

## Footnotes and References

* Condensed from LBL-7103, published in Phys. Rev. Lett. 39, 450 (1977).

Table 2. $^6Li + {}^{28}Si$ Woods-Saxon optical model potentials.

| Set | Parameters | | | | | | $\chi^2/F$ | Volume Integral | $\theta_R$[b] |
|---|---|---|---|---|---|---|---|---|---|
| | $V_0$(MeV) | $r_0$[a](fm) | $a_0$(fm) | $W_0$(MeV) | $r_I$[a](fm) | $a_I$(fm) | (135.1 MeV data) | (MeV fm$^3$) | (deg) |
| Z8 | 10 | 1.34 | 0.809 | 82.1 | 0.955 | 0.727 | 12 | 478 | - 11 |
| V27 | 100 | 0.828 | 0.833 | 53.2 | 0.841 | 1.10 | 3.0 | 1384 | - 56 |
| R22 | 150 | 0.727 | 0.877 | 44.4 | 0.904 | 1.06 | 2.6 | 1587 | - 72 |
| R27 | 150 | 0.682 | 0.828 | 38.8 | 1.02 | 0.889 | 28 | 1318 | - 71 |
| Q5 | 200 | 0.679 | 0.871 | 66.1 | 0.795 | 1.08 | 2.8 | 1809 | - 95 |
| M4 | 250 | 0.636 | 0.872 | 54.7 | 0.848 | 1.07 | 2.7 | 1964 | -112 |

[a] $R = r(28^{1/3} + 6^{1/3})$, i.e., the heavy-ion convention -- more reasonable values of r are obtained with the light-ion convention $R = r(28^{1/3})$.

[b] Nuclear rainbow angle (Ref. 2).

†Nuclear Structure Research Laboratory, University of Rochester, Rochester, N.Y. 14627

‡Department of Physics and Astronomy, University of Maryland, College Park, MD 20743

§Department of Physics, University of Manitoba Winnepeg, Manitoba, Canada R3T 2N2 and Crocker Nuclear Laboratory, University of California, Davis, CA 94720

‖Nuclear Physics Laboratory, University of Washington, Seattle, WA 98195

1. J. G. Cramer, R. M. DeVries, D. A. Goldberg, M. S. Zisman and C. F. Maguire, Phys. Rev. C 14, 2158 (1976).

2. D. A. Goldberg and S. M. Smith, Phys. Rev. Lett. 29, 500 (1975); D. A. Goldberg, S. M. Smith and G. F. Burdzik, Phys. Rev. C 10, 1367 (1974).

3. P. P. Singh, P. Schwandt and G. C. Yang, Phys. Lett. 59B, 113 (1975); S. M. Smith, et al., Nucl. Phys. A 207, 273 (1973); L. W. Put and A. M. J. Paans, Phys. Letts. 49B, 266 (1974).

4. R. M. DeVries, D. S. Shapira, N. Anantaraman, R. Cherry, M. R. Clover and H. E. Gove, to be published.

5. J. S. Eck, T. J. Gray and R. K. Gardner, Bull. Am. Phys. Soc. 22, 563 (1977).

6. I. Kohno, S. Nakajima, T. Tonuma and M. Odera, J. Phys. Soc. Japan 30, 910 (1971).

7. F. Perey, unpublished.

8. Braun-Munzinger et al., [Phys. Rev. Lett. 38, 944 (1977)] have been able to fit such data but only by employing direct modification of the S-matrix elements.

9. D. F. Jackson and R. C. Johnson, Phys. Lett. 49B, 249 (1974).

# ENERGY DEPENDENCE OF THE $^{208}Pb(^{16}O,^{15}N)^{209}Bi$ AND $^{208}Pb(^{16}O,^{15}O)^{209}Pb$ REACTIONS*

C. Olmer,† M. C. Mermaz,‡ M. Buenerd,§ C. K. Gelbke,‖ D. L. Hendrie, J. Mahoney, D. K. Scott, M. H. Macfarlane,¶ and S. C. Pieper¶

Studies of direct reactions over a wide range of incident energy may be able to reveal new features of the reaction mechanism which can not be discerned in studies at any one energy due to various uncertainties in the internal structure of the nuclear states. We have investigated the $^{208}Pb(^{16}O,^{15}N)^{209}Bi$ and $^{208}Pb(^{16}O,^{15}O)^{209}Pb$ single nucleon transfer reactions at 312.6 MeV, using an $^{16}O^{6+}$ beam and the QSD magnetic spectrometer at the 88-in cyclotron, and have compared the results to those obtained at lower incident energies,[1-4] thereby spanning the region from below to more than 200 MeV above the Coulomb barrier. Since both the projectile and target are closed-shell nuclei, and since the low-lying levels in the residual nuclei are known to have a strong single particle character, such an investigation can provide an extremely sensitive test of the distorted wave Born approximation (DWBA) model, which is, at present, our most useful model of the reaction mechanism.

Energy spectra for the $^{208}Pb(^{16}O,^{15}N)^{209}Bi$ and $^{208}Pb(^{16}O,^{15}O)^{209}Pb$ reactions at various incident energies, each measured near the respective grazing angle, are shown in Figs. 1 and 2. (The data displayed in Figs. 1(a-c) and 2(a) were obtained from Refs. 1 and 4, respectively.) Prominent in all these spectra are transitions to several well-known single particle states, and these are indicated by their shell model orbitals. In addition, several broad structures appear in the spectra. The qualitative features of these spectra (for example, the relative population of the discrete final states and the nature of the broad structures) have been discussed earlier.[5] Here, we discuss the more quantitative features of these data, and attempt to use the DWBA to reproduce the observed absolute intensity of each transition at the various incident energies.

Angular distributions for the $^{208}Pb(^{16}O,^{15}N)^{209}Bi$ and $^{208}Pb(^{16}O,^{15}O)^{209}Pb$ reactions at 312.6 MeV are shown in Figs. 3 and 4, and are observed to have nearly identical bell-shaped behavior, similar to what was observed at the other incident energies above the Coulomb barrier. Finite range DWBA calculations for each of these transitions at all measured incident energies were made with the program PTOLEMY.[6] The bound state and optical potential parameters used in the calculations are presented in Table 1, and the latter are discussed in an accompanying report.[7] Identical optical potential parameters were used in both the entrance and exit channels, except for optical potential Q2, for which the exit channel parameters were adjusted according to the reaction Q-value and the empirically determined energy dependence of the parameters. The resulting DWBA calculations are shown in Figs. 3 and 4, using optical potential Q2 and the experimentally determined relative spectroscopic factors listed in Tables 2 and 3. As may be seen, the DWBA accounts reasonably well for the shape and position of the angular distributions, as well as the observed relative yields. However, the

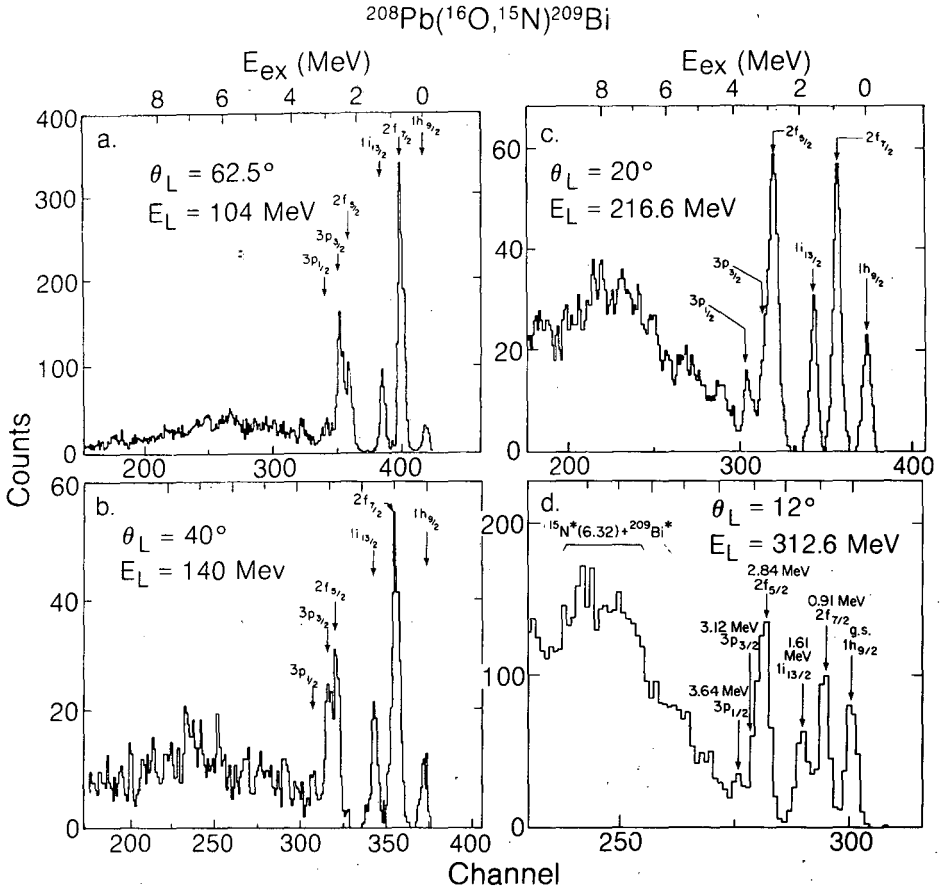


Fig. 1. Energy spectra obtained for the $^{208}Pb(^{16}O,^{15}N)^{209}Bi$ reaction at incident energies of 104, 138.5, 216.6 and 312.6 MeV. Transitions to known proton single-particle states are labeled according to their shell model orbitals.
(XBL 7612-4518)

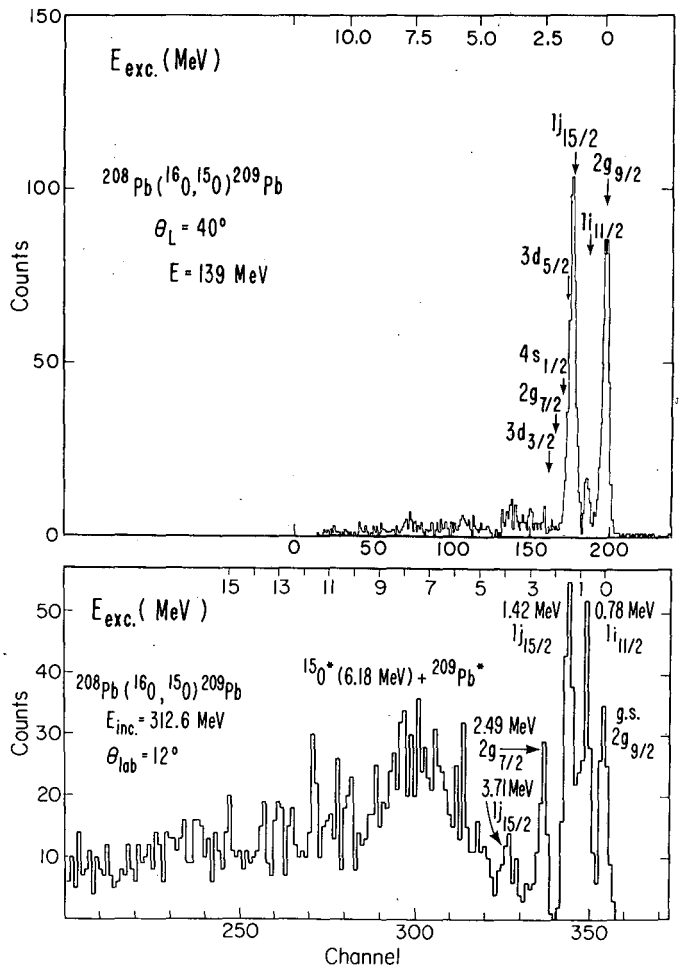


Fig. 2. Energy spectra obtained for the $^{208}Pb(^{16}O,^{15}O)^{209}Pb$ reaction at incident energies of 139 and 312.6 MeV. Transitions to known neutron single-particle states are labeled according to their shell model orbitals.
(XBL 777-1370)

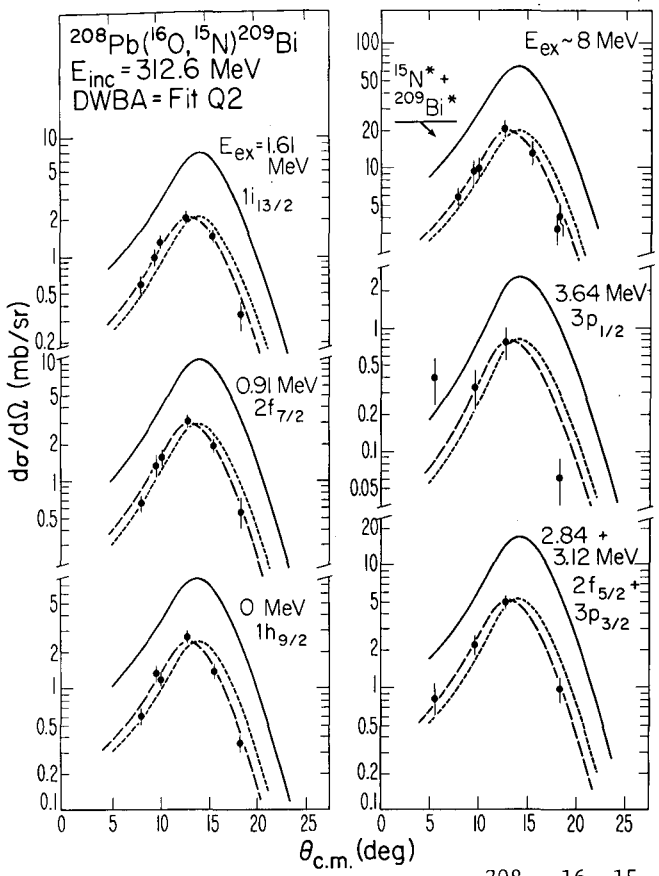


Fig. 3. Angular distributions of the $^{208}Pb(^{16}O, ^{15}N)^{209}Bi$ reaction at 312.6 MeV. The solid lines represent DWBA calculations using optical model potential Q2. The short dashed lines indicate the DWBA predictions when the theoretical ground state angular distribution is normalized to the experimental result; better agreement with the data is obtained when the predictions are shifted by 1°, as indicated by the long dashed lines. (XBL 777-1357)

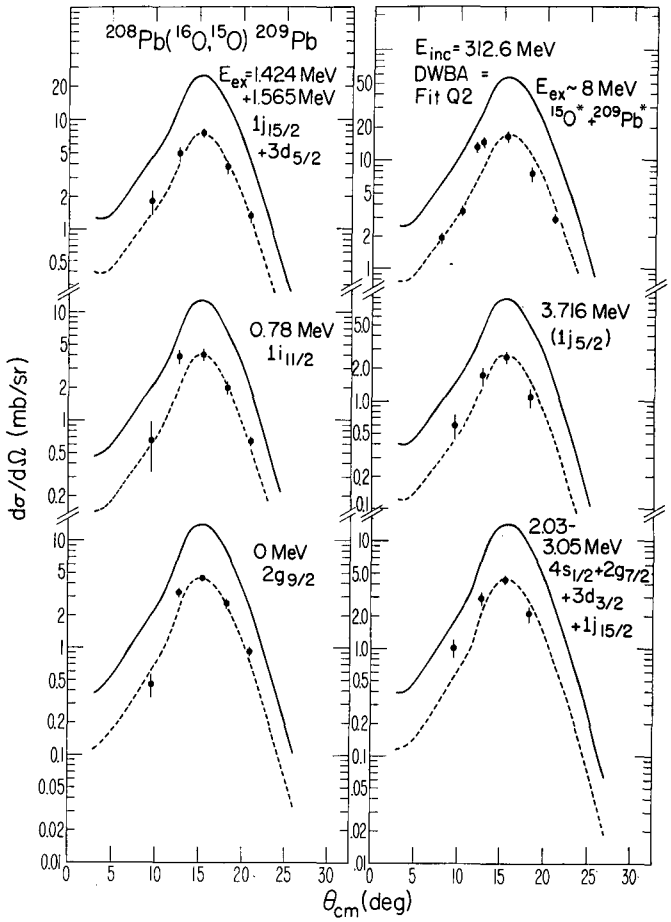


Fig. 4. Angular distributions of the $^{208}Pb(^{16}O, ^{15}O)^{209}Pb$ reaction at 312.6 MeV. The solid lines represent DWBA calculations using optical model potential Q2. The dashed lines indicate the DWBA predictions when the theoretical ground state angular distribution is normalized to the experimental result. (XBL 777-1369)

Table 1. Bound state and optical potential parameters.

| System | $r_o$ (fm) | a (fm) | $V_{so}$ (MeV) | $r_{so}$ (fm) | $a_{so}$ (fm) | $r_{co}$ (fm) |
|---|---|---|---|---|---|---|
| $^{208}Pb+p$ | 1.28 | 0.76 | 6 | 1.09 | 0.60 | 1.30 |
| $^{208}Pb+n$ | 1.25 | 0.63 | 7 | 1.10 | 0.50 | |
| $^{15}N+p$ | 1.20 | 0.65 | 7 | 1.20 | 0.65 | 1.20 |
| $^{15}O+n$ | 1.20 | 0.65 | 7 | 1.20 | 0.65 | |

| Potential | V (MeV) | W (MeV) | $r_o$ (fm) | $r_{oi}$ (fm) | a (fm) | $a_i$ (fm) | $r_c$ (fm) |
|---|---|---|---|---|---|---|---|
| Q2 | 51.09 | 51.46 | 1.114 | 1.114 | 0.7964 | 0.7410 | 1.300 |
| I2 | 50.00 | 50.00 | 1.181 | 1.145 | 0.6820 | 0.6820 | 1.300 |
| C1 | 100.00 | 20.00 | 1.090 | 1.273 | 0.7770 | 0.5970 | 1.300 |

Table 2. Spectroscopic factors for the $^{208}Pb(^{16}O,^{15}N)^{209}Bi$ reaction.

| State | $E_{ex}$ (MeV) | Fit Q2 | Fit I2 | $(^{16}O,^{15}N)^a$ S | $(^{12}C,^{11}B)^b$ S | $(^{3}He,d)^c$ S | Theory[d] S |
|---|---|---|---|---|---|---|---|
| $1h_{9/2}$ | 0.00 | 0.95[e] | 0.95[a] | 0.95 | 0.84 | 1.17 | 0.95 |
| $2f_{7/2}$ | 0.90 | 0.81 | 0.82 | 0.74 | 0.81 | 0.78 | 0.85 |
| $1i_{13/2}$ | 1.61 | 0.73 | 0.68 | 0.61 | 0.75 | 0.56 | 0.70 |
| $2f_{5/2}$ | 2.84 | 0.73[f] | 0.67[f] | 0.61 | 0.54 | 0.88 | 0.66 |
| $3p_{3/2}$ | 3.12 | 0.70[f] | 0.70[f] | 0.55 | 0.69 | 0.67 | 0.74 |
| $3p_{1/2}$ | 3.64 | 0.66 | 0.50 | 0.52 | | 0.45 | 0.54 |

a) From Ref. 1.
b) From Ref. 11, $E_{inc}$ = 97.9 MeV.
c) From Ref. 10.
d) From Ref. 8.
e) Theoretical ground state spectroscopic factor is assumed.
f) Spectroscopic factor for the $2f_{5/2}$ level has been corrected for a small contribution from the unresolved $3p_{3/2}$ level (S=0.70 assumed).

DWBA is unable to accurately predict the absolute magnitude of the transfer cross sections, and overestimates the magnitude of the cross section by more than a factor of three for both the proton and neutron transfer data. This effect is also apparent when other optical potentials are employed, although the magnitude of the effect (a factor between 2 and 4) is sensitive to the choice of optical potential parameters.

That the DWBA calculations at 312.6 MeV predict cross sections significantly different from those observed experimentally is also true at other incident energies, as is shown in Figs. 5 and 6. At the top of each figure are plotted the angle-integrated cross sections for each transition at the various incident energies. The data are indicated by the solid black dots and the corresponding DWBA calculations, using the theoretical spectroscopic factors[8,9] (see Tables 2 and 3), are indicated by the dotted lines. The 69.9 MeV sub-Coulomb transfer data of Ref. 2 are included in Fig. 5, although certain weak transitions were not observed in that work. (The optical potential parameters used in the analysis of the 69.1 MeV data were those derived at 104 MeV since the DWBA calculations are somewhat insensitive to the choice of nuclear potential parameters.)

For the proton transfer data, the DWBA reproduces reasonably well the energy dependence of the transfer cross sections at low incident energies, although the actual magnitudes of the cross sections for all transitions are underestimated by the DWBA. At energies above approximately 140 MeV, however, the energy dependence of the DWBA no longer resembles that of the data. Whereas the experimental cross sections generally decrease fairly rapidly with incident energy, the predicted cross sections either remain constant in magnitude or increase as the incident energy is increased, resulting in an overestimate by the DWBA of the transfer cross sections at high incident energies. These observations are more apparent at the bottom of the figure, where the ratios of the DWBA to experimental cross sections for all observed transitions are contained within the cross-hatched area. As can be seen, the DWBA accurately predicts the energy dependence of the data at low energies, but drastically fails, by nearly a factor of seven, to predict the energy dependence between 140 and 312.6 MeV. This failure of the DWBA is not the result of the particular optical potential used in the analyses. Calculations using potentials I2 and C1 indicated that the ability of the DWBA to accurately reproduce the energy dependence of the transfer cross sections at low incident energies appears to depend upon the optical potential. However, the general trend of decreasing experimental cross sections and constant or increasing theoretical cross sections as the incident energy is increased, remains, independent of which set of optical potential parameters is employed.

The experimental angle-integrated cross sections for the $^{208}Pb(^{16}O,^{15}O)^{209}Pb$ reaction at 138.5 and 312.6 MeV are displayed in Fig. 6(a) and (b) for optical potentials Q2 and I2, respectively, and the theoretical spectroscopic factors[8,9] listed in Table 3. (Since the theoretical spectroscopic factor for the possible $1j_{15/2}$ fragment state at 3.72 MeV is extremely uncertain, the energy-averaged experimental spectroscopic factor for each optical potential was used for display purposes.) As may be seen, there is a general tendency of the DWBA calculations to increase with incident energy more rapidly than the data. This effect is similar to what was

Table 3. Spectroscopic factors for the $^{208}Pb(^{16}O,^{15}O)^{209}Pb$ reaction.

| State | $E_{ex}$ (MeV | $E_{inc}$ = 312.6 MeV Fit Q2 | Fit I2 | 138.5 MeV[a] Fit Q2 | Fit I2 | (d,p)[b] | Theory[c] |
|---|---|---|---|---|---|---|---|
| $2g_{9/2}$ | 0.00 | 0.89[d] | 0.89[d] | 0.89[d] | 0.89[d] | 0.92 | 0.89 |
| $1i_{11/2}$ | 0.78 | 0.87 | 0.86 | 0.51 | 0.47 | 1.14 | 0.96 |
| $1j_{15/2}$ | 1.424 | 0.85[e] | 0.86[e] | 0.75[e] | 0.78[e] | 0.77 | 0.65[f] |
| $3d_{5/2}$ | 1.565 | 0.89[d] | 0.89[d] | 0.89[d] | 0.89[d] | 0.89 | 0.91 |
| $4s_{1/2}$ | 2.03 | 0.89[d] | 0.89[d] | 5.94[g] | 6.44[g] | 0.85 | 0.94 |
| $2g_{7/2}$ | 2.49 | 0.89[d] | 0.89[d] | 1.42 | 1.61 | 0.95 | 0.84 |
| $3d_{3/2}$ | 2.54 | 0.89[d] | 0.89[d] | 0.89[d] | 0.89[d] | 0.99 | 0.90 |
| $1j_{15/2}$ | 3.05 | 0.20[h] | 0.20[h] | 0.07[h] | 0.07[h] | | 0.26[f] |
| $(1j_{15/2})$ | 3.72[i] | 0.26 | 0.25 | 0.24 | 0.22 | | - |

a) Data from Ref. 4 and reanalyzed in the present work.
b) From Ref. 12, for an incident energy of 20 MeV.
c) From Ref. 8.
d) Theoretical ground state spectroscopic factor is assumed.
e) Spectroscopic factor for the $1j_{15/2}$ level has been corrected for an equally large contribution from the unresolved $3d_{5/2}$ level (s = 0.89 assumed).
f) From Ref. 9.
g) Approximate spectroscopic factor (upper limit) since the experimental yields are small and the fits to the data are poor.
h) Spectroscopic factor for the $1j_{15/2}$ level has been corrected for an equally large contribution from the unresolved $2g_{7/2}$ level and for small contributions from the unresolved $4s_{1/2}$ and $3d_{3/2}$ levels (s = 0.89 assumed).
i) Approximate excitation energy. This group could contain transitions to several neighboring states.

observed in analyses of the proton-transfer data, although the severity of this discrepancy appears to be less for the neutron transfer data.

In this work, it has been demonstrated that the energy dependence of the transfer cross sections predicted by the DWBA fails to reproduce the experimentally observed energy dependence. It should be again noted that the overall absolute normalization of the DWBA calculations is not unique, and can be varied, in an energy-independent way by, for example, adjustments of the bound state parameters. In this way, the DWBA cross sections for the proton-transfer reaction at 312.6 MeV can be reduced by a factor of 2.54 by employing the $^{15}N+p$ bound-state potential parameters at both light- and heavy-ion vertices. However, this adjustment has a similar effect at 104 MeV (by a factor of 2.86), so that the discrepancy in the energy dependence is not removed. One consequence of this observation is that the precise energy at which the experimental and DWBA cross sections are equal is not physically significant since it is a function of the absolute normalization of the DWBA.

Adjustments of the optical potential parameters can also affect the absolute normalization of the DWBA, as well as the specific details of the predicted energy dependence. The important point to note, however, is that no reasonable adjustment of the model parameters can rectify this failure of the DWBA. Of course, agreement between the DWBA and experimental cross sections at the various incident energies could be obtained by ad hoc variations carried out at each energy, of the bound state and optical potential parameters and, as a result, sacrificing, if necessary, both the qualitative relationship of the bound state potentials to the nucleon-nucleus optical model as as well as the quality of optical model fits to the elastic scattering data. Such modifications, however, miss the point of the DWBA-optical model treatment of direct reactions and, moreover, have no predictive power. If as is shown in the present work a systematic application of the model uncovers major shortcomings, then this result should be taken as an indication that the physical premises of the model have broken down.

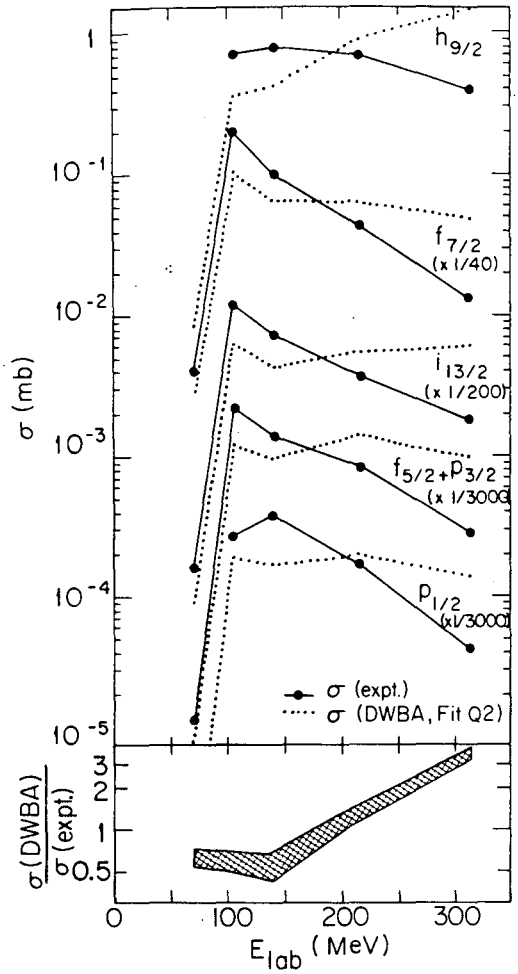


Fig. 5. Experimental and DWBA angle-integrated cross sections for the $^{208}Pb(^{16}O,^{15}N)^{209}Bi$ reaction as a function of incident energy, using optical model potential Q2. The ratios of DWBA to experimental cross sections for all measured transitions are contained within the cross-hatched area at the bottom of the figure. (XBL 777-1362)

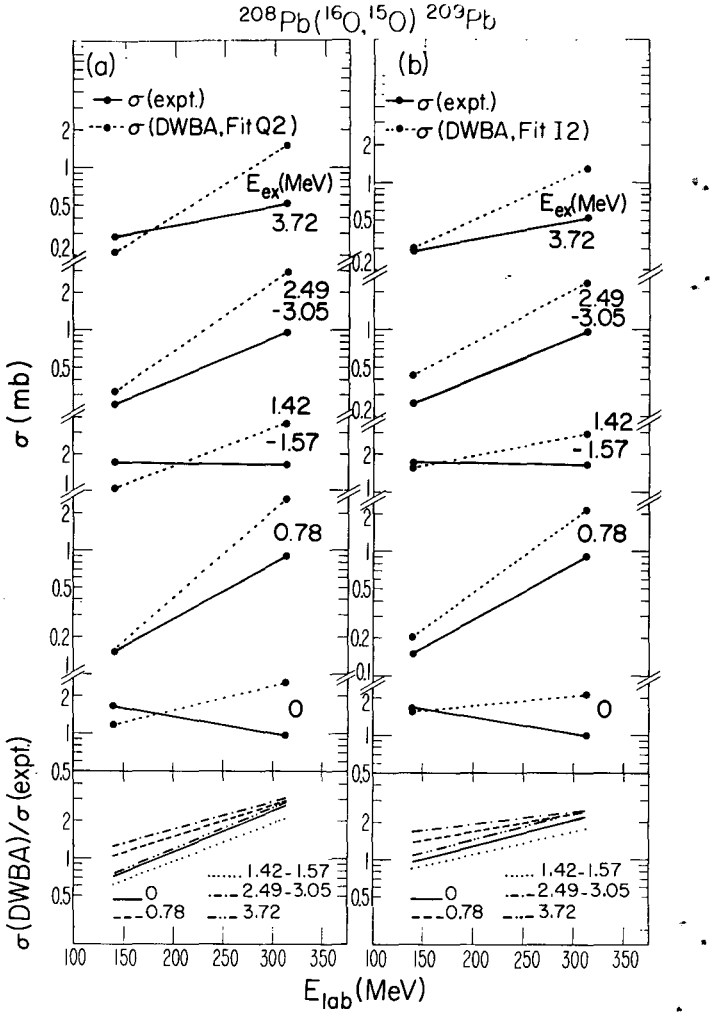


Fig. 6. Experimental and DWBA angle-integrated cross sections for the $^{208}Pb(^{16}O,^{15}O)^{209}Pb$ reaction as a function of incident energy, using optical model potentials Q2 (part a) and I2 (part G). The ratios of DWBA to experimental cross sections for all measured transitions are shown at the bottom of the figure. (XBL 777-1361)

Footnotes and References

*Condensed from LBL-6553.

†Present address: Physics Division, Argonne National Laboratory, Argonne, Illinois 60439.

‡Permanent address: Centre d'Etudes Nucleaires de Saclay, Gif-sur-Yvette 91190, France.

§Permanent address: Institut des Sciences Nucleaires, Grenoble, France.

‖Present address: Department of Physics, Michigan State University, East Lansing, Michigan 48824.

¶Argonne National Laboratory, Argonne IL 60439.

1. S. C. Pieper, M. H. Macfarlane, D. G. Kovar, D. H. Glockner, F. D. Becchetti, B. G. Harvey, D. L. Hendrie, H. Homeyer, J. Mahoney, R. Puhlhofer, W. von Oertzen and M. Zisman, in preparation.

2. A. R. Barnett, W. R. Phillips, P. J. A. Buttle and L. J. B. Goldfarb, Nucl. Phys. 176, 321 (1971).

3. D. G. Kovar, B. G. Harvey, F. D. Becchetti, J. Mahoney, D. L. Hendrie, H. Homeyer, W. von Oertzen and M. A. Nagarajan, Phys. Rev. Lett. 30, 1075 (1973).

4. F. D. Becchetti, B. G. Harvey, D. Kovar, J. Mahoney, C. Maguire and D. K. Scott, Phys. Rev. C 12, 894 (1975).

5. C. Olmer, M. Buenerd, C. K. Gelbke, D. L. Hendrie, J. Mahoney, A. Menchaca-Rocha and D. K. Scott, Nuclear Science Division Annual Report LBL-5075 (1975), p.102.

6. D. H. Glockner, M. H. Macfarlane and S. C. Pieper, Argonne National Laboratory, Report ANL-76-11 (1976).

7. C. Olmer, M. C. Mermaz, M. Buenerd, C. K. Gelbke, D. L. Hendrie, J. Mahoney and D. K. Scott, The Elastic Scattering of $^{16}O$ + $^{208}Pb$ and the Energy Dependence of the Interaction Radius, this Annual Report.

8. P. Ring and E. Werner, Nucl. Phys. A 211, 198 (1973).

9. I. Hamamoto, Nucl. Phys. A 126, 545 (1969); A 141, 11 (1970).

10. C. Ellegarrd and P. Vedelsby, Phys. Lett. 26B, 155 (1968).

11. K. S. Toth, J. L. C. Ford, Jr., G. R. Satchler, E. E. Gross, D. C. Hensley, S. T. Thornton and T. C. Schweizer, Phys. Rev. C, (1977).

12. D. G. Kovar, N. Stein and C. K. Bockelman, Nucl. Phys. A 231, 266 (1974).

# SIMILARITIES OF CROSS SECTIONS AND ISOTOPE YIELDS FOR PERIPHERAL COLLISIONS AT 140, 315 and 33600 MeV

M. Buenerd,* C. K. Gelbke, B. G. Harvey, D. L. Hendrie, J. Mahoney, A. Menchaca-Rocha,†
M. Mermaz, C. Olmer, and D. K. Scott

The measurement of cross sections for particles produced by heavy ions of relativistic energies at forward angles[1,2] has evoked substantial theoretical study.[3-7] Bombardments of a 0.7 mg/cm$^2$ thick $^{208}Pb$ target with 315 MeV $^{16}O^{6+}$ ions at the 88-in. cyclotron[8] yielded results that show similarity in both isotope yields and total reaction cross sections between this experiment at 20 MeV/A and those performed at 2.1 GeV/A[2,9] Although differences do exist, there being a general trend toward greater production of neutron-deficient isotopes at this higher energy, the relative cross sections for isotope production at the two energies are generally of the same magnitude and the relative element yields are identical within the experimental errors. This similarity was an unexpected result, since similar experiments at energies only a few MeV/A above the Coulomb barrier give entirely different distributions of reaction products.[10,11] At those energies, the relative ion velocities are smaller than the Fermi velocity and the interaction times are long enough to permit at least partial equilibration of the system, while at 20 MeV/A the relative velocities of the interacting nuclei are comparable to the Fermi velocity and consequently perhaps provide results bridging the low and high energy regions with characteristics of both types of reactions.

The small ratio $\sigma(^{15}N,^{16}O,315\ MeV)/\sigma(^{15}N,^{15}O,$ 33.6 GeV) is presumably due to the contribution of the $^{16}O(\gamma,p)$ and $(\gamma,n)$ reactions at the higher energy, where the $\gamma$ represents the virtual photon field of the high-Z target nucleus.[2] Assuming that the total reaction cross section is the sum of the cross sections for peripheral ($\sigma_p$) and central collisions ($\sigma_c$), one obtains $\sigma_c \approx 2100$ mb at 20 MeV/A and $\sigma_c \approx 2200$ mb at 2.1 GeV/A, which agrees with the high energy limit for the estimated fusion cross section.[12]

These results gave rise to two questions: (1) At what lower energy do the particle yields begin to differ significantly from the high energy results and how do they differ? (2) Are the relative cross sections at the lower energies target independent as has been observed[2] and explained[3,4,6] at 2.1 GeV/A? To answer these questions we used beams of 140 and 315 MeV $^{16}O$ to bombard targets of $^{94}Zr$, $^{197}Au$, $^{208}Pb$ and $^{232}Th$ [13] using triple $\Delta E - \Delta E - E$ solid-state telescopes to obtain isotope separation. To reduce the effect of different angular distributions for different reaction intervals the cross sections have been summed over an angular interval of 15 to 30° for the $^{94}Zr$ target and 10 to 45° for the $^{197}Au$ and $^{208}Pb$ targets at 140 MeV. At 315 MeV the cross sections were integrated between 10 and 20° for the $^{197}Au$ and $^{232}Th$ targets and the differential cross section at 10° for the $^{94}Zr$ target was used for the comparison of particle yields. The total yields for $^{16}O$ + $^{208}Pb$ at 315 MeV was taken from the earlier experiment and the cross sections for 33.6 GeV from Ref. 2. The relative particle yields vary significantly, as shown in Fig. 1, between 140 and 315 MeV and remain nearly constant between 315 MeV and 33.6 GeV, suggesting that cross sections do vary significantly for relative particle velocities smaller than the Fermi velocity and tend to be constant for larger velocities.

Figures 2 and 3 show a comparison of relative yields for different targets at 33.6 GeV and 315 MeV, respectively. From Ref. 2 the ratios of $\sigma(a + b \rightarrow x)/\sigma(a + b' \rightarrow x)$ where a is the projectile, b and b' the targets and x the observed particle should be independent of x for different targets, and this is shown to be true at these energies. Figure 4 shows the plots for 140 MeV and while the ratio of $\sigma(^{197}Au)/\sigma(^{208}Pb)$ remains constant, $\sigma(^{94}Zr)/\sigma(^{208}Pb)$ shows increasing yields for the lighter elements, possibly caused by the fact that the energy above the Coulomb barrier increases from 3.5 MeV/A for $^{16}O$ + $^{208}Pb$ to 5.4 MeV/A for $^{16}O$ + $^{94}Zr$. An increase of light particle yields is also seen when the beam energy is increased to 315 MeV from 140 MeV [see Fig. 1(a)].

The similarity of particle yields for $^{16}O$ + $^{197}Au$ and $^{16}O$ + $^{208}Pb$ at 140 MeV cannot be

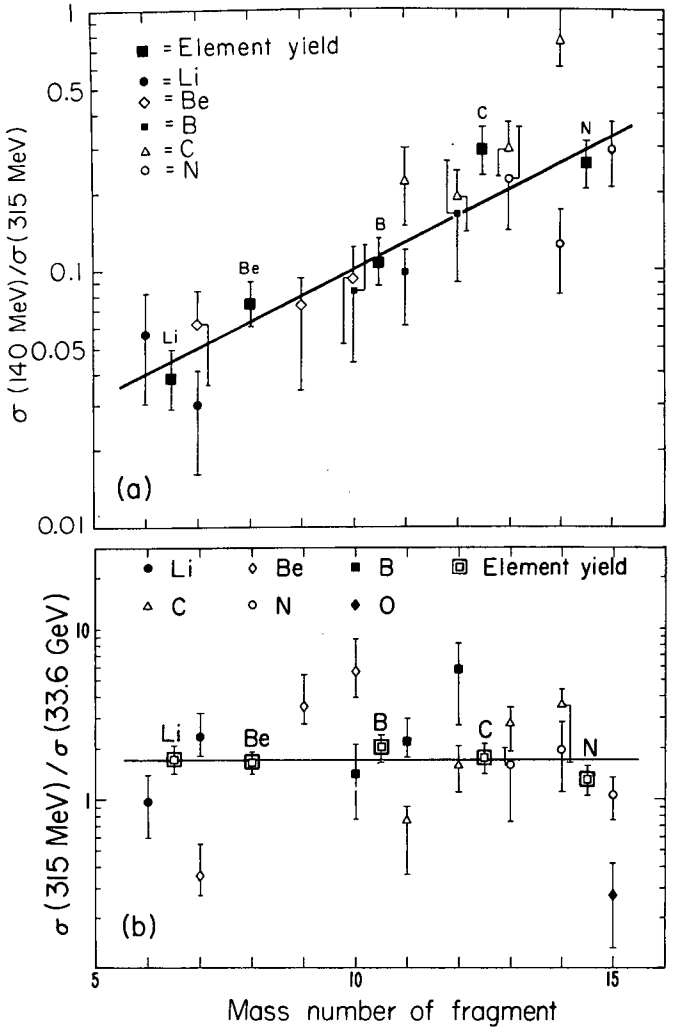


Fig. 1. Comparison of isotope yields for reactions induced by $^{16}O$ on $^{208}Pb$ at incident energies of (a) 140 and 315 MeV and (b) 315 MeV and 33.6 GeV. The vertical scale of part (a) is in arbitrary units
(XBL 768-3340A)

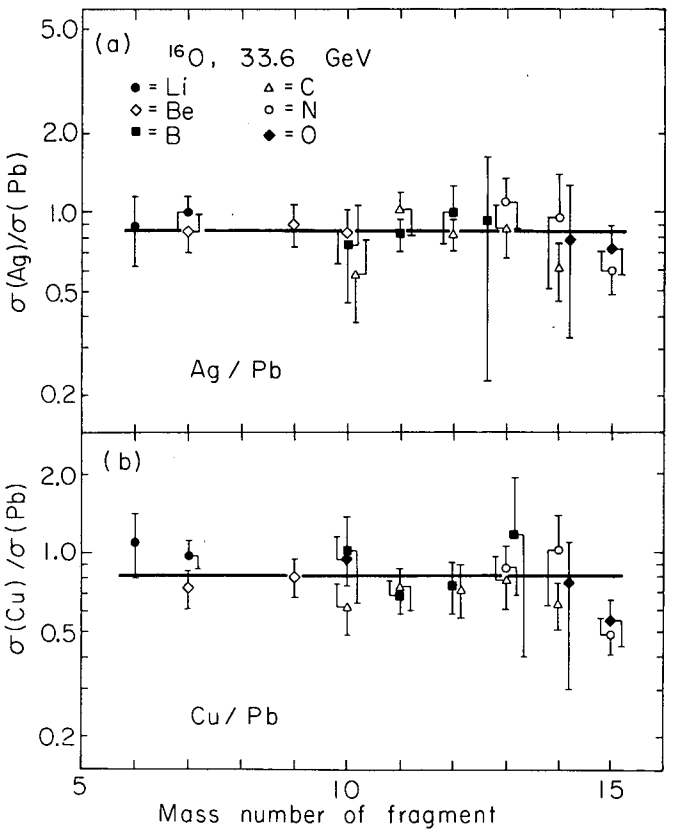


Fig. 2 Comparison of isotope yields observed in the bombardment of $^{16}O$ ions on Cu, Ag and Pb targets at 33.6 GeV laboratory energy. Data have been taken from Ref. 2.
(XBL 769-3953)

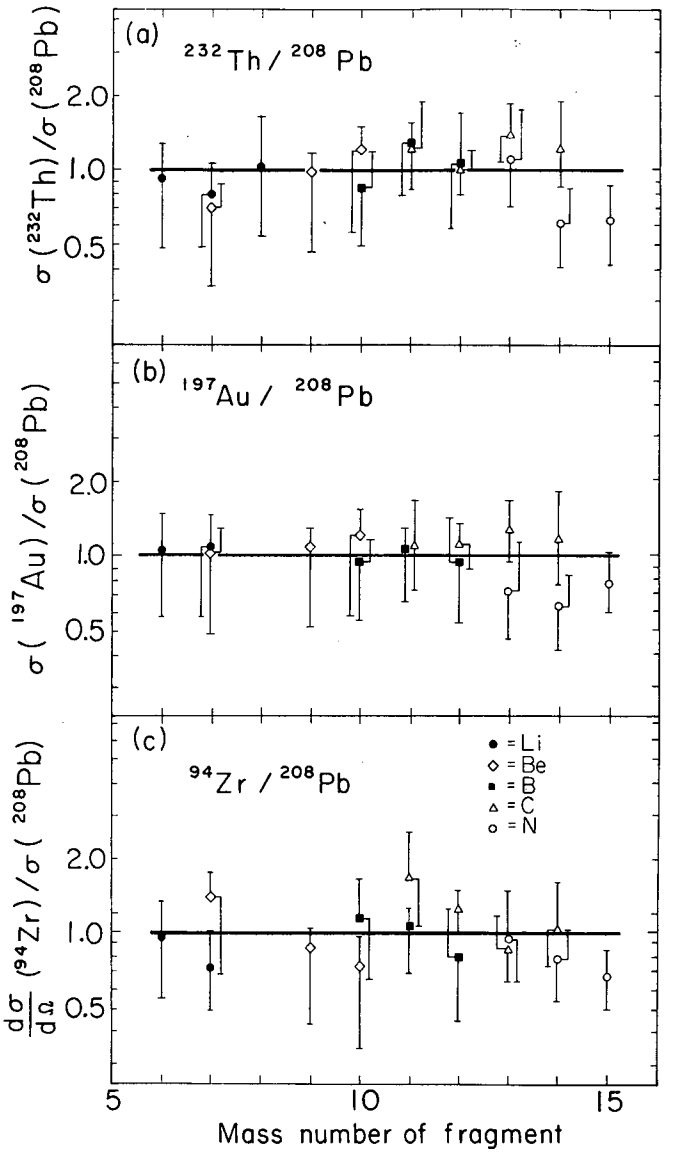


Fig. 3 Comparison of isotope yields observed in the bombardment of $^{232}Th$, $^{208}Pb$, $^{197}Au$ and $^{94}Zr$ targets by $^{16}O$ ions at 315 MeV laboratory energy. The vertical scale is in arbitrary units.
(XBL 769-3954)

anticipated from the systematics[10] which predicts the isotope production cross sections to be given by[10,14,15]

$$\sigma(A,Z) \propto \exp([\Delta v_c + Q_{gg}]/T) \quad . \qquad (1)$$

A and Z are the mass and charge of the observed nucleus, $\Delta V_c$ is the difference between the entrance and exit channel Coulomb barriers, $Q_{gg}$ is the ground state Q value of the corresponding transfer reaction and T is an effective temperature. Since T should not change significantly[14,15] between $^{16}O + ^{197}Au$ and $^{16}O + ^{208}Pb$, constant relative yields are expected only if the difference

$$\Delta = \Delta V_c(^{197}Au) + Q_{gg}(^{197}Au) - \Delta V_c(^{208}Pb) - Q_{gg}(^{208}Pb) \approx \text{constant} \qquad (2)$$

for each exit channel. $\Delta$ changes by more than 10 MeV, however, for the range of particles considered here. Calculating $Q_{gg}$ by using the liquid drop masses causes a smooth change with target mass and charge and could account for the similarity observed in the cross sections from $^{197}Au$ and $^{208}Pb$.

The assumption that the reaction products are highly excited and decay in flight[16] could explain the similarities of yields at 140 MeV. The decay in flight of the excited projectile has been assumed to be very important at relativistic energies[3,6,7] and it would be interesting to use the same approach over the entire energy range, from nonrelativistic to relativistic, in attempting to predict the energy dependence of peripheral reactions between heavy ions.

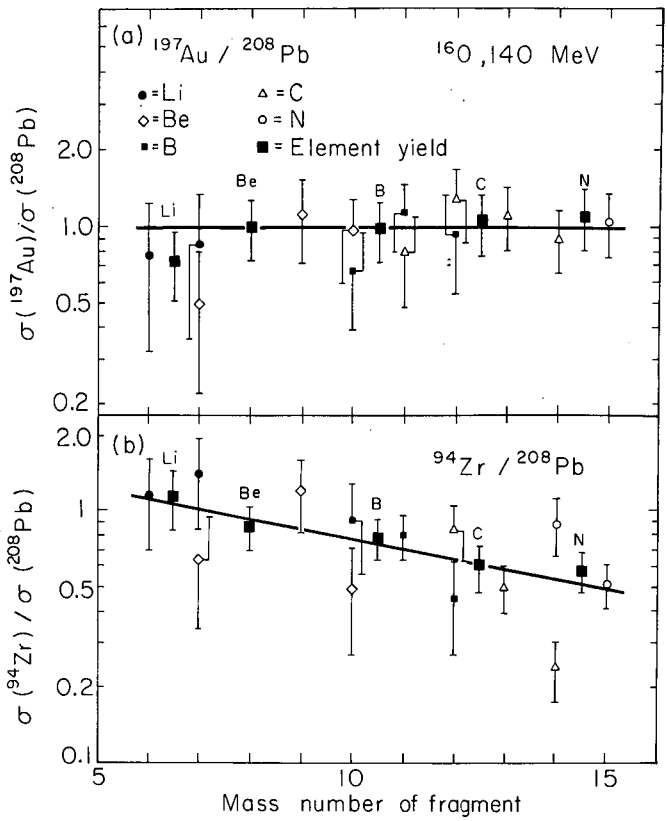


Fig. 4 Comparison of isotope yields observed in the bombardment of $^{208}Pb$, $^{197}Au$ and $^{94}Zr$ targets by $^{16}O$ ions at 140 MeV laboratory energy. The vertical scale is in arbitrary units. (XBL 769-3949)

## Footnotes and References

*Permanent address: Institute des Sciences Nucleaires, Cedex 257, 38044, Grenoble, France.

†Permanent address: Instituto de Fisica, U. N. A. M., Mexico.


1. D. E. Greiner, P. J. Lindstrom, H. H. Heckman, B. Cork and F. S. Bieser, Phys. Rev. Lett. 35, 152 (1975).

2. P. J. Lindstrom, D. E. Greiner, H. H. Heckman, B. Cork and F. S. Bieser, LBL-3650 (1975).

3. H. Feshbach and K. Huang, Phys. Lett. B 47, 300 (1973).

4. S. Barshay, C. B. Dover, and J. P. Vary, Phys. Lett. B 51, 5 (1974).

5. A. S. Goldhaber, Phys. Lett. B 53, 306 (1974).

6. V. K. Lukyanov and A. I. Titov, Phys. Lett. B. 57, 10 (1975); V. K. Lukyanov, Y. A. Panebratsev and A. I. Titov, Dubna preprint E2-9089.

7. J. Hüfner. K. Schäfer and B. Schürmann, Phys. Rev. C 12, 1888 (1975); A. Abul-Magd, J. Hüfner and B. Schürmann, Phys. Lett. B 60, 327 (1976).

8. M. Buenerd, C. K. Gelbke, B. G. Harvey, D. L. Hendrie, J. Mahoney, A. Menchaca-Rocha, C. Olmer, and D. K. Scott, Phys. Rev. Lett. 37, 1191 (1976).

9. P. J. Lindstrom, D. E. Greiner, H. H. Heckman, B. Cork and F. S. Bieser, Lawrence Berkeley Laboratory Preprint, HE-3-4.

10. V. V. Volkov, in Classical and Quantum Mechanical Aspects of Heavy-Ion Collisions, edited by H. L. Harney, P. Braun-Munzinger and C. K. Gelbke (Springer-Verlag, Heidelberg, 1975), p. 274, and Refs. therein.

11. A. G. Artukh, V. V. Avdeichikov, J. Erö, G. F. Gridnev, V. L. Mikheev, V. V. Volkov and J. Wilczynski, Nucl. Phys. A 160, 511 (1971).

12. M. Lefort, see Ref. 10, loc. cit., p. 275.

13. C. K. Gelbke, M. Buenerd, D. L. Hendrie, J. Mahoney, M. C. Mermaz, C. Olmer and D. K. Scott, Phys. Lett. 65B, 227 (1976).

14. A. Y. Abul-Magd, K. El-Abed and M. El-Nadi, Phys. Lett. B 39, 166 (1973).

15. J. P. Bondorf, F. Dickmann, D. H. E. Gross and P. J. Siemens, J. de Phys. 32, C6-145 (1971).

16. J. P. Bondorf and W. Nörenberg, Phys. Lett. 44B, 487 (1973).

# EXCITATION OF GIANT RESONANCES IN $^{208}Pb$ BY INELASTIC SCATTERING OF HEAVY IONS

A. Guterman,* D. Ashery,* D. K. Scott, M. S. Zisman, H. Wieman, C. K. Gelbke, and J. Alster*

The region of excitation of energy in nuclei where giant resonances are expected, has been extensively studied in recent years. Enhancement in the cross sections was observed in photonuclear reactions and in inelastic scattering of electrons, protons, deuterons, $^3$He and $^4$He particles. The existence of the resonance was established and various properties were studied. However, a definite conclusion about the multipolarity of the observed resonances has not been reached, although there is a tendency to believe that giant quadrupole resonances were identified. Still, a monopole resonance at the same excitation energy could be populated.

An attempt to selectively populate the giant quadrupole resonance was made[1] by using the Coulomb excitation process which should not populate a monopole resonance. This was done by bombarding $^{197}$Au and $^{208}$Pb with $^{16}$O and $^{20}$Ne ions from the 88-in. cyclotron at sub-Coulomb energies. Due to the large background and small cross section for this process, only upper limits for the cross section could be deduced. The experiment was continued at the 88-in. cyclotron by bombarding $^{208}$Pb with 140 MeV $^{16}$O ions. At this energy the Coulomb excitation cross section is larger but there is also a large contribution to the cross section from nuclear excitation. Coulomb nuclear interference may then be observed if a quadrupole resonance is populated. No such interference is expected for a monopole resonance because of the vanishing Coulomb contribution.

The angular distribution of the inelastically scattered $^{16}$O was measured between 31 to 50° in 2° to 3° steps. Preliminary results indicate a fine structure in the observed broad peak (see Figs. 1 and 2). Several peaks with possible different angular distributions are observed. The energies of two of these peaks are consistent with the results recently observed by inelastic scattering of 120 MeV α particles from $^{208}$Pb.[2] The results are being analyzed with a program which includes Coulomb nuclear interference terms.

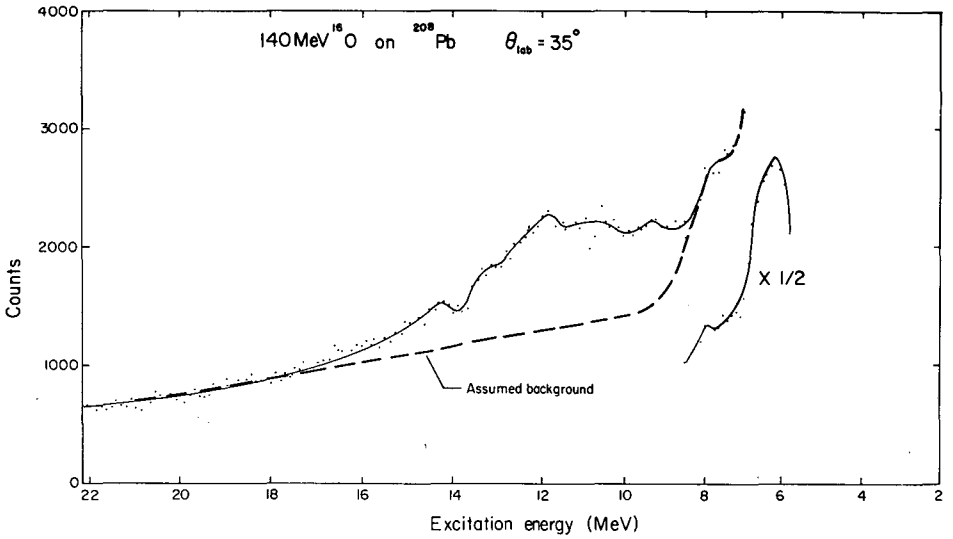


Fig. 1. Inelastic scattering of 140 MeV $^{16}$O on $^{208}$Pb at a lab scattering angle of 35°. The broad structure above the dashed background line is the assumed giant resonance. (XBL 778-1705)

Fig. 2. Inelastic scattering of 140 MeV $^{16}$O on $^{208}$Pb at a lab scattering angle of 40°. Bound state peaks are included. (XBL 778-1706)

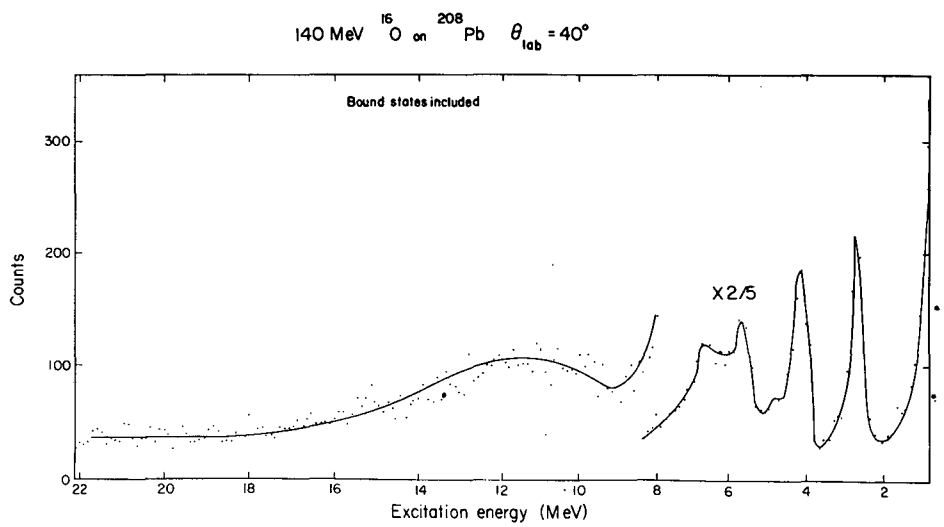


Footnote and References

*Tel Aviv University, Israel.

1. D. Ashery et al., LBL-5075, p. 97.

2. Harakeh et al., Phys. Rev. Lett. 38, 676 (1977).

# EXPERIMENTAL STUDY OF THE E2 STRENGTH DISTRIBUTION IN $^{12}C$ and $^{16}O$ NUCLEI*

M. Buenerd,† C. K. Gelbke, D. L. Hendrie, J. Mahoney, C. Olmer, and D. K. Scott

The giant quadrupole resonance (GQR) in nuclei with mass $A > 28$ lies around $63\ A^{-1/3}$ (MeV) excitation energy and exhausts most ($\gtrsim$ 60%) of the energy weighted sum rule (EWSR). In lighter systems, the $^{16}O$ nucleus has been investigated via the reaction $^{15}N(p,\gamma)$[1] and more recently by inelastic hadron scattering experiments.[2,3] All these measurements concur as to the existence of a noticeable E2 strength between 15 and 30 MeV excitation energy. It is clearly shown in Ref. 2 that the GQR does not appear as a single broad (4-5 MeV) bump, as in medium mass and heavy nuclei, but is spread over several individual states. This trend is quite analogous to that of the isovector giant dipole resonance (GDR)[4] which also appears as a single broad state in nuclei with $A > 40$ and shows spreading over several fine structure states in lighter systems. It is of interest to pursue the study of the GQR in lighter nuclei tracking the E2 strength and its spreading into the continuum. We report measurements of the distribution of E2 states in $^{12}C$ and $^{16}O$ nuclei by inelastic scattering of 130 MeV $^3He$ particles. The $^{16}O$ data have been used for comparison with the results from the $^{16}O(\alpha,\alpha')$ study[2] in order to check that the weak $^3He$-nucleus isovector effective interaction[5] does not produce a noticeable excitation of the isovector states (especially the GDR) in the 20 to 30 MeV excitation energy region.

The experiments were performed at the 88-in. cyclotron. The scattered particles were identified with two $\Delta E$ - E(2.5 to 5 mm) silicon detector telescopes. The $^{12}C$ target had a thickness of 650 $\mu g/cm^2$. The gas cell for the $^{16}O$ experiment consisted of a cylinder of 60 mm diam. with a 3 $mg/cm^2$ Havar window; the pressure of the cell was between 8 and 13 psi. Spectra were recorded between 12.5 and 40°, with an overall resolution of about 300 to 400 keV for both targets.

The measured spectra have been separated into background and peaks. The background was approximated by fitting by computer a set of five points of the spectrum with a polynomial. The points were chosen so that the background joined the high-lying continuum smoothly down to the $\alpha$-particle threshold region, passing by the minima between the peaks in the 10 to 20 MeV excitation energy region. The results obtained are illustrated in Fig. 1. After subtraction of the background, the difference spectra have been unfolded into single peaks using a computer code performing a $\chi^2$ search in each region of the spectrum and fitting at most 4 three-parameter Gaussian shaped peaks.

The $^{16}O$ spectra (Fig. 1) are identical to those obtained from the $(\alpha,\alpha')$ reaction[2]. Furthermore, no E1 contribution was detected in the analysis of the angular distributions of the individual levels. Moreover, in the $^{12}C$ spectrum we have found no evidence for the strong E1 state at $E_x \approx 22$-23 MeV.[4] This confirms that the strength observed in the present experiments is mostly isoscalar, and that the cross section for the excitation of the GDR can be neglected. For both nuclei, the peak structure of the spectrum between 15 MeV and 30 MeV excitation energy, exhibit the same overall shape across the angular range investigated; we see this feature as an indication that the continuum is dominated by one excited multipole with negligible inclusion of other L values. Indeed, assuming that two states with different multipolarities and comparable cross section are excited, the calculations (see below) predict that the extrema of their relative cross sections would be different by a large factor ($\gtrsim$ 3) between 15 and 30° c.m., and this was not observed above $E_x \approx 15$ MeV. The experimental angular distributions displayed in Fig. 2 exhibit shapes with quite similar structure, slightly changing with the excitation energy.

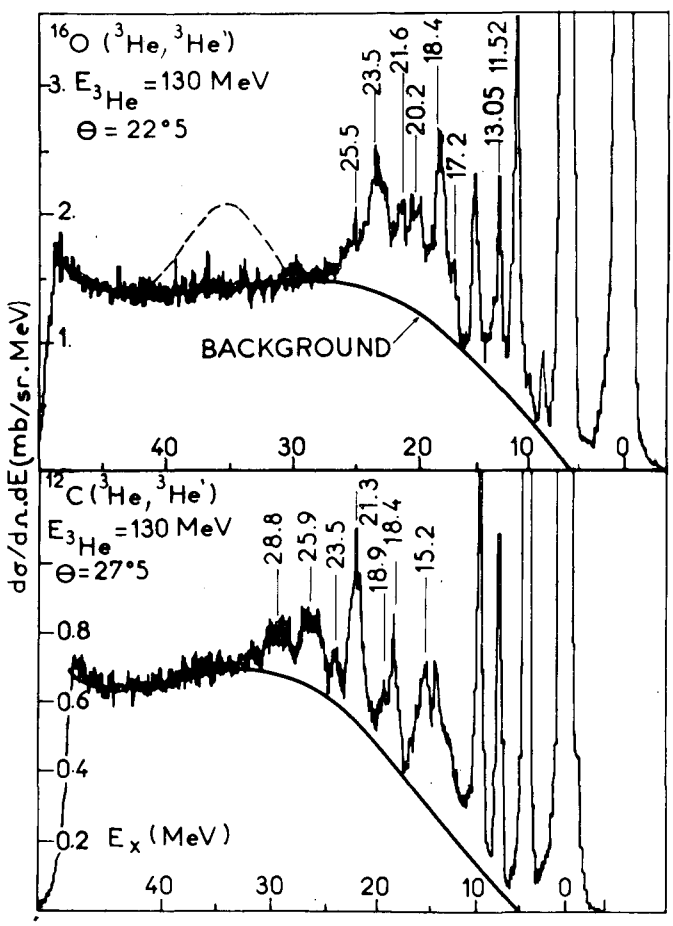


Fig. 1. Examples of measured spectra. Excitation energies of the E2 states above 10 MeV are indicated. The dashed bump is the expected cross section for giant octupole resonance (see text).

(XBL 778-1811)

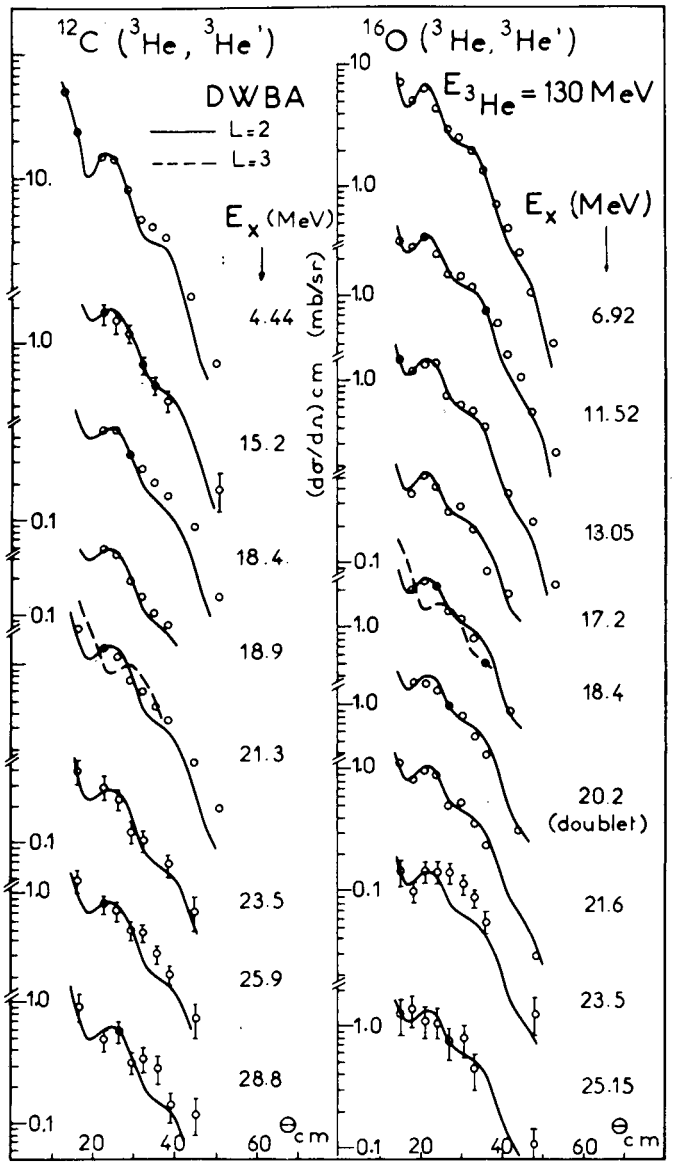


Fig. 2 Angular distributions of the E2 transitions. The error bars are ±5% for the first $2^+$ state, ±10% for states below $E_x$ = 15 MeV and ±15% above; larger error bars are indicated. The points are fitted with DWBA calculations for L = 2 transitions (solid line). The dashed line is an example of L = 3 calculation.
(XBL 778-1812)

DWBA calculations have been performed with the code DWUCK (version DWUCK 4). Optical model parameters have been obtained by fitting the inelastic scattering data; they are for $^{12}C$: V = 83.6 MeV; $r_V$ = 1.2, $a_V$ = 0.77 fm; W = 13.45 MeV; $r_W$ = 1.83; $a_W$ = 0.59 fm; and for $^{16}O$ : V = 89.7; $r_V$ = 1.2; $a_V$ = 0.84 fm; W = 15.51 MeV; $r_W$ = 1.73; $a_W$ = 0.58 fm. The experimental angular distributions have been compared to collective model calculations.[6] Multipolarities and deformation parameters $\beta_L$ have been deduced from this comparison, the latter expressed in terms of percentage of the EWSR limit given by the formula:[6]

$$\sum_n \hbar\omega_L^{(n)} \left(\beta_L^{(n)} R\right)^2 = \frac{4\pi}{A} \frac{\hbar}{2m} \frac{L(2L+1)^2}{(L+2)^2} \frac{\langle r^{2L-2}\rangle}{\langle r^{L-1}\rangle^2} , \quad (2)$$

where R is the radius of the real part of the optical potential, all other notations being the same as in Ref. 6. The multipole-moments of the nuclear matter distribution have been calculated using parameters taken from Ref. 7, assuming a Saxon-Wood shape.

For the two nuclei, the DWBA calculations using complex form factor fit the first $2^+$ (Fig. 2) and $3^-$ levels, providing a sound basis for L-assignments to high excitation energy states. However the deduced ($\beta_L$ R) values are much smaller than those obtained from other reactions due to very different real and imaginary radii of the $^3He$ optical potential. Hence, the deformation lengths have been extracted using real form factor calculations as they fit correctly the forward angles cross sections and provide ($\beta_L$ R) values in agreement with other experimental values for the first $2^+$ and $3^-$ states of both $^{12}C$ (Ref. 8) and $^{16}O$ (Ref. 9). The angular distributions of the assigned E2 transitions are shown in Fig. 2, which fit with L = 2 DWBA calculations; one L = 3 calculated shape is also indicated for comparison. For the $^{16}O$ nucleus they confirm the results of Ref. 2. However the angular distribution of the 23.5 MeV state exhibits a slight bump in the 25 to 30° region, rather than a rapid fall off observed for the other angular distributions, perhaps due to a contamination by another multipolarity.

In Ref. 10 evidence has been obtained for a large E3 strength (≈ 70% EWSR) centered around $E_x \approx 35$ MeV. We have calculated the expected cross section in our data and found that for 50% EWSR and assuming a 5 MeV FWHM this giant octupole resonance should appear as shown in Fig. 1. Its non-observation raises some questions about the assumptions made in Ref. 10. For the $^{12}C$ nucleus[1] E2 assignments have previously been made for the 15.2 MeV[1] and the 18.4 MeV[12,15] states. A state found at 21.3 MeV from inelastic scattering of 155 MeV protons was assigned E3 on a solid basis[12] and some other E3 strength has been located around 21.6 MeV.[13] The present results suggest that the latter could be isovector, but there is some uncleared ambiguity about the presence of E2 and E3 strength in the 21 to 22 MeV excitation energy region of $^{12}C$. The present results also suggest that the E1 strength reported in Ref. 14 could have been overestimated because of undetected E2 strength.

For the two nuclei studied, the percentages of the EWSR limit exhausted in the observed E2 transitions are listed in Table 1 together with the excitation energies, widths and deformation lengths. The total E2 strength exhausted up to 30 MeV excitation energy is around 46% in $^{12}C$ and 55% in $^{16}O$, the latter value in reasonable agreement with previous measurement[2]. In both nuclei, the giant quadrupole resonance is split into several states and its strength is spread over a larger excitation energy range (∿ 13 MeV) for $^{12}C$ than for $^{16}O$ (∿ 8 MeV). The centroid of the GQR (assumed to include states at $E_x$ > 15 MeV) lies around 21.5 MeV in both nuclei and the

Table 1. Excitation energies $E_x$ full width at half maximum (FWHM) corrected from experimental resolution $\Gamma$, deformation length ($\beta_2 R$) and percentage of the EWSR for the measured quadrupole transitions. Associated uncertainties are indicated for the first two quantities. (a) doublet (19195 MeV to 20.6 MeV) resolved at $\theta_{lab} = 17°5$.

| $E_x \pm \Delta E_x$ (MeV) | $\Gamma \pm \Delta\Gamma$ (MeV) | $\beta_2 R$ | $\%S_2$ |
|---|---|---|---|
| 4.4 | | 1.60 | 15.7 |
| 15.2 ± 0.3 | 1.8 ± 0.3 | 0.55 | 6.4 |
| 18.4 ± 0.1 | 0.4 ± 0.1 | 0.35 | 3.1 |
| 18.9 ± 0.15 | 0.7 ± 0.15 | 0.27 | 2.0 |
| 21.3 ± 0.15 | 1.4 ± 0.2 | 0.51 | 7.6 |
| 23.5 ± 0.2 | 0.6 ± 0.2 | 0.23 | 1.7 |
| 25.9 ± 0.3 | 2.2 ± 0.3 | 0.39 | 5.5 |
| 28.8 ± 0.4 | 2.7 ± 0.4 | 0.34 | 4.5 |
| $^{12}C$ | Total $^{12}C$ | | 46% |
| 6.92 | | 0.83 | 7.9 |
| 11.52 | | 0.57 | 6.2 |
| 13.05 ± 0.1 | | 0.42 | 3.7 |
| 17.20 ± 0.15 | < 0.2 | 0.25 | 1.8 |
| 18.40 ± 0.1 | 1.0 ± 0.2 | 0.56 | 9.4 |
| 20.2 ± 0.2(a) | doublet | 0.46 | 7.0 |
| 21.6 ± 0.2 | 1.0 ± 0.3 | 0.36 | 4.7 |
| 23.50 ± 0.15 | 1.5 ± 0.2 | 0.43 | 7.1 |
| 25.15 ± 0.3 | 2.8 ± 0.6 | 0.40 | 6.8 |
| $^{16}O$ | Total $^{16}O$ | | 55% |

strength corresponds to 31% and 37% of the EWSR for $^{12}C$ and $^{16}O$, respectively. Thus, in light nuclei the GQR exhausts a markedly smaller part of the sum rule limit and lies at a smaller excitation energy ($\sim$ 50 to 53 $A^{-1/3}$ MeV) than in heavier nuclei, exhibiting trends similar to those observed for the isovector giant dipole resonance.

## Footnotes and References

*Condensed from Le Journal de Physique-Lettres Tome 38, 15 Janvier 1977, page L-53.

†Now at Institut des Sciences Nucleaires, Grenoble, France.


1. S. S. Hanna et al., Phys. Rev. Lett. 32, 114 (1974).

2. K. T. Knöpfle et al., Phys. Rev. Lett. 35, 779 (1975).

3. M. Buenerd, P. Martin, P. de Saintignon and J. M. Loiseaux, Phys. Rev. C 14, 1316 (1976).

4. B. L. Bermann, Nuclear Data Tables 15, 319 (1975).

5. A. Moalem, W. Benenson, and G. M. Crawley, Nucl. Phys. A 236, 307 (1974).

6. G. R. Satchler, Nucl. Phys. A 195, 1 (1972).

7. R. Hofstadter, Nuclear and Nucleon Structure (Benjamin) 1963.

8. G. R. Satchler, Nucl. Phys. A 100, 97 (1967); J. D. Walecka, Phys. Rev. 126, 663 (1962).

9. F. Ajzenberg-Selove, Nucl. Phys. A 188, 1 (1971) and to be published in Nucl. Phys. See also Ref. 2 and references therein.

10. D. Lebrun et al., Nucl. Phys. A 265, 291 (1976)

11. M. Buenerd et al., La Physique Nucleaire autour des Cyclotrons et des Tandems, Louvain-la-Neuve, Belgium (1974). J. Physique Colloq. 35, C5-4 (1974).

12. M. Buenerd, Thesis, Universite de Grenoble (1975).
M. Buenerd, P. Martin, P. de Saintignon and J. M. Loiseaux, in preparation.

13. A. Yamagushi, T. Terasawa, K. Nakahara and Y. Yorizuka, Phys. Rev. C 3, 1750 (1971).
M. Buenerd, P. Martin, P. de Saintignon, and J. M. Loiseaux, Int. Conf. on Nuclear Structure and Spectroscopy, Amsterdam, Vol. II (1974) p. 286.

14. M. Buenerd, P. Martin, P. de Saintignon and J. M. Loiseaux, Phys. Rev. Lett. 33, 1233 (1974).

15. K. T. Knöpfle et al., Phys. Lett. 64B, 263 (1976).

# 2. Macroscopic

## MEASUREMENTS OF THE FUSION OF $^{12}C + ^{14}N$ AND THE LIQUID-DROP LIMIT FOR $^{26}Al$

R. G. Stokstad,* R. A. Dayras,* J. Gomez del Campo,* P. H. Stelson,* C. Olmer, and M. S. Zisman

The value of the angular momentum J for which the fission barrier $B_f$ is zero is often referred to as the liquid-drop limit.[1] It represents an absolute maximum angular momentum, $J_{max}$, above which an equilibrated compound nucleus probably does not exist and, therefore, is not expected to be formed in a heavy-ion reaction. Efforts to determine $J_{max}$ have been difficult because the liquid-drop limit is not always the most restrictive limitation on the heavy-ion fusion cross section, $\sigma_{fus}$.[2] A large amount of data for projectiles with $A \leq 40$ is explained by one-dimensional potential models[3] in which entrance-channel requirements, such as penetration to a critical radius, limit $\sigma_{fus}$. In a few cases, at very high bombarding energies, the deduced critical angular momenta equal or sometimes exceed the predicted values of $J_{max}$ by 10 to 15 percent.[4,5] Entrance-channel models seem to provide a good explanation of these data. Experiments with very heavy projectiles, in which even the predicted entrance-channel limitations allow angular momenta far in excess of the predicted liquid-drop limit, are difficult to interpret because of the problem of distinguishing the products of equilibrium fission from those of quasi-fission or deep inelastic scattering.[5] A measurement of $J_{max}$ is important, however, in that it probes one of the fundamental limits to the stability of the nucleus and tests the ability of a basic nuclear model to predict this limit.

Beams of 248 MeV and 158 MeV $^{14}N$ from the 88-in. cyclotron were used to bombard a 304 $\mu g/cm^2$ natural carbon target. Reaction products were detected by two separate solid-state counter telescopes having three detector-elements of 11, 44, and 3000 μm, and 14, 70, and 2000 μm, respectively. The data were recorded event-by-event on magnetic tape for later analysis. Measurements were made over the laboratory angular region of 3 to 40°. The target thickness was determined both by weighing and by α-ranging; the telescope solid angles of 0.16 msr and 0.35 msr were measured with a calibrated α-source.

The energy spectra of the reaction products with Z = 5-9 exhibit two components at forward angles. As discussed in Ref. 6, the lower energy component corresponds to evaporation residues and the higher energy component to direct-reaction products which have an energy-per-nucleon similar to that of the projectile and a very forward-peaked angular distribution. The features of the energy spectra taken at 248 MeV were qualitatively similar to those observed at lower energies and therefore could be analyzed in the manner described in Ref. 6. Care was taken to unfold the evaporation-residue and direct-reaction components of the spectra in a consistent way for data obtained at all bombarding energies in the present work and in Ref. 6.

At sufficiently high bombarding energies there can be a non-negligible probability for the compound nucleus to evaporate five α-particles or four α-particles plus several nucleons, leaving a Li or a Be nucleus as the residue. Since it was not possible to identify the evaporation-residue component in the Li and Be spectra, we have used the evaporation code LILITA[7] to estimate the fraction of the fusion cross section which would appear as residues with Z less than 5. These values are (4 ± 2)% and (13 ± 3)% at 158 and 248 MeV, respectively. This procedure includes an estimate of the "α-particle residues" which result from the decay of $^9B$, $^8Be$ and particle unstable excited states of Li and Be. The predicted relative intensities are not sensitive to reasonable variations in the value of $J_{max}$ assumed in the calculation.

Figure 1 shows the measured and predicted relative intensities of the evaporation residues at $E_{^{14}N}$ = 158 and 248 MeV, respectively. Figure 2

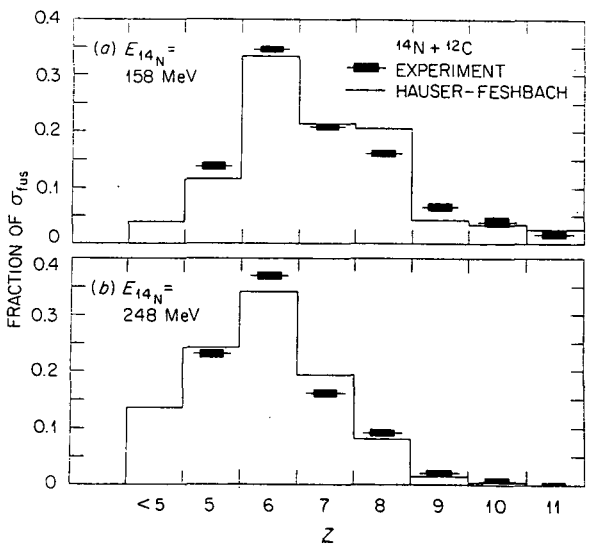


Fig. 1. Angle integrated yields for evaporation residues with Z = 5-11, expressed as a fraction of $\sigma_{fus}$. The histograms are the predictions of the code LILITA.

(XBL 777-9737)

presents the new experimental results for $\sigma_{fus}$ at $E_{^{14}N}$ = 158 and 248 MeV together with earlier results[6] for $\sigma_{fus}$ at energies ranging from 34 MeV to 178 MeV. The values obtained for $E_{^{14}N} \geq 145$ MeV have been revised upward slightly by small amounts corresponding to $Z < 5$ residues.

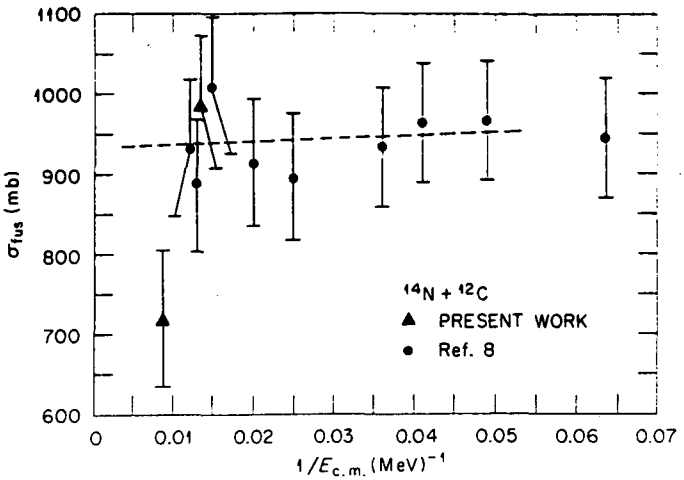


Fig. 2. Values of $\sigma_{fus}$ vs $1/E_{c.m.}$. The dashed line is a fit to all data points except those at the lowest and highest bombarding energies. (XBL 777-9735)

One-dimensional entrance-channel models[3] predict that the fusion cross section should vary approximately linearly with $E_{c.m.}^{-1}$ for energies well above the interaction barrier. The dashed line in Fig. 2 is a least-squares fit to the values $\sigma_{fus}$ for $E_{c.m.}^{-1} = 0.012 - 0.049$ MeV$^{-1}$ corresponding to $E(^{14}N) = 43 - 178$ MeV. An entrance-channel limitation would thus indicate a fusion cross section at 248 MeV of 936 mb or $J = 31.6\ \hbar$. We observe, however, only 717 ± 85 mb corresponding to a critical angular momentum of 27.5 ± 1.7 ħ. Clearly, at the highest energy there is a limitation on the fusion cross section which is more restrictive than that imposed by the entrance channel.

Figure 3 presents the critical angular momenta deduced from the measured values of $\sigma_{fus}$ using the sharp-cutoff relation $\sigma_{fus} = \pi \lambda^2 (J+1)^2$. The excitation energy in $^{26}$Al is defined as the center-of-mass bombarding energy plus the 15 MeV separation energy for $^{12}C + ^{14}N$. The dashed line represents a linear fit for excitation energies between 30 and 100 MeV. The solid line at $J(J+1) = 734\ \hbar^2$ corresponds to the predicted liquid-drop limit[1] of $J_{max} = 26.6\ \hbar$. Thus, the smaller fusion cross section observed at 248 MeV is consistent with the prediction of the rotating liquid-drop model and a value of ≈ 27 h for the maximum angular momentum which the $^{26}$Al compound nucleus may have.

It is important to account for the "missing" portion of cross section which does not appear as fusion residues at 248 MeV and which should be reflected in a larger direct-reaction cross section. We find that the direct-reaction yield rises from 476 mb at 158 MeV to 734 mb at 248 MeV.

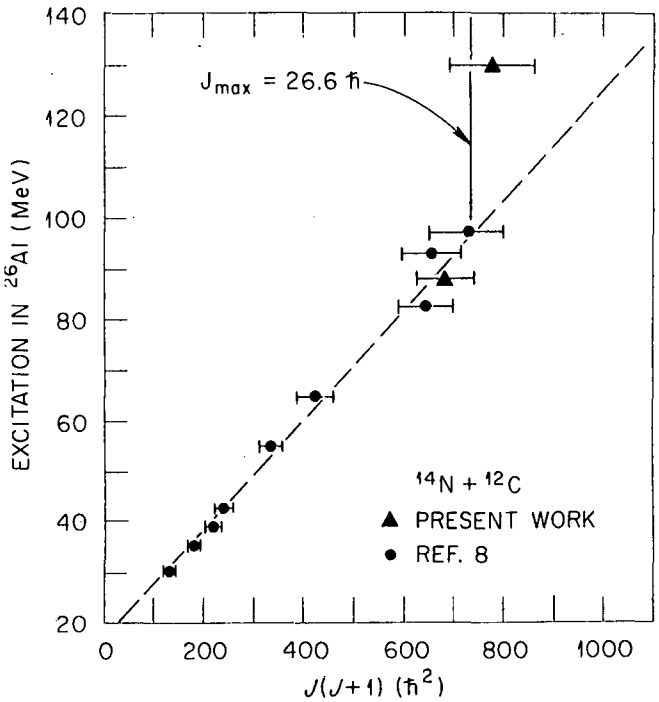


Fig. 3. Values of the critical angular momentum, J, plotted as J(J+1), vs excitation energy in $^{26}$Al. The dashed line is a fit to all data points except that at 130 MeV excitation. (XBL 777-9734)

This increase accounts within errors for the 270 mb decrease in the fusion cross section from the value of 987 ± 80 mb at 158 MeV to the value of 717 ± 85 mb at 248 MeV. The total reaction cross sections of 1460 ± 120 mb (at 158 MeV) and 1450 ± 120 mb (at 248 MeV) compare favorably with optical model estimates of 1450 and 1515 mb based on optical parameters deduced from measurements of $^{12}C + ^{12}C$ scattering.[8] This comparison also indicates that the emission of protons, neutrons and α-particles continues to be the main mode of decay for these light compound systems, even though the predicted barrier for symmetric fission is small for large angular momenta.

In summary, the measured fusion cross section for $^{14}N + ^{12}C$ shows a marked decrease when the $^{14}N$ bombarding energy is increased from 158 to 248 MeV. Considered together with previous experiments at other energies below 180 MeV, the present results suggest that the absolute maximum angular momentum which the $^{26}$Al nucleus can support has been observed, in agreement with the predictions of the rotating liquid-drop model.

## Footnote and References

*Oak Ridge National Laboratory, Oak Ridge, TN 37830

1. S. Cohen, F. Plasil and W. J. Swiatecki, Ann. of Phys. 82, 557 (1974).

2. A. M. Zebelman and J. M. Miller, Phys. Rev. Lett. 30, 27 (1973).

3. R. Bass, Phys. Lett. 47B, 139 (1973); D. H. E. Gross and H. Kalinowski, Phys. Lett. 48B, 302 (1974); D. Glas and U. Mosel, Nucl. Phys. A 237, 429 (1974).

4. M. N. Namboodiri, E. T. Chulick, J. B. Natowitz and R. A. Kenefick, Phys. Rev. C 11, 401 (1975); M. N. Namboodiri, E. T. Chulick and J. B. Natowitz, Nucl. Phys. A 263, 491 (1976).

5. H. C. Britt et al., Phys. Rev. C 13 1483 (1976).

6. R. G. Stokstad et al., Phys. Rev. Lett. 36, 1529 (1976); J. Gomez del Campo et al., to be published.

7. J. Gomez del Campo, Computer Code LILITA (unpublished).

8. R. M. Wieland, R. G. Stokstad, G. R. Satchler and L. D. Rickertsen, Phys. Rev. Lett. 37, 1458 (1976).

## DISTRIBUTION OF REACTION STRENGTH OBSERVED IN $^{16}O + ^{40}Ca$ COLLISIONS

S. E. Vigdor,* D. G. Kovar,* P. Sperr,* J. Mahoney, A. Menchaca-Roca, C. Olmer, and M. S. Zisman

The distribution of strength among all reaction channels in the interaction of $^{16}O + ^{40}Ca$ has been investigated over a wide range of bombarding energies, in collaboration with a group from Lawrence Berkeley Laboratory.[1] Angular distributions for transfer reactions and inelastic scattering, as well as for elastic scattering, were obtained at $E_{lab}(^{16}O)$ = 56 and 75 MeV at Argonne, and at 104, 140, and 214 MeV at the LBL 88-in. cyclotron. The complete fusion cross section was measured at these energies and in addition at 40, 45, 50, and 63 MeV by detection of the heavy fragments (evaporation residues) remaining after particle decay of the compound nucleus $^{56}Ni$. All the measurements were made with silicon-detector telescopes; for the fusion measurements, $\Delta E$ detectors of thickness 2.3 μm or 3.6 μm were used. A representative two-dimensional (E vs $\Delta E$) spectrum acquired with the fusion telescope at $E_{lab}$ = 140 MeV is shown in Fig. 1.

In Fig. 2 the measured fusion cross sections ($\sigma_{fus}$) are compared to the total reaction cross sections ($\sigma_{reac}$) as a function of bombarding energy. At energies up to about twice the Coulomb barrier height $\sigma_{fus}$ accounts for most of $\sigma_{reac}$. However, whereas the fusion cross section saturates at $E_{lab} \approx 70$ MeV, the reaction cross section continues to rise rapidly toward higher energies. This "break" between $\sigma_{fus}$ and $\sigma_{reac}$ is consistent with the model of Glas and Mosel,[2] which assumes that fusion occurs only upon penetration to a critical distance $R_c$; the solid line through the fusion measurements in Fig. 2 is calculated using this model and the parameters indicated in the figure.

While the data analysis for the nonfusion reactions is still in progress, it is clear that most of the "missing" reaction cross section at high energies in Fig. 2 is accounted for by inelastic scattering and by stripping of relatively few nucleons into the target nucleus, accompanied by substantial (but not complete) damping of the initial kinetic energy into internal excitation of the fragments. The cross section for transfer of more than two units of charge increases with increasing bombarding energy, but remains a small fraction of $\sigma_{reac}$ even at 214 MeV. The angular distributions of the transfer reaction products at the high energies are strongly forward peaked, as has been observed also for other light systems.[3]

Little is yet known about the decomposition of the total reaction cross section in collisions between light nuclei at very high energies.

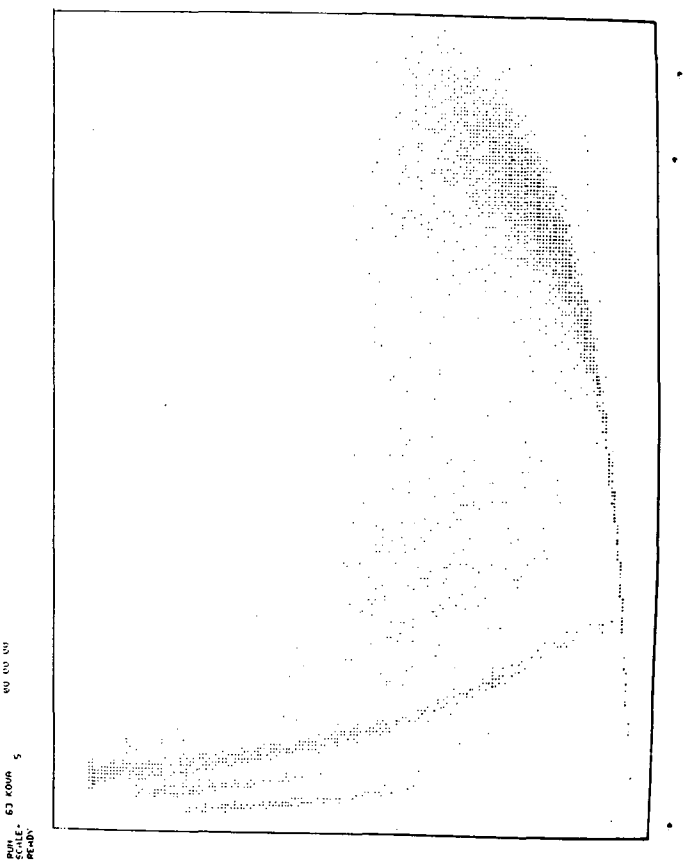

Fig. 1. Two-dimensional display of $\Delta E$ (horizontal) vs $E_{total}$ (vertical) obtained at $\theta_L = 6°$ for $^{16}O + ^{40}Ca$ at 140 MeV.
(XBL 778-177.4)

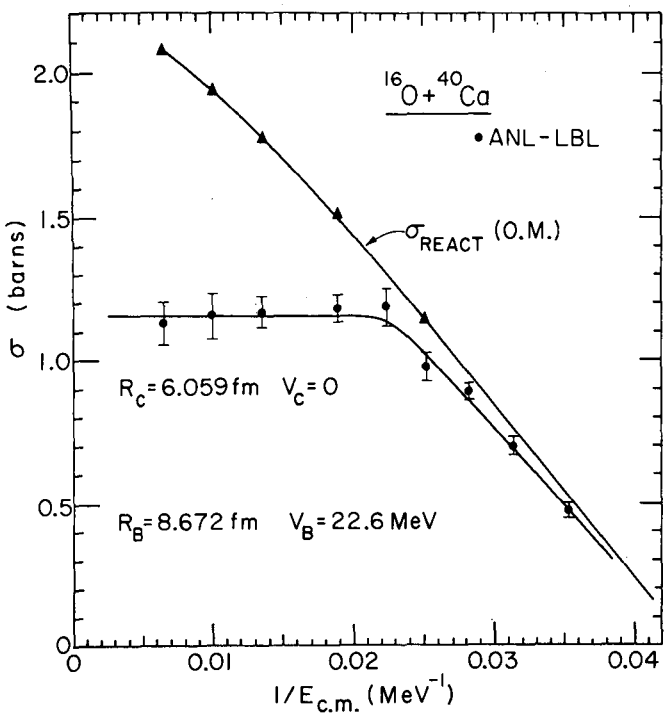


Fig. 2. Energy dependence of the fusion and total reaction cross sections for $^{16}O + ^{40}Ca$. The fusion cross sections are shown as solid dots and were obtained by measurement of the evaporation residues. The triangles represent the total reaction cross sections as obtained from optical model fits to the elastic scattering. The solid curve for $\sigma_{fus}$ is calculated using the model of Ref. 2 with the parameters indicated in the figure.
(XBL 778-1775)

Several models[4,5] predict that a compound nucleus cannot be formed with more than a certain critical angular momentum $\ell_{cr}$; at energies above that for which the partial wave $\ell_{cr}$ first contributes to the fusion cross section, $\sigma_{fus}$ is predicted to drop toward zero. In the rotating liquid drop model (RLDM) of Ref. 5, $\ell_{cr}$ is associated with the vanishing of the fission barrier ($B_{fiss} = 0$). The corresponding falloff predicted for the total fusion cross section is not inconsistent with our measurements. However, the experimental results do exceed the estimated limit on the evaporation-residue cross section which is considerably lower than the limit on $\sigma_{fus}$ because fission is the favored decay mode of the compound nucleus for those angular momenta for which $B_{fiss} < 10$ MeV. The present results, together with other recent measurements,[6,7] suggest that the RLDM limits, based on calculations for rigidly rotating nuclei in thermal equilibrium, are not applicable to the highly excited composite systems formed in the fusion of light nuclei.

Footnote and References

*Argonne National Laboratory, Argonne, Ill. 60439

1. S. E. Vigdor et al., Bull. Am. Phys. Soc. 21, 680 (1976).

2. D. Glas and U. Mosel, Nucl. Phys. A 237, 429 (1975).

3. T. M. Cormier et al., Phys. Rev. C 13, 682 (1976); R. Albrecht et al., Phys. Rev. Lett. 34, 1400 (1975).

4. R. Bass, Nucl. Phys. A 231, 45 (1974).

5. S. Cohen, F. Plasil and W. J. Swiatecki, Ann. Phys. 82, 557 (1974).

6. R. G. Stokstad et al., Phys. Rev. Lett. 36, 1529 (1976).

7. M. N. Namboodiri, E. T. Chulick, and J. B. Natowitz, Nucl. Phys. A 263, 491 (1976).

## ENERGY AND SPIN DEPENDENCE OF FISSION AND $^4$He EMISSION FROM $^{194}$Hg COMPOUND NUCLEI

J. M. Miller,* D. Logan,† G. L. Catchen,† M. Rajagopalan,‡ J. M. Alexander,‡ M. Kaplan,§ L. Kowalski,|| and M. S. Zisman

This work was undertaken to investigate fission-evaporation competition of highly excited, broad spin distribution compound nuclei in the mass region of $A \approx 200$. The general strategy employed is well known[1] and in the present case involved measuring the energy and angular distributions of evaporation residues, fission fragments and isotopes of H and He for the Ghoshal system of $^{12}C + ^{182}W$ and $^{19}F + ^{175}Lu \rightarrow ^{194}Hg$, each at excitation energies of 98 and 142 MeV.

Light charged particles were detected with a three member solid state telescope. The $^4$He energy distributions were found to be indicative of compound evaporation at backward angles while showing a direct component of forward angles. The shape of such energy spectra at backward angles, together with experimentally estimated fission-$^4$He cross sections, suggested that alpha emission following fission did not lead to a serious overestimate of the evaporated alpha cross section.

Fission products and evaporation residues were detected with a Fowler-Jared gas ionization telescope.[2] Fission cross sections were calculated by direct integration of the angular distributions for the $^{19}F$ bombardments, in which a large number of angles were covered. For the less intensively

studied $^{12}C$ bombardments, the cross sections were calculated under the same assumptions used by Sikkeland et al.[3] Evaporation residues were detected to as low as 3° and their cross sections were integrated to 0° with the requirement that $d\sigma/d\theta$ (0°) = 0.

Table 1 indicates the experimentally measured quantities together with a number of calculated quantities for the four entrance channels in question. The fusion cross section was taken to be the sum of the evaporation residue and fission cross sections.

The critical angular momenta ($\ell_{crit}$) were calculated under the sharp cutoff approximation while the total reaction cross sections were inferred from reaction systematics.[4] Table 2 shows the cumulative decay probabilities calculated for the listed exit channels. Spin domains were isolated under the independence hypothesis and contributions to each domain were calculated under the formalism of Reedy et al.[1]

A comparison of columns 3 and 4 of Table 1 suggests that increasing the excitation energy from 98 to 142 MeV while essentially maintianing the same spin distribution results primarily in an increase in alpha decay probability, while that of fission remains relatively unchanged. Table 2 seems to indicate that fission does become more likely as spin increases while the probability of alpha decay becomes somewhat smaller.

The $\ell_{crit}$ values of Table 1 (44, 59, 64, 76) may in some cases be overestimates due to the problem of distinguishing evaporation residues from products following direct H or He emission. However, the degree of overestimation is not expected to be serious as such direct reaction

Table 1. Values of the cross sections and other parameters.

| Reaction | $^{12}C$ + $^{182}W$ | $^{19}F$ + $^{175}Lu$ | $^{12}C$ + $^{182}W$ | $^{19}F$ + $^{175}Lu$ |
|---|---|---|---|---|
| Beam energy | 121 MeV | 135 | 168 | 184 |
| Product Excitation of $^{194}Hg$ | 98 MeV | 98 | 142 | 142 |
| | | Cross Sections (mb) | | |
| $^4He$ [a] | 165 | 152 | 405 | 324 |
| Evaporation residues [a] | 458 | 351 | 539 | 312 |
| Fission [a] | 577 | 780 | 1021 | 1066 |
| Complete fusion | 1035 | 1131 | 1560 | 1378 |
| Total reaction [b] | 2238 | 1861 | 2736 | 2264 |
| | | Critical angular momenta ($\hbar$) | | |
| $\ell_{crit}$ | 44 | 59 | 64 | 76 |
| | | Fraction of fusion cross section | | |
| $^4He$ | $0.16_{\pm.02}$ | $0.13_{\pm.03}$ | $0.26_{\pm.03}$ | $0.24_{\pm.04}$ |
| Evaporation residues | $0.44_{\pm.03}$ | $0.31_{\pm.04}$ | $0.35_{\pm.02}$ | $0.23_{\pm.03}$ |
| Fission | $0.56_{\pm.03}$ | $0.69_{\pm.04}$ | $0.65_{\pm.03}$ | $0.77_{\pm.03}$ |

[a] Estimated uncertainties are ≈ 20% absolute or 10% relative.

[b] Calculated as described in Ref. 4.

Table 2. Cumulative decay probabilities.

| Product \ Initial excitation energy | 98 MeV | 98 MeV | 142 MeV | 142 MeV |
|---|---|---|---|---|
| Spin domain | 0-44 ħ | 44-59 ħ | 0-64 ħ | 64-76 ħ |
| | fraction | fraction | fraction | fraction |
| $^4$He | 0.16 | 0.10 | 0.26 | ≈ 0.2 |
| Evaporation residues | 0.44 | 0.14 | 0.35 | ≈ 0. |
| Fission | 0.56 | 0.86 | 0.65 | ≈ 1. |

products for the C bombardments would have been lower than our detection threshold. For the F bombardments where direct reaction products might have been detected, the residue cross section decreased with bombarding energy as opposed to the behavior expected from direct reaction systematics. The above $\ell_{crit}$ values also tend to agree with the Bass[5] model calculated values of (52,66,66,79).

It was found, somewhat surprisingly, that the fission probability did not rapidly increase with excitation energy in the region studied here. We are at present investigating this behavior with evaporation calculations in hopes of extracting level density information. Further, the behavior of $^{156}$Er compound nuclei is shortly scheduled to be studied in an analogous fashion. Lastly, the alpha decay probabilities reported herein have been profitably employed in Monte-Carlo calculations simulating alpha emission in the reaction of 724 MeV $^{86}$Kr + $^{197}$Au.

Footnotes and References

*Deceased

†Columbia University

‡State University of New York at Stony Brook

§Carnegie-Mellon University

‖Montclair State College


1. See for example: A. M. Zebelman, L. Kowalski, J. M. Miller, K. Beg, Y. Eyal, S. Yaffe, A. Kandil, and D. Logan, Phys. Rev. C 10, 200 (1974).

2. M. M. Fowler and R. C. Jared, Nucl. Instrum. and Meth. 124, 341 (1975).

3. J. Sikkeland, J. E. Clarkson, N. H. Steiger-Shafrir and V. E. Viola, Phys. Rev. C 3, 329 (1971); J. Sikkeland, Phys. Rev. 135, B669 (1964).

4. L. C. Vaz and J. M. Alexander, Phys. Rev. C 10, 464 (1974); J. M. Alexander, H. Delagrange and A. Fluery, Phys. Rev. C 12, 149 (1975).

5. R. Bass, Nucl. Phys. A 231, 45 (1974).


## A COINCIDENCE STUDY OF $^4$He AND HEAVY FRAGMENTS IN THE REACTION OF 724 MeV $^{86}$Kr WITH Au

J. M. Miller,* G. L. Catchen,† D. Logan,† M. Rajagopalan,‡ J. M. Alexander,‡ M. Kaplan,§ and M. S. Zisman

We have sought to determine the mechanisms of $^4$He production for the reaction of 724 MeV $^{86}$Kr + $^{197}$Au. One of the foremost reasons for choosing this system is that it is typical[1] of systems characterized by large cross sections for deeply inelastic scattering. Our approach has been to measure the differential cross section of $^4$He in coincidence with heavy fragments and to ask whether they could be accounted for by evaporation from either of the deeply inelastic scattering products "Kr*" or "Au*".

The Kr* product was detected by a Fowler-Jared gas ionization telescope[2] (GT) while alphas were detected with a 3 member solid state telescope (SST). The detection threshold of the latter was 9 MeV. Following pulse height defect and energy determinations, identification of the heavy fragment was made utilizing Northcliffe-Schilling tables.[3] Estimated Z and A uncertainties were ±3 and ±10%, respectively.

The GT was placed at either 36° or 42° and the SST was varied over the range of 80° to 320°. Based on velocities expected of evaporated $^4$He from Au* and Kr*, the latter two products average velocities and our $^4$He detection threshold, kinematic claculations suggested the following: At > 200° the efficiency of observing Au* evaporated $^4$He was maximized while that due to Kr* was essentially zero. At < 80° the opposite was true (see Fig. 1).

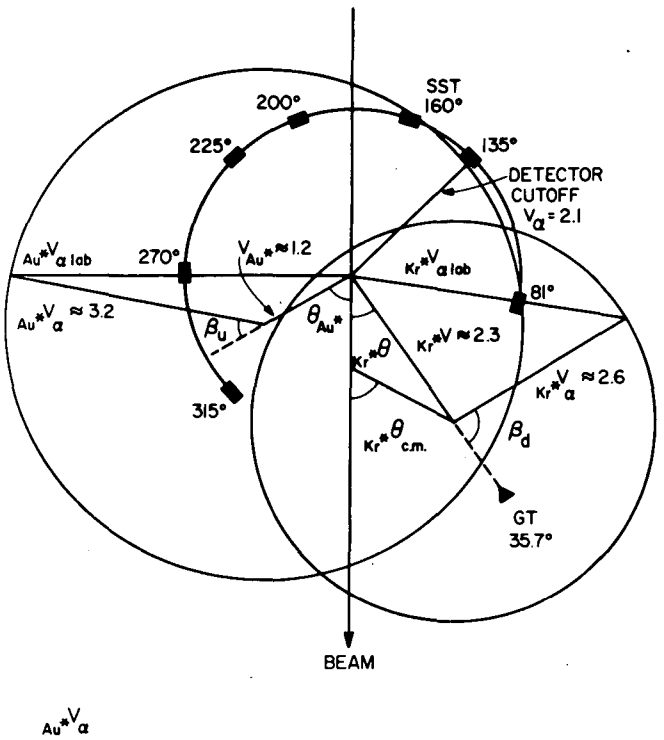


Fig. 1. Velocity vector diagram of a typical hard reactive collision. Velocities are given in cm/nsec. The fragment labeled Kr* was detected in a gas telescope GT at 36° lab or ≈ 65° c.m. The undetected fragment Au* recoiled at 300-340°, lab depending on the Q value. The velocities of $^4$He particles emitted at Coulomb barrier energies are shown. Their angles of emission $\beta_d$ and $\beta_u$ are also shown in the frames of the detected and undetected fragments. The solid state telescope for $^4$He detection was situated at angles near to those shown with velocity threshold for $^4$He of ≈ 2.1 cm/nsec. The lab system velocities for the cases shown are well above the detection thresholds at 81° and 270°, respectively.

(XBL 778-9874)

With the above expectation the data were treated in the following manner. Each coincident event, representing a triple differential cross section, was transformed into three moving frames: that of the detected Kr*, the undetected Au*, and lastly, the center-of-mass (c.m.) frame (see Fig. 2). An examination of these spectra suggested that at 270° the $^4$He could have indeed resulted from Au* evaporation, while at 80° the same could be said for Kr*. However, as it is conceivable that there may exist a direct component at these angles, the above spectra must be considered as upper limits for Au* and Kr* evaporation. With previous work[4] indicating that essentially isotropic emission was expected from either Au* or Kr*, the above differential cross sections were then subtracted from the remaining spectra in each frame and the sum subtracted from the c.m. spectra. The remaining cross section, shown as the unshaded area in Fig. 2, thus represents a lower estimate of $^4$He not associated with evaporation from Au* or Kr*. It was also apparent that the above alphas were emitted with greatest probability between 60° and 125° relative to Kr* in the c.m. system, and with energies typical of emission from a composite system. These angular preferences and energies are reminiscent of $^4$He emitted in low energy fission wherein particles are emitted from the neck joining the separating fission fragments. It is thus possible that such a neck region is also emitting alpha particles in the deeply inelastic scattering process.

## Footnotes and References

*Deceased

†Columbia University

‡State University of New York at Stony Brook

§Carnegie-Mellon University

1. J. Galin, J. Physique C 5, 83 (1976); M. Lefort, J. Physique C 5, 57 (1976); J. Bondorf, J. Physique C 5, 195 (1976); L. G. Moretto and R. Schmitt, J. Physique C 5, 109 (1976).

2. M. M. Fowler and R. C. Jared, Nucl. Instrum. and Meth. 124, 341 (1975).

3. L. C. Northcliffe and R. F. Schilling, Nucl. Data A7, (1970).

4. R. C. Reedy, M. J. Fluss, S. F. Herzog, L. Kowalski, J. M. Miller, Phys. Rev. 188, 1771 (1969); J. M. Miller, D. Logan, G. Catchen, M. Rajagopalan, J. M. Alexander, M. Kaplan, M. S. Zisman and L. Kowalski, preprint 1977.

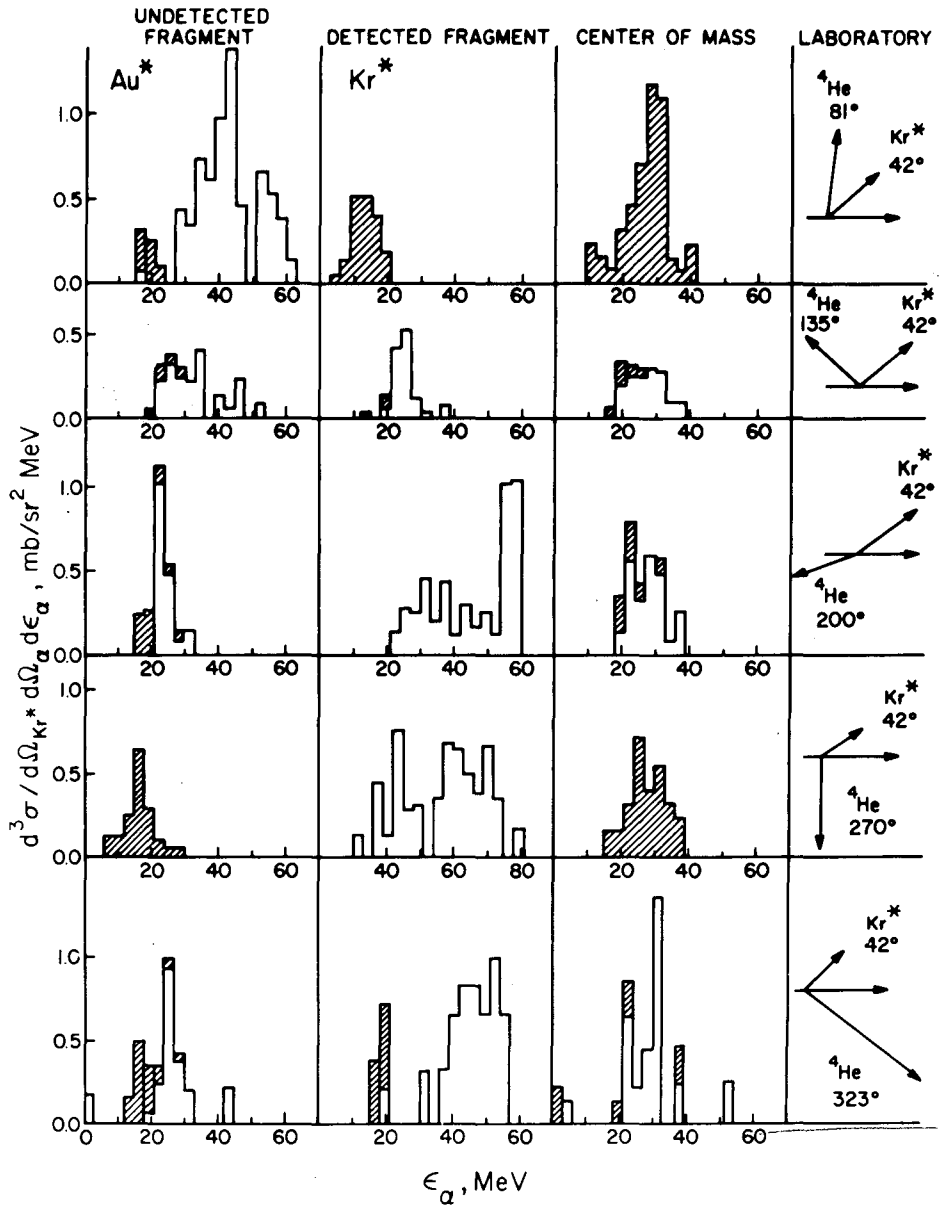


Fig. 2. Values of $d^3\sigma/d\Omega_{Kr^*}d\Omega_\alpha d\epsilon_\alpha$ vs energy in the frame of the undetected fragment Au*, the detected fragment Kr*, and the c.m. The vector diagram on the right gives for the α and Kr* the average lab angles and velocities for each spectrum in that row. Shaded areas are attributed to evaporation from the fragments. (XBL 778-9875)

## ANGULAR CORRELATIONS IN PERIPHERAL HEAVY-ION REACTIONS

C. K. Gelbke,* M. Bini,† C. Olmer,‡ D. L. Hendrie, J.-L. Laville,§ J. Mahoney, M. C. Mermaz,‖ D. K. Scott, and H. H. Wieman

Angular correlations between fast alpha particles and outgoing heavy reaction products have been measured for the reactions ($^{16}O$, $^{12,13,14}C\alpha$) and ($^{16}O$, $^{14}N\alpha$) on $^{208}Pb$ and $^{197}Au$ targets with beams of 140 and 310 MeV $^{16}O$ at the 88-in. cyclotron. Coincident reaction products from the bombardment of a 3 mg/cm$^2$ thick $^{208}Pb$ target at both incident energies and of a 15 mg/cm$^2$ thick $^{197}Au$ target at 310 MeV were detected by two solid state ΔE-E counter telescopes. Five-parameter events (two ΔE signals, two E signals and the timing signal between the two telescopes) were stored on magnetic tape and analyzed off line. A three-body kinematic analysis[1] of the data event by event determined the mean values $\langle E_{c.m.}(\alpha)\rangle$ $\langle E_{12}\rangle$ and $\langle E_{23}\rangle$ where the sub-indices denote

1) the heavy fragments (C and N nuclei), 2) the coincident alpha particles and 3) the target residues, and $E_{c.m.}(\alpha)$ is the energy of the alpha particle in the center-of-mass system.

Because of target impurities which affect the cross section data at more negative Q values, the values reported in Ref. 2 are not reliable and only events with three-body Q values $Q_3 \geq -20$ MeV for the Pb target and $Q_3 \geq -100$ MeV for the Au target are discussed. Figure 1 shows plots of three regions of Q-value for C-α coincidences and two regions for $^{14}$N-α coincidences. Over the entire range of Q values the coincident particles peak on the same side of the beam axis (positive $\theta_\alpha$) and only for the most quasi-elastic events in the $^{12}$C + α channel are two peaks observed. For more negative Q values the $^{12}$C + α channel closely resembles the others and at 140 MeV its cross section is smaller than those for $^{13,14}$C-α, indicating that pure projectile break-up is not the dominant reaction mechanism.

The mean values of $E_{c.m.}(\alpha)$ and $E_{23}$ are not precisely defined by the statistics of the experiment but a general trend of smaller values for more negative Q values can be seen in Fig. 2, as well as a strong angular dependence which implies that the alpha particles do not originate from a sequential decay of the ejectile[3] or from a transfer process followed by alpha particle emission as seen[4,5] at lower energies. Furthermore, the narrow widths of the angular correlations (see Fig. 1) indicating a time scale shorter than the rotational periods of the systems (1+3) and (2+3) and the high velocities of the alpha particles emitted at forward angles (Fig. 2) suggest that they are produced mainly in a fast,

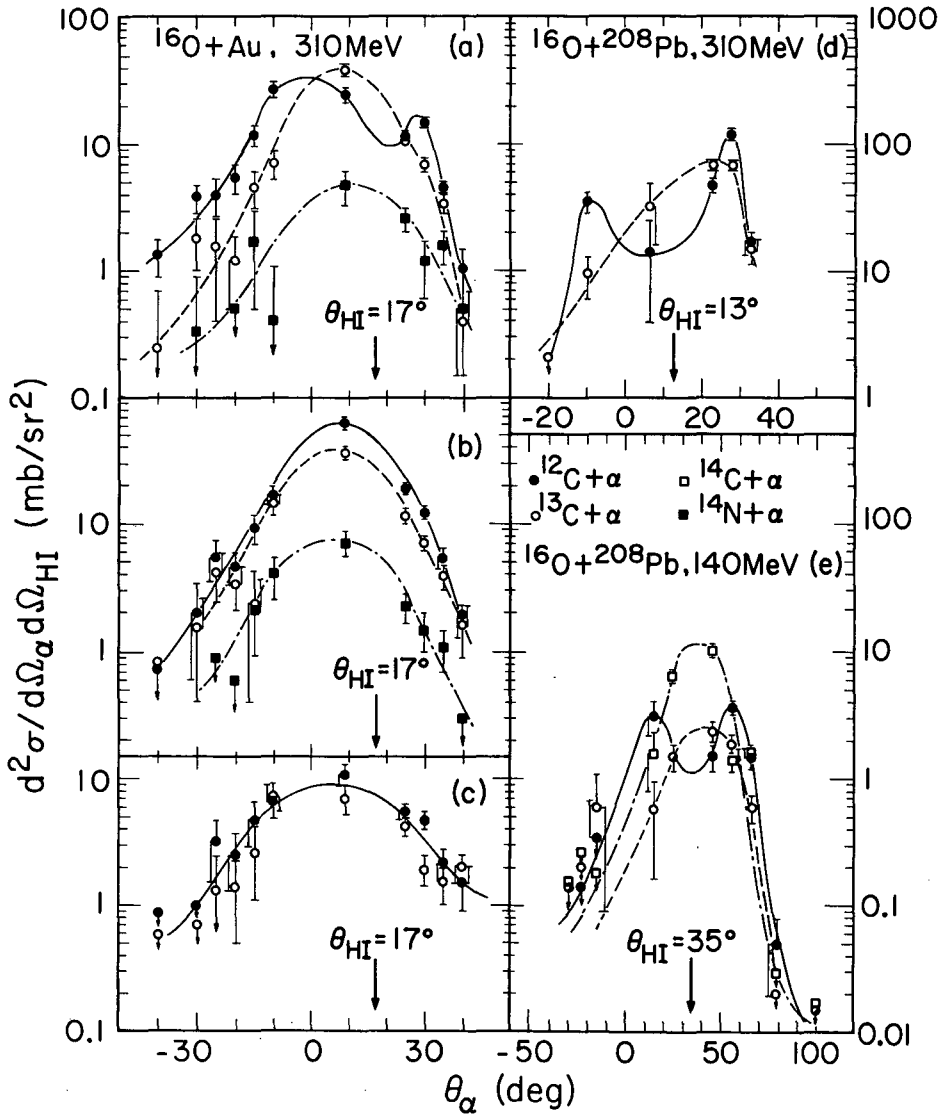


Fig. 1. In-plane angular correlations:
(a) $^{16}$O + $^{197}$Au, $Q_3$(C-α) ≥ -20 MeV; $Q_3$(N-α) ≥ -30 MeV; $\theta_{HI}$ = 17°
(b) $^{16}$O + $^{197}$Au, -60 MeV ≤ $Q_3$(C-α) < -20 MeV; -80 MeV ≤ $Q_3$(N-α) < -30 MeV; $\theta_{HI}$ = 17°
(c) $^{16}$O + $^{197}$Au, -100 MeV ≤ $Q_3$(C-α) < -60 MeV; $\theta_{HI}$ = 17°
(d) $^{16}$O + $^{208}$Pb, $Q_3$(C-α) ≥ -20 MeV; $\theta_{HI}$ = 13°
(e) $^{16}$O + $^{208}$Pb, $Q_3$(C-α) ≥ -20 MeV; $\theta_{HI}$ = 35° (XBL 777-3611)

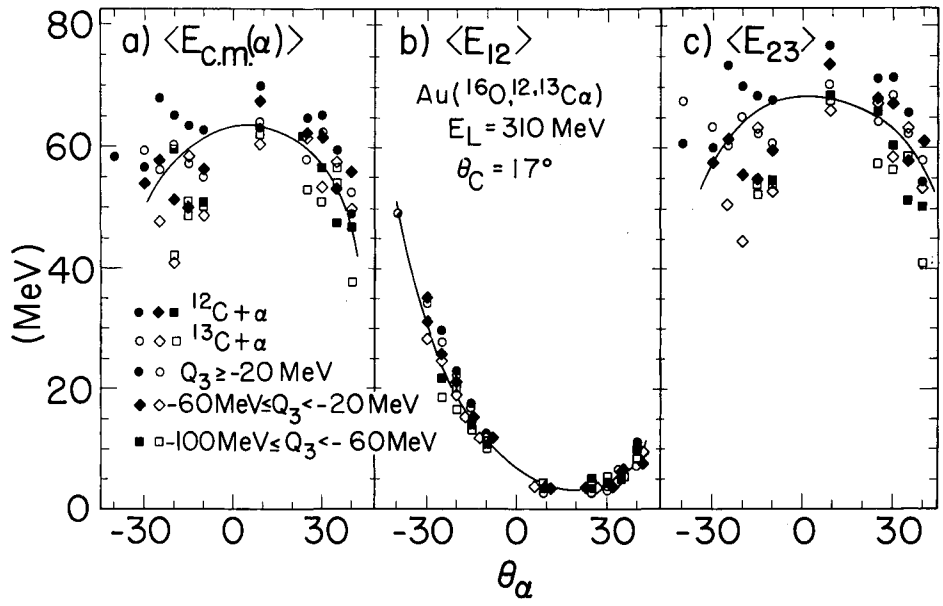


Fig. 2. Mean values of the center-of-mass energy $E_{c.m.}(\alpha)$ of coincident alpha-particles and the excitation energies $E_{12}$ and $E_{23}$ of the systems 12 and 23, respectively, observed in the reactions $^{197}$Au($^{16}$O,$^{12,13}$Cα) at 310 MeV. (XBL 777-3612)

nonequilibrium process at an early stage of the collision.

The piston model,[6] which assumes that such fast alpha particles are produced by the radial component of the dissipative force, predicts that the alpha particles will be emitted from the side of the target nucleus opposite to the point of impact, and if the quasi-elastic and deeply inelastic collisions are associated with positive and negative deflection angles of the heavy ion,[7] then for quasi-elastic events the coincident particles should be found on opposite sides of the beam axis and on the same side for deeply inelastic, as shown schematically in Fig. 3(a). Our results show the particles to be emitted on the same side for both quasi-elastic and more inelastic events and a possible interpretation, illustrated in Fig. 3(b), involves the emission of fast alpha particles mainly from the region of initial impact along the direction of the classical Coulomb trajectories of the incoming projectile.[8] In a macroscopic friction model, these alpha particles could be associated with the tangential rather than the radial friction force. The experimental angular correlations are then consistent with positive deflection angles for the entire region of Q-values considered in this experiment.

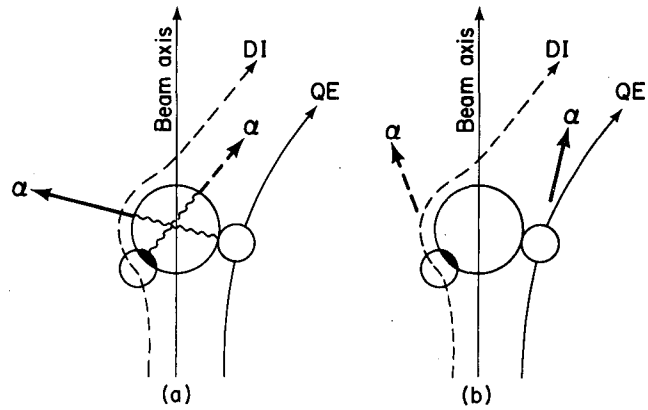


Fig. 3. Schematic illustration of angular correlations between fast alpha particles and heavy fragments in quasi-elastic (QE) and deeply-inelastic (DI) collisions. In (a) alpha particle production by radial friction[7] leads to alpha particles and heavy fragments from deeply-inelastic scattering preferentially on the same side of the nucleus, and on opposite sides for quasi-elastic scattering. The inverse correlations are illustrated in (b), where the alpha particles are assumed to be produced mainly at the initial stage of the collision, and to follow the Coulomb trajectory of the incident ion. (XBL 774-695)

Footnotes and References

*Present address: Physics Department, Michigan State University, East Lansing, Michigan 48824.

†Nato Fellow, on leave from the University of Florence, Florence, Italy.

‡Present address: Physics Division, Argonne National Laboratory, Argonne, Illinois 60439.

§On leave from C.N.R.S., Caen, France.

‖On leave from C.E.N., Saclay, France.

1. G. G. Ohlsen, Nucl. Instrum. and Meth. 37, 240 (1965).

2. C. K. Gelbke, C. Olmer, D. L. Hendrie, J-L. Laville, J. Mahoney, M. C. Mermaz, and D. K. Scott, LBL-5821, 1976, unpublished.

3. J. P. Bondorf and W. Nörenberg, Phys. Lett. 44B, 487 (1973).

4. D. C. Slater, J. R. Hall, J. R. Calarco, B. A. Watson, and J. A. Becker, Phys. Rev. Lett. 33, 784 (1974).

5. J. W. Harris, T. M. Cormier, D. F. Geesaman, L. L. Lee, Jr., R. L. McGrath, and J. P. Wurm, Phys. Rev. Lett. 38, 1460 (1977).

6. D. H. E. Gross, and J. Wilćzynski, Phys. Lett. 67B, 1 (1977).

7. J. Wilćzynski, Phys. Lett. 47B, 484 (1973).

8. H. C. Britt and A. R. Quinton, Phys. Rev. 124, 877 (1961).

# INFLUENCE OF INTRINSIC NUCLEON MOTION ON ENERGY SPECTRA AND ANGULAR DISTRIBUTIONS FOR $^{16}$O-INDUCED REACTIONS AT 20 MeV/A*

C. K. Gelbke,† D. K. Scott, M. Bini,‡ D. L. Hendrie, J. L. Laville,§ J. Mahoney, M. C. Mermaz,|| and C. Olmer¶

At relativistic energies a broad peak found in the continuum of the energy spectra of heavy-ion reactions is explained by projectile fragmentation[1] in which the intrinsic motion of the nucleons inside the projectile determines the main features of the momentum distributions of the observed fragments.[2,3,4] At lower energies (5 MeV/A or less above the Coulomb barrier) this peak is thought to be due to two body reactions populating a high density of final states in the residual nucleus. Recent experiments show the energy spectra and angular distributions from peripheral reactions at 20 MeV/A can also be well understood in terms of the intrinsic nucleon motion in the projectile.

The reaction products from a 315 MeV $^{16}O^{6+}$ beam on $^{208}Pb$ were identified by a $\Delta E$-$\Delta E$-$E$ solid-state detector telescope and absolute cross sections were obtained to an accuracy of within 15%. Using simple models that describe the momentum distribution for projectile fragmentation at relativistic energies,[1,2] we derived the equation

$$\frac{d^2\sigma}{d\Omega dE_L} \sim m_f \sqrt{2m_f E_L} \exp\left[-\frac{m_f}{\sigma^2}\left(E_L - 2aE_L^{1/2}\cos\theta + a^2\right)\right] \quad (1)$$

with

$$a^2 = m_f \frac{V_R^2}{2} ,$$

where $E_L$ is the laboratory energy, $m_f$ is the mass of the observed fragment and $V_R$ is the velocity of the rest frame in which fragments $m_f$ are emitted isotropically. From this equation we were able to produce energy spectra and angular distributions which compare very well with our data, as shown in Figs. 1 and 2. Table 1 lists the parameters used for each curve. Although an exact description of the experimental data cannot be expected from such a simple approach, the widths of the energy spectra and the slopes of the angular distributions are reproduced remarkably well, indicating that intrinsic nuclear motion is a dominant factor at this energy as well as relativistic energies.

## Footnotes and References

*Condensed from LBL-6551.

†Present address: Department of Physics, Michigan State University, East Lansing, Michigan 48824.

‡Nato fellow, on leave from the University of Florence, Florence, Italy.

§On leave from C.N.R.S., Caen, France.

||On leave from C.E.N., Saclay, France.

¶Present address: Physics Division, Argonne National Laboratory, Argonne IL 60439.

1. D. E. Greiner, P. J. Lindstrom, H. H. Heckman, B. Cork, and F. S. Bieser, Phys. Rev. Lett. 35, 152 (1975).

2. A. S. Goldhaber, Phys. Lett. 53B, 306 (1974).

3. H. Feshbach and K. Huang, Phys. Lett. 47B, 300 (1973).

4. A. Abdul-Magd and J. Hüfner, Z. Physik A 277, 379 (1976).

5. J. V. Lepore and R. J. Riddell, LBL-3086, 1974, unpublished.

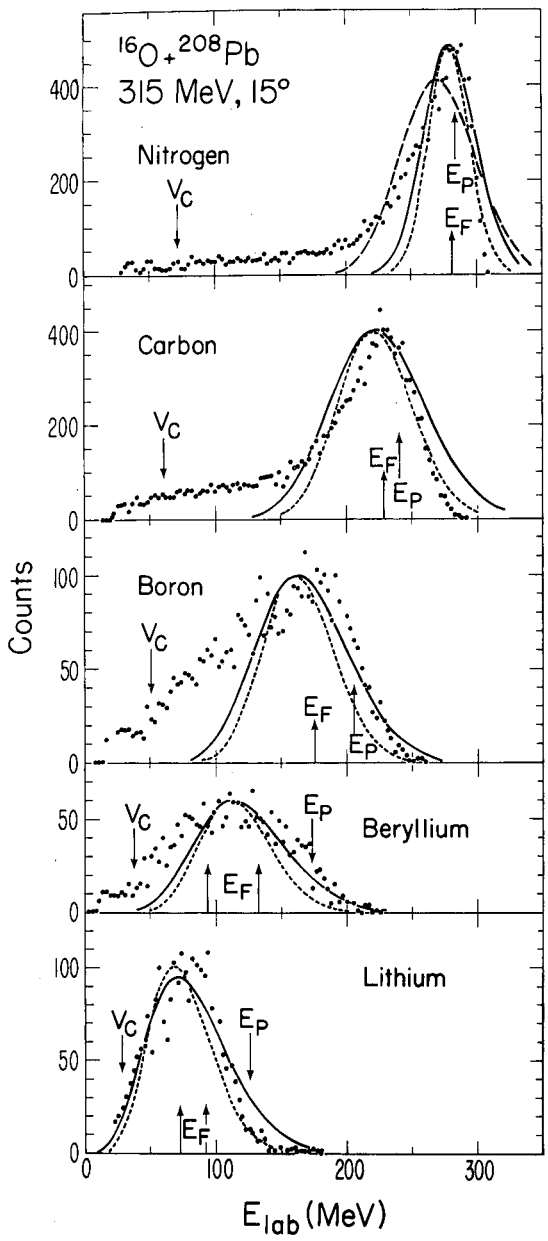


Fig. 1. Energy spectra of reaction products N, C, B, Be, Li measured in the bombardment of $^{208}Pb$ by $^{16}O$ ions of 315 MeV at the laboratory angle of 15°. The curves are calculated from Eq. (1) as explained in the text. The arrows denoted by $V_C$, $E_F$ and Ep correspond to the exit-channel Coulomb barrier, the energy predicted for a fragmentation of the projectile into the observed fragment together with individual nucleons and alpha particles,[5] and the energy of a product with the projectile velocity. (XBL 776-1141)

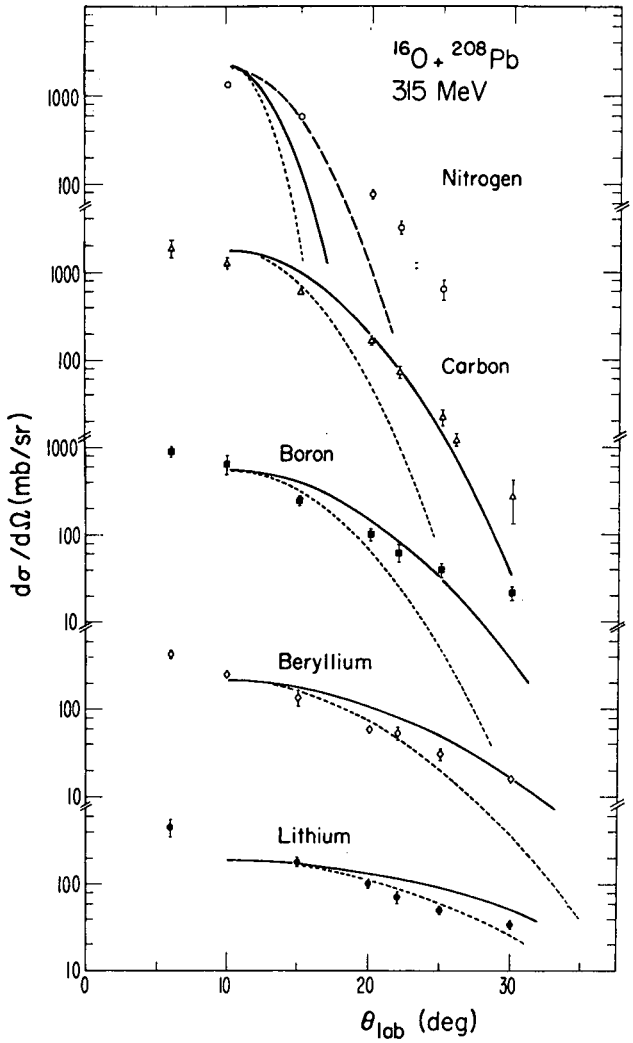


Fig. 2. Angular distributions of reaction products N, C, B, Be, and Li measured in the bombardment of $^{208}Pb$ by $^{16}O$ ions of 315 MeV. The curves are calculated from Eq. (1) as explained in the text. (XBL 776-1142)

Table 1. Parameters used for the calculated curves in Figs. 1 and 2. The widths $\sigma_0$ = 103 MeV/c and $\sigma_0$ = 80 MeV/c have been used for the solid and dotted curves, respectively.

| Element | N | | C | B | Be | Li |
|---|---|---|---|---|---|---|
| $m_f$(amu) | 15 | (14) | 12 | 11 | 9 | 7 |
| $a^2$(MeV) | 280 | (270) | 220 | 160 | 110 | 65 |

# ANGULAR MOMENTUM TRANSFER IN THE DEEPLY INELASTIC SCATTERING OF 610 MeV $^{80}$Kr by $^{209}$Bi

P. Dyer,* R. J. Puigh,* T. D. Thomas,† R. Vandenbosch,* and M. S. Zisman

The reaction cross section for 610 MeV $^{86}$Kr + $^{209}$Bi is dominated by the deeply inelastic scattering process, which is characterized by strong damping of the initial kinetic energy, little net charge or mass transfer, and angular distributions peaked near the grazing angle.[1,2] In classical descriptions of the reaction mechanism, phenomenological viscous friction forces, with radial and tangential components, are used to describe the dissipation of initial kinetic energy and angular momentum into internal degrees of freedom. We are studying the angular momentum transfer in order to determine the strength of the tangential friction. This is done by measuring angular correlations of fragments from fissioning heavy reaction products relative to the recoil axis.

The geometry of the experiment is shown in Fig. 1. Fission fragments were detected in coincidence with the projectile-like reaction product, and correlations in and out of the reaction plane were measured. A 610 MeV $^{86}$Kr beam from the SuperHILAC was incident on a target consisting of 300 μg/cm$^2$ $^{209}$Bi on a 50 μg/cm$^2$ carbon backing. Light (projectile-like) products were detected by a semiconductor counter telescope fixed at 40° lab, where the deeply inelastic scattering cross section is at a maximum. Two single counters detected fission fragments, one of which was mounted on an arm that could be moved to various out-of-plane angles. Timing signals from each detector were fed into time-to-amplitude converters (TAC's), so that each event was characterized by four linear signals, ΔE, E+ΔE, fission fragment energy, and TAC, which were digitized and recorded event-by-event. In a two-dimensional array of counts vs telescope energy and fission fragment energy (after a subtraction of random events), the events of interest were easily separable from other events.

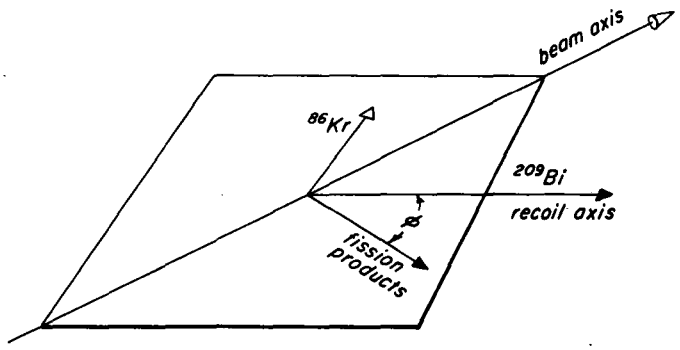


IN-PLANE CORRELATION

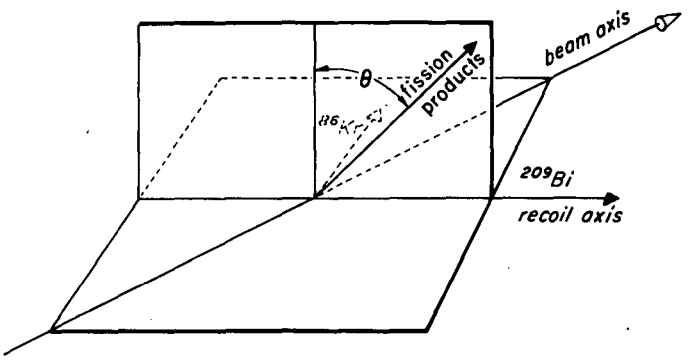


OUT-OF-PLANE CORRELATION

Fig. 1. Geometry of the experiment. (XBL 778-9872)

The angular distribution, with respect to a space-fixed z axis, of fission fragments from a nucleus having quantum numbers J, M, and K is given by

$$W^J_{MK}(\theta) = \frac{(2J+1)}{2} \left| d^J_{MK}(\theta) \right|^2 ,$$

where J is the intrinsic angular momentum of the fissioning nucleus, M is the projection of J on the z axis, K is the projection of J on the nuclear symmetry axis, θ is the angle measured from the z axis, and the $d^J_{MK}(\theta)$ are rotational wave-functions. In order to calculate a family of angular correction curves that can be compared to experimental data, it is necessary to sum the above distribution over J, M, and K with the appropriate weighting functions. The K distribution depends only on the properties of the fissioning nucleus, and is taken from previous experiments. The J and M distributions depend on the reaction mechanism; these are to be determined from the present experiment. The out-of-plane correlation is more sensitive to the J distribution; the in-plane, to the M distribution. In the limit of M=J (that of equatorial collisions in the classical limit) the in-plane correlation would be isotropic and the out-of-plane correlation would be anisotropic, with the anisotropy increasing with increasing J.

A Gaussian distribution of K values is assumed. The parameter $K_0^2$ characterizing the width of the distribution is taken from previous measurements of fragment correlations from fissioning compound nuclei.[3-6] We use $K_0^2 = 132$. No further assumptions about the properties of the fissioning nucleus are required.

For the J distribution, we take $P(J) \propto (2J+1)$ up to some maximum $J_{max}$, where there is a sharp cutoff. This form follows from a model in which all partial waves up to some maximum ℓ give rise to particles scattered to about 40° lab (an

assumption supported by the sharply peaked differential cross section) and in which the fraction of orbital angular momentum transferred into intrinsic angular momentum is the same for all partial waves (an assumption which holds in the rolling or sticking friction limits).

The measured in- and out-of-plane fission correlations are shown in Fig. 2. Lab angles and cross sections have been converted to those of the $^{209}$Bi center-of-mass coordinate system. Also shown for the out-of-plane case are a family of curves calculated for $K_0^2 = 132$, M=J, and varying $J_{max}$. The large out-of-plane anisotropy is a direct indication of sizable angular momentum transfer with the resulting intrinsic angular momentum being predominantly oriented perpendicular to the reaction plane. Comparison of the anisotropy with the model calculations just described leads to an initial estimate of the angular momentum transferred to the recoil of 55 ħ.

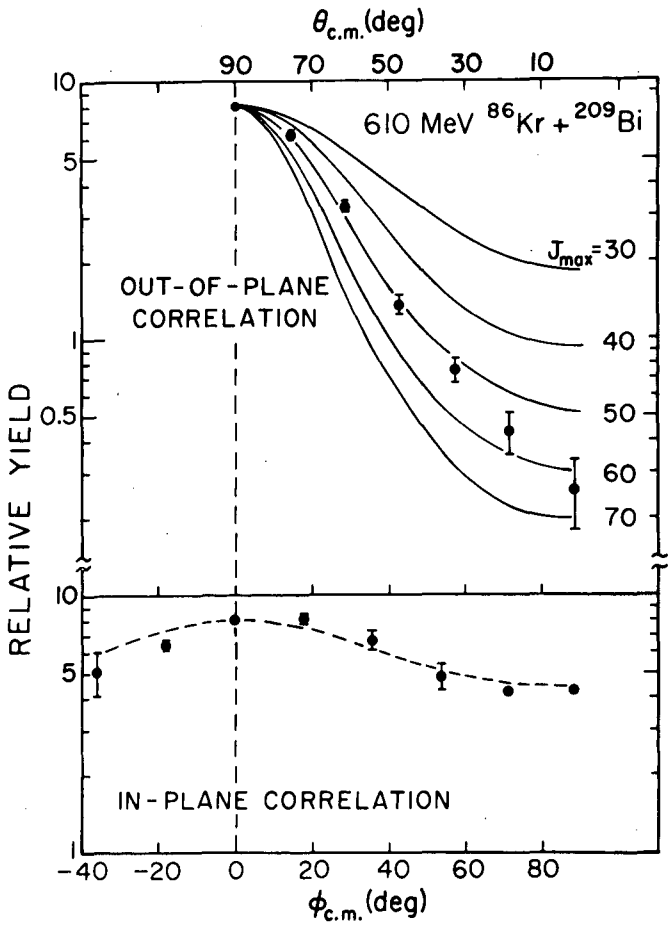


Fig. 2. Fission angular correlations measured in and out of the reaction plane. The family of solid curves is calculated for the out-of-plane case with M=J, $K_0^2 = 132$. The dashed curve is with $J_{min}$=18, $J_{max}$=58 and with contributions from M≠J (see text). (XBL 778-9873)

Two corrections to this result are presently being estimated. We believe the anisotropy in the in-plane correlation arises from interactions (such as those of non-equatorial collisions) that lead to angular momentum vectors whose projections in the reaction plane are not isotropically distributed. Comparison of the out-of-plane correlation data to the family of curves in Fig. 2 then results in an underestimate of $J_{max}$ by 15 to 20 units. Another effect that must be considered is that partial waves of small ℓ may not contribute to the observed deeply inelastic cross section. Considering upper limits on the fusion cross section, we see that such an effect could lower our estimate of the maximum angular momentum transfer by 10 to 15 units. The dashed curves in Fig. 2 are from a preliminary calculation taking these factors into account, with $J_{max}$=58 and $J_{min}$=18. The angular momentum vectors were assumed to lie in the plane perpendicular to the recoil axis with a Gaussian (σ=27°) distribution of angles with respect to the z axis.

We thus conclude that the maximum angular momentum transferred to the heavy reaction product is between 50 and 70 ħ. This is higher than the value of 39 ħ expected in the limit of rolling friction, and is less than but consistent with the value of 68 ħ expected in the sticking limit. The result implies that the tangential friction component is very important. The only calculation that has been performed for this particular system and bombarding energy is a friction model of Gross et al.,[7] who obtain a total loss (that going into both fragments) of orbital angular momentum of 38 ħ. This calculation thus underestimates the tangential component.

Similar data have also been acquired for the 730 MeV $^{86}$Kr + $^{238}$U reaction in a search for the instantaneous fission predicted by Deubler and Dietrich.[8] These data are presently under analysis.

## Footnotes and References

*University of Washington, Seattle, WA 98195
†Oregon State University, Corvallis, OR

1. K. L. Wolf, J. R. Huizenga, J. Birkelund, H. Friesleben, and V. E. Viola, Phys. Rev. Lett. 33, 1105 (1974).

2. R. Vandenbosch, M. P. Webb, and T. D. Thomas, Phys. Rev. C 14, 143 (1976).

3. R. Chaudhry, R. Vandenbosch, and J. R. Huizenga, Phys. Rev. 126, 220 (1962).

4. L. G. Moretto, R. C. Gatti, and S. G. Thompson, LBL-1666, unpublished.

5. S. S. Kapoor, H. Baba, and S. G. Thompson, Phys. Rev. 144, 965 (1966).

6. R. G. Clark, W. G. Meyer, M. M. Minor, C. T. Roche, and V. E. Viola, Z. für Physik 274, 131 (1975).

7. D. H. E. Gross, H. Kalinowski, and J. N. De, in Classical and Quantum Mechanical Aspects of Heavy Ion Collisions, H. L. Harney,

P. Braun-Munzinger and C. K. Gelbke, eds. Lecture Notes in Physics, Vol. 33, pg. 194 (Springer-Verlag, Berlin-Heidelberg-New York, 1975).

8. H. H. Deubler and K. Dietrich, Phys. Lett. 62B, 369 (1976).

# ENERGY DEPENDENCE OF ENERGY LOSS IN THE INTERACTIONS OF $^{86}$Kr WITH $^{139}$La

P. Dyer,* R. J. Puigh,* T. D. Thomas,† R. Vandenbosch,* M. P. Webb,‡ and M. S. Zisman

Our previous studies[1] of the Kr + La system at 710 MeV have been extended to lower bombarding energies. The primary motivation of this extension was to see how the double-peaked energy spectra observed at the higher energy change in character with decreasing energy. We also wished to see if we could test the presumed dependence of the energy loss on the relative velocity of the two reactants.

We have made new measurements at 610 MeV and 505 MeV. The energy spectra obtained at 610 MeV exhibit two components at certain angles although not as prominently as at 710 MeV. The overall features of the dependence of energy loss on angle at 610 MeV and 505 MeV are shown in Figs. 1 and 2.

At the lower bombarding energies the quasi-elastic ridge running down in energy from the entrance channel energy does not move forward in angle as rapidly as it did at the higher bombarding energy. It also merges more quickly with the fully damped events. The indication at the higher energy that the fully damped events orginated from negative deflection angles is less clear. A deflection function giving the nuclear rainbow at a small (< 10°) positive or negative angle could

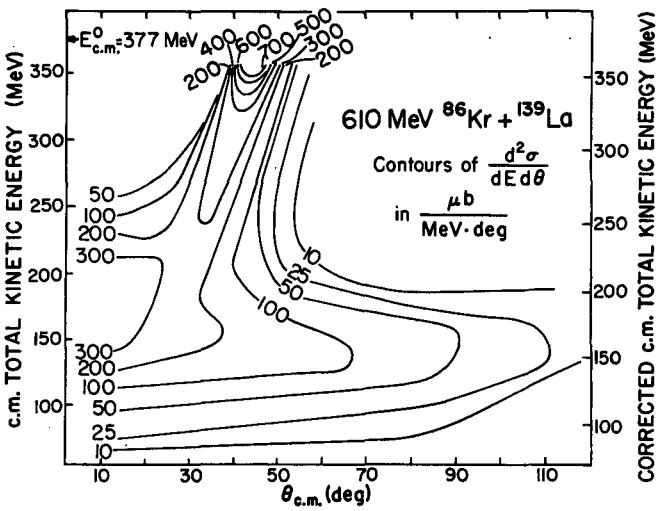


Fig. 1. Contours of double differential cross section $d^2\sigma/dEd\theta$ in μb $MeV^{-1}$ $deg^{-1}$. The ordinate is the total kinetic energy in the exit channel derived from the light-particle kinetic energy with the assumption of no net mass transfer. No corrections for neutron emission have been made. (XBL 778-9869)

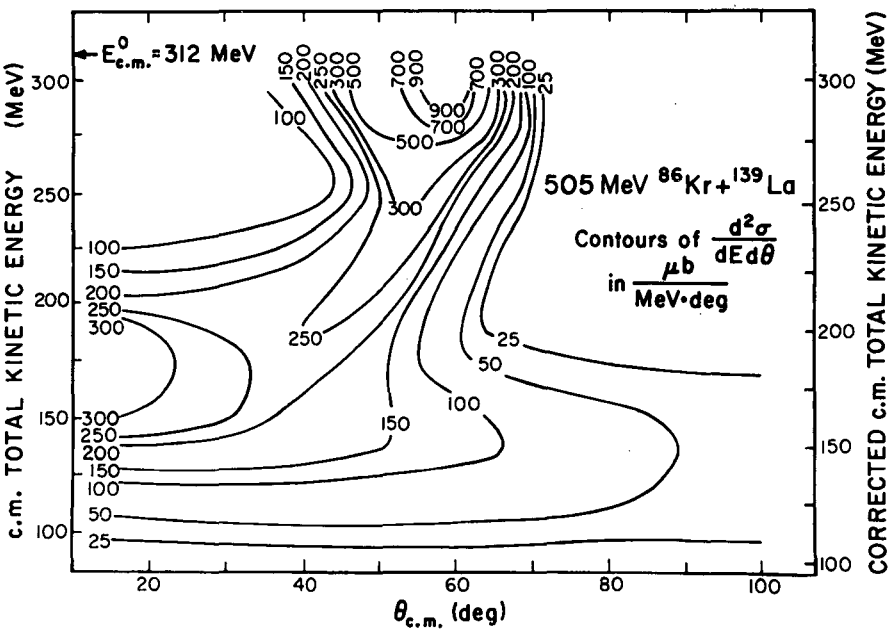


Fig. 2. Contours of double differential cross section as in Fig. 1. (XBL 778-9870)

be consistent with the observations. The two possibilities would lead to ridge lines in a contour plot given by either the dashed or full curves in Fig. 3.

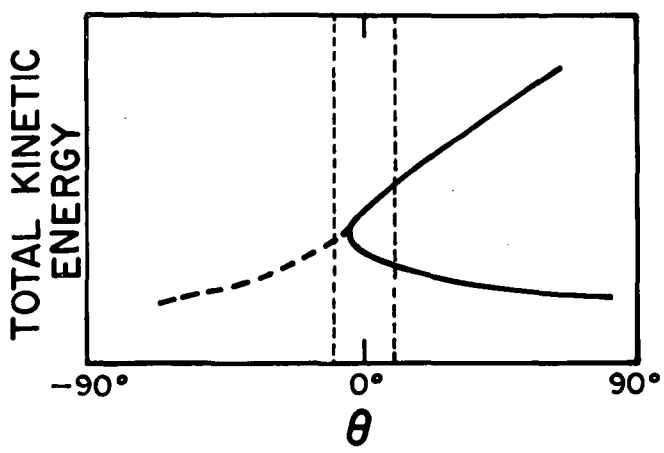


Fig. 3. Two possible trajectories of the ridge line in an E vs θ cross section contour diagram. (XBL 778-9867)

In order to understand the processes responsible for the energy loss in these reactions, we have undertaken some calculations of the energy loss associated with one-body dissipation. Swiatecki[2] has derived a simple "window" formula from which one can calculate the energy loss due to transfer of nucleons between two nuclei moving with a relative velocity $\vec{v}$. Randrup[3] has recently generalized this using a proximity model to obtain the dependence of the dissipation on the separation between the nuclei. The model takes into account the radius of curvature of the two nuclei, the surface diffusivity, and the transparency of the "window" between the two nuclei to particle transfer. We have integrated the dissipation predicted by the resulting dissipation function along various classical trajectories using a trajectory program described elsewhere. The trajectory calculations performed thus far have neglected the effect of energy loss and orbital angular momentum loss on the trajectories. Sample calculations indicate these corrections largely cancel for the relatively small energy losses for which the generalized window treatment might be expected to be valid.

The calculations are quite sensitive to the conservative potential determining the trajectories. For self-consistency we have used the proximity potential.[4] As a partial test of the validity of this potential we have modified our optical model code so as to replace the usual Woods-Saxon real potential with the proximity potential. With the imaginary potential retained from previous fits to the elastic data, use of the proximity potential with the suggested parameters gave a satisfactory fit to the elastic scattering, and with a slight adjustment of the radius parameter (by an amount consistent with the uncertianty in the absolute bombarding energy) gave essentially as good a fit as the three-parameter Woods-Saxon real potential.

The results of some of the calculations are given in Fig. 4. The experimental energy losses are obtained from the dependence of the most probable energy loss on angle using the deflection function obtained with the proximity potential. The apparent energy losses have been corrected for neutron emission assuming the excitation energy is divided according to the masses of the products. The calculations seem to underestimate the energy loss by about a factor or two. It must be emphasized that there are no adjustable parameters in this calculation. The dependence of the energy loss on impact parameter (or ℓ) and on the bombarding energy seems to be qualitatively correct.

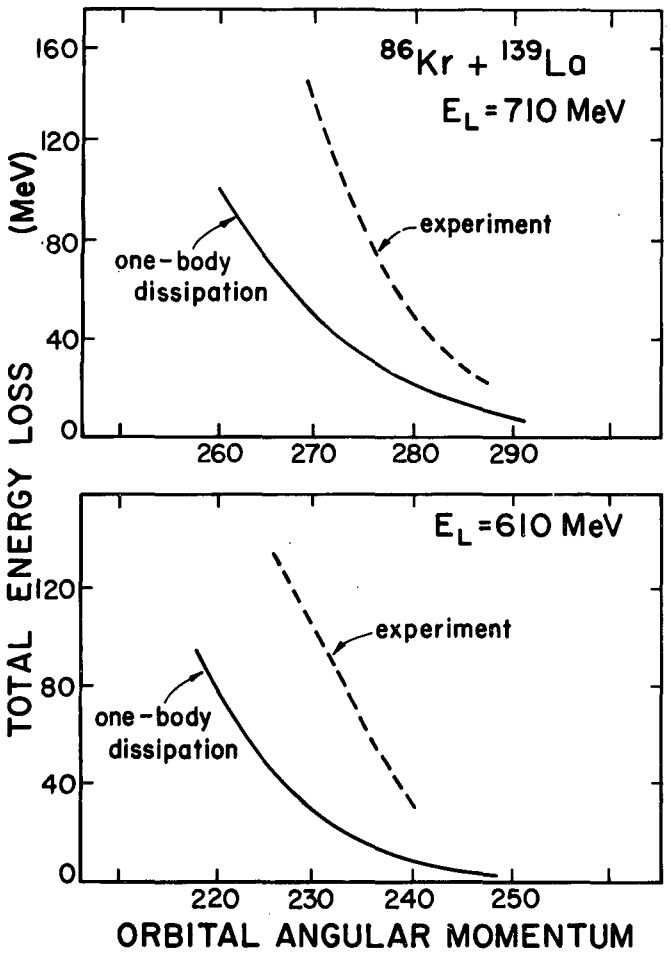


Fig. 4. Comparison of observed energy loss (corrected for neutron emission) with that calculated using one-body proximity friction at two bombarding energies. (XBL 778-9868)

A more model-independent test of the importance of one-body dissipation via nuclear transfer can be performed by deducing the number of particles transferred from the variance of the experimental charge distributions at a particular energy loss. From the number of particles transferred and the known relative velocity the expected energy transfer can be calculated and compared with the measured energy loss. If neutrons and protons are transferred independently and if

the total number of particles transferred is A/Z times the number of protons transferred then $\Delta E = A/Z\ E_n \sigma_Z^2$ where $E_n$ is the energy transfer per particle (from the known relative velocities) and $\sigma_Z^2$ is the variance of the charge distributions. We have measured $\sigma_Z^2$ as a function of energy loss in the $^{86}Kr + ^{139}La$ system. A comparison of the calculated to experimental energy losses for the 710 MeV bombardment is given in Fig. 5. The theory again accounts for less than half of the observed loss, in agreement with our previous calculations. We emphasize that the latter comparison employing the variances of the charge distribution is independent of any assumptions about the form factor of the dissipation function or the influence of the conservative potential on the trajectory. (For larger energy losses than considered here one would have to worry about nuclear deformations and their effect on the Coulomb interaction potential and hence the relative velocity of the nuclei in the interaction region). We conclude from the comparison given here that the transfer component of one-body dissipation is incapable of explaining the energy loss. Whether other one-body effects such as energy exchange generated by the deformation of the potential walls during the collision or two-body mechanisms are responsible for the energy loss is not clear.

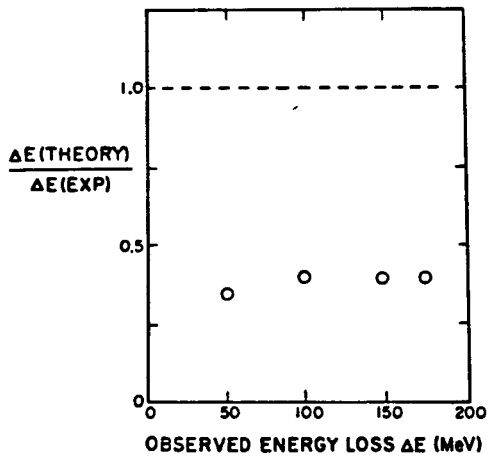


Fig. 5. Dependence of the ratio of calculated to experimental energy loss as a function of observed energy loss for 710 MeV $^{86}Kr + ^{139}La$. (XBL 778-9871)

Footnotes and References

*University of Washington, Seattle WA 98195

†Oregon State University, Corvallis, OR 97331

‡Present address: Oak Ridge National Laboratory, Oak Ridge, TN 37831

1. M. P. Webb, R. Vandenbosch, and T. D. Thomas, Phys. Letters 62B, 407 (1976).

2. W. J. Swiatecki, J. de Physique Colloque C 5, 45 (1972).

3. J. Randrup, to be published

4. J. P. Blocki, J. Randrup, W. J. Swiatecki, and C. F. Tsang, Ann. Phys. to be published.

## EVIDENCE FOR THE CHARACTERIZATION OF HEAVY-ION REACTIONS BY THE RATIO E/B*

G. J. Mathews,† G. J. Wozniak, R. P. Schmitt, and L. G. Moretto‡

Two very different patterns have been observed in heavy-ion collisions. The "quasi-fission" process[1] is characterized by rather narrow mass (or charge) distributions and side-peaked gross-product (all masses) angular distributions. This phenomenon has been observed in relatively heavy projectile-target collisions.[2] In contrast, "deep-inelastic scattering" (generally applied to lighter projectile-target systems)[3] is characterized by relatively broad mass distributions, and forward-peaked angular distributions. These different patterns are shown to have characteristic values of the ratio E/B (c.m. kinetic energy to Coulomb barrier) and are correlated with different lifetime regimes for the intermediate complex as it diffuses along the mass-asymmetry coordinate.

In a diffusion model the characteristic features of the mass (or charge) distribution are intimately related to the lifetime of the system. For example, the Fokker-Planck equation for a mass-asymmetry driving potential of constant slope yields that the variance, $\sigma^2$, of the charge distribution is given by $\sigma^2 \propto t$. Thus narrow charge distributions correspond to short lifetimes and broad ones to long lifetimes.

Angle-integrated charge distributions for four reactions are presented in order of increasing values of E/B in Figs. 1 and 2. To facilitate comparison, the members of each pair of distributions in both Figs. 1 and 2 have been shifted to align the entrance channels (the projectile Z-value has been left off both figures because of background contamination). Comparing the four spectra in Figs. 1 and 2, it is evident that the width of the charge distributions increases dramatically as the ratio E/B increases. For an E/B of 1.2 (170 MeV $^{40}Ar + ^{nat}Ag$) the peak in the integrated charge distribution centered at the projectile is very narrow (see Fig. 1a). When E/B is increased to 1.4 (620 MeV $^{86}Kr + ^{197}Au$), the integrated charge distribution broadens dramatically although it is still centered at the projectile Z-value (see

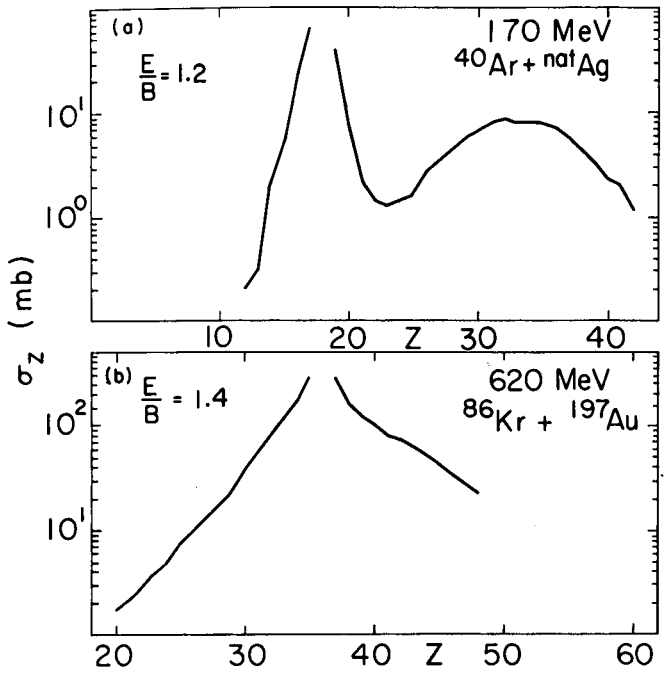


Fig. 1. Integrated laboratory charge distributions for (a) 170 MeV $^{40}Ar + ^{nat}Ag$ (E/B = 1.2), and (b) 620 MeV $^{86}Kr + ^{197}Au$ (E/B = 1.4). These distributions have been shifted to align the projectile Z-values and exhibit relatively narrow mass distributions. (XBL 7612-11057)

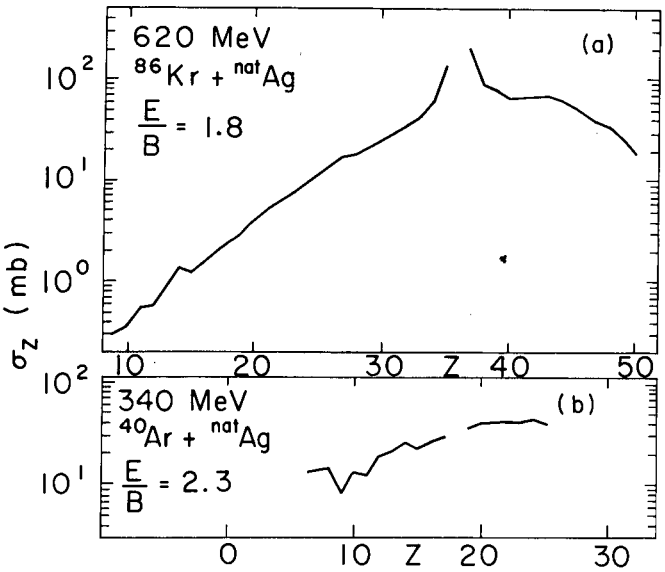


Fig. 2. Integrated laboratory charge distributions for (a) 620 MeV $^{86}Kr + ^{nat}Ag$ (E/B = 1.8) and for (b) 340 MeV $^{40}Ar + ^{nat}Ag$ (E/B=2.3). These distributions have been shifted to align the projectile Z-values; they are rather broad and have drifted towards symmetry. (XBL 7612-11056)

Fig. 1b). If E/B is raised to 1.8 (620 MeV $^{86}Kr + ^{nat}Ag$), the integrated charge distribution is broader still and a drift toward symmetry is observed in the centroid (see Fig. 2a). For a still larger value of E/B = 2.3 (340 MeV $^{40}Ar + ^{nat}Ag$), the integrated charge distribution becomes relatively flat with no evidence of any peaking near the projectile Z-value (see Fig. 2b). Insofar as these Z-distributions can be interpreted in terms of a diffusion process, the increasing charge widths imply longer average lifetimes for the systems which correlates with increasing values of E/B.

In addition, one observes side peaking in the angular distributions near the projectile Z-value (see Fig. 3a) in the system 170 MeV $^{40}Ar + ^{nat}Ag$ (E/B = 1.2), which indicates that the lifetime of the intermediate complex is small relative to its rotational period. However, for large mass transfers 1/sin θ angular distributions occur. For the case of 620 MeV $^{86}Kr + ^{197}Au$ (E/B = 1.4) side peaking is also observed (see Fig. 3b). One should note that in both of the above systems there is no clear-cut distinction between quasi-elastic and deep-inelastic processes; only a single broad peak is seen near the grazing angle. For the case of 620 MeV $^{86}Kr + ^{nat}Ag$, the angular distributions are for the most part forward peaked (see Fig. 4a). The extensive forward peaking indicates that the average system lifetime is long enough so that rotation can proceed through 0° (i.e., orbiting). In Fig. 4b the angular distributions are shown for two systems with longer lifetimes, 288 MeV (E/B = 2.0) and 340 MeV (E/B = 2.3) $^{40}Ar + ^{nat}Ag$, which are strongly forward peaked. A comparison of these data with those in Fig. 3a demonstrates that it is possible to change the angular distribution pattern from a forward- to a side-peaked one by simply decreasing the bombarding energy.

These data indicate that side-peaked angular distributions (short lifetimes) tend to occur for values of E/B ≤ 1.5 and forward-peaked distributions for larger values of E/B; providing further evidence for the characterization of heavy-ion reactions by this parameter. Thus the apparent dichotomy presented by reaction studies of light and heavy systems can be explained by differences in the average lifetime of the system.

## Footnotes and References

*Condensed from LBL-5812, to be published in Z. Physik

†AWU-ERDA Fellow on leave from the University of Maryland

‡Sloan Fellow 1974-1976

1. F. Hanappe et al., Phys. Rev. Lett. 32, 738 (1974).

2. L. G. Moretto and R. Schmitt, J. de Phys. Colloque C5, 109 (1976).

3. A. G. Artukh et al., Nucl. Phys. A 215, 91 (1973).

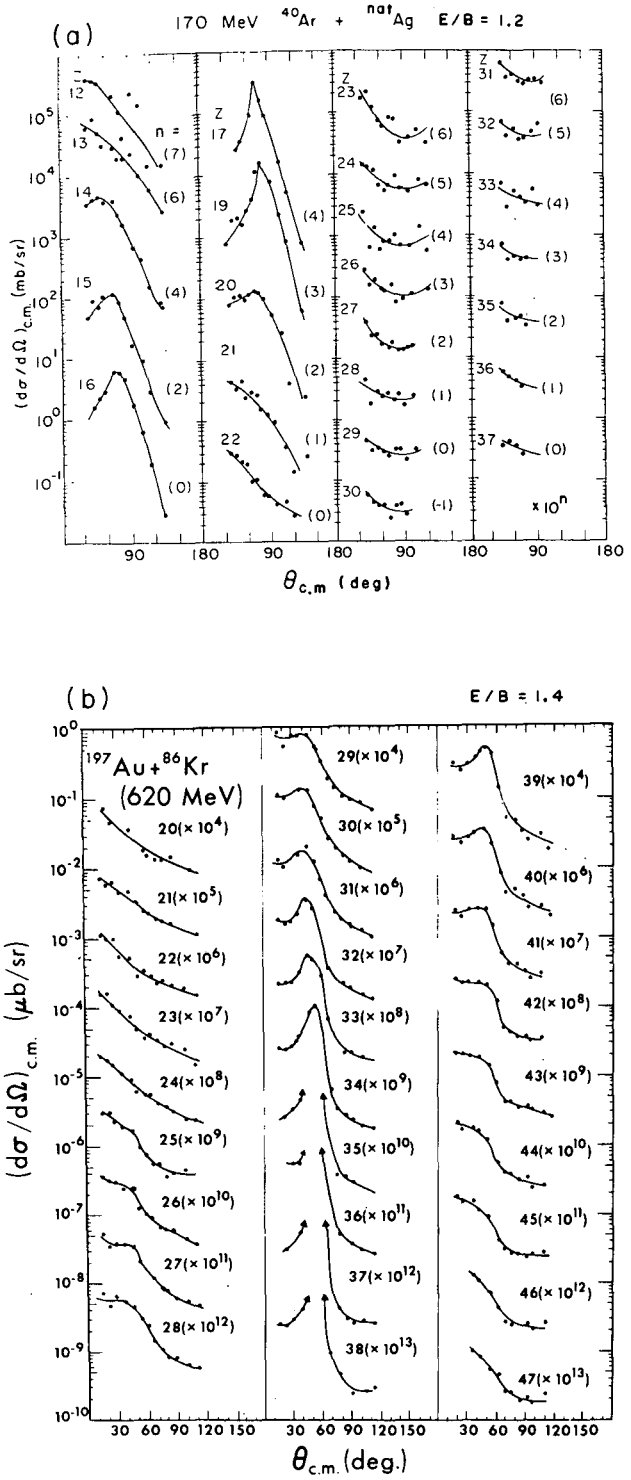


Fig. 3. Center-of-mass angular distributions for (a) 170 MeV $^{40}Ar + ^{nat}Ag$ (E/B=1.2), and (b) 620 MeV $^{86}Kr + ^{197}Au$ (E/B=1.4). The occurrence of side peaking near the projectile Z is clearly evident (the solid lines drawn through the data points are solely to quide the eye). The number in parentheses is the common log of the multiplication factor in Fig. 3a whereas in 3b it is the multiplication factor.
(XBL 7612-10982)

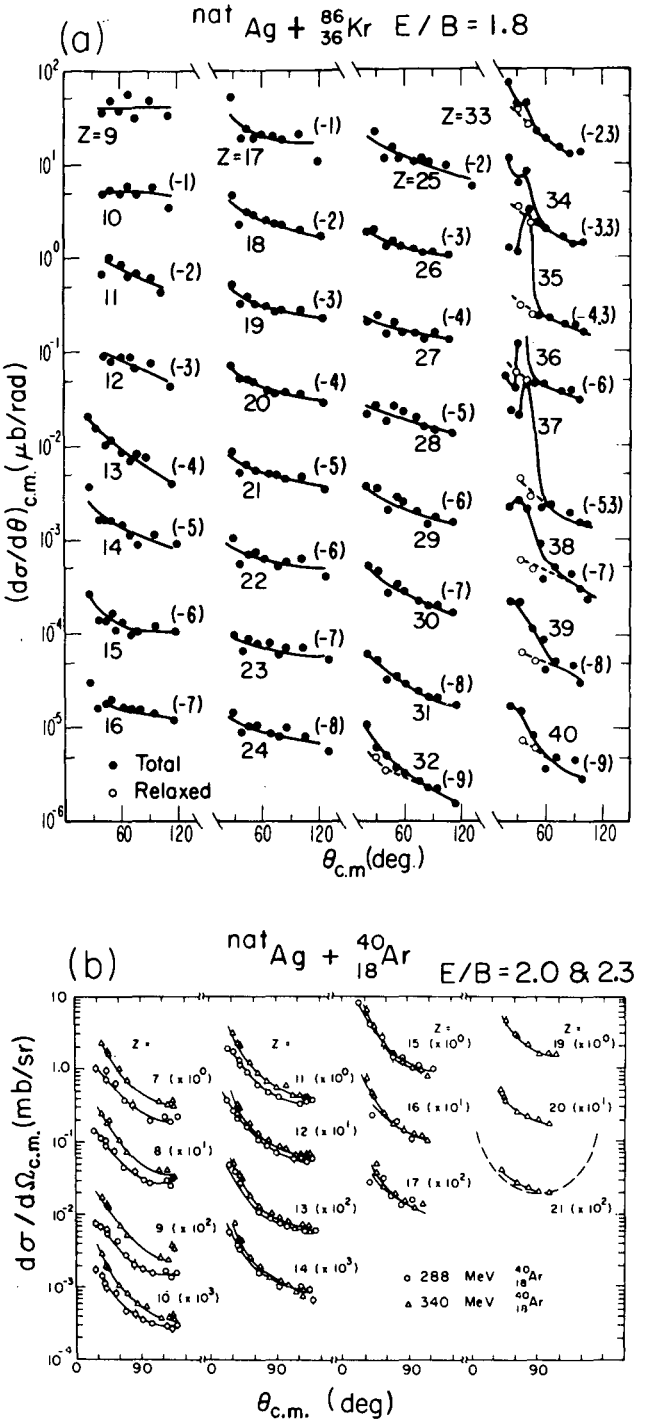


Fig. 4. Center-of-mass angular distributions, (a) ($d\sigma/d\theta$) for 620 MeV $^{86}Kr + ^{nat}Ag$ (E/B = 1.8) and (b) ($d\sigma/d\Omega$) for 288 and 340 MeV $^{40}Ar + ^{nat}Ag$ (E/B = 2.0, 2.3). Here one finds the forward peaking which is typical of lighter ion reactions (the solid lines drawn through the data points are solely to guide the eye). The number in parentheses in Fig. 4a is the common log of the multiplication factor whereas in 4b it is the multiplication factor.
(XBL 7612-10981)

# ANGULAR MOMENTUM TRANSFER IN DEEP INELASTIC PROCESSES*

P. Glässel,† R. S. Simon,‡ R. M. Diamond, R. C. Jared, I. Y. Lee, L. G. Moretto,§ J. O. Newton,‖ R. P. Schmitt, and F. S. Stephens

The transfer of entrance-channel orbital angular momentum into intrinsic spin of the two fragments of the intermediate complex was studied in the reaction 175 MeV $^{20}Ne + ^{nat}Ag$. To determine the total spin of the fragments associated with a given mass asymmetry in the exit channel, the $\gamma$ multiplicity was measured as a function of the fragment atomic number.

The de-excitation $\gamma$ radiation was observed in two 3 × 3 in. NaI detectors at 75° and 105° relative to the beam direction and 60 cm from the target. The $\gamma$ rays were recorded in coincidence with one fragment, which was detected in either of two telescopes consisting of a solid state E and gas $\Delta$E counters.[1] The measurements were performed at telescope angles of 25° (the grazing angle), 35° and 90° with respect to the beam direction. To obtain $\gamma$ multiplicities, the coincident $\gamma$ spectra were corrected for random events (10%) and then unfolded using a carefully adjusted response function and the absolute efficiency of the NaI detectors. When normalized to the number of singles events in the gated Z and kinetic-energy region, the unfolded $\gamma$ spectra can be integrated to give the average $\gamma$ multiplicities.

In Fig. 1 the $\gamma$ multiplicity $M_\gamma$ is shown as a function of Z for the relaxed component at the three lab angles. Some typical error bars are given, referring only to statistical uncertainties. For comparison, calculated $\gamma$ multiplicities for the limiting cases of rolling (dashed lines) and sticking (solid lines) are plotted for two values of the entrance-channel orbital angular momentum (50$\hbar$ and 70$\hbar$), assuming two sharp spheres in contact ($R = 1.225\,(A_1^{1/3} + A_2^{1/3})$fm). The intrinsic angular momentum is assumed to be twice the $\gamma$ multiplicity. This represents a balance between some $\gamma$ rays carrying less than 2$\hbar$ and some particle emission that carries angular momentum, and it is consistent with compound-nucleus studies.[2] The value of 70$\hbar$ for the entrance channel is in fair agreement with the value to be expected from the sum of the known evaporation-residue cross section[3] of 900 ± 200 mb (corresponding to an upper angular momentum cut-off $\ell_{ER} = 57 \pm 7$), and the deep-inelastic cross section of 400 mb, bringing the angular momentum cut-off close to $\ell = 70$.

Comparing the data with the calculated lines, one sees that at 90° the fairly rapid increase of $M_\gamma$ with decreasing Z suggests that the sticking limit is approached, indicating that the decay times are probably longer at this angle. The 70$\hbar$ line for sticking agrees better at high Z's, while the 50$\hbar$ line agrees best for the lower Z's. The substantially lower multiplicities observed for the lower Z values at 25° and 35° could be due to a very strong preference of these Z's for lower $\ell$-waves, but this behavior can be better understood

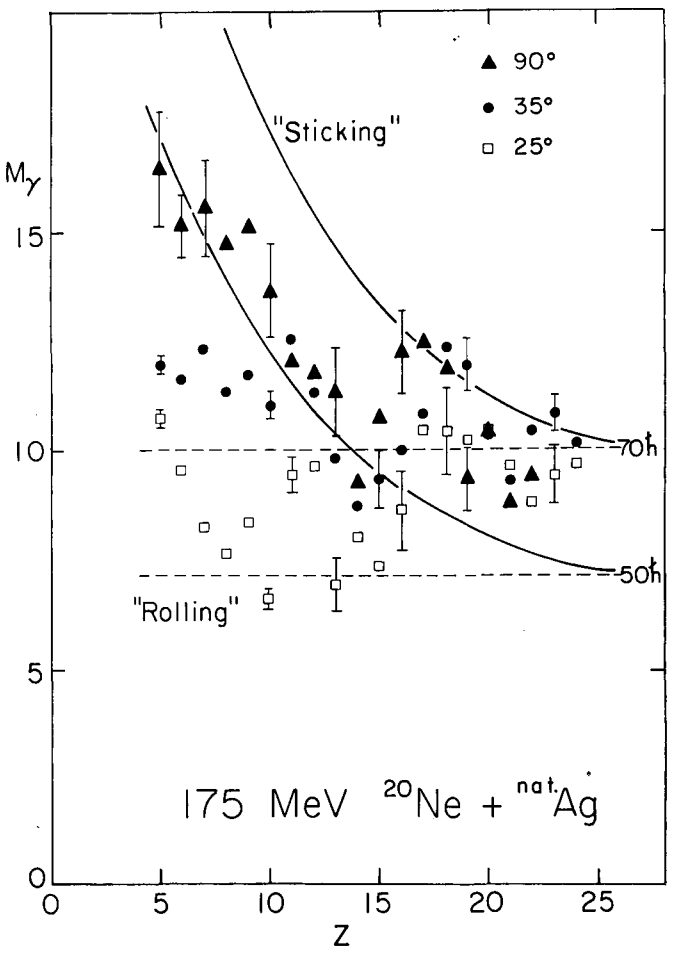


Fig. 1. Gamma-multiplicity vs Z for the relaxed component. (XBL 7611-4446)

in terms of incomplete angular momentum transfer. The lowest multiplicities are observed at the grazing angle 25° and may be thought to contain the shortest decay times.

The $\gamma$ multiplicity for the quasi-elastic component and for the Z = 10 "elastic" component are shown in Fig. 2. It is seen that, as one moves away from the Z of the projectile, the $M_\gamma$ rises very rapidly from extremely low values to around the "rolling" limit. It is tempting to relate such a rapid increase in $M_\gamma$ with the corresponding rapid decrease in kinetic energy of the quasi-elastic peak as one moves from Z = 10 towards lower Z's. The dependence of both kinetic energies and $\gamma$ multiplicities seems to be consistent with that predicted by a direct mass transfer (dashed line in Fig. 2).[4]

In conclusion, the data presented here furnish strong evidence that the intermediate complex approaches rigid rotation in a time

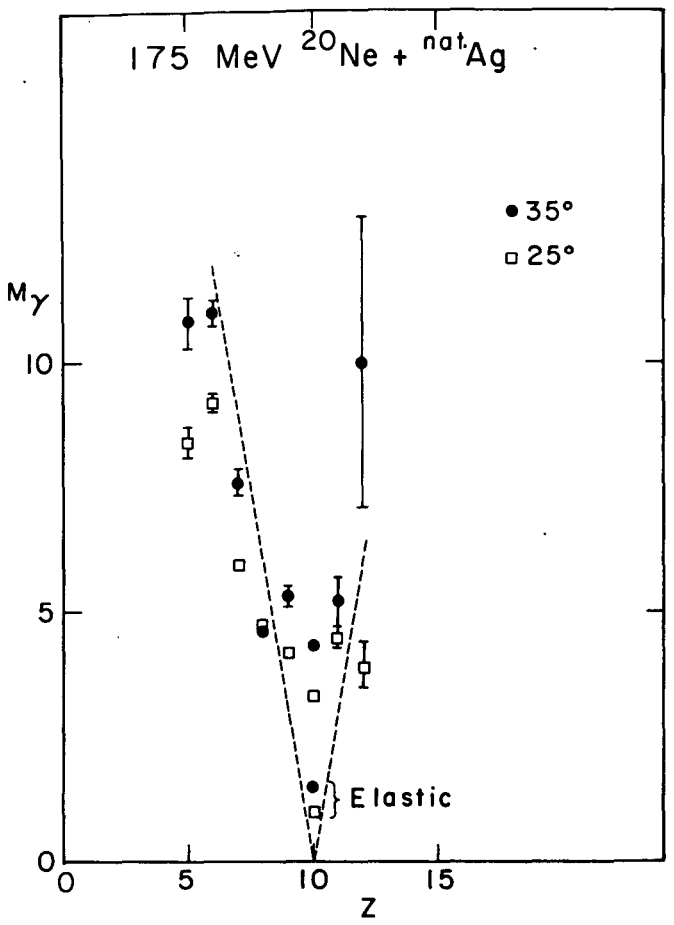


Fig. 2. Gamma-multiplicity vs Z for the quasi-elastic component. (XBL 7611-4445)

comparable to the rotational period of the complex. The evidence from the low-Z quasi-elastic component is consistent with the suggestion that the fastest transfer of angular momentum is accomplished by direct mass transfer.

Footnotes and References

*Condensed from LBL-5086 and Phys. Rev. Lett. 38, 331 (1977).

†Present address: Physikalisches Institut der Universität Heidelberg Philosophenweg, Z2, 0-69, Heidelberg, W. Germany.

‡On leave from Sektion Physik der Ludwig-Maximilians-Universität München, 8046 Garching, Germany; sponsored by the Bundesministerium für Forschung and Technologie.

§Sloan Fellow 1974-76

‖On leave from the Australian National University, Canberra, Australia.

1. M. M. Fowler, R. C. Jared, Nucl. Instrum. Meth. 124, 341 (1975).

2. R. S. Simon et al., Phys. Rev. Lett. 36, 359 (1976).

3. F. Plasil and M. Blann, Phys. Rev. C 11, 508 (1975).

4. M. Ishihara et al., Proc. Symp. on Macroscopic Features of Heavy-Ion Collisions, Argonne (1976) p. 617.

## NUCLEAR RELAXATION PHENOMENA, DIFFUSION AND ORBITING IN THE REACTION $^{107,109}$Ag + $^{84,86}$Kr AT 7.2 MeV/NUCLEON*

R. P. Schmitt, P. Russo,† R. Babinet,‡ R. Jared and L. G. Moretto§

Charged particles produced from the interaction of a 7.2 MeV/n Kr beam and a natural Ag target have been studied. Fragments up to Z = 50 have been identified by means of a ΔE, E telescope. Kinetic energy distributions, charge distributions and angular distributions have been measured for the individual atomic numbers.

The kinetic energy distributions of the reaction products [see Figs. 1(a) & (b)] reveal the existence of two components (in addition to elastic scattering): a quasi-elastic peak, at near elastic energies; and a deep-elastic, or relaxed, component at substantially lower energies. The existence of these two components has already been confirmed with lighter projectiles like $^{14}$N, $^{20}$Ne and $^{40}$Ar (Refs. 1-3). This is somewhat atypical of Kr reactions since with heavier targets the quasi-elastic and relaxed components often lose their separate identities.[4] Note also that the quasi-elastic component is restricted to forward angles and to atomic numbers close to that of the projectile. For angles forward of the grazing, the distinction between quasi-elastic and deep-inelastic diminishes, and very broad distributions are observed for elements around Kr (Z = 36). Sufficiently behind the grazing angle, a single, fully relaxed peak is visible. In this angular range the spectra are approximately Gaussian. The width of this peak is essentially independent of angle implying a constant degree of energy relaxation over a broad angular range.

The shape dependence of the kinetic energy distributions with angle can be interpreted in terms of orbiting. For rather high impact parameters only small amounts of matter and/or energy are transferred. Fragments produced in these collisions follow near Coulomb trajectories and account for the quasi-elastic component near the grazing angle. As the impact parameter is decreased, more energy and mass are transferred

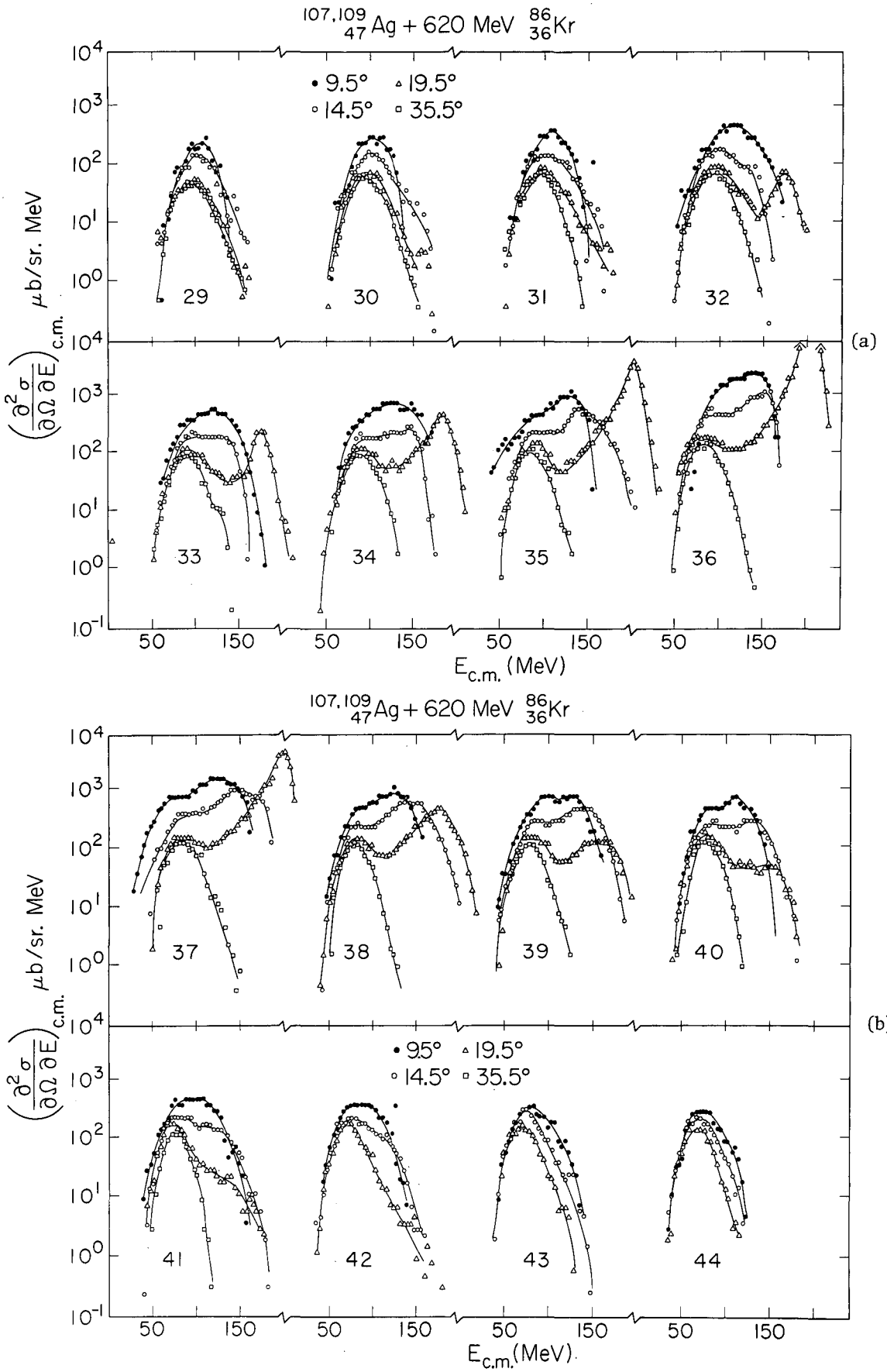


Fig. 1. (a) and (b) The c.m. kinetic energy distributions for various atomic numbers at four lab angles. For purpose of comparison with other Z-values the elastic component has been extracted from Z = 36 at 9.5° and 19.5°. [(a) XBL 766-3004; (b) XBL 766-3005]

and the fragments are deflected towards smaller angles. At still lower impact parameters, "sticking" of the fragments occurs, and the complex may rotate past 0° to negative angles in the reaction plane. At backward angles, only the damped, long-range "orbiting" component is observed. The overlap of the positive and negative angle contributions leads to the broad energy distributions observed at forward angles.

Lab cross sections integrated over energy for various atomic numbers and for several angles are given in Fig. 2(a) and (b). For angles behind the grazing, only the deep-inelastic, or relaxed, component contributes to the cross section. The observed charge distributions for these angles are very broad and the cross section increases with increasing Z. At more forward angles the quasi-elastic component becomes dominant for Z close to Z = 36, and a good deal of the cross section is concentrated in this region. The yield for the quasi-elastic component is distributed more or less symmetrically about Z = 36. This is not surprising since the target and projectile are similar in mass so that stripping and pickup are similar processes. When the quasi-elastic component is removed, the distributions look very similar to those obtained at backward angles and peak near symmetry (Z = 41.5).

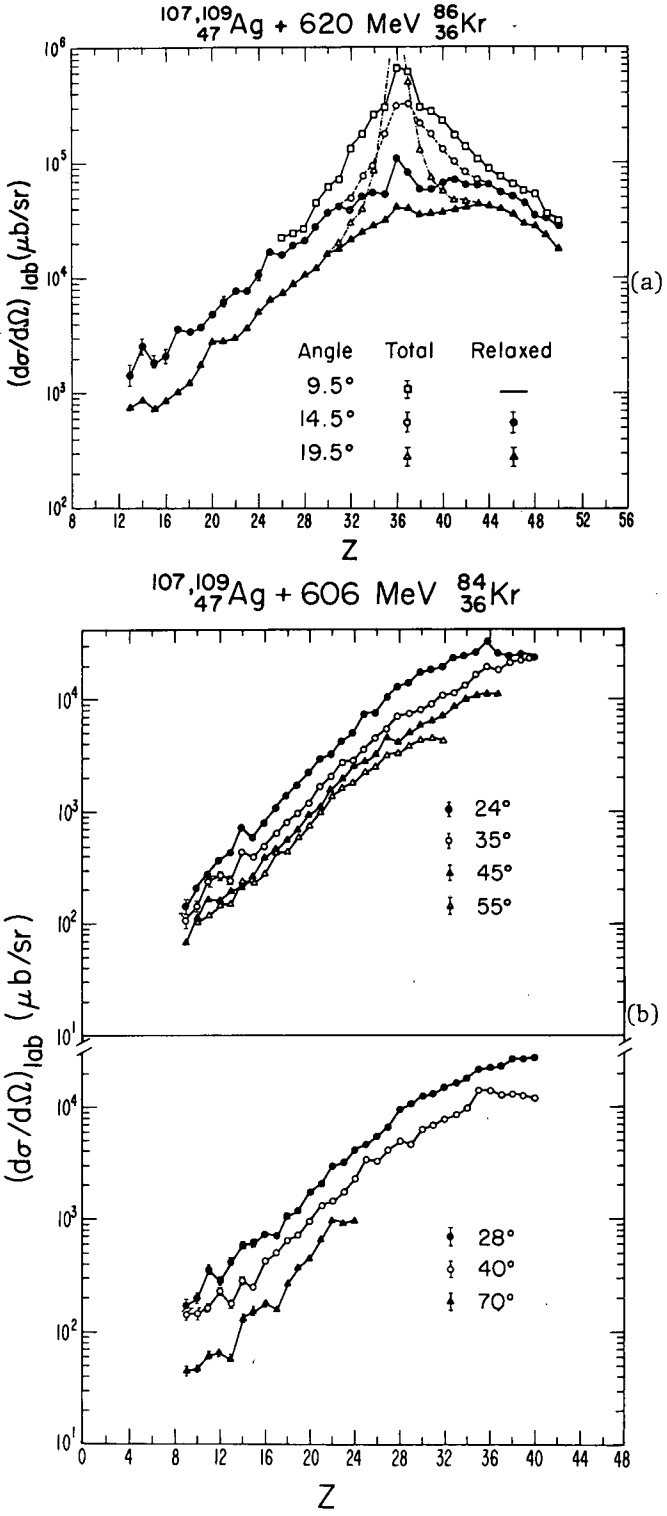


Fig. 2. (a) Lab charge distributions for $^{107,109}$Ag+620 MeV $^{86}$Kr at various lab angles. The cross section for the relaxed component is shown when it was possible to make a distinction between it and the quasi-elastic one. (b) Same as (a) for $^{107,109}$Ag+606 MeV $^{84}$Kr. At these more backward angles, the kinetic energy spectra are essentially all relaxed. [(a) XBL 768-3265; (b) XBL 768-3226]

The c.m. angular distributions are given in Fig. 3. In the cases where a decomposition of the quasi-elastic and relaxed components was feasible, both the relaxed and total are given. The angular distributions ($d\sigma/d\Omega$ vs $\theta$) are all forward peaked in excess of $1/\sin\theta$ (with the exception of Z = 9,10). To make this more readily visible we have plotted $d\sigma/d\theta$ rather than $d\sigma/d\Omega$. The forward peaking in excess of $1/\sin\theta$ implies that the lifetime of the intermediate complex is comparable to the rotational period (about $6 \times 10^{-21}$ sec for the rms angular momentum assuming that the complex consists of spherical fragments in contact and rotating rigidly). The excess forward peaking is strongest in the vicinity of the projectile. As one moves down in Z, the forward peaking decreases gradually until about Z = 17, where it tends to increase again, and then decreases again. This behavior for the very low Z-values is not easily explained, and may be an experimental effect due to secondary reactions with a low-Z material like Al.

This pattern of angular distributions can be qualitatively accounted for within the framework of the diffusion model. One expects to see the greatest forward peaking for the shortest lifetimes. At the same time, short lifetimes imply small mass transfers. Hence, one observes the greatest forward peaking in the vicinity of the projectile. Atomic numbers far from the projectile are populated on a much longer time scale, so the complex has, on the average, rotated through much larger angles. As a result, the angular distributions are less forward peaked. Such contrasting behavior can be attributed to differences in the ratio $\tau_{life}/\tau_{rot}$, where $\tau_{life}$ and $\tau_{rot}$ represent the average lifetime and the average rotational period of the complex. For small values of this ratio, the complex does not live long enough to reach 0°, and the fragments are emitted on the side of impact. For slightly

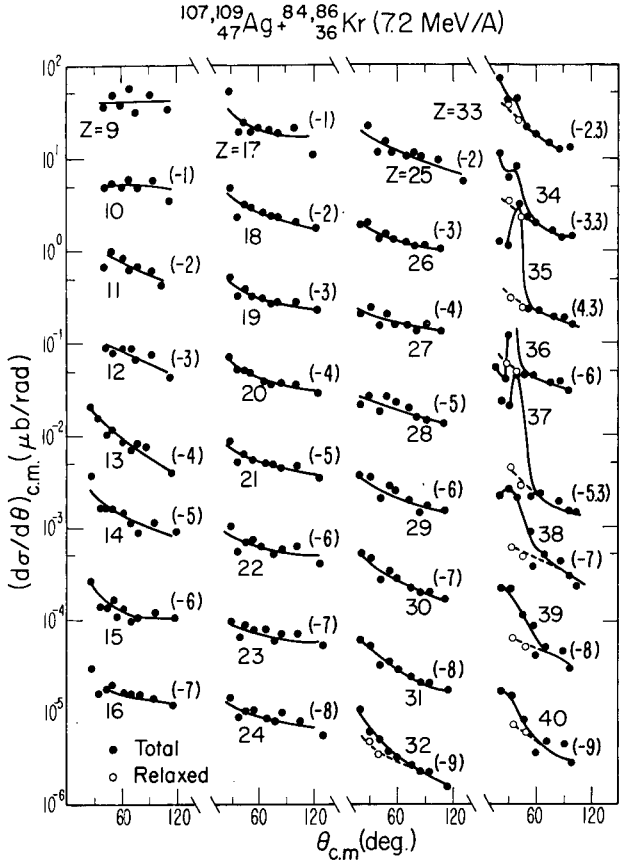


Fig. 3. The c.m. angular distributions for 32 atomic numbers. The quantity $d\sigma/d\theta$ is plotted. Both the relaxed and total contributions are given when the relaxed component appeared as a distinct component. The number in parentheses is the common log of the multiplication factor. (XBL 768-10148)

larger values, the complex decays at angles near 0° producing angular distributions that are forward peaked. As the value of this ratio increases further, the complex rotates to larger negative angles before decaying, resulting in decreased forward peaking and enhanced yields in the backward hemisphere. In the limit of large $\tau_{life}/\tau_{rot}$, the complex may undergo one or more complete revolutions, and the angular distributions tend to the $1/\sin\theta$ behavior expected for the decay of a compound nucleus with large angular momentum.

Nuclear relaxation phenomena are clearly visible in the reaction Ag+Kr. Most apparent are the relaxation of energy, as seen in the kinetic energy spectra for the Z close to that of the projectile, and relaxation of the mass/charge asymmetry mode, as reflected in the charge and angular distributions. The relaxation along the mass asymmetry mode seems to be slower than the relaxation of kinetic energy and appears to be diffusive in nature. The charge and angular distributions have been interpreted within the framework of the diffusion model of Moretto and Sventek and provide evidence for such a unified approach in the interpretation of heavy-in reaction phenomena. Finally, the experimental data show that nuclear orbiting is well developed in the reaction Ag+Kr.

Footnotes and References

*Condensed from LBL-5042 and Nucl. Phys. A 279, 141 (1977).

†Present address: University of Rochester, Rochester, New York 14627

‡Present address: OphN/MF-CEN, Saclay, France.

§Sloan Fellow 1974-1976

1. L. G. Moretto et al., Physics and Chemistry of Fission, 1973, Vol. 2 (IAEA, Vienna, 1974) p. 351.

2. A. G. Artukh et al., Nucl. Phys. A 215, 91 (1973).

3. L. G. Moretto et al., Nucl. Phys. A 255, 491 (1975).

4. P. Russo et al., Nucl. Phys. A 281, 509 (1977).

## A STUDY OF DIFFUSION PHENOMENA IN THE INTERMEDIATE MASS REGION: THE REACTION $^{159}$Tb + 620 MeV $^{86}$Kr†

G. J. Wozniak, R. P. Schmitt, P. Glässel,* and L. G. Moretto‡

With the advent of heavy-ion accelerators, many new physical phenomena have been revealed in heavy-ion reactions studies. In particular, early studies with Kr beams gave evidence for phenomena which were characterized by a large energy dissipation and a relative small amount of mass transfer. Recent detailed studies[1-3] of the $^{86}Kr + ^{197}Au$, $^{86}Kr + ^{181}Ta$ and $^{86}Kr + ^{107,109}Ag$ systems at 620 MeV bombarding energy demonstrated that as the mass of the target is decreased from $^{197}Au$ to $^{107,109}Ag$ the integrated charge distribution broadens and the side peaking in the angular distributions diminishes. For the two heavier systems[1,2] these features have been semi-quantitatively reproduced with the Diffusion Model of Moretto and Sventek.[4] In addition, the broader

charge distributions and the forward peaked angular distributions observed in the $^{86}Kr$ + $^{107,109}Ag$ system[3] have also been qualitatively explained in terms of this model. To further investigate the transition region between the light and heavy targets and to determine whether the Diffusion Model could successfully quantitatively describe the observed phenomena over the mass region from $^{107,109}Ag$ to $^{197}Au$ with a consistent set of parameters, we have investigated the $^{86}Kr + ^{159}Tb$ system and performed Diffusion Model calculations for this system plus the previously studied $^{86}Kr + ^{107,109}Ag$ system.

Previously, Diffusion Model calculations semi-quantitatively reproduced data from $^{181}Ta$ and $^{197}Au$ targets with the following parameters values:[1,2]

$$\tau(0) = 35 \times 10^{-22} \text{ sec} ,$$

$$\sigma(0) = 10 \times 10^{-22} \text{ sec} ,$$

$$\kappa = 0.5 \times 10^{+21} \text{ fm}^{-2}\text{sec}^{-1} ,$$

$$\delta = -2.0 \text{ fm} .$$

Diffusion Model calculations of the angle integrated charge distributions from the $^{159}Tb$ target utilizing these values (solid curve) are presented in Fig. 1. The experimental values (circles) in Fig. 1 were obtained by integrating over the experimental range of measurements. Because of the limited angular range of the measurements and the steeply falling angular distributions for low and high Z values, a sizable fraction of the cross section is missed. (Forward angle data requires long counting times because the large elastic rate severely restricts the beam intensity.) This fact can account for the calculations overestimating the cross section for the low and high Z values, since if one extrapolates the experimental data using the shapes of the theoretical angular distributions, the discrepancy is reduced to about 20%. Near Z = 36 the calculations grossly underestimate the cross section. However, this failure is not unexpected because the theory is not readily applicable[4] to partially damped events and the energy spectra for these elements near the grazing angle show large contributions from such events.

Since the potential energy of the intermediate complex depends on its shape, we investigated this dependence by varying the overlap parameter δ. Diffusion Model calculations for two smaller values of δ (dashed lines) are also shown in Fig. 1. Decreasing the overlap from -2.0 to -1.0 fm shifts cross section from elements below the projectile to those above it. For the smaller overlaps the potential energy is steeper at the injection point, which inhibits diffusion to greater asymmetry and favors diffusion toward symmetry. Because of the arguments enumerated above, it is felt that the calculations with δ = -2.0 fm best reproduce the data. Since this value also gave the best agreement with the integrated charge distributions from the $^{181}Ta$ and $^{197}Au$ targets, it seems to be target

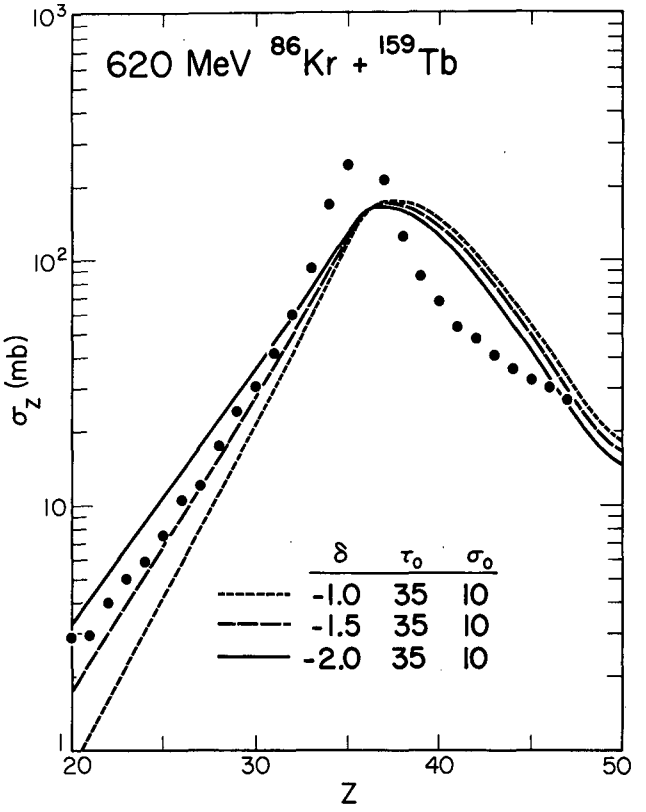


Fig. 1. A comparison between the experimental angle-integrated cross section (points) and the diffusion model calculation (smooth curves) for fragments ($20 \leq Z \leq 47$) produced in the reaction $^{159}Tb$ + 620 MeV $^{86}Kr$ (see text). Calculations are shown for three values of the overlap parameter δ and the experimental values were obtained by integrating over the experimental range of measurements. (XBL 777-1274)

independent over a large mass range for Kr-induced reactions.

To test more rigorously the Diffusion Model, calculations of the angular distributions were performed with the values (δ = -2.0, τ(0) = 35, σ(0) = 10 and κ = 0.5) which gave the best fit to the data from the $^{181}Ta$ and $^{197}Au$ targets. In Fig. 2 an absolute comparison is made between the experimental (solid circles) and calculated (curves) angular distributions for the $^{159}Tb$ + 620 MeV $^{86}Kr$ system. The overall agreement between the theoretical predictions and experiment is quite good with both the shape and magnitude being reproduced for elements 3 or more Z's above the projectile and 5 or more below. Although the calculations indicate substantially less side peaking than observed for elements adjacent the projectile, most of this side peaking is due to quasi-elastic processes that the present model neglects. However, the overall fall off of the cross section from forward to backward angles is well reproduced. To illustrate that these cross sections are more forwarded peaked than the compound nucleus limit, a 1/sin θ curve is included in the bottom of the right column.

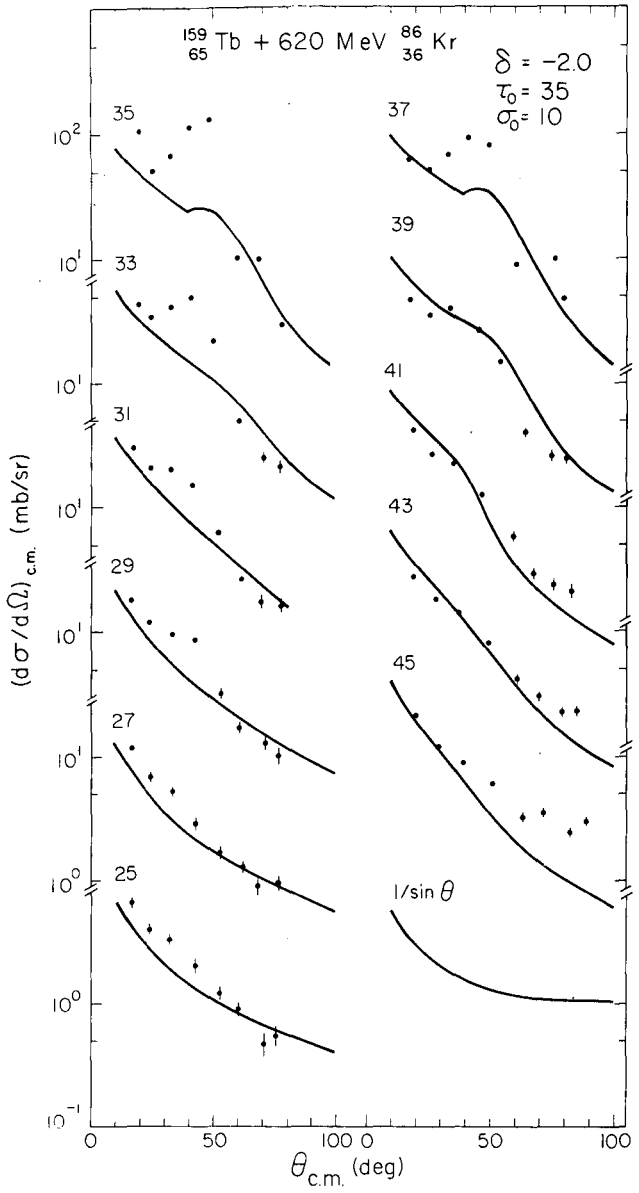


Fig. 2. Absolute comparison between experimental (points) and calculated angular distributions (solid curve) for representative elements produced from the reaction $^{159}$Tb + 620 MeV $^{86}$Kr (see text).
(XBL 777-1272)

An extensive discussion of the $^{107,109}$Ag + 620 MeV $^{86}$Kr system has been presented by Schmitt et al. in Ref. 3. This investigation demonstrates that the experimental charge and angular distributions are dramatically different from those observed in $^{86}$Kr induced reactions on heavier systems like $^{181}$Ta and $^{197}$Au. In particular the charge distributions are very broad and the angular distributions are essentially forwarded peaked. This broadening of the charge distributions and weakening of the side peaking in the angular distributions as one goes from $^{197}$Au to $^{107,109}$Ag targets was explained qualitatively in terms of the Diffusion Model and correlated with the increasing value of the ratio E/B. Because no quantiative Diffusion Model calculations were available when Ref. 3 was published and because subsequently the Diffusion Model with a single set of parameters has been able to semi-quantitatively reproduce the measured data from three targets over a mass range from 159 to 197, it is interesting to determine if these parameters will reproduce the $^{107,109}$Ag + 620 MeV $^{86}$Kr data or whether some parameter adjustments are required.

To this end angular distributions (solid curves) were calculated for fragments produced in the reaction $^{107,109}$Ag + 620 MeV $^{86}$Kr utilizing the parameters which gave the best fits to the data from other targets and are presented with the experimental data (solid circles) in Fig. 3. Although the overall agreement with the data is somewhat poorer than that obtained for the other systems with these parameter values, the calculations do reproduce the forward angle region for several Z values around the projectile. However, for elements 31 - 27 this region is overestimated by the calculations. In addition the

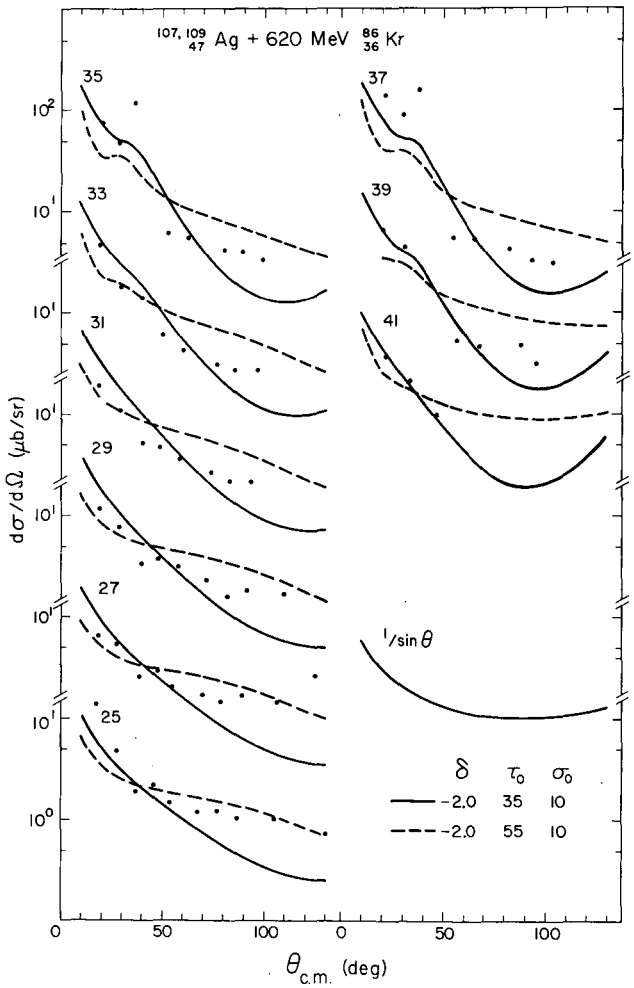


Fig. 3. Absolute comparison between experimental (points) and calculated (curves) angular distributions for representative elements produced from the reaction $^{107,109}$Ag + 620 MeV $^{86}$Kr. Calculations are presented for two values of the mean lifetime $\tau(0)$ of the intermediate complex.
(XBL 777-1276)

backward angle region is consistently underestimated. These two features indicate that the intermediate complex's lifetime is too short so that the complex does not rotate enough before decaying. To determine if increasing the lifetime would give a better fit to the data, calculations (dashed lines) were performed for $\tau(0) = 55$. For Z values several charge units removed from the projectile, this longer lifetime gives a better fit to the data, but the yield at backward angles is consistently overestimated. An intermediate value for the lifetime $\tau(0)$ of $45 \times 10^{-21}$ sec would decrease the backward angle yield while maintaining the agreement at forward angles. Thus it seems that the $^{107,109}$Ag + 620 MeV $^{86}$Kr system is best described by increasing the intermediate complex's lifetime by 30%.

Recent investigations have demonstrated that the character of the charge and angular distributions from $^{86}$Kr induced reactions at 620 MeV change dramatically when making the transition between light ($^{107,109}$Ag) and heavy ($^{197}$Au) targets. By investigating the transition region ($^{159}$Tb) and successfully reproducing the experimental data and the previously published $^{107,109}$Ag data with Diffusion Model calculations utilizing a consistent set of parameters which also fit the data from the heavier $^{181}$Ta and $^{197}$Au targets, we have demonstrated the applicability of the Diffusion Model and its ability to quantitatively describe deep inelastic phenomena. In particular it seems that the disappearance of the side peaking observed when one goes from Au to Ag is mainly due to the decreasing moment of inertia of the intermediate complex. Thus for the same lifetime distribution there is much more rotation through 0° for the lighter complex, resulting in flatter angular distributions. Even though the initial damping of the projectile kinetic energy is neglected in this model, good agreement with the data is obtained, illustrating the importance of the diffusion process in these heavy-ion reactions.

Footnotes and References

†Condensed from LBL-6532, submitted to Nucl. Physics.

*Present address: Physikalisches Institut der Universitat Heidelberg Philosophenweg 12, D-69, Heidelberg, W. Germany.

‡Sloan Fellow 1974-76, extended support.

1. P. Russo et al., Nucl. Phys. A 281, 509 (1977).

2. B. Cauvin et al., LBL-6506, Nucl. Phys. (in press).

3. R. P. Schmitt et al., Nucl. Phys. A 279, 141 (1977).

4. L. G. Moretto and J. S. Sventek, Phys. Lett. 58B, 26 (1975).

## TRANSITIONAL FEATURES OBSERVED IN THE CHARGE AND ANGULAR DISTRIBUTIONS OF DEEPLY INELASTIC FRAGMENTS PRODUCED IN THE REACTION $^{181}$Ta + 620 MeV $^{86}$Kr†

B. Cauvin,* R. P. Schmitt, G. J. Wozniak, P. Glässel,‡ P. Russo,§ R. C. Jared, J. B. Moulton, and L. G. Moretto‖

In previous papers we have reported on the results obtained in 620 MeV $^{86}$Kr bombardments of Ag and Au targets.[1,2] These studies demonstrated that these systems belong to the short- and long-lifetime regimes, respectively. In order to study the transition between these regimes, we have bombarded a target of intermediate mass $^{181}$Ta with 620 MeV $^{86}$Kr ions. Charged fragments produced in this reaction have been studied with ΔE-E telescopes. Kinetic energy spectra, charge distributions, and angular distributions have been measured for atomic numbers in the range $12 \leq Z \leq 49$. For all observed atomic numbers and for all angles, the energy spectra show the presence of energetically relaxed products in the vicinity of the Coulomb barrier. The spectra for elements near the projectile also show a large contribution from incompletely damped events at angles close to the grazing angle. For these elements the spectra show no clean separation between the relaxed and partially damped components. The charge distributions peak at or slightly above the projectile Z. For elements well removed in Z from the projectile, the angular distributions are forward peaked, whereas elements near Kr have angular distributions which are side peaked. The transition from side peaking to forward peaking takes place over a smaller range of Z-values than was observed for the reaction $^{197}$Au + 620 MeV $^{86}$Kr.

A direct comparison between the calculated angle-integrated charge distribution and the experimental values is presented in Fig. 1. The following values of the parameters were used in this calculation:[3]

$$\tau(0) = 35 \times 10^{-22} \text{ sec},$$

$$\sigma(0) = 10 \times 10^{-22} \text{ sec},$$

$$\kappa = 0.5 \times 10^{+21} \text{ fm}^{-2} \text{ sec}^{-1},$$

$$\delta = -2.0 \text{ fm}.$$

These values were used initially because they had previously yielded good agreement with the experimental angular distributions for the system $^{197}$Au + $^{86}$Kr.

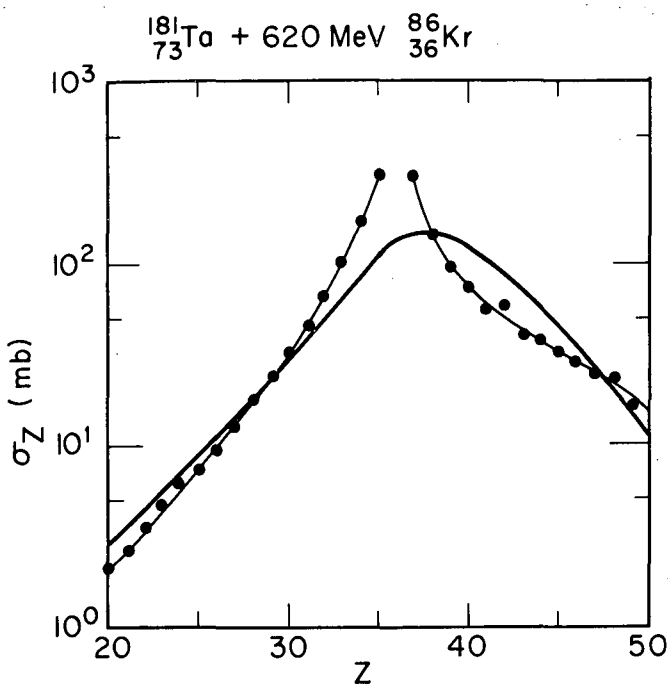


Fig. 1. A comparison between the experimental angle-integrated cross section (points) and diffusion model predictions (heavy curve). The experimental values were obtained by integrating between $\theta_{lab}$ = 10 to 80°. (XBL 775-3455)

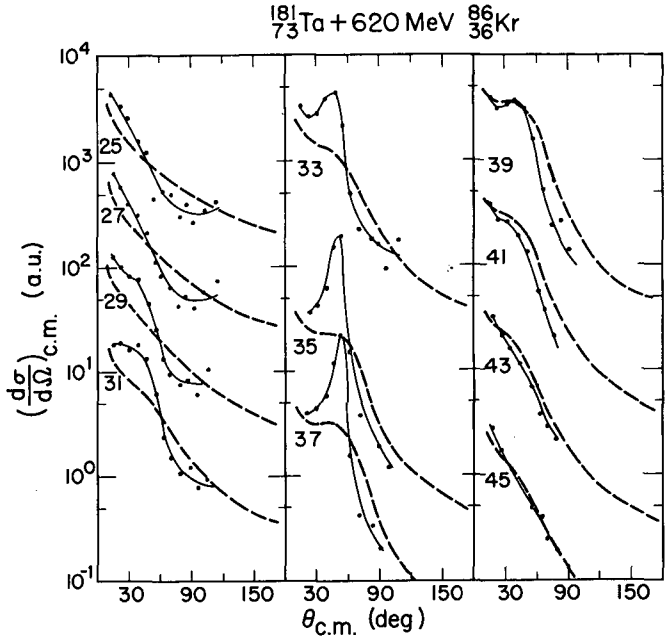


Fig. 2. Absolute comparison between experimental (points) and calculated angular distributions (heavy dashed curves). The thin solid curves through the data points serve only to guide the eye. (XBL 775-3453)

The experimental values in Fig. 1 were obtained by integrating over the experimental range of measurements. Because of the limited angular range of the measurements, a sizable fraction of the cross section may be missed, particularly for high Z-values. As is seen from the figure, the fit to the low Z data (i.e., $Z \gtrsim 31$) is quite good. Both the magnitude and slope of the cross section is reproduced within 30%. Although near Z = 36 the theory grossly underestimates the cross section, this failure is not unexpected since the energy spectra clearly show a large contribution of incompletely damped events for these elements. The theory is not directly applicable in this region since the overlap parameter $\delta$ and the form factor f have been held constant for all $\ell$-values [ $f = 2\pi R_1 R_2/(R_1+R_2)$ as in Ref. 4]. Both of these quantities are expected to decrease for high $\ell$-waves. Since the theory does not take this into account, the highest $\ell$-waves have been left out of the calculations ($P(\ell) = 0.5$ for $\ell \approx 250$). The fit to the high Z data (i.e., Z > 36) is rather poor. The theoretical values are almost a factor of two larger than the experimental numbers around Z = 40. However, if one extrapolates the experimental data using the shapes of the theoretical angular distributions, the discrepancy is reduced to about 30%.

A more rigorous test of the diffusion model calculations is given in Fig. 2 where an absolute comparison is made between the experimental and calculated angular distributions. The same values of the parameters given above were used in these calculations. The agreement is quite good. Both the magnitude and shape of the angular distributions are very accurately reproduced for the high Z's (see Z = 39 - 45). For Z's near the projectile, of course, the peak magnitude is grossly underestimated due to the omission of the quasi-elastic component in the calculations. Nevertheless, the agreement at angles well removed from the grazing angle is reasonable, in particular the slope of the fall-off at backward angles is correctly predicted for Z = 35 and 37. The agreement with the data for Z's below the projectile is less satisfactory. For Z = 25 and 27 the experimental angular distributions show stronger forward peaking than the calculations predict. In addition, the behavior at backward angles is not reproduced by the model: while the data shows some evidence of backward peaking (perhaps due to orbiting), the calculations decrease monotonically with increasing angle.

The effects of varying $\tau(0)$ and $\sigma(0)$ are illustrated in Fig. 3. The first and third columns show the effect of varying $\tau(0)$ (the second column repeats some of the calculations of Fig. 2). For $\tau(0) = 45$ (unless otherwise stated, units of $10^{-22}$ sec are used) one sees that the side peaking has almost vanished, leaving a small shoulder for Z = 35, 39, 43. The loss of side peaking is due to the fact that, for a majority of $\ell$-waves, the complex lives long enough to rotate past 0°. While the fit to the experimental high Z data is spoiled, the slope for Z = 27 at forward angles is in much better agreement with the data. There is, however, no evidence for any backward peaking; in fact, the yield at backward angles is depleted because of the longer lifetime.

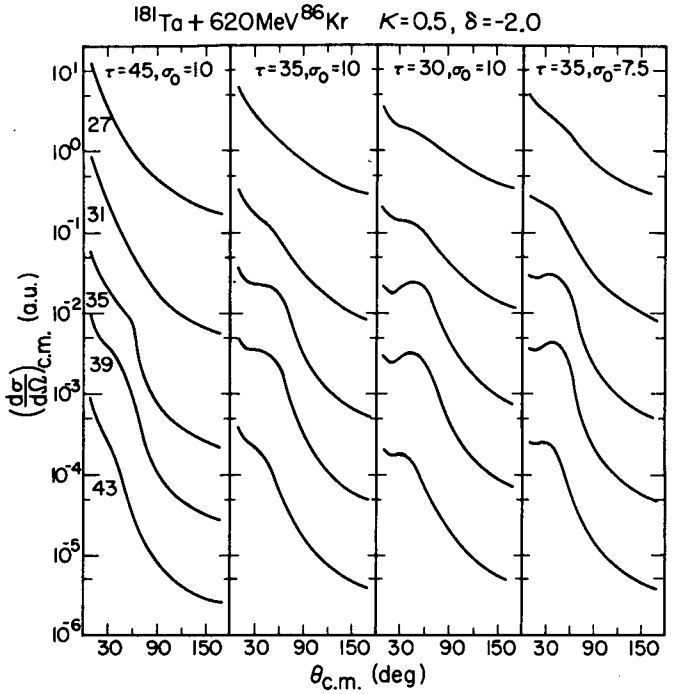


Fig. 3. Calculated angular distributions for several values of $\tau(0)$ and $\sigma(0)$ (in units of $10^{-22}$ sec). The Z-values are given only once at the extreme left of figure. (XBL 775-3452)

Apparently, the lifetime would have to be increased substantially to allow the system to orbit past 0° to backward angles.

The effect of decreasing $\tau(0)$ to 30 is shown in the third column. For all Z's the side peak has moved to slightly greater angles and become more pronounced with even Z = 27 showing a weak bump. A comparison to the data reveals that the overall agreement is poorer than for $\tau(0) = 35$. In the right-most column $\sigma(0)$ has been decreased by 25%. This variation causes the side peak to become narrower and moves it to somewhat smaller angles [compared to $\tau(0) = 35$, $\sigma(0) = 10$]. The side peak is also more persistence, as evidenced by the calculations for Z = 27 and 41. The agreement with the data is slightly better near Z = 36 but it is worse for atomic numbers removed in Z from the projectile (e.g., 27,43). Thus, we feel that the best overall agreement with the data is obtained with $\tau(0) = 35$ and $\sigma(0) = 10$.

Previous studies of the $^{107,109}$Ag + 620 MeV $^{86}$Kr and $^{197}$Au + 620 MeV $^{86}$Kr reactions revealed two distinct regimes of charge distributions and angular distributions. The current investigation of the system $^{181}$Ta + 620 MeV $^{86}$Kr exhibits intermediate characteristics and demonstrates that the transition between the regimes apparently takes place rather quickly. Even a variation of about 10% in the charge of the target in going from $^{197}$Au to $^{181}$Ta has a strong effect on the character of the angular distributions. For the slightly heavier $^{197}$Au + $^{86}$Kr system, side peaking is observed over a greater range of mass transfer than in the case of Ta + Kr. On the other hand, the angular distributions for $^{107,109}$Ag + $^{86}$Kr are markedly different from those of the two heavier systems. The dependence of the charge distributions on the mass of the target (at fixed bombarding energy) is quite smooth. The fact that the charge distributions widths tend to be narrow for the heavy systems is consistent with E/B systematics.

The most important conclusions of this work are in connection with the comparison of the diffusion model calculations to the experimental data. The fits to the experimental angular distributions strongly support this approach in interpreting and understanding heavy-ion reactions. It should be stressed that the transitional features observed in the Ta + Kr study present a critical test for the model which must systematically reproduce data from a range of systems.

## Footnotes and References

†Condensed from LBL-6506, submitted to Nuclear Physics.

*Present address: Dphn/Mf-CEN, Saclay, France.

‡Present address: Physikalishches Institut der Universitat Heidelberg Philosophenweg Z2, Heidelberg, W. Germany.

§Present address: University of Rochester, Rochester, New York 14627.

‖Sloan Fellow 1974-76.

1. R. P. Schmitt et al., Nucl. Phys. A 279, 141 (1977).

2. P. Russo et al., Nucl. Phys. A 281, 509 (1977).

3. J. S. Sventek and L. G. Moretto, Phys. Lett. 65B, 25 (1976).

4. L. G. Moretto and J. S. Sventek, Phys. Lett. 58B, 26 (1975).

# CHARGE AND ANGULAR DISTRIBUTIONS AND SECONDARY FISSION OF DEEP INELASTIC PRODUCTS FROM THE REACTION $^{197}$Au + 979 MeV $^{136}$Xe†

P. Russo,* R. P. Schmitt, G. J. Wozniak, B. Cauvin,‡ P. Glässel,§ R. C. Jared, and L. G. Moretto‖

Fragments from the reaction $^{197}$Au + 979 MeV $^{136}$Xe were detected with four telescopes, each consisting of a gas-ionization ΔE counter and a solid-state E-counter. The process of Z-identification was accomplished by means of a computerized method for the automatic location and subsequent fitting of Z-ridges in the two-dimensional E vs ΔE map.[1] The laboratory kinetic energy spectra for individual elements produced in the Xe + Au experiments reveal two well-resolved peaks at forward angles, particularly near Z = 40. Figure 1a shows the charge distributions of the higher energy component at several laboratory angles. This component peaks at the projectile Z-value and near the grazing angle (38°), indicating that it consists of light fragments produced in deep inelastic reactions.

The charge distributions for the low-energy component are plotted in Fig. 1b. These are peaked near one half the target Z-value suggesting that this component originates from fission of target-like fragments. This fission component for Xe + Au dominates the differential cross section near Z = 37. The peak near Z = 42 in the charge distributions suggests that the fissioning nucleus is a product of the transfer of several nucleons to the gold target resulting in a higher fission yield from the less abundant, but more fissionable nuclei. This is the first direct evidence of secondary fission of the target-like fragments produced in deep inelastic collisions. These observations support radiochemical yield studies of the more fissile system Xe + U.[2] It should be pointed out that for targets with $Z \gtrsim 79$ the large contribution of secondary fission could cause considerable distortion in the mass distributions for $A = 1/2\ A_{target}$.

Center-of-mass angular distributions for individual elements from Co to Er are presented in Fig. 2. The extensive side peaking observed for such a broad range of Z-values is unique among the very heavy-ion reactions investigated so far. If the Xe + Au and the Kr + Au[3] systems have similar lifetimes, one might expect comparable side peaking since the calculated mean rotational periods for spherical configurations are very similar. The observed difference between the angular distributions of the two systems can be explained by enhanced deformations in the Xe + Au system, which would increase the rotational period so that even the slower large-mass transfer processes give side-peaked angular distributions.

Differences in potential energy surfaces may also explain the above differences since, compared to Xe + Au, the potential for Kr + Au is steeper. Elements below the projectile are populated more slowly for the Kr + Au system compared to Xe + Au, so rotation proceeds further, causing the side peak to vanish sooner with decreasing Z. A related feature of the angular distributions for Xe + Au is the observed forward shift in angle of the side peak as Z decreases from the projectile Z-value. The angular distribution of events arising from a longer-lived complex is shifted forward since rotation and mass transfer proceeds further with increased time.

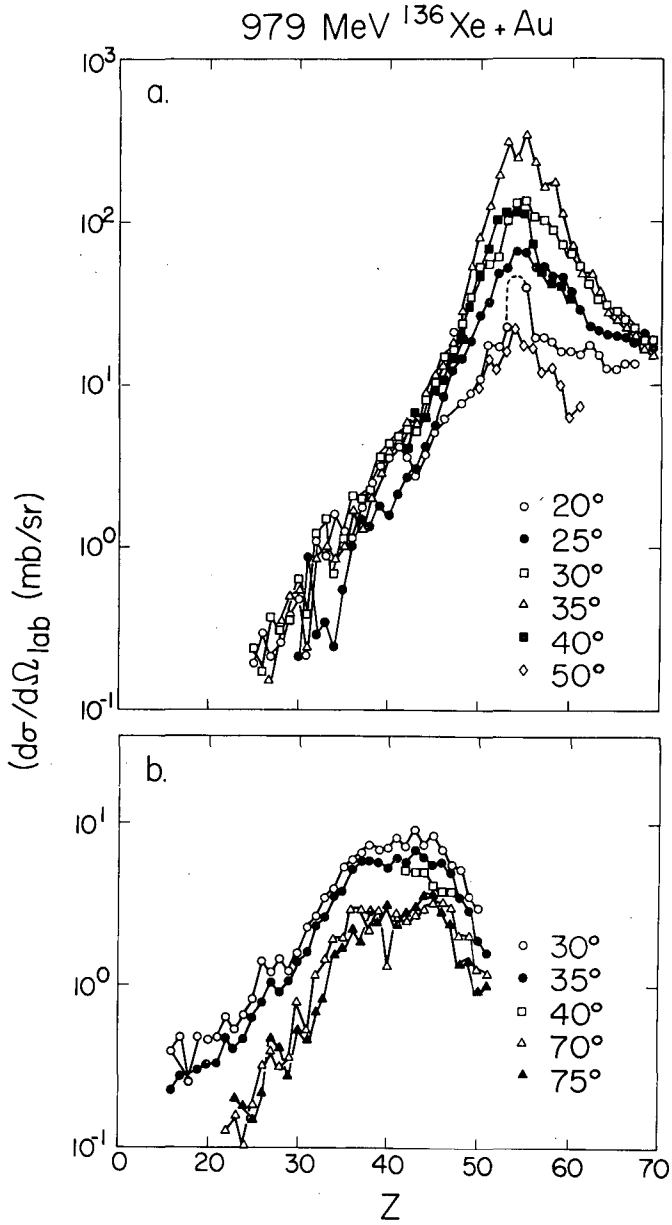


Fig. 1. (a) Laboratory differential cross section vs Z for the deep inelastic component: (b) same as (a) for the fission component. (XBL 767-3171)

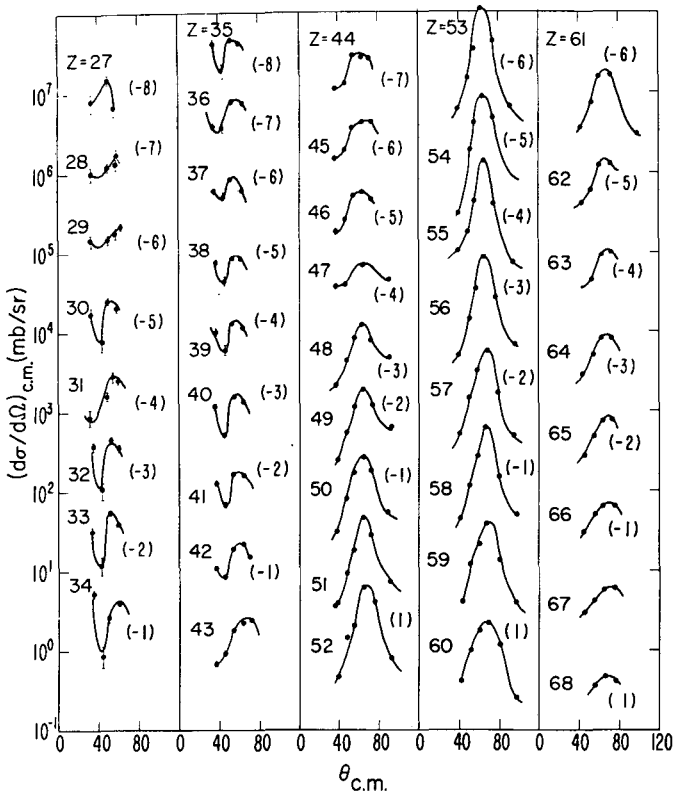


Fig. 2. Center of mass angular distributions of the deep inelastic component for individual Z-values. The number in parentheses is the common log of the multiplication factor. (XBL 766-3007A)

In summary, the first direct evidence of secondary fission in heavy-ion reactions has been presented. Furthermore, the comparable charge distribution widths, the lower ratio of the mean fragment energy to its calculated Coulomb energy and the much more pronounced side-peaking of the angular distributions for the Xe + Au relative to the Kr + Au system, seem consistent with larger fragment deformations in the former system.

## Footnotes and References

†Condensed from LBL-5050 and Phys. Lett. 67B, 15 (1977).

*Present address: University of Rochester, Rochester NY 14627.

‡Present address: DphN/MF-CEN, Saclay, France.

§Present address: Physikalisches Institut der Universitat Heidelberg Philosophenweg 12, D-69, Heidelberg, W. Germany.

||Sloan Fellow 1974-1976.


1. P. Glässel, R. Jared and L. G. Moretto, Nucl. Instrum. and Method, 142, 569 (1977).
2. R. J. Otto et al., Phys. Rev. Lett. 36, 135 (1976).
3. L. G. Moretto et al., Phys. Rev. Lett. 36, 1069 (1976).


# SECONDARY FISSION OF TARGET-LIKE NUCLEI PRODUCED IN DEEP INELASTIC COLLISIONS: $^{197}$Au + 620 MeV $^{86}$Kr

G. J. Wozniak, P. Glässel,* R. P. Schmitt, J. B. Moulton, G. Bizard,† R. C. Jared, and L. G. Moretto‡

A recent study of the system 979 MeV $^{136}$Xe + $^{197}$Au produced evidence of substantial secondary fission of the target-like fragments formed in deep inelastic collisions.[1] These secondary fission events were characterized by an atomic number Z of approximately one-half that of the target, a maximum cross section at an angle where the deep inelastic target-like products would peak and energies substantially larger than Coulomb energy expected for deep inelastic events. These observations are consistent with a binary reaction process wherein the initial kinetic energy of the projectile is damped into internal degrees of freedom. A rotating intermediate complex is formed and nucleons are exchanged between the two excited fragments. The intermediate complex undergoes decay and the two fragments separate. At a later time when the excited heavy fragment has left the nuclear field of the light fragment, it may undergo fission. To investigate whether secondary fission of the Au-like products occurs with a lighter projectile at a lower bombarding energy and to explore in more detail the dependence of the fissionability on the atomic number and the excitation energy of the heavy fragment, we performed a coincidence study of deep inelastic products from the reaction 620 MeV $^{86}$Kr + $^{197}$Au.

A self-supporting target of $^{197}$Au was bombarded with a 620 MeV $^{86}$Kr beam from the SuperHILAC and the light and heavy reaction products were detected in coincidence on opposite sides of the beam. A ΔE-E telescope with a 1 msr solid angle was used to measure the atomic number $Z_3$, the lab angle $\theta_3$, and the energy $E_3$ of the light fragment. The complementary heavy fragment or one of its secondary fission fragments was detected in coincidence with a large solid angle (~100 msr) X-Y position-sensitive telescope[2] which measured the in-plane lab angle $\theta_4$, the out-of-plane angle $\phi_4$ and the energy $E_4$ of this fragment. For binary events the ΔE-E telescope localized the light fragment to ± 1°, and because

subsequent neutron evaporation caused only small perturbations, the massive heavy fragment's direction is restricted to a narrow angular region. As result of this localization of the heavy fragment and the large solid angle of the X-Y telescope, events from a binary reaction process not followed by secondary fission could be detected with an efficiency of essentially 100%. (This 100% detection efficiency was verified with elastic scattering data.) Thus by comparing the singles to non-fission coincident events for a light fragment of a particular Z, the fissionability of the complementary heavy element can be measured.

To eliminate electrons and reduce the numbers of photons striking the X-Y counter (a parallel plate avalanche detector), a 2 kG magnetic field was created and a 0.5 mg/cm$^2$ Au foil placed in front of the counter. To maintain a position resolution of ~1°, the counting rate in the X-Y counter was limited to 5,000 s$^{-1}$. Both singles (2 parameters; $\Delta E_3$, $E_3$) and coincidence (8 parameters; $\Delta E_3$, $E_3$, $X^+$, $X^-$, $Y^+$, $Y^-$, $E_4$ and TAC) data were taken event-by-event and written on magnetic tape. Off-line, gates were set around the Z of the light fragment, the TAC peak, and a threshold in $E_4$ which separated the non-fissioning heavy-fragments from the fissioning ones.

In Fig. 1 some results of such a gating technique are shown for a light fragment $Z_3 = 38$ detected at $\theta_3 = 50°$ and the X-Y telescope at -50° (subtended 20° in both radial vertical directions). The entire histogram is the singles data, the unshaded part the non-fission coincidence data and the shaded area is the difference. From this figure it is apparent that the probability with which a $Z_4$=77 nucleus undergoes secondary fission depends strongly on the energy of the light fragment $E_3$. For large light fragment energies,

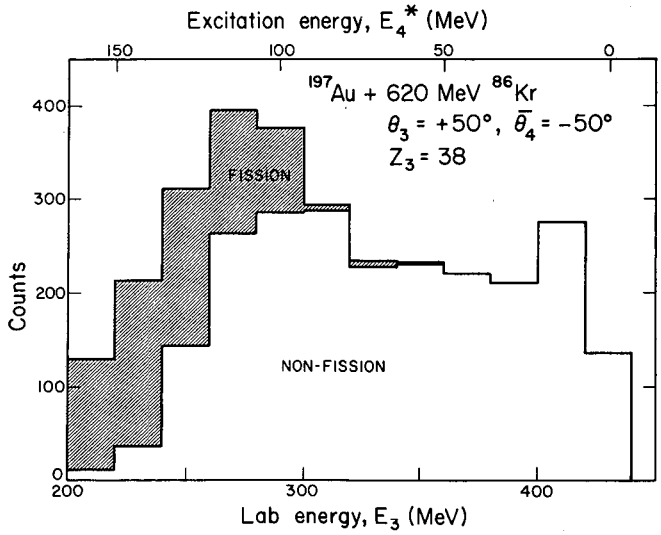


Fig. 1. Energy spectra of $Z_3 = 38$ fragments detected in the $\Delta E$-E telescope. The entire histogram is the singles data; the unshaded part, the non-fission coincidence events; and the unshaded area, the $Z_3 = 38$ events whose complementary $Z_4 = 77$ fragment fissioned. (XBL 778-1666)

very little secondary fission is observed whereas at low energies almost all the heavy fragments undergo secondary fission. In the top of the figure, the estimated excitation energy ($E_4$) of the heavy fragment (Z=77) is shown. This data indicates that secondary fission begins to occur for excitation energies of ~70 MeV and increase rapidly with further increases in $E_4^*$. In Fig. 2 this point is better illustrated. Increasing the excitation energy from 50 to 150 MeV causes the probability that the $Z_4 = 77$ fragment will undergo secondary fission to increase from 0 to 93%.

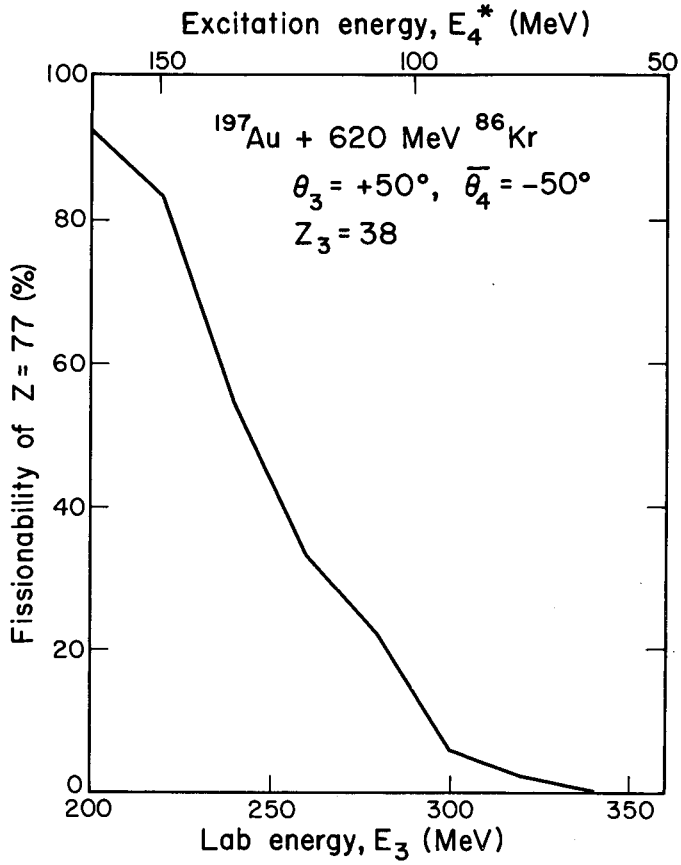


Fig. 2. Percent fissionability of the $Z_4 = 77$ fragment plotted vs both the energy ($E_3$) of the $Z_3 = 38$ fragment and the calculated $E_4^*$ excitation energy. (XBL 778-1665)

Since the fission barriers for elements above and below Au show a strong Z-dependence, it is interesting to determine the mean fissionability as a function of the number of charge units transferred to or from the target. By integrating over $E_3$ for each $Z_3$ for both the singles and non-fissioning coincidence events, an experimental value of the fission probability, $P_f$ was determined. In Fig. 3 this ratio is plotted vs the Z of the light fragment. As charge units are transferred to the target ($Z_3 < 35$), the probability of the heavy fragment undergoing secondary fission increases dramatically. In fact when 5 or more charge units are transferred to Au, essentially all of the heavy fragments ($Z_4 \geq 84$) undergo

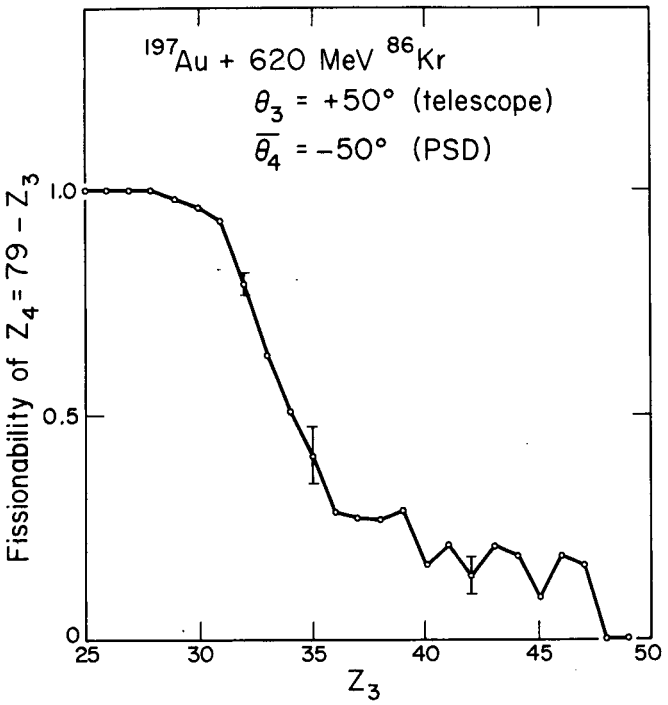


Fig. 3. Percent fissionability of the heavy fragment ($Z_4$) vs $Z_3$ of the light fragment. (XBL 778-1664)

secondary fission. For heavy fragments, lighter than Au ($Z_3 > 36$), the fissionability falls off very slowly and $P_f$ has a value of 0.2 even after the transfer of 10 charge units. The non-zero values of $P_f$ for large $Z_3$ (> 40) is partly caused by contamination of the singles data by secondary fission events which will have a mean Z of $\sim 1/2\ Z_{tgt}$.

In conclusion, preliminary results of a coincidence study of the $^{86}Kr + ^{197}Au$ system at $\theta_3 = +50°$ and $\theta_4 = -50°$ indicate substantial degree of secondary fission following deep inelastic collisions, in which charge units are transferred to the target. Similar studies at other angles, different bombarding energies and targets are in progress. These results should give further insight into the relaxation of the entrance channel kinetic energy, the sharing of excitation energy between the fragments and an estimate of the angular momentum transfer as a function of both charge and energy transfer.

Footnotes and References

*Physikalisches Institut der Universität Heidelberg Philosophenweg 12-D-69, Heidelberg, W. Germany

†Laboratoire de Physique Corpusculaire, Universite de Caen 140000 CAEN-FRANCE.

1. P. Russo, R. P. Schmitt, G. J. Wozniak, B. Cauvin, P. Glässel, R. C. Jared, and L. G. Moretto, Phys. Lett. 67B, 15 (1977).

2. R. C. Jared, P. Glässel, J. Hunter, and L. G. Moretto, see Instrumentation Section of this Annual Report.

## EXPERIMENTAL EVIDENCE AND PHYSICAL IMPLICATIONS OF THE TIME EVOLUTION ALONG THE MASS ASYMMETRY MODE IN HEAVY-ION REACTIONS

L. G. Moretto* and R. P. Schmitt

The complex experimental features associated with the mass or charge distributions, and with the angular distributions as a function of fragment mass or charge, are interpreted as evidence of an intermediate structure, or intermediate complex, evolving in time along the mass asymmetry mode. Strong circumstantial evidence suggests that this time evolution is diffusive in nature and can be described in terms of the Master Equation or the Fokker-Planck Equation. The experimental evidence of broad mass distributions for large ratios E/B, where E is the center-of-mass energy and B is the interaction barrier, and narrow mass distributions peaked at the projectile and target mass for small ratios E/B, is interpreted as due to an increasing lifetime of the complex with energy. For short lifetimes, the system has little time to evolve in mass asymmetry and gives rise to rather narrow distributions centered about the target and projectile mass. For long lifetimes the system undergoes extensive relaxation in mass asymmetry and gives rise to very broad mass distributions. Similarly the angular distributions seem to evolve from side peaked to forward peaked with increasing E/B. This is interpreted as due to a transition from a short lifetime-slow angular velocity regime which does not allow for orbiting beyond 0°, to a long lifetime-large angular velocity regime which produces orbiting past 0°. The evolution from side peaking to forward peaking in the same reaction as one moves away in Z from the projectile is interpreted as due to the time lag introduced by diffusion in the population of fragments farther removed in Z from the projectile. The variation of charge and angular distributions with the fragment kinetic energy allows one to connect the energy relaxation to the mass asymmetry relaxation. Theoretical calculations based on diffusion models allow one to fit mass and angular distributions as well as to extract transition probabilities and Fokker-Planck coefficients. The reliability of various methods of analysis is discussed in Ref. 1.

Footnote and Reference

*Sloan Fellow 1974-76.

1. Abstract from LBL-5057; J. de Phys. Colloque C5, 109 (1976).

# EVIDENCE FOR DIFFUSIVE RELAXATION ALONG THE MASS ASYMMETRY COORDINATE IN THE REACTION $^{197}$Au + 620 MeV $^{86}$Kr†

P. Russo,* R. P. Schmitt, G. J. Wozniak, R. C. Jared, P. Glässel,‡ B. Cauvin,§ J. S. Sventek, and L. G. Moretto||

Nuclei have been identified by atomic number up to Z = 50 using ΔE-E telescopes. Kinetic energy spectra, charge and angular distributions have been measured from $\theta_{lab}$ = 10 to 80°. At angles removed from the grazing, a single peak with a mean energy somewhat below the calculated Coulomb energy is observed for all elements. Near the grazing angle, a much broader peak appears, which extends from near elastic energies down to the Coulomb barrier. The charge distributions were peaked near the projectile Z and demonstrate a strong shape dependence on the angle of observation. The angular distributions for elements near the projectile are strongly side-peaked; however, as Z is increased or decreased from Z = 36 they gradually become forward peaked.

A Diffusion Model[1] which assumes the formation of a rotating intermediate complex, an overlap of the densities of the two fragments and an ℓ-dependent lifetime has been utilized to calculate angular distributions and integrated charge distributions. Values for the diffusion constant $\kappa$ of $0.5 \times 10^{+21}$ fm$^{-2}$ sec$^{-1}$, the overlap parameter $\delta$ of -2.0 fm and the mean lifetime of the intermediate complex for ℓ = 0 of $\tau(0) = 35 \times 10^{-22}$ sec were used to calculate the angle integrated charge distribution shown in Fig. 1 (heavy curve). Impressive agreement between theory and experiment (circles) is observed. Both the shape and magnitude of the data are reproduced to approximately 50% with the largest deviations occurring for elements near the projectile where there are large quasi-elastic contributions (neglected in the calculations which assume an upper ℓ cutoff of 252ħ).

Angular distributions were also calculated and are presented in Fig. 2 along with the experimental data for every other element. These distributions are presented (from top to bottom of Fig. 2) in order of increasing mass transfer to the target (left column) and to the projectile (right column). For elements above the projectile, the position and magnitude of the side peak as well as the shape of the experimental data are quite well reproduced. For elements below the projectile, the magnitude of the side peak is underestimated, but its position as well as the magnitude of the backward angle points is correctly predicted. The underestimation of the magnitude of the side peak observed for elements close to the projectile is due to the strong quasi-elastic contribution in the data and the neglect of partially damped processes in the calculations. It should be stressed that no normalization between calculations and experiment has been performed.

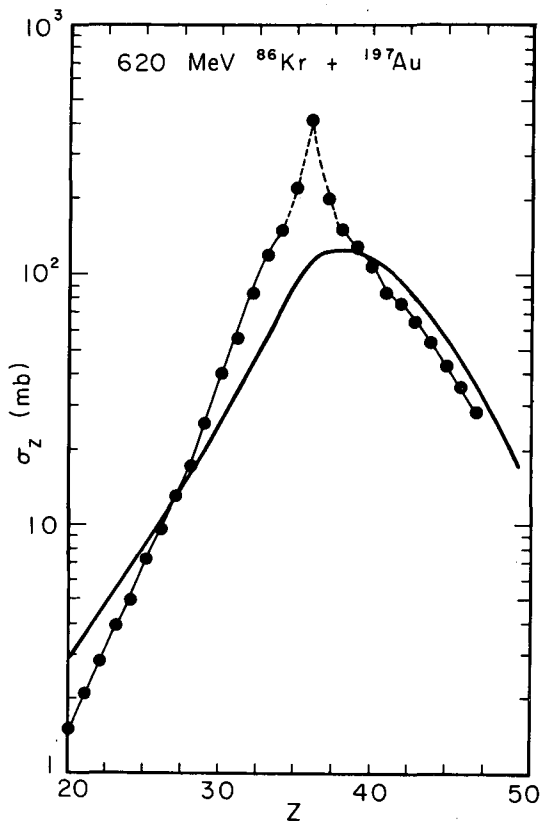


Fig. 1. Total experimental (circles) and calculated (heavy curve) cross sections as a function of Z for the reaction $^{197}$Au + 620 MeV $^{86}$Kr. The data points were integrated from $\theta_{lab}$ = 10 to 80° and the thin line connecting the data points is to guide the eye. (XBL 7611-4461)

The dominant influence of the interaction time on the character of the charge and angular distributions produced in heavy-ion reactions is clearly visible in the $^{197}$Au + 620 MeV $^{86}$Kr data. The evolution from side to forward peaked angular distributions with both increasing energy dissipation and increasing mass transfer beautifully illustrates the transition from short to long lifetimes for the intermediate complex.[2] This

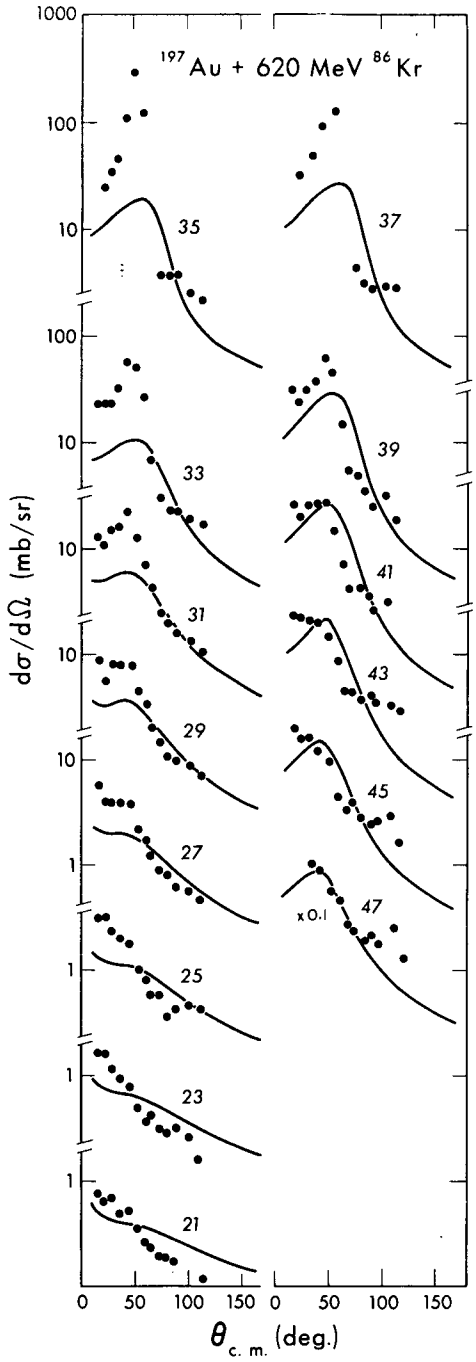


transition is also seen in the evolution of the charge distributions from narrow ("young") to broad ("old") with energy dissipation and with lab angle. Thus it appears that the differences between the deep-inelastic and quasi-fission behavior appear to be related to differences in the lifetime of the reaction intermediate.

Footnotes and References

†Condensed from LBL-5810 and Nucl. Phys. A281, 509 (1977).

*Present address: University of Rochester, Rochester, New York 14627.

‡Present address: Physikalisches Institut der Universitat Heidelberg Philosophenweg 12, D-69, Heidelberg, W. Germany.

§Present address: DphN/MF-CEN, Saclay, France.

‖Sloan Fellow 1974-1976

1. J. S. Sventek and L. G. Moretto, Phys. Lett 65B, 326 (1976).

2. L. G. Moretto and R. Schmitt, J. de Phys. Collogue C5, 109 (1976).

Fig. 2. Calculated (curves) and experimental (circles) angular distributions for the reaction $^{197}$Au + 620 MeV $^{86}$Kr. (XBL 7611-4486)

## BINARY ASPECTS AND MULTIPLICITIES OF EVAPORATED PARTICLES FROM THE FRAGMENTS OF 340 MeV $^{40}$Ar + $^{nat}$Ag DEEP INELASTIC COLLISIONS*

B. Cauvin,† R. C. Jared, P. Russo,‡ R. P. Schmitt, R. Babinet,§ and L. G. Moretto‖

After the break-up of the intermediate complex formed in heavy-ion collisions, the fragments are highly excited and are expected to emit neutrons, protons, and α particles through the evaporation process. A detailed investigation of the charges and masses of the fragments as well as their charge and mass loss through evaporation allows us to learn about the fragment neutron to proton ratio and the sharing of the excitation energy between the two fragments. A coincidence experiment was performed on the system Ar + Ag at 340 MeV bombarding energy in which the measurement of the Z of the light fragment, along with the energies and angles of both fragments, which

permits the determination of the masses before evaporation and some insight on the evaporation process.

The $^{40}Ar$ beam of the SuperHILAC with an energy of 340 MeV was used to bombard a natural, self-supporting, 350 μg/cm$^2$ Ag target. Two detectors measured the light and heavy fragment energies and angles in coincidence. The light fragment detector, which consisted of an ionization chamber[1] telescope, measuring both energy ($E_3$) and the atomic number ($Z_3$), was placed at 42° from the beam direction.

On the other side of the beam axis, a high resistivity silicon position-sensitive detector (PSD) was placed parallel to the reaction plane and successively at 30 and 50° from the beam axis to explore the 20 to 60° in plane distribution of the correlated heavy fragment. The measured quantities were the energy ($E_4$) and the in-plane angle ($\theta_4$) of the heavy fragment.

Out-of-plane angular distributions were also measured keeping the light fragment telescope at the same angle (42°) but at three different angle settings of the position sensitive detector (29, 42, and 50°).

Very accurate energy measurements are necessary in this experiment. While the pulse height defect (PHD) is very small for low Z ions detected in silicon, it is significantly higher for a high Z ion of the same kinetic energy. In a calibration experiment a beam of 163 MeV Ar from the 88-in. cyclotron was incident on thin (200 to 350 μg/cm$^2$) self supporting foils of natural gold, silver, and copper. The observed energies of the elastically scattered nuclei were corrected for energy defects due to dead layers and target and window thicknesses and were then compared to the calculated elastic energies of both nuclei and the differences were attributed to the PHD. The PHD for gold, silver and copper ions in the high-resistivity silicon of the PSD are plotted in Fig. 1 as a function of the energy of the ion as it enters the silicon in dimensionless energy units (LSS units).[2]

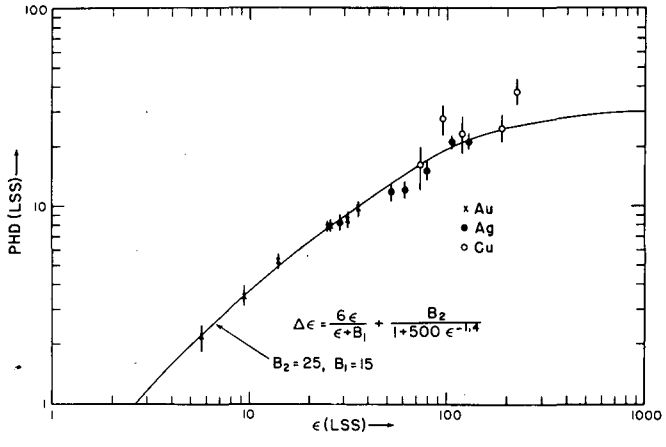


Fig. 1. Pulse height defect for Au, Ag and Cu. LSS units are used for the energy and the pulse height defect. (XBL 766-8212)

A critical test of the accuracy of the energy corrections for heavy ions is the ability to reproduce the kinematics of elastic scattering. The results of correlated elastic scattering measurements made with 163 MeV argon incident on gold, silver and copper targets are shown in Fig. 2. The agreement with calculations (solid lines) is good except when the recoil energy drops below about 15 MeV.

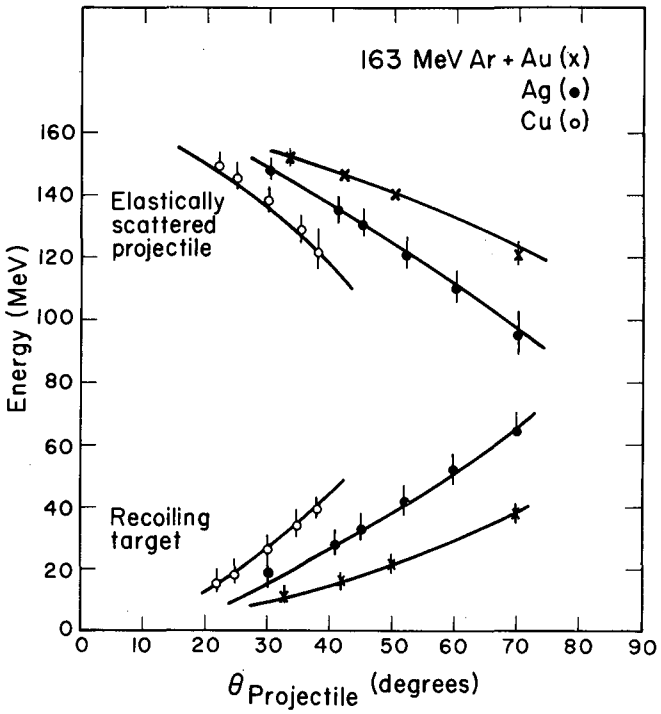


Fig. 2. Comparison of experimental and calculated energies of the scattered projectile and target in the elastic scattering of 163 MeV $^{40}Ar$ on Au(x), Ag(•), and Cu(o). The solid lines represents the calculated values. (XBL 766-8213)

In the case of a binary breakup of the intermediate complex, the conservation of linear momentum and mass can be expressed through the following set of equations in the lab system:

$$E_3^* A_3^* = A_1 E_1 \frac{\sin^2 \theta_4}{\sin^2(\theta_3 + \theta_4)} \quad (1)$$

$$E_4^* A_4^* = A_1 E_1 \frac{\sin^2 \theta_3}{\sin^2(\theta_3 + \theta_4)} \quad (2)$$

$$A_3^* + A_4^* = A_1 + A_2 \quad (3)$$

The energy $E_i$ of a primary fragment of mass $A_i^*$ becomes on the average after evaporation of $\bar{\nu}_i^T$ nucleons of mean energy $\bar{\eta}_i$

$$\bar{E}_i = E_i^* \left(1 - \frac{\bar{\nu}_i^T}{A_i^*} \left(1 - \frac{\bar{\eta}_i}{E_i^*}\right)\right) \qquad (4)$$

The second term of the inner brackets represents the recoil corrections which are small (6%) in our experiment. To first order Eq. (4) can be written as

$$E_i^* = \bar{E}_i \left(1 + \frac{\bar{\nu}_i^T}{A_i}\right)$$

If we define

$$K_i = \frac{E_1 A_1}{\bar{E}_i} \frac{\sin^2 \theta_j}{\sin^2(\theta_i + \theta_j)} \qquad \begin{matrix} i = 3,4 \\ j = 4,3 \end{matrix}$$

which contains all measured quantities, Eq. (1) to (3) become:

$$A_3^* + \bar{\nu}_3^T = K_3$$

$$A_4^* + \bar{\nu}_4^T = K_4$$

$$A_3^* + A_4^* = A_1 + A_2 \,.$$

This set of equations shows that the total number of evaporated nucleons from the two fragments ($\bar{\nu}_3^T + \bar{\nu}_4^T$) can be obtained to first order without any assumptions on $A_3^*$ and $A_4^*$. This simple analysis yields the values plotted in Fig. 3 as a function of the Z of the light fragment. The quantity $\bar{\nu}_3^T + \bar{\nu}_4^T$ appears to be reasonably constant throughout the Z range of this experiment.

Since atomic numbers have been resolved up to Z = 32, data are available for nearly symmetric break-up. Near symmetry it is reasonable to assume that the relative loss of mass $\bar{\nu}^T/A^*$ is the same for both fragments. With this assumption and Eqs. (1) to (4), the masses of both fragments $A_{3,4}^*$ prior to particle evaporation, and the total number of evaporated nucleons $\bar{\nu}_{3,4}^T$ can be calculated for each fragment using the experimental data. The results of these calculations are shown in Fig. 4a. It is interesting to notice that a sizable discontinuity is visible in the masses at symmetry. This is an indication of the evaporation of charged particles. Since the fragments should be identical at symmetry, the number of evaporated charges per fragment is given by the downward and upward shift in Z that must be applied to the two

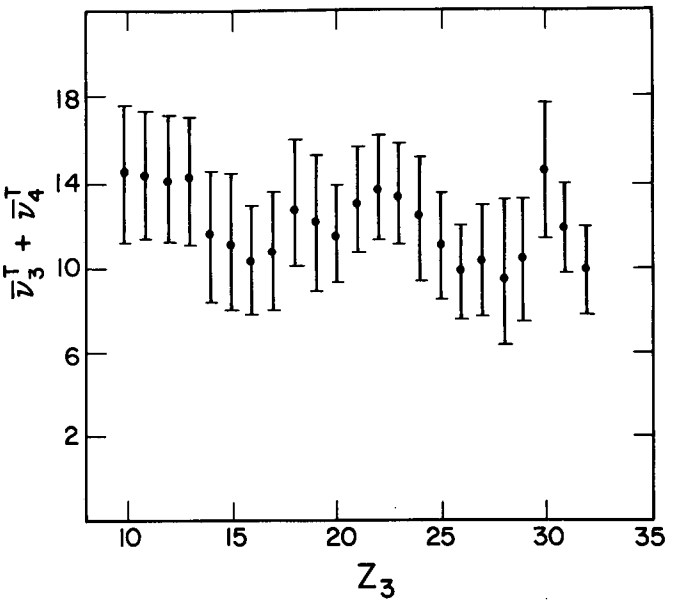


Fig. 3. Total number of nucleons evaporated by the fragments. (XBL 778-1731)

branches so that they coincide. This shift is 1.3 charge units per fragment. In Fig. 4b such a shift has been applied, thus generating a continuous curve. Evaporation calculations predict an average of 1.2 evaporated charges at symmetry in good agreement with our data.

In order to extract the masses and number of emitted particles from the data away from symmetry, the assumption made in the previous paragraph, namely that the ratio $\bar{\nu}^T/A^*$ is the same for the two fragments, is not necessarily valid. Instead we can use the conservation of the energy in the laboratory system, assuming again a binary splitting of the system. The conservation of energy can be expressed as:

$$E_1 + B(A_1,Z_1) + B(A_2,Z_2) =$$

$$E_3^* + E_4^* + B(A_3^*,Z_3^*) + B(A_4^*,Z_4^*) + E_n^T + E_p^T + E_\alpha^T + E_\gamma^T \,, \qquad (5)$$

where $E_3^*$ and $E_4^*$ can be calculated from Eq. (4); $B(A^*,Z^*)$ is the binding energy of a fragment of mass $A^*$ and charge $Z^*$ before evaporation. $E_n^T$, $E_p^T$, $E_\alpha^T$, $E_\gamma^T$ are the total excitation energies released by the fragments in the evaporation of neutrons, protons, alpha particles and $\gamma$ rays, respectively.

Using Eq. (5), along with Eqs. (1) to (4) in which now one must use: $\bar{\nu}_{3,4}^n + \bar{\nu}_{3,4}^p + 4\bar{\nu}_{3,4}^\alpha$. A self-consistent procedure was developed to obtain the mass and the number of evaporated neutrons for each fragment.

The results of these calculations are given in Fig. 5 which shows the masses prior to evaporation and the number of evaporated neutrons as a

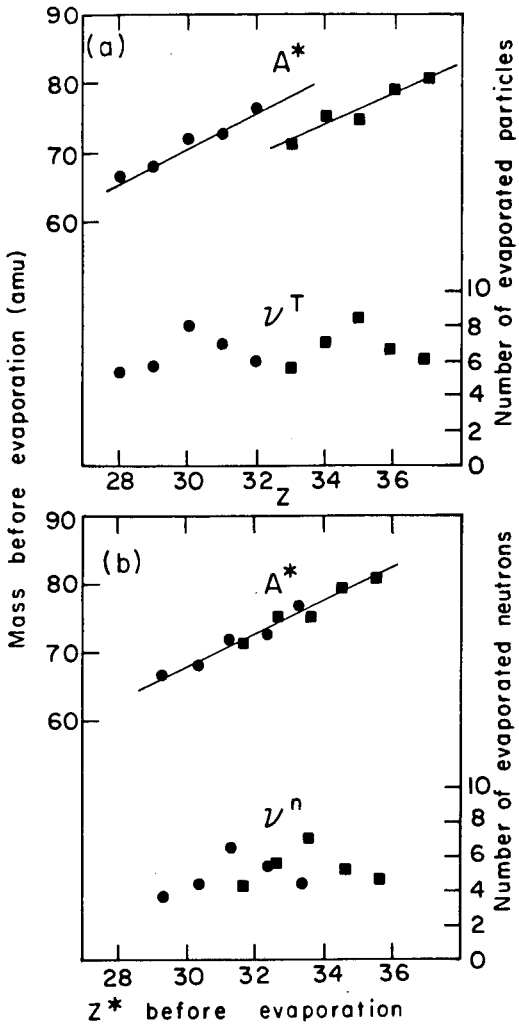


function of the Z before evaporation of the fragment. Around symmetry, the agreement with the simple analysis done before (Fig. 4) is good. The upper solid line represents the masses calculated by assuming charge equilibrium between two liquid drops in contact.[3] The good agreement with this model confirms that charge equilibrium is indeed achieved in deep inelastic collisions for the part of the angular distribution beyond the grazing angle. The lower solid line represents the calculated values of $\bar{\nu}^n$ from an evaporation code. The good agreement with the experimental values also suggests that thermal equilibrium is achieved between the fragments as was postulated when establishing the input parameters of the evaporation calculations.

Emission of particles prior to or after the break-up of the system perturbs the direction of the velocity of the fragments and leads to a spreading of the heavy fragment direction in the plane as well as out of the plane of the reaction. The widths of the in plane and out of plane angular distributions are given by the following expression, in which $\bar{\nu}$ is the average multiplicity, $\bar{\eta}$ the average kinetic energy of the neutrons and E* is the KE of the fragment of mass number A*:

Fig. 4. (a) Masses before evaporation and number of nucleons evaporated relative to fragments close to symmetry plotted vs the Z after evaporation. (b) Masses before evaporation and number of neutrons evaporated plotted vs the Z before evaporation. The symbols (Δ) and (•) refers to the light and heavy fragment, respectively. (XBL 766-8209)

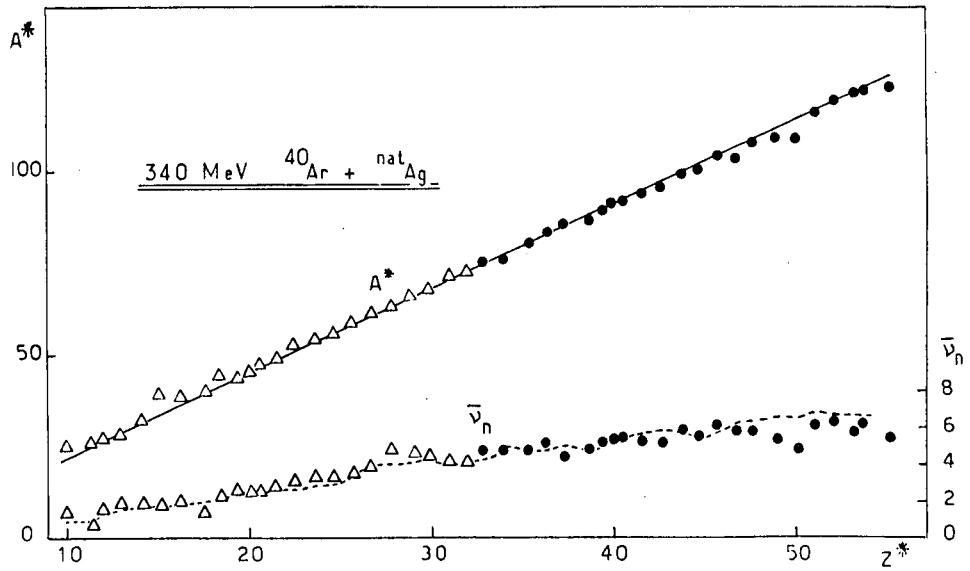


Fig. 5. Masses prior to evaporation and number of evaporated neutrons as a function of the Z before evaporation of the fragments. Symbols (Δ) and (•) refers to light and heavy fragments, respectively. The upper solid line represents the masses calculated with the charge equilibrium model. (XBL 766-8210)

$$\sigma_\theta^2 = \frac{1}{2}\,\frac{\bar{\nu}\bar{n}}{A^*E^*} \quad . \qquad (6)$$

The following first order expression contains contributions from both fragments:

$$\sigma_\theta^2 = \frac{1}{2}\,\frac{\bar{n}_3\,\bar{\nu}_3 + \bar{n}_4\bar{\nu}_4}{A_4^*\,E_4^*} \quad .$$

This equation reduces to

$$\sigma_\theta^2 = T\,\frac{\bar{\nu}_3 + \bar{\nu}_4}{A_4^*\,E_4^*} \quad , \qquad (7)$$

if we assume that the nuclear temperatures of the fragments are the same. These calculations are compared to the experimental values in Fig. 6.

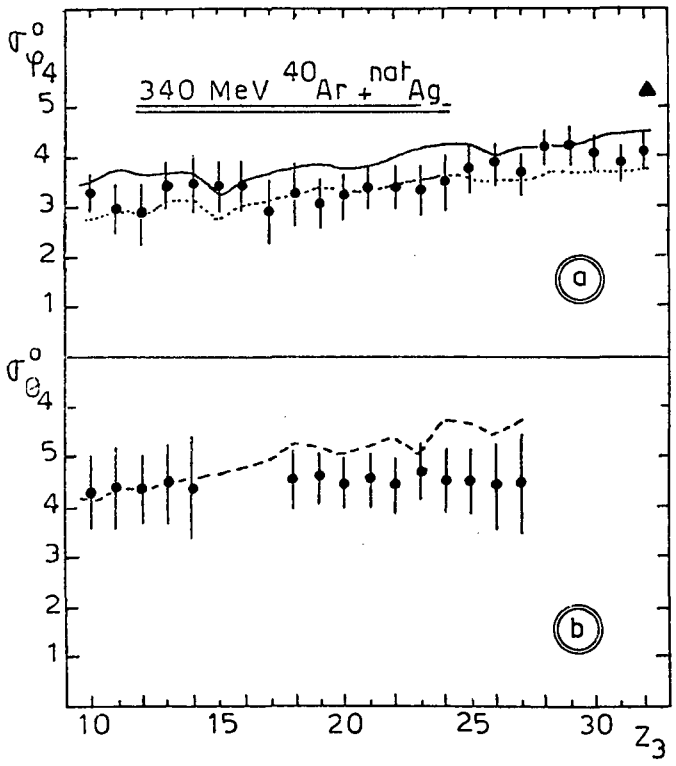


Fig. 6. a) Standard deviations of the out-of-plane (laboratory frame of reference) angular distributions of the heavy fragments in coincidence with light fragments of Z ranging from 10 to 32. Experimental points are compared to calculated values from Eq. (7) in three cases: (i) all evaporated particles are neutrons (dashed curve); (ii) neutrons, protons, and alpha particles are emitted (solid curve); (iii) all charged particles evaporated at symmetry are alpha particles (Δ). b) Same as Fig. 6a for the in-plane angular distribution of the heavy fragment. The dashed curve refers to case (ii). Kinematical broadening has been included.

(XBL 778-2624)

Footnotes and References

* Condensed from LBL-5099

† Present address: DpHN/MF-CEN, Saclay, France.

‡ Present address: University of Rochester, Rochester, N.Y. 14627.

§ Present address: DphN/MF-CEN, Saclay, France.

¶ Sloan Fellow 1974-1976

1. M. F. Fowler and R. C. Jared, Nucl. Instrum. and Meth. 124, 341 (1975).

2. J. Lindhard, M. Scharff, and H. E. Schiott, Mat. Fys. Medd. Dam. Vid. Selsk. 33, 14 (1963).

3. B. Gatty, D. Guerreau, M. Lefort, X. Tarrago, J. Galin, B. Cauvin, J. Girard, and H. Nifenecker, Nucl. Phys. A 253, 511 (1975).

## CHARGED PARTICLE EVAPORATION FROM THE SYSTEM $^{63}Cu + {}^{20}Ne$ AT 7.9, 12.6 AND 17.2 MeV/NUCLEON*

R. P. Schmitt, G. Bizard,† G. J. Wozniak, and L. G. Moretto

It is rather ironic that since the discovery of deeply-inelastic reactions the energy dissipation process has itself received little attention experimentally. Most of the experiments performed to date have been focused on the relaxation of other modes, the mass-asymmetry mode being the most studied. The reason for this state of affairs stems largely from the fact that most of the studies of deep-inelastic collisions (DIC) have been single particle inclusive

experiments in which only the mass or charge of a single fragment has been measured. While it is obvious from the energy spectra of these fragments that much of the entrance channel kinetic energy has been dissipated, it is by no means obvious how this has been accomplished. Recent experiments with $^{14}N$ and $^{16}O$ projectiles have hinted that a fragmentation processes may be occurring.[1,2] In order to shed light on the energy dissipation mechanism, we have undertaken a series of coincidence experiments in which the atomic number Z of both of the primary charged fragments have been identified. The system studied, $^{20}Ne$ + $^{63}Cu$, was chosen for a variety of reasons: the charge and angular distributions for singles events have already been measured; it is possible to vary the bombarding energy over a broad range; and the technique of simultaneous Z-determination is optimized for relatively light systems.

A self-supporting 0.560 μg/cm$^2$ thick $^{63}Cu$ foil (99% enrichment) was bombarded with $^{20}Ne$ ions produced by the Berkeley 88-in. cyclotron. The detection apparatus consisted of two large solid angle (5° angular acceptance) particle telescopes, each having a gas ionization ΔE detector and a solid state E detector. The gas counters were operated with pure methane at a pressure of 4 cm Hg. The entrance windows consisted of thin (60 μg/cm$^2$) polypropylene foils mounted on circular collimators 1 cm in diameter. The initial measurements made with 252 MeV $^{20}Ne$ ions were aimed at studying the de-excitation products of the symmetric decay mode (i.e., $Z_1 = 19$, $Z_2 = 20$) at near symmetric angles ($\theta_1 = 42°$, $\theta_2 = 44°$). In this configuration adequate Z-resolution was obtained up to the low 20's.

In addition to the symmetric angle measurements, data was taken over the range of the angular correlation ($\theta_1$ fixed at 42°), both in-plane and out-of-plane. The in-plane correlation is broad (≈ 15° FWHM). Out-of-plane the distribution is somewhat narrower, the FWHM being slightly less than 10°. Neither of the quantities varies much as a function of the detected charges. For the 158 and 343 MeV lab energies, measurements were taken only at symmetric angles.

In Fig. 1 the $Z_2$ distribution for fixed $Z_1$ is plotted for various cuts in the total lab kinetic energy, $E_T$. The total energy was chosen since it is most closely related to the excitation energy. The FWHM of the distributions is large (≈ 4-5 charge units), and is, to first order, constant for different $Z_1$ and different $E_T$. The centroids of the distributions exhibit an interesting trend: as $E_T$ is decreased, the position of the centroid moves towards lower $Z_2$. Presumably, this just reflects the fact that the excitation energy increases for lower values of $E_T$.

To investigate the in-plane angular dependence of the evaporated charge, the average missing charge $\Delta Z$(i.e., $39-Z_1-Z_2$) is plotted vs $E_T$ for various $Z_1$ and $\theta_2$ (see Fig. 2). Several points are immediately obvious: (1) the number of charges evaporated is large, $\Delta Z$ ranging from 8-4 as $E_T$

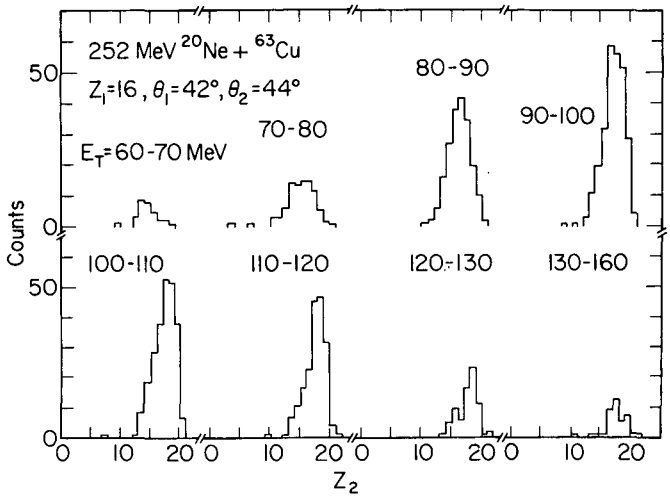


Fig. 1. Distributions of Z2 for Z=16 and various bins in total kinetic energy.
(XBL 777-1517)

ranges from 60 to 150 MeV; (2) $\Delta Z$ decreases with increasing $E_T$; (3) the magnitude and shape of the $\Delta Z$ curve is essentially independent of the asymmetry of the fragments (note the clustering of the value for different asymmetries); (4) the above trends do not change appreciably over the in-plane correlation. Point (1) is understandable since we are dealing with a light system (low Coulomb barrier) at high excitation energies. The gross dependence of $\Delta Z$ on $E_T$ can be attributed to an excitation energy effect: as the lab energy increases, the available excitation energy decreases so that fewer particles are emitted. The insensitivity of $\Delta Z$ on asymmetry is explained by virtue of the fact that the Q values leading to different exit channels for this system are small and essentially independent of asymmetry (assuming constant Z/A for the fragments). The fourth point (i.e., the lack of angular dependence) is probably just an artifact of the evaporation process itself. There is so much evaporation that the width of the in-plane distribution is largely a result of it.

The out-of-plane data (see Fig. 3) does, however, show angular effects. The symmetric angle setting ($\theta_1 = 42$, $\theta_2 = 44°$) is again shown for comparison. For $\theta_2 = 44°$, $\phi_2 = 10°$ the mean evaporated charge $\Delta Z$ is slightly higher by about 0.5 charge units. For $\phi_2 = 20°$ $\Delta Z$ has increased by almost 1 Z-unit. (From now on we shall present only the average $\Delta Z$; the "error bars" represent one standard deviation in the spread of the data for the various asymmetries.) It is reasonable to assume that in looking at out-of-plane, one is preferentially selecting those events in which more extensive evaporation has occurred, perhaps via α emission, which tends to impart high recoil momentum. The correlation data can also be used to estimate the total evaporated mass. Simple calculations yield 15 ± 3 units of evaporated mass. The large error is due to uncertainties in the angles associated with the large angular acceptance. This result is consistent with preliminary data on light charged particles (p's and α's) which were detected in a third telescope (28 μm ΔE, 5 mm E).

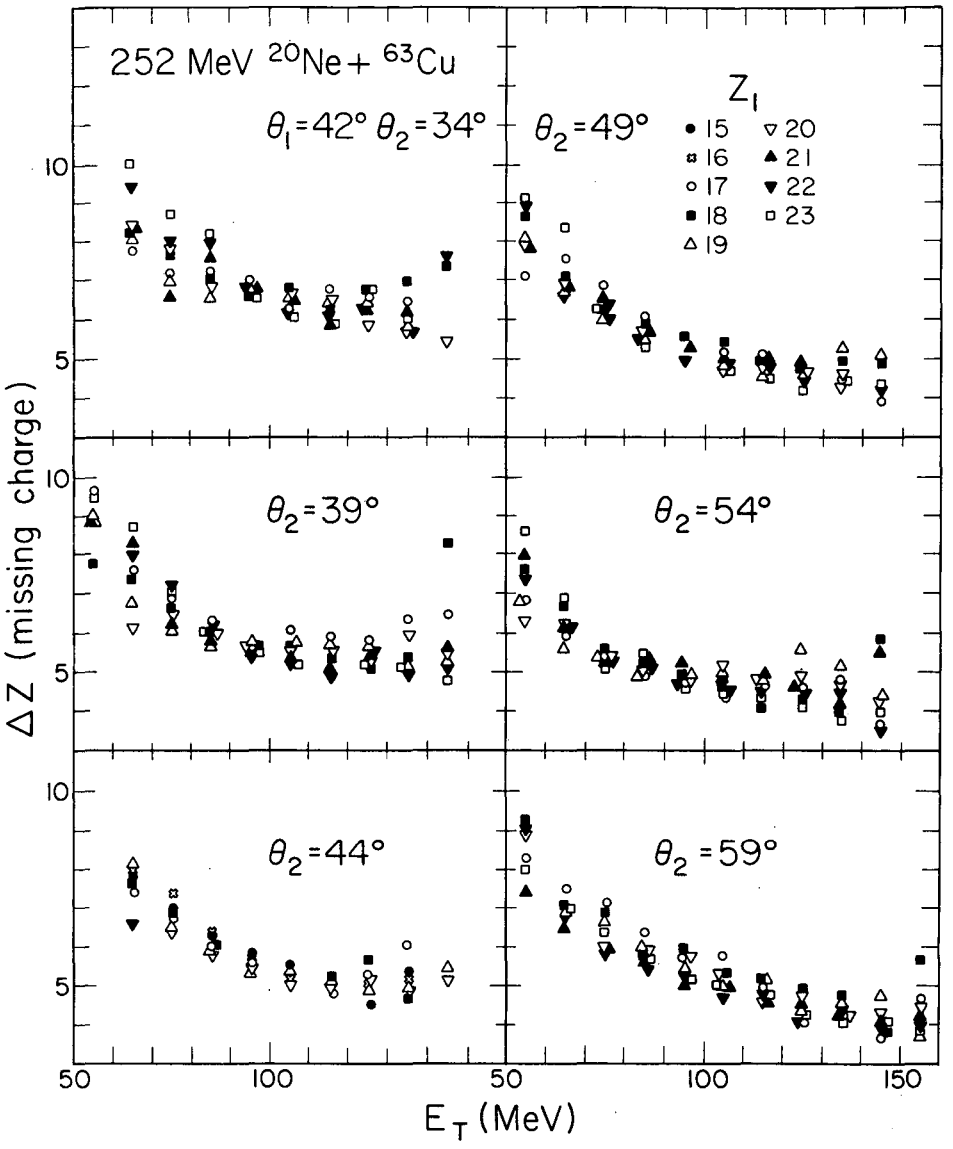


Fig. 2. Missing charge as a function of total kinetic energy for three values of the azimutheal angle. (XBL 777-1398)

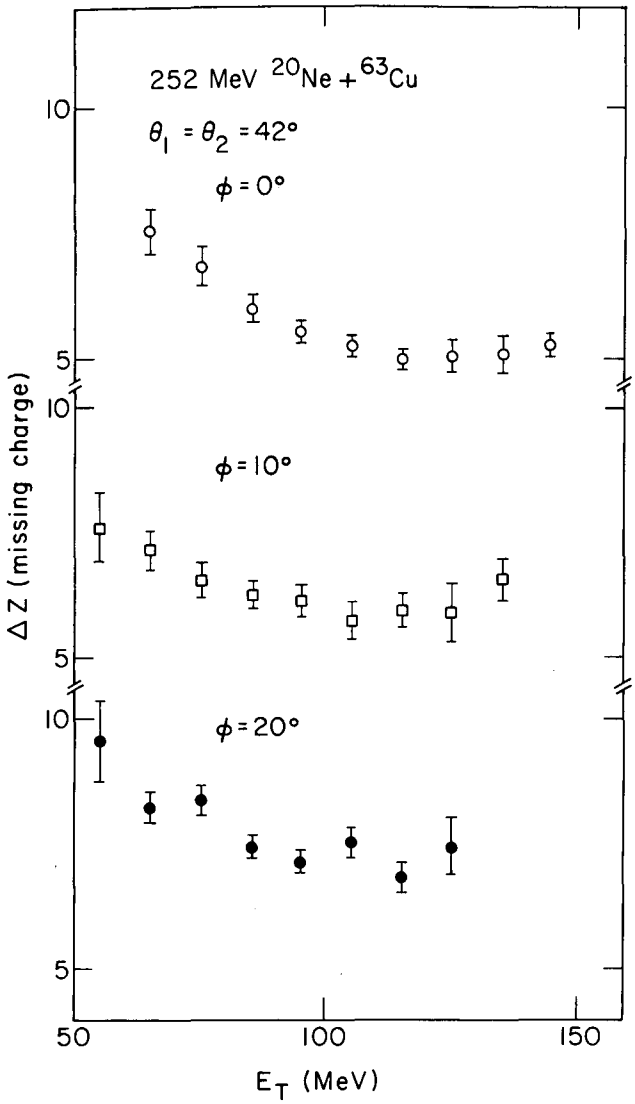


Fig. 3. Average missing charge as a function of total kinetic energy for three values of the azimuthal angle. (XBL 777-1398)

In Fig. 4 the average ΔZ is plotted vs $E_T$ for the three bombarding energies. Again the angles have been chosen at the peak of the correlation for symmetric division. The gross trend favoring higher ΔZ for bombarding energy is, perhaps, to be expected for the resulting higher excitation energies.

It is more important to note that the average in ΔZ increases monotonically with bombarding energy. This observation is strong evidence that the incident energy is thermalized over a broad range of bombarding energies. While such behavior is, perhaps, not unexpected at low energies, it is not obvious that this should be the case at high energies. Another immediate consequence of this data is that DIC are essentially binary over a very broad energy range.

Yet another interesting feature is manifested in this data: the pronounced dip in the 158 MeV curve and the change of slope at intermediate $E_T$

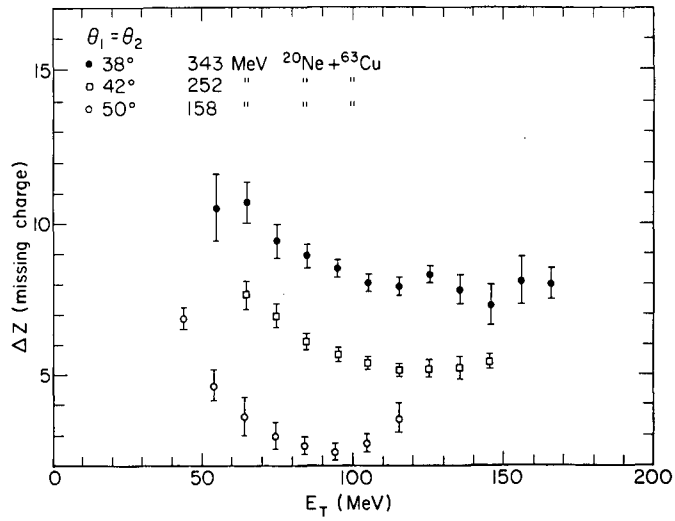


Fig. 4. Average missing charge as a function of total kinetic energy for three beam energies. (XBL 777-1400)

for 252 and 343 MeV data. We believe that this effect is due to the competition between p, α and n emission. For low temperature the differences in the effective barriers between the various decay modes can enhance a particular decay. Since the effective ΔZ/ΔE is different for the various channels (e.g., ΔZ = 0 for n decay), the slope of the curve can change with $E_T$. For high temperatures the ratio of the decay widths tends to 1, which accounts for the general observation that minima are not present at higher energies.

In conclusion correlated charged fragments from the reaction $^{20}$Ne + $^{63}$Cu have been investigated over a broad range of energies. The results show the power of this technique for extracting many details of DIC. Evidence has been presented that the process remains essentially binary and that the entrance channel kinetic energy is effectively thermalized over a broad energy range. The missing charge has been directly measured and the total missing mass has been deduced from angular correlation data. The data are consistent with sequential particle evaporation from two excited fragments. These data also provide information on the competition between various decay modes, and with detailed comparison with calculation, may yield valuable insight into the DIC mechanism.

## Footnotes and References

*Condensed from LBL-6571

†Present address: Laboratory de Physique Corpuseulaire, Université de Caen, 14000 CAEN-FRANCE

1. A. Albrecht, C. Bercks, W. Dunnweber, G. Graw, H. Ho, J. P. Wurm, D. Disdier, V. Rauch, and F. Scheibling, Proceedings of the European Conf. on Heavy Ions, Caen, France (1976).

2. M. Ishihara, H. Kamitsubo, T. Shimoda, F. Fukuda, T. Motobayashi, T. Ohi, I. Kohno, Proc. of the European Conf. on Heavy Ions, Caen, France (1976).

# STUDIES OF DEEP INELASTIC PROCESSES IN THE REACTION OF 175 AND 252 MeV $^{20}Ne$ + $^{197}Au$

J. B. Moulton, G. J. Wozniak, R. P. Schmitt, and L. G. Moretto*

An investigation of a system with a very asymmetric entrance channel Ne+Au has been performed at the 88-in. cyclotron. The beam was focused on a thin metal target (300 to 800 $\mu g/cm^2$) and the Z and kinetic energies of the reaction products measured in E-ΔE detectors. The ΔE counter was a gridded (methane-gas) ionization chamber[1] and the E counter was a surface-barrier Si detector. Fragments with atomic numbers from 5-32 were identified with the upper value restricted by the low MeV/A of the heaviest fragments. The detector signals were amplified by a modular electronic system, converted to digital form via a 4096-channel ADC, and stored on magnetic tape. This event-by-event data was sorted by atomic number and for each Z lab and c.m. energies and cross sections were calculated. The data analysis was performed on a PDP-9 computer.

The products of the Ne plus Au reactions at both bombarding energies and at most angles have c.m. kinetic energies which are essentially identical and approximately equal to the Coulomb repulsion of the two separating fragments (see Fig. 1). The kinetic energy brought in by the projectile has been relaxed into internal degrees of freedom. Products observed around the grazing angle and for lighter than Z = 11 products have broadened or two-lobed kinetic energy spectra. The upper lobe arising from reactions in which the energy has not been completely relaxed. All products produced far from the grazing angle or differing appreciably from the projectile mass have fully relaxed, single-peaked kinetic energy spectra. The above observations can be interpreted in terms of an intermediate complex diffusing along its mass asymmetry coordinate. Thus for products observed far from the grazing angle, or which are quite different from the projectile, the intermediate complex had to rotate and diffuse longer to reach the mass asymmetry at which it eventually split and the resulting kinetic energy spectra are relaxed and angle-independent.

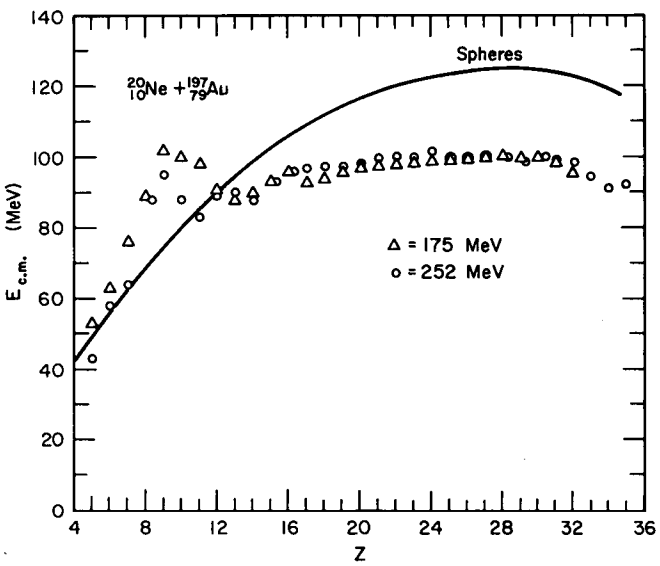


Fig. 1. Mean c.m. kinetic energy vs Z averaged over angle. The solid line is the Coulomb repulsion energy for two spheres calculated as $E = 1.44\ Z_1Z_2/(1.225\ (A_1^{1/3} + A_2^{1/3}) + 2\ fm)$. (XBL 778-1667)

Laboratory charge distributions are presented for both bombarding energies in Figs. 2 and 3. For Z-values greater than the projectile and for angles for which the kinetic energies are fully relaxed, the cross section rises three orders of magnitude. For energetically relaxed products lighter than the projectile the cross section increases by one factor of 10 from Z = 9 to Z = 4. The cross section for products lighter than Ne whose kinetic energies are significantly above the Coulomb energy is quite large, indicating a fast, nonequilibrium transfer process.

Important differences between the 175 and 252 MeV reactions show up in the angular distributions presented in Fig. 4. The distributions from the lower bombarding energy have shown strong forward peaking from the lowest Z's up to about Z = 15, and angular asymmetry is present in all products observed. Products of the high energy reaction are strongly forward peaked up to about Z = 12, with angular asymmetry remaining only until about Z = 20. Products with larger Z's display angular distributions which are symmetrical about 90° and follow a 1/sin θ curve. The degree of forward peaking of the angular distributions can be related to the reaction time. Events which decay in less than about 1 rotational period will be peaked in the forward direction, and violate the angular symmetry about 90° expected from a true compound nucleus reaction and from fission. Thus the steeper angular distributions observed at 175 MeV indicates a shorter decay time for the intermediate complex formed at the lower bombarding energy. Two distinct mechanisms seem to be available to explain this difference. First, a greater contribution from fission of the $^{197}Au$ and/or from a "Au-like" nucleus enlarged by the diffusion of nucleons from the projectile, might be expected in the 252 MeV system because of the greater

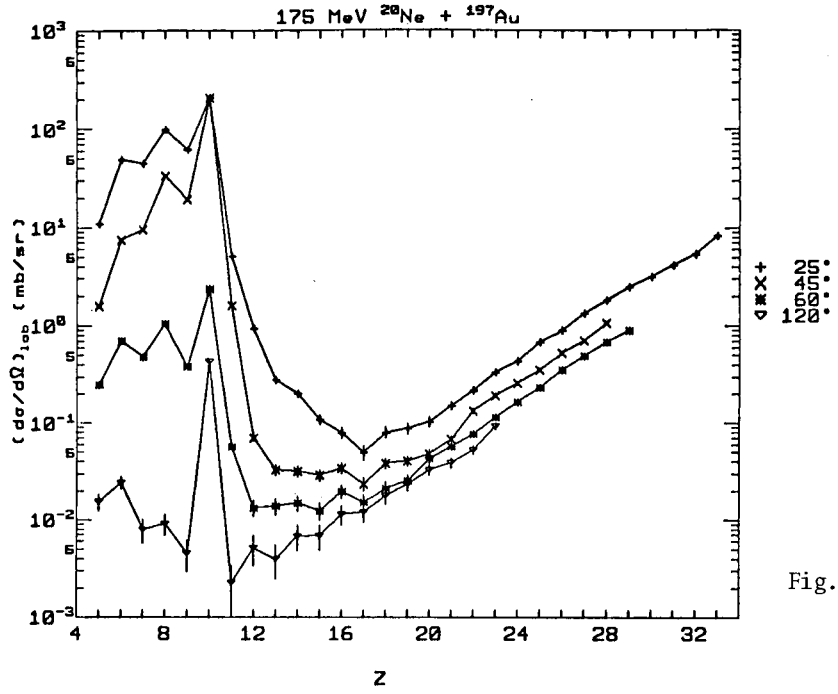


Fig. 2. Lab differential cross section vs Z averaged over angle for 175 Ne + Au. (XBL 778-9581)

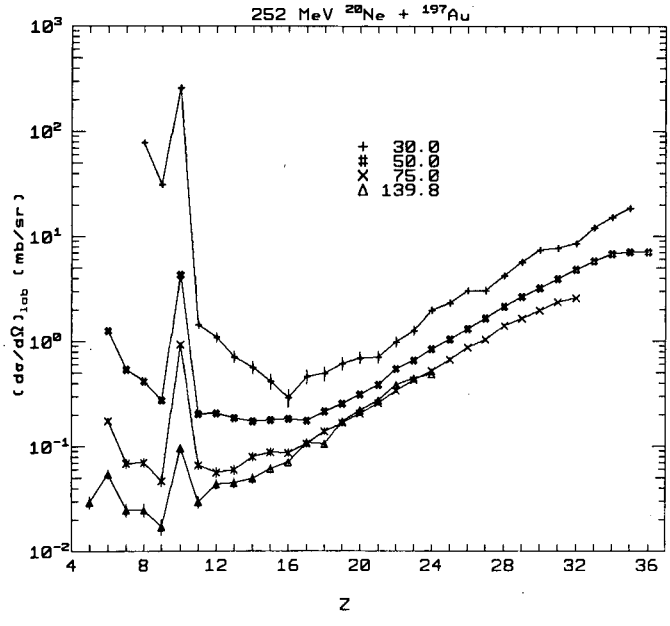


Fig. 3. Lab differential cross section vs Z averaged over angle for 252 MeV Ne + Au. (XBL 778-9948)

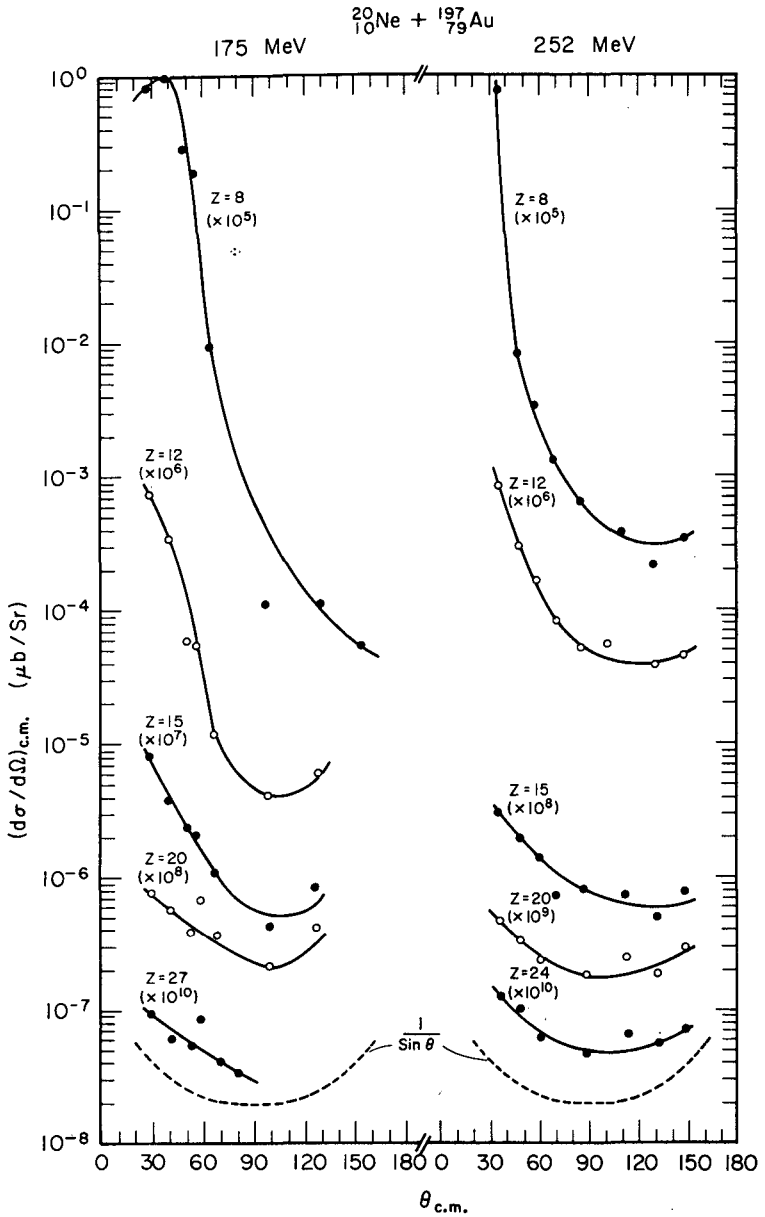


Fig. 4. C.m. differential cross section vs angle for various Z's at both bombarding energies. (XBL 778-1669)

excitation energy. This could possibly explain the symmetry about 90° for Z = 24, but it seems unreasonable to adduce a fission component as the explanation of the more moderate forward peaking of such light products as Z = 12 to 15. In a second explanation, the difference in decay times for the intermediate complex formed at 175 and 252 MeV could be based on a greater interpenetration of the two colliding nuclei at the higher energy. Having come to a closer radial turning point, the higher energy system requires more time for the nuclei to slide back down a quite viscous radial potential.

The mass yield of the Ne + Au system can be viewed as combining the characteristics of the Ne + Ag and the Ar + Au systems. Like the Ne + Ag system, the cross section rises from Z = 9 toward lower Z's. This is due to the very large initial mass-asymmetry of the Ne + Au system. Like the Ar + Au system, the cross section rises dramatically with Z, above Z = 10. This indicates that the system readily samples the large potential energy dip around symmetric masses even though the initial asymmetry is quite large and the system probably is initially on the down slope leading to greater mass asymmetry. The extent to which this population of masses above the projectile is due to fission of a compound nucleus rather than diffusion between two distinct fragments remains to be determined.

## Footnote and Reference

*Sloan Fellow 1974-1976

1. M. M. Fowler et al., Nucl. Instrum. Meth. 24, 341 (1975).

# PRODUCT MASS AND CHARGE DISTRIBUTIONS IN THE REACTION OF $^{48}$Ca WITH SILVER*

W. Loveland,† D. J. Morrissey, R. J. Otto, D. Lee, and G. T. Seaborg

We have measured the product mass and charge distributions radioanalytically for the reaction of natural Ag with ~224 MeV $^{48}$Ca ions, focusing upon the complete fusion process. A natural Ag foil of thickness 230 mg/cm$^2$ was irradiated by a $^{48}$Ca beam of average intensity $5.4 \times 10^{13}$ particles/min for ~450 min at the SuperHILAC. Following irradiation, the target was divided into two fractions. The Sc reaction products were chemically separated from the first fraction by solvent extraction and a Sc sample prepared for $\gamma$-ray spectrometry. The $\gamma$-radiation from the separated Sc sample and the second fraction of the Ag target was then measured with a 54 cc Ge(Li) spectrometer system. Gamma-ray spectra were measured starting one hour after irradiation and continuing for a period of one month.

The independent yield radionuclide cross sections for the $^{48}$Ca + Ag reaction derived from the above procedures are shown in Fig. 1(a). The apparent scatter in the data in Fig. 1(a) occurs because the independent yields generally represent only a fraction of the total mass yield. The (Z,A) distributions of the products for various mass regions are shown in Fig. 1(b). Gaussian charge distribution curves fitted to the data of Fig. 1(a) and (b) were integrated to give the yield of each A where a radionuclide was observed in the reaction. The resulting product post-neutron emission mass distribution is shown in Fig. 1(c) along with the data of Hille et al.[1] In preparing Fig. 1(c), the data were normalized so that the experimental total reaction cross section [the area under the curve in Fig. 1(c)] equals the mean geometric reaction cross section for a thick target reaction as given by:

$$\bar{\sigma}_R = \frac{\pi R^2 \int_B^E (1 - (\frac{B}{E}))dE}{E - B} = 1319 \text{ mb} , \quad (1)$$

where the interaction radius R=12.1 fm, the interaction barrier B=110 MeV, and the incident projectile energy (cms) E=209.8 MeV. This would imply the effective projectile energy in the thick target in the center-of-mass system was

$$E_{eff} = \frac{B}{1 - \frac{\bar{\sigma}_R}{\pi R^2}} = 155 \text{ MeV} , \quad (2)$$

i.e., $E_{eff}$(lab) $\approx$ 224 MeV.

The evaporation residue cross section, $\sigma_{ER}$, was taken to be the area under the curve for $124 \leq A \leq 153$ and is $700 \pm 100$ mb. To extract the fission cross section, $\sigma_F$, we did a least squares decomposition of the mass yield curve for $24 \leq A \leq 124$ into components representing deep inelastic scattering, fission and quasi-elastic scattering. Based upon an extrapolation of the data of Britt et al.,[2] we chose Gaussian shapes of specific width and center for the mass distribution associated with each of these components. The fission mass distribution was assumed to have a FWHM of 28 A units centered at A = 71.5. The deep inelastic distribution was represented by two Gaussian distributions (constrained to have equal area) of FWHM 27 and 40 A units, centered at A = 44 and A = 104, respectively. The quasi-elastic distribution was also represented by two Gaussian distributions of equal area, centered at A = 48 and 108 of FWHM ~4 A units. The magnitude of each component of the mass distribution was then determined by a nonlinear least squares fit of the component shapes to the data. The results give $\sigma_F \approx 100 \pm 10$ mb, $\sigma_{\text{QUASI-ELASTIC}} \approx 250 \pm 25$ mb and $\sigma_{\text{DEEP INELASTIC}} \approx 270 \pm 30$ mb. The above estimate of uncertainty in the fission cross section does not take into account uncertainties in the shapes of the deep inelastic component and should probably be regarded as $\sigma_F \sim 100 \pm 50$ mb, taking these uncertainties into account. From these cross sections, we calculate the complete fusion cross section, $\sigma_{CF}(=\sigma_{ER} + \sigma_F)$, as $800 \pm 110$ mb. Using the critical distance formulation for the complete fusion cross section given by Glas and Mosel[3] one calculates $\sigma_{CF}$ for the $^{48}$Ca + Ag reaction to be 797 mb, a value in remarkably good agreement with the experimental value of $800 \pm 110$ mb.

Another intriguing feature of the data is the ratio $\sigma_F/\sigma_{ER}$ which is $100 \pm 50/700 \pm 100$ for this study and was found to be $300 \pm 100/620 \pm 90$ for the $^{40}$Ar + $^{109}$Ag reaction at $E_{cms} = 144$ MeV by Britt et al.[2] A standard statistical de-excitation calculation involving neutron-fission-charged particle emission competition using the OVERLAID ALICE code[4] with level density parameter ratio $a_f/a_n = 1.0$, $\Delta J$=no option and the rotating liquid drop fission barriers of this code, that sums all partial waves up to an $\ell_{cr} = 75\hbar$, predicts $\sigma_F/\sigma_{ER} = 220/619$ for the $^{40}$Ar + $^{109}$Ag reaction, in rough agreement with the experimental data. Using the same parameters to describe the $^{48}$Ca + Ag reaction, one calculates that $\sigma_F/\sigma_{ER} \approx 297/488$ when one sums all partial waves up to $\ell_{cr} = 79\hbar$. Calculations performed with the best new values[5] of the ground state fission barriers give essentially similar results, i.e., an inability to account for the increased survival of the compound nuclei made in the $^{48}$Ca + Ag reaction (in both cases, the excitation energies, E ~ 90 MeV, are similar). Since in both cases the rotational energies of the system are quite high for those partial waves contributing most to the complete fusion cross section, the exact ratio of $\sigma_F/\sigma_{ER}$ will depend sensitively upon how the fission barrier is lowered as a function of angular momentum. These data may suggest that the prescription of Cohen, Plasil and Swiatecki[6] used in the de-excitation calculation simply are not

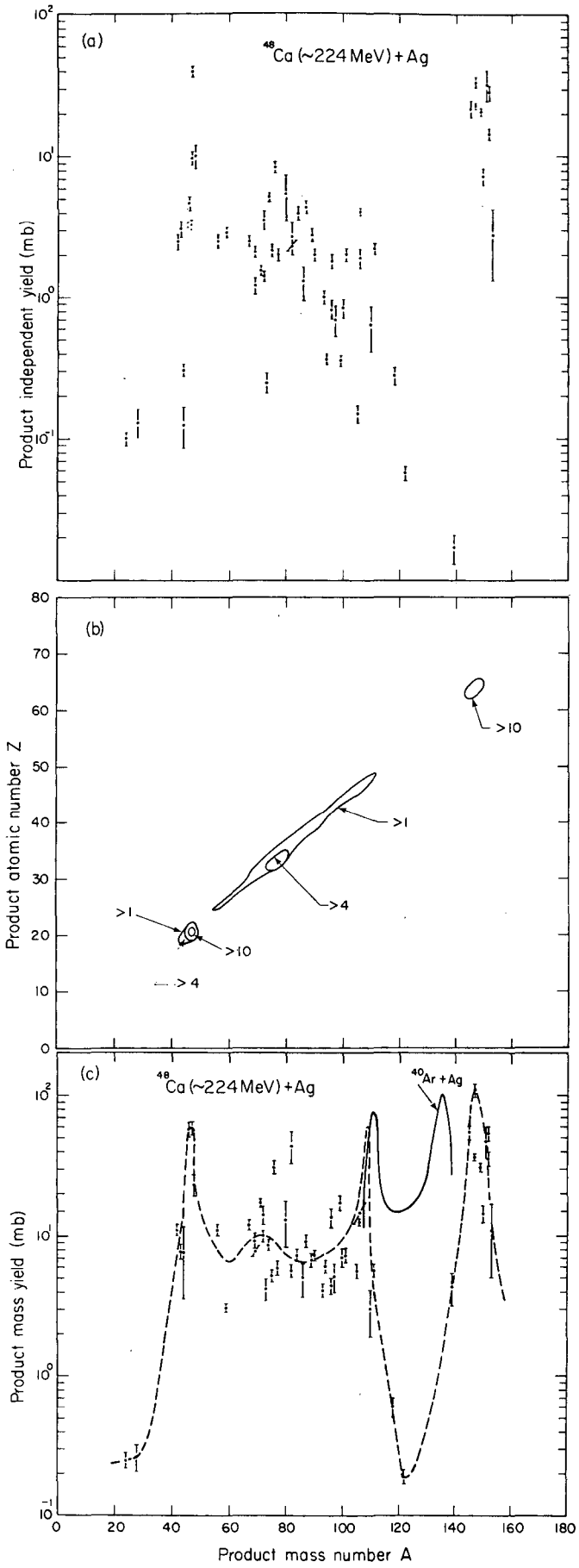


accurate enough to account for the detailed variation of $\sigma_F/\sigma_{ER}$ in the region where the rotating liquid drop fission barriers are small (<2 MeV, as compared to a J=0 barrier of ~30 MeV).

## Footnotes and References

*Condensed from LBL-6527, submitted to Nucl. Phys. A.

†Permanent address: Department of Chemistry, Oregon State University, Corvallis, OR 97331.

1. M. Hille, P. Hille, H. H. Gutbrod and M. Blann, Nucl. Phys. A 252, 496 (1975).

2. H. C. Britt, B. H. Erkkila, R. H. Stokes, H. H. Gutbrod, F. Plasil, R. L. Ferguson, and M. Blann, Phys. Rev. C 13, 1483 (1976).

3. D. Glas and U. Mosel, Nucl. Phys. A 237, 429 (1973).

4. M. Blann, USERDA Report COO-3494-29 (1976).

5. W. D. Myers and W. J. Swiatecki, private communication.

6. S. Cohen, F. Plasil and W. J. Swiatecki, Ann. Phys. (NY) (1974), p.557.

Fig. 1. (a) Independent yield formation cross sections for individual radionuclides. (b) Contour lines of equal independent yields in millibarns. (c) Total integrated mass yields. The dashed curve is intended as a guide to the data. The solid curve is for the reaction $^{40}$Ar + $^{109}$Ag (ref. 1). (XBL 776-1138)

# OBSERVATIONS ON THE MASS DISTRIBUTIONS FROM HEAVY-ION-URANIUM REACTIONS

D. J. Morrissey, R. J. Otto, and G. T. Seaborg

Over the past several years our research group has conducted a systematic study of the mass distributions of the reaction products formed by the interaction of heavy-ion projectiles with $^{238}U$ targets. Projectiles that have been studied by our group at the SuperHILAC have been $^{40}Ar$, $^{84}Kr$, and $^{136}Xe$.[1-3] The results of two similar studies of the systems $^{56}Fe + ^{238}U$ and $^{238}U + ^{238}U$ have recently become available.[4,5] In all of these studies three major reaction channels have been identified for heavy-ion interactions, the quasi-elastic transfer (QET) reaction, the deep inelastic transfer (DI) reaction, and for the lighter projectiles the complete fusion (CF) reaction.

Table 1 summarizes the thick target cross sections for each of these mechanisms for the HI plus uranium reactions. We have found that in order to make comparisons between these systems it is instructive to use the percentage of the total reaction cross sections that each reaction mechanism has been found to represent. In Fig. 1 these percentages are plotted as a function of the projectile atomic number ($Z_{HI}$). This figure helps us to identify several features of heavy-ion reactions that have only recently become apparent. First, the fraction of the total reaction cross section, $\sigma_R$, that goes into the complete fusion process rapidly decreases with increasing $Z_{HI}$. Since the value of $\sigma_{CF}$ for $^{84}Kr + ^{238}U$ of 4% may actually represent an upper limit to $\sigma_{CF}$, the complete fusion cross section could well fall below 5% of $\sigma_R$ when $Z_{HI}$ is greater than 30. Second, the deep inelastic fraction of $\sigma_R$ slowly rises with increasing $Z_{HI}$ and appears to go through a maximum somewhere between Kr($Z_{HI}$=36) and uranium ($Z_{HI}$=92). This is a new observation only made possible by the recent study of $^{238}U + ^{238}U$ which showed that the percent DI for $^{238}U$ projectiles is below the percent DI previously observed with $^{136}Xe$ projectiles.[5] Thirdly, there is the more subtle point that the increase in the

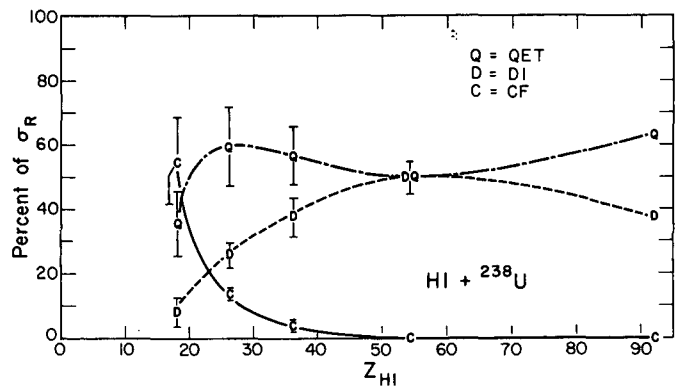


Fig. 1. Plotted are the percent of the total reaction cross section for the three reaction channels, quasi-elastic transfer (QET), deep inelastic (DI), and complete fusion-fission (CF) as a function of projectile Z for the interaction of $^{40}Ar$, $^{56}Fe$, $^{84}Kr$, $^{136}Xe$ and 238U with $^{238}U$ targets. (XBL 778-1694)

DI process does not correspond to the rapid decrease in the CF process. The resulting effect is an increase in the percent QET for intermediate values of $Z_{HI}$. This can be seen at $Z_{HI} \sim 25$ where the CF and DI reaction mechanisms only account for 40% of $\sigma_R$, thus making $\sigma_{QET}$ = 60% of $\sigma_R$.

Here we note that the separation of the QET and DI reaction mechanisms is quite good with the radiochemical techniques used in these studies. The QET process results in two narrow distributions of products centered at the projectile and target. Some of the target-like products are sufficiently excited to undergo fission; however, this excitation is low enough that fission results in an easily

Table 1. Thick target cross sections for $Z_{HI}$ plus $^{238}U$.

| System | $E_{lab}$ | $B/E_{eff}$ | $\sigma_{QET}$ (mb) | $\sigma_{DI}$ (mb) | $\sigma_{CF}$ (mb) |
|---|---|---|---|---|---|
| $^{40}Ar + ^{238}U$ | ≤288 | .828 | 400±120 | 100±50 | 620±150 |
| $^{56}Fe + ^{238}U$ | ≤538 | .755 | 810±160 | 350±55 | 190±30 |
| $^{84}Kr + ^{238}U$ | ≤605 | .859 | 700±120 | 470±70 | 55±15 |
| $^{136}Xe + ^{238}U$ | ≤1150 | .800 | ~600 | 600±125 | <<1 |
| $^{238}U + ^{238}U$ | ≤1785 | .874 | 610 | 365 | <<1 |

identifiable asymmetric mass distribution of neutron-rich fragments. However, most of the primary target-like products of the DI reaction are sufficiently excited to undergo fission de-excitation and, because of the higher excitation result in a broad symmetric mass distribution that is clearly distinguishable from the QET-induced fission products. But not all of the DI target-like fragments undergo fission de-excitation. These survivors are seen as a peak or bump in the mass distribution somewhat below the target mass. This peak has been referred to as the "Goldfinger" and was first observed in the $^{84}Kr + ^{238}U$ reaction[2] where the DI process becomes a significant portion of the reaction cross section. The top of the Goldfinger is seen to move from $_{79}Au$ (in the $^{84}Kr + ^{238}U$ reaction) to $_{85}At$ ($^{136}Xe + ^{238}U$) and finally to $_{90}Th$ ($^{238}U + ^{238}U$).

Several factors contribute to the formation of products in the final DI mass distribution near the target. The primary product formation cross section is determined by the diffusion of nucleons between the target and projectile. For the Uranium + Uranium reaction the net driving forces for nucleon transfer must be zero so that any distribution of mass about uranium is a result of statistical fluctuation about mass symmetry. Secondly, the survival of the deep inelastic products is determined by the distribution of excitation energy in each fragment and their fissionability. The increasing survival for the heavy DI products in the progression from Kr to Xe to U suggests that there is a decreasing amount of excitation energy associated with these products as the mass of the projectile increases. The latter conclusion is consistent with the data obtained by the in-beam counter studies of the $^{136}Xe + ^{197}Au$ and $^{136}Xe + ^{209}Bi$ systems[6,7] which show a large number of partially damped, and thus, more nearly quasi-elastic events. By extension a large number of the $^{238}U + ^{238}U$ collisions must result in partially or incompletely damped collisions leaving the fragments relatively unexcited. Thus, for the heavy symmetric $^{238}U + ^{238}U$ system it is not clear that the two reaction mechanisms, QET and DI, can be totally separated by radiochemical techniques.

In summary, the CF cross section for heavy-ion reactions disappears rapidly for $Z_{HI} > 30$, while the percent DI rises only slowly. Thus at the same time there is a compensating increase in the percentage $\sigma_{QET}$. And finally, the fraction of the reaction cross section that goes into the DI process never exceeds 50% although the exact evaluation of the ratio $\sigma_{DI}/\sigma_{QET}$ for the $^{238}U + ^{238}U$ system is difficult.

## References


1. J. V. Kratz, J. O. Liljenzin, A. E. Norris, and G. T. Seaborg, Phys. Rev. C 13, 2347 (1976).
2. J. V. Kratz, A. E. Norris and G. T. Seaborg, Phys. Rev. Lett. 33, 502 (1974).
3. R. J. Otto, M. M. Fowler, D. Lee, and G. T. Seaborg, Phys. Rev. Lett. 36, 135 (1976).
4. U. Reus, A. M. H. Wätzig, R. A. Esterlund, P. Patzelt and I. S. Grant, Phys. Rev. Lett. 39, 171 (1977).
5. J. V. Kratz et al., GSI Annual Report, 1977, GSI-J1-77, p.60, unpublished.
6. P. Russo, B. Gauvin, P. Glassel, R. C. Jared, R. P. Schmitt, G. J. Wozniak, and L. G. Moretto, Phys. Lett. 67B, 155 (1977).
7. W. U. Schröder et al., Phys. Rev. Lett. 36, 514 (1976).


# LOWERED FUSION CROSS SECTION IN THE QUADRUPLY MAGIC HEAVY-ION SYSTEM, $^{48}Ca + ^{208}Pb$†

D. J. Morrissey, W. Loveland,* R. J. Otto, and G. T. Seaborg

Concurrent with attempts to produce superheavy elements (SHE) in reactions involving the bombardment of highly fissionable heavy element targets such as $^{248}Cm$ with doubly-magic, neutron rich $^{48}Ca$,[1] and in an attempt to understand better the reactions of this unique projectile, we have studied the reaction of the doubly-magic $^{48}Ca$ projectile with the relatively nonfissionable doubly-magic $^{208}Pb$ target.

Isotopically pure $^{208}Pb$ targets of thickness 42 to 45 mg/cm$^2$ were irradiated with beams of $^{48}Ca$ ions of incident energy 303 and 408 MeV from the SuperHILAC of the Lawrence Berkeley Laboratory. Following the bombardments the induced radioactivities in the target were detected with a Ge(Li) $\gamma$-ray spectrometer. The decay of the observed activities was followed for a period of approximately two months. Specific radionuclides produced were identified on the basis of $\gamma$-ray energy, half-life and relative abundance of associated $\gamma$ rays.

In this manner 94 and 109 radionuclides were identified in the low and high energy reactions, respectively. Using the procedures we have previously developed to analyze heavy-ion reaction mass distributions,[2] we calculated independent

yields for each observed radionuclide and the isobaric yield for each mass number where a radionuclide was observed. The resulting mass distributions are shown in Figs. 1(a) and (b). The relative contributions to the measured mass distributions from complete fusion-fission and the fission of Pb-like species were evaluated by a nonlinear least squares fitting to the measured data of our best estimates for the shapes of the mass distributions from these processes.

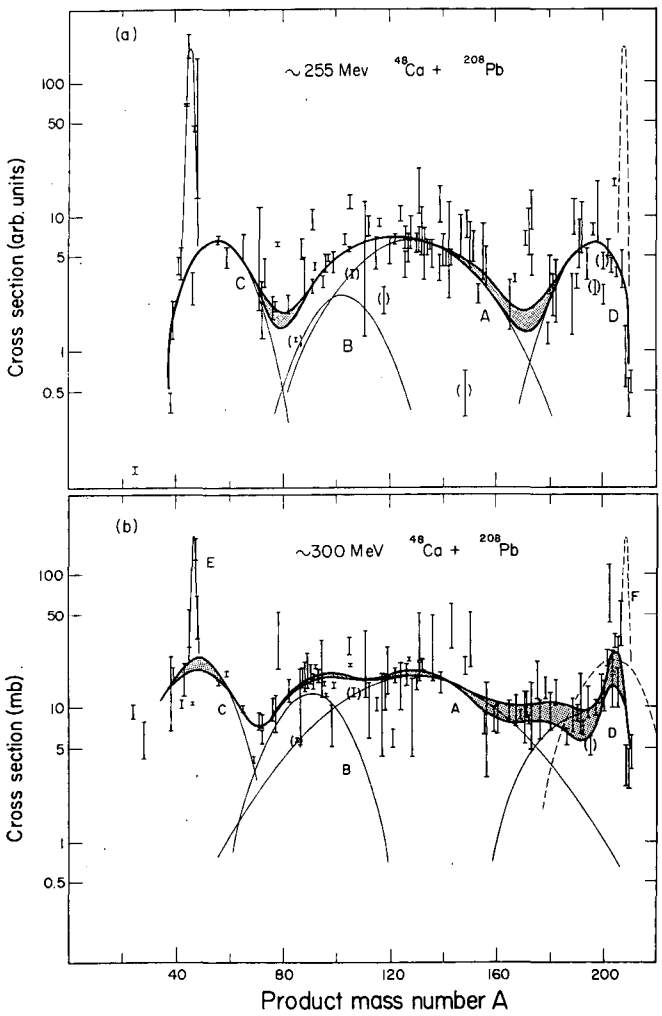


Fig. 1. (a) Product mass distributions from the bombardment of the $^{208}$Pb with ~255 MeV $^{48}$Ca. (b) Same as (a) except $^{48}$Ca energy ~300 MeV. Parenthetical points indicate members of an isomeric pair where the isobaric yield can be split between both members. For an explanation of curves see text. (XBL 779-2016)

Figure 1(a) shows the results of the best least squares component analysis of the mass distribution for the low energy reaction. The curve labeled A represents fusion-fission, component B the deep inelastic induced fission of Pb-like products and component C the light deep inelastic mass distribution. Component B(÷2) plus the heavy deep inelastic peak, component D, is approximately equal to component C, as expected. However, our main interest is in the value of the complete fusion cross section, $\sigma_{CF}$, component A(÷2). Because of the relatively clean separation of the complete fusion-fission and deep inelastic components the value of $\sigma_{CF}$ is not strongly dependent on the deep inelastic component. We can calculate the absolute magnitude of the complete fusion-fission cross section by knowing what fraction of the measured total reaction cross section, $\sigma_R$, it represents. The area under curve A in Fig. 1(a) represents 24 ± 10% of the total measured reaction cross section. The mean geometrical reaction cross section, $\bar{\sigma}_R$, is 990 mb. This gives $\sigma_{CF}$ = 235 ± 99 mb and an effective projectile energy in the thick target of 255 MeV.

The component analysis of the mass distribution from the high energy reaction, Fig. 1(b), is possibly more clear. A range of values of $\sigma_{CF}$ (from 530 to 670 mb) was obtained by varying the shape of the deep inelastic component from one that minimized $\sigma_{CF}$ to one that maximized $\sigma_{CF}$ while maintaining a meaningful fit to the data. Figure 1(b) shows this mass distribution as well as the best least squares fit to the distribution Reasoning at the 95% confidence level, we can say that $\sigma_{CF}$ = 600 ± 70 mb. The measured reaction cross section is 1770 ± 90 mb. The calculated total reaction cross section is 1750 mb corresponding to an effective projectile energy of 300 MeV.

These values of $\sigma_{CF}$ seemed low compared to values obtained for $^{40}$Ar induced reactions.[3-5] In order to make meaningful comparisons, we have plotted (in Fig. 2) the values of $\sigma_{CF}$ from this work and measurements of $\sigma_{CF}$ for the interaction

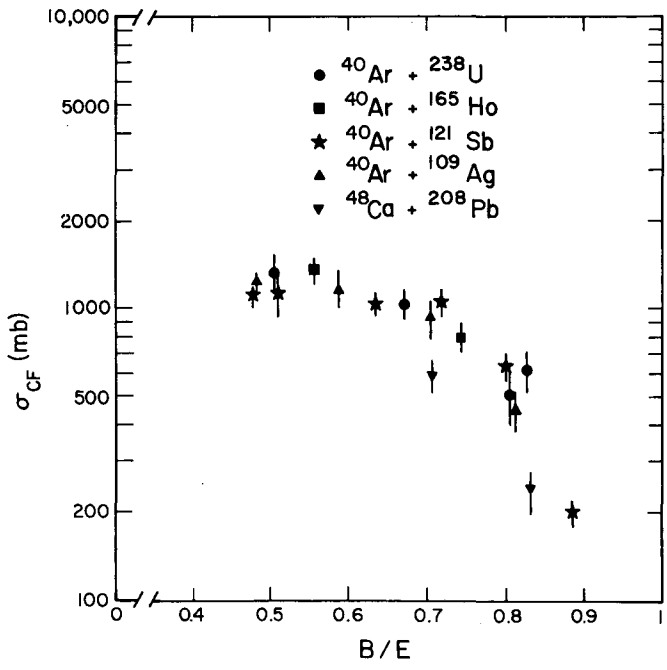


Fig. 2. Representation of the complete fusion cross section, $\sigma_{CF}$, for $^{40}$Ar and $^{48}$Ca induced reactions vs the parameter B/E. (XBL 775-1007)

of $^{40}Ar$ projectiles with medium and high mass targets[3-5] vs the parameter B/E, the laboratory interaction barrier divided by the effective laboratory energy of the projectile. Figure 2 presents a simple method for the comparison of values of $\sigma_{CF}$ for a given projectile with those that would be expected for $^{40}Ar$ projectiles, essentially independent of target. On this basis we conclude that the value of $\sigma_{CF}$ for the $^{48}Ca + ^{208}Pb$ system is significantly lower than that found for $^{40}Ar$ induced reactions, with nonmagic targets, at comparable energies. Glas and Mosel[6] have predicted the general behavior of the complete fusion cross sections that is seen in Fig. 2 and have suggested that a lower fusion cross section might be observed for doubly-magic systems due to a smaller critical radius.

Additional evidence for this comes from mass distribution studies of the reaction of $^{40}Ar$ with nonmagic $^{197}Au$ and magic $^{209}Bi$ targets.[7,8] These thick target experiments were done at effective B/E values of 0.71 and 0.74, respectively, and are therefore directly comparable with the high energy $^{48}Ca$ results. The cross section for the quasi-elastic transfer reaction represents 30% to 35% of the total reaction cross section for all three reactions ($^{40}Ar$ + Au, $^{40}Ar$ + Bi and $^{48}Ca$ + Pb). The deep inelastic cross sections, however, are ~20% (for $^{40}Ar$ + Au), ~30% (for $^{40}Ar$ + Bi) and 30% (for $^{48}Ca$ + Pb) while the complete fusion cross sections show the opposite trend, ~50% ($^{40}Ar$ + Au), ~40% ($^{40}Ar$ + Bi) and ~34% ($^{48}Ca$ + Pb). These trends support the conclusion that the closed shell nature of the target and projectile contribute effectively to the reduction of $\sigma_{CF}$. This finding of a depressed fusion cross section for the $^{48}Ca + ^{208}Pb$ reaction should serve as a challenge for theoretical studies of these reactions to explain the apparent effect of projectile-target nuclear structure on the complete fusion cross section.

## Footnotes and References

†Condensed from LBL-6539, submitted to Physics Letters.

*Permanent address: Department of Chemistry, Oregon State University, Corvallis, OR 97331.

1. E. K. Hulet et al., Phys. Rev. Lett., submitted for publication; R. J. Otto et al., LBL-6509; J. Inorg. and Nucl. Chemistry, to be published. See also R. J. Otto, et al., A Search for Superheavy Elements with Half-Lives Between a Few Minutes and Several Hundred Days in the $^{48}Ca + ^{248}Cm$ Reaction, in this Annual Report.

2. R. J. Otto, M. M. Fowler, D. Lee and G. T. Seaborg, Phys. Rev. Lett. 36, 135 (1976).

3. H. C. Britt et al., Phys. Rev. C 13, 1483 (1976).

4. B. Tamain et al, Nucl. Phys. A 252, 187 (1975).

5. T. Sikkeland, Ark. Fys. 36, 539 (1967); Phys. Lett. 27B, 277 (1968).

6. D. Glas and U. Mosel, Nucl. Phys. A 237, 429 (1975).

7. I. Binder, Ph.D. Thesis, LBL-6526, University of California, Berkeley, 1977.

8. R. J. Otto, I. Binder, M. M. Fowler, D. Lee, I. Binder, and G. T. Seaborg, in Nuclear Chemistry Annual Report, 1974, LBL-4000, p.44.

# C. EXPERIMENTAL HEAVY IONS

## 1. Projectile and Target Fragmentation

### GAMMA-RAYS FROM TARGET EXCITATIONS IN HIGH-ENERGY HEAVY-ION REACTIONS

T. Shibata,* H. Ejiri,* J. Chiba,† S. Nagamiya, K. Nakai,† H. R. Bowman, J. Ioannou, and J. O. Rasmussen

Studies of in-beam gamma rays following high-energy heavy-ion reactions provide information on target excitations in peripheral processes complementary to that from projectile fragmentation studies. We measured prompt and delayed gamma-rays in bombardments of α and $^{12}C$ beams from the Bevalac on Na, S and Ca targets with Ge(Li) detectors. Energies of the beams were 250 and 400 MeV/n.

Many gamma-ray lines from target fragments were observed, and each line was assigned to a nucleus by its energy. Those were mainly transitions from the first excited states to ground states in product nuclei. Plotted in Fig. 1 are gamma-ray production cross sections vs $-Q_{min}$ (minimum Q values to produce the nuclei). In the cases of doubly-even product nuclei, we can assume all gamma transitions feed through the first excited state, so that the gamma-ray production cross section is equal to that for production of the nucleus. In Fig. 2, cross sections only for

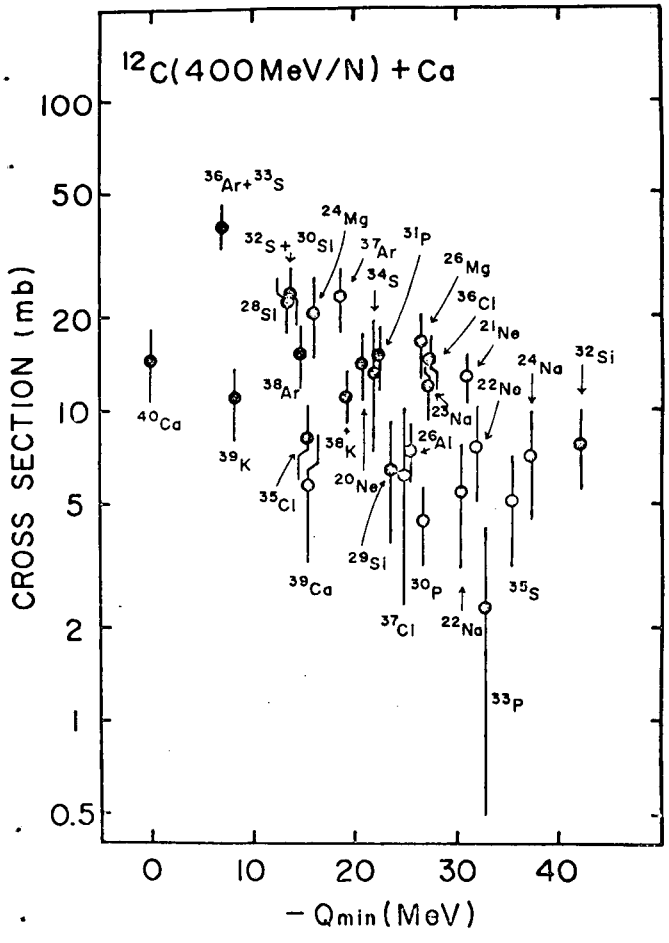


Fig. 1. Gamma-ray cross sections for 400 MeV/n $^{12}C$ on calcium target. (XBL 777-9597)

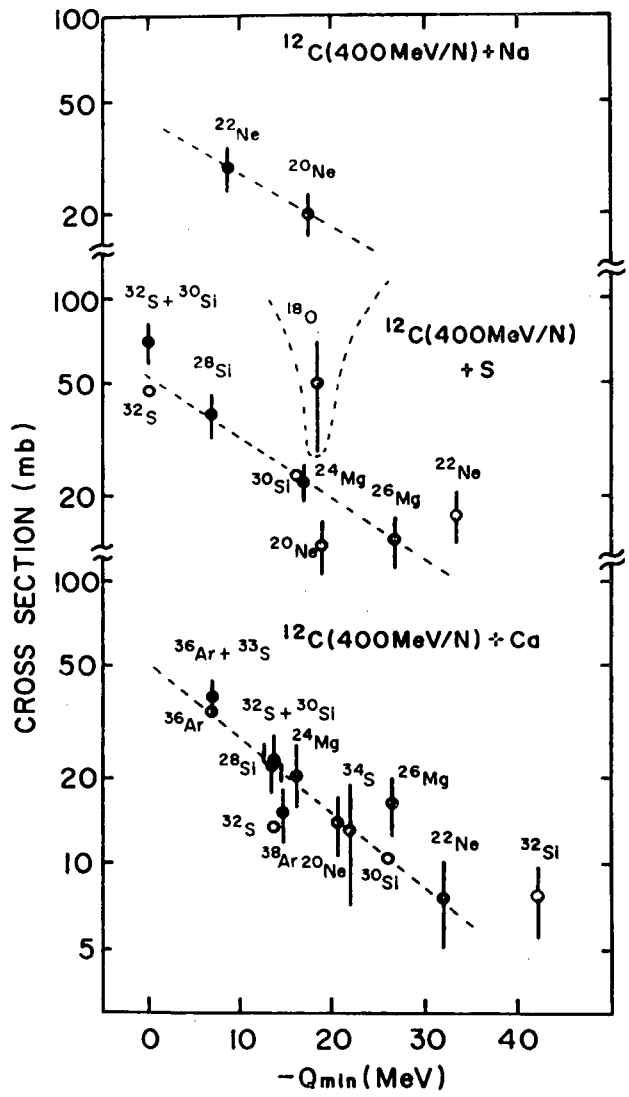


Fig. 2. First-excited-state-to-ground state gamma ray cross sections for 400 MeV/n $^{12}C$ on Na, S, and Ca targets. (XBL 776-9057)

doubly-even products were plotted. The cross sections appear to show an exponential dependence on the $-Q_{min}$; $\sigma \propto \exp(-Q_{min}/a)$, similar to that shown by Lukyanov[1] for $^{16}O$ fragmentation using data of Lindström et al.[2] The values of "a" for 400 and 250 MeV/n $^{12}C$ on S were 20 and 14 MeV, and on Ca they were 17 and 10 MeV respectively. Comparison data for Ca target with proton and pion beams of relativistic energies are available.[3,4]

Ratios of cross sections by α beams to $^{12}C$ beams were about 1.2 for all product nuclei from three different targets, and agreed with ratios calculated assuming $\sigma \propto (A_p^{1/3} + A_T^{1/3} - 1.6)$. This result is consistent with the picture of peripheral processes.

The gamma-ray lines observed at 90° to the beam showed Doppler broadening which provides information on transverse momentum distribution of target fragments. The momentum transfers deduced from the broadening were rather small, ($\Delta p_\perp$ = 100-200 MeV/c) again in agreement with the peripheral picture.

Footnotes and References

*Present address: Physics Dept., Osaka University, Toyonaka, Osaka, Japan.

†Dept. of Physics, University of Tokyo, Bunkyo-ku, Tokyo.

1. V. K. Lukyanov et al., Phys. Lett. 57B, 10 (1975).

2. P. J. Lindström et al., LBL-3650 (1975).

3. O. Artum et al., Phys. Rev. Lett. 35, 773 (1975).

4. H. E. Jackson et al., Phys. Rev. Lett. 35, 1170 (1975).

## PROJECTILE FRAGMENTATION-TARGET EXCITATION CORRELATIONS

H. J. Crawford,* H. R. Bowman, J. Chiba,† D. E. Greiner, J. Ioannou, P. J. Lindstrom, K. Nakai,† J. O. Rasmussen, T. Shibata‡

We performed an experiment which coupled "in beam" Ge(Li) gamma-ray spectroscopy with a multi-element fragmentation telescope to see if we could detect correlations between projectile fragmentation modes and excitation energy deposited in a target as revealed through subsequent gamma decay of target residues. The specific reaction we studied was

$$400 \text{ MeV/amu } C + Na \rightarrow {}^{A}Z + \gamma + x$$

In which we detected fragment, or fragments, $^{A}Z$ in coincidence with the gamma ray. The experiment was run in 2 modes, one requiring the gamma in the trigger and one without the gamma in the trigger scheme.

Although we obtained very good resolution of several first-excited-state-to-ground gamma lines, allowing taggins of $^{23}Na^*$, $^{22}Na$, g $^{22}Ne$ and $^{19}F$, we were somewhat limited by poor statistics in the detailed coincidence sorting of events. There seems to be little or no correlation between target excitation-fragmentation and projectile excitation-fragmentation. To gain improved statistics, we analyzed the gamma-ray spectrum seen in coincidence with each type of projectile fragmentation and, conversely, the fragment charge distribution seen in coincidence with different broad energy segments of the gamma spectrum. In addition we could compare relative branching ratios for the projectile decay both with and without requiring a gamma ray in the coincidence logic.

The experimental results indicate that the overall gamma-ray spectrum obtained with the gamma in coincidence is very insensitive to the specific forward-going fragment formed. Thus the gamma spectrum associated with charge 4 fragments is virtually identical to the spectrum associated with charge 2 fragments. The charge spectrum associated with a high energy gamma ray (>3 MeV) is also virtually identical to the charge spectrum associated with a low energy gamma ray (<1 MeV). Our final and most definite experimental conclusion derives from the fact that the branching ratio does not depend on whether we required a gamma in coincidence or not. This indicates that the multiplicity of gamma rays (presumably from the target residue) is independent of whether the carbon projectile fragmented into protons and alphas or into larger fragments like Be or B.

In the standard geometrical (abrasion-ablation) interpretation of heavy-ion interactions, we would expect production of smaller projectile fragments to be accompanied by greater disruption of the target nucleus. One would expect this to lead to a different probability for gamma ray production. Since we do not see a difference in the projectile branching ratio, we can conclude that for the target products we could tag by gamma lines (mass range 23 to 19) the dominant mechanism, involves target and projectile nuclei independently extracting excitation energy from the translational kinetic energy of a grazing collision. That is,

there is an interaction produced by the time-varying potential field from the collision partner, a process we have called the "stochastic grazing" process. Since target fragments below mass 19 had no observable discrete gamma ray tags, we cannot draw conclusions about possible correlations with projectile fragmentation for these more violent collisions.

Footnotes and References

*University of California Space Sciences Laboratory, Berkeley, California.

†Dept. of Physics, University of Tokyo, Bunkyo-ku, Tokyo.

‡Present address: Physics Dept., Osaka University, Toyonaka, Osaka, Japan.

1. J. D. Bowman, W. J. Swiatecki, and C. F. Tsang, LBL-2908 (1973).

2. J. Hufner, K. Schafer, and B. Schurmann, Phys. Rev. C 12, 1888 (1975).

3. J. O. Rasmussen, R. Donangelo, and L. Oliveira, Theoretical Calculations of Peripheral Reaction Yields from Relativistic Heavy Ions, LBL-6580 (1977).

## INCLUSIVE CHARGED PARTICLE PRODUCTION IN COLLISIONS OF RELATIVISTIC LIGHT NUCLEI

L. Anderson, W. Bruckner, O. Chamberlain, S. Nagamiya, S. Nissen-Meyer, D. Nygren, B. Ockel, L. Schroeder, S. R. Schnetzer, G. Shapiro, H. Steiner, and I. Tanihata

In an experiment at the Bevalac we have measured single particle inclusive production of charged particles in collisions of protons, deuterons, alphas, and carbon particles at 1.75 GeV/c/n and 2.88 GeV/c/n and alpha particles at 0.93 GeV/c/n with targets of C, $CH_2$, Cu, and Pb. The $CH_2$ anc C targets were used to obtain cross sections for hydrogen. Measurements of the longitudinal and transverse momentum distributions extend over magnetic rigidities from 0.25 to 9.0 GV/c, laboratory production angles from 0 to 12°, and transverse rigidities from 0 to 0.8 GV/c.

Typical results are shown in Figs. 1 and 2. On the basis of an analysis of our data for the alpha particle beams we point out the following dominant features of the data:

1. As in previous measurements[1] a peak which is sharp in angle and momentum is observed at the projectile velocity for each stable nucleus of mass less than that of the projectile. The peaks are identified as projectile fragmentation peaks. The Lorentz invariant cross section for these fragments is independent of beam energy in the energy range T/N = 1-2 GeV for fragment momenta out to 0.4 GeV/c in the forward and transverse directions in the projectile frame. The momentum distribution in the projectile frame is not isotropic; the cross section is lower in the forward direction than in the backward or transverse directions. The momentum at which the cross section reaches its maximum for a given transverse momentum shifts to lower values with increasing transverse momentum.

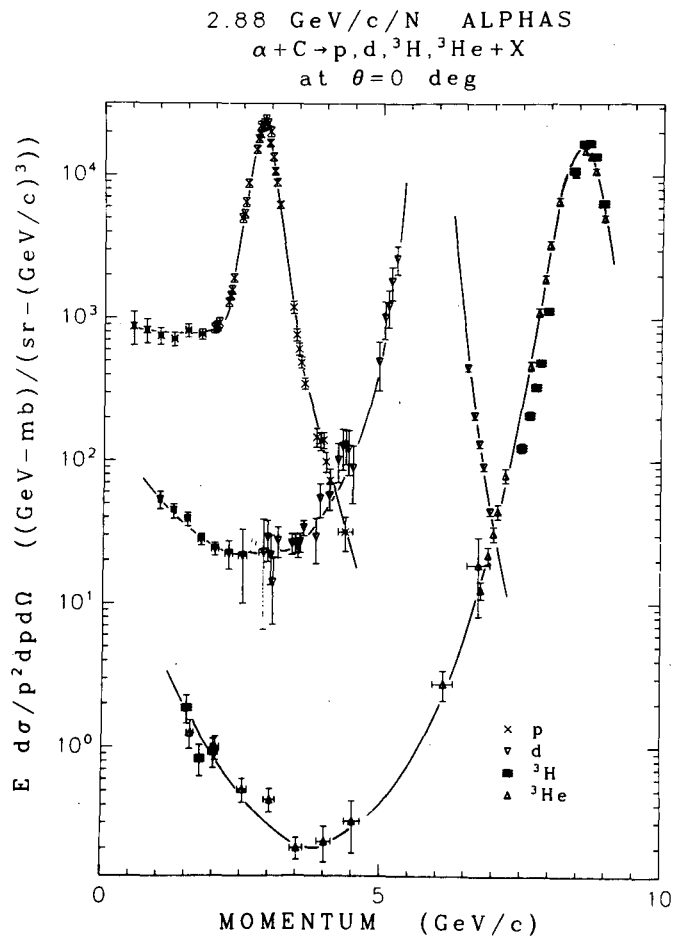


Fig. 1. Momentum distributions at θ = 0° for the reactions 2.88 GeV/c/n α + C → p, d, $^3$H, and $^3$He + X. (XBL 778-9778)

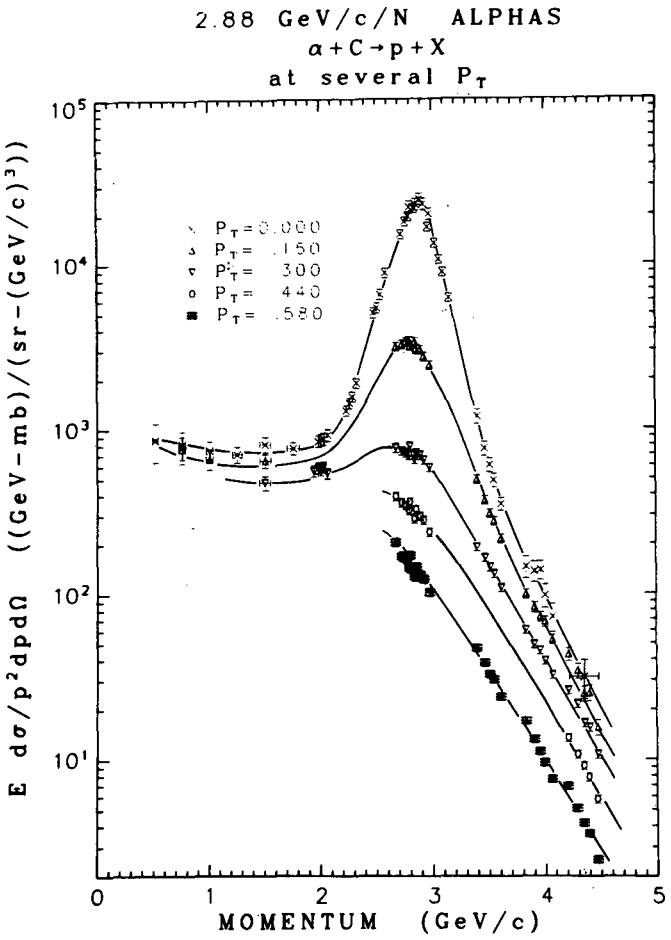


Fig. 2. Momentum distributions for protons for the reaction 2.88 GeV/c/n α + C → p + X at several transverse momenta. The large $p_T$ points plotted do not join continuously since they are not at exactly the same $p_T$. (XBL 778-9780)

2. A target fragmentation region, of which we see only the tail, is apparent.

3. A central plateau (for protons) or valley (for heavier fragments) with a very shallow angular dependence is observed. With increasing beam energy, this region becomes deeper (and, of course, broader), especially for the heavier fragments.

4. We have fit the target mass dependence of the cross section for the C, Cu, and Pb targets to the form $A_T^N$ where $A_T$ is the target mass. For protons at the beam velocity we find N = 0.24 at $p_T = 0$ and N = 0.4 for $p_T \geq 0.15$ GeV/c, N rises to approximately 0.4 for products in the central region and higher in the target fragmentation region where we find $N > 1$ for the heavier fragments.

As yet the longitudinal and transverse momentum distributions we have measured are not accurately predicted by any model. However, the predominance of the fragmentation peaks and the fact that they obey limiting fragmentation (energy independence in the projectile frame) indicate that our data should be useful for studying the structure of the projectile particles and the fragmentation mechanism.

Reference

1. J. Papp, Thesis, University of California, Berkeley, LBL-3633, May 1975, unpublished.

## PROJECTILE FRAGMENTS FROM HIGH MOMENTUM TRANSFER RELATIVISTIC HEAVY-ION COLLISIONS

M. M. Grazzaly,* V. Perez-Mendez, A. L. Sagle, E. T. B. Whipple, F. Zarbakhsh, G. Iga,* J. B. Carroll,*†
J. V. Geaga,*† J. B. McClelland,* M. A. Nasser,* H. Spinka,*‡ and R. Talaga*†

The production of light fragments ($\pi$,p,d,t,$^3$He, and $^4$He) has been measured for relativistic heavy-ion collisions of 1.8 GeV/n $^{40}$Ar and 2.1 GeV/n $^{12}$C beams on Be and Cu targets. Single particle inclusive double differential cross sections $d^2\sigma/dpd\Omega$ were obtained using a movable magnetic spectrometer, spanning the angular region between 3.5 and 15.2°; the momentum, $\theta$, and $\phi$ were measured for each particle detected by the spectrometer. The present work extends projectile fragmentation data to higher momentum transfers than the previous work at 0°[1] and 2.5°[2]. The rapidities of the detected particles extend to regions midway between the target and beam rapidities. The momentum transfers involved in these collisions are typically much larger than the Fermi momentum. When viewed in the projectile rest frame, the present data correspond to fragment energies as high as 1 GeV/n over an angular range from 20 to 160°.

An array of 30 lucite Cherenkov detectors was used to measure the multiplicity distribution of fast charged particles associated with each particle detected by the spectrometer. This array has a $\theta_L$ acceptance of 4 to 12° or 5 to 16° which is selected by varying the target-to-detector distance. The multiplicity (or tag) counters have a velocity threshold of $\beta_{th} \simeq 0.7$ and are in the form of azimuthal segments covering all of the azimuthal coordinate not occupied by the spectrometer acceptance. The kinematics of the reaction ensure that the tag counters accept a large fraction of the fragments from the projectile which have received momentum transfers greater than the Fermi momentum.

Preliminary results for $^{40}$Ar-Cu collisions are presented in Figs. 1-3. The invariant inclusive cross section for proton production as a function of laboratory momentum at $\Theta_L = 5°$ and $\Theta_L = 14.7°$ is plotted in Fig. 1. The deuteron and triton production cross sections are shown in Figs. 2 and 3, respectively. At 5° the cross section peaks at a fragment velocity slightly below $\beta_p$, the projectile velocity. The fragment energies, when viewed in the projectile rest frame, are as low as 25 MeV/n for $\Theta_L = 5°$ and as low as 250 MeV/n for $\Theta_L = 14.7°$.

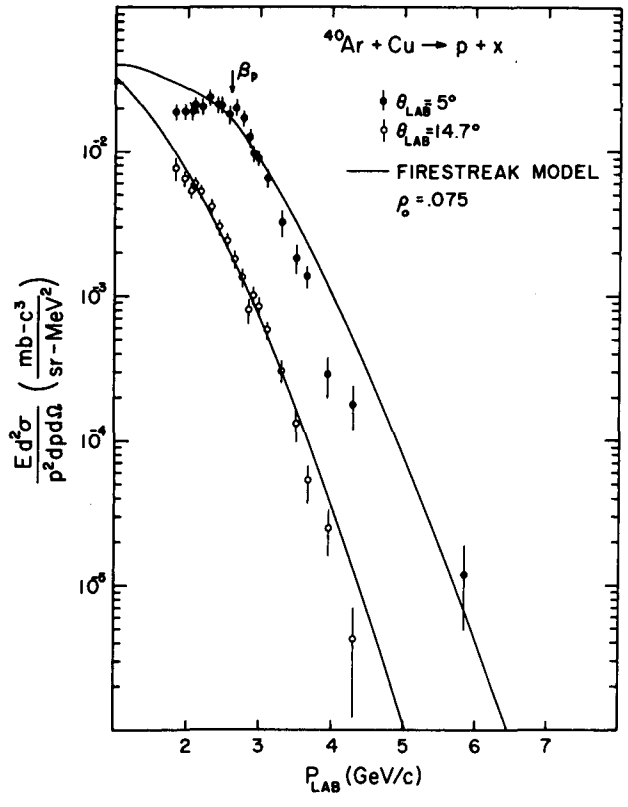


Fig. 1. The invariant inclusive cross section for proton production resulting from collisions between 1.8 GeV/n $^{40}$Ar and Cu. The solid lines are theoretical calculations based on the Firestreak model. (XBL 778-1629)

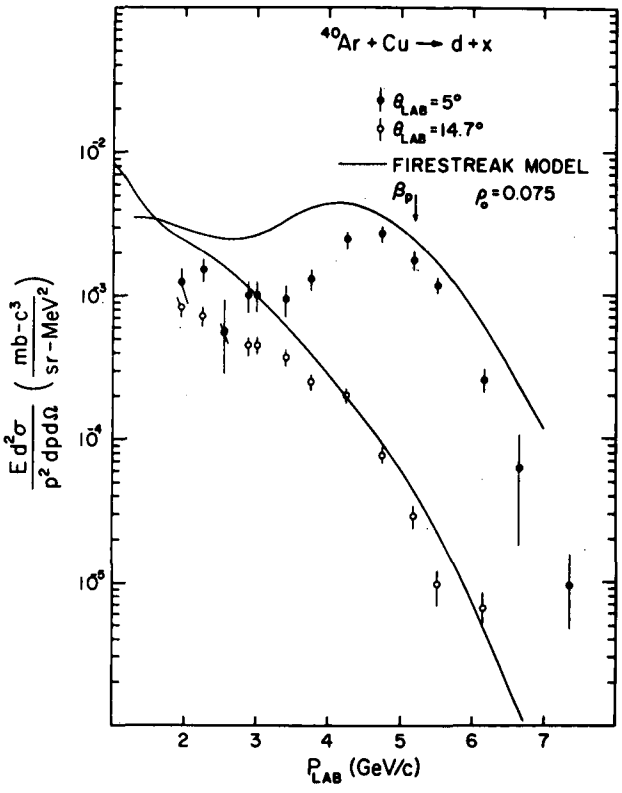


Fig. 2. The invariant inclusive cross section for deuteron production. (XBL 778-1630)

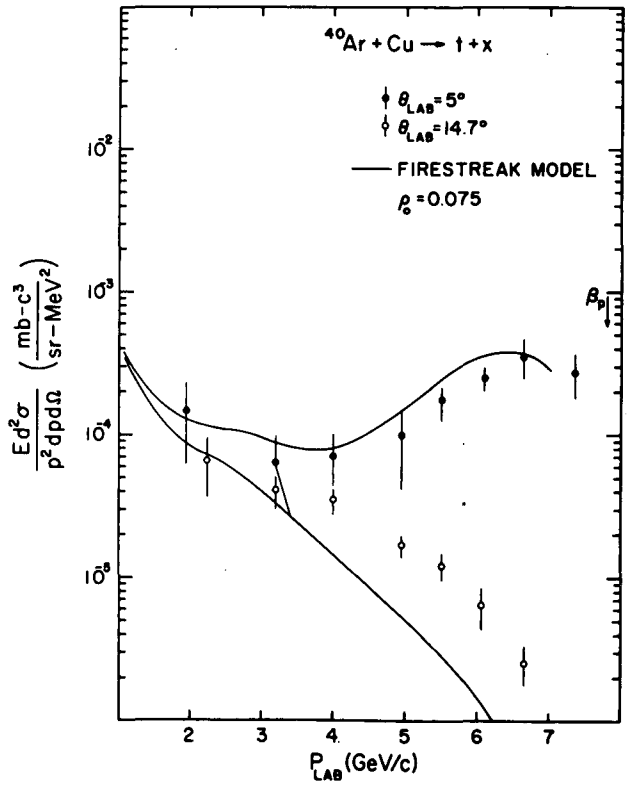


Fig. 3. The invariant inclusive cross section for triton production. (XBL 778-1631)

The curves shown in Figs. 1-3 are predictions from the Diffuse Firestreak model.[3,4] In this model, the projectile and target are divided into tubes. At a given impact parameter the overlapping projectile and target interaction tubes, as defined in this model, undergo a completely inelastic one-dimensional collision in the beam direction. The resulting composite system of "firestreaks" decays thermodynamically after expanding to a freeze-out density $\rho_o$. The calculations for our data were done using $\rho_o = 0.075$ fm$^{-3}$, which is about half of the normal nuclear density.

This model fits the proton data quite well but overestimates the deuteron production at low momenta (Fig. 2). The triton production is underestimated at large angles and high momenta (Fig. 3). We intend to compare our data to the predictions of other models. In particular, we await the results of the internucleon cascade model calculations of Smith and Danos.[5]

The target dependence of the inclusive cross sections is plotted in Fig. 4 as the ratio $R_a \equiv (^{40}\text{Ar+Cu} \to \text{a+X})/(^{40}\text{Ar+Be} \to \text{a+X})$, where a is either p, d, or t and X is anything. The dashed lines in the figure indicate the beam rapidity, $Y_B$, and the rapidity midway between the beam and target, $Y_B/2$. The solid horizontal lines indicate the ratios expected if the cross sections depend on the area ($A_T^{2/3}$) or volume ($A_T$) of the target nucleus. At rapidities near $Y_B/2$, the deuteron data show a clear trend toward volume dependence for the target. This is consistent with the hypothesis that particles emitted in this rapidity region are from "central" (small impact parameter) collisions.

The data from the multiplicity counters are in the early stages of analysis and tentative results are available. To within statistical uncertainties, the average multiplicity is independent of both the type and momentum of the fragment detected in the spectrometer. The multiplicity (uncorrected for efficiency) is never greater than 20 and its average varies between 5 and 8 for argon projectiles.

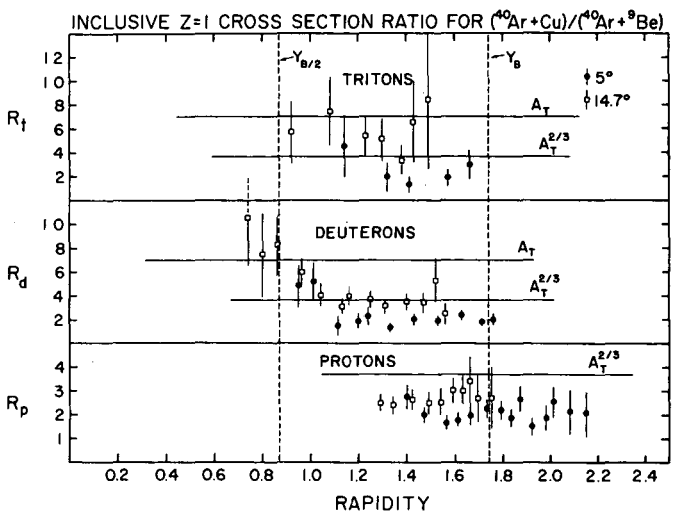


Fig. 4. A plot of the ratio of the reactions $(^{40}\text{Ar+Cu} \to \text{a+X})/(^{40}\text{Ar+Be} \to \text{a+X})$, where a is either p,d, or t and X is anything, as a function of the fragment rapidity.
(XBL 778-1632)

As a test for possible correlation between high multiplicity, m, and some particular region of the inclusive cross section, W, we have selected events with $m \geq 7$ and studied the ratio $C \equiv (W_{m\geq 7}(\Theta_L, P_L))/(W_{m=all}(\Theta_L, P_L))$ as a function of angle and momentum. At a given angle C is independent of momentum. As shown in Table 1,

Table 1. $\bar{C}^a$ for $^{40}\text{Ar} + T \to d + X$

| $\Theta_{Lab}$ | T = Be | T = Cu |
|---|---|---|
| 5° | 0.294±0.025 | 0.373±0.034 |
| 14.7° | 0.495±0.043 | 0.736±0.068 |

[a] $\bar{C}$ is the ratio of cut to uncut cross section averaged over fragment momentum for a given angle.

$\bar{C}$ (averaged over momentum at a given angle) increases by almost a factor of 2 as $\Theta_L$ increases from 5 to 14.7°. At 5°, $\bar{C}$ (Cu)/$\bar{C}$(Be) = 1.27 ± 0.16, and at 14.7° this ratio increases to 1.49 ± 0.19. The multiplicity associated with a given fragment detected in the spectrometer has only a small dependence on the type of target nucleus. This might be because the multiplicity counters subtend $\Theta_L$ as low as 4°. From Fig. 4 it is seen that the single particle inclusive cross sections do not have a strong target dependence at 5°. In future, data will be taken with the tag counters intercepting larger $\Theta_L$. This will be equivalent to raising the low energy threshold in the projectile rest frame.

## Footnotes and References

*Physics Dept., University of California, Los Angeles, CA 90024

†Present address: Lawrence Berkeley Laboratory, Berkeley, CA 94720

‡Present address: Argonne National Laboratory, Argonne, IL 60439

1. D. E. Greiner, P. J. Lindstrom. H. H. Heckman, B. Cork and F. S. Bieser, Phys. Rev. Lett. 35, 152 (1975).

2. J. Papp, Ph.D. Thesis, LBL-3633 (May 1975).

3. W. D. Myers, LBL-6569 (1977).

4. J. Gosset, J. Kapusta, and G. D. Westfall, to be published.

5. R. K. Smith and M. Danos, to be published.

# UNIVERSAL FRAGMENT-MOMENTUM DISTRIBUTION IN HIGH ENERGY NUCLEUS-NUCLEUS COLLISIONS*

P. B. Price, J. Stevenson, and K. Frankel

We have reported[1] energy and angular distributions of complex nuclei ($3 \leq Z \leq 9$) with energies ~15 to ~60 MeV/n produced in the reactions 20 GeV Ar + Au and 8 GeV Ne + U at the Lawrence Berkeley Laboratory Bevalac. The angular distributions were consistent with isotropic emission from a source moving in the beam direction with a velocity $\beta_o \approx 0.08 \pm 0.02$. The energy distributions in the moving frame were about equally consistent with Maxwellian's with a very high temperature, $\tau \approx 50$ to 70 MeV, or with exponentials in momentum. We pointed out that a source in thermal equilibrium at such a high temperature and low velocity would be incompatible with energy-momentum conservation. We concluded that most of these complex nuclei must have been emitted nonthermally.

We show that the momentum distribution of fragment from the slow source appears to be a universal curve, exponential in form, for all species near the stability line, at least up to mass 19.

Figure 1 shows the invariant cross section, $f \equiv P^{-1} d^2\sigma/dEd\Omega$, as a function of P', the momentum in a frame moving at $\beta_o = 0.08$. The open and closed symbols refer to the two inclusive reactions 400 MeV/n Ne + U → X + anything, and 500 MeV/n Ar + Au → X + anything, where X is one of the species $^8$Li (detected visually by its distinctive "hammer" track from the decay $^8\text{Li} \to {}^8\text{Be} \to 2\alpha$), and B,C,N,O, or F (its charge but not mass determined by its ionization rate). The data were reported in Ref. 1. With a Lorentz transformation using a single value of the source velocity determined by a least-squares calculation to be $\beta_o = 0.08$, all of the data from a given reaction lie within a factor of 3 of a single exponential curve

$$f \equiv P^{-1} d^2\sigma/dEd\Omega = K \exp(-P'/P_c), \qquad (1)$$

where

$$P' = \{\gamma_o^2 [P_\parallel - \beta_o (P^2 + M^2)^{1/2}]^2 + P_\perp^2\}^{1/2}, \qquad (2)$$

and the characteristic momentum $P_c = 236$ MeV/c for the Ne + U reaction and $P_c = 340$ MeV/c for the Ar + Au reaction. Thus, for a given reaction the invariant cross section for any charge from 3 to 9 at a given momentum is predicted rather well by three parameters, K, $P_c$, and $\beta_o$, that are independent of Z, A, and $\beta'$, the fragment velocity in the moving frame.

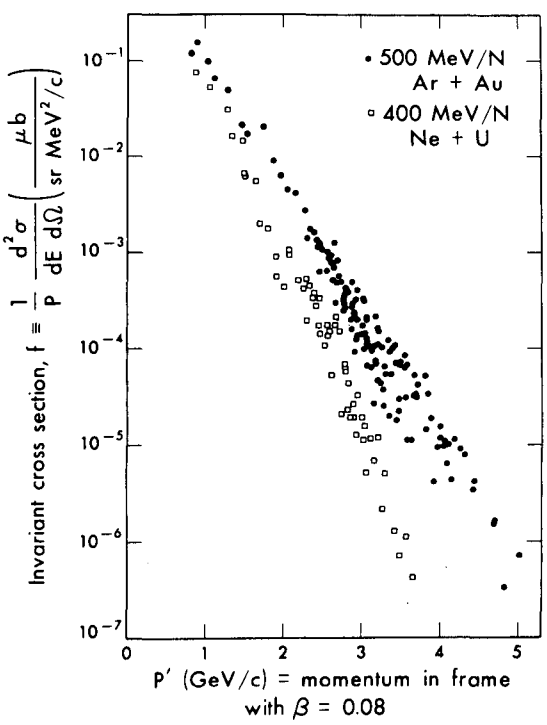


Fig. 1. Invariant cross sections for fragments ranging from $^8$Li to fluorine as a function of total momentum evaluated in a frame moving in the beam direction with speed 0.08 c. Data are from Ref. 1.
(XBL 779-4860)

We find that data for H and He isotopes with energies from ~20 to ~120 MeV/n produced in 400 MeV/n Ne + U reactions[2,3] lie on an extension of our curve for complex nuclei in the same reaction. We also find that complex nuclei with Z from 3 to 12 at energies all the way from 3 up to ~50 MeV/n from the 2.1 GeV/n C + Au reaction (data from Ref. 4 and our own unpublished measurements) are consistent with a single exponential in momentum. These results are shown in Fig. 2. Curves are identified for the different species so one can see the range of momenta for which measurements of each species have been made. We also take into account the dependence of the fragment velocity $\beta'$ on the source velocity $\beta_o$.

We sometimes find large deviations from a single exponential line. Contributing sources of the deviations are systematic error, statistical error, and plotting data for single isotopes of a given charge. We expect as more data for individual nuclides on the stability line become available, the deviation from a universal line will decrease if only the most stable nuclides are considered.

We have applied the same analysis to the published[5] fragment yields from the reaction 5.5 GeV p + U → X + anything. The invariant cross sections for the various fragments from

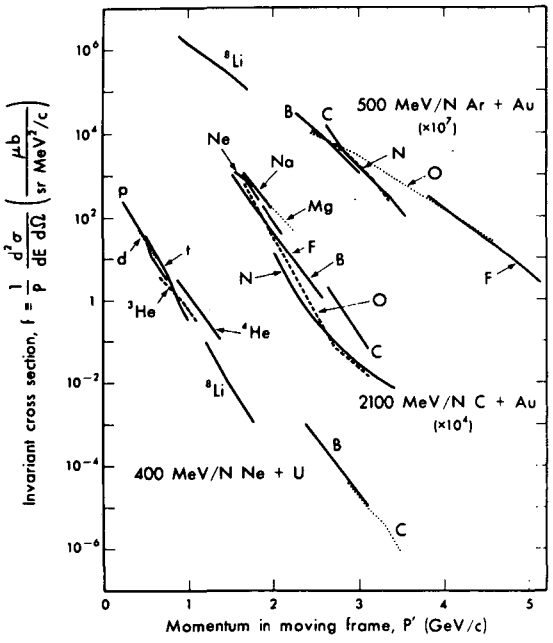


Fig. 2. Invariant cross sections for fragments from three different reactions. Data for p, d, t, $^3$He, and $^4$He are from Refs. 2 and 3. In the C + Au reaction the data for B, C, N and O are from Ref. 4. Remaining data are ours.
(XBL 779-4861)

p to Ar fall off roughly exponentially with momentum, with $P_c \sim 100$ to 150, but fail by many orders of magnitude to lie on a single curve. When fitted to Maxwellian distributions in the moving frame, the apparent temperatures[5] are of order 10 to 20 MeV, very much lower than the apparent temperatures for nucleus-nucleus collisions. We conclude that there may be a qualitative difference between nucleus-nucleus collisions and proton-nucleus collisions, one manifestation of which is a universal fragment-momentum distribution for nucleus-nucleus collisions.

Footnote and References

*Condensed from Phys. Rev. Lett. 39, 177 (1977).


1. J. Stevenson, P. B. Price and K. Frankel, Phys. Rev. Lett. 38, 1125 (1977).
2. H. H. Gutbrod, A. Sandoval, P. J. Johansen, A. M. Poskanzer, J. Gosset, W. G. Meyer, G. D. Westfall, and R. Stock, Phys. Rev. Lett. 37, 667 (1976).
3. G. C. Westfall, J. Gosset, P. J. Johansen, A. M. Poskanzer, W. G. Meyer, H. H. Gutbrod, A. Sandoval, and R. Stock, Phys. Rev. Lett. 37, 1202 (1976).
4. H. J. Crawford, P. B. Price, J. Stevenson and L. Wilson, Phys. Rev. Lett. 34, 329 (1975).
5. A. M. Poskanzer, G. W. Butler, and E. K. Hyde, Phys. Rev. C 3, 882 (1971).


## LARGE COLLISION RESIDUES AND NUCLEAR FISSION IN THE INTERACTION OF 25.2 GeV $^{12}$C WITH URANIUM*

W. Loveland,† R. J. Otto, D. J. Morrissey, and G. T. Seaborg

Target residue mass and charge distributions have been measured for 76 products of the interaction of 25.2 GeV $^{12}$C with U. The purpose of this investigation was to see if the target residue mass and charge distributions show any unusual features that could help us to understand the mechanism of these relativistic heavy ion (RHI) reactions with heavy targets. Other radioanalytical studies of RHI reactions with lighter targets by Rudy and Porile[1] (Ag + C), and by Cumming et al.[2,3] (Cu + C,N) indicated little difference (except in the light product yields) between the RHI reactions and reactions induced by GeV protons, although track detector studies by Katcoff and Hudis[4] (U + N) did show enhanced fission cross sections in the RHI reactions.

The target array for this experiment consisted of three foils of natural uranium separated from each other by ~150 mm. The foils, varying in thickness from 33 to 72 mg/cm$^2$ and surrounded by ~15 mg/cm$^2$ Al catcher foils, were irradiated for 162 min in a beam of 25.2 GeV $^{12}$C ions of intensity $\sim 2.5 \times 10^{10}$ particles/min at the Bevalac. Gamma and x-ray spectroscopic measurements of the radioactivity induced in the target and catcher foils began one hour after bombardment and continued for about three weeks. Over 75 radionuclides were identified on the basis of their γ-ray energy, half-life and relative γ-ray abundance. Based upon the variation of activity with foil thickness, corrections (of ~10 to 30%) were made to each measured activity to account for the effects of secondary-induced reactions.

The experimentally determined independent and cumulative yields for individual radionuclides are shown in Fig. 1(a). Figure 1(b) depicts the data of Fig. 1(a) plotted to show the (Z,A) distribution of the products while Fig. 1(c) shows the mass yield distribution for the reaction. The dramatic bump in the mass yield curve in the region from $160 \leq A \leq 190$ is also seen in the measured nuclide yields shown in Fig. 1(a), thus indicating it is not an artifact of the data reduction procedures.

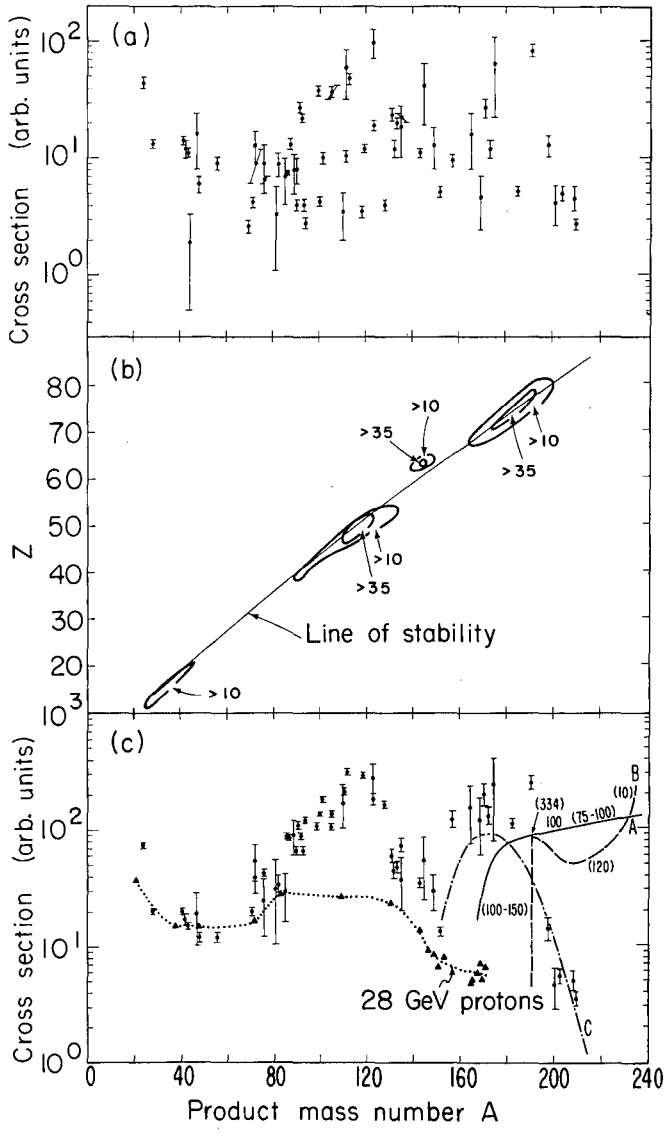


Fig. 1. (a) Independent and cumulative yield formation cross sections for individual radionuclides. (b) Contour lines for equal independent yields. The two main bumps observed are due to the fission product and central collision survivor distributions. Subsidiary features include enhanced yields of products with N=82 and low Z products. (c) Total integrated mass yields. Dotted curve is from Ref. 5. See text for explanation of other curves. The numbers in parentheses along curves A and B refer to the excitation energies in MeV of species of given mass. (XBL 774-806A)

Based upon the shapes of the mass and charge distributions, product nuclei with $70 \leq A \leq 140$ are assumed to result from binary fission of a target-like residue. As seen in Fig. 1(c) the mass distribution for the 25.2 GeV $^{12}C$ ion induced fission of U is similar in shape to the distribution for the 28 GeV p induced fission of U.[5] As pointed out by Katcoff and Hudis,[4] the higher absolute cross sections observed in the RHI reactions are due mostly to the increased total reaction cross section for RHI's. The fission product charge dispersions are characterized by width parameters $\sigma \sim 0.9$-$1.2$ Z units. Direct comparison of these width parameters with those from a number of other higher energy fissioning systems of known excitation energy[6] allows one to infer the average excitation energy for the fissioning system(s) to be 50 to 100 MeV. The fission product charge dispersions observed in this work are very different from those observed in GeV proton induced fission of U. Our charge dispersion curves for the region of $110 \leq A \leq 140$ are single Gaussians with $\sigma \sim 0.9$ while the dispersions observed for 11 GeV proton induced fission of U[7] are interpreted as the sum of two Gaussians with widths $\sigma$=1.0 and 1.8 for the neutron excessive and deficient components, respectively. The Zp for our data occurs approximately halfway between the n-excessive component and n-deficient component Zp values of Yu and Porile.[7]

The most interesting new feature observed by us is the surprising large bump in the mass yield curve in the region from $160 \leq A \leq 190$, a feature totally absent from the GeV p reaction mass yield curve. The preferential population of the low spin member of the isomeric pair $^{186m,g}Ir$ [$\sigma(^{186m}Ir(2-))/\sigma(^{186}Ir(6-)) \approx 12 \pm 4$] implying low final product angular momentum is another intriguing feature of yields in this region. We have done a statistical de-excitation calculation using a modified version of the ALICE code,[8] which allows for fission-neutron charged particle emission competition with $J_{rms} \leq 10\hbar$ (as suggested by our isomer ratio data). By assuming various sets of initial product yields and excitation energies and tracing their de-excitation, we were able to determine what set of initial conditions lead to the observed product yields. Assuming the data are properly represented by the curve C in Fig. 1(c), the product yields and excitation energies at the time at which fission begins to compete with particle emission (i.e., the start of the statistical de-excitation process) are shown by curveA. Curve B in Fig. 1(c) shows the predictions for product yields and excitation energies as given by a calculation employing the geometrical concepts of the fireball model.[9] Clearly a more refined version of this model is needed to fit the data. On the other hand, reasoning from the fact that the fission cross section is ~1/2 the total reaction cross section[4] and the mean fissioning system mass is greater than

the mean mass of the "large residue nuclei," we are lead to conclude that the impact parameter $b \lesssim 0.7\ (R_t + R_p)$ for events leading to the "large residue nuclei."

Footnotes and References

*Condensed from Phys. Rev. Lett. 39, 320 (1977).

†Permanent address: Department of Chemistry, Oregon State University, Corvallis, OR 97331.


1. C. R. Rudy and N. T. Porile, Phys. Lett. 59B, 240 (1975).
2. J. B. Cumming, R. W. Stoenner, and P. E. Haustein, Phys. Rev. C 14, 1554 (1976).
3. J. B. Cumming et al., Phys. Rev. C 10, 739 (1974).
4. S. Katcoff and J. Hudis, Phys. Rev. C 14, 628 (1976).
5. Y. Y. Chu, E. M. Franz, G. Friedlander, and P. J. Karol, Phys. Rev. C 4, 2202 (1971).
6. See, for example, R. L. Folger, P. C. Stevenson, and G. T. Seaborg, Phys. Rev. 98, 107 (1955); J. A. McHugh and M. C. Michel, Phys. Rev. 172, 1160 (1968); A. C. Wahl, Proc. Sym. Physics and Chemistry of Fission, Salzburg, Austria, 1965.
7. See, for example, Y. W. Yu and N. T. Porile, Phys. Rev. C 7, 1597 (1973).
8. F. Plasil and M. Blann, Phys. Rev. C 11, 508 (1975).
9. G. D. Westfall et al., Phys. Rev. Lett. 37, 1202 (1976).


# FURTHER STUDIES OF LARGE COLLISION RESIDUES IN RELATIVISITIC HEAVY-ION REACTIONS WITH HEAVY NUCLEI*

W. Loveland,† R. J. Otto, D. J. Morrissey, and G. T. Seaborg

Target residue mass and charge distributions have been measured radioanalytically for the reaction of 25.2 GeV $^{12}C$ ions with Au and Pb. This investigation was carried out as a complement to a study[1] with a U target, since the interpretation of the data was expected to be more straight-forward for the case of the less fissionable Pb and Au targets.

Foils of Au and Pb (of thickness 25 and 480 mg/cm$^2$ respectively and surrounded by ~15 mg/cm$^2$ Al catcher foils) were irradiated for 162 min in a beam of 25.2 GeV $^{12}C$ ions of intensity $\sim 2.5 \times 10^{10}$ particles/ min at the Bevalac. Gamma and x-ray spectroscopic measurements of the radioactivity induced in the target and catcher foils began one hour after bombardment and continued for about three weeks. Over 75 radionuclides were identified in this work on the basis of their $\gamma$-ray energy, half-life and radiation intensity. Secondary corrections for these experiments were estimated to be <7%, based on out-of-beam monitor foil activity. Recoil losses from the target were negligibly small although enough activity was found in the Al catcher foils surrounding the Au target to measure by x-ray spectrometry forward/backward (F/B) ratios of $1.5 \pm 0.6$, $2.7 \pm 1.2$ and $1.9 \pm 1.0$ for nuclei in the Xe-Pr, Dy-Yb and Pt-W regions, respectively.

The experimentally determined independent and cumulative yields for individual radionuclides from the Au and Pb targets are shown in Figs. 1(a) and 2(a). Figures 1(b) and 2(b) depict the relative yield of species of given (Z,A) for the Au and Pb targets while Figs. 1(c) and 2(c) show the mass yield distributions. As partially shown in Figs. 1 and 2, Zp, the most probable fragment charge, moves to more neutron deficient values and the charge dispersion widths, $\sigma$, increase as the product mass decreases from A=208 to A=140. The mass yield curves for Au and Pb could be superimposed with no discernible difference except for (a) the position of the target peak and (b) the position of the steeply sloping region of the mass yield curve appears to start at A~140 for the Au target and at A~150 for the Pb target.

Also shown in Fig. 2(c) is the mass yield curve for the reaction of GeV protons with Pb as deduced from a combination of data from Friedlander[2] and Grover.[3] Comparison of the two curves shows very similar shapes for the region $40 \leq A \leq 100$, with modest enhancements of the yield of the lightest products and enhanced product yields in the $140 \leq A \leq 170$ regions in the RHI reactions. While there is no clear cut separation of fission product yields from other reaction product yields in these RHI mass distributions, one can note a relatively broad charge dispersion ($\sigma = 1.5$ Z units) for the A~100 products in the Pb mass distribution thus implying[1] an excitation energy of the fissioning system of 100 to 130 MeV.

Of most interest is the question of the origin of the enhanced product yields in the

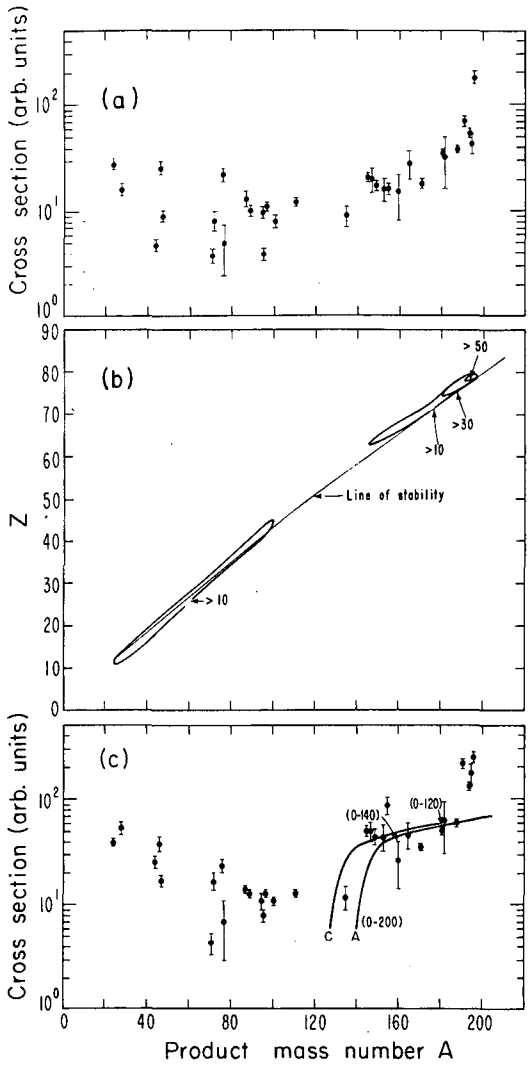


Fig. 1. (a) Independent and cumulative yield formation cross sections for individual radionuclides for the reaction of 25.2 GeV $^{12}C$ with Au. (b) Contour lines for equal independent yields. (c) Total integrated mass yields. See text for explanation of curves. The numbers along curve A in parentheses represent the excitation energy in MeV for species of a given mass.
(XBL 775-984)

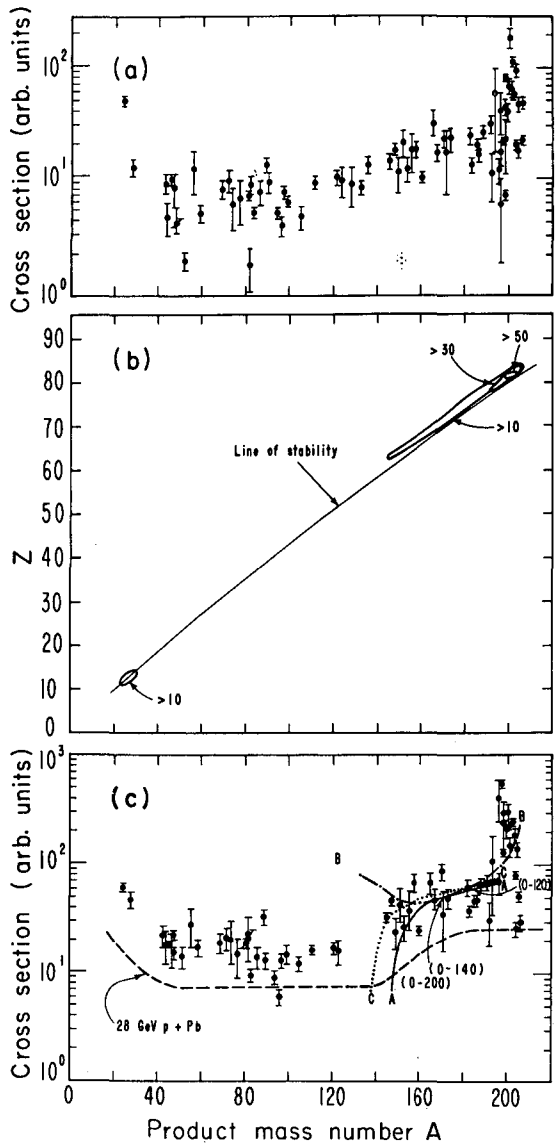


Fig. 2. Same as Fig. 1 except target is Pb. The dashed curve in Fig. 2(c) is a combination of the data of Refs. 2 and 3. The dot-dashed curve (B) represents the prediction of the abrasion-ablation model.
(XBL 775-985)

$140 \leq A \leq 170$ regions. We used a modified version of the computer code ALICE,[4] to trace the course of the neutron-fission-charged particle emission competition as the precursors of the $140 \leq A \leq 170$ products de-excited. By assuming various shapes for the initial precursor mass, charge and energy distribution, and tracing their de-excitation, we were able to set ranges on what the product distribution must have been at the end of the initial interaction-fast pre-equilibrium particle emission (i.e., pre-statistical evaporation) stage of the RHI reaction. Assuming the data are represented by curve C, such precursor distributions are shown in Figs. 1(c) and 2(c) as curve A. These precursor distributions are remarkably similar in shape to that inferred for the reaction of 25.2 GeV $^{12}C$ with U.[1] Since very different amounts of fission and neutron emission are involved in the de-excitation of products of the U, Pb, Au systems, we can now conclude, in a

relatively model independent manner, that similar mechanisms are acting in the initial interaction of RHI's with Au, Pb and U targets, and that curve A is a proper representation of the initial product distribution.

It is interesting to see what the geometrical "abrasion-ablation" ideas[5] used in the fireball model to describe the projectile-target interaction might predict for the product distribution from these reactions. Curve B in Fig. 2(c) shows the result of such a calculation for the C + Pb reaction. The agreement between the calculation and the data is reasonable except for the events with $A<150$ which result from impact parameters $b \leq 5$ fm. It will be interesting to see what success more sophisticated approaches to RHI interactions have in treating our data.

Footnotes and References

*Condensed from Phys. Lett. 69B, 284 (1977).

†Permanent address: Department of Chemistry, Oregon State University, Corvallis, OR 97331.


1. W. Loveland, R. J. Otto, D. J. Morrissey, and G. T. Seaborg, Phys. Rev. Lett. 39, 320 (1977).
2. G. Friedlander, Proc. Sym. Physics and Chemistry of Fission, Salzburg, Austria (IAEA, Vienna, 1965).
3. J. R. Grover, Phys. Rev. 126, 1540 (1962).
4. F. Plasil and M. Blann, Phys. Rev. C 11, 508 (1975).
5. J. D. Bowman, W. J. Swiatecki, and C. F. Tsang, LBL-2908 (1973).


# 2. Central Collisions

## THE NUCLEAR FIREBALL MODEL*

G. D. Westfall, J. Gosset,† P. J. Johansen,‡ A. M. Poskanzer, W. G. Meyer, H. H. Gutbrod, A. Sandoval, and R. Stock

In relativistic heavy-ion reactions both projectile fragmentation[1] and target evaporation[2] are qualitatively understood. In order to describe the emission of nucleons in the intermediate-velocity region, a very simple model is proposed consisting of a fireball, formed from the nucleons mutually swept out from the target and projectile, which decays as an ideal gas. This model uses the geometrical concepts of the abrasion model[3] and the free expansion of an ideal gas.

This "nuclear fireball" model fits the gross features of the existing data on proton inclusive spectra in this intermediate-velocity region. The agreement of this geometrical, thermodynamic model with the data presents a challenge to understand its success microscopically. The geometrical concepts of this model are illustrated in Fig. 1. It is assumed that the target and projectile are spheres with radius equal to $1.2A^{1/3}$, and that the projectile and target make clean cylindrical cuts through each other[3], leaving a spectator piece of the target and, if the impact parameter is sufficiently large, also a spectator piece of the projectile. These spectator pieces eventually lead to the products of target spallation and projectile fragmentation, which are not considered further.

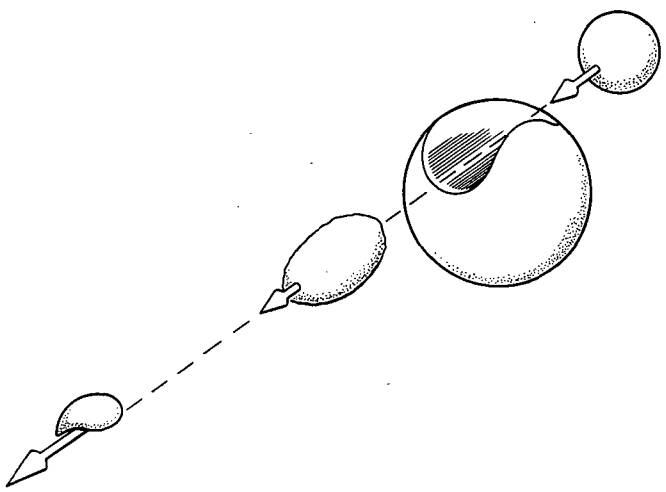

Fig. 1. In the fireball model, the target and projectile make clean cylindrical cuts through each other leaving a target spectator, and if the impact parameter is large enough, a projectile spectator. The fireball is made up from the participant nucleons mutally swept out in the primary interaction. (XBL 7610-4265)

One can calculate, as a function of impact parameter (b), the number (N) of nucleons swept out from both the projectile and target. The laboratory velocity (β) of the center of mass of the swept-out nucleons is then calculated from kinematics. In the center of mass of these nucleons, the available energy per nucleon (ε) is assumed to be their kinetic energy minus an 8-MeV binding energy. It is then assumed that the available energy in the center of mass heats up the swept-out nucleons leading to a quasi-equilibrated nuclear "fireball." The fireball is treated relativistically as an ideal gas whose temperature (τ) is determined by the available energy per nucleon. At the 250- and 400-MeV/n incident energies $\varepsilon \approx (3/2)\tau$, and one has a Maxwell-Boltzman energy distribution.

The laboratory distributions are calculated assuming isotropic decay in the rest frame of the fireball, transforming relativistically to the laboratory frame, and summing over all impact parameters. The importance of each impact parameter is given by the number of protons in the fireball times $2\pi b$. The characteristics of the fireball for the impact parameter at the maximum weight are listed in Table 1.

Table 1. Calculated properties of the fireball at the impact parameter with the maximum weight ($b_{mw}$) on a uranium target.

| Projectile | $\beta_{inc}$ | $b_{mw}$ | N | ε | τ | β |
|---|---|---|---|---|---|---|
| | (MeV/N) | (fm) | | (MeV/n) | (MeV) | |
| $^{20}$Ne | 250 | 0.61 | 4.8 | 64 | 44 | 28 | 0.22 |
| $^{20}$Ne | 400 | 0.71 | 4.8 | 64 | 74 | 47 | 0.27 |
| $^{4}$He | 400 | 0.71 | 4.7 | 25 | 51 | 33 | 0.17 |
| $^{20}$Ne | 2100 | 0.95 | 4.8 | 64 | 363 | 92 | 0.56 |

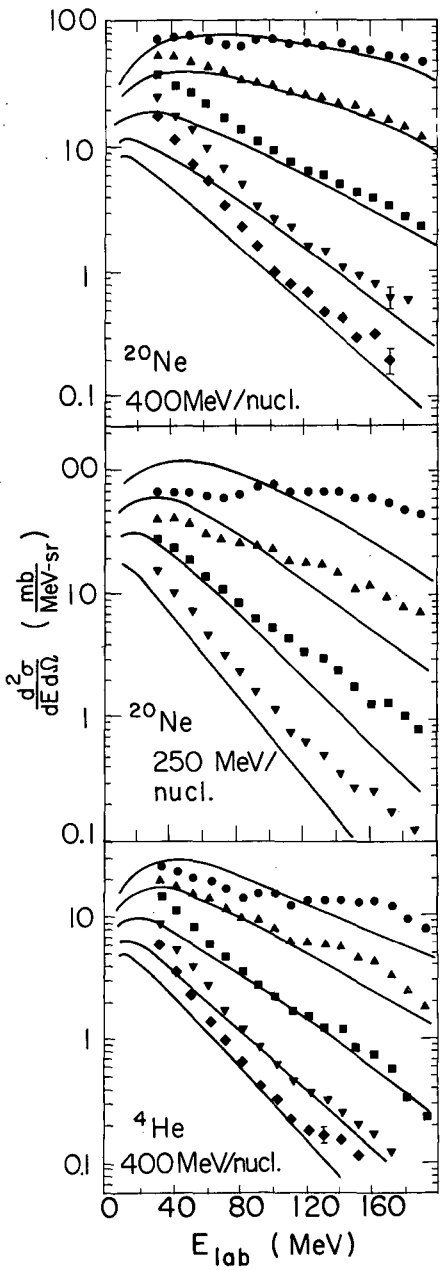


Fig. 2. Measured proton inclusive spectra at 30°, 60°, 90°, 120°, and 150° in the laboratory. For the 250-MeV/n Ne on U data, 150° was not taken. The solid lines are calculated with the fireball model. (XBL 768-3873)

The experimental proton spectra obtained in our previous experiment are shown in Fig. 2. The spectra at the lower proton energies probably include a contribution from the proton evaporation from the target residue.

Also at 250-MeV/n incident energy the most forward angle probably includes some contribution from fragmentation of the projectile residue. Considering these points, the overall agreement with the 250- and 400-MeV/n data is good. Notice that the considerably lower cross sections with the He projectile are also described and that there are no adjustable parameters in the calculation.

The above formulations were applied in the 250 and 400 MeV/n incident energy cases. However, in the case of 2.1 GeV/n incident energy, the temperature can no longer be related to the available kinetic energy through the ideal gas formulation because of the creation of baryonic resonances.[4]

The surprising success of the simple model for proton inclusive spectra indicates the importance of the use of thermodynamic concepts in relativistic heavy-ion reactions. The large number of swept-out nucleons combined with an anticipated, fairly large number of interactions per particle is presumably responsible for a quasi-equilibrated system--the fireball--which can then be described in terms of mean values and statistical distributions.

Footnotes and References

*Condensed from Phys. Rev. Lett. 37, 1202 (1976); Also see Phys. Rev. C 16, 629 (1977).

†Permanent address: Département de Physique Nucléaire et Moyenne Energie, Centre d'Etudes Nucléaires de Saclay, 91190 Gif-sur-Yvette, France.

‡Permanent Address: Niels Bohr Institute, University of Copenhagen, DK-2100 Copenhagen, Denmark.

1. D. E. Greiner, P. J. Lindstrom, H. H. Heckman, B. Cork, and F. S. Bieser, Phys. Rev. Lett. 35, 152 (1975); A. S. Goldhaber, Phys. Lett. B 53, 306 (1974); J. Hüffner, K. Schäfer, and B. Schürmann, Phys. Rev. C 12, 1888 (1975).

2. A. M. Zebelman, A. M. Poskanzer, J. D. Bowman, R. G. Sextro, and V. E. Viola, Jr., Phys. Rev. C 11, 1280 (1975); and references therein.

3. J. D. Bowman, W. J. Swiatecki, and C. F. Tsang, LBL-2908 (1973) unpublished.

4. R. Hagedorn and J. Ranft, Nuovo Cimento 6, 300 (1968).

## CENTRAL COLLISIONS OF RELATIVISTIC HEAVY IONS*

J. Gosset,† H. H. Gutbrod, W. G. Meyer, A. M. Poskanzer, A. Sandoval, R. Stock, and G. D. Westfall

A systematic study of central collisions has been undertaken. We have measured single particle inclusive spectra for the hydrogen and helium isotopes, and in another experiment, for the elements from lithium through oxygen, together with the associated multiplicity of charged particles. The projectile-target combinations studied so far are $^{20}$Ne on U at 250 MeV/n, 400 MeV/n and 2.1 GeV/n, $^{4}$He on U at 400 MeV/n, and $^{20}$Ne on Al at 2.1 GeV/n. The H and He isotopes were measured with a silicon-plastic scintillator telescope, the heavy fragments with a large area silicon-intrinsic germanium telescope, and the associated multiplicity was recorded in a fifteen-fold plastic scintillator array covering one third of the forward hemisphere.

The double differential cross sections for $^{20}$Ne on U at 400 MeV/n presented in Fig. 1 are smooth and exponentially decaying with increasing energy, being flattest for the protons and becoming steeper as the mass of the fragment increases. For a given fragment the slope of the energy spectra rapidly increases with increasing angle, and the yield of each fragment decreases as the mass or charge of the fragment increases. A deviation from this general trend is observed in the vicinity of the evaporation region where the yield is higher for $^{4}$He than for $^{3}$He. In turn, $^{3}$He exhibits a relatively more prominent high energy cross section.

For the heavier fragments at intermediate energies in Fig. 2 the slopes of the spectra also get steeper with increasing angle for each fragment. The changes of the slopes with fragment mass at a given angle are less pronounced than before, but note that here the spectra are plotted in MeV instead of MeV/n as in the case of the hydrogen and helium isotopes previously shown.

The associated multiplicities should give us a hint whether we are indeed observing near central collisions. Figure 3 shows from the 15 tag counter array the m-fold coincidence cross sections associated with three different fragments detected in the telescope at 90°. For all fragments the average multiplicity is large reflecting quite a large transverse momentum transfer since the tag array is sensitive to particles like protons above 50 MeV.

In summary the qualitative features of the data are:

1) All light fragment energy spectra are smooth except for an "evaporation peak" at very low energies.

2) The most neutron deficient isotopes exhibit spectra with a relatively higher cross section in the high energy tail.

3) The slope of the fragment spectra in the intermediate energy range gets steeper with increasing detection angle. Angular distributions are forward peaked.

4) The double differential cross sections for Ne on U at 30° are approximately independent of the incident energy for a given fragment. At larger angles the yield increases and the slope decreases with increasing bombarding energy.

5) The slope of the fragment spectra in energy/nucleon at a given angle gets steeper with increase in fragment mass.

6) The total yields of light fragments fall off with increase in mass. At energies of 30 to 50 MeV/n cluster emission comprises a significant

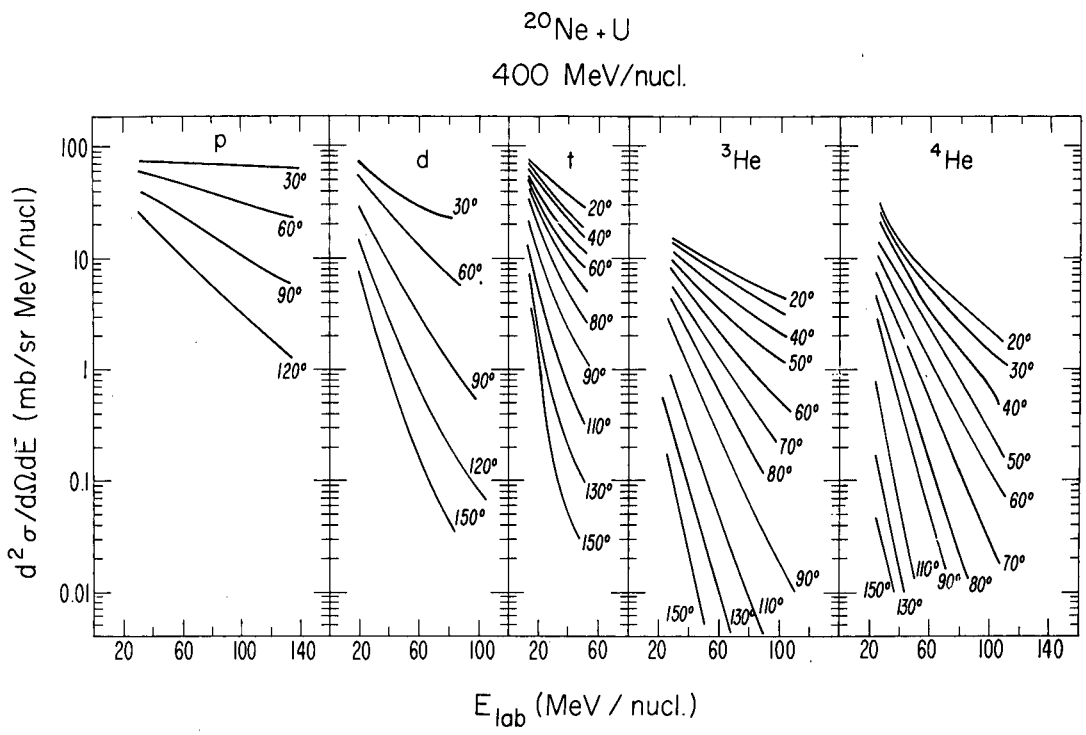


Fig. 1. Double differential cross sections of light fragments emitted from the irradiation of uranium with $^{20}$Ne ions at 400 MeV/n (XBL 771-71)

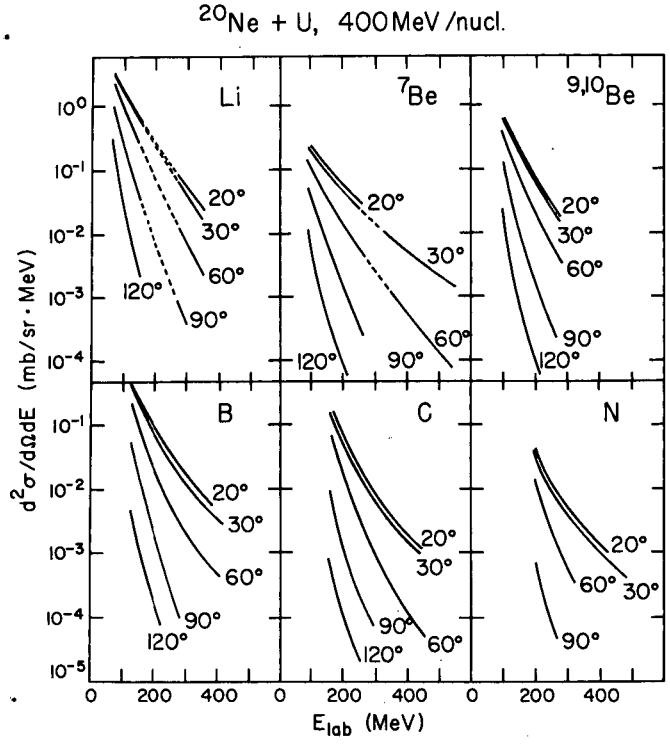


Fig. 2. Double differential cross sections for the heavy fragment production for Ne on U at 400 MeV/n. (XBL 771-218)

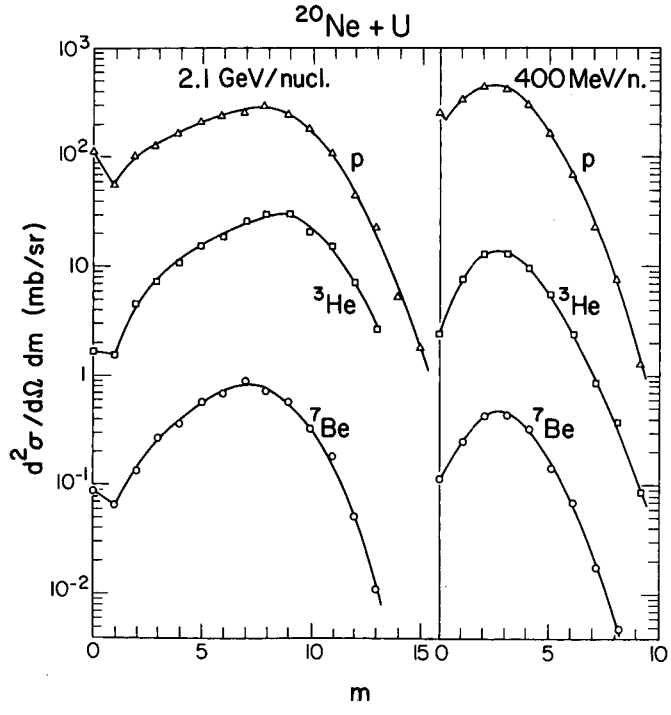


Fig. 3. Comparison of the 90° charged particle coincidence distributions associated with different fragments for two bombarding energies of Ne on U. (XBL 773-694)

fraction (about 50%) of the total baryonic cross section. Towards higher energies protons become predominant.

7) Increasing the projectile mass at a fixed incident energy per nucleon leads to a small increase in the cross section for low energy fragments but to a larger increase at high fragment energies, especially for the heavier clusters.

8) In Ne bombardment of U and Al targets, besides the differences in overall absolute cross section, one finds for Al a depletion of cross section at back angles.

9) For all particles detected at angles between 20° and 160° the mean associated multiplicity is high and not changing remarkably with fragment mass or energy.

10) The mean associated multiplicity increases with the projectile mass and with the target mass.

11) Large angle emission of energetic fragments is enhanced in high multiplicity events.

In Fig. 4 the $^3$He invariant cross sections have been plotted as contour lines in a diagram of perpendicular momentum per nucleon vs. fragment rapidity for three bombarding energies. It is clear that at these $^3$He energies their sources are neither the target nor the projectile but are at intermediate rapidities. Also, it is not a single source, since the more energetic fragments come from a faster moving system.

The proton double differential cross section at the lower bombarding energies can be very well described as being due to the decay of a nuclear fireball (see preceding contribution). The composite particles have been interpreted as due to final state interaction of the nucleons from the fireball decay which coalesce into heavier fragments.[1] Recently it has been proposed[2] that they can be produced in the fireball itself in a chemical equilibrium between the various species.

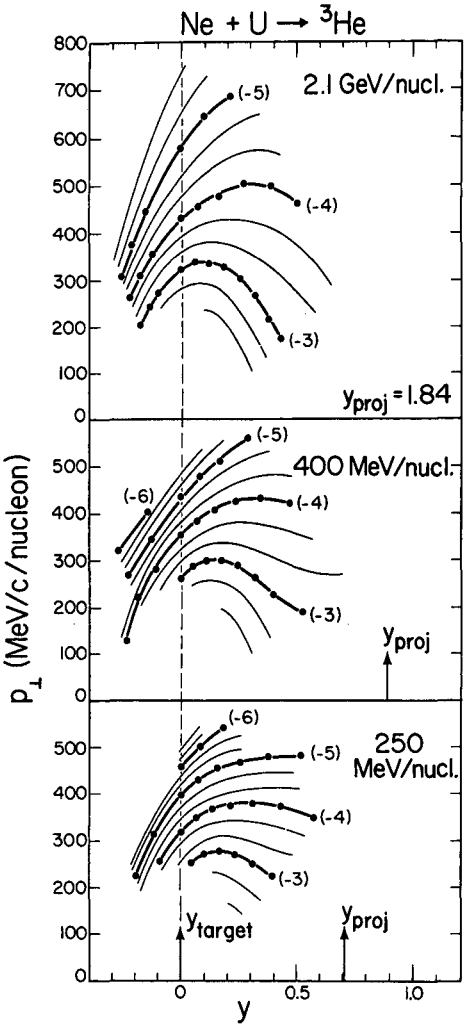


Fig. 4. Contours of constant $^3$He invariant cross section in the (y, $P_\perp$) plane. $P_\perp$ is the $^3$He perperdicular momentum per nucleon, y is the rapidity defined as $y = 1/2\ \ell n[(E + p_\parallel)/(E - p_\parallel)]$. The thick lines are labeled by the power of the invariant cross-section magnitude. (XBL 775-926)

Footnotes and References

*Condensed from Phys. Rev. C 16, 629 (1977).

†Permanent Address: Département de Physique Nucléaire et Moyenne Energie, Centre d'Etudes Nucléaires de Saclay, 91190 Gif-sur-Yvette, France.

1. H. H. Gutbrod, A. Sandoval, P. J. Johansen, A. M. Poskanzer, J. Gosset, W. G. Meyer, G. D. Westfall, and R. Stock, Phys. Rev. Lett. 37, 667 (1976).

2. A. Mekjain, Phys. Rev. Lett. 38, 640 (1977).

# FURTHER STUDIES OF COLLISIONS OF RELATIVISITIC HEAVY IONS

J. Gosset,* H. H. Gutbrod, Ch. Lukner, W. G. Meyer, A. M. Poskanzer, A. Sandoval, R. Stock, and G. D. Westfall

A second series of measurements have begun to study large momentum transfer in central collisions[1] between relativistic heavy ions and light, medium, and heavy target nuclei. The goal of the experiment is to investigate the reaction mechanism; to determine whether hot, dense nuclear matter is created and hopefully to gather information about the equation of state of finite nuclear systems. To accomplish this goal, we are measuring angular distributions (20° to 160°) and energy spectra of $\pi^+$, p, d, and t produced in the target and intermediate rapidity regions (i.e., 17-100, 5-200, 6-250, and 7-300 MeV, respectively). Several combinations of projectiles of p, $^4$He, $^{20}$Ne, $^{40}$Ar with targets of Al, Ca, Ag, and U at projectile velocities of 0.1, 0.25, 0.40, 1.05, and 2.1 GeV/n are being studied.

The $\pi^+$, p, d, and t reaction products are identified by their energy loss in a five element silicon-germanium telescope. For each particle detected in the telescope, the multiplicity of charge particles produced in the interaction is determined by recording the coincidences between the telescope and any of the members of the 80 counter tag array (shown schematically in Fig. 1).

The tag counter array consists of 80 6-mm thick plastic scintillators (Pilot B) coupled to 80 photomultiplier tubes by means of lucite light pipes. The counters are mounted symmetrically around the outside of a one meter diameter spherical scattering chamber with 3-mm thick aluminum walls, as shown in Fig. 1. The tag counters cover 40% of 4 $\pi$ and are sensitive to charged particles from 25 MeV/n up to minimum ionizing.

The five element particle telescope (Fig. 2) consists of a 150 μm phosphorous diffused silicon detector, a 5-mm lithium drifted silicon detector, a 7-cm intrinsic germanium detector (consisting of two germanium crystals with thicknesses in the fragment direction of 2.8 and 4.2 cm), and a

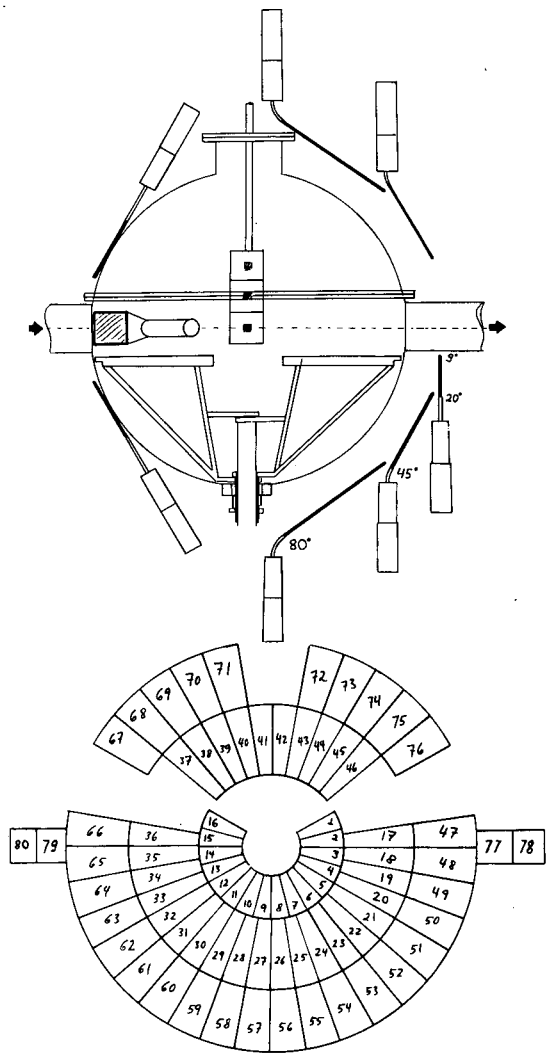


Fig. 1. Schematic of the 1 m diameter spherical scattering chamber. Lower section shows the arrangement of the 80 plastic scintillators as seen looking down the beam pipe. (XBL 776-9100)

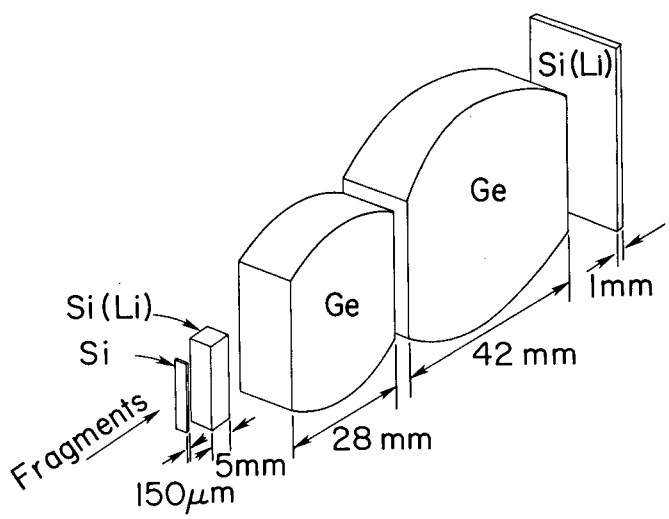


Fig. 2. Silicon-germanium telescope. The germanium detectors are in an isolated vacuum at LN temperature. The silicon detectors are at -20° C. (XBL 778-1638)

1-mm lithium drifted silicon E reject detector. The 150-μm and 5-mm silicon detectors are used to measure p, d, and t up to energies of 30, 40, and 50 MeV respectively with a solid angle of 0.55 msr. The 5-mm silicon and 7-cm germanium detectors are used to measure $\pi^+$, p, d, and t up to energies of 100, 200, 250, and 300 MeV respectively with a solid angle of 0.94 msr. A silicon ΔE-E monitor telescope is permanently affixed to the inner wall of the chamber and is designed to measure low energy alpha particles and is used for relative normalization of the data.

The $\pi^-$'s which stop in the particle telescope produce stars and are not useful. In order to produce clean $\pi^+$ spectra, use is made of the $\pi^+$ decay to a $\mu^+$ and the subsequent decay of the muon to a positron. A delayed coincidence between the $\pi^+$ and the $e^+$ is used to tag each positive pion that stops in the telescope. A delayed coincidence decay curve exhibiting the 2.2 μsec mean life expected is shown in Fig. 3.

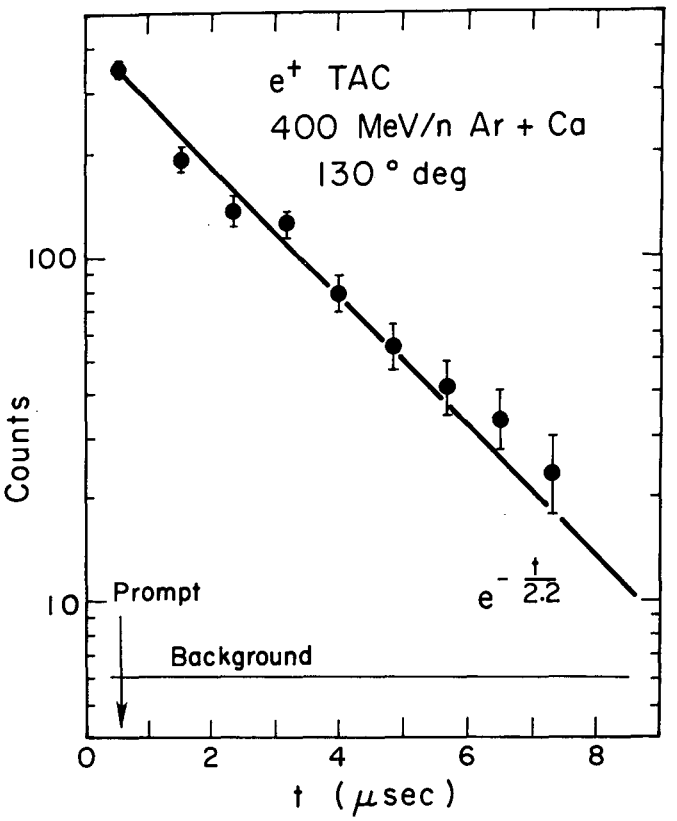


Fig. 3. Observed delayed coincidence curve showing the expected 2.2 μsec mean life used for identifying the positive pions. (XBL 778-1637)

Footnote and Reference

*Present address: Département de Physique Nucléaire et Moyenne Energie, Centre d'Etudes Nucléaires de Saclay, 91190 Gif-sur-Yvette, France.

1. J. Gosset, H. H. Gutbrod, W. G. Meyer, A. M. Poskanzer, A. Sandoval, R. Stock, and G. D. Westfall, Phys. Rev. C 16, 629 (1977).

## STUDY OF CENTRAL COLLISIONS PRODUCED BY RELATIVISTIC HEAVY IONS IN NUCLEAR EMULSION*

H. H. Heckman, H. J. Crawford,† D. E. Greiner, P. J. Lindstrom, and Lance W. Wilson

We have performed an experimental study on the angular and momentum distributions of fragments emitted from central collisions between emulsion nuclei (AgBr) and heavy-ion projectiles $^4$He, $^{16}$O, and $^{40}$Ar at beam rigidity 5.72 GV. The criterion we have adopted for a central collision is that it exhibits an absence of projectile fragmentation, i.e., no beam-velocity fragments ($Z_F \geq 1$ from $^4$He interactions, $Z_F \geq 2$ from $^{16}$O and $^{40}$Ar interactions) are produced within 5° of the incident beam direction.

Production angles have been measured for all fragments having a restricted grain density $g \geq 2\ g_{min}$, corresponding to $E \leq 250$ MeV/A for singly-charged particles. Both range and angle measurements have been made for fragment ranges $\leq 4$ mm, equivalent to E = 31 MeV/A for protons (and $^4$He). The experimental data are analyzed in terms of a modified Maxwell-Boltzmann velocity distribution, from which estimates of the longitudinal velocity $\beta_\parallel$ and the characteristic spectral velocity $\beta_o$ of the particle-emitting systems, are made. This distribution, expressed in a covariant, nonrelativistic form, is:

$$d^2N/d\beta d\mu \propto \beta^2 e^{-(\beta^2 - 2\beta_\parallel \beta\mu)/\beta_o^2},$$

where $\beta$ = fragment velocity, obtained from the proton range-energy relation for emulsion, and $\mu = \cos\theta$, where $\theta$ is the production angle of the fragment. The equivalent temperature of the system is given by $\tau(\text{MeV/A}) = M_p/2\ \beta_o^2$, where $M_p$ is the proton mass.

Tabulated in Table 1 are the range-velocity parameters $B_\parallel$ and $\beta_o$, and the quantity $\chi_o = \beta_\parallel/\beta_o$ evaluated therefrom, obtained by least-square fits

Table 1. Range-velocity parameters $\beta_{\parallel}$, $\beta_o$, and $\chi_o = \beta_{\parallel}/\beta_o$ vs. range interval for R ≤ 4 mm. ε is the proton energy corresponding to range R.

| RANGE (mm) | ε (MeV) | | $^4$He | $^{16}$O | $^{40}$Ar |
|---|---|---|---|---|---|
| | | $\beta_{\parallel}$ | 0.016 ± 0.004 | 0.015 ± 0.002 | 0.012 ± 0.002 |
| 0 - 4 | 0 - 31 | $\beta_o$ | 0.117 ± 0.002 | 0.115 ± 0.002 | 0.117 ± 0.002 |
| | | $\chi_o$ | 0.14 ± 0.04 | 0.13 ± 0.02 | 0.10 ± 0.02 |
| | | $\beta_{\parallel}$ | 0.010 ± 0.002 | 0.012 ± 0.002 | 0.014 ± 0.004 |
| 0 - 1 | 0 - 14 | $\beta_o$ | 0.105 ± 0.003 | 0.104 ± 0.003 | 0.110 ± 0.003 |
| | | $\chi_o$ | 0.10 ± 0.02 | 0.11 ± 0.02 | 0.13 ± 0.04 |
| | | $\beta_{\parallel}$ | 0.030 ± 0.011 | 0.016 ± 0.005 | 0.016 ± 0.003 |
| 1 - 4 | 14 - 32 | $\beta_o$ | 0.169 ± 0.015 | 0.122 ± 0.004 | 0.143 ± 0.012 |
| | | $\chi_o$ | 0.18 ± 0.07 | 0.13 ± 0.04 | 0.11 ± 0.02 |

of the range and angle data to Eq. 1. The results show that as the range, hence energy, of the fragment increases, both $\beta_{\parallel}$ and $\beta_o$ increase. The ratio $\chi_o$, however appears to remain constant, all values being compatible with a mean value $\langle \chi_o \rangle$ = 0.11 ± 0.01. The longitudinal velocities of the particle-emitting system, $\beta_{\parallel}$, are typically 0.01 - 0.03, and within the accuracy of the measurements, independent of projectile. The values of $\beta_{\parallel}$ observed here are equal to those measured for low-energy fragment-emitting systems produced in proton-nucleus collisions over a broad range of energies.[1] We also point out that the temperatures τ implied by the velocities $\beta_o = \sqrt{2\tau/M_n}$ are typically 6 to 7 MeV/A, characteristic of the binding energies of nuclei and also compatible with the temperatures associated with projectile fragmentation.[2,3]

Fig. 1 presents the range-angle data in terms of the rapidity variable, $y \approx \beta_L$, where $\beta_L$ is the longitudinal component of the quantity $\vec{\beta}$. The mean value $\langle y \rangle \approx \beta_{\parallel}$ is indicated for each distribution, as is the standard deviation $\sigma_y = \beta_o/\sqrt{2} = \sqrt{\tau/M_p}$. The cutoff values of y at R = 4 mm are ± 0.260, which are indicated by the arrows in the figure. The average standard deviation of the three rapidity distributions is $\langle \sigma_y \rangle$ = 0.082 ± 0.001, corresponding to a longitudinal momentum $P_L$ = 77 MeV/c per nucleon.

The angular distributions observed for fragments with energies $E_p$ < 31 MeV produced by each of the incident projectiles, are shown in Fig. 2. The distributions are presented as functions of both θ and cos θ. Drawn through the data are curves derived from the fitted Maxwell-Boltzmann

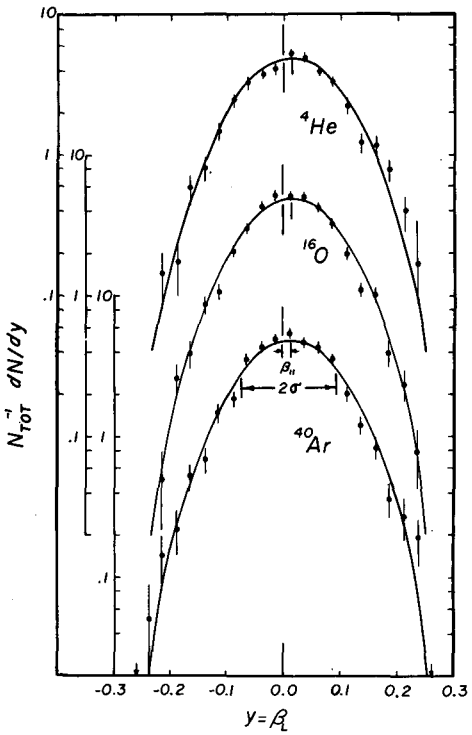


Fig. 1. Rapidity distributions $y = \beta_L$ of fragments with ranges R ≤ 4 mm, assuming $m/z^2 = 1$. Cut off valves of $\beta_L$ = 0.26 are indicated by the arrows on the abscissa. Values of $\beta_{\parallel}$ and $\beta_o = \sqrt{2}\sigma$ are given in Table 1, $E_{beams}$ = 2.1 (1.8) GeV/A. (XBL 778-1645)

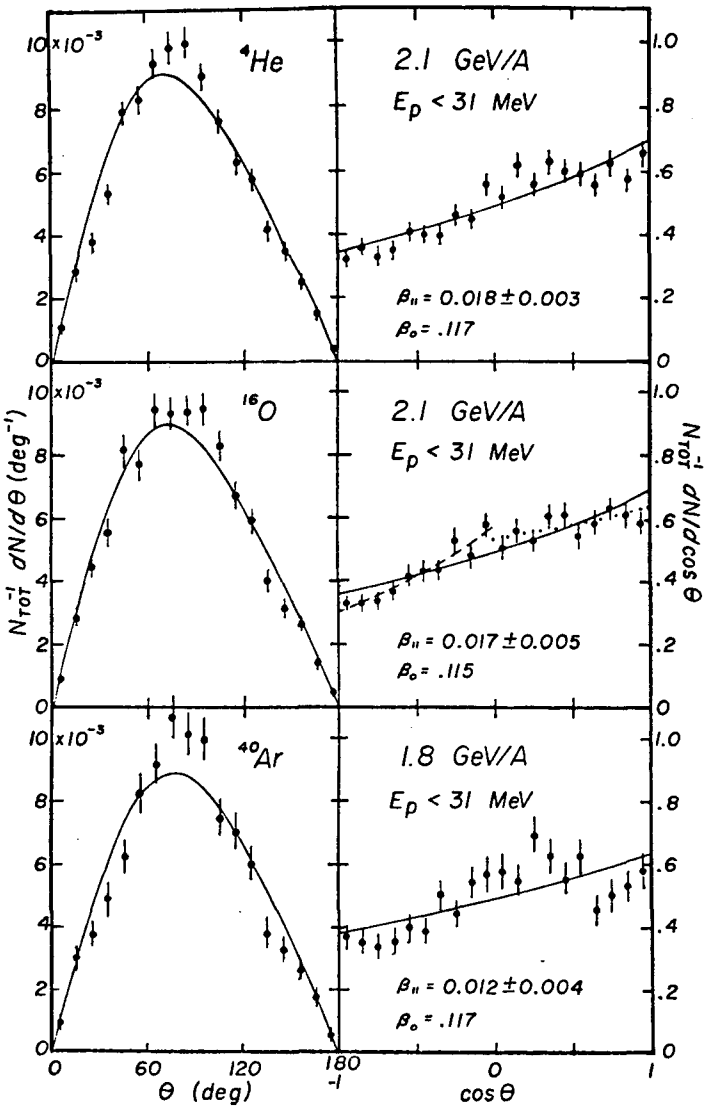


Fig. 2. Angular distributions for fragments, $E_p$ < 31 MeV. Solid curves are fits of the data to Eq. (1), $-1 \leq \cos\theta \leq 1$, using the parameters indicated. The dashed and dotted curves are fits to the data, for the backward and forward hemispheres, respectively. (XBL 778-1646)

distributions. In the case of the $^{16}$O data, the fits to the data in the backward and forward hemispheres are indicated, which illustrates that the distributions of dN/dcos θ consistently show greater isotropy in the forward, relative to backward, hemisphere.

Similar observations are made from the angular distributions for higher energy fragments, i.e., $E_p$ <250 MeV. Notable differences between the angular spectra for low energy ($E_p$< 31 MeV) and the high energy ($E_p$ < 250 MeV) fragments are evident, however. For example, the maxima in the dN/dθ distributions occur at smaller angles as the fragment energy increases, and the angular distributions clearly show a dependence on the mass of the projectile.

We obtain no evidence in this experiment for structure in either range or angular distributions of fragments emitted from non-peripheral collisions between 2 GeV/n, $^4$He, $^{16}$O, and $^{40}$Ar projectiles and heavy emulsion nuclei. We also find there is no unique Maxwellian distribution that successfully describes both the angular and momentum distributions of the observed fragments, hence no unique particle-emitting system characterized by a longitudinal velocity $\beta_{\parallel}$ and spectral velocity $\beta o = \sqrt{2\tau/M_p}$.

Footnotes and References

*Condensed from LBL-6561.

†University of California Space Sciences Laboratory, Berkeley, California.

1. E. K. Hyde, G. W. Butler, and A. M. Poskanzer, Phys. Rev. C 4, 1759 (1971).

2. D. E. Greiner, P. J. Lindstrom, H. H. Heckman, Bruce Cork, and F. S. Bieser, Phys. Rev. Lett. 35, 152 (1975).

3. A. S. Goldhaber, Phys. Lett. 53B, 306 (1974).

## INCLUSIVE PROTON AND PION SPECTRA AT LARGE ANGLES IN RELATIVISTIC HEAVY-ION COLLISIONS

S. Nagamiya, I. Tanihata, S. R. Schnetzer, W. Brückner, L. Anderson, G. Shapiro, H. Steiner, and O. Chamberlain

Proton and negative pion inclusive spectra were measured with a magnetic spectrometer at laboratory angles from 15 to 145° in collisions of 800 MeV/n C on C and Pb and of 800 MeV/n Ne on NaF, Cu and Pb. Pions of energies from 50 MeV to 1 GeV and protons from 50 MeV to 2 GeV were analyzed.

Typical results are shown in Figs. 1 and 2, where particle energy distributions in the carbon-

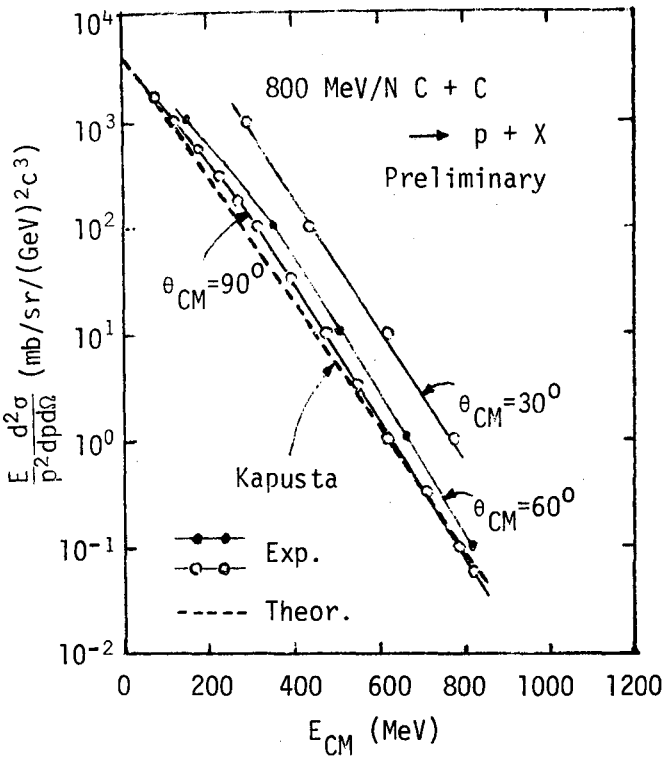


Fig. 1. Observed energy distribution of protons in the CM frame, as compared with theoretical prediction. (XBL 778-2699)

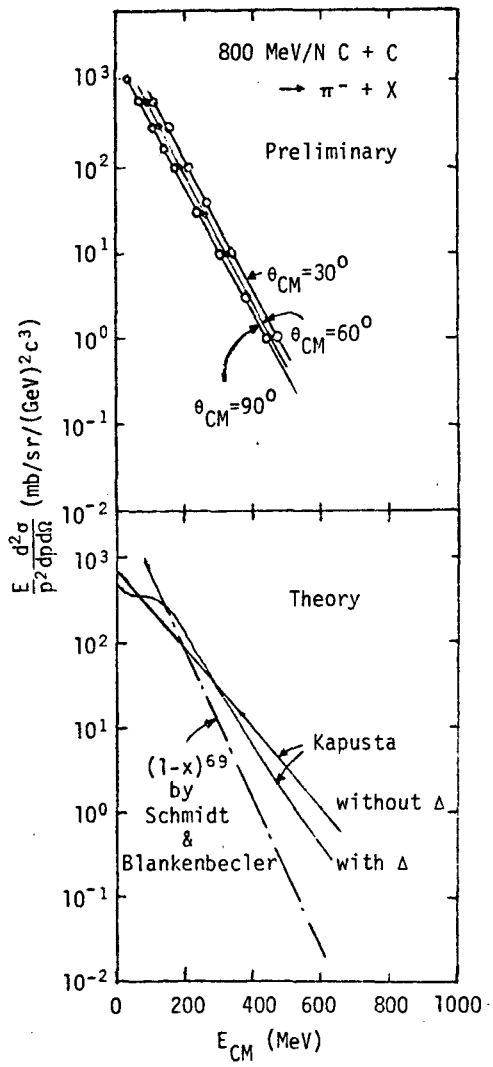


Fig. 2. Pion inclusive spectra in the c.m. frame (upper), compared with two theoretical curves (lower). (XBL 778-2700)

carbon center-of-mass frame are plotted. For protons the yield is higher for smaller c.m. angles, showing forward and backward peaking, while the yield for pions is close to isotropic in that frame. In Fig. 1 the proton yield is compared with a theory by Kapusta[1] which is an extended fireball model[2] calculation by including a pion degree of freedom. The theory explains the spectrum for θ(CM)=90°, but there is a significant deviation for smaller c.m. angles. Two theories are compared with the pion data, as shown in Fig. 2; one by Kapusta of fireball model and the other a very simple formula of $(1-x)^{69}$ proposed by Schmidt and Blankenbecler[3] based on a parton model of hadrons, where x is the scaling variable defined by $x \equiv k^*/k^*_{max}$. Comparison with other theories are now under study.

Although they are very preliminary, the following observations can be made:

1) We have prepared 5 sets of counter telescopes arranged in azimuthally symmetric way. When events are selected in which several high-energy protons (> 200 MeV) count in the telescopes, the cross section seems to fall less steeply with energy than in the inclusive case.

2) Except for very low energy pions, energy spectra of pions at a given laboratory angle seem to be almost independent of target. Pion production is roughly proportional to $A_T^{2/3}$ in the energy range below 1 GeV.

3) Proton yield in the laboratory frame is about proportional to $A_T^{2/3}$ at θ(lab) = 15°, but it becomes proportional to $A_T$ at 70°, and the yield ratio between targets exceeds $A_T$ at 145°.

References

1. J. I. Kapusta, private communication (1977).

2. G. D. Westfall et al., Phys. Rev. Lett. 37, 1202 (1976).

3. I. A. Schmidt and R. Blankenbecler, SLAC-PUB-1881 (1977).

## MULTIPION PRODUCTION BY RELATIVISTIC HEAVY IONS

Bruce Cork, H. H. Heckman, F. S. Bieser,* H. J. Crawford,* P. J. Lindstrom, and D. E. Greiner

If high energy heavy ions produce superdense matter, one decay scheme may be by the production of a large number of charged and neutral pions. Since the production of this state may depend critically on the mass of the two interacting systems, as well as the relativistic momentum, a whole family of experiments may be required to set limits on the multipion process, and to distinguish it from the simple nucleon-nucleon pion production process.

Experiment 271H is an experiment designed to select multipion production events by counting only high velocity reaction products. An array of 18 water Cherenkov counters is mounted in a duo-decahedron that surrounds a production target, typically a 1/2-in. long $^{238}U$ target. The initial experiment has had 400 and 900 MeV/n $^{40}A$ ions incident on various targets.

The pulse height of each of the 18 counters is digitized and recorded on a PDP 11/45 computer and the system is triggered on a preselected trigger coincidence rate, typically 2 to 5 coincidences.

The water Cherenkov counter detects charged particles of $\beta > 0.75$, and a lucite Cherenkov detector detects particles of $\beta > 0.67$. Table 1 gives the energy, momentum, velocity, and range of various values for electrons, muons, pions, and protons.

The initial experiment in February 1977, allowed us to adjust the gain of the Cherenkov counters and calibrate the pulse height with 900 MeV protons. The calibration was done with each of the 18 water Cherenkov counters placed directly in the proton beam. The counters were

Table 1. Energy momentum β range of various charged particles.

| Electrons | | | | Pions | | | | Protons | | | | Muons | | | |
|---|---|---|---|---|---|---|---|---|---|---|---|---|---|---|---|
| T MeV | P MeV/e | β | Range g/cm | T MeV | P MeV/e | β | Range g/cm | T MeV | P MeV/e | β | Range g/cm | T MeV | P MeV/e | β | Range g/cm |
| 1 | | | 0.4 | 41 | 100 | 0.60 | 9 | 5.3 | 100 | | 0.1 | 20 | 68 | 0.54 | 5 |
| 10 | 11 | 1 | 5. | 50 | 130 | 0.67 | 17 | 47 | 300 | | 5 | 30 | 86 | 0.62 | 10 |
| 20 | | | 10 | 58 | 140 | 0.71 | 20 | 80 | 400 | 0.4 | 70 | 40 | 100 | 0.69 | 15 |
| 30 | | | ∿20 | 80 | 175 | 0.78 | 40 | 100 | | | | 50 | 115 | 0.74 | 20 |
| | | | | 100 | 200 | 0.81 | 50 | 310 | 850 | 0.67 | 110 | | | | |
| | | | | 180 | 290 | 0.90 | | 430 | 1000 | 0.72 | 180 | | | | |
| | | | | | | | | 470 | 1050 | 0.75 | 200 | | | | |
| | | | | | | | | 600 | 1230 | 0.78 | 300 | | | | |
| | | | | | | | | 1000 | 1700 | 0.88 | | | | | |
| | | | | | | | | 1100 | 1800 | 0.89 | | | | | |
| | | | | | | | | 1250 | 2000 | 0.90 | | | | | |

then installed in the duo-decahedron array and various targets were bombarded with 400 MeV/n $^{40}A$.

The solid angle of the detectors during the experiment was approximately $0.3 \times 4\pi$. The system was adjusted to trigger on two or more counters giving a pulse greater than 0.075 V, compared to a 1 GeV proton of 0.500 V. The spectrum of pulses from the various Cherenkov counters was observed, with good statistics, and a wide range of pulse heights was observed, with many small pulses, 0.030 V; and a few percent of the pulses with 1.0 V.

In a separate experiment, the large background is explained as due to Compton electrons from high energy gamma rays. This background could be reduced by requiring the detection of an energetic charged particle in a second scintillator or Cherenkov counter telescope. However, the detectors necessary for this modification have not been built.

In spite of the large background, an upper limit on the cross section for production of more than 12 charged pions by 400 MeV/n $^{40}Ar$ incident on $^{238}U$ is 10 microbarns per nucleus. Also 900 MeV/n $^{40}A$ incident on $^{238}U$ was observed to have an upper limit of 10 microbarns per nucleus for production of more than 30 charged pions per interaction.

The addition of a scintillation counter in coincidence with each Cherenkov counter would probably reduce the background by an order of magnitude.

Footnote

*University of California Space Sciences Laboratory, Berkeley, California.

## INCLUSIVE CROSS SECTIONS FOR LOW-ENERGY PION PRODUCTION IN HIGH-ENERGY NUCLEUS-NUCLEUS COLLISIONS

K. Nakai,* J. Chiba,* I. Tanihata, S. Nagamiya, H. R. Bowman, J. Ioannou, and J. O. Rasmussen

Doubly differential cross sections for low-energy ($20 < T_\pi < 100$ MeV) $\pi^+$ production in bombardments of 800-MeV/n $^{20}Ne$ beams on Pb, Cu and NaF targets ($\sim 1$ g/cm$^2$) were measured. We used a multielement pion-range-telescope for detection of $\pi^+$, consisting of a stack of eight plastic scintillators. The stopped $\pi^+$ was identified by detecting a delayed-pulse due to the $\pi^+ \to \mu^+$ decay. When a pion comes in and stops in one of the scintillators, a double pulse appears in that scintillator, one due to a $\pi^+$ followed by the second pulse due to a $\mu^+$. We took both timing (of the delayed pulse) and pulse-height information from each element and stored these on magnetic tapes event-by-event. In off-line analyses we found that we had much redundancy in identifying pions by analyzing both time and pulse-height spectra, and were able to measure pion yields even at forward angles where backgrounds due to accidental coincidences of protons were large.

The cross sections obtained are shown in Fig. 1. The data were corrected for the following effects: 1) $\pi^+$ decay in flight, 2) multiple scattering of $\pi^+$ in the scintillator and absorbers, 3) $\pi^+$-nucleus reaction in the scintillators, 4) detector edge effect and 5) target thickness.

The results are preliminary, and overall uncertainties may be as large as 40 to 50 percent. Nevertheless we were able to deduce the following significant results.

Experimental cross sections for three targets are compared with calculated cross sections in the figure. Assuming no coherence among nucleons in the projectile $^{20}Ne$ we calculated the cross sections using experimental data[1] for $p + A \to \pi^\pm + X$ at Ep = 730 MeV,

$$\left(\frac{d^2\sigma}{dEd\Omega}\right) = Z_{proj}\left(\frac{d^2\sigma}{dEd\Omega}\right)_{p + A \to \pi^+ + X} + N_{proj}\left(\frac{d^2\sigma}{dEd\Omega}\right)_{n + A \to \pi^+ + X} . \quad (1)$$

The second term may be replaced with $\left(\frac{d^2\sigma}{dEd\Omega}\right)_{p + A \to \pi^- + X}$ assuming charge symmetry.

However, for target nuclei with $N_{target} \neq Z_{target}$ we need an additional factor $\left(\frac{Z}{N}\right)^2_{target}$.

$$\left(\frac{d^2\sigma}{dEd\Omega}\right) = Z_{proj}\left(\frac{d^2\sigma}{dEd\Omega}\right)_{p + A \to \pi^+ + X} + N_{proj}\left(\frac{Z}{N}\right)_{target}\left(\frac{d^2\sigma}{dEd\Omega}\right)_{p + A \to \pi^- + X} . \quad (2)$$

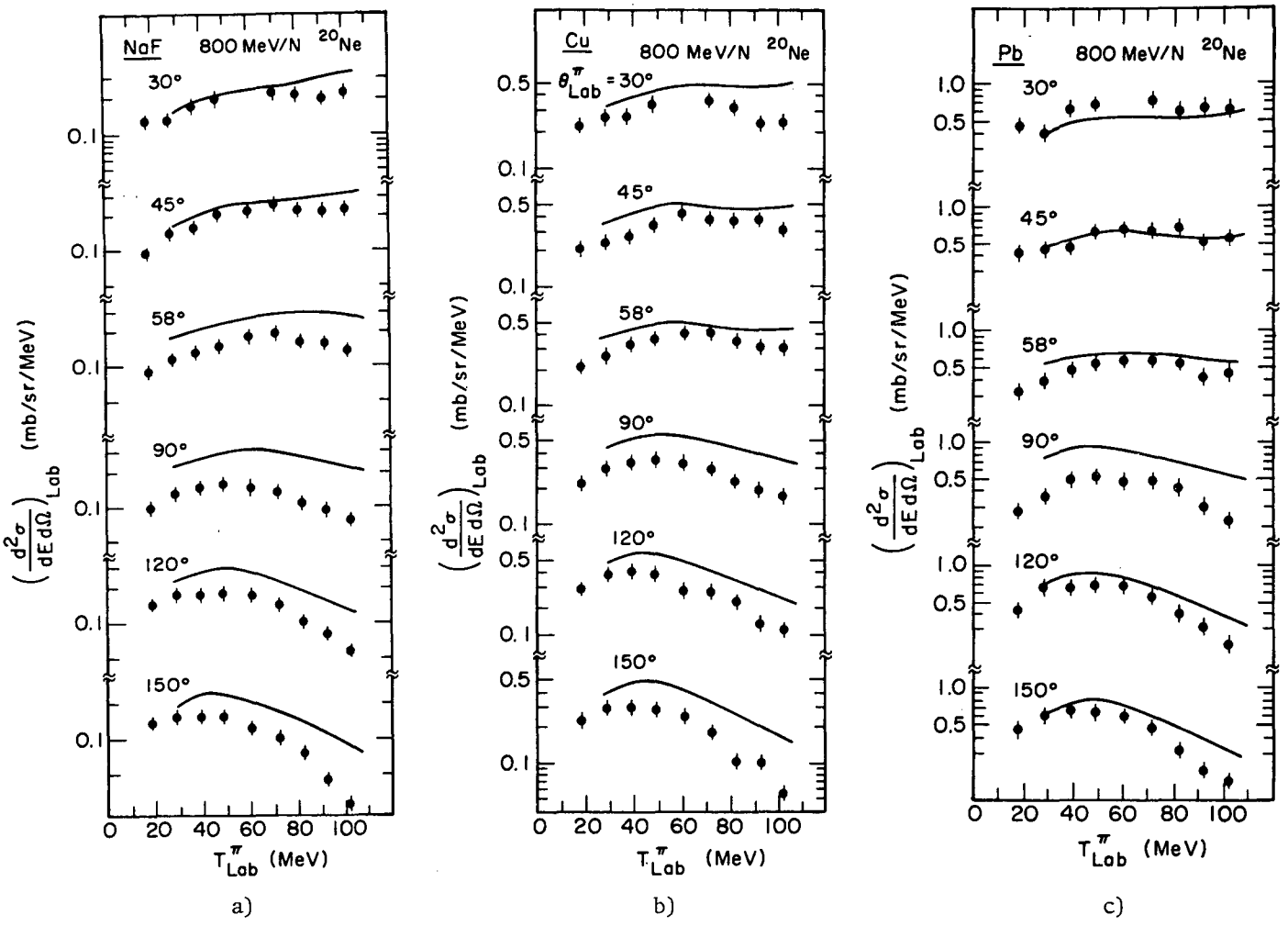


Figs. 1a,b,c. Doubly differential cross sections for pion production in bombardments of 800 MeV/n $^{20}$Ne beams on NaF, Cu and Pb targets. The solid curves are "incoherent" pion production cross sections calculated from experimental data for $p + A \rightarrow \pi^+ + X$.
[(a) XBL 7710-10281; (b)7710-10280; (c) 7710-10279]

The calculated cross sections are shown with solid curves in Fig. 1. Surprisingly good agreement was obtained between experimental and calculated cross sections without normalization, particularly for Pb and Cu targets at large angles. The agreement implies that those pions emitted in backward directions were produced incoherently and are not from a thermally-equilibrated system. The agreement is relatively poor for the NaF target. In this calculation, effects of pion absorption, scattering, and charge exchange in the target nucleus were included atuomatically by using the experimental (p + nucleus) cross sections. However, such effects in the projectile nucleus were neglected. The approximation would therefore be good when the projectile nucleus is much smaller than the target.

We noticed that at forward angles ($\theta_{lab}$ = 30° and 60°) the measured pion yields were higher than those calculated. These excess pions, being specific to the heavy-ion reactions, are of special interest and will be further investigated.

Footnote and References

*Dept. of Physics, University of Tokyo, Bunkyo-ku, Tokyo.

1. Cochran et al., Phys. Rev. D 6, 3085 (1972).

2. This factor may be between $\left(\frac{Z}{N}\right)$ target and $\left(\frac{Z}{N}\right)^{2/3}$ target depending upon relative contributions of direct and indirect (charge exchange) processes. Since the contribution of the first term in Eq. (2) is much larger than the second, the uncertainty in this factor is not so important in this rather crude comparison.

# NEGATIVE PION PRODUCTION IN RELATIVISTIC HEAVY-ION COLLISIONS*

S. Y. Fung,† W. Gorn,† G. P. Kiernan,† F. F. Liu,‡ J. J. Lu,† Y. T. Oh,§ J. Ozawa,‖ R. T. Poe,† L. Schroeder, and H. Steiner

In the study of relativistic heavy-ion collisions, considerable interest has been focused on the production of pions. Theoretical speculations[1-5] on the occurrence of exotic phenomena such as nuclear collective effects, shock waves, or quark matter production[5] all predict pion production significantly greater than what is expected from an aggregate of individual nucleon-nucleon collisions. The study of pion production in heavy-ion collisions will also shed light on less exotic but equally important questions such as multiple scattering and thermalization processes in nuclear matter.

A series of runs utilizing the LBL streamer chamber to investigate some of the characteristics of pion production in nucleus-nucleus collisions has been performed. The streamer chamber offers the advantage of $4\pi$ geometry, the capability of being triggered on selected events of interest, and very high multiple track efficiency (events with over 125 charged tracks have been observed). Results are presented from 20 sets of runs with an $^{40}Ar$ beam at 0.4 GeV/n, 0.9 GeV/n, and 1.8 GeV/n, and a $^{12}C$ beam at 0.4 GeV/n and 2.1 GeV/n, incident on targets of LiH, NaF, $BaI_2$, and $Pb_3O_4$. Each run consisted of ∿2000 pictures with the chamber triggered in the "inelastic mode," a trigger condition which rejects most non-interesting events but is relatively unbiased for inelastic events. Figure 1 shows an example of a very high multiplicity event.

Scanning for negative tracks yielded predominantly negative pions. We estimate that electron contamination from pair production to be <1%. Measurements of the negative pion tracks were carried out on standard Micrometric scanner-digitizer tables and the track reconstruction used a modified version of TVGP. The use of thin targets allowed the low momentum cutoff of the observed pion spectrum to be ∿50 MeV/c.

Table 1 shows the average negative pion production $< N_{\pi^-} >$ per (inelastic) interaction. Also shown is the ratio of the average negative pion production $< N_{\pi^-} >$ to the average number of charged fragments $<N>$. This ratio is seen to rise sharply as the incident energy increases, but with the ratio remaining roughly independent of the projectile or target at a given energy. A recent emulsion study by McNaulty et al.[6] reported the observation of copious pion production for heavy-ion collisions in the energy range of 275 MeV/n and below. Our far lower $\pi^-$ production observed at higher energy (400 MeV/n) is difficult to reconcile with their result.

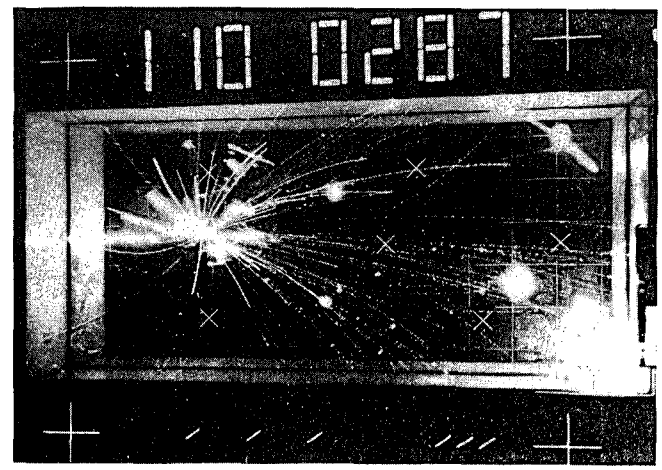


Fig. 1. 1.8 GeV/n $^{40}Ar$ projectile interacting with a thin $Pb_3O_4$ target inside LBL streamer chamber. Positive particles bend down in magnetic field of chamber, and negative particles bend up.
(XBB 7411-8445)

Table 1.

| Projectile | Projectile Energy (GeV/n) | TARGET: LiH $<N_{\pi^-}>$/int. | LiH $<N_{\pi^-}>/<N>$ | NaF $<N_{\pi^-}>$/int. | NaF $<N_{\pi^-}>/<N>$ | $BaI_2$ $<N_{\pi^-}>$/int. | $BaI_2$ $<N_{\pi^-}>/<N>$ | $Pb_3O_4$ $<N_{\pi^-}>$/int. | $Pb_3O_4$ $<N_{\pi^-}>/<N>$ |
|---|---|---|---|---|---|---|---|---|---|
| $^{40}Ar$ | 0.4 | 0.043 ± 0.022 | 0.006 ± 0.003 | 0.034 ± 0.015 | 0.003 ± 0.001 | 0.107 ± 0.019 | 0.007 ± 0.001 | 0.099 ± 0.020 | 0.007 ± 0.001 |
| | 0.9 | 0.31 ± 0.04 | 0.033 ± 0.004 | 0.60 ± 0.09 | 0.044 ± 0.005 | 0.87 ± 0.09 | 0.045 ± 0.003 | 0.92 ± 0.88 | 0.045 ± 0.003 |
| | 1.8 | 0.97 ± 0.05 | 0.08 ± 0.003 | 1.91 ± 0.12 | 0.104 ± 0.004 | 3.27 ± 0.18 | 0.106 ± 0.003 | 3.27 ± 0.15 | 0.104 ± 0.002 |
| $^{12}C$ | 0.4 | 0.02 ± 0.01 | 0.004 ± 0.002 | 0.038 ± 0.013 | 0.006 ± 0.002 | 0.078 ± 0.014 | 0.010 ± 0.002 | 0.066 ± 0.014 | 0.009 ± 0.002 |
| | 2.1 | 0.68 ± 0.07 | 0.095 ± 0.008 | 1.03 ± 0.08 | 0.108 ± 0.006 | 1.91 ± 0.17 | 0.110 ± 0.006 | 1.79 ± 0.16 | 0.101 ± 0.006 |

Negative pion multiplicity distributions for four high energy runs are shown in Fig. 2. These distributions extend to fairly larger values for the case of $^{40}Ar$ on $Pb_3O_4$ at 1.8 GeV/n. The total number of pions of all charges is of course considerable higher. We point out that the negative pion multiplicity distributions are, to first approximation, not incompatible with those expected from independent nucleon-nucleon collisions. Further work is underway to look at the high multiplicity end, a region where new and exotic phenomena might manifest themselves.

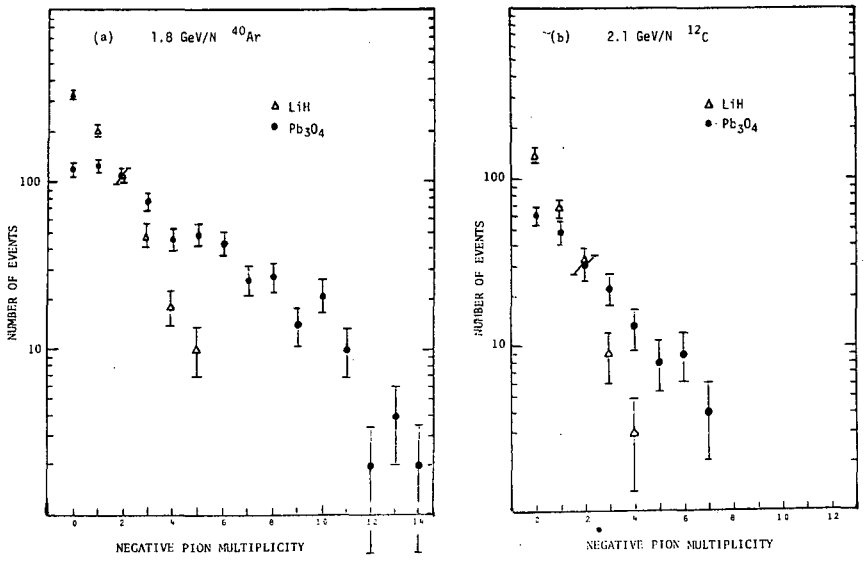


Fig. 2. Negative pion multiplicity for (a) 1.8 GeV/n $^{40}Ar$ and (b) 2.1 GeV/n $^{12}C$ beams incident on LiH and $Pb_3O_4$.

(XBL 778-2740)

Footnotes and References

*Condensed from an article submitted to Phys. Rev. Lett.

†Dept. of Physics, University of California, Riverside, CA 92521

‡Present Address: Physics Dept., California State College, San Bernadino, CA 92407

§Present Address: Physics Dept., University of Hawaii, Hilo, Hawaii 96720

‖Present Address: Lawrence Livermore Laboratory, University of California, Livermore, CA 94550

1. G. Chapline, M. Johnson, E. Teller, and M. Weiss, Phys. Rev. D 8, 4302 (1973).

2. W. Scheid, H. Muller, and W. Greiner, Phys. Rev. Lett. 32, 741 (1974).

3. M. Sobel, P. J. Siemans, J. P. Bondorf, and H. A. Bethe, Nucl. Phys. A 251, 502 (1975).

4. Y. Kitazoe, M. Sano, and H. Toki, Nuovo Cimento Lett. 13, 139 (1975).

5. G. Chapline and A. Kerman, to be published.

6. P. McNaulty, G. E. Farrell, R. C. Filez, W. Schimmerling, and K. G. Vosburgh, Phys. Rev. Lett. 38, 1519 (1977).

# D. ATOMIC PHYSICS AND QUARK SEARCH

## MEASUREMENT OF ELECTRON CAPTURE AND STRIPPING CROSS SECTIONS OF HIGH ENERGY HEAVY IONS

Grant Raisbeck,* H. J. Crawford,† F. S. Bieser,† D. E. Greiner, H. H. Heckman, P. J. Lindstrom, and Lance W. Wilson

The data aquisition phase of Experiment 239H (Atomic Charge Exchange Cross Sections for High Energy Heavy Ions) was completed in the Fall of 1976. The experiment consisted of passing beams of C, Ne, and Ar with a variety of energies through a number of targets (see Table 1). The Bevalac Beam 33 spectrometer was then used to separate the emerging beam into two atomic charge states, (Z-1) and Z (Z is the ion's nuclear charge). A detector telescope and a secondary emission monitor were placed at the bending angles corresponding to the trajectories of the (Z-1) and Z beams. Thus the experiment was able to count the number of ions emerging from the target with an electron attached, N(Z-1), and the number that emerged fully stripped, N(Z).

In principle, the experimental ratio N(Z-1)/N(Z) varies as a function of target thickness, x, in accordance with the curve of growth formula:

$$\frac{N(Z-1)}{N(Z)}(x) = \frac{\sigma_a}{\sigma_s}(1-e^{-\sigma_s n_T x}) \quad , \qquad (1)$$

where $\sigma_a$ is the attachment cross section, $\sigma_s$ is the stripping cross section, and $n_T$ is the number of target atoms per unit volume. Note that for thick targets, i.e., for $(n_T x) \gg 1/\sigma_s$, this equation becomes independent of x and reaches a plateau at the equilibrium ratio $\sigma_a/\sigma_s$.

For some of the combinations in Table 1 it was possible to obtain thin enough targets to see the increase of N(Z-1)/N(Z) as a function of target thickness. In these cases, least squares fits of Eq. (1) to the data yielded the cross sections $\sigma_a$ and $\sigma_s$. For the remaining cases, the data provided the equilibrium ratios, $\sigma_a/\sigma_s$. These experimentally determined cross sections and ratios will be compared to theoretical predictions in the coming year.

Footnotes

*Laboratoire Rene Bernas, Orsay, France

†University of California Space Science Laboratory, Berkeley, California

Table 1. The combinations of projectile, solid target and beam energy per nucleon used in this experiment.

| | Projectile and Energy/Nucleon | | | | | | | | |
|---|---|---|---|---|---|---|---|---|---|
| | C | | | Ne | | | | Ar | |
| Target | 140 | 250 | 400 | 250 | 400 | 1050 | 2100 | 400 | 1050 |
| Be | * | * | * | * | * | * | * | * | * |
| C | | * | * | | | * | * | * | * |
| Mylar | | * | * | * | * | * | * | * | * |
| Al | | * | * | * | * | * | * | * | * |
| Ni | | * | | * | * | * | | * | * |
| Cu | * | * | * | | | * | * | * | * |
| Ag | | | * | | | * | | * | * |
| Ta | | * | * | * | * | * | * | * | |
| Au | * | * | * | | | * | * | * | * |

# POSITRON PRODUCTION IN HEAVY-ION COLLISIONS*

W. E. Meyerhof,† R. Anholt,† Y. El Masari,‡ I. Y. Lee, D. Cline,§ F. S. Stephens, and R. M. Diamond

In order to interpret positron spectra from GeV U+U and similar collisions[1] in terms of new quantum electrodynamic processes[2] it is crucial to understand the positron background from nuclear reactions[3] and from instrumental effects.[4] We have developed a method which can predict the shape and the intensity (within a factor of ~2) of positrons from heavy-ion nuclear reactions, independent of the reaction mechanism (nuclear Coulomb excitation[5] or nuclear reactions). From the measured pulse-height spectrum $N_e(E_e)$ in a Ge(Li) detector we unfold the gamma-ray spectrum $G(E_\gamma)$, which in a heavy-ion reaction is a continuum for $E_\gamma \gtrsim 1$ MeV, except for possible isolated gamma transitions. Figure 1 shows $N_e(E_e)$ and $G(E_\gamma)$ for 624-MeV $^{136}$Xe+Th, using a $Xe^{+28}$ beam from the LBL SuperHILAC. Following Ref. 5, we assume that internal pair production is mainly responsible for the positrons. Fortunately the pair conversion coefficient $\beta(E_\gamma)$ depends rather little on Z and on gamma multipolarity, except for E1 radiation. We assume Z = 0 and compute the positron spectrum

$$N_+(E_+) = \int_{E_+ + 2mc^2}^{\infty} G(E_\gamma)\beta(E_\gamma)P(E_+,E_\gamma)dE_\gamma,$$

where $P(E_+,E_\gamma)$ is the positron energy distribution normalized to unity. Figure 2 shows positron

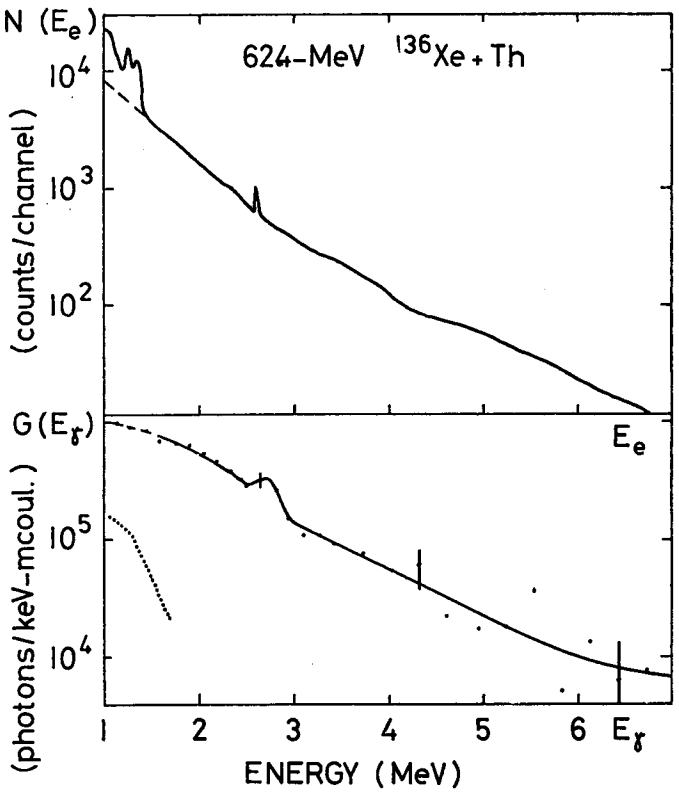


Fig. 1. Pulse-height spectrum $N(E_e)$ in a 45-cc GeLi detector and the derived gamma-ray spectrum $G(E_\gamma)$ for the 624-MeV $^{136}$Xe+Th reaction. The 1.32-MeV $^{136}$Xe gamma-ray line, Doppler shifted in $N(E_e)$, is omitted in $G(E_\gamma)$. The origin of the 2.62-MeV gamma ray is uncertain. This line, unfolded in $G(E_\gamma)$, gives an indication of the resolution of the method. Computed points are shown and the curve is drawn to guide the eye. The dotted curve gives the spectral shape computed for 1600-MeV $^{238}$U + $^{238}$U Coulomb excitation (Ref. 5). (XBL 778-1625)

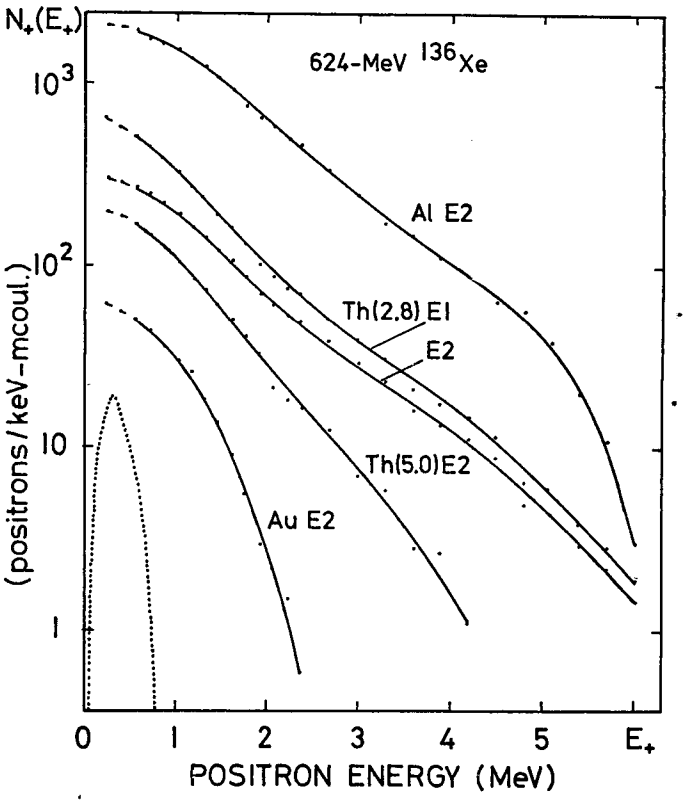


Fig. 2. Internal-pair-conversion positron spectra derived from gamma-ray spectra for 624-MeV $^{136}$Xe+Th, Au and Al bombardments. The spectrum from the 1.32-MeV $^{136}$Xe gamma transition is omitted and the dashed lines correspond to an extrapolation of the continuum spectra (see Fig. 1). Target thickness in mg/cm$^2$ is given in parentheses. Assumed E1 or E2 multipolarity is indicated. Computed points are shown and the curves are drawn to guide the eye. The dotted curve gives only the spectral shape calculated for 778-MeV $^{136}$Xe + $^{238}$U Coulomb excitation ($\sigma_+$ = 59 μb)(Ref. 6). (XBL 778-1626)

spectra computed for various targets bombarded by 624-MeV $^{136}$Xe, assuming E1 and E2 multipolarity. Two different Th targets, presumably differently oxidized, give different gamma and positron spectra.

To test our method we measured the positron spectra from the same targets as in Fig. 2. A broad-range mini-orange magnetic spectrometer with a Si(Li) positron detector was used.[6] To assure sensitivity only to positrons, a 45-cc Ge(Li) detector was placed as close as possible behind the Si(Li) and coincidences with the annihilation peak in the Ge(Li) were required. Figure 3 gives measured detected spectra $D_+(E_+) = N_+(E_+)t(E_+)$ for 624-MeV $^{136}$Xe+Th and the predicted E1 and E2 curves, where t is the known transmission and detection function of the spectrometer. Two different magnet configurations are shown. Since $N_+(E_+)$ is rather featureless (Fig. 2), the curves essentially reflect $t(E_+)$. Good agreement is obtained between experiment and prediction, as can also be seen from Table 1 which gives the predicted and detected integral counts between $E_+ = 0.3$ and 0.9 MeV.

Our work shows: 1) important positron production from light-element target impurities; 2) a method for predicting the internal pair-conversion positron background from any heavy-ion nuclear reaction.

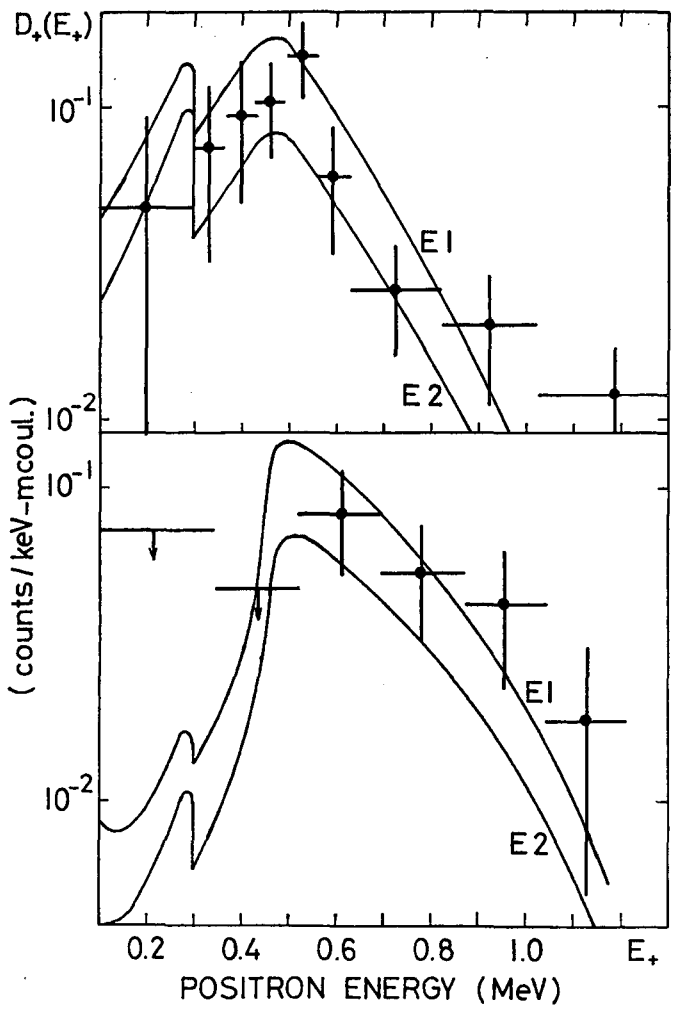


Fig. 3. Positron spectral distribution from 624-MeV $^{136}$Xe + Th detected in the mini-orange spectrometer. Top and bottom are for two different magnet configurations (A and B in Table 1). The curves are predicted positron spectra for E1 or E2 radiation; the predicted spectrum from the 1.32-MeV $^{136}$Xe gamma transition (E2) is included. (XBL 778-1627)

Table 1. Integral positron yield between 0.3 and 0.9 MeV in spectrometer.

| Target | Thickness ($mg/cm^2$) | Magnet Configuration | Detected counts $(mC)^{-1}$ E1 | E2 | Exp. | Cross sect.[a] (μb) |
|---|---|---|---|---|---|---|
| Th | 2.8 | A | 25 | 51 | 37 ± 6 | 101 ± 16 |
| | | B | 22 | 44 | 28 ± 9 | 109 ± 35 |
| | | C | 8 | 17 | 17 ± 9 | 141 ± 75 |
| Th | 5.0 | A | 17 | 35 | 21 ± 7 | 30 ± 10 |
| Au | 2.0 | A | 5 | 11 | 11 ±10 | 33 ± 30 |
| Al | 2.4 | A | 192 | 371 | 220 ± 49 | 78 ± 17 |

[a]Average over target thickness, for 624-MeV Xe beam.

Footnotes and References

*An expanded version in Phys. Lett. 698, 4 (1977).

†Dept. of Physics, Stanford University, Stanford, CA 94305.

‡On leave from Inst. de Physique Corpusculaire, Louvain-la-Neuve, Belgium.

§Permanent address: Dept. of Physics & Astronomy, Univ. of Rochester, NY.

1. H. Backe et al., ICPEAC, Paris, July 1977.

2. K. Smith et al., Phys. Rev. Lett. 32, 544 (1974); W. Betz et al., Phys. Rev. Lett. 37, 1046 (1976); G. Soff et al., Phys. Rev. Lett. 38, 592 (1977).

3. B. Müller, Ann. Rev. Nucl. Sci. 26, 351 (1976).

4. H. Backe et al., Technische Hochschule, Darmstadt, Rept. No. 67 (1975).

5. V. Oberacker, G. Soff, and W. Greiner, Nucl. Phys. A 259, 324 (1976) and private communications.

6. J. van Klinken, S. J. Feenstra, K. Wisshak, and H. Faust, Nucl. Instrum. Meth. 130, 427 (1975).

# QUARKS WITH UNIT CHARGE: A SEARCH FOR ANOMALOUS HYDROGEN*

Richard A. Muller, Luis W. Alvarez, William R. Holley, and Edward J. Stephenson

Quarks, the components of the nucleon proposed by Gell-Mann and Zweig,[1] have been the subject of extensive searches by both elementary-particle and cosmic-ray physicists.[2] In most of these experiments the quark's fractional charge (1/3 or 2/3 that of the proton) was the distinctive signature that would have indicated its presence. But fractional charge is not required by all quark models; in particular, theories proposed by Lee[3] and by Han and Nambu[4] have quarks of integral charge. It seems reasonable to speculate that the quark searches failed because they assumed the wrong signature; perhaps quarks have integral charge. Quarks with Z = +1 would be equivelent chemically to a new isotope of hydrogen, and would be found on the earth mixed with that element. With this in mind, we decided to search in terrestrial hydrogen for Z = +1 quarks using the same technique that was used in the discovery of stable (and natural) $^3$He by Alvarez and Cornog,[5] i.e., to use a cyclotron as a high-energy mass spectrometer.

We used the 88-inch sector-focused cyclotron at the Lawrence Berkeley Laboratory for our search. Both hydrogen and deuterium gases were introduced as sample materials into the filament ion source. Only those ions with the appropriate value of Z/m, given by the cyclotron resonance equation, were accelerated. In our search we kept the magnetic field constant and scanned in frequency.

For the 88-inch cyclotron to be "in tune", i.e., for it to accelerate particles into our detectors, several criteria must be met. The magnetic field profile (i.e., the field as a function of radius) must be appropriate to compensate the relativistic increase in mass as the particle is accelerated, and the voltages applied to the electrostatic deflector and dee must be at the correct values to assure efficient beam extraction. In order to eliminate the need to change the magnetic-field profile during a scan, we operated the cyclotron in the third-harmonic mode, where the particle revolution frequency is 1/3 of the oscillator frequency and the maximum particle velocity is only 0.1 c. During scans we changed the deflector and dee voltages in proportion to the change in frequency. The ultimate proof that we were in tune in our scans came from the observation of expected beams; for example, when we set the cyclotron to accelerate Z/m = 1/2 ($D^+$) and scanned to Z/m = 1/3, we found that $DH^+$ molecular ions were being efficiently accelerated and extracted.

The emerging beam from the cyclotron was focused onto two silicon detectors: a thin one (20-60 μ) to measure the ionization rate dE/dx, followed by a thick one (1 mm) to measure the total energy. By requiring a coincident signal between the two detectors, and that the signals in them correspond to a single Z = 1 particle with the correct energy, we were able to discriminate against heavier particles, molecules, and background radiation from the cyclotron. Except when the cyclotron was tuned near the resonant frequency for known species (integral values of Z and m), the number of background counts was essentially zero; during one run we operated for over an hour with no background counts. The rapid fall-off of the tails of the cyclotron resonance allowed us to search within 1% of values of Z/m for which known particles exist.

For quark masses above 2 amu, we used deuterium gas in the cyclotron ion source. The deuterium had been separated from water at the Savannah River Heavy Water Plant, using the GS process followed by vacuum distillation and electrolysis.[6] The efficiency for each of these concentration processes increases as the mass of the isotope increases; thus for masses just above 2 amu quarks would have been concentrated by at least a factor of 6,600, the ratio of $^1$H to $^2$H in river water. For masses $\gg$ 2 amu we know that the concentration of quarks could not have been increased by more than a factor of $5 \times 6600 = 33 \times 10^3$, since 20% of the original deuterium in the water was recovered, and obviously no more than 100% of the original quarks could have been recovered. Kaufman and Libby[7] have shown that for electrolytic separation, this transistion to maximum concentrations takes place below mass 3 amu. Thus by searching in deuterium, the sensitivity is 6600 times greater than a search in hydrogen for quark masses near 2 amu, and 33,000 times as sensitive for quark masses above 3 amu.

In a typical run a 13 μA deuterium beam was observed as we tuned through the $^2H^+$ frequency, corresponding to $8 \times 10^{13}$ ions/sec. The deuterium beam was measured with a Faraday cup, preceded by collimators which simulated the acceptance geometry of the silicon detectors. Our typical dwell time for a particular value of Z/m as we manually scanned in frequency was 2 seconds, during which time we would have recorded as significant the observation of even a single particle with the proper signature in the dE/dx and total E detectors; no quarks were observed. Thus the ratio of quarks to deuterons was less than $6 \times 10^{-15}$. The ratio of quarks to $^1$H is then less than $10^{-18}$ near mass 2, and less than $2 \times 10^{-19}$ for masses $\geq$ 3 amu.

For quark masses in the range 1 to 2 amu we used ordinary hydrogen in the source rather than deuterium; our sensitivity was correspondingly 6,600 times poorer. We repeated the scan in the mass range 1.5 to 2 amu using deuterium, with the thought that it would give us some additional sensitivity in the range just below 2 amu. We saw no quark events in this scan. It is difficult to estimate the sensitivity of this scan without studying the detailed physical chemistry of the isotope separation process; thus we claim

no limit obtained from this scan. For the mass range 0 to 1, we looked for quark-hydrogen molecules Hq, assuming that they would have chemistry similar to $H_2$. The mass range was covered in two runs; for quark masses 1/3 to 1 amu, the $H_2^+$ current we obtained was 1.7 μA, and for the mass range 0 to 1/3 amu, the $H_2^+$ current was 0.16 μA. The corresponding sensitivities are in the range $q/H = 10^{-14}$ to $10^{-13}$.

We have observed no quarks of Z = +1, nor other anomalous isotopes of hydrogen. The limits from our search and previous experimental results, are plotted in Fig. 1. These limits correspond to one standard deviation, i.e., a confidence level of 67%. For 95% confidence levels, each limit must be adjusted upward by a factor of three, as is indicated on the plot. In addition, we have taken the calculations of Zeldovich, Okun, and Pikelner,[8,9] and, after scaling them appropriately with energy, plotted the predicted quark-to-proton ratios. For several regions corresponding to integral values of Z and m, the intensity from known ions (such as $^2H_2^+$ and $^{14}N^{2+}$) was sufficiently high to require the removal of the silicon detectors from the beam. As a result there are regions, generally less than 1% wide in mass, in which we were unable to search for quarks. These regions are indicated in Fig. 1 by short vertical bars. The existence of these beams served the useful purpose of proving that the cyclotron was still in tune, and that if there were quarks at concentrations greater than the limits we have placed, they would have been observed.

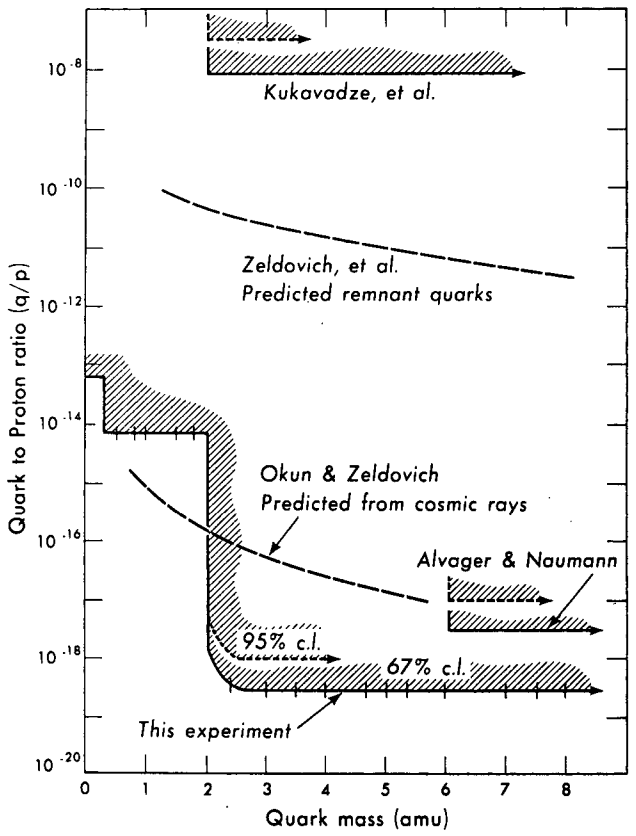


Fig. 1. Quark-to-proton ratio as a function of quark mass. Shown are the experimental limits, as well as predictions of the levels expected from cosmic-ray and big bang production if Z = +1 quarks exist. The predictions were scaled with mass to take into account changing cross sections and cosmic-ray fluxes. The short vertical bars indicate the narrow regions (generally less than 1% wide) where we could not search because of the existence of beams of common ions with integral values of Z and m. The experimental limits plotted as solid lines are for the 67% confidence level, corresponding to approximately 1 standard deviation. Each limit must be raised by a factor of 3 (as indicated with dashed lines) for a 95% confidence level. (XBL 7611-4480)

## Footnote and References

*Condensed from LBL-5399; Science 196, 521 (1977).

1. M. Gell-Mann, Phys. Lett. 8, 214 (1964); G. Zweig, CERN 8182 TH/401 (1964), unpublished.

2. An extensive list of searches can be found in the Review of Particle Properties by the Particle Data Group, Rev. Mod. Phys. 48, No. 2, Part II, 100-102 (1976).

3. T. D. Lee, Nuovo Cimento XXXV, 933 (1965).

4. M. Han and Y. Nambu, Phys. Rev. 139, B1006 (1965).

5. L. Alvarez and R. Cornog, Phys. Rev. 56, 379 (1939); Phys. Rev. 56, 613 (1939).

6. See, for example, the Kirk-Othmer Encyclopedia of Chemical Technology, 2nd Ed., Vol. 6, p. 815-918 (Wiley, 1968).

7. S. Kaufman and W. F. Libby, Phys. Rev. 93, 1337 (1954).

8. Ya. Zeldovich, L. Okun, S. Pikelner, Usp. Fix. Nauk 87, 113 (1965); Sov. Phys. Uspekhi 8, 702 (1966).

9. L. Okun and Ya. Zeldovich, Comments Nucl. Part. Phys. 6, 69 (1976).

# II.

# THEORY

# A. NUCLEAR REACTIONS

## 1. Microscopic

### LONG RANGE ABSORPTION IN THE HEAVY-ION OPTICAL POTENTIAL*

A. J. Baltz,† S. K. Kauffmann, N. K. Glendenning, and K. Pruess

A long range absorption in the heavy-ion optical potential due to Coulomb excitation has been the subject of some interest recently. An experimental specimen is the elastic scattering data of 90 MeV $^{18}O$ on $^{184}W$.[1] These data show a Fresnel pattern damped below the Rutherford cross section that is well reproduced by a coupled channels calculation which includes Coulomb excitation of the 111 keV $2^+$ rotational state in $^{184}W$. An alternative theoretical description is the construction of an optical model component arising from two step contributions to elastic scattering. Love, Teresawa, and Satchler (LTS) have recently obtained an approximate formula for a long range imaginary potential with radial dependence $(1/R^5)\ [1-(Z_1Z_2e^2/R\,E_{cm})]^{-1/2}$, based on plane wave scattering states and a classical Coulomb correction.[2] We have derived a more exact formula for this long range potential based on the use of Coulomb wavefunctions throughout.

The potential component to be evaluated may be written[3]

$$V = V_f\, G_2\, V_i \qquad (1)$$

where $G_2$ is the Green's function for the intermediate $2^+$ state, and $V_f$, $V_i$ are the quadruple operators with $1/R^3$ dependence connecting ground and excited state. We assume no energy loss in the quadrupole transition, but an adiabaticity correction factor, $g_2(\xi)$[2,4] may be applied later as needed. $G_2$ is written in terms of Coulomb wavefunctions in coordinate space, and a local potential is constructed making use of the known analytical forms for integrals of $1/R^3$ times Coulomb wavefunctions along with recurrence relations. The dominant imaginary part of the potential is obtained in closed form, good for large $\eta$ or $\hat{\ell}$ with $\hat{\ell} = \ell + 1/2$:

$$U_\ell(r) = \frac{-i\,2\mu}{k\hbar^2}\,\frac{\pi}{50}\,Z_p^2 e^2 B(E2)\uparrow \cdot \left[\left(\frac{\eta^2 k^2}{\hat{\ell}^2}\,\frac{(3\hat{\ell}^2+\eta^2)}{(\hat{\ell}^2+\eta^2)^2} - \frac{\eta k^2}{\hat{\ell}^3}\arctan\frac{\hat{\ell}}{\eta}\right)\frac{1}{r^3} + \frac{4\,\eta k\hat{\ell}^2}{(\hat{\ell}+\eta^2)^2}\,\frac{1}{r^4} + \frac{2\hat{\ell}^4}{(\hat{\ell}^2+\eta^2)^2}\,\frac{1}{r^5}\right] \qquad (2)$$

In contrast to the $\ell$-independent, dominantly $1/R^5$ behavior of the LTS potential, our potential is specifically $\ell$-dependent with $1/R^5$, $1/R^4$ and $1/R^3$ radially dependent terms. As $\ell \to \infty$ our $1/R^5$ term dominates and the ratio of LTS to ours approaches 4/3.

The physical correspondence between the approximate LTS potential and our more exact form may be seen in Fig. 1. The LTS potential crosses our $\ell$-dependent potential several Fermis outside of the classical turning point for each $\ell$. Our analytical closed form for the potential agrees quite well with computer evaluation of the potential using Coulomb wavefunctions throughout.

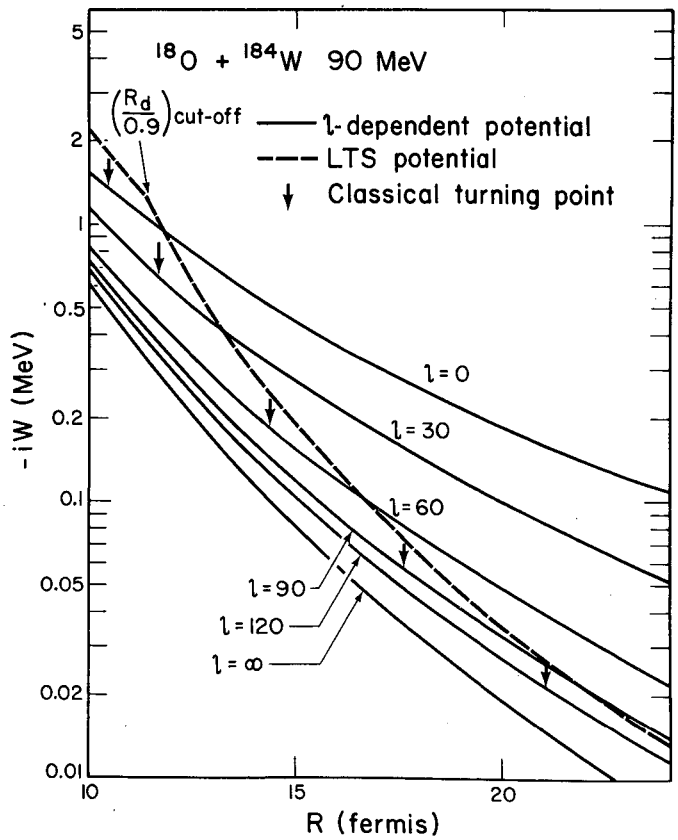


Fig. 1. $\ell$-dependent imaginary optical potential obtained from Eq. (2) compared with the LTS potential for $^{18}O$+$^{184}W$ at 90 MeV. (XBL 778-1635)

Although this potential is appropriate for incorporation into existing optical model codes we have not yet pursued this. Rather we have considered the effects of long range absorption in the case of sub-Coulomb elastic scattering and we have derived a formula for the cross section in analytical closed form.

Since our long range imaginary potential is weak and smoothly varying in both r and $\ell$, it will produce a nondiffractive quasi-classical absorptive effect on trajectories passing a few diffuseness lengths or more outside the nuclear surface. Thus the effect of our imaginary potential on the elastic scattering cross section may be readily calculated in a perturbative JWKB approximation developed previously.[5] Detailed application of this approach to elastic scattering above the Coulomb barrier has been carried out but is not discussed here. The usual Coulomb trajectory angular momentum substitution $\ell = \eta \cot \theta/2$ is made.

We then obtain the remarkable result that below the Coulomb barrier the elastic scattering ratio to Rutherford cross section takes the simple form

$$\sigma(\theta)/\sigma_R(\theta) = \exp(-K f(\theta)) \qquad (3)$$

where all the specific parameters of the reaction are contained in the constant

$$K = \frac{16\pi}{225} \frac{k^4}{\eta^2} \frac{B(E2)\uparrow}{Z_t^2 e^2} \qquad (4)$$

and $f(\theta)$ is a universal function of angle

$$f(\theta) = \frac{9}{4}\left[(\cos\tfrac{\theta}{2})^4\left(\tfrac{4}{3}D^4 + \tfrac{104}{105}D^5\right) + (\sin\theta)^2\left(\tfrac{\pi}{4}D^3 + \left(\tfrac{64-15\pi}{30}\right)D^4\right) + \left((3+(\tan\tfrac{\theta}{2})^2)(\sin\tfrac{\theta}{2})^4 - (\tan\tfrac{\theta}{2})^3\left(\tfrac{\pi-\theta}{2}\right)\right)(D^2+\tfrac{2}{3}D^3)\right] \qquad (5)$$

with

$$D = \frac{1}{1+\csc\frac{\theta}{2}} \quad . \qquad (6)$$

This analytical form for $f(\theta)$ has the smooth behavior exhibited in Fig. 2a.

We may also obtain an expression identical to the above for the cross section produced by the LTS potential except that a different universal function of angle $\bar{f}(\theta)$ is involved. We have plotted the universal below-barrier ratio $\bar{f}(\theta)/f(\theta)$ in Fig. 2b. This ratio deviates from unity by up to 33 1/3% at forward angles but this will not show up in most reactions due to the small magnitude of $f(\theta)$. At intermediate angles of about 40 to 110° the ratio deviates little from unity implying excellent agreement for the predictions of the two potentials. However, beyond 110° (corresponding to LTS cut off at $R_d/0.9$ of the Coulomb correction factor) there is no theory from the LTS potential but only a possible prescription. For the sake of analytical tractability we have merely ignored the cut off in the ratio calculation. Clearly without the arbitrary cut off, LTS predictions deviate substantially from those of our potential at very large angles as is illustrated in Fig. 2c. Here are plotted predicted cross sec-

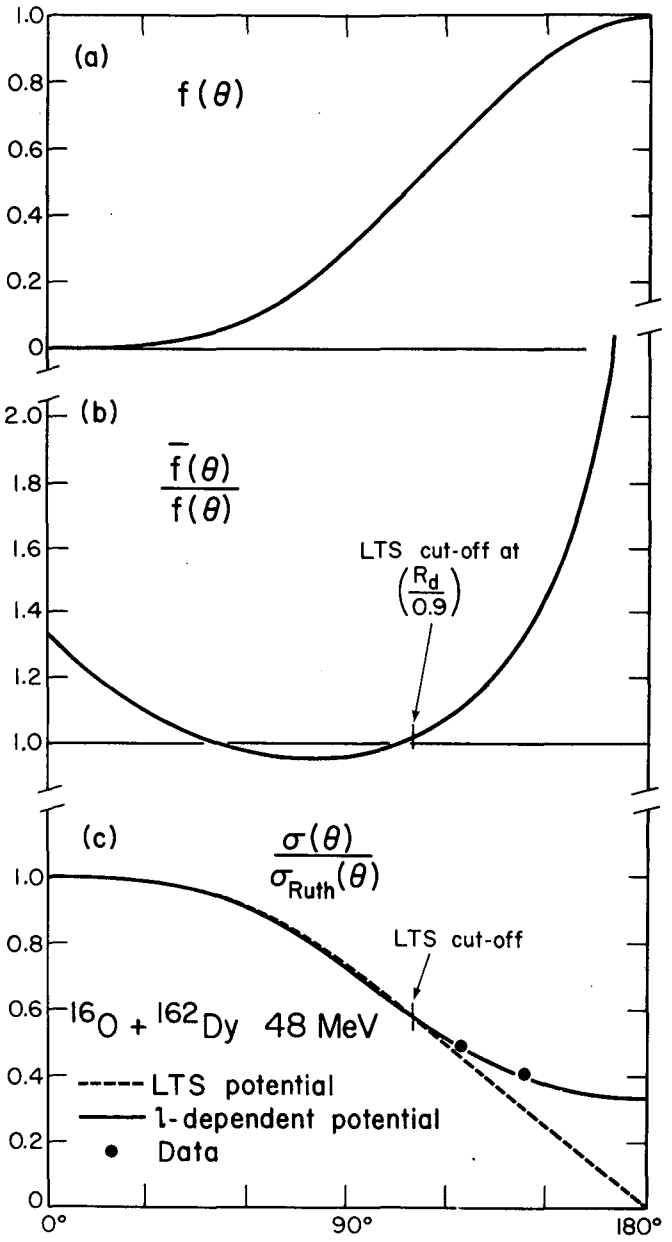


Fig. 2. a) Universal function of angle $f(\theta)$. b) Ratio of $\bar{f}(\theta)$ for the LTS potential to $f(\theta)$ for our potential. c) Elastic cross section for $^{16}O+^{162}Dy$ at 48 MeV calculated from Eq. (3) incorporating $f(\theta)$ for our potential and $\bar{f}(\theta)$ for the LTS potential. Data are from Lee and Saladin (Ref. 6).

(XBL 778-1636)

tions in a realistic case for which data exists at two angles:[6] $^{160}$ + $^{162}$Dy at 48 MeV. The excellent agreement between the calculated cross section and the two data points seems to encourage further experiments to obtain complete angular distributions in sub-Coulomb elastic scattering. The remarkable point of such experiments is that there is a nontrivial theory with no free parameters, which can be evaluated without a computer, that gives specific cross-section predictions. Indeed, in the situation where the long range potential arises dominantly from a single state, sub-Coulomb elastic scattering analyzed in terms of our analytical expression might provide an alternate method of determining the experimental B(E2) to that single state.

Footnotes and References

*Condensed from LBL-6581.

†Permanent address: Brookhaven National Laboratory, Upton, NY 11973

1. C. E. Thorn, M. J. Levine, J. J. Kolata, C. Flaum, P. D. Bond and J. C. Sens, Phys. Rev. Lett. 38, 384 (1977).

2. W. G. Love, T. Terasawa, and G. R. Satchler, Phys. Rev. Lett. 39, 6 (1977); Nuclear Physics, to be published.

3. H. Feshbach, Ann. of Phys. 19, 287 (1962).

4. K. Alder, A. Bohr, T. Huus, B. Mottelson and A. Winther, Rev. Mod. Phys. 28, 432 (1956).

5. S. K. Kauffmann, Relation of Phase Shifts to Potential Parameters in the Elastic Scattering of Very Heavy Ions, University of Cape Town, Department of Physics preprint, Cape Town, 1976.

6. I. Y. Lee and J. X. Saladin, Phys. Rev. C 9, 2406 (1974).

## POLARIZATION OF NUCLEAR WAVEFUNCTIONS IN HEAVY-ION REACTIONS*

L. A. Charlton,† G. Delic,‡ N. K. Glendenning, P. Lichtner,§ K. Pruess

Most direct reactions between heavy ions can be interpreted in terms of a transition between shell model states of the isolated nuclei with the transition amplitude calculated in DWBA, or, when important multiple step transitions through low-lying collective states are important, in CCBA. However, there are some experimental measurements that cannot be so interpreted.[1,2] They exhibit a systematic discrepancy when compared with DWBA having the three features: (1) for weakly bound states the observed angular distribution is shifted toward smaller angles than expected (by as much as 15°); (2) the shift grows with decreasing binding for a sequence of levels in the same nucleus (dashed curves of figure); (3) the magnitude of the shift decreases as the bombarding energy increases. The uniform systematic behavior suggests that it is not due to two-step transitions through one or several low-lying intermediate states because the different parentage amplitudes could hardly be of the same sign and uniform magnitude for a whole sequence of states, implying therefore nonsystematic interference between one and two-step transitions. On the other hand the above three features would follow if the weakly bound state is modified by the field of the approaching nucleus. While such a polarization is intuitively plausible, such a phenomenon has never been needed to understand the direct reactions between light particles and nuclei, and possibly for this very reason they have been so useful to the nuclear spectroscopist. Our first goal therefore is to assess whether the magnitude of the effects due to such a polarization of the wavefunctions is comparable to the discrepancies observed. We have done this in a schematic way by employing the two-center shell model to generate polarized states in $^{209}$Bi as a function of the distance of the polarizing nucleus $^{11}$B. Transitions to these states are computed in DWBA. The trend of growing shift with decreasing binding is reproduced as is the magnitude of the shift (Fig. 1, solid curves). Thus we have demonstrated that this phenomenon is a likely explanation for the observed discrepancies.

While the calculations that we have done, which correspond to a particle transfer to a two-center shell model state, seem plausible under the circumstances, we now show that the transition amplitude actually takes this form in lowest approximation, when the binding is weak and bombarding energy is low.

Our calculation can be understood as the lowest order approximation to a dynamical process involving transitions through many high-lying levels. If the Hilbert space is truncated to include only the initial channel $\alpha$, the final (weakly bound) channel $\beta$ and many high-lying levels $\beta'$ in the nucleus having the weakly bound state, the transition amplitude is

$$T_{\alpha\to\beta} = \langle \chi_\beta^{(-)} | (\phi_\beta | \hat{V}_\alpha | \phi_\alpha) + \sum_{\beta'} (\phi_\beta | \hat{V}_\beta | \phi_{\beta'}) \frac{1}{E_{\beta'}^{(+)} - H_\beta} (\phi_{\beta'} | \hat{V}_\alpha | \phi_\alpha) | \chi_\alpha^{(+)} \rangle , \quad (1)$$

where the first term is the usual DWBA. We neglect rescattering among the intermediate states

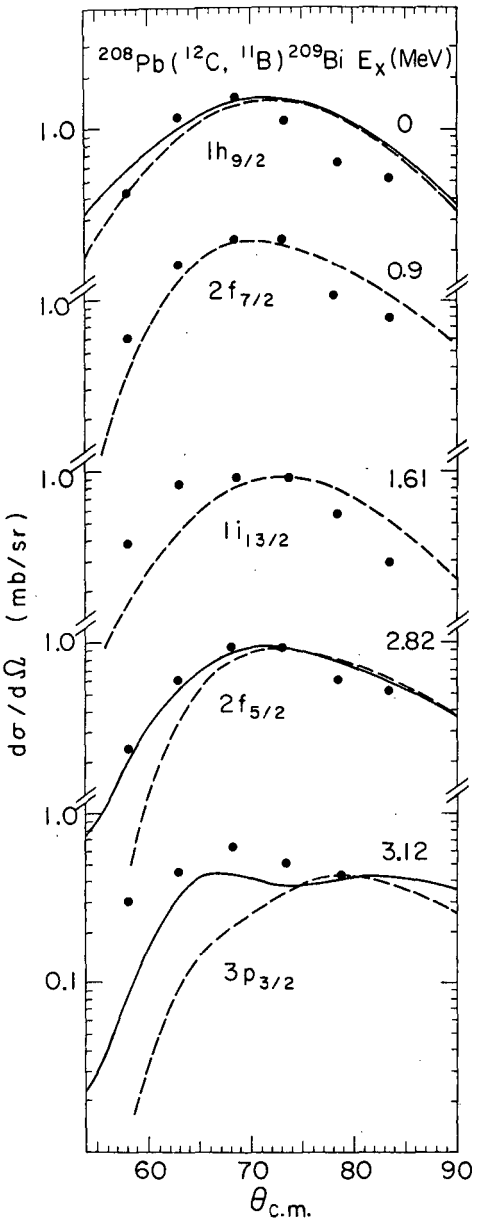


Fig. 1. The usual DWBA transition between the isolated states of the nuclei shows a growing discrepancy through the sequence of levels (dashed lines). The transition to polarized states reproduces approximately the experimental features (solid curves). (XBL 771-122)

β' by replacing the interaction in $H_\beta$ by an optical potential so that $H_\beta = T_\beta + U_\beta$, being the Hamiltonian and $E_{\beta'} = E - \varepsilon_{\beta'}$ the energy of relative motion with $\varepsilon_{\beta'}$ the excitation energy of the nucleus. The long-range and smooth behavior of the nucleon-nucleus interaction $\hat{V}$ and the narrow Q-window especially at low energy ensure that intermediate scattering states of $H_\beta$ with energy far from $E_\beta$ can be neglected. Defining a projection operator P which projects on eigenstates of $H_\beta$ with energy $E_i$ such that $|E_i - E_\beta| < |\varepsilon_\beta - \varepsilon_{\beta'}|$ the Green's function can be expanded as

$$P \frac{1}{E_\beta^{(+)} - H_\beta} = P \frac{1}{\varepsilon_\beta - \varepsilon_{\beta'}} \sum_{n=0}^{\infty} \left( \frac{H_\beta - E_\beta}{\varepsilon_\beta - \varepsilon_{\beta'}} \right)^n . \quad (2)$$

If we were to keep only the n=0 term we get

$$T_{\alpha \to \beta} = \langle \chi_\beta^{(-)} \left( \phi_\beta + \sum_{\beta'} \frac{(\phi_\beta | \hat{V}_\beta | \phi_{\beta'})}{\varepsilon_\beta - \varepsilon_{\beta'}} \phi_{\beta'} \right) | \hat{V}_\alpha | \phi_\alpha \chi_\zeta^{(+)} \rangle . \quad (3)$$

This shows that the transition is from the state α to a polarized state β with the polarization amplitudes corresponding to first order perturbation theory. It is the theoretical justification for our schematic calculation.

However, since the dependence on the bombarding energy is contained in the n > 0 terms, we are in the process of calculating the full expression (1) which contains the dynamical aspects of the process.

## Footnotes and References

*Condensed from LBL-6517.

†Now at Oak Ridge National Laboratory, Oak Ridge, Tennessee.

‡Now at Technische Hochschule Darmstadt, Darmstadt, Germany.

§University of Maryland, College Park, Maryland.

1. K. S. Toth et al., Phys. Rev. C 14, 1471 (1976).

2. G. Delic, K. Pruess, L. A. Charlton, N. K. Glendenning, Phys. Rev. Lett. 69B, 20 (1977). and Argonne Symposium on Macroscopic Features of Heavy Ion Collisions II (1976) 723.

# THREE-DIMENSIONAL TIME DEPENDENT HARTREE-FOCK CALCULATIONS FOR $^{16}O + ^{16}O$ AND $^{40}Ca + ^{40}Ca$

H. C. Flocard and M. S. Weiss*

A method has been developed to solve the three-dimensional time dependent Hartree-Fock (TDHF) equations in coordinate space. This is applied to the study of $^{16}O + ^{16}O$ collision at $E_{lab} = 105$ MeV for incident angular momenta varying from 0 to 40ħ. We find fusion for L = 13ħ through 27ħ and highly inelastic scattering for L < 11ħ. Some calculations have been made at other energies to study the fusion regime.

Figure 1 shows different stages of the collision for L = 13ħ which leads to fusion. We have drawn on the x-y plane (the reaction plane) the contour lines of the integral of the nuclear density along the three axes. The times t are given in units $10^{-22}$S. In Fig. 2 we have plotted the deflection function and the kinetic energy loss in the c.m. frame as a function of the initial angular momentum. The shaded area indicates where we have obtained fusion. It is interesting to note the large energy loss 35 MeV obtained for low values of the angular momentum. This is to be compared to the energy available in the c.m.: 52.5 MeV.

The most interesting phenomenon we have observed in our calculation is a region of fusion which yields a fusion cross section consistent

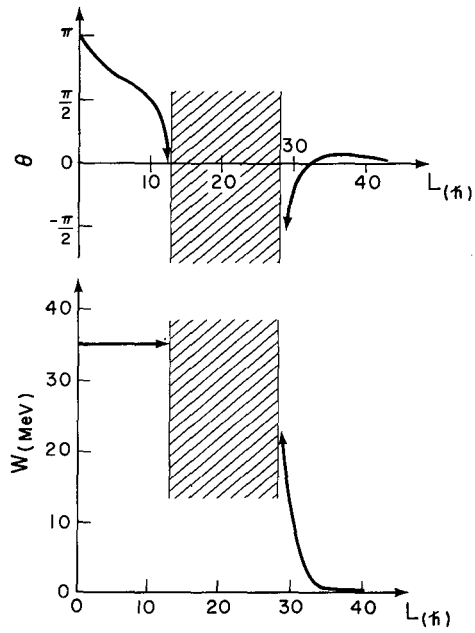


Fig. 2. The deflection function and energy loss. (XBL 777-1524)

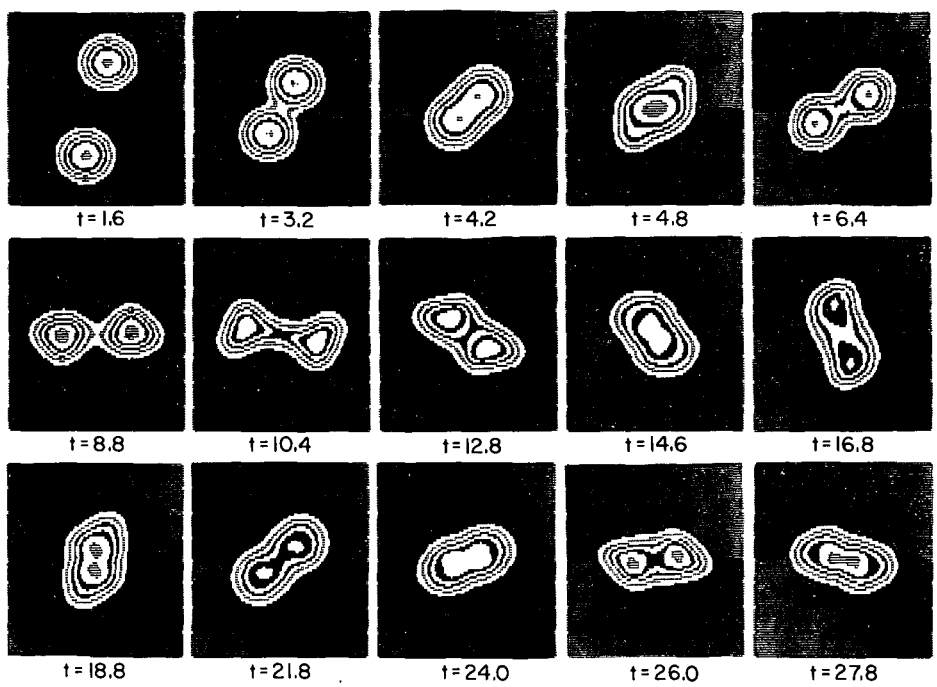


Fig. 1. Time evolution of the collision $^{16}O + ^{16}O$ at $E_{lab} = 105$ MeV. (XBL 777-1527)

with experiment 1. This is in contrast with previous TDHF calculations in two dimensions[2] (2-D) which showed no fusion for high-energy collisions. Therefore triaxiality is important in the dissipative process that leads to fusion.

It is also important to note the lack of fusion for small angular momentum at high bombarding energy. For these small values of the angular momentum we calculated the scattering angle and energy loss of the outgoing fragments. These predictions are amenable to experimental verifications. We also find that the absence of fusion for head-on collision disappears at sufficiently low bombarding energies. However, our calculations contain several technical restrictions (e.g. spin, isospin, and two spatial symmetries) which may affect the specific numerical values that we give.

A comparison with other 3-D calculations[3] indicates a probably dependence of the results on the interaction. Therefore it is quite possible that TDHF calculations of heavy-ion scattering will provide a means to study the characteristics of the nucleon-nucleon effective interaction.

We have also examined $^{40}Ca + {}^{40}Ca$ at $E_{lab}$ = 278 MeV both because of its intrinsic interest[4] and because 2-D[2] calculations with the same effective interaction exist. We find significant differences relative to the 2-D[2] calculations. Particularly, they did not observe any fusion, whereas in 3-D there is a wide band of impact parameters for which the system fuses. In addition, although both 2-D and 3-D have the same large kinetic energy loss for small impact parameters, the 3-D calculation has considerably more energy going into "heat" relative to the 2-D result once the impact parameter exceeds the maximum for which fusion takes place. It therefore appears that 3-D dynamics are required for an adequate description of heavy ion collisions once the impact parameter exceeds relatively small values ($\ell$=10$\hbar$ for $^{16}O + {}^{16}O$, $E_{lab}$ = 105 MeV; $\ell$=20$\hbar$ for $^{40}Ca + {}^{40}Ca$,, $E_{lab}$ = 278 MeV).

Footnote and References

*Lawrence Livermore Laboratory.


1. P. Sperr et al., Phys. Rev. Lett. 37, 321 (1977).
2. S. Koonin et al., Phys. Rev. C 15, 1359 (1977).
3. R. Y. Cusson, J. A. Maruhn, and H. W. Meldner, to be published.
4. P. Colombani, et al., Phys. Lett. 55B, 45 (1975).


# 2. Macroscopic

## DIFFUSION MODEL PREDICTIONS FOR HEAVIER SYSTEMS: THE REACTION $^{197}Au$ + 620 MeV $^{86}Kr$*

J. S. Sventek and L. G. Morettot

We have used the Master Equation to follow the time-dependent population $\phi_Z(t)$ of systems whose mass-asymmetry is characterized by the atomic number Z of one of the fragments. We have assumed an equilibrated neutron to proton ratio, as shown to be true by Galin et al.[1] The potential energies used are those for two touching spherical fragments as in Ref. (2). A plot of a typical potential energy curve vs asymmetry can be seen in Fig. 1a.

The time dependence of the population $\phi_Z$ is given by:

$$\dot{\phi}_Z = \sum_{Z' \neq Z} \lambda_{ZZ'}[\phi_{Z'}\rho_Z - \phi_Z\rho_{Z'}] \quad , \qquad (1)$$

where $\lambda_{ZZ'} = \lambda_{Z'Z}$ is the microscopic transition probability between systems specified by the asymmetries Z and Z', and $\rho_Z$ is the level density of the system specified by Z. The level densities can be written in terms of the potential energy of the intermediate complex $V_Z$, discussed above, measured with respect to the rotating ground state, as $\rho_Z = \rho(E - V_Z)$. The $\lambda_{ZZ'}$ are the product of a diffusion constant $\kappa$ and a normalized form factor.[2] We have assumed that the high nuclear temperatures involved (2-3 MeV) eliminate correlations between nucleons, so that, in the limit of the independent particle model, the sum in Eq. (1) is restricted to $Z' = Z \pm 1$.

The system of equations in Eq. (1) can be solved by standard matrix techniques to give the time-dependent populations $\phi_Z(t)$ (normalized to 1). Fig. 1b is a map of contours of constant probability, calculated for the potential energy given in Fig. 1a, plotted as a function of mass-asymmetry Z and the time t (in units of $10^{-22}$ s). Note that the drift and spread of the distribution can be easily discerned for short times, and the equilibration of the distribution can be seen for long times.

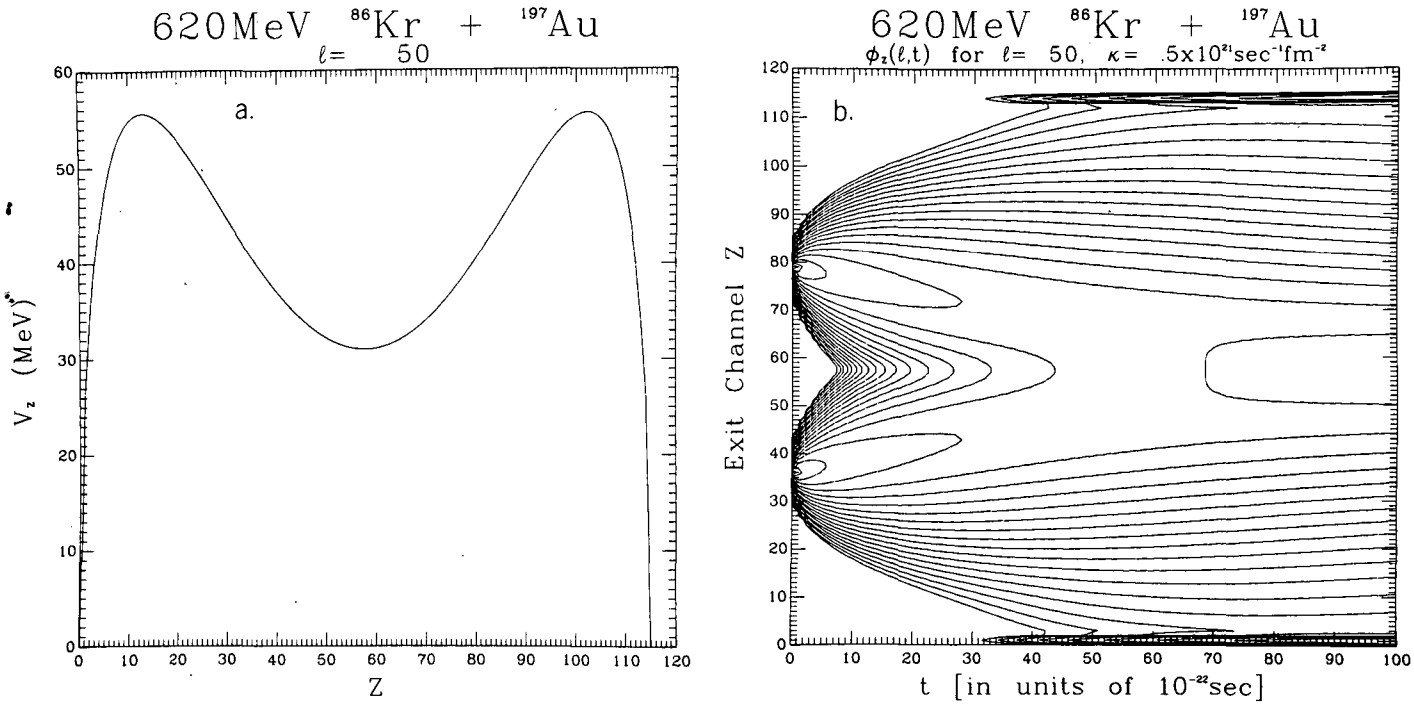


Fig. 1. (a) Potential energy of the intermediate complex as a function of Z for ℓ = 50. (b) Probability distributions along the mass-asymmetry coordinate as a function of time calculated for ℓ = 50. (XBL 766-8131)

With the $\phi_Z(t)$'s, we can calculate the differential cross sections as:

$$\frac{d\sigma}{d\Omega}(\theta) = \int_0^\infty dt \left\{ \sum_b \frac{bP(b)}{\sin\theta\,|d\theta/db|} \phi_z(b,t)\Pi(t;b) \right\} \quad (2)$$

where P(b) is the probability that a collision at impact parameter b leads to a deep inelastic reaction. For this calculation, P(b) = 1 for all impact parameters $b \leq b_{lim}$, and P(b) = 0 for $b > b_{lim}$. The quantity $b_{lim}$ is such that the cross section resulting from collisions at impact parameters in the range $b_{lim} \leq b \leq b_{max}$ ($b_{max}$ corresponds to a grazing collision) is equal to the quasi-elastic cross section measured for Z's near the projectile Z at lab angles near the grazing angle. The sum in Eq. (2) is carried over all impact parameters b which result in a particle Z being emitted at the angle θ after the complex has lived a time t. The quantity Π(t;b) is the probability that the complex formed by a collision at impact parameter b will live a time t. In previous work, we have assumed $\Pi(t;b) = (1/\tau)\exp(-t/\tau)$ independent of b with τ being the average lifetime of the intermediate complex. Moretto et al.[3], have shown that the variation in the width of the Z distributions with angle can be explained by an average lifetime for the complex which decreases with increasing b. In the light of these results, these calculations have been performed with:

$$\Pi(t;b) = \frac{1}{N(b)} \exp\left[-(t - \tau(b))^2/\sigma^2(b)\right] \quad , \quad (3)$$

where N(b) is a normalization factor and $\tau(b) = \tau(0)\,(1 - b/b_{max})$.

This linear form for τ(b) is the simplest that such a decreasing lifetime can take, and trajectory calculations using a volume-type friction in the radial coordinate (similar to the calculation performed by Tsang[4] have yielded a T(b) similar to the linear form used. Since the dispersion in any random walk process varies linearly with the elapsed time,[5] we have assumed that $\sigma^2(b) = \sigma^2(0)(1 - b/b_{max})$. The quantity τ(b) represents the average lifetime of the complex formed at impact parameter b, and $\sigma^2(b)$ represents the dispersion of the distribution of lifetimes about this average value. For these calculations, the values of $\sigma^2(0)$ and τ(0) are paramaters but can in principle be determined from trajectory calculations.

The parameters used were: $\kappa = 0.25 \times 10^{21}$ $s^{-1}fm^{-2}$, $\tau(0) = 3.5 \times 10^{21}$ s, and $\sigma(0) = 1.0 \times 10^{21}$ s. The calculations have not been optimized with respect to the value of κ, and the value used was chosen because of the success of the previous work on light systems. The position and width of the side peak depends very strongly upon τ(0) very uniquely, and $\sigma^2(0)$, as one might expect. The position of the side peak in the experimental angular distribition determines τ(0) very uniquely, and $\sigma^2$ has the effect of making the side peak broader or narrower. The value of τ(0) should be compared with the rotational period of $8.6 \times 10^{-21}$s for the average ℓ-value of 185. The value of σ(0) would seem to indicate a very strong coupling of intrinsic modes to the collective motion during the collision.

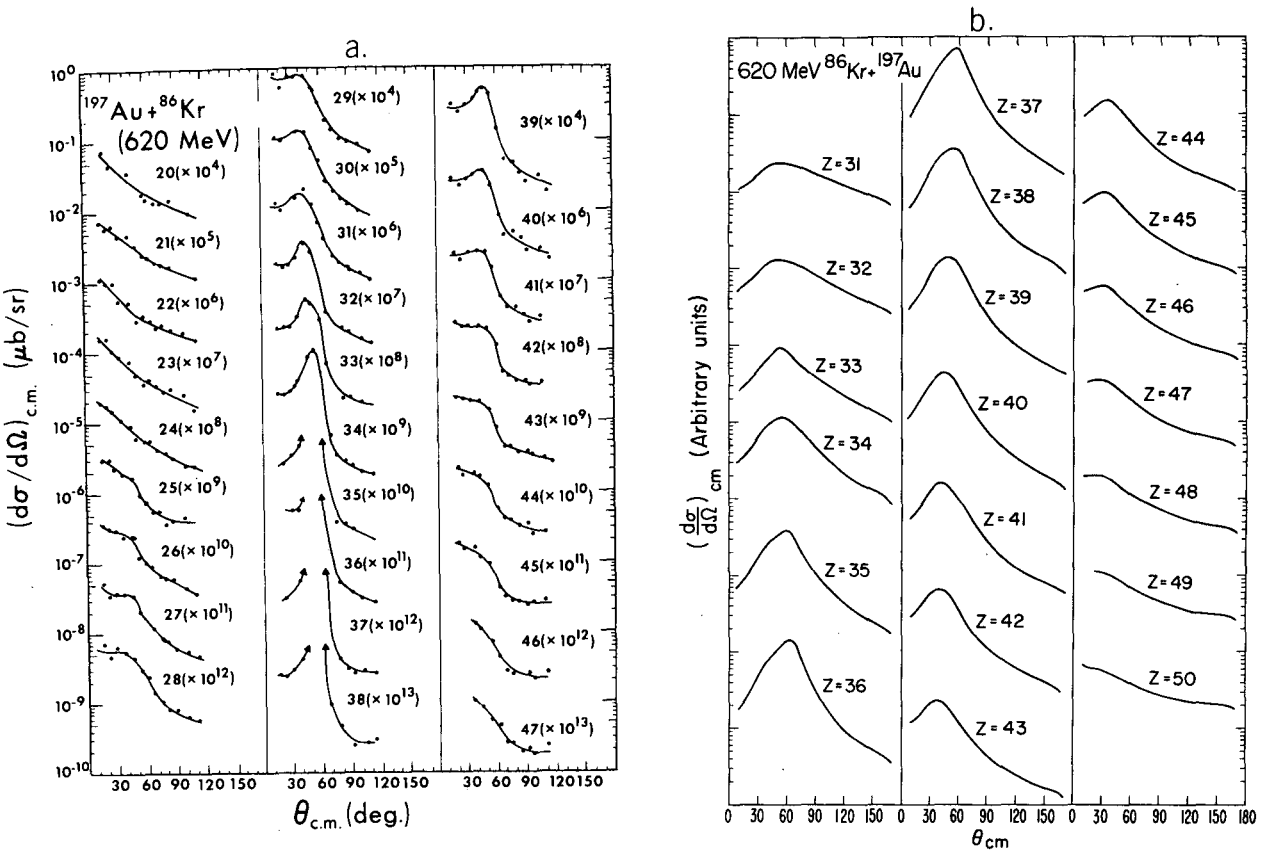


Fig. 2 (a) Experimental center-of-mass angular distributions for the reaction $^{197}$Au + 620 MeV $^{86}$Kr. (b) Theoretical center-of-mass angular distributions for the same reaction using model described in the text. (XBL 776-2905A)

The angular distributions measured recently by our group[3] for 620 MeV $^{86}$Kr + $^{197}$Au are displayed in Fig. 2(a). The general features discussed above, such as the Z dependent side peaking, can be seen quite clearly as one scans Z's both above and below Z = 36. Fig. 2(b) shows the angular distributions calculated for this system using the model described above. Note that the magnitude of the side peaking is greatest for Z = 36 and decreases on either side of the projectile. The gradual disappearance of the side peak for Z's above the projectile almost exactly parrots the experimental distributions. The distributions for Z's below the projectile follow a similar pattern, but the side peaking disappears too quickly (after too few Z's). This seems to be due to the assumption of two touching spheres for the shape of the intermediate complex.

In conclusion, the Diffusion Model is able to duplicate the qualitative experimental features of the relaxed component observed in the reactions of "heavy" systems like $^{86}$Kr + $^{197}$Au. Calculations are currently being performed in which the time-dependence of the kinetic energy of the relative motion of the projectile and target is explicitly followed, thereby generating kinetic energy distributions as well as Z distribution. Such an approach should describe the features of both relaxed and quasi-elastic components in a continuous manner.

## Footnotes and References

*Condensed from Phy. Lett. 65B, 326 (1976).

†Sloan Fellow 1974-1976.

1. J. Galin et al., Nucl. Phys. A 255, 472 (1975).

2. L. G. Moretto and J. S. Sventek, Phys. Lett. 58B, 26 (1975).

3. L. G. Moretto et al., Phys. Lett. 36, 1069 (1976).

4. C. F. Tsang, Physica Scripta 10A, 90 (1974).

5. S. Chandrasekhar, Rev. Mod. Phys. 15, 1 (1943).

# INCLUSION OF RADIAL AND TANGENTIAL MOTION IN AN IMPROVED DIFFUSION MODEL FOR HEAVY ION REACTIONS*

L. G. Moretto†

In a previous formulation of the diffusion model,[1-4] the dynamics of the radial motion was simplified by freezing the two interacting fragments to a fixed overlap. Furthermore, it was assumed that the two interacting fragments were rapidly rotating. The realization that the form factor of the diffusion constant as well as the potential energy vs mass asymmetry and the interaction times are strongly affected by the radial motion has led to a more detailed recasting of the model as follows.

We assume that the intermediate complex has a shape close to that of two touching fragments. Charge to mass equilibration is assumed to be a rather fast process, so that the asymmetry of the system can be characterized by the mass or by the charge of one of the two fragments. We further assume that the time evolution along the asymmetry coordinate is diffusive in nature and describable in terms of the Master Equation:

$$\dot{\varphi}(Z,t) = \int dz' [\Lambda(Z,Z')\varphi(Z') - \Lambda(Z',Z)\varphi(z)] \qquad (1)$$

where $\varphi(Z,t)$, $\dot{\varphi}(Z,t)$ are the populations of the configurations characterized by the atomic number $Z$ of one of the fragments and their time derivating at time $t$; and $\Lambda(Z,Z')$, $\Lambda(Z',Z)$ are the macroscopic transition probablilties.

If in Eq. (1) one writes: $Z' = Z + h$ and all the quantities are expanded about $Z$ in powers of h, one obtains to lower order:

$$\dot{\varphi}(Z,t) = -\frac{\partial}{\partial Z}[\mu,\varphi] + \frac{1}{2}\frac{\partial}{\partial Z^2}[\mu_2\varphi] \qquad (2)$$

which is the well-known Fokker-Planck equation.[5] The quantities $\mu_1$ and $\mu_2$ are the first and second moment of the transition probabilities:

$$\mu_1 = \int h\Lambda(Z,h)dh \quad ; \quad \mu_2 = \int h^2\Lambda(Z,h)dh \quad . \qquad (3)$$

An analytical solution is available when the force is harmonic or $Z_Z = c/2\ (Z-Z_{sym})^2 = 1/2\ ch^2$; the solution is:

$$\varphi(h,t) = c^{1/2}\left[2\pi T\left(1 - \exp - \frac{2ct}{K}\right)\right]^{1/2} \times \exp - \frac{c[h-h_o \exp - ct/K]^2}{2T(1-\exp - 2ct/K)} \quad , \qquad (4)$$

where we have made use of the Einstein relation $\mu_1/\mu_2 = - V_Z'/2T$ where $T$ is the temperature and $F = - V_Z'$ is the driving force.

From general phase-space considerations one can consider the following ansatz for the transition probabilities:[2] $\Lambda(Z,Z') = \lambda(Z,Z')\rho_Z = \kappa f \rho_Z/(\rho_Z\rho_{Z'})^{1/2}$, where $\lambda(Z,Z')$ is the microscopic transition probability, $\rho_Z$ is the final state density, K is a particle flux and $f$ is the window area between the two fragments. This can be rewritten as

$$\Lambda(Z,h) = \kappa f \exp - V_Z'h/2T \quad . \qquad (5)$$

The Fokker-Planck coefficients can then be calculated:

$$\mu_1 = 2Kf \sinh V_Z'/2T \simeq - Kf\, V_Z' \quad ;$$

$$\mu_2 = 2\, Kf \cosh V_Z'/2T \approx 2Kf \qquad (6)$$

which for large $T$ satisfy the Einstein relation.

Such an ansatz implies for the friction coefficient: $K = T/\kappa f$. Alternatively if the particle transfer between two fragments with chemical potential differing by an energy $a = V'h$ is considered, one can write:

$$\Lambda(Z,h) = Ag\int \frac{d\varepsilon}{1 + \exp(\varepsilon - a)/T}\left(1 - \frac{1}{1 + \exp \varepsilon/T}\right) = \frac{AgV_Z'h}{1 - \exp - \frac{V_Z'}{T}} \qquad (7)$$

where $A$ is some strength constant and $g$ the average single particle level density. The final result is:

$$\mu_1 = - AgV_Z' \quad ; \quad \mu_2 = Ag\, V_Z' \coth V_Z'/2T \simeq 2AgT \qquad (8)$$

again satisfying the Einstein relation. The friction coefficient is $K = 1/Ag$. The two approaches lead to different results, namely the first predicts a friction coefficient proportional to the temperature, the second to a constant.

The quantity $\kappa f$ in Eq. (7) depends upon the overlap between the two fragments. It can be written as suggested by Randrup[6] as follows:

$$\kappa f \equiv \int h\, d\sigma = 2\pi\, n_o\, \bar{R}\, b\, \psi(\zeta) \quad , \qquad (9)$$

where $n_o$ is the particle flux in nuclear matter at saturation density, $\bar{R} = c_1c_2/c_1 + c_2$ is a reduced radius expressed in terms of the central

radii of the two fragments, b is the skin thickness and $\psi(\zeta)$ is a universal function depending upon the separation between the sharp surface of the two fragments in units of the surface thickness. This approach neatly factors out the geometrical features of the problem.

In general, the potential energy of the intermediate complex as a function of Z can be written as

$$V(Z,\ell) = V_{LD}(Z) + V_{LD}(Z_T - Z) + V_{Prox}(Z,\ell) + V_{Coul} + V_{Rot} \qquad (10)$$

where $\ell$ is the total angular momentum, $V_{LD}$ represent the liquid drop energies of the two fragments, and $V_{prox}$ is the nuclear interaction or proximity energy[7]. The total potential V depends on the fissionability of the system x, on $\ell$ and on the distance between centers D. The driving force which arises from this potential depends dramatically on the entrance channel asymmetry, as well as on x, $\ell$, D. It may either drive the system towards symmetry or towards extreme asymmetries. For a reaction like 600 MeV Kr + Au the driving force is always in the direction of symmetry.

Both the diffusion constant and the asymmetry potential energy depend upon the distance between the two fragments. Furthermore the extent to which the diffusion proceeds depends upon the interaction time. One needs then to study the radial motion in some detail.

The radial potential can be written as:

$$V(C) = V_{prox} + \frac{Z(Z_T-Z)e^2}{D} + \frac{\hbar^2\ell^2}{2\mathcal{J}(\ell)} \qquad (11)$$

$\mathcal{J}(\ell)$ being an appropriate moment of inertia. We shall just use it to calculate the average force $F_R(\ell) = \frac{\partial V(D)}{\partial D}\Big|_{D_{int}}$. From the knowledge, at interaction radius, of the reduced mass $\mu$, of the radial velocity $v_R$ and of the radial force $F_R$ for each $\ell$ value, one can introduce the following two ansatz for the interaction time $\tau$ and the average penetration $\bar{x}$:

$$\tau(\ell) = \frac{2\mu v_R}{F_R} = 2\sqrt{\frac{2\mu(E-B)}{F_R}}\left(1 - \frac{\ell^2}{\ell_{max}^2}\right)^{1/2};$$

$$\bar{X}(\ell) = \frac{\alpha}{2}\,\frac{\mu v_R^2}{F_R}. \qquad (12)$$

The tangential motion is treated assuming, for the equation of motion the simple form: $F_T = \mu\gamma(\omega_o - \omega_{Rig})$ where $\omega_o$ and $\omega_{Rig}$ are the two limiting angular velocities corresponding to sliding and sticking.

The interaction times calculated for the reaction Au + Kr at three energies are shown in Fig. 1a as a function of angular momentum. There is good experimental evidence for the angular momentum dependence predicted by our ansatz. In Fig. 1b the average deflection function is shown. Notice the well pronounced deep inelastic rainbow which moves from positive to negative angles as the bombarding energy increases, in excellent agreement with experiment. In Figs. 2 and 3 the calculated angle-integrated Z distributions are compared with experiment for the reactions Au + Kr and Ta + Kr at 620 MeV.[1] In Figs. 4 and 5 examples of the angular distributions for fragments of various Z are shown for both reactions.

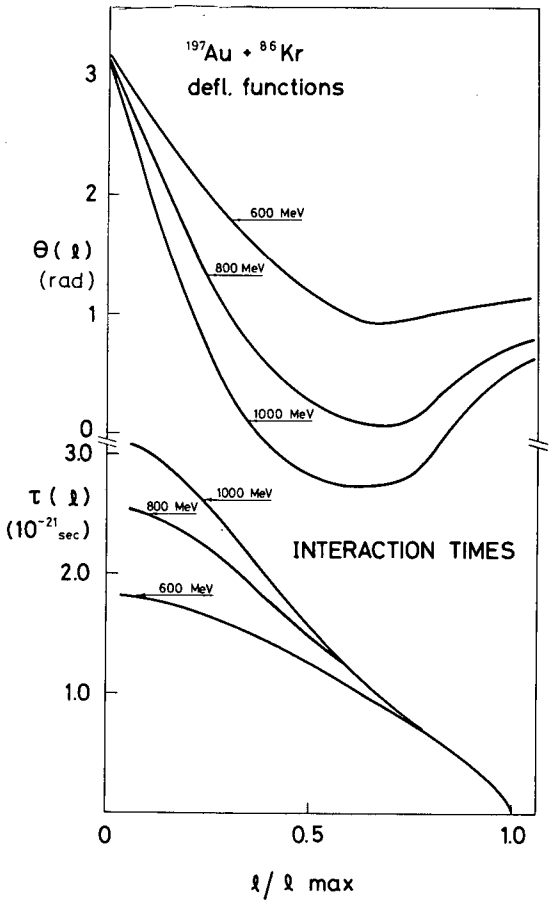


Fig. 1. Top. Dependence of the interaction time upon angular momentum at three bombarding energies for the reaction Au + Kr. Bottom. Average deflection functions for the same bombarding energies.
(XBL 778-9815)

There is an additional confirmation of the validity of the diffusion model. The intrinsic angular momenta for each asymmetry have been studied by measuring the $\gamma$-ray multiplicities as a function of Z.[7] Our model can readily predict the total average angular momentum for a given Z. By assuming an arbitrary shape, like two touching rigidly rotating spheres, one can calculate the angular momentum partition. Rigid rotation is most likely a good approximation 2 or 3 units beyond the projectile. In Fig. 6 the estimated multiplicities and the corresponding widths are shown together with the experimental data.[7] The rise of the multiplicity at low Z's, expected for

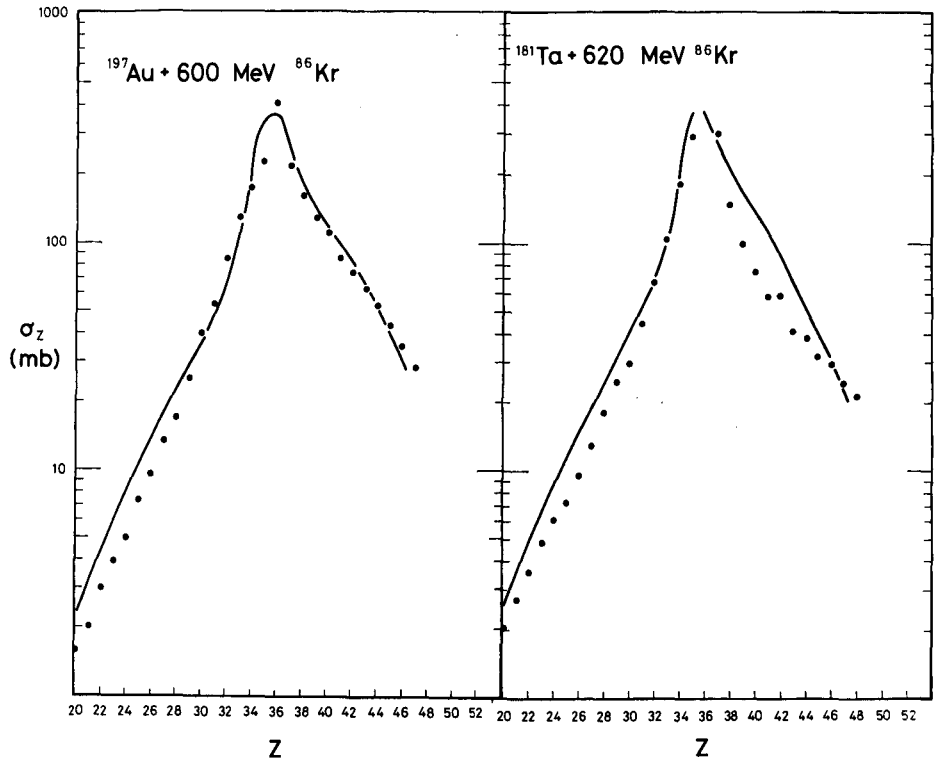


Fig. 2. Angle integrated Z distribution for the reaction Au + 600 MeV Kr. The dots are the experimental points and the solid line the theoretical calculation. (XBL 778-9817;left)

Fig. 3. Same as in Fig. 2 for the reaction Ta + 620 MeV Kr. (XBL 778-9817;right)

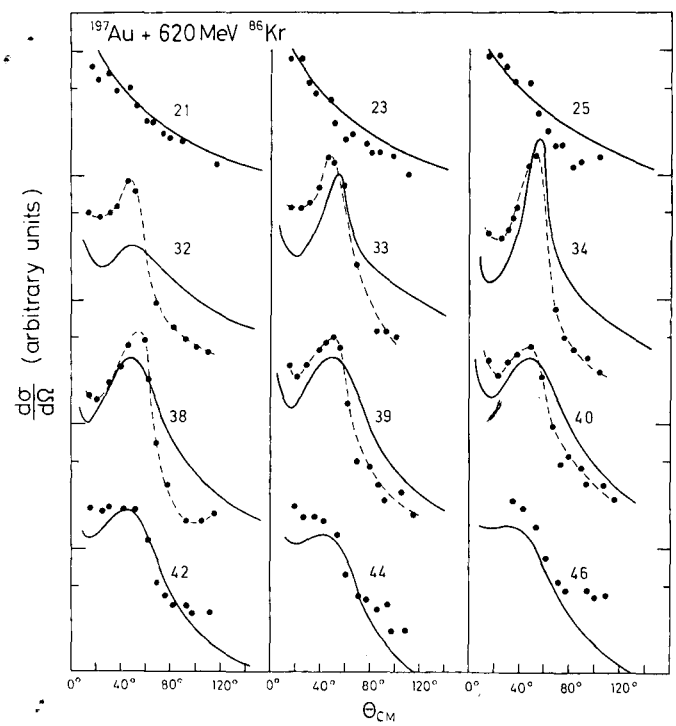


Fig. 4. Angular distributions of fragments of selected Z for the reaction Au + 600 MeV Kr. The dots are the experimental points and the solid lines the theoretical calculations. (XBL 778-9811)

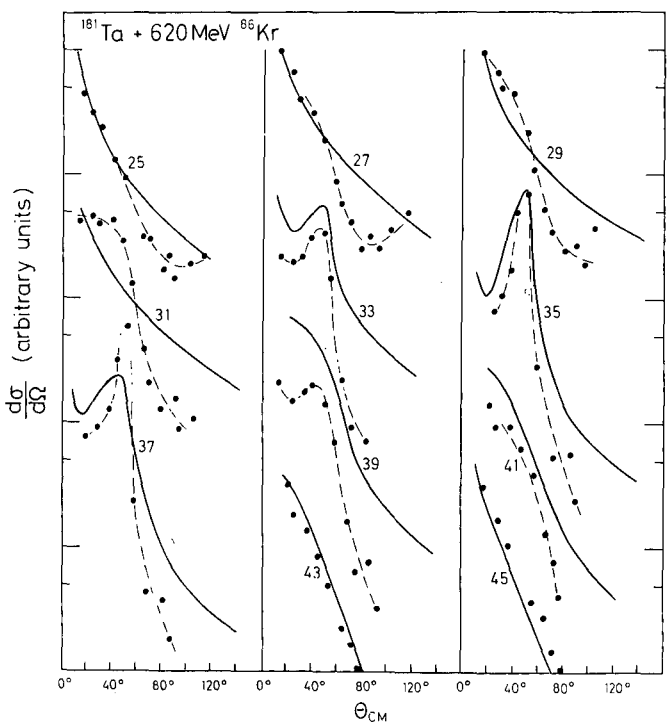


Fig. 5. Same as in Fig. 4 for the reaction Ta + 600 MeV Kr. (XBL 778-9816)

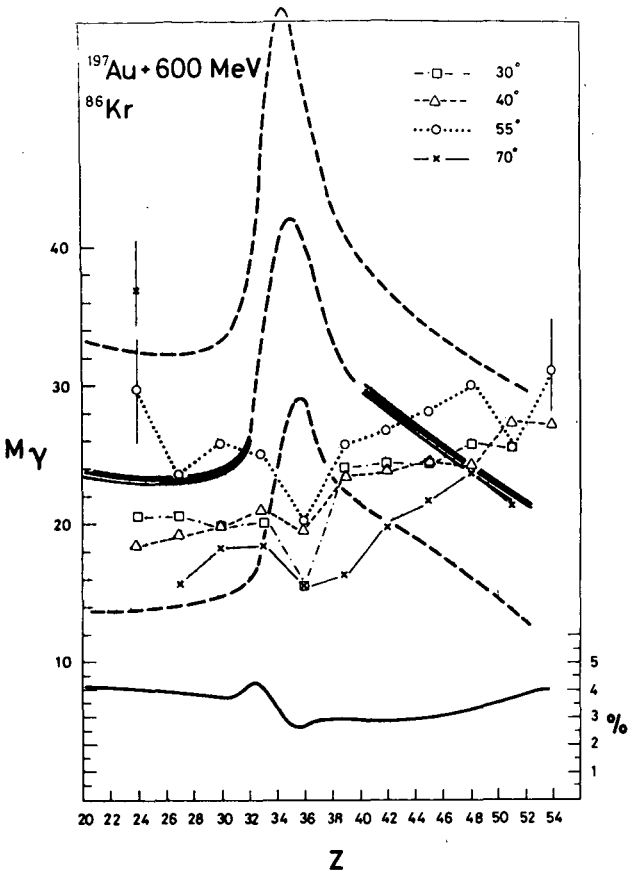


Fig. 6. Experimental and theoretical γ-ray multiplicities as a function of Z. The large band represents the theoretical width (± σ) which is also plotted in the lower part of the figure. (XBL 778-9813)

rigid rotation at constant angular momentum, is not seen in the calculation nor in the experiment. The reason lies in that the driving force towards symmetry is much stronger at high than at low angular momentum. The diffusion process therefore selects out low angular momenta to populate the low Z configurations with the consequent low values of the γ-ray multiplicity.

## Footnotes and References

*Work supported in part by the Niels Bohr Institute, Copenhagen, Denmark.

†Sloan Fellow 1974-1976.

1. L. G. Moretto and R. Schmitt, J. de Physique C 5 no. 11, 37 (1976); 109 and references therein.

2. L. G. Moretto and J. S. Sventek, Phys. Lett. B 58, 26 (1975).

3. W. Nörenberg, Z. Physik A 274, 241 (1975).

4. L. G. Moretto, B. Cauvin, P. Glässel, R. Jared, P. Russo, J. Sventek and G. Wozniak, Phys. Rev. Lett. 36, 1069 (1976).

5. W. Nörenberg, J. de Physique C 5, no. 11, 37, 141 (1976).

6. J. Randrup, Proceedings of the International Workshop on Gross Properties of Nuclei and Nuclear Excitations, AED Conf. 77-017-001, Hirschegg 1977.

7. Preliminary results from L. G. Moretto and Diamond-Stephens groups, Berkeley.

# NUCLEAR ONE-BODY PROXIMITY FRICTION*

J. Randrup†

A variety of experiments have established the importance of dissipative processes in nuclear dynamics. At moderate energies, where the nucleon mean free path is long, the dissipation is expected to be predominantly produced by the inelastic collisions of individual nucleons with the time-dependent average single-particle potential. This one-body dissipation mechanism has received increased interest in recent times.[1-3] In particular, Ref. 3 explores simple formulas for the dissipation rate, based on a picture of independent classical particles confined by a time-dependent container.

In the simplest version, this picture assumes that for colliding nuclei the individual nucleons are exchanged via a sharply defined and fully open window.[3,4] Although qualitatively correct, this treatment neglects the diffuseness of the nuclear surface. If quantitative applications are to be made the separation dependence of the friction must be treated with the same care that is accorded to the conservative part of the force between the nuclei. The calculation of the one-body friction between nuclei can be brought to the same level of accuracy as has been accomplished for the calculation of the conservative nuclear force by virtue of the proximity treatment.[5]

The general expression for the Rayleigh dissipation function F, which is half the rate of energy dissipation, is given by

$$F = \frac{1}{2} N \left(2u_n^2 + u_t^2\right) \qquad (1)$$

From this function the friction forces acting on the collective variables can be obtained by

partial differentiation with respect to the corresponding collective velocities. The normal and tangential components of the relative velocity between the two nuclei at the window are denoted by $u_n$ and $u_t$. Furthermore, N denotes the total one-way current of mass from one nucleus to the other through the window, $N = \int n\, d\sigma$, where n is the local mass flux. An approximate but quite general scheme for calculating the current N can be made in analogy with the calculation of the proximity potential between leptodermous systems.[5]

Consider two juxtaposed leptodermous systems with slightly curved surfaces. In the limit of small curvature the local flux n from one system to the other depends only on the separation s between the local elements of the two surfaces. To leading order, this separation has a quadratic dependence on the distance from the point of smallest separation: $s \approx s_o + \rho/2\bar{R}$. Hence $d\sigma = 2\pi \bar{R}\, ds$ and the integral can be reduced, in the usual way, to a one-dimensional integral over the surface separation s:

$$N = \int n\, d\sigma \approx 2\pi\bar{R} \int_{s_o}^{\infty} n(s)ds = 2\pi\bar{R}\, N(s) \quad (2)$$

As in Ref. 5, $1/\bar{R} = 1/C_1 + 1/C_2$ is the mean curvature of the gap between the two surfaces and the matter density profile radii $C_i$ are related to the equivalent sharp radii $R_i$ by $C_i = R_i - b^2/R_i$ where b is the surface diffuseness of the matter density distribution. Moreover, the function $N(s)$ is the incomplete integral of $n(s)$, the flux between two semi-infinite systems positioned with surface separation s.

The functions $n(s)$ and $N(s)$ can be expressed in dimensionless form by adopting the inherent surface diffuseness b as the unit of length and the inherent bulk flux $n_o$ as the unit of flux. Thus $\zeta = s/b$ is the dimensionless separation and we define the universal proximity transparency function by

$$\psi(\zeta) = n(\zeta b)/n_o \quad (3)$$

and its incomplete moments by

$$\Psi_n(\zeta_o) = \int_{\zeta_o}^{\infty} \zeta^n \Psi(\zeta)\, d\zeta \quad (4)$$

In terms of $\Psi(\zeta)$ the total flux across the curved gap can be written

$$N = \int n\, d\sigma = 2\pi\, n_o\, \bar{R}\, b\, \Psi(\zeta_o) \quad (5)$$

with $\zeta_o = s_o/b$. The advantage of introducing the dimensionless form is that a calculation of the friction will then tend to be less sensitive to possible defects of the model employed; the model is only asked to yield the form of the friction function and not its absolute scale. This leaves the possibility of adjusting the parameters b and $n_o$ to experimental values.

The final proximity formula for the Rayleigh dissipation function thus becomes

$$F = \frac{1}{2}\, 2\pi\, n_o\, \bar{R}\, b\, \Psi(\zeta_o)(2u_n^2 + u_t^2) \quad (6)$$

The usefulness of this result lies in the separation of the geometry (entering here as $\bar{R}$) from the inherent surface properties of the particular matter under study. The geometrical part may vary from case to case and is easy to calculate while the second part is specific to the type of material considered and can thus be calculated once and for all, in a suitable model (and it is in this sense universal). It should be added that the present appraoch is not restricted to parabolic gap geometries. Indeed, as discussed in Ref. 5, a wider class of geometries can be reduced to simple expressions containing the dimensionless functions $\Psi_n(\zeta)$. Moreover, the effect of gentle variations of the relative velocity $\vec{U}$ over the window region can also easily be expressed in terms of the functions $\Psi_n(\zeta)$.

The dimensionless transparency function $\Psi(\zeta)$ has been calculated in the nuclear Thomas-Fermi model based on the phenomenological Seyler-Blanchard nucleon-nucleon interaction. The method is similar to the one employed in Ref. 5. The resulting function $\psi(\zeta)$ is displayed in Fig. 1 and the integrated function $\Psi(\zeta)$ is displayed in Fig. 1 and the integrated function $\Psi(\zeta)$ in Fig. 2 It should be noted that in contrast with the proximity force function $\varphi(\zeta)$ the transparency function $\psi(\zeta)$ tends to zero at a finite separation, $\zeta \approx 3.60$, corresponding to the "breakthrough" distance at which the barrier in the potential just coincides with the Fermi level. As the two systems approach the barrier decreases and the transparency function $\psi(\zeta)$ quickly tends to unity.

For practical applications it is useful to have available a simple analytical representation of the flux function $\Psi(\zeta)$ appearing in the proximity expression for the Rayleigh dissipation function. One such approximation is

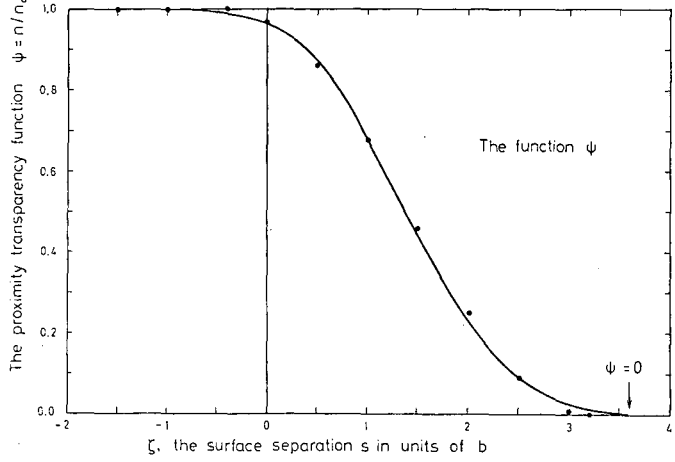


Fig. 1. The universal proximity transparency function $\psi(\zeta)$. The circles indicate values given by the analytic approximation to $\psi(\zeta)$. (XBL 778-1761)

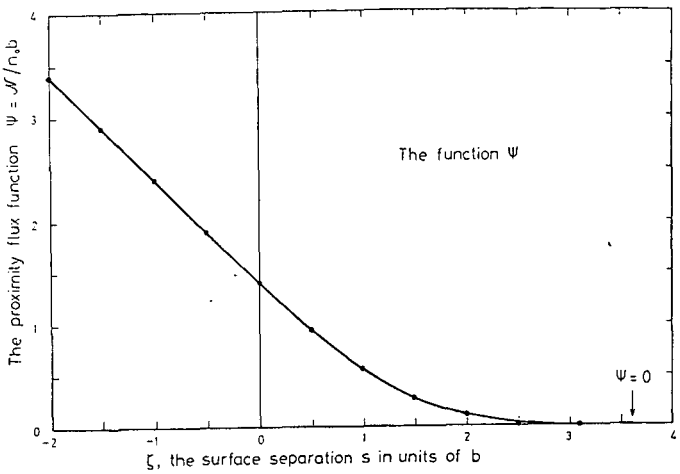


Fig. 2. The universal proximity flux function $\Psi(\zeta)$ [identical to the incomplete moment $\Psi_0(\zeta)$]. The circles indicate values given by the analytic approximation to $\Psi(\zeta)$. (XBL 778-1762)

$$\begin{cases} \Psi(\zeta \leq -0.4) = 1.4 - \zeta \\ \Psi(-0.4 \leq \zeta \leq 3.2) = 1.6 - 0.5\zeta - \frac{1.8}{\pi} \sin\left(\frac{\zeta + 0.4}{3.6}\right)\pi \\ \Psi(3.2 \leq \zeta) = 0 \quad . \end{cases} \tag{7}$$

Included in Figs. 1 and 2 are some values resulting from this approximate expression, in order to make possible a quick judgement of the degree of validity of these representations. Corresponding representations of the higher moments $\Psi_n(\zeta)$ can be obtained on the basis of the above approximation to $\psi(\zeta)$ .

Combining the proximity friction calculated in this paper with the proximity potential of Ref. 5, one should be in a position to calculate the features of collisions between idealized nuclei without introducing any adjustable parameters. Along this line, we are planning to calculate the angular deflections and energy losses in grazing collisions and by a comparison with experimental (Wilczynaki-type) plots to confront the one-body dissipation theory with collision measurements in a relatively unambiguous way.

Footnotes and References

*Condensed from LBL-5847.

†Present address: NORDITA, Blegdamsvej 17, DK-2100 Copenhagen Ø, Denmark.

1. W. J. Swiatecki (1975) LBL-4296.

2. S. E. Koonin, R. L. Hatch and J. Randrup, Nucl. Phys. A 227, 509 (1977).

3. J. P. Błocki, Y. Boneh, J. R. Nix, J. Randrup, M. Robel, A. Sierk, W. J. Swiatecki, LBL-6100 (1977).

4. W. J. Swiatecki, J. Phys. C 5, 45 (1972).

5. J. P. Błocki, J. Randrup, W. J. Swiatecki and C. F. Tsang, Ann. Phys. 105, 427 (1977).

## ONE-BODY DISSIPATION AND THE SUPER-VISCIDITY OF NUCLEI*

J. Błocki,† Y. Boneh,‡ J. R. Nix,§ J. Randrup,‖ M. Robel, A. J. Sierk,¶ and W. J. Swiatecki

By taking at face value the independent-particle model of nuclear structure, even when the nuclear potential well is a slowly varying function of time, one is led to suspect that macroscopic nuclear dynamics might often be dominated by dissipative effects originating in a "one-body" dissipation mechanism[1] expected to be relevant for an assembly of particles whose mean-free-paths are comparable to or larger than the size of the system. By introducing a certain "randomization hypothesis" we have derived two simple dissipation formulae, one relevant for the process of nuclear fission and the other for nuclear collisions. The fundamental time unit for energy dissipation implied by these formulae turns out to be the relatively short single-particle transit time (in order of magnitude). The wall formula, when applied to the description of nuclear fission, does not lead to serious disagreement with experiment (Fig. 1). The window formula, when applied to nucleus-nucleus collisions, implies a fairly rapid dissipation of the energy of relative motion (see Fig. 2), but whether there is quantitative agreement or not with experimental data is not certain.

Further theoretical studies (see also Ref. 2) bring out the expected failure of the randomization hypothesis for nuclear shapes and motions characterized by special regularities and symmetries. Quantal effects, which we have studied by numerically solving the time-dependent Schrödinger equation, also set a limit to the applicability of simple macroscopic formulae, especially for small systems at low temperatures. Finally at high temperatures approaching the Fermi energy, the independent-particle model and the associated dissipation formulae are expected

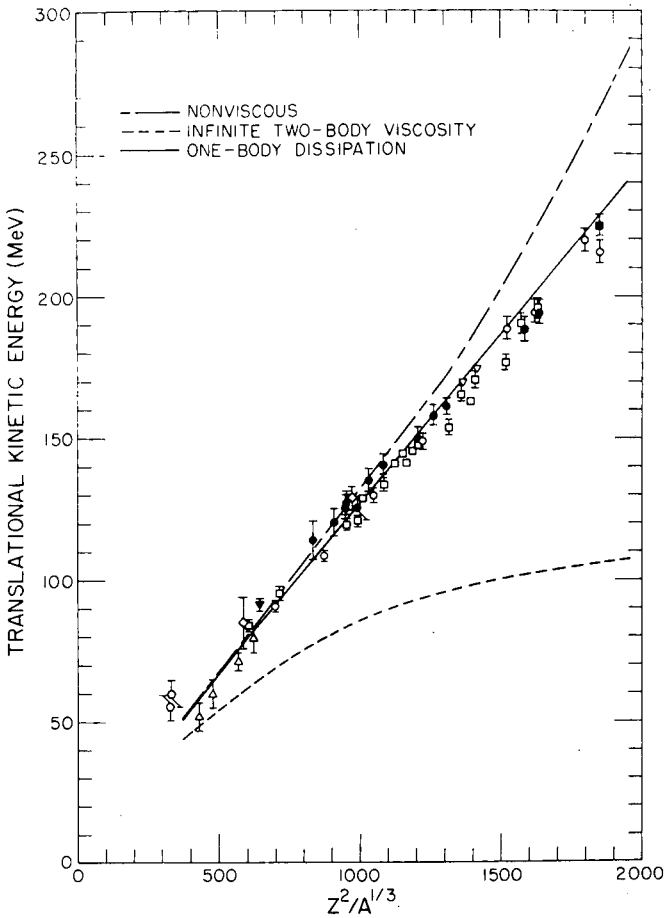


Fig. 1. Comparison of calculated and experimental most probable fission-fragment kinetic energies as a function of $Z^2/A^{1/3}$. The kinetic energies calculated for nonviscous flow are given by the dot-dashed curve. The dashed curve shows the results for infinite conventional (two-body) viscosity, and the solid curve shows the results for the one-body dissipation considered here. The experimental data are for cases in which the most probable mass division is into two equal fragments; the open symbols represent values for equal mass divisions only and the solid symbols represent values averaged over all mass divisions. (XBL 777-9492)

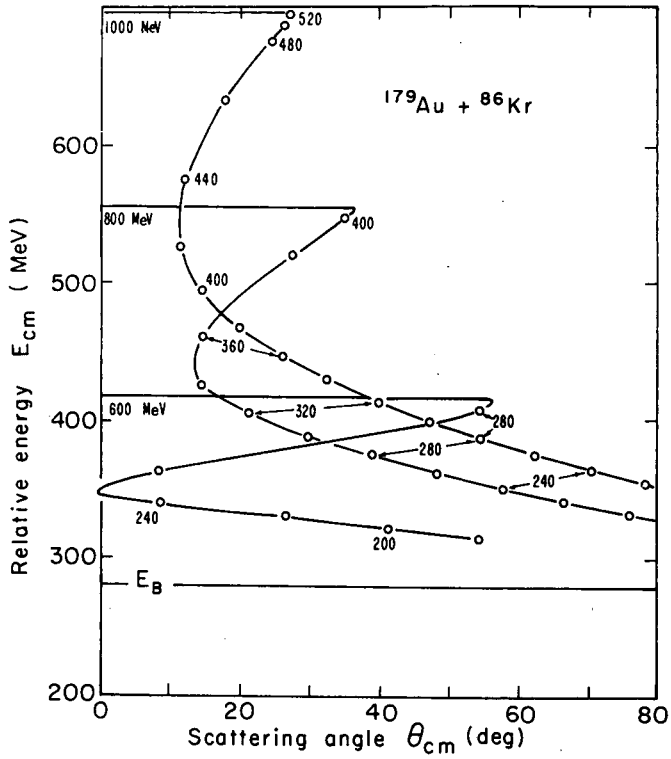


Fig. 2. Energy vs angle plots (Wilczyński diagrams) for the idealized collision of $^{86}$Kr on $^{179}$Au at three (lab) energies. The labels on the circled points give the final orbital momentum appropriate to the angle and energy indicated. The interaction barrier $E_B$ (the same, in the model used, for the entrance and exit channels) is indicated. (XBL 776-1302)

to break down, the nuclear medium becoming more like an ordinary fluid (which, however, is still expected to be dominated by viscosity).

Taking a broad view of the situation, the following features appear to emerge. A two-part approach to nuclear dynamics, in which effects of shell structure are added to a smooth background, somewhat analogous to the two-part approach to nuclear statics,[3] should be useful. Apart from super-fluidity at very low nuclear excitations, the smooth background dynamics would appear to be characterized by super-viscidity, i.e., a pronounced dominance of the motions by dissipative effects. At moderate temperatures, in the domain of the approximate validity of the independent-particle model, the dissipation is probably largely of the one-body kind, giving place to more conventional two-body viscosity at high temperatures. These smooth dynamics (whose key equations are relatively simple, especially in the one-body domain) are expected to be modified more or less drastically at moderate and low temperatures by symmetries and quantal features.

The future development of macroscopic nuclear dynamics might thus be found to parallel the development of macroscopic nuclear statics. There, the simple smooth background equations for the macroscopic nuclear potential energy (written down in the thirties) were followed (in the sixties) by a gradual understanding of the special effects of symmetries and quantization.

## Footnotes and References

*Condensed from LBL-6536.

†Permanent address: Institute for Nuclear Research, Swierk, Poland.

‡Permanent address: Weizmann Institute, Rehovot, Israel.

§Los Alamos Scientific Laboratory, Los Alamos, NM.

‖ Permanent address: Niels Bohr Institute, Coopenhagen, Denmark.

¶ Los Alamos Scientific Laboratory, Los Alamos, NM, and California Institute of Technology, Pasadena, CA.

1. W. J. Swiatecki, Proc. Int. School-Seminar on Reactions of Heavy Ions with Nuclei and Synthesis of New Elements, Dubna, Sept. 23-Oct. 4, 1975, p. 89; LBL-4296 (1975).

2. S. E. Koonin, R. L. Hatch, and J. Randrup, Nucl. Phys. A 283, 87 (1977).

3. W. D. Myers and W. J. Swiatecki, Nucl. Phys. 81. 1 (1966); M. Brack et al., Rev. Mod. Phys. 44, 320 (1972).

# EXTENSION OF THE CLASSICAL-LIMIT S-MATRIX TO ALPHA TRANSFER REACTIONS

L. F. Oliveira, R. Donangelo, H. Radi, M. W. Guidry, and J. O. Rasmussen

The theory of the classical-limit S-matrix (CLSM) has been successfully applied to the problem of Coulomb excitation of rotational states in deformed heavy ions.[1,2] More recently the problem of Coulomb-nuclear interference was also studied using this formalism.[3] In the present work we extend the theory to the investigation of alpha transfer into different rotational levels at bombarding energies slightly below the Coulomb barrier.

As in previous works, the relative motion of the colliding nuclei is described classically. The rotational signature is again caused by the interaction of the electric field of the projectile and the quadrupole moment of the deformed target. In our new code the transfer is taken care of through the inclusion of a form factor in our expression for the Coulomb excitation S-matrix. This form factor or transfer amplitude expresses both the alpha tunneling amplitude through the barrier and the effect of the zones of most probable alpha emission on the nuclear surfaces.

With the inclusion of this transfer amplitude $a_t(\chi_o)$ our expression for the integral representation of the S-matrix becomes

$$S_{0\to I} = \frac{\sqrt{2I+1}}{2} \int_0^{\pi} \sqrt{\sin\chi_o \sin\bar{\chi}\, \frac{d\bar{\chi}}{d\chi_o}} \times P_I(\cos\bar{\chi})\, a_t(\chi_o)\, e^{i\Delta/\hbar}\, d\chi_o \quad , \quad (1)$$

where $\chi_o$ is the initial angle between the symmetry axis of the target and the line joining the centers of the projectile and target. All other variables are explained in Ref. 1. We note that this expression for the S-matrix applies only for the case of backward scattering, however this is not a serious restriction since in sub-barrier interactions transfer is expected to be maximal for backward angles.

The transfer amplitude is given by the equation

$$\frac{da_t(\chi_o,t)}{dt} = T(\chi(t))\; e^{iQ_{eff}\, t/\hbar}\; W(\chi(t)) \quad (2)$$

which is then integrated along the trajectory defined by the initial angle $\chi_o$. The amplitude appearing in Eq. (1) is defined as

$$a_t(\chi_o) = \lim_{t\to\infty} a_t(\chi_o,t) \quad (3)$$

In Eq. (2) T is the tunneling amplitude, which will be approximated by the WKB expression, the term $e^{iQ_{eff}\, t/\hbar}$ takes care of the Q-mismatch between the entrance and exit channels and W describes the α emission amplitude in different zones of the nuclear surface.

In the WKB approximation T can be written as

$$T = \exp\left[-\sqrt{\frac{2\mu}{\hbar}} \int_{R_2}^{R(t)-R_1} \times \sqrt{Q_i + \frac{2Z_p e^2}{R(t)-x} + \frac{2Z_T e^2}{x} + \frac{Q_o e^2 P_2(\cos\chi)}{x^3}} + V_{P\alpha} + V_{T\alpha}\, dx\right] \quad (4)$$

where $Q_i$ is the α-binding energy in the projectile, $Z_P$ and $Z_T$ are the charges of projectile and target respectively, $Q_o$ is the quadrupole moment of the target and μ is the reduced mass of the system. $V_{P\alpha}$ and $V_{T\alpha}$ are the nuclear potentials seen by the α-particle in the projectile and target respectively. The radius of the projectile is given by $R_1$, and $R_2(\chi)$ is the radial coordinate of the target surface. The variable R(t) describes the relative separation between the centers of projectile and target, while x is the distance between the center of the α particle and that of the target (see Fig. 1).

For backward scattering $Q_{eff}$ can be approximated by

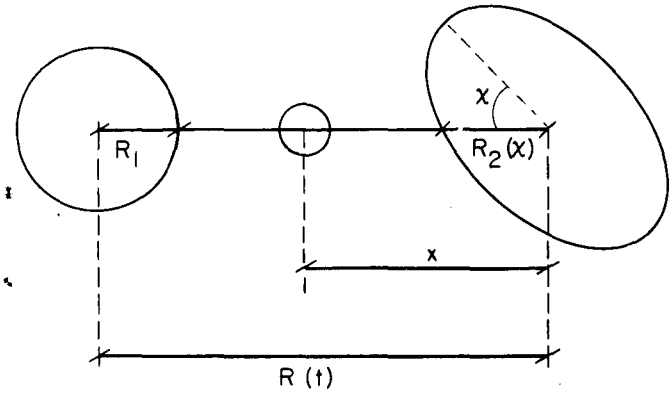


Fig. 1. Geometrical parameters which describe the system. (XBL 778-9954)

$$Q_{eff} = Q_R + \left[\frac{Z_P Z_T e^2}{2a}\right]_{entrance} - \left[\frac{Z_P Z_T e^2}{2a}\right]_{exit} \quad (5)$$

Here $Q_R$ is the reaction Q-value, a the half distance of closest approach on the Rutherford trajectory with the same impact parameter and energy. The above correction to $Q_R$ can be understood as a renormalization of the α-particle energy in one nucleus due to the Coulomb field of the other.[4]

The α-emission amplitude $W(\chi)$[5] is given by

$$W(\chi) = \sum_{\ell \text{ even}} a_\ell Y_{\ell 0}(\chi) \quad , \quad (6)$$

where $Y_{\ell 0}(\chi)$ are spherical harmonies. The coefficients $a_\ell$ used in the present work were calculated by Radi et al.[6]

Figure 2 presents the results of two calculations, curve labeled (1) was obtained using the present formalism while curve (2) is the Coulomb excitation probabilities without transfer [that is, setting $a_t(\chi_0) = 1$ in Eq. (1)].

We notice that the interference structure of curve (2) does not appear in curve (1). We interpret this in the USCA approach[7] as due to the fact that trajectories approaching the target close to its tip are much more favored for transfer to take place than those which approach the nucleus close to its equator. In practice this is equivalent to having just one trajectory contributing to transfer of the two that appear in the Coulomb excitation case. The interference between these two trajectories is responsible for the structured behavior of the Coulomb excitation probabilities, and as we see, is lacking in the case where transfer takes place. It is interesting to see that transfer takes place mostly to states other than the ground state.

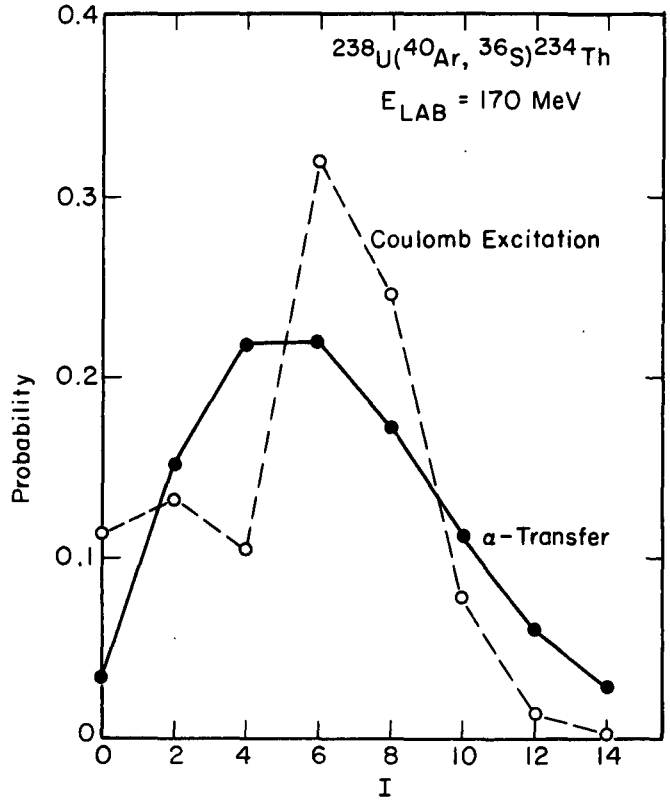


Fig. 2. Alpha transfer (full circles) and pure Coulomb excitation (open circles) probabilities for the system $^{40}Ar + ^{238}U$. The alpha transfer probabilities are normalized to 1 for comparative purposes. (XBL 778-9953)

References

1. R. Donangelo, M. W. Guidry, J. P. Boisson, and J. O. Rasmussen, Phys. Lett. 64B, 377 (1976).

2. R. Donangelo, Ph.D. Thesis, University of California, Berkeley (1977), unpublished.

3. M. W. Guidry, H. Massmann, R. Donangelo, and J. O. Rasmussen, Nuc. Phys. A 274, 183 (1976).

4. R. Broglia and A. Winther, Nuc. Phys. A 182, 112 (1972).

5. I. Perlman and J. O. Rasmussen, Handbuch der Physik, Springer Verlag (1957).

6. H. Radi, J. O. Rasmussen, L. Oliveira, R. Donangelo and A. Shihab-Eldin, unpublished report.

7. H. Massmann and J. O. Rasmussen, Nuc. Phys. A 243, 155 (1975).

# THE CLASSICAL-LIMIT S-MATRIX AND ORBITAL DYNAMICS IN SEMICLASSICAL COULOMB EXCITATION THEORY*

R. Donangelo, M. W. Guidry, J. P. Boisson, and J. O. Rasmussen

The recent availability of very heavy ions has made it possible to populate high spin states with multiple Coulomb excitation processes. Exact partial-wave, coupled-channel calculations are possible for Coulomb excitation with light projectiles,[1] but such calculations are not feasible at present for heavy-ion systems. The most common approach to this problem has used the semiclassical methods developed by Alder and Winther[2] (A-W) to calculate multiple Coulomb excitation probabilities. In this approach the internal degrees of freedom are treated quantum-mechanically but the projectile dynamics are taken as that of a classical particle on an energy-symmetrized hyperbola.

Initial attempts to account for the corrections arising from the use of approximate orbital dynamics have involved extrapolations from exact light-ion calculations and sophisticated energy and angular momentum symmetrizations in the semiclassical limit. In Ref. 3 a third approach was introduced, using classical-limit S-matrix (CLSM) methods originally developed in atomic and molecular scattering problems. It was suggested that this approach might be capable of supplying corrections due to the semiclassical orbital dynamics. In this paper we apply recently introduced refinements to the CLSM method,[4,5] and provide evidence that this approach can be used with confidence to determine excitation probabilities for heavy-ion multiple Coulomb excitation. The reader should refer to Refs. 4 and 5 for a description of this method.

It is important to consider carefully the nature of the approximations implicit in the Alder-Winther (A-W) semiclassical method and in the classical-limit S-matrix method. In the (A-W) approch the wavefunction is expanded on the unperturbed nuclear eigenstates, but the time dependence of the interaction potential in the resulting coupled Schrödinger equations is approximated as due to a projectile moving on a classical Rutherford trajectory. In this sense the method may be characterized as one which treats the target internal excitation degrees of freedom quantum mechanically, but which treats the projectile degrees of freedom using approximate classical dynamics. The dynamics are approximate because 1) all coupling of the projectile motion to the noncentral part of the potential (e.g., the quadrupole field) is ignored, and 2) because the energy difference in the entrance and exit channels for an inelastic process is only approximately accounted for by the introduction of energy-symmetrized hyperbolas.

The validity of this approximation rests on whether the wave-packet representing a projectile in a given situation behaves as a localized particle subject to classical equations of motion and, if so, whether the deviation from a Rutherford trajectory arising from coupling to the quadrupole field and from finite energy transfer sufficient to invalidate the approximate classical dynamics employed. The first question relates to whether there are explicit quantum dynamical effects operating that cast doubt on the concept of a classical trajectory. It is a question about phenomena which vanish in the limit $\hbar \to 0$ and which can only be fully answered in the context of a rigorous quantum mechanical analysis. The second question concerns effects which are due to approximations in the classical dynamics employed and which are independent of $\hbar$. This question might reasonably be answered within a classical or classical-limit framework.

In the classical-limit S-matrix method one forsakes the semiclassical prescription of a quantum mechanical treatment for the internal degrees of freedom and approximate classical treatment of the projectile motion. Instead, both the internal and projectile degrees of freedom are approximated by exact classical dynamics. Although the dynamics are those of classical mechanics, one retains certain quantum-mechanical features since the superposition principle and quantized boundary conditions are implicit in the CLSM method. The validity of this approximation depends upon the validity of using classical mechanics to describe both the particle and the rotor dynamics. Two things should be carefully noted: 1) If the concept of a classical trajectory is valid, the CLSM trajectories are dynamically exact, while the A-W trajectories employ dynamical approximations; 2) The A-W treatment of the target internal degrees of freedom is a quantum-mechanical one, while the CLSM method employs an approximation which, at first glance, might seem severe.

As pointed out in Refs. 4 and 5 the approximations employed in the CLSM method are expected to be more valid for heavy projectiles and the excitation of large numbers of rotational states. Since this is exactly the situation for which quantum-mechanical calculations are not yet practical, this represents one of the attractive features of the method. On the other hand, this means that comparisons to quantum-mechanical calculations are easily done only for lighter systems in which the CLSM method might not be expected to work very well. In fact, we have found that the CLSM gives a highly accurate description of the Coulomb excitation process even for the lightest ions. This is illustrated in Figs. 1 and 2 for several representative target-projectile systems. In the upper part of each figure we have plotted the amplitude and phase of the complex S-matrix for the $\ell = 0$ incident partial wave as a function of angular momentum, both for a quantum mechanical calculation and for the CLSM calculation (note that the radial scale is logarithmic). The coupled-channels quantum mechanical calculation

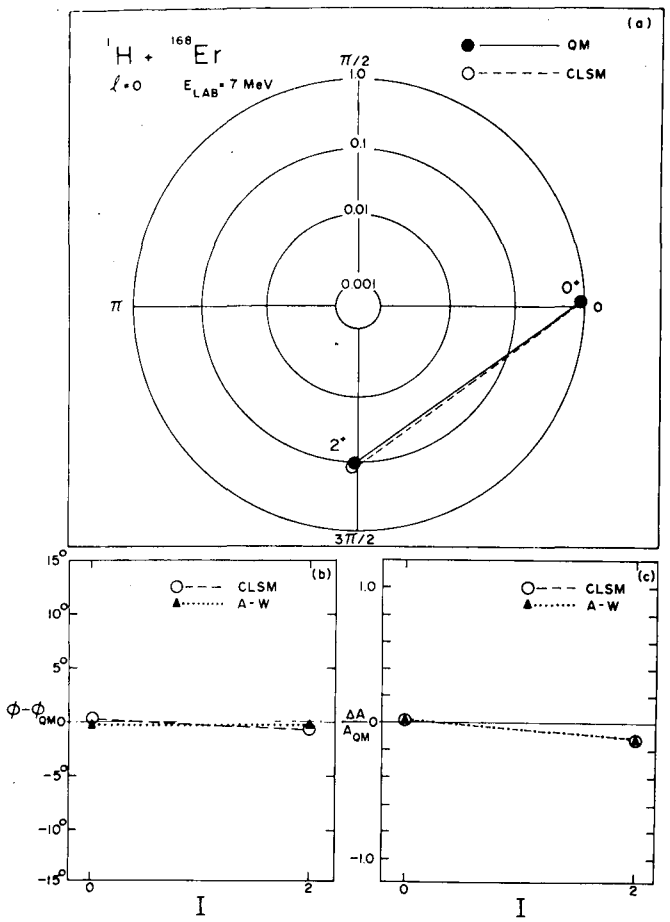


Fig. 1. (a) The $\ell = 0$ R matrix elements for Coulomb excitation of the ground band of $^{168}Er$ by 7 MeV $^{1}H$ projectiles. The radial scale is logarithmic. The quadrupole moment of $^{168}Er$ is taken to be $Q_0(2) = 7.673$ b and the energy levels are taken from the rotational model with $E_{2+} = 0.0798$ MeV. The classical limit S-Matrix (CLSM) calculations are in good agreement with the quantum mechanical calculations done using the computer code AROSA (QM). (b) The difference in phase between the $\ell = 0$ quantum mechanical R-matrix elements and the CLSM and Alder-Winther (A-W) semiclassical calculations. (c) The relative difference in amplitudes between the $\ell = 0$ quantum mechanical R-matrix elements and the CLSM and A-W ones. (XBL 774-8303)

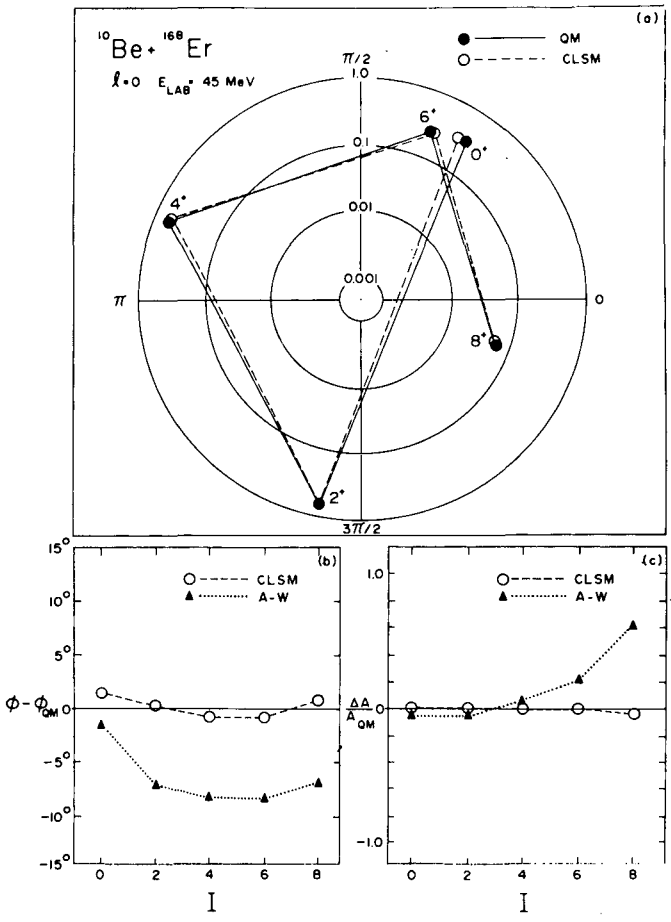


Fig. 2. Same as Fig. 1 for the projectile $^{10}Be$ at 45 MeV laboratory energy. (XBL 774-8302)

was made with the code AROSA.[1] In the lower part of each figure we show the relative deviation of the amplitude and the deviation of the phase of the S-matrix from the quantum mechanical calculation, both for the CLSM method and for the A-W method, with the A-W values calculated using a version of the standard Winther-deBoer code and with the semiclassical amplitudes identified with the elements of the reaction matrix.[2] The agreement between the CLSM method and the quantum-mechanical calculation for the amplitude and the phase of the $\ell = 0$ S-matrix, even for protons, is remarkable. Furthermore, even for many of the cases where $\bar{q}_2$ and $\eta$ are rather small there is clear evidence for superior accuracy of both the amplitude and the phase of the CLSM $\ell = 0$ relative to the A-W one. As discussed, the CLSM method should improve as one goes to heavier projectiles transferring larger amounts of angular momentum.

In Fig. 3 we show calculated excitation probabilities for head-on collisions in several representative heavy-ion systems using CLSM and A-W methods. Overall, the calculations are in rather good agreement with each other, but there are some systematic differences for the highest spins. The preceding arguments suggest that these differences are primarily due to the approximate classical orbital dynamics of the A-W method. If those arguments are correct, the differences between the CLSM and A-W curves in Fig. 3 represent the orbital dynamics component of the correction to semiclassical (A-W) Coulomb excitation theory.

Finally, we note that the relatively good agreement between the CLSM and A-W calculations except at the highest spins is consistent with recent experimental evidence setting upper limits on any corrections to A-W semiclassical calculations.[6,7] For example, an extensive comparison of transition probabilities for states in $^{232}Th$

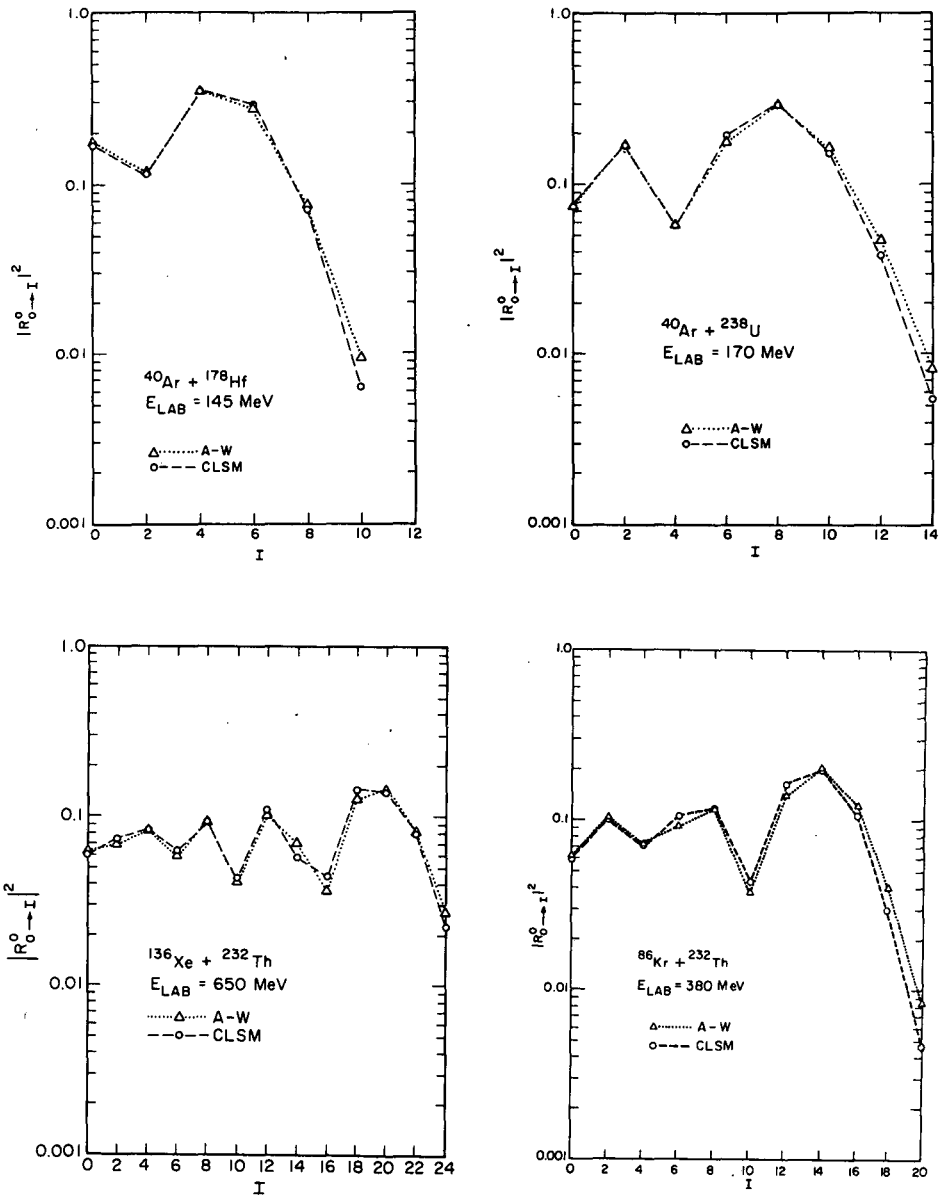


Fig. 3. Excitation probabilities for $\ell = 0$ in several representative heavy-ion systems. The A-W probabilities were calculated using a standard Winther-deBoer code. (XBL 777-5727)

determined by various Doppler-shift lifetime methods and by multiple Coulomb excitation places an upper limit of 15-20% on the semiclassical probability correction for $I^\pi < 16^+$ with 623-MeV $^{136}Xe$ projectiles.[6] This upper limit is consistent with the indicated differences in Fig. 3.

## Footnote and References

*Condensed from LBL-4363.

1. F. Roesel, J. X. Saladin, and K. Alder, Compt. Phys. Commun. 8, 35 (1974).

2. K. Alder and A. Winther, "Electromagnetic Excitation," North Holland, 1975.

3. H. Massmann and J. O. Rasmussen, Nucl. Phys. A 243, 155 (1975).

4. R. Donangelo, M. W. Guidry, J. P. Boisson, and J. O. Rasmussen, Phys. Lett. 64 B, 377 (1976).

5. R. Donangelo, Ph.D. Thesis, University of California (1977), unpublished.

6. M. W. Guidry, P. A. Butler, P. Colombani, I. Y. Lee, D. Ward, R. M. Diamond, F. S. Stephens, E. Eichler, N. R. Johnson, and R. Sturm, Nucl. Phys. A 266, 228 (1976).

7. D. Ward, P. Colombani, I. Y. Lee, P. A. Butler, R. S. Simon, R. M. Diamond and F. S. Stephens, Nucl. Phys. A 266, 194 (1976).

# CLASSICAL-LIMIT DESCRIPTION OF THE OCTUPOLE BAND EXCITATION IN DEFORMED EVEN-EVEN NUCLEI*

R. Donangelo, L. F. Oliveira, and J. O. Rasmussen

Recently Grosse et al.[1] have excited the lowest octupole vibrational band of $^{238}U$ up to spin 19. They found that this band has (initially) a predominant K value of zero. This corresponds to an oscillating deformation in the nuclear shape proportional to $P_3(\cos\theta)$, where $\theta$ is the azimuthal angle and $P_3$ the standard third order Legendre polynomial.

A classical description of the process shows that the excitation of this vibration by the electric field of an incident heavy ion is strongly dependent on the particular trajectory followed by the projectile, especially at the point of closest approach. In Fig. 1 we expect that trajectories such as (1) that approaches the target along a node of the octupole vibration will excite it little or not at all, while those like (2) will excite it much more. In general the excitation will go as $P_3(\cos\chi_{CA})$ where $\chi_{CA}$ is the angle between the symmetry axis of the target and the line joining its center with that of the projectile at the distance of closest approach.

The introduction of this $P_3(\cos\chi_{CA})$ form factor into the expression for the classical-limit S-matrix for backscattering Coulomb excitation results in the following expression:

$$S_{0\to I} = iK\sqrt{2I+1}\int_0^{\pi} d\chi_0 \sqrt{\sin\chi_0 \sin\bar{\chi}\,\frac{d\bar{\chi}}{d\chi_0}} \times P_I(\cos\bar{\chi})P_3(\cos\chi_{CA})\exp(i\phi') \quad ,$$

where K is a constant and all other quantities are the same as in Ref. 2. We applied this equation to different physical systems and the excitation probabilities defined as $P_{0\to I} = |S_{0\to I}|^2$ obtained by this method were compared with those obtained by a standard semiclassical method.[3] Typical results are shown in Fig. 2, which indicate a very good agreement, in spite of the fact that the descriptions of the internal degrees of freedom of the target are radically different in the two methods.

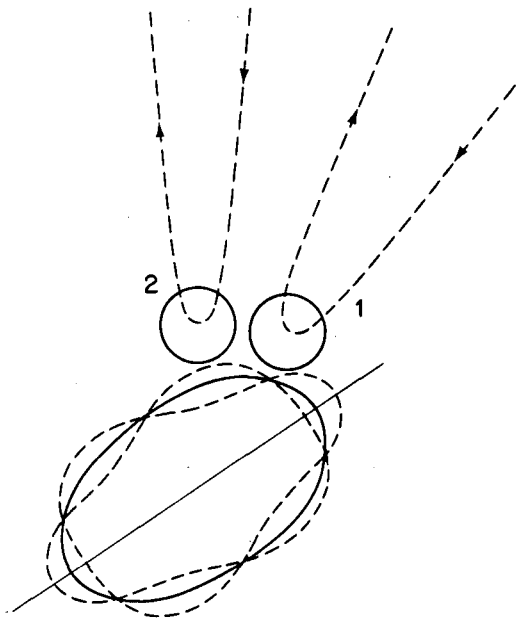


Fig. 1. The K = 0 octupole vibration is represented as a standing wave on the nuclear surface. Trajectory labeled (2), which has its point of closest approach close to a maximum in the vibration amplitude, excites the octupole vibration much more than trajectory (1), which has it close to a node in the vibration. (XBL 775-8586)

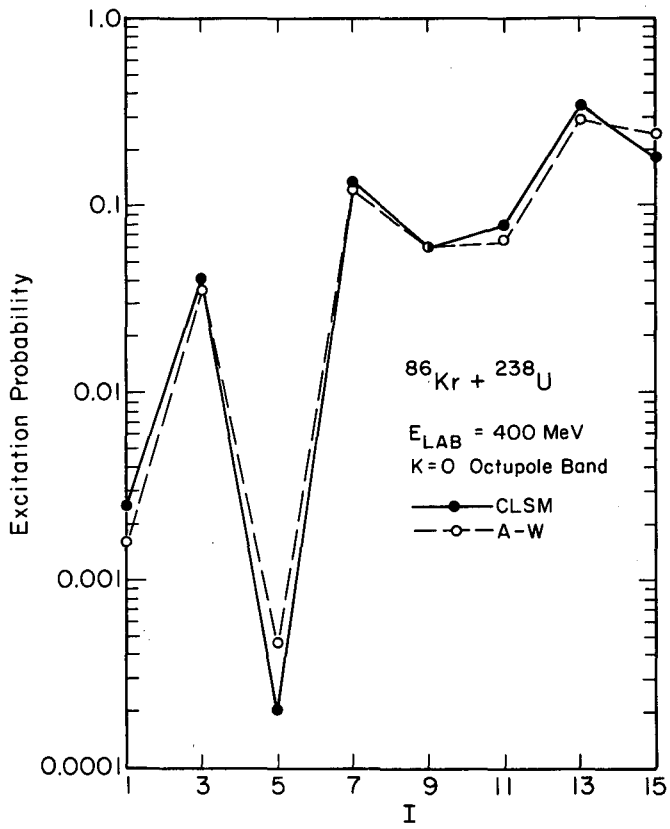


Fig. 2. Signature of the K = 0 octupole band excitation in $^{238}U$ by 400 MeV $^{86}Kr$ ions. The energies are taken from the rotational model with $E_{1^-} = 0.6798$ MeV and $E_{3^-} = 0.7313$ MeV for the octupole band and $E_{2^+} = 0.0449$ MeV for the ground band. The quadrupole moment of $^{238}U$ is taken to be 11.12b for both bands. (XBL 775-8589)

We should remark that these calculations apply to the K = 0 band only. For the high spin states the Coriolis coupling mixes all four octupole bands by aligning the vibrational angular momentum along the rotation axis. In this case the octupole vibration will look classically as a wave propagating on the nuclear surface, orthogonally to the rotation axis, and not as a standing wave as it was the case for the K = 0 band; therefore the rotational signature for the high spin states of the octupole band predicted by this model will be that of the ground band states which have three units less of angular momentum.

The success found in this case suggests the possibility of using the same approach for other physical processes. We are presently studying the rotational signature of the alpha-transfer reactions at energies around the Coulomb barrier.

Footnote and References

*Condensed from LBL-5825.

1. E. Grosse et al., Phys. Rev. Lett. 35, 565 (1975).

2. R. Donangelo et al., Phys. Lett. 64B, 377 (1976).

3. K. Alder and A. Winther, Mat. Fys. Medd. Dan. Vid. Selsk. 32, 8 (1960).

# 3. Relativistic

## NUCLEON NUMBER TRANSPORT EQUATION AS A MODEL FOR BEVALAC COLLISIONS

R. Malfliet* and Y. Karant

We assume that the nucleon number transport equation (a "closed form" intranuclear cascade model) is the governing dynamics of Bevalac collisions. To solve this equation, we use numerical intergration in a perturbation expansion, in which we perturb about the initial nuclear states. Specifically, we assume that an expansion in order of scattering (number of collisions) is possible. Thus, we consider a classification of particles into those which have not undergone scattering ("fixed" particles) and those which have ("moving" particles). At present, we neglect moving-moving collisions in order to simplify the calculation. Since this simplification is strictly valid only for small A projectile, we consider at present projectiles only up to Ne.

The actual method employed is to start the iteration with the initial nuclear distributions, that is, with a Fermi distribution in coordinate space and a zero temperature degenerate Fermi gas in momentum space. The space distribution is based upon electron scattering data,[1] and also has a simple analytic fit.[2] Normalization is such that before interaction, the integral over all classical Lorentz invariant phase space yields the mass number of each nucleus separately. The ideal method we would follow is to allow each fixed distribution to interact (recall our definition of fixed and moving particles) at fixed center-to-center impact parameter, giving the first moving distribution (first iteration). The number of particles in the moving distribution is determined, and the fixed distributions are renormed (depleted) to conserve nucleon number. We assume that, because of the short time of the collision, no nuclear changes occur, except for a change in the density because of particle knock-out. This moving distribution then is allowed to interact with the fixed distribution, generating the second iteration, and the process continues. Then, the iteration is repeated for several impact parameters.

To verify the general method, comparison was made with the published results of cascade programs.[3] A typical spectrum appears as Fig. 1; note that good agreement is obtained. To do this calculation, several additional approximations were made.

1) A single nucleon was taken as the projectile, and thus a steady state approximation (no explicit time dependence) was made.

2) Depletion was ignored. Numerically this is a small effect in these light systems.

3) A nonrelativistic closed form approximation for the cross section from a Fermi gas model of the nucleus was used,[4] requiring nonrelativistic formalisms throughout. At 300 MeV, this is valid.

We are currently in the process of extending this to relativistic nucleus-nucleus collisions. We have also calculated two systems, p + $^{16}$O at 2 GeV and p + $^{40}$Ca at 600 MeV. Those were picked because of experimental interest[5,6] and comparisons with experiment are under way. The preliminary results appear in Tables 1 and 2. The tables may be explained as follows. Impact is the impact parameter. At the impact, we indicate that after the proton has undergone one collision, the target has A* nucleons left with an excitation energy per

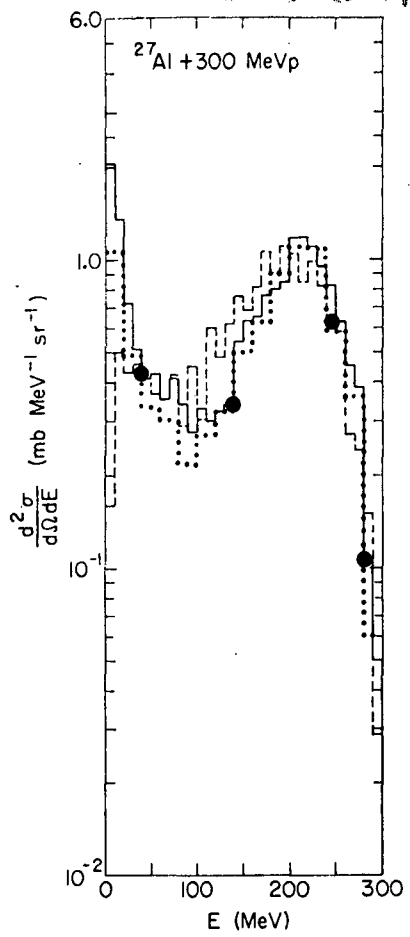


Fig. 1. Energy distributions of emitted protons at 30° ± 5°. The solid, dashed, and dotted histograms are the results obtained from the JINR, BNL-CU, and ORNL models, respectively. The heavy circles represent our results. (XBL 778-1791)

Table 1. $P + {}^{40}Ca \rightarrow A^* + nP$; $T_{beam}$ = 600 MeV

| Impact (fm) | No. of Collisions | A* | E*(MeV) | Probability |
|---|---|---|---|---|
| 1.88 | 1 | 39 | 250 | .23 |
| | 2 | 38 | 186 | .26 |
| 4.38 | 1 | 39.7 | 262 | .82 |
| | 2 | 39.5 | 356 | .08 |
| 6.88 | 1 | 39.99 | .80 | .996 |
| | 2 | 39.98 | 1.20 | .001 |

Table 2. $P + {}^{16}O \rightarrow A^* + nP$; $T_{beam}$ = 2 GeV.

| Impact (fm) | No. of Collisions | A* | E*(MeV) | Probability |
|---|---|---|---|---|
| 1.38 | 1 | 15.2 | 600 | .27 |
| | 2 | 14.1 | 656 | .26 |
| 3.21 | 1 | 15.7 | 130 | .71 |
| | 2 | 15.4 | 212 | .097 |
| | 3 | 14.9 | 255 | .071 |
| 5.04 | 1 | 15.98 | 11.3 | .972 |
| | 2 | 15.97 | 15.8 | .003 |

residual nucleus E*; and that at this impact, this process has a given probability, (which must be weighted by the geometrical probability of this impact). Because of the cost of running the code, we have not evaluated small impacts to many collisions. The next stop is to consider the decay of the residual nucleus, which is also under current consideration.

These results are approximate, however, because of the truncations made again to give a manageable calculation. Specifically:

1) While relativistic kinematic has been used, Fermi momentum has been ignored.

2) The total N-N (isospin and spin averaged) cross section has been used. Thus, particle creation has been implicity considered, but an approximate form for the differential cross section was used. Specifically, the cross section was assumed to be isotropic in the N-N center-of-mass frame, and pions (or other particles) were ignored. The actual forward peaked cross section would be made somewhat more isotropic by the Pauli principle in nuclear matter, and since we ignored the explicit inclusion of the Pauli principle, we in part compensated for this effect.

3) Depletion has been ignored, but as the results indicate, this is not a large effect for these systems.

We are presently considering methods to improve these calculations.

Footnote and References

*Present address: KVI, Univ. of Groningen, Netherlands.


1. R. Horman and R. Hofstadter, High-Energy Electron Scattering Tables Stanford (1960).
2. P. J. Karl, Phys. Rev. C 11, 1208 (1975).
3. V. S. Barashenkov, et al., Nucl. Phys. A 187, 531 (1972).
4. K. Kikuchi and M. Kawai, Nuclear Matter and Nuclear Reactions, Interscience, (1968) p. 44.
5. P. J. Lindstrom, D. G. Greiner, H. H. Heckman, B. Cork, and F. S. Bieser, LBL-3650.
6. O. Artun et al., Phys. Rev. Lett. 35, 773 (1975).


# THEORETICAL CALCULATIONS OF PERIPHERAL REACTION YIELDS FROM RELATIVISTIC HEAVY IONS*

John Rasmussen, Raul Donangelo, and Luiz F. Oliveira†

We direct attention mainly toward interpreting the experimental results of Shibata et al[1] with 250 MeV/n and 400 MeV/n carbon ions and alpha particles on calcium targets at the Berkeley Bevalac.

We have drawn on the works of J. D. Bowman and W. Swiatecki[2] and of Hüfner et al.[3] that were directed toward understanding the $^{16}O$ projectile fragmentation cross sections at 1 and 2 GeV/n. We take note also of the calculations of Loveland et al[4] on product yields in the gold region following relativistic carbon bombardment of uranium.

For the fast process we have used two related but different models, Swiatecki's abrasion (fireball) model and Myers' firestreak model.

In the abrasion model one calculates geometrically as a function of impact parameter, b, the volume fractions $f_T$ and fp remaining in the spectator pieces of target and projectile, respectively. From the inverse function $b(f_T)$ the partial cross section for a primary fragment of mass A is determined as

$$\sigma(A) = \pi \left[ b\left(\frac{A+0.5}{A_T}\right)^2 - b\left(\frac{A-0.5}{A_T}\right)^2 \right] .$$

In our calculations we introduce a dispersion in charge-to-mass ratio much as did Hüfner. That is, each struck target nucleon is assumed to have a Z/A probability of being a proton. Hence, the charge dispersion for constant A has the form of a hypergeometric distribution

$$P_{(z,n)} = \frac{\binom{Z}{z}\binom{N}{n}}{\binom{A}{a}} ,$$

where the capitals refer to the target nucleus and lower case letters refer to the knocked-out protons z, neutrons n, and total nucleons a(=z+n) respectively.

Before beginning the evaporation calculations to determine final products, it is necessary to specify an excitation energy distribution for the primary fragments. Swiatecki proposed an excitation energy term equal to the excess surface energy of the abrasion product, and we calculate and include this term. Following Hüfner we also add a final state interaction, assuming each struck nucleon has a 50% chance of passing through the spectator and depositing 40 MeV of excitation. (This energy value, the dominance of (N,N'), and the balancing out of capture against (N,2N) processes can be rationalized from Monte Carlo work of Metropolis et al.[5]) Thus, each primary spectator with A-a mass number has a final state interaction with a number of nucleons $m_{FSI}$ which have a binomial distribution given by

$$\text{Prob}(m_{FSI}) = \frac{\binom{a}{m_{FSI}}}{2^a} . \qquad (3)$$

The excitation energy is given, for each $m_{FSI}$, by

$$E_{FSI} = 40\ m_{FSI} \qquad (3')$$

With the primary fragment Z, N, and E distributions from the fast process determined we begin calculation of the statistical evaporation of nucleons, deuterons, and alpha particles using Blann's code ALICE[6] as a subroutine. We use his options of Myers-Swiatecki shell-corrected formula masses and level density constant a = A/8 $MeV^{-1}$. We assume zero angular momentum throughout the evaporation cascades, since it is not obvious how

to calculate spin distributions in the fast process and they may well be generally small.

There is the feature that the abrasion model implies a strong correlation between target spectator excitation and projectile spectator excitation. The smaller the impact parameter the greater this excitation. Photographic emulsion experiments of Heckman's group[7] have shown, however, the presence of considerable pure target or pure projectile fragmentation events (some 7 to 16% of each with nitrogen and oxygen beams at 2 GeV/n). Furthermore, there are the correlation experiments of Crawford et al.[8] between sodium target gamma rays and carbon beam fragmentation patterns at 400 MeV/n. These results suggest very little correlation between the fates of the two collision partners, a-proaching the particle-physics limiting factorization behavior. This near factorization necessitates in addition to abrasion a grazing "stochastic" excitation mechanism in which internal degrees of freedom of each collision partner independently extract translational energy through the time-dependent field of the other nucleus.

To bring a greater measure of sophistication to the fast process we have gone on to explore the "firestreak" model of Myers.[9] In this model the collision is subdivided into a set of "tubes" parallel to the relative velocity vector, with the matter within each tube assumed to thermally equilibrate all energy in excess of the translational kinetic energy for momentum-conserving center-of-mass motion of the tube. In order to divide the tubes between spectators and escaping firestreak it is necessary to specify some critical tube momentum $p_c$ above which the tube escapes from the spectator. Clearly there will be a dependence on bombarding energy in the relationship between impact parameter and spectator mass. We have performed the firestreak calculation for several values of the critical momentum $p_c/p_{Fermi}$ (0.2, 0.45, and 1.0). These $p_c$ values correspond respectively to tube translational energies of 1 MeV/n, 8 MeV/n, and 38 MeV/n.

Let us turn to consider the grazing "stochastic" excitation mechanism mentioned earlier. It has been shown by Boisson et al.[10] (Eq. 12) that the time-dependent nuclear potential energy felt at the nearest point on the target surface during a grazing collision has a Gaussian dependence on time near time zero $V(t) \propto \exp(-t^2/t_o^2)$, where $t_o = [2\, r_o(R_t+R_p)]^{1/2}/v$, with $R_t$ and $R_p$ the radii of target and projectile nuclei, $r_o$ the range of the interaction and v speed of the projectile. The relativistic modification would replace v by $c\beta/\sqrt{1-\beta^2}$. In general terms the nucleus is exposed to a perturbing field with energy (frequency) spectrum, a Gaussian, the Fourier transform of V(t). That is, the characteristic energy $E_o = 2\hbar/t_o$. For $^{12}C + ^{40}Ca$ with force range and radius constant 1.4 Fm we get $E_o = 83\ \beta/\sqrt{1-\beta^2}$ MeV, which gives 85 MeV at 400 MeV/n and gives 65 MeV at 250 MeV/n. The actual nuclear excitation spectrum will depend on various nuclear strength functions, most likely the isoscalar multipoles, quadrupole, octupole and higher. For orientation purposes if we assume flat nuclear strength functions, the stochastic grazing process would leave the $^{40}Ca$ target with a Gaussian distribution of excitation energy with the above widths (85 MeV or 65 MeV, respectively). It may be that the nuclear strength function falls off with characteristic Fermi energy if particle-hole excitation is the main mode of energy absorption. In that case the 85 and 65 MeV figures might be reduced.

The total cross section involved in the stochastic process may be estimated from the emulsion studies cited. About one-tenth of observed heavy-ion events are pure target fragmentation, and the contributing range of impact parameters should be of the order of the force range of ~1.4 Fm. Then we can be consistent with emulsion observations if we say there is an 0.5 probability of a quantum of excitation being absorbed in this grazing zone, for then the $1.4 \times 2\rho \times (R_t+R_p)$ rim cross section of 0.70 barns divides into 4 equal parts: (1) pure target excitation, (2) pure projectile excitation, (3) both excited, and (4) neither excited. The 0.70/4 (≈0.175 barns) to each process is only slightly less than 10% of the geometrical cross section $(R_t+R_p)^2$ of ≈2.00 barns.

Table 1 presents our best calculated cross sections for C + Ca reactions. We prefer firestreak 2 plus the stochastic grazing process, although the total theoretical cross sections generally exceed those measured. The absolute normalization of the experimental cross sections is less certain than the determination of relative cross sections. We are looking forward to comparison with beam fragmentation data from $^{56}Fe$ in unpublished experimental studies of Lindstrom et al.[11] From preliminary comparisons our theory gives an odd-even difference not seen in experiment. The defect is probably in the ALICE code usage of the same level density formula for odd and even nuclear types.

As it affects these calculations, the firestreak model at low critical momentum $p_c$ for knock out (calculations 1 and 2) is not very different from the simpler abrasion (fireball) model, and the latter might continue to be used.

There is much yet to be done, and we hope the present work helps define the questions for further studies.

We are most grateful to Marshall Blann for making the ALICE code available and to Bill Myers for generously giving and helping us adapt key portions of his firestreak code. Wladyslaw Swiatecki, Walter Loveland, and Roland Otto generously helped and made available the abrasion model code.

Various members of the TOSABE (Tokyo, Berkeley, Osaka) group have contributed significantly to development of the concepts behind these calculations, notably K. Nakai, T. Shibata, H. Ejiri, J. Ioannou, and J. Chiba.

Footnotes and References

*Condensed from LBL-6580.

†Supported by CNEN-Brazil

Table 1. Theoretical and experimental cross sections (>1.0 mb) for all products.

| | | 250. MeV/n | | | 400. MeV/n | | | |
|---|---|---|---|---|---|---|---|---|
| Z | A | Firestreak 2 | Stochastic $E_o$=65 MeV | Total | Firestreak 2 | Stochastic $E_o$=85 MeV | Total | Exp. $\gamma_{2\rightarrow 0}$ |
| 20 | 40 | - | 60.2 | 60.2 | - | 46.2 | 46.2 | 14.4 ± 3.8[a] |
| 20 | 39 | 50.7 | 4.9 | 55.6 | 48.2 | 3.8 | 52.0 | |
| 20 | 38 | - | 1.0 | 1.0 | - | 1.0 | 1.0 | 5.7 ± 2.8 |
| 19 | 39 | 0 | 56.0 | 56.0 | 48.2 | 43.8 | 92.0 | |
| 19 | 38 | 0 | 6.3 | 6.3 | 0 | 5.4 | 5.4 | |
| 19 | 37 | 8.8 | 1.8 | 10.6 | 8.1 | 1.5 | 9.5 | |
| 18 | 38 | 50.7 | 40.3 | 91.0 | 7.8 | 34.0 | 41.8 | 15.2 ± 3.5 |
| 18 | 37 | 19.7 | 16.1 | 35.8 | 19.8 | 15.4 | 35.2 | |
| 18 | 36 | 32.1 | 30.8 | 62.9 | 39.2 | 27.7 | 66.9 | ≤38.6 ± 6.2[b] |
| 18 | 35 | 3.7 | 3.9 | 7.6 | 4.2 | 3.9 | 8.1 | |
| 17 | 37 | 4.3 | 3.9 | 8.2 | 1.1 | 3.8 | 4.9 | |
| 17 | 36 | 5.9 | 1.4 | 7.3 | 5.9 | 1.4 | 7.3 | |
| 17 | 35 | 19.5 | 23.8 | 43.5 | 16.0 | 22.2 | 38.2 | |
| 17 | 34 | 4.4 | 3.9 | 8.3 | 4.2 | 4.2 | 8.4 | |
| 17 | 33 | 8.5 | 1.3 | 9.8 | 7.8 | 1.7 | 9.5 | |
| 16 | 36 | 3.8 | 1.0 | 4.8 | 3.8 | 1.1 | 4.9 | |
| 16 | 35 | 1.7 | 0.4 | 2.1 | 1.9 | 0.6 | 2.5 | |
| 16 | 34 | 25.0 | 23.9 | 48.9 | 23.7 | 25.5 | 49.2 | 13.2 ± 6.0 |
| 16 | 33 | 29.4 | 10.1 | 39.5 | 29.1 | 12.9 | 42.0 | |
| 16 | 32 | 29.4 | 14.4 | 43.8 | 30.7 | 17.8 | 48.5 | ≤23.5 ± 5.1[c] |
| 16 | 31 | 4.7 | 1.6 | 6.3 | 4.8 | 2.3 | 7.1 | |
| 16 | 30 | 3.3 | 0.6 | 3.9 | 3.1 | 0.9 | 4.0 | |
| 15 | 33 | 4.3 | 1.2 | 5.5 | 4.1 | 1.6 | 5.7 | |
| 15 | 32 | 2.8 | 0.5 | 3.3 | 2.6 | 0.9 | 3.5 | |
| 15 | 31 | 19.8 | 8.4 | 28.2 | 17.0 | 12.1 | 29.1 | |
| 15 | 30 | 6.4 | 1.4 | 7.8 | 6.4 | 2.2 | 8.6 | |
| 15 | 29 | 4.3 | 0.4 | 4.7 | 4.3 | 0.9 | 5.2 | |
| 14 | 32 | 1.7 | - | 1.7 | 1.8 | 0.4 | 2.2 | 7.7 ± 2.2 |
| 14 | 31 | 1.3 | - | 1.3 | 1.3 | - | 1.3 | |
| 14 | 30 | 24.1 | 5.9 | 30.0 | 23.6 | 9.3 | 32.9 | ≤23.5 ± 5.1[c] |
| 14 | 29 | 15.2 | 2.2 | 17.4 | 14.7 | 4.6 | 19.3 | |
| 14 | 28 | 25.0 | 3.6 | 28.6 | 24.1 | 8.0 | 32.1 | 22.0 ± 4.5 |
| 14 | 27 | 4.8 | 0.5 | 5.3 | 4.9 | 0.9 | 5.8 | |
| 14 | 26 | 3.1 | 1.4 | 4.5 | 3.0 | 0.4 | 3.4 | |
| 13 | 29 | 1.9 | - | 1.9 | 1.7 | 0.4 | 2.1 | |
| 13 | 28 | 1.8 | - | 1.8 | 1.9 | - | 1.9 | |
| 13 | 27 | 14.3 | 1.4 | 15.7 | 14.9 | 2.9 | 17.8 | |
| 13 | 26 | 4.0 | - | 4.0 | 3.8 | 0.5 | 4.3 | |
| 13 | 25 | 3.8 | - | 3.8 | 3.7 | - | 3.7 | |
| 12 | 26 | 17.3 | 0.7 | 18.0 | 17.0 | 2.1 | 19.1 | 16.5 ± 3.9 |
| 12 | 25 | 11.9 | - | 11.9 | 12.1 | 0.9 | 13.0 | |
| 12 | 24 | 25.8 | 0.7 | 26.5 | 25.9 | 1.6 | 27.5 | 20.5 ± 5.7 |
| 12 | 23 | 4.6 | - | 4.6 | 4.6 | - | 4.6 | |
| 12 | 22 | 3.4 | - | 3.4 | 3.5 | - | 3.5 | |
| 11 | 23 | 11.1 | - | 11.1 | 11.2 | - | 11.2 | |
| 11 | 22 | 2.9 | - | 2.9 | 2.9 | - | 2.9 | |
| 11 | 21 | 3.0 | - | 3.0 | 3.0 | - | 3.0 | |
| 10 | 22 | 10.6 | - | 10.6 | 10.8 | - | 10.8 | 7.6 ± 2.6 |
| 10 | 21 | 8.4 | - | 8.4 | 8.6 | - | 8.6 | |
| 10 | 20 | 18.7 | - | 18.7 | 18.6 | - | 18.6 | |
| 10 | 18 | 2.3 | - | 2.3 | 2.2 | - | 2.2 | |
| 9 | 19 | 3.8 | - | 3.8 | 3.9 | - | 3.9 | |
| 8 | 18 | 3.4 | - | 3.4 | 3.4 | - | 3.4 | |
| 8 | 17 | 2.3 | - | 2.3 | 2.4 | - | 2.4 | |
| 8 | 16 | 4.8 | - | 4.8 | 4.7 | - | 4.7 | |

[a] $3^- \rightarrow 0^+$ (g.s.) transition.

[b] Gamma unresolved from transition in $^{33}Si$; 38.6 mb is total.

[c] Gammas unresolved for $^{32}S$ and $^{30}Si$; 23.5 mb is total.

1. T. Shibata et al., Contribution to the International Conference on Nuclear Structure, Tokyo (1977).

2. J. D. Bowman, W. J. Swiatecki and C. F. Tsang, LBL-2908 (1973).

3. J. Hüfner, K. Schäfer and B. Schürmann, Phys. Rev. C 12, 1888 (1975).

4. W. Loveland et al., Phys. Rev. Lett. 39, 320 (1977).

5. N. Metropolis et al., Phys. Rev. 110, 185 (1958).

6. M. Blann, "OVERLAID ALICE", COO-3494-29, Rochester University Report.

7. H. H. Heckman et al., "An Atlas of Heavy Ion Fragmentation Topology", unpublished.

8. H. J. Crawford et al., Bull. Am. Phys. Soc. 22, 594 (1977).

9. W. D. Myers, private communication (1977).

10. J. P. Boisson et al., LBL-5814 (1976).

11. P. J. Lindstrom, private communication, (1977).

# A MODEL FOR HIGH ENERGY HEAVY ION COLLISION*

William D. Myers

A schematic model has been developed for predicting the distributions of products from high energy heavy ion collisions whose source seems to be the overlap region between the target and projectile. (Some of the geometrical features of the model are similar to those employed in Ref. 1-3). It includes a recognition that a velocity shear exists across the overlap region that depends, locally, on the amount of material coming from the projectile. In addition the model is based on nuclear density distributions with diffuse (rather than sharp) surfaces. A special way of summarizing the geometrical aspects of the model has been found that allows one to immediately assess the importance of its various features.

For any given collision the ratio of the amount of projectile matter to the amount of target matter it is aimed at, varies with position in the plane normal to the beam direction. The diffuse nature of the nuclear surface region tends to smooth out these variations so that a continuous range of $\eta$ (the "projectile fraction") values is expected, where

$$\eta = \frac{\text{number of particles from the projectile}}{\text{number of projectile plus target particles}} . \quad (1)$$

The local value of $\eta$ can vary from zero (for the target spectator) smoothly through intermediate values (corresponding to the overlap region) to one (for the projectile spectator fragment). Between the target and projectile spectators (if the impact parameter is large enough for any of the projectile to survive) distribution of material, is expected which contains a large amount of internal energy and which is drawn out into a streak by the velocity shear across the overlap region.

Figure 1 is a schematic two-dimensional representation of the model to illustrate how the nuclear density distributions are expected to evolve with time. In part (a) of the figure the material in the overlap region is seen to be moving with velocities spread uniformly between those of the target and projectile spectators. Some of the material has already "burned off" because of its high degree of internal excitation. In part (b) the process has continued, and in part (c) the hottest part of the streak has completely dissipated leaving behind the spectator fragments that continue to burn off particles from the excited regions on their surfaces.

For the actual case of a particular projectile and target combination, the geometrical aspects of the problem can be condensed into an especially simple form based on the quantity $\eta$. To see this we need only consider the origin of the functions $F_j(\underset{\sim}{p})$, which are the laboratory momentum space densities (in barns) for particles of type j which are produced in the collision. These quantities can be approximated by the expression (see Ref. 4 for details),

$$F_j(\underset{\sim}{p}) = \sum_{i=1}^{n} Y(\eta_i)\, J_{\underset{\sim}{p}'\to\underset{\sim}{p}}\, f_j(\underset{\sim}{p}') . \quad (2)$$

With this expression many of the results of high energy heavy ion collisions can be calculated by summing over a relatively small number of terms, each one of which consists of a geometrical, a kinematical, and a statistical factor. All of the geometry in this approach is contained in the function $Y(\eta)$ which can be tabulated for any target projectile combination. The kinematic considerations are all in the Jacobian $J_{\underset{\sim}{p}'\to\underset{\sim}{p}}$,

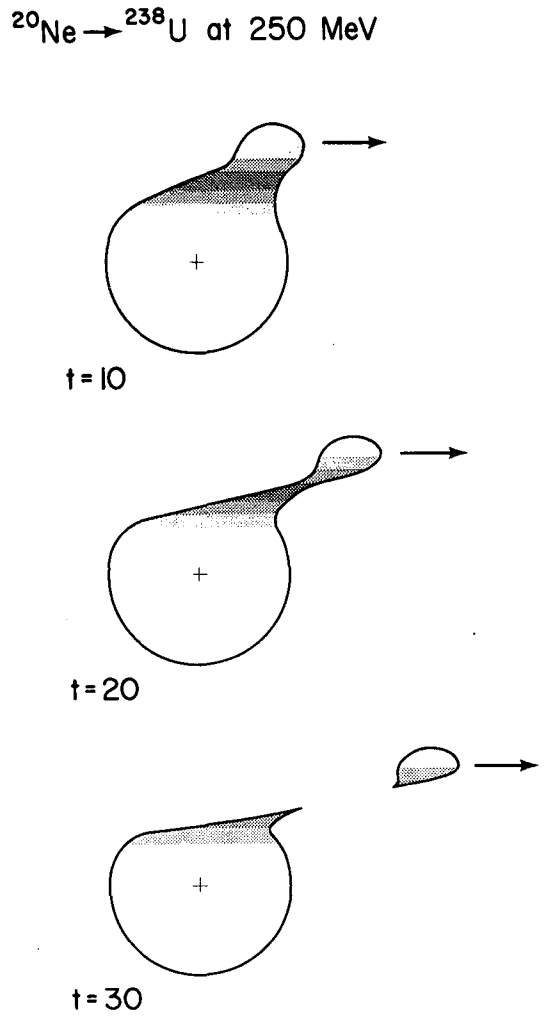


Fig. 1. Schematic two-dimensional representation of a collision between 250 MeV/n $^{20}Ne$ projectile with a $^{238}U$ target at a impact parameter of 8 fm. The three parts of the figure show how the system is expected to have evolved at times t = 10, 20 and 30 fm/c. The intensity of the shading is proportional to the degree of internal excitation generated by the collision. (XBL 778-1679)

and all of the statistical considerations are contained in the functions $f_j$.

The relative importance of different assumptions regarding geometrical aspects of high energy heavy ion collisions can be understood in terms of the functions $Y(\eta)$. For example consider the much studied case of $^{20}Ne \rightarrow ^{238}U$. In Fig. 2 the function $Y(\eta)$ is plotted for three different models. In part (2) the nuclei has been assumed to be sharp surface spheres and the entire target and projectile contributions to the overlap region are assumed to form 2 single composite (the "fireball model" of Ref. 2) with 2 single value for the velocity and local internal energy. The distribution in $\eta$, which is quite narrow, is created solely by the sum over impact parameters.

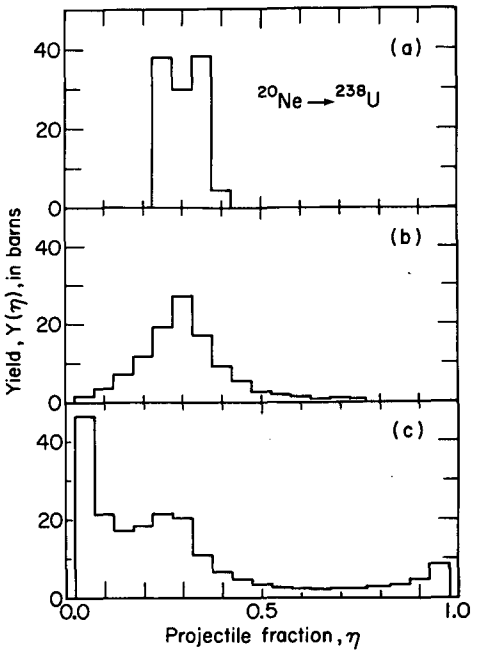


Fig. 2. The yield function $Y(\eta)$ for $^{20}Ne$ on $^{238}U$ is plotted against $\eta$ for three different geometrical models. (XBL 778-1567)

Part (b) shows the effect of including the dependence of $\eta$ upon position in the x-y plane. Finally, part (c) shows the result for the model being proposed here, where not only is the dependence of $\eta$ upon position in the x-y plane included, but the density distributions of both the target and projectile are taken to have diffuse (rather than sharp) surfaces.

The ease with which this approach can be applied, and its flexability with regard to the incorporation of alternative forms for the functions $f_j$ is its major strength. The predictions of this method can be compared with a wide range of experimental observations in order to help to identify experimental results that suggest collective or otherwise anomalous effects.

## Footnote and References

*Condensed from LBL-6569.

1. J. D. Bowman, W. J. Swiatecki and C. F. Tsang, LBL-2908, July 1973, unpublished.

2. G. D. Westfall, et al., Phys. Rev. Lett. 37, 1202 (1976).

3. J. Knoll, Proceedings of the International Workshop on Gross Properties of Nuclei and Nuclear Excitations V, Hirschegg, Austria, January, 1977 (Technische Hochschule Darmskdt Report No. AED - Conf 77-017-001).

4. W. D. Myers, LBL-6569.

# THERMODYNAMIC MODEL FOR COMPOSITE-PARTICLE EMISSION IN RELATIVISTIC HEAVY-ION COLLISIONS*

Aram Mekjian†

Properties of the spectra of high-energy composite particles emitted in a relativistic heavy-ion collision[1,2] are studied in the framework of a thermodynamic picture whose foundation is based on the big-bang equilibrium model.[3] The basis of the model to be discussed is the nuclear fireball picture used to describe proton inclusive spectra.[2] In this picture, nucleons mutually swept out from the combined system of target and projectile form an equilibrated fireball which then expands freely. The results of this model[2] fit the gross features of the proton inclusive spectra for 400-MeV/A $Ne^{20}$ and $He^4$ on uranium for proton energies above 80 MeV.

On the other hand, the composite-particle spectra seen in the same experiments have been interpreted in terms of a model in which nucleons with small relative momenta coalesce.[1,4] Specifically, this model imposes a momentum-space restriction for formation of composite particles; and this restriction, in turn, leads to correlations in energy and angle between double differential cross sections of composite particles and powers of the corresponding proton cross sections. These features are borne out in the experimental results as shown in the figures of Ref. 1. Now, within the framework of the coalescence model,[1] no explicit reference has been made to the spatial evolution of the cascade nucleons and to the possible equilibration properties that they may have. It is this aspect and its consequences that will be investigated.

Since a detailed description of an expanding collection of strongly interacting nucleons raised to a high temperature (the fireball) is impossible, simplifying assumptions or idealizations have to be made. Here, the idealization is based on the three phases that this collection goes through in its expansion. First, when densities and temperatures are high, mean free paths are short ($\ell_0 \approx 1$ fm or less), and collisions are then frequent in the bulk of the material, causing scattering to all possible states (continuum and bound), with composite-particle formation and break-up having its equal place in the system. In this phase, a temporal thermodynamic equilibrium could perhaps be established. In a second stage as the collection of these nucleons and nuclei expands, nonequilibrium few-collision processes dominate until the density is so low that a third phase is reached in which all collisions cease and the gas expands freely.

Now, as a working idealization, we replace this complicated evolution with a much simpler one in which the fireball expands through a set of equilibrium states until a volume $V_0$ or density $\tilde{\rho}$ is reached, after which all collisions cease instantaneously. The system then expands freely.

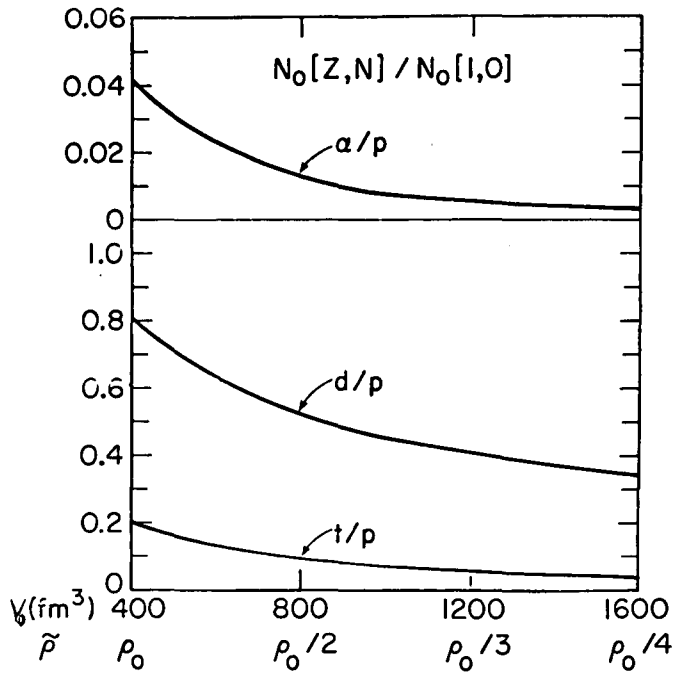


Fig. 1. The ratio of d,t α to p as a function of the thermodynamic volume $V_0$ or density $\tilde{\rho}$. The evaluation is for $kT_0 = 50$ MeV and for $\tilde{Z} = 30$, $\tilde{N} = 30$, which are typical values in Ref. 2. For sixty nucleons, normal nuclear matter with density $\rho_0 = 0.15$ nucleons/fm$^3$ occupies a volume 400 fm$^3$. From the figure, we note the persistence of a large d/p ratio even in diffuse regions. A small observed d/p ratio could indicate a diffuse $\tilde{\rho}$. A large α/p ratio could indicate a dense $\tilde{\rho}$. (XBL 7612-11104)

Under the assumption that thermodynamic equilibrium is established in a volume $V_0$ and at a temperature $T_0$, the number $N_0[Z,N]$ in equilibrium is determined by statistical factors alone and is[3]

$$N_0[Z,N] = \left(\frac{[\lambda(T_0)]^3}{V_0}\right)^{A-1} \frac{f(Z,N)}{2^A} (N_0[1,0])^Z (N_0[0,1])^N, \tag{1}$$

where $\lambda(T) = hc(2\pi m_p c^2 kT)^{-1/2}$, $A = Z+N$, and

$$f(Z,N) = A^{3/2} \exp[E_0(Z,N)/kT_0] \times \sum_j (2S_j + 1) \exp(-E_j/kT_0) . \tag{2}$$

The summation is over the ground and excited states of the nucleus (Z,N), with $S_j$ being the spins of these states and $E_j$ being their excitation energy measured from the ground state energy $E_o(Z,N)$. $N_o[1,0]$ and $N_o[0,1]$ are, respectively, the number of protons and neutrons in $V_o$ at equilibrium. If we define $\tilde{Z}$ and $\tilde{N}$ as the initial numbers of protons and neutrons, respectively, in the fireball, the following auxiliary conditions must be satisfied:

$$\sum_{Z,N} N_o[Z,N] = \tilde{Z}; \quad \sum_{Z,N} NN_o[Z,N] = \tilde{N} . \quad (3)$$

Next, the momentum distribution of the individual species of this composite gas is given by the Maxwell-Boltzmann distribution in the rest frame of the fireball; thus,

$$d^3N_o[Z,N;\vec{P}]/d^3P = N_o[Z,N]\exp(-E_K/kT_0)(2\pi Am_p kT_0)^{-3/2},$$

where $E_K = P^2/2m_A$ is the total kinetic energy of the nucleus [Z,N] whose abundance $N_o[Z,N]$ is determined by Eq. (1).

At this point a formal correspondence with the results of the coalescence model can be made. In this model, the momentum phase-space restriction that composite particles be constructed from nucleons whose momenta lie within a sphere of radius $P_0$ of each other leads to[1]

$$\frac{d^2n[Z,N]}{P_n^2 dP_n d\Omega} = \frac{2S_A+1}{2^A}\frac{1}{Z!N!}R_{p,t}^N\left(\frac{4\pi}{3}\gamma P_0^3\right)^{A-1}\left(\frac{d^3n[1,0]}{P_n^2 dP_n d\Omega}\right). \quad (5)$$

The $P_n$ is the momentum per nucleon, $d^2n[Z,N]/P_n^2 dP_n d\Omega$ is the number of nuclei [Z,N], or protons [1,0], per event per unit element of phase space; $\gamma = (1 + P_n^2/m_p^2)^{1/2}$ and $R_{p,t} = (N_p + N_t)/(Z_p + Z_t)$, where the target is $[Z_t,N_t]$ and projectile is $[Z_p,N_p]$. In Eq. (5) we have explicitly included the spin-alignment factor $(2S_A + 1)/2^A$ between the individual nucleons and the composite [Z,N] (implicit in Ref. 1). Now, it is interesting to note that the result of Eq. (5), relating the momentum-space density of the composite system to powers of the proton density, is also a feature of the equilibrium model. Specifically, Eq. (4) can be rewritten as

$$\frac{d^2N_0[Z,N;\vec{P}]}{A^3P_n^2 dP_n d\Omega} = \frac{f(Z,N)}{A^{3/2}2^A}R_0^N\left(\frac{h^3}{V_0}\right)^{A-1}\left(\frac{d^2N_0[1,0;P_n]}{P_n^2 dP_n d\Omega}\right)^A, \quad (6)$$

where $P_n^2/2m_p = E_K/A$ and where $R_0 = N_0[0,1]/N_0[1,0]$. In obtaining Eq. (6), we have used the result $A^3P_n^2dP_n = P^2dP$, where $\vec{P}$ is the total momentum. Thus, the equilibrium model has all the essential features of the coalescence model since Eq. (6) is formally similar to Eq. (5). However, a difference exists (apart from combinatorial and phase-space factors), which is that the proton density in momentum space in the thermodynamic model is fixed by Eq. (4) to be the equilibrium thermal distribution.

The composite-particle cross section can also be obtained as

$$\frac{d^2\sigma[Z,N]}{dtd\Omega} = \quad (7)$$

$$A^{3/2}\frac{f(Z,N)}{2^A}\bar{R}_o^N\left(\frac{h^3\tilde{\rho}_p}{G_0}\right)^{A-1}[f(t,\theta)]^{A-1}\left(\frac{d^2\sigma[1,0]}{dtd\Omega}\right)^A .$$

Here

$$[f(t,\theta)]^{-1} \equiv [t(t+2m_p)]^{1/2}\,\bar{\gamma}\{t+m_p - \bar{\beta}[t(t+2m_p)]^{1/2}\cos\theta\}$$

with t the kinetic energy per particle, $G_p \equiv \int 2\pi bN_0[1,0;b]db$, and $\tilde{\rho}_p = N_0[1,0;b]/V_0(b)$; $\bar{T}_0$, $\bar{\beta}$, $\bar{\gamma} = (1-\bar{\beta}^2)^{-1/2}$, and $\bar{R}_0$ are the constant values of these quantities. The result of Eq. (7) is of the form of the coalescence result, [Eq. (2) of Ref. 1]. It thus contains the same correlation in energy and angle between composite-particle cross sections and powers of the proton cross sections.

Moreover, the result of Eq. (7) allows a formal identification

$$\left(\frac{4\pi P_0^3}{3\sigma_0}\right)^{A-1}R_{t,p}^N\frac{1}{Z!N!} \leftrightarrow A^3R_0^N\exp(E_0/kT_0)\left(\frac{h^3\tilde{\rho}_p}{G_p}\right)^{A-1}, \quad (8)$$

where $\sigma_0$ is the total reaction cross section. This equation can next be utilized to obtain properties of the fireball density at freeze out. With use of the extracted $p_0$'s of Ref. 1 for the 400-MeV/n $Ne^{20}$ and U data, values of $\tilde{\rho}_z$ follow when use is made of the approximate scaling $\tilde{\rho}_z/G_z \approx \tilde{\rho}_p/G_p$ so that $\tilde{\rho}_z = \tilde{Z}(b)/V_0(b)$ and $G_z = \int 2\pi b\tilde{Z}(b)db = 4800$ fm$^2$. The resulting values depend on the composite particle and are $\tilde{\rho}_z/\rho_1 \cong 2/3$, 1/3, and 1/5 for α, t, and d, respectively, where $\rho_1 = 0.075$ protons/fm$^3$ is the nuclear matter density of protons.

Footnotes and References

*Abstracted from Phys. Rev. Lett. 38, 640 (1977).

†Present address: Rutgers University, Dept. of Physics, New Brunswick, NJ 08904

1. H. Gutbrod, A. Sandoval, P. Johansen, A. Poskanzer, J. Gosset, W. Meyer, G. Westfall, and R. Stock, Phys. Rev. Lett. 37, 667 (1976).

2. G. D. Westfall, J. Gosset, P. Johansen, A. Poskanzer, W. Meyer, H. Gutbrod, A. Sandoval, and R. Stock, Phys. Rev. Lett. 37, 1202 (1976).

3. E. Burbidge, G. Burbidge, W. Fowler, and F. Hoyle, Rev. Mod. Phys. 29, 547 (1957).

4. A. Schwarzschild and C. Zupanicic, Phys. Rev. 129, 854 (1963).

# EXPLOSIVE NUCLEOSYNTHESIS, EQUILIBRIUM THERMODYNAMICS AND RELATIVISTIC HEAVY-ION COLLISIONS*

A. Mekjian†

The underlying picture for the formation of composite nuclei to be developed is one of an expanding collection of strongly interacting nucleons raised to a high temperature which evolves from a high density region to a low density free expansion. Now, in the initial stages of the expansion, when densities are high and mean free paths are small compared to the size of the system, collisions are then frequent, causing scattering to all possible states. These collisions will then have a three-fold role. First, they will produce the thermal equilibrium generating the randomized final state from the ordered initial state. Second, they will lead to particle production ($N + N \rightarrow N + N + \pi$) and transformation ($N + \pi \rightarrow \Delta$) when incident incoming energies are above particle production thresholds. Third, these interactions result in composite particle formation and break up ($n + p \rightleftharpoons d$).

Then, in the initial stages, when interactions are important, transformations and transitions occur between all strongly interacting constituents so that a transient character is ascribed to each element of the system. Only conserved quantities will have a permanence. For example, a "deuteron" (or more precisely, a pair correlation) will be a metastable resonance in the interacting stage which will appear at one point and then disappear only to reappear at another point possibly in a disguised form with a $\Delta$ replacing a nucleon.

Now the high temperatures ($kT \sim 50$ MeV) and densities ($\rho \sim$ nuclear matter) involved in the interaction region also imply that composite particles can be produced in a profusion of reactions whose rates will be large since energies encountered ($\langle E \rangle \sim 3/2\ kT \sim 75$ MeV) are above all barriers. Furthermore, if these rates are comparable or shorter than expansion time scales, then the rates of formation for various reactions become equal to the rates of their break up (detailed balance) and a chemical equilibrium between all constituents is achieved. Under these circumstances, the dynamical build up of various nuclei quickly takes the system to its equilibrium distributions. In turn, properties of phase space distributions, which, for example, maximize the entropy of the distribution of products in this space, play a more fundamental role than the details of the various cross sections.

If a complete thermodynamic equilibrium is established, then the average behavior of the system is describable in terms of a few state functions which will be taken as the volume of the interaction region and the temperature of the system. It is important to note that the establishment of thermodynamic equilibrium in this volume destroys the history of the system for all previous times except for the information related to conserved quantities. As an example, the number of $\alpha$-particles will reflect a randomized state of the system at some volume and temperature, and will not reflect, except for nucleon number conservation, the ordered initial state. Similarly, any exotic previous state of the system which must evolve through a quasi-equilibrium state of the system at some later stage in the time development of the system will also have its information lost, except for any conserved quantities related to it.

In the results to be presented below, the volume of the interaction region (or density of the system) is a physical quantity that will remain in the final expressions; this volume can therefore be extracted. Specifically, the volume reflects an idealization of the dynamic space-time evolution of the system, representing a sharp cut-off from an interacting to a noninteracting system as it expands. The metastable resonances in this transition eventually become the stable composites. Thus, in an equilibrium model, the observed properties will reflect a "frozen in" equilibrium distribution of an emitting system as it evolved through space and time. Within the framework to be developed, interactions and these ranges are then both included in producing thermal and

chemical equilibrium and in determining the size of the volume where they are established.

Starting with the assumption that the average behavior of a system of nucleons, nuclei and particles produced in a central collision of two heavy ions at relativistic energies might approximate a thermodynamic system in equilibrium, the hope is that the simple and eloquent mathematical framework of equilibrium thermodynamics can lead to some useful insights into the collision. With this qualification in mind, we will proceed on two levels of complexity, the simplest level being defined by a model with the following constraints:

1. Impose the condition that the interactions have produced a thermal equilibrium.
2. Impose the condition that the interactions produce composite nuclei in their bound states with all species in chemical equilibrium.
3. Neglect the structure in the continuum due to the unbound states.
4. Otherwise treat particles as noninteracting ideal gases.

Now, the above model leads to a simple and complete solution to the average behavior of a system of nucleons and nuclei in a box of volume V and temperature T. This solution can be obtained from statistical mechanics using the Gibbs grand canonical partition function. For a system of noninteracting ideal gases of different species, this partition function is given by

$$\mathcal{Z}[V,T,\{\mu_s\}] = \pi_s \left[ \sum_{N_s} e^{\mu_s N_s/kT} \mathcal{Z}_{N_s} \right], \qquad (1)$$

where $\mu_s$ is the chemical potentials of specie S and $\mathcal{Z}_{N_s}$ is the canonical partition function for $N_s$ particles of a particular specie. In turn, the canonical partition function with $N_s$ noninteracting particles is

$$\mathcal{Z}_{N_s} = \frac{\mathcal{Z}_1(S)^{N_s}}{N_s!} \qquad (2)$$

with $\mathcal{Z}_1^{(s)}$ the one-body partition function given by the product of the internal partition function $\mathcal{Z}_{int}$ for that specie and the ratio of the volume V of the thermodynamic box to the thermal volume defined in terms of the thermal de Broglie wavelength $\lambda_T(s)$:

$$\mathcal{Z}_1(s) = \frac{V}{\lambda_T^3(s)} \mathcal{Z}_{int}^{(s)} . \qquad (3)$$

The internal partition function $\mathcal{Z}_{int}^{(s)}$ is given by

$$\mathcal{Z}_{int}^{(s)} = \left[ \Sigma\, (2S_j+1) e^{-E_j/kT} \right] e^{E_0/kT} . \qquad (4)$$

The connection of thermodynamics to statistical mechanics can next be introduced through the thermodynamic potential $\Omega$:

$$\Omega = kT \ln \mathcal{Z}[V,T,\{\mu_s\}] . \qquad (5)$$

All thermodynamic properties then follow from $\Omega$.

The first quantity of interest is the average number of a particular specie in the thermodynamic volume. This number is obtained from the partial derivative of the thermodynamic potential with respect to the chemical potential:

$$N_s = -\frac{\partial \Omega}{\partial \mu_s} = \mathcal{Z}_{int}^{(s)} \frac{V}{\lambda_T^3(s)} e^{\mu_s/kT} . \qquad (6)$$

When the interaction conditions of thermal and chemical are imposed on the system an interesting result is obtained. First, imposing the condition of chemical equilibrium, which is just the statement

$$\mu_{Z,N} = Z\,\mu_p + N\,\mu_n , \qquad (7)$$

the law of mass action immediately follows:

$$\frac{N_0[Z,N]}{N_0[1,0]^Z\, N_0[0,1]^N} = \left[\frac{\lambda_T^3}{V}\right]^{A-1} \frac{A^{3/2}\, \mathcal{Z}_{int}[Z,N]}{2^A} . \qquad (8)$$

The $\lambda_T$ is the thermal wavelength of the proton. The above result can also be derived by the Darwin-Fowler method or method of steepest descent; this result is also the nuclear analog of the Saha equation for ionization.

Letting $\tilde{Z}$ and $\tilde{N}$ be the total number of protons and neutrons in the system, including those contained in composite nuclei, the following auxiliary conditions must be satisfied:

$$\Sigma N_0[Z,N]Z = \tilde{Z} , \quad \Sigma N_0[Z,N]N = \tilde{N} . \qquad (9)$$

Secondly, imposing the condition of thermal equilibrium, which is just the statement that momentum distributions are Maxwell-Boltzman, the momentum space density of a composite is

$$\frac{d^3N_0[Z,N]}{d^3P_A} = N_0(Z,N) \frac{e^{-E_K/kT}}{(2\pi M_A kT)^{3/2}} . \qquad (10)$$

The $P_A$ is the total momentum of the composite and $E_K$ is its total kinetic energy $E_K = P_A^2/2M_A$. The phase space distribution of Eq. (10) can be cast into a Lorentz invariant form when Eq. (10) is

multiplied by E, since $d^3P/E$ is a Lorentz invariant phase space element. The E, here, now includes the rest mass.

The above results show that a thermodynamic model gives rise to an isotropic distribution of fragments. Contrarily, the observed cross sections in the laboratory are forward peaked and, thus, apparently nonthermal in this system. The asymmetry is due to the persistence of the longitudinal momentum of the initial incident state required by overall momentum conservation. In order to avoid a major failure of the model on the most trivial of grounds, one has to allow for nonturbulent collective motion coexistent with local thermal equilibrium. Then, in some rest system in which this collective motion has been separated off, distributions will again be isotropic. The results of Eq. (10) apply to this rest system if it exists.

The Lorentz transformation of the distribution of Eq. (10) from this rest system to the laboratory system gives rise to a forward peaking of the distribution. If, for example, this rest system moves with velocity $\beta$ with respect to the lab, then from the Lorentz invariance of $Ed^3N/d^3p = E'd^3N/d^3p'$, the phase space distributions in the laboratory are

$$\frac{d^3N_0[Z,N]}{d^3P_A} = \frac{E'}{E} N_0[Z,N] \frac{e^{-E'_K/kT}}{(2\pi M_A kT)^{3/2}} \quad . \qquad (11)$$

The primed quantities refer to the rest system and the unprimed quantities to the lab system. The energy E' can be written in terms of the laboratory energy E through the relationship $E' = \gamma(E - \beta P_A \cos\theta_L)$, where

$$\gamma = 1/\sqrt{1-\beta^2}$$

and $\theta_L$ is the angle between $\vec{P}_A$ and $\vec{\beta}$. The $E'_K = E_K - \beta P_A \cos\theta_L + \frac{1}{2} M_A \beta^2$ in the nonrelativistic limit.

Footnotes

*Condensed from LBL-6545.

†Present address: Rutgers University, Dept. of Physics, New Brunswick, NJ 08904.

# PIONIC INSTABILITIES I: SPONTANEOUS $\pi^+\pi^-$, $\pi^\circ\pi^\circ$ PHONON PAIR PRODUCTION IN NONEQUILIBRIUM NUCLEAR MATTER

Miklos Gyulassy

The expectation of reaching high nuclear densities ($\rho \sim 2$-$4\ \rho_0$; $\rho_0 = 0.17\ fm^{-3}$) in heavy-ion collisions has led to much theoretical speculation about the possible unusual properties of such systems. These speculations mainly involve the possibility of observing collective instabilities or phase transitions at such densities. Since pion exchange is the longest range nuclear force as well as being perhaps the best understood of nucleon interactions, it has been natural to first look for collective instabilities involving pion fields.

Previous studies[1] of pion modes in cold (T=0) nuclear matter indicated that above a critical density $\rho_c \sim (1\text{-}2)\rho_0$, nuclear matter is unstable with respect to forming a pion condensate, which in turn leads to a spin-isospin lattice. These studies were extended in Ref. 2 to high temperatures T. The analogue, $T_{crit}(\rho)$, of the Curie temperature in ferromagnets was calculated for pion condensation. The results showed that for sufficiently high densities $\rho \gtrsim 2\rho_0$, the pion condensate phase can be expected to survive the rather high temperatures ($T \sim 50$ MeV) that may arise in heavy-ion collisions. Encouraged by these results, we pursued[3,4] the question of pionic instabilities in non-quilibrium nuclear systems. The problem here is then analogous to the study of the two stream instability in colliding plasmas. The main results are summarized below.

As a model of the non-equilibrium nucleon momentum distribution, $n(\tilde{p})$, we took[3]

$$n(\tilde{p}) = \Theta(P_F - |\tilde{P} + \tilde{P}_{cm}|) + \Theta(P_F - |\tilde{P} - \tilde{P}_{cm}|) \ , \qquad (1)$$

where $P_F$, $P_{cm}$ specify the Fermi and c.m. momenta of the separate colliding nuclei. To look for pionic instabilities in such configurations, the pion propagator $\Delta(\omega,\tilde{k}) = (\omega^2 - k^2 - m_\pi^2 - \Pi(\omega,\tilde{k}))^{-1}$ was calculated. The dominant interactions that had to be taken account of in the pion self-energy $\Pi$ were[1] (1) the P-wave $\pi$ NN interaction that gives the nucleon particle-hole propagator $\Pi_{NN}$, (2) the p-wave $\pi N\Delta$ interaction that gives the $\Delta_{33}(1236)$ particle-nucleon hole propagator $\Pi_{N\Delta}$, and (3) the hard core NN, N$\Delta$, $\Delta\Delta$ interactions that are approximated[1] by $G_c(k) = g/k^2$, with $g = 0.5 \pm 0.1$. The self-energy is then given by[1-4]

$$\Pi = (\Pi_{NN} + \Pi_{N\Delta})/(1 - G_c(\Pi_{NN} + \Pi_{N\Delta})). \qquad (2)$$

The search for pionic instabilities involves looking for complex roots $\omega(\tilde{k}) = \omega_R + i\gamma$ of $\Delta^{-1}(\omega(\tilde{k}), \tilde{k}) = 0$. In Ref. 3, $\gamma(k)$ was shown to be the rate of spontaneous $\pi^+ \pi^-$ or $\pi^o \pi^o$ phonon pair creation where one phonon has wavenumber $\tilde{k}$ while the other has $-\tilde{k}$. The total number of unstable modes is given by[3]

$$n^{\pi}_{crit} = \int \frac{3Vd^3k}{(2\pi)^3} \Theta(\gamma(\tilde{k})) \equiv V/V^{\pi}_{crit} \quad , \qquad (3)$$

while the total phonon pair creation rate is

$$\Gamma_{col} = n^{\pi}_{crit} \langle \gamma(\tilde{k}) \rangle \, , \qquad (4)$$

where V is the volume of the system. $\Gamma_{col}$ measures the growth rate of unstable collective pion fields.

The interest in calculating $\gamma(\tilde{k})$ is (1) to map out the regions of pion phase space $\tilde{k}$ where such instabilities occur and (2) to check if such instabilities have enough time to develop during the short interaction time $\tau \sim$ (5-10) fm/c. The magnitude of $\gamma(\tilde{k})$ necessary for one phonon to be created in mode $\tilde{k}$ during this time is $\gamma_{min} = 1/2\ \tau \sim (0.07 - 0.14)\ m_\pi$, $m_\pi^{-1} = 1.4$ fm/c. We expect that only those unstable modes $\tilde{k}$ with $\gamma(\tilde{k}) \gtrsim \gamma_{min}$ can develop and effect the dynamics in heavy-ion collisions.

Figure 1 shows a contour plot of $\gamma(\tilde{k})$ as a function of $|\tilde{k}|$ and $\cos\theta_\pi = (\tilde{k} \cdot \tilde{p}_{CM})/(kp_{CM})$ for a typical case studied in Ref. 4. This corresponds to a lab kinetic energy of 670 MeV/n. Note first that regions with $\gamma(\tilde{k}) > \gamma_{min}$ do exist, indicating that there is enough time in heavy-ion collisions for such instabilities to develop. Next, note that because of the p-wave nature of the $\pi N$ interaction, the wavenumbers k of those modes are large: $k \sim$ (2-3) $m_\pi$. This is crucial for the existence of such modes in the finite geometries $R \sim$ (5-10) fm in heavy-ion collisions since then $\lambda = 2\pi/k$ can satisfy the boundary condition $\lambda < R$. Note further that there are two distinct regions in Fig. 1. Zero frequency (static) instabilities occur in region I, while finite frequency (dynamic) instabilities occur in region II. The instabilities in region II are the direct analogues of two stream instabilities in colliding plasmas and disappear when the system reaches thermal equilibrium. On the other hand, those in region I survive even in thermal systems[2] and are more analogous to ferromagnetic instabilities.

Finally we note the great sensitivity of $\gamma(k)$ to the value of the correlation parameter[1] $g = 0.5 \pm 0.1$. Thus $\Gamma_{col}/V = 0.18\ m_\pi^4$ for $g = 0.5$ in Fig. 1a, while it is only $0.025\ m_\pi^4$ for $g = 0.6$ in Fig. 1b. Because of this sensitivity, all calculations on pionic instabilities must be viewed only as indicative of possible interesting phenomena that may arise in the dense nuclear medium formed in heavy-ion collisions.

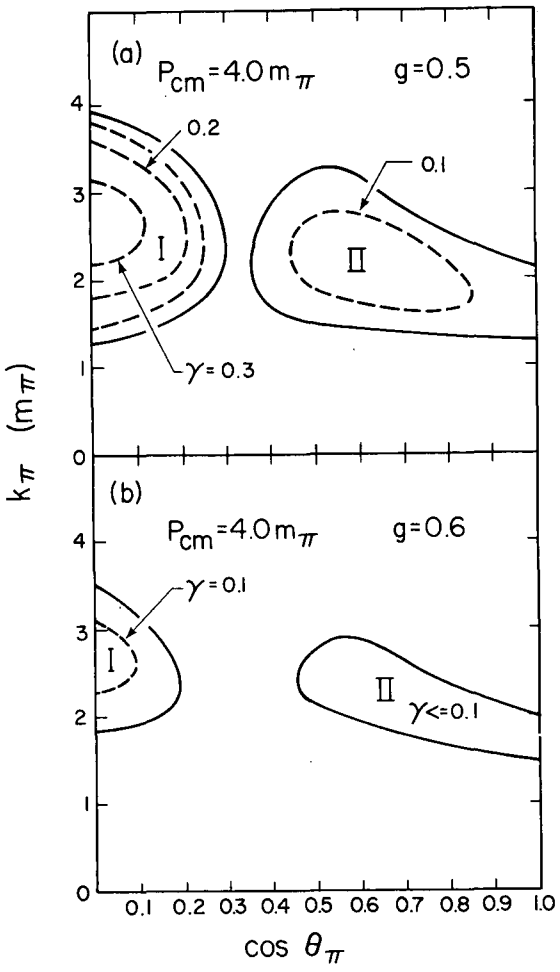


Fig. 1. Contour plot of $\gamma(\tilde{k})$ for $p_{CM} = 4\ m_\pi$, $p_F = 2m_\pi$ in Eq. (1) giving the spontaneous $\pi^+\pi^-$ or $\pi^o\pi^o$ phonon pair creation rates in units of $m_\pi c^2/\hbar$. (XBL 776-1093)

## References


1. A. B. Migdal, et al., Sov. Phys. JETP 39, 212 (1974); G. E. Brown, W. Weise, Phys. Reports 27C, 1 (1976); and references therein.

2. V. Ruck, M. Gyulassy, W. Greiner, Z. Physik A 277, 391 (1976).

3. M. Gyulassy, W. Greiner, Critical Scattering and Pionic Instabilities in Heavy Ion Collisions, University of Frankfurt, Germany, preprint Jan. 1977; Ann. Phys. in press.

4. M. Gyulassy, Pionic Instabilities in High Energy Heavy Ion Collisions, LBL-6525 (June 1977).

# PIONIC INSTABILITIES II: EFFECTS ON HEAVY ION DYNAMICS

Miklos Gyulassy

In Part I of this work,[1] the existence of pionic instabilities in thermal and non-equilibrium configurations of high density nuclear matter was studied. The results indicated that pionic instabilities can occur in heavy-ion collisions in spite of the high excitations energies, short interaction times, and small nuclear dimensions. Part II of this study concerns the role of pionic instabilities on the dynamics itself.

Collective instabilities can affect dynamics in two essential ways: (1) through the growth of collective fields via spontaneous phonon pair creation, and (2) through the modification of two body scattering rates via phonon rather than bare meson exchange. To evaluate the importance of each effect, a formalism was found in Ref. 1 that incorporates them both. This formalism involves the calculation of the complex correlation energy density $M_{RPA}$ of the system in the Random Phase Approximation (RPA). In terms of $M_{RPA}$, the decay rate of the system is given by $\Gamma = -2V \text{ Im } M_{RPA}$. The resulting expression for $\Gamma$ is

$$\Gamma = \text{Re} \int \frac{3Vd^4k}{(2\pi)^4} \log \varepsilon(\omega,\tilde{k}) \ , \qquad (1)$$

where $\varepsilon(\omega,\tilde{k})$ is the pion "dielectric" function in the nuclear system and is closely related to the pion propagator $\Delta(\omega,\tilde{k})$. From the analytic properties of $\varepsilon(\omega,\tilde{k})$, it was possible to derive a decomposition of $\Gamma$as

$$\Gamma = \Gamma_{col} + \Gamma_{NN} + \Gamma_{N\Delta} + \Gamma_{\Delta\Delta} \ , \qquad (2)$$

where $\Gamma_{col}$ is the phonon pair creation rate (see Part I) and $\Gamma_{ij}$ are the effective two body $NN \to ij$ scattering rates in the medium. $\Gamma_{ij}$ could be cast into the Boltzmann collision integral form, which in short hand is

$$\Gamma_{ij}/V = \rho^2 \ \langle \sigma_{eff}(NN \to ij) \ v_{rel} \rangle \ , \qquad (3)$$

where the average is over the nucleon distribution. The effective differential cross section $d\sigma_{eff}$ that appears in that average was related to the free space cross section $d\sigma_o$ through

$$d\sigma_{eff} = P(\omega,\tilde{k}) \ d\sigma_o \ , \qquad (4)$$

where $\omega,\tilde{k}$ are the energy, momentum transfers involved. The polarization form factor, $P(\omega,\tilde{k})$, contains the configuration and density dependence of the effective cross sections. See Ref. 1 for details.

The significance of P in Eq. (4) is that when pionic instabilities occur, there appears a range of $\omega,\tilde{k}$ for which $P(\omega,\tilde{k})$ is logrithmically divergent. This property is related to well-known critical scattering phenomena in Solid State physics. To illustrate this phenomena in connection with pionic instabilities $d\sigma_{eff}$, $d\sigma_0$, and P are plotted in Fig. 1 for a typical configuration studied in

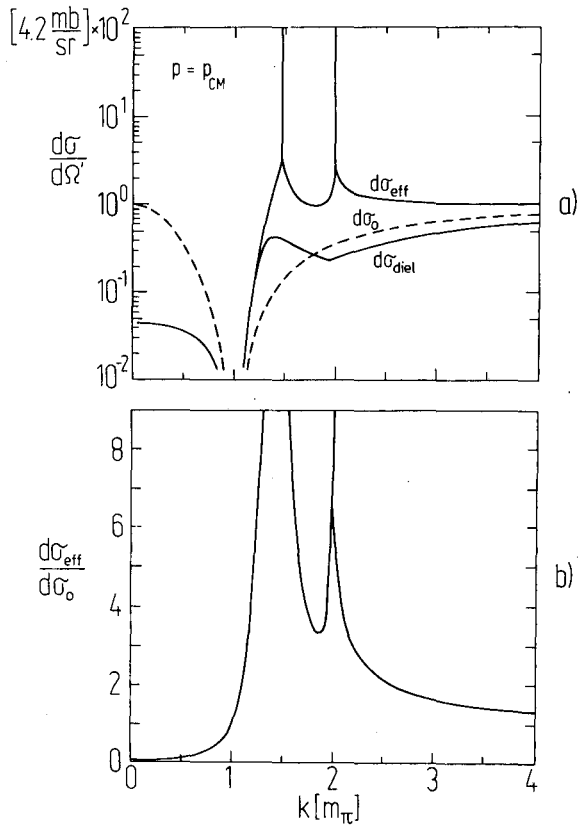


Fig. 1. a) Elastic cross sections[1] in ($d\sigma_{eff}$) and out ($d\sigma_o$) of non-equilibrium nuclear matter for $P_{CM} = 4m_\pi$, $P_F = 2m_\pi$ as a function of momentum transfer k.
b) Polarization form factor, Eq. (4), for this case. (XBL 772-7475)

Ref. 1. This corresponds to elastic scattering of two nucleons of momentum $\vec{P}_{cm}$ and $-\vec{P}_{cm}$ in a system specified by $P_{cm} = 4m_\pi$, $P_F = 2m_\pi$ that was discussed in Part I. Note the logrithmic singularities of $d\sigma_{eff}$ and P that arise as a result of pionic instabilities.

The simple physical picture behind this critical scattering phenomena is as follows: In vacuum, nucleons interact via the exchange of a bare pion. Because that pion is far off shell it cannot propagate freely and the interaction range is limited to $\sim m_\pi^{-1} = 1.4$ fm. In nuclear matter, that pion can propagate much further by jumping from one nucleon to another (the skipping stone effect). This becomes especially true as the mean spacing between nucleons approaches $m_\pi^{-1} \Rightarrow \rho \to 2\rho_o$. This increased range at high densities then leads to the enhanced effective cross sections in the medium.

The overall enhancement of these effective cross sections because of pionic instabilities was found to be on the order of 2-4 for a variety of configurations studied.[1] Typical value of $\Gamma_{NN}$ and $\Gamma_{N\Delta}$ found were $\Gamma_{NN}/V \approx 0.3 \pm 0.1\ m_\pi^4$ and $\Gamma_{N\Delta}/V \approx 0.6 \pm 0.2\ m_\pi^4$. The growth rate of collective fields, on the other hand, was $\Gamma_{col}/V \approx 0.2 \pm 0.1\ m_\pi^4$.

The implication of these results for the dynamics is that the dominant effect of pionic instabilities is to enhance two body cross sections via critical scattering. The dynamics is expected to be collision dominated, $(\Gamma_{NN} + \Gamma_{N\Delta})/\Gamma_{col} \sim 5$, rather than dominated by the collective pion fields. This indicates that a cascade or hydrodynamic approach to the dynamics of medium energy heavy-ion collisions is more appropriate than one based on the Vlasov or TDHF equations. Further implications of pionic instabilities, especially with regard to real pion production, are currently under investigation.

Reference

1. See references in "Pionic Instabilities I: Spontaneous $\pi^+\pi^-$, $\pi^o\pi^o$ Phonon Pair Production...," M. Gyulassy, this Annual Report, p. 197.

## PION MULTIPLICITIES IN HEAVY-ION COLLISIONS

S. K. Kauffmann and M. Gyulassy

The gross features of single particle p, d, t, He, ... (Ref. 1) and $\pi^+$, $\pi^-$ (Ref. 2) inclusive spectra have been interpreted successfully in terms of simple thermodynamic models[1,3,4,5] involving only geometry, kinematics, and statistical mechanics. More detailed models[6] such as hydrodynamics and intranuclear cascade involving quite distinct dynamical assumptions have also been able to reproduce the main features. Therefore, single particle measurements by themselves have not provided strong enough tests to differentiate various possible dynamical models of heavy-ion collisions. To provide more stringent tests of the theories, multiparticle correlations must then be considered.

One such correlation that has been recently measured[7] is the negative pion multiplicity distribution p(n), which is the probability that n $\pi^-$ are produced in a given heavy-ion collision. The only calculation of p(n) until now has been the analytic cascade model of Ref. 8. The central assumption there is that p(n) can be obtained by the superposition of p(n) from independent nucleon-nucleon collisions. The data[7] for Ar+Pb3O4 at 1.8 GeV/n is plotted in Fig. 1a along with the predictions of Ref. 8. As seen from the figure, points $\nabla$ overestimate the high multiplicity tail and do not reproduce the bump at n=1. We report on the results of a thermodynamic calculation[9] of p(n) that fit all features of the measured distribution rather well.

We calculate p(n) assuming that, as a result of the relatively long interaction times ~10 fm/c compared to inverse pion production and absorption rates, pions come to chemical as well as thermal equilibrium in the nuclear medium.[5,10] For a given impact parameter b, corresponding to an interaction volume V(b) and temperature T(b), the average number of $\pi^-$ produced is[5,10] (for symmetric N=Z nuclei

$$\langle n(b) \rangle = \sum_{n=o}^{\infty} n\, p(n;b)$$

$$= \frac{V(b)}{2\pi^2} \int_{m_\pi}^{\infty} d\varepsilon\ \varepsilon\sqrt{\varepsilon^2 - m_\pi^2}\ \frac{1}{e^{\varepsilon/T(b)} - 1} \quad . \qquad (1)$$

The multiplicity distribution is obtained[9] from the generating function

$$F(\lambda) = \sum_{n=o}^{\infty} \lambda^n\, p(n) \qquad (2)$$

$$= \exp\left\{ \frac{V}{2\pi^2} \int_{m_\pi}^{\infty} d\varepsilon\ \varepsilon\sqrt{\varepsilon^2 - m_\pi^2}\ \log\left[ \frac{1 - e^{-\varepsilon/T}}{1 - \lambda e^{-\varepsilon/T}} \right] \right\} .$$

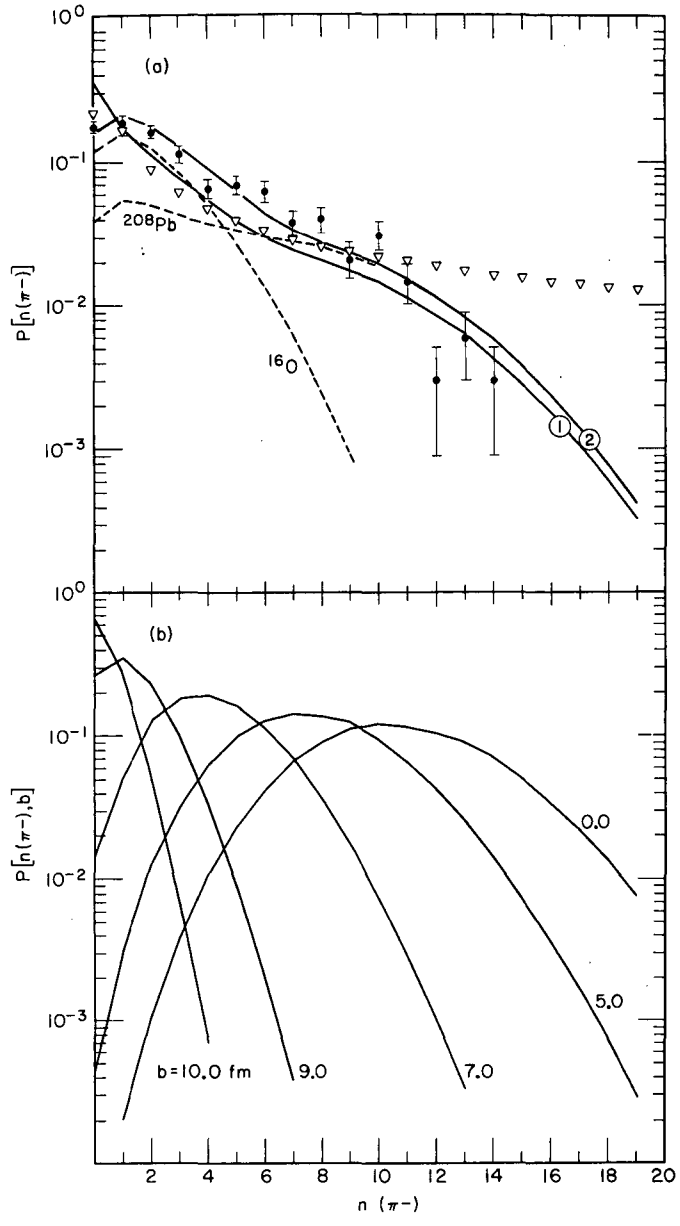


Fig. 1. (a) The $\pi^-$ multiplicity distribution for Ar+$Pb_3O_4$ at 1.8 GeV/n: ♦, Ref. 7; ∇, Ref. 8; Curve 1, Eq. (4), no b cutoff; $\rho_c = 0.16\ m_\pi^3$; Curve 2, Eq. (4) with $b_{max}$ (Pb) = 9.6 fm, $b_{max}$ (O) = 5.0 fm; dashed curves give contributions to Curve 2 from Pb and O targets. (b) The $\pi^-$ multiplicity distributions, Eq. (3), as a function of impact parameter b for Ar+Pb at 1.8 GeV/n. (XBL 778-1599)

In the limit $(\lambda_\pi^3/V)^{2/3} \ll T/m_\pi \ll 1$, p is found[9,11] to be

$$p(m;b) \approx e^{-\langle n(b)\rangle} \frac{\langle n(b)\rangle^m}{m!} , \qquad (3)$$

with $\langle n(b)\rangle$ given by Eq. (1). Finally,

$$p(n) = \int_0^{b_{max}} \frac{2bdb}{b_{max}^2}\, p(n;b) . \qquad (4)$$

For a mixed target such as $Pb_3O_4$, p(n) is appropriately averaged over the distinct elements.

For a model of V(b) and T(b) in Eq. (1), we use the geometry and kinematics of the fireball model[1,3] that gives the total number of nucleons N(b) and excitation energy E*(b) as a function of b. The relation between T(b) and E*(b) follows from the assumption of equilibrium between nucleons and pions, which leads to the approximate form[5]

$$T(b) = T_o(1 - \exp(-2E^*(b)/3T_o)) , \qquad (5)$$

with $T_o \approx 92$ MeV. The volume V(b) corresponding to the form Eq. (5) is[5]

$$V(b) = (N(b) + \langle n(b)\rangle)/\rho_c \approx N(b)/\rho_c , \qquad (6)$$

with $\rho_c \approx 0.16\ m_\pi^3$ being the "freezeout" density below which thermal equilibration ceases. The observed $\pi^-$ multiplicity distribution as well as the single particle spectra are then assumed[1,3,4,5] to reflect only on the V and T of the system at that freezeout density. Clearly, $\rho_c$ is an adjustable parameter of the theory.

One constraint on $\rho_c$ is the fit to the single pion inclusive cross section.[2] Calcultions in progress[5] indicate that the gross features of that cross section are reproduced with $\rho_c \approx 0.05$ fm$^{-3}$. We varied $\rho_c$ about that value to obtain a good fit in Fig. 1a. Curve 1 is obtained by taking $b_{max}$ as the sum of the radii of Ar+Pb and Ar+O. As with points ∇, too many n=o events are predicted, although the high multiplicity end fits well. As a possible explanation for the bump at n=1 in the data we assumed that very peripheral collisions are excluded in Ref. 7 by the triggering of the streamer chamber only on events involving at least a few charged fragments. Indeed, the charged particle multiplicity measurements peak at 5-10 particles for n=o negative pions. Therefore we reduced $b_{max}$ in Eq. (4) by ~ 1 fm corresponding to the requirement that $N(b) \geq 8$ for $b \leq b_{max}$. The resulting curve 2 now shows a bump at n=1 of the correct magnitude. To understand why an impact parameter cutoff produces this bump, we plot p(n;b) in Fig. 1b. As the impact parameter decreases, $\langle n(b)\rangle$ increases as V(b) increases,[1,5] shifting p(n;b) to higher multiplicities. The largest impact parameters are weighed the most in Eq. (4), but have the smallest $\langle n(b)\rangle$, resulting in the excess of n=o events in curve 1. The point we wish to emphasize is that with a reasonable cutoff all features of the data are reproduced.

References


1. H. Gutbrod, A. Sandoval, P. Johansen, A. Poskanzer, J. Gosset, W. Meyer, G. Westfall, et al., Phys Rev. Lett. 37, 1202 (1976); J. Gosset, et al., LBL-5820, preprint (May 10, 1977).

2. H. Bowman, J. G. Ioannou, S. Kaplan, J. O. Rasmussen, J. Chiba, S. Nagamiya, K. Nakai, K. Sugimoto, I. Tanihata, Low Energy Pion Production in Heavy Ion Collisions, LBL preprint in preparation.

3. W. D. Myers, A Model for High Energy Heavy Ion Collisions, LBL-6569 and this Annual Report.

4. A. Mekjian, Phys. Rev. Lett. 38, 640 (1977).

5. J. I. Kapusta, Particle Production in the Nuclear Fireball Model, LBL-6504, preprint and to be published.

6. A. A. Amsden, J. N. Ginocchio, F. H. Harlow, J. R. Nix, M. Danos, E. C. Halbert, R. K. Smith, LA-UR-77-152 preprint (January 15, 1977).

7. S. Y. Fung, W. Gorn, G. P. Kiernan, F. F. Liu, J. J. Lu, Y. T. Oh, J. Ozawa, R. T. Poe, L. Schroeder, H. Steiner, G. Van Dalen, preliminary data, manuscript in preparation.

8. J. P. Vary, Multiple Collision Model for Pion Production in Relativistic Nucleus-Nucleus Collisions, Iowa State preprint IS-4184, (1977)

9. M. Gyulassy and S. K. Kauffman, Pion Multiplicity Distributions in Heavy-Ion Collisions, LBL-6593.

10. G. Chapline, M. Johnson, E. Teller, M. Weiss, Phys. Rev. D 8, 4302 (1973); M. I. Sobel, P. J. Siemens, J. P. Bondorf, H. A. Bethe, Nucl. Phys. A 251, 502 (1975).

11. R. Hagedorn, in Cargèse Lectures in Physics, Vol. 6, p. 707, Ed. E. Schatzman, 1973.


## CAN THE HADRONIC MASS SPECTRUM BE DETERMINED BY HIGH ENERGY NUCLEAR COLLISIONS?

Norman K. Glendenning and Yasha Karant

One of the fundamental properties of matter is the mass spectrum of the hadrons. Besides being an object of interest in particle physics, it has profound cosmological significance. The spectrum starts with the pion and rapidly becomes dense up to masses of about 2 GeV. Thereafter, according to our present knowledge, but most likely due to the difficulty of measurement, there are only a few additional known particles and resonances. The experimental spectrum is shown in Fig. 1 with the exception of isolated recent discoveries. According to the bootstrap hypothesis the spectrum continues beyond the known region and in effect, exponentially. The hypothesis can be stated simply as follows: from among the known particles or resonances select two (or more) and combine their quantum numbers. The multiplet so obtained are also particles or resonances (at something like the sum of the masses). Add these to the pool of particles and continue. The spectrum so obtained by Hamer and Frautschi[1] is also shown in Fig. 1. The implication is astonishing. The number of particles and resonances grows so fast that at masses of only 2.5 GeV the number in a mass interval of the pion mass, expected from the bootstrap hypothesis, is $\sim 10^4$. The number of known hadrons is $\sim 10^2$. If new particles were discovered at the rate of one a day it would require a hundred years to confirm the bootstrap prediction by a direct count, and that in only such a small mass interval and at such a low mass!

We suggest as an alternative that it may be possible to determine the general behavior of the spectrum without the necessity of discovering the individual particles and resonances. The decay of hadronic matter produced in ultra high energy collisions between nuclei will depend upon the type and masses of particles that can energetically be produced, that is, on the mass spectrum of the hadrons. After that obvious statement, there remain two important questions. At what energy does the outcome of the collision depend sensitively on the (unknown) spectrum and what is the dynamical description of the reaction? We shall here assume that the colliding nucleons, assisted by particle production and the resulting subsequent collisions, attain a temporary state of equilibrium among the large number of hadrons, and shall answer the first question in the context of that dynamics. We conjecture that the energy at which sensitivity is achieved will not depend crucially on the dynamics assumed, although the observable signals may. To the nuclear physicist, the possibility that an equilibrium state would be temporarily reached in a nuclear collision at high energy may seem remote. Nonetheless thermodynamic models in particle physics are not new, and they enjoy some success.[2] A collision involving initially many nucleons is even more likely to reach an equilibrium state that one involving initially only two.

It is the aim of this research to determine whether the thermodynamic properties of hot hadronic matter occupying a volume of the order of nuclear dimensions is sufficiently sensitive to the unknown hadronic mass spectrum as to encourage

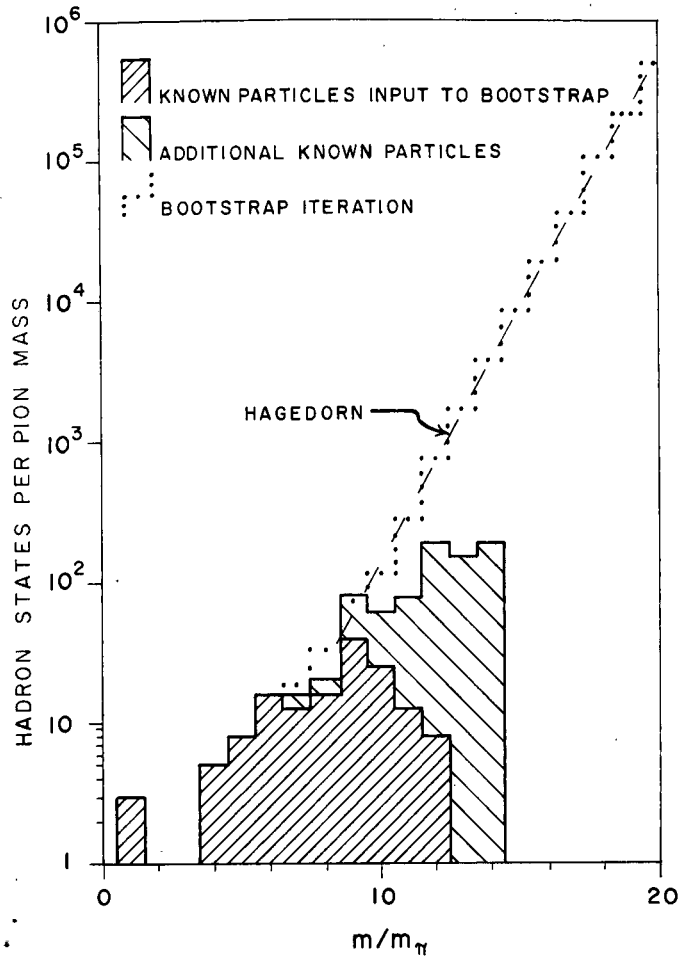


Fig. 1. The density of different hadrons, ρ, in unit interval is plotted as a function of the mass in units of the pion mass. The experimentally known particles and resonances with their multiplicities are shown in the shaded areas. The dotted histogram is a bootstrap iteration[1] on the known spectrum and the dashed curve is a Hagedorn type spectrum, fitted to the bootstrap. (XBL 778-2819)

an attempt to discover it experimentally in this way. We shall refer hereafter to such hadronic matter as a nuclear fireball, it being suggested by the thermodyanmic bootstrap theory of hadrons due to Hagedorn[3] and already used in the context of nuclear collisions.[4,5]

The partition function and momentum distribution function for an ideal relativistic gas of fermions or bosons of mass m and statistical weight g = (2J+1)(2I+1) occupying a volume V at temperature T are[3]

$$\ln Z(V,T) = \frac{gV}{2\pi^2} m^2 T \sum_1^\infty \frac{(\mp)^{n+1}}{n^2} K_2\left(\frac{nm}{T}\right), \quad \begin{pmatrix} F \\ B \end{pmatrix} \tag{1}$$

$$f(p,T)d^3p = \frac{gV}{2\pi^2} \frac{p^2 dp}{\exp\left(\frac{1}{T}\sqrt{p^2+m^2}\right) \pm 1}, \quad \begin{pmatrix} F \\ B \end{pmatrix} \tag{2}$$

from which the various thermodynamic quantities can be calculated. We want to describe a gas of baryons and mesons distributed in mass according to some unknown functions $\rho_B(m)$ and $\rho_M(m)$ for which bargon number is conserved. This conservation can be achieved as usual by introducing a chemical potential μ for the baryons.[6] The average number and energy for baryons and mesons are

$$B = \frac{VT}{2\pi^2} \int_{m_N}^\infty dm\ \rho_B(m)\ m^2 \sum_1^\infty \frac{(-)^{n+1}}{n} \times K_2\left(\frac{nm}{T}\right) \exp\left(\frac{n\mu}{T}\right) \tag{3}$$

$$E_B = \frac{VT}{2\pi^2} \int_{m_N}^\infty dm\ \rho_B(m) m^3 \sum_1^\infty \frac{(-)^{n+1}}{n} \times \left[K_1\left(\frac{nm}{T}\right) + \frac{3T}{nm} K_2\left(\frac{nm}{T}\right)\right] \exp\left(\frac{n\mu}{T}\right) \tag{4}$$

$$M = \frac{VT}{2\pi^2} \int_{m_\pi}^\infty dm\ \rho_M(m) m^2 \sum_1^\infty \frac{1}{n} K_2\left(\frac{nm}{T}\right) \tag{5}$$

$$E_M = \frac{VT}{2\pi^2} \int_{m_\pi}^\infty dm\ \rho_M(m) m^3 \times \sum_1^\infty \frac{1}{n}\left[K_1\left(\frac{nm}{T}\right) + \frac{3T}{nm} K_2\left(\frac{nm}{T}\right)\right] \tag{6}$$

We shall consider collisions between identical nuclei with isospin I=0. In that case charge conservation is implied already. For a grid of values of T, we solve the first equation for the value of μ which yields the baryon density desired. The remaining equations then tell us the corresponding energy and meson number.

It may seem strange that a strongly interacting hadronic system is discussed in terms

of an ideal gas. However Hagedorn has argued convincingly, on the basis of statistical mechanical techniques introduced by Beth, Uhlenbech, and Belenkij[7] that the hadronic spectrum is the manifestation of the hadronic interactions; that by introducing the complete hadronic mass spectrum one has accounted for their interactions completely.

We consider two extreme possibilities for the mass spectrum of hadrons. One is a caricature of the experimental spectrum of Fig. 1.

$$\rho_{exp}(m) = \begin{cases} 20 \text{ discrete hadrons}, & m < 12\ m_\pi \\ 27.5 \text{ per pion mass}, & m > 12\ m_\pi \end{cases} \qquad (7)$$

where $\rho(m)$ is the number of different hadrons in the interval of a pion mass. The other is a Hagedorn mass spectrum which fits the bootstrap iteration of the known particles as shown in Fig. 1.

$$\rho_{exp}(m) = \begin{cases} 20 \text{ discrete hadrons}, & m < 12\ m_\pi \\ \dfrac{1.12\ e^{m/T_0}}{(m/T_0)^3} \text{ pion mass}, & m > 12\ m_\pi \end{cases} \qquad (8)$$

$$T_0 = 0.958\ m_\pi \quad , \quad m_\pi = 140 \text{ MeV}$$

$$m_\pi$$

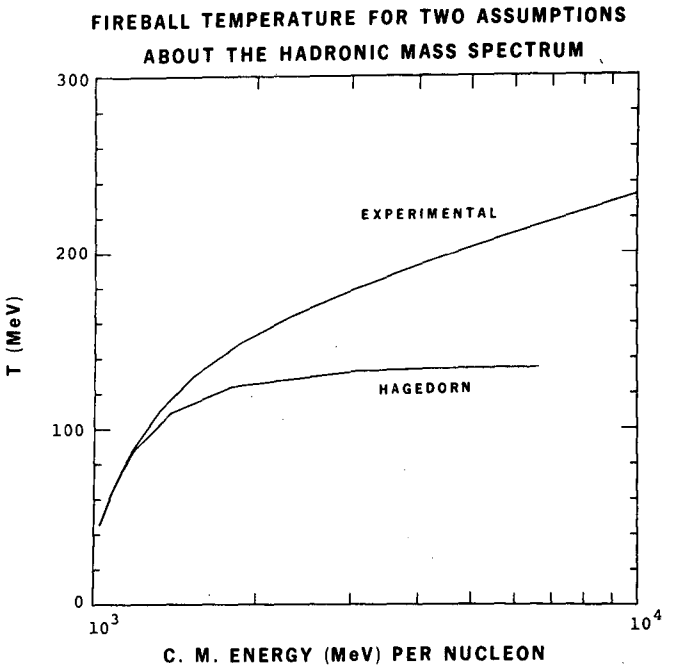


Fig. 2. The temperature of hot hadronic matter assumed to be produced in a symmetric nuclear collision is plotted as a function of the c.m. kinetic energy per nucleon of the colliding nuclei for a volume corresponding to about the initial density of nucleons. The curve labeled "experimental" corresponds to a mass spectrum that approximates the known spectrum Eq. (7), while that labeled "Hagedorn" corresponds to a Hagedorn spectrum, Eq. (8). (XBL 779-4875)

In both cases we include as a discrete spectrum the known hadrons up to and including the $\Delta(1650)$ and g(1690) with their widths, and continue the spectrum with one or other of the above continua. The number of baryons and mesons in the continuous region at each mass are assumed equal.

The temperature is plotted in Fig. 2 as a function of the center-of-mass kinetic energy per nucleon for the symmetric collision at a baryon density of $0.25/fm^3$. For an exponentially increasing mass spectrum the temperature is limited to $T_0$, but the temperature can increase without bound for the less rapidly increasing spectrum. What we see is a moderate difference in the temperature of the two assumed spectra at energies in range of the CERN storage rings. This encourages us to believe that even at presently attainable energies, one might be able to distinguish between various hadronic spectra.

The next steps in our research will involve invoking several different models for the expansion of the fireball to a freezeout density. We hope that the moderate difference between the two assumed spectra will persist to the freezeout density where thereafter it will be preserved in the spectra of observed particles.

We interpret our suggestion and result as follows. The true dynamics is without doubt much more complicated than equilibrium thermodynamics. Extensive theoretical developments in understanding the dynamics of high energy nuclear collisions, assisted by much experimentation are needed before we can even contemplate extracting the hadronic mass spectrum from data on nuclear collisions. What this paper shows is that the sensitivity to the mass spectrum is most probably present in ultra high energy nuclear collisions and it therefore provides the motive for pursuing what is surely a long and difficult task.

## References

1. C. J. Hamer and S. C. Frautschi, Phys. Rev. D 4, 2125 (1971).

2. There is a long literature but perhaps the paper of most direct interest here is Ref. 3.

3. R. Hagedorn in Cargèse Lectures in Physics, Vol. 6, ed. by E. Schatzman, (Gordon Breach, NY) 1973.

4. G. F. Chapline, M. H. Johnson, E. Teller, and M. S. Weiss, Phys. Rev. D 8, 4302 (1973).

5. G. D. Westfall, I. Gosset, P. J. Johansen, A. M. Poskanzer, W. G. Meyer, H. H. Gutbrod, A. Sandoval, and R. Stock, Phys. Rev. Lett. 37, 1202 (1976).

6. J. I. Kapusta, (LBL-6504) has considered pion production in nuclear collisions also assuming a relativistic ideal gas of π, N, and Δ. Our equations are a natural extension of his, and both follow from the literature on ideal relativistic gases.

7. S. Z. Belenkij, Nucl. Phys. 2, 259 (1956).

## RELATIVISTIC MEAN FIELD THEORIES: NUCLEAR MATTER vs PCAC

D. Vautherin and M. Gyulassy

To explore possible unusual properties of dense nuclear systems generated in high energy heavy-ion collisions, many groups[1-4] have recently investigated the consequences of Lorentz invariant Lagrangian theories in the mean field approximation. There have been up to now two distinct approaches to the study of high density matter within this framework.

These differ in the constraints imposed on the parameters (coupling constants and masses) of the theory. In the first approach,[1,3] the theory is constrained to reproduce normal saturation properties of nuclear matter:

$$E/A = \omega(\rho_0) = -16 \text{ MeV}; \quad \rho_0 = 0.17 \text{ fm}^{-3} . \quad (1)$$

In the second approach,[4] the theory is constrained to reproduce properties of strong interactions summarized by current algebra and Partially Conserved Axial Currents (PCAC)

$$\partial_\mu A_\mu^{\,i}(x) = c_\pi \, m_\pi^{\,2} \, \pi_i(x) \quad (2)$$

with $c_\pi$ = 94 MeV and $\pi_i$ being the pion fields. In both approaches the objective is to calculate the equation of state $\omega(\rho)$ at higher densities $\rho > \rho_0$ and look for phase transitions characterized by $\sigma$ and/or $\pi$ condensates.

A disturbing feature of both approaches is that the two constraints, Eqs. (1,2), seem to be mutually exclusive in the models studied. Therefore, the class of theories[1,3] that gave good saturation properties did not give PCAC and, hence, ignored the Goldberger-Treiman, the Adler-Weisberger relations, and other cherished properties of strong interactions. On the other hand, theories[2,4] motivated by PCAC and current algebra did not give normal saturation properties and, hence, ignored nuclear physics. We have found[5] that a simple theory can be constructed that incorporates the best of both worlds, giving both nuclear saturation as well as PCAC and current algebra.

Consider the class of theories involving the nucleon $\psi$, scalar sigma $\sigma$, pseudo-scalar pion $\pi_i$, and vector omega $\omega_\mu$ fields of the form

$$\begin{aligned}\mathcal{L}(x) = {} & \bar\psi \{(i\partial_\mu - g_v\omega_\mu)\gamma_\mu - g_s(\sigma + i\gamma_5 \, \vec\tau\cdot\vec\pi)\} \psi \\ & + \frac{1}{2}\{(\partial_\mu\sigma)^2 + (\partial_\mu\pi)^2\} \\ & - \frac{1}{2}\left\{\frac{1}{2} F_{\mu\nu} F_{\mu\nu} + m_\omega^{\,2} \omega_\mu^{\,2}\right\} \\ & - U(\sigma,\pi_i) \quad , \end{aligned} \quad (3)$$

where the potential density U is parametrized as

$$\begin{aligned} U(\sigma,\pi_i) = {} & \frac{a}{2}\left[\left(\frac{\sigma}{\sigma_0}\right)^2 + \left(\frac{\pi}{\sigma_0}\right)^2\right] + \frac{b}{4}\left[\left(\frac{\sigma}{\sigma_0}\right)^2 + \left(\frac{\pi}{\sigma_0}\right)^2\right]^2 . \\ & - (a+b)\,\frac{\sigma}{\sigma_0} + \frac{a}{2}(c-1)\left(\frac{\pi}{\sigma_0}\right)^2 + \frac{a}{2} + \frac{3}{4} b \end{aligned} \quad (4)$$

The vacuum is then specified by $\langle\sigma\rangle = \sigma_0$ and $\langle\pi_i\rangle = 0$ at which point $U = \partial U/\partial\sigma = \partial U/\partial\pi = 0$.

The divergence of the axial current $A_\mu^{\,i}(x)$ is computed from the variation of $\mathcal{L}$ under a chiral transformation:

$$\sigma \to \sigma + \vec\varepsilon\cdot\vec\pi, \; \vec\pi \to \vec\pi - \vec\varepsilon\sigma, \; \psi \to (1+i\gamma_5 \, \vec\varepsilon\cdot\vec\tau)\, \psi \, ,$$

$$\Rightarrow \partial_\mu A_\mu^{\,i} = -\frac{\partial U}{\partial\sigma}\pi_i + \frac{\partial U}{\partial\pi_i}\sigma \, . \quad (5)$$

Equation (5) shows that $\partial_\mu A_\mu^i = 0$ if $\mathcal{L}$ were chiral symmetric, i.e., $U = U(\sigma^2+\pi^2)$. Note that the form of the current $A_\mu^i = \delta\mathcal{L}/\delta(\partial_\mu\varepsilon_i)$ does not depend on U since U involves no derivatives. Hence, current algebra is not effected by the specific form of U. However, PCAC requires $\partial_\mu A_\mu^i$ to be given by Eq. (2). The PCAC constraint on U is then

$$\left[ -\frac{\partial U}{\partial \sigma}\pi_i + \frac{\partial U}{\partial \pi_i}\sigma \right]_{\sigma=\sigma_0} = c_\pi m_\pi^2 \pi_i \quad . \quad (6)$$

Observe that Eq. (6) is only a local constraint on U near the vacuum point $\sigma = \sigma_0$, $\pi_i = 0$. This is a reminder of the well known (but sometimes forgotten) fact that while approximate chiral symmetry is sufficient for PCAC, it is by no means necessary. The existence of models with badly broken chiral symmetry satisfying Eq. (2) is the key to reconciling constraints Eqs. (1) and (2).

Now note that Eq. (1) also requires[1,3] only a limited knowledge of $U(\sigma,\omega)$. In particular, the addition of any function of $\pi^2$ to U has no effect on the calculation leading to Eq. (1). Since Eq. (1) then only constrains $U(\sigma,0)$ while Eq. (2) only constrains the derivatives of U near the vacuum, it is not surprising that a form of $U(\sigma,\pi)$ can be found that leads to both Eqs. (1) and (2).

To illustrate the differences between models satisfying Eq. (1) and/or Eq. (2), we plot in Fig. 1 equipotential surfaces of $U(\sigma,\pi)$ in three models. Fig 1(a) corresponds to the $\sigma$ model[2,4] with a = -507 MeV/fm$^3$, b = 530 MeV/fm$^3$, c = 1 in Eq. (4). The approximate chiral invariance is reflected in the approximate rotation symmetry of U about $\sigma = \pi = 0$. As discussed in Refs. 2 and 3, normal nuclei [Eq. (1)] are however unstable in this model. In Fig. 1(b) a Walecka type model[1] is illustrated for which a = 379 MeV/fm$^3$, b = 0, c = 1. In this case Eq. (1) is satisfied, but $\partial_\mu A_\mu^i = (a/\sigma_0)\pi_i$. To recover Eq. (2) requires $\sigma_0 = 1580$ MeV, which then implies $m_\sigma = m_\pi = 34$ MeV. If, on the other hand, $m_\pi$ is taken as the physical pion mass then $\partial_\mu A_\mu^i \approx 4\, c_\pi m_\pi^2 \pi_i$ which is inconsistent with Goldberger-Triemann relation, pion decay width, etc. In this model chiral symmetry is clearly broken badly. Finally, Fig. 1(c) illustrates a $U(\sigma,\pi)$ satisfying both Eqs. (1) and (2). This model[5] differs from Walecka's model only in that c = 0.0625 which leads to $m_\sigma/m_\pi = 4$ and $\sigma_0 = c_\pi$.

Comparing Figs. 1(a), 1(c) near the vacuum point, one can see how the local property, Eq. (3), can be simultaneously satisfied by both models. Comparing Figs. 1(b), 1(c) shows that $U(\sigma,0)$ is identical and, hence, both models lead to the same condition Eq. (1). The interesting point to observe is that Eq. (1) was made consistent with Eq. (2) simply by retaining both of the commonly employed versions of symmetry breaking:[4] $\mathcal{L}_{SB}^{(1)} = c_1\sigma$ and $\mathcal{L}_{SB}^{(2)} = c_2\pi^2$. In this model then, chiral symmetry is also badly broken on a global scale.

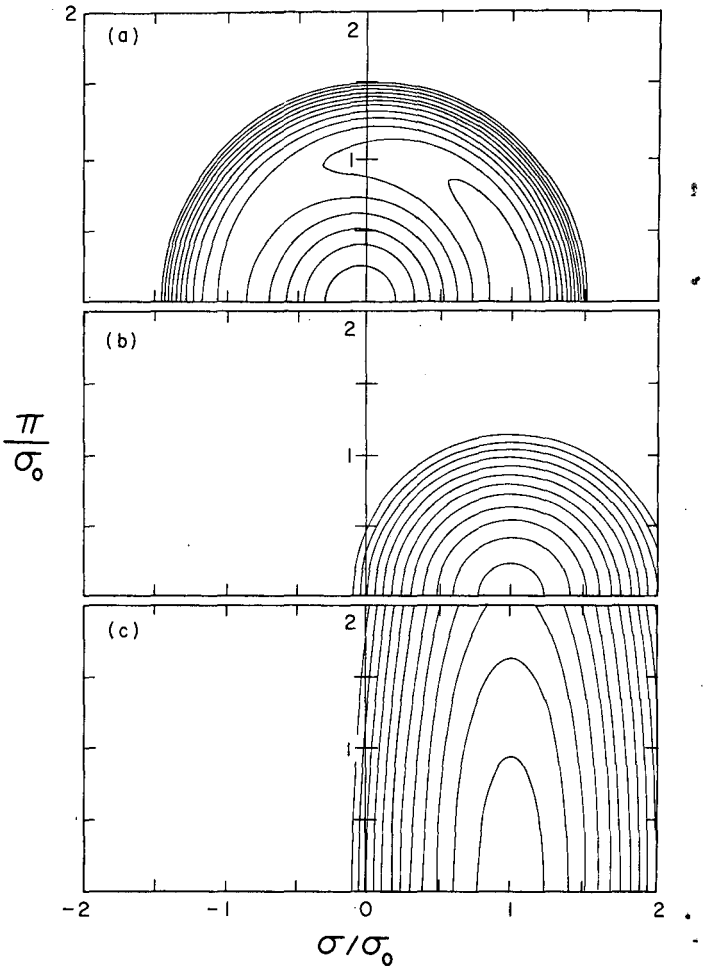


Fig. 1. Contour plot of $U(\sigma/\sigma_0, \pi/\sigma_0)$, Eq. (4), in steps of 20 MeV/fm$^3$. a) Model satisfying Eq. (2) but not Eq. (1); b) Model satisfying Eq. (1) but not Eq. (2); c) Model satisfying both Eqs. (1) and (2). See discussion in text.
(XBL 778-1676)

We are currently investigating the consequences of this model in connection with pion condensation since the largest differences between conventional approaches based on chiral models [Fig. 1(a)] and the one proposed here [Fig. 1(c)] which satisfies both Eqs. (1) and (2) should arise for $\langle \pi_i \rangle \neq 0$.

## References

1. J. D. Walecka, Ann. Phys. 83, 491 (1974); S. A. Chin, J. D. Walecka, Phys. Lett. 52B, 24 (1974).

2. A. K. Kerman, L. D. Miller, Contribution to Heavy Ion Summer Study, LBL July 1974, MIT-CTP Pub. 449.

3. S. A. Moszkowski, C. G. Kallman, Abnormal Neutron Star Matter, UCLA preprint (1977); J. Boguta, A. R. Bodmer, Relativistic Calculation of Nuclear Matter and the Nuclear Surface, Argonne preprint (1977).

4. T. D. Lee, Rev. Mod. Phys. 47, 267 (1975); D. Campbell, R. Dashen, J. Mannassah, Phys. Rev. D 12, 979, 1010 (1975); M. Chanowitz, P. J. Siemens, Pion Condensation and Abnormal Nuclear Matter, LBL-5597, (1977).

5. D. G. Vautherin, M. Gyulassy, Nuclear Matter, PCAC, and Chiral Symmetry, manuscript in preparation.

# BREMSSTRAHLUNG IN THE NUCLEAR FIREBALL MODEL*

J. I. Kapusta

In a recent paper[1] a nuclear fireball model was used to calculate the proton inclusive spectra from relativistic heavy-ion collisions. The essential ingredients of the model are: geometry, to calculate the number of nucleons in the fire ball; kinematics, to calculate the velocity of the fireball and the energy deposited in it; and thermodynamics, to describe the decay of the fireball.

Without making any further assumptions it is possible to calculate the low-energy bremsstrahlung radiated during the direct collision process. The fireball model does not specify how the system evolves from projectile plus target to fireball(s) plus fragments. For relativistic heavy-ion collisions the inverse collision time is of order $c/2R$, where R is a nuclear radius. To a photon with frequency $\omega \ll c/2R$ the collision will appear as instantaneous. Thus we assume that the acceleration of charge which produces the bremsstrahlung can be treated as a delta-function. All that need be specified then are the incoming and outgoing currents. This limits us to calculating bremsstrahlung photons with energy less than 10 MeV. This assumption is equivalent to a long-wavelength approximation so that all nuclear form factors which might appear can be set equal to one. The use of classical electrodynamics is justified since all photon energies will be negligible compared to nucleon and pion masses. Note that the decay of the fireball(s) will not contribute substantially to the bremsstrahlung since it is a thermodynamic expansion.

The bremsstrahlung calculation proceeds in the standard way.[2] Figure 1 shows the double

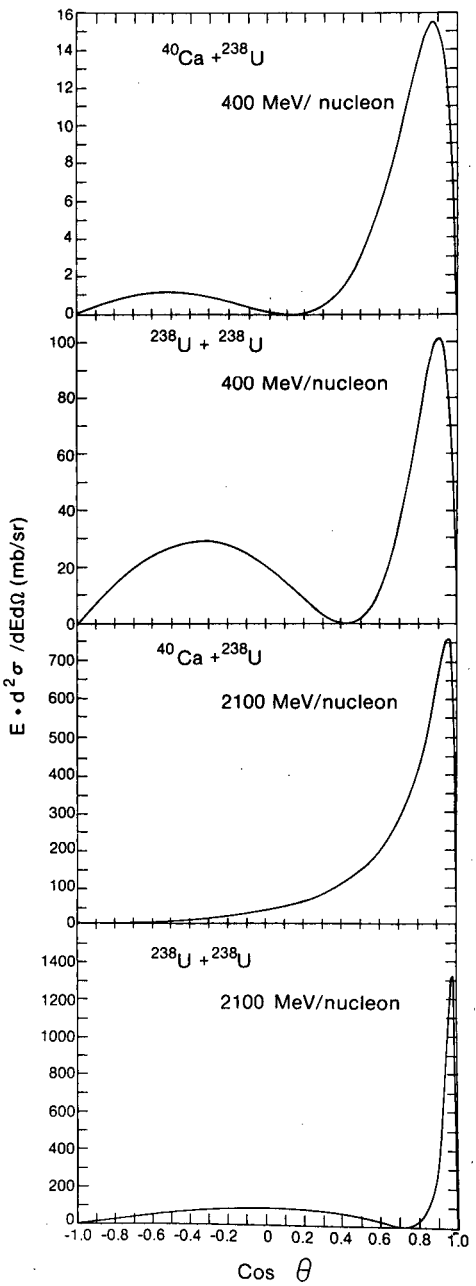


Fig. 1. Bremsstrahlung cross sections as a function of angle. (a) and (b) assume one fireball, (c) and (d) assume two fireballs with a transparency of 75%. (XBL 7611-4383)

differential cross section for photon production for $^{40}Ca$ and $^{238}U$ on $^{238}U$ at 400 and 2100 MeV/n. At the higher energy two fireballs have been assumed with a transparency of 75%. The sharp peak in the forward direction, which is present in all the cross sections, is because of relativity. The broad hump in the backward direction, which is not even noticeable in one of the graphs, arises for the same reason. The dip in the central region is because of interference between the incoming and outgoing currents.

In this paper only the bremsstrahlung from the direct nucleus-nucleus collision has been considered. There are other sources which might interfere with the observation of this bremsstrahlung. In the low keV region there may be photons emitted during electronic transitions. In the high keV and low MeV region there may be photons emitted by the residual projectile and target nuclei (if any) making EM transitions after the direct collision.

Experimental confirmation of these calculations would be an independent verification of the validity of the nuclear fireball concept. On the other hand the low energy bremsstrahlung does not provide any information on the details of the collision process since it only depends on the incoming and outgoing currents. One should be able to obtain much more information about how the nuclear system evolves during the collision by examining the bremsstrahlung in the 10 to 140 MeV region.

Footnote and References

*Condensed from Phys. Rev. C 15, 1580 (1977).

1. G. D. Westfall, J. Gosset, P. J. Johansen, A. M. Poskanzer, W. G. Meyer, H. H. Gutbrod, A. Sandoval and R. Stock, Phys. Rev. Lett. 37, 1202 (1976).

2. J. D. Jackson, Classical Electrodynamics, 2nd edition, Wiley, New York (1975), p. 671.

## PARTICLE PRODUCTION IN THE NUCLEAR FIREBALL MODEL

J. I. Kapusta

In a recent paper[1] it was found that the gross features of the proton inclusive spectra in relativistic heavy-ion collisions could be described by a nuclear fireball model. In this model the projectile and target nuclei are taken to be uniform density spheres. For a given impact parameter the fireball consists of those nucleons whose extrapolated straight line trajectories intersect the other nucleus. The baryon number and charge of the fireball are thus determined by geometry. The mass and velocity of the fireball are then determined uniquely by kinematics. We assume that enough interactions occur during the initial formation and subsequent expansion of the fireball that thermal equilibrium occurs among all the hadrons consistent with the conservation laws.

In the spirit of Hagedorn we will use noninteracting gas formulae to describe each hadron type which we expect to be a statistically significant component of the fireball when it decays. Hagedorn's mass spectrum[2] is not directly applicable here because, for instance, the number of protons and neutrons will not in general be equal. The distribution of particles of type i in momentum space is:

$$\frac{d^2N_i}{dp^3} = \frac{(2S_i+1)V}{(2\pi)^3}\left(\exp\left(\frac{\sqrt{p^2+m_i^2}-\mu_i}{T}\right)\pm 1\right)^{-1} \quad (1)$$

Here $S_i$ is the spin, $m_i \neq 0$ is the mass and $\mu_i$ the chemical potential. $V$ is the volume of the fireball at the instant of decay and $\pm$ refers to fermion/boson. We use $\hbar = c = k = 1$.

Pomeranchuk[3] has observed that one should not choose a fireball volume independent of the number of hadrons it contains and then expect to use noninteracting gas formulae to describe them. If the hadron density is high there will be many interactions. As the system expands its density will decrease and so will the number of interactions. Due to the short range nature of the strong interactions one might expect that some critical density $\rho_c$ will be reached after which most of the particles effectively cease to interact. This hadron density is expected to be of the order of $(4/3\ \pi\ m_\pi^3)^{-1}$. Of course the use of a critical density is only an approximation but it makes the problem much more tractable. The critical density is the only parameter in the model. We would expect that $0.04 \lesssim \rho_c(fm^{-3}) \lesssim 0.12$.

The statement of thermal equilibrium implies certain relations among the chemical potentials. For instance, $p + n \leftrightarrow n + n + \pi^+$ implies that $\mu_{\pi^+} = \mu_p - \mu_n$. For a given impact parameter we can calculate the mass M, charge Q and baryon number B of the fireball. The unknown quantities which are to be determined are the proton and neutron chemical potentials, the temperature and the volume at the critical density. They are found by solving the equations for the conservation

of energy, charge and baryon number, and the constraint that the number density be $\rho_c$.

Up to several GeV beam energy the most important contributions to the fireball are the pions, nucleons and deltas. The nucleon cross sections are independent, and the pion cross sections nearly independent, of the inclusion or exclusion of the delta. The slope of the nucleon differential cross section is made slightly steeper by the inclusion of the delta, whereas the shape of the pion differential cross section is changed significantly. For neutron rich projectile-target combinations there is a net conversion of neutrons to protons and a larger number of negative than positive pions. This conversion will affect the relative abundance of various isotopes of light nuclei.

A serious approximation in the model is that the transition from thermal equilibrium to a freely expanding system of particles is made instantaneously. For long-lived particles this is not too much of a problem but for short-lived particles it may be. For instance, the doubling time of the fireball volume is the same order of magnitude as the lifetime of the $\Delta(1232)$.

The possibility of a transparency between target and projectile at higher energy leading to two fireballs was not considered, although it is clear how to include it. Transparency affects the kinematics, not the thermodynamics of the model. Finally when making a detailed comparison with experiment for the spectra of nucleons and light nuclei it may be necessary to take account of the evaporation of the target and spectator pieces. Also the spectra of nucleons from the fireball need to be corrected for depletion due to the production of light nuclei.

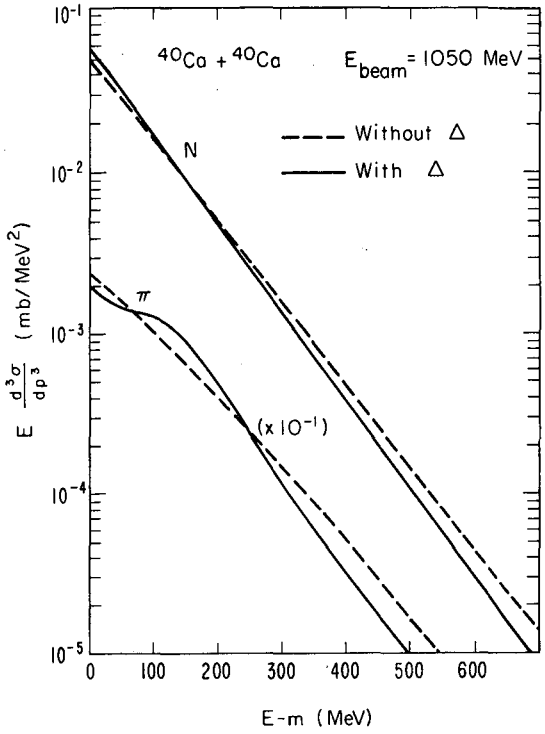


Fig. 1. Influence of the $\Delta(1232)$ on the pion and nucleon differential cross sections for the reaction $^{40}Ca + ^{40}Ca$ at 1050 MeV. (XBL 774-888)

Footnote and References

*Condensed from LBL-6504.

1. G. D. Westfall, J. Gosset, P. J. Johansen, A. M. Poskanzer, W. G. Meyer, H. H. Gotbrod, A. Sandoval, and R. Stock, Phys. Rev. Lett. 37, 1202 (1976).

2. R. Hagedorn, in Cargèse Lectures in Physics VI, edited by E. Schatzmann (Gordon and Breach, New York, 1973), p. 643.

3. I. Ya. Pomeranchuk, Dokl. Akad. Nauk SSSR 78, 889 (1951).

# A NEW APPROXIMATION FOR GLAUBER THEORY ON STRIPPING OF RELATIVISTIC DEUTERONS

Sven A. Nissen-Meyer

We present a new approximation for the Glauber theoretical model of Bertocchi, Tekou, and Treleani (BTT)[1,2] on the neutron stripping off of relativistic deuterons in collisions with nuclei. Their original ansatz overestimated the stripping cross section by including parts of the elastic cross section for $d+A \rightarrow d+A$. This comes about by approximating the wavefunction for the dissociated deuteron by a plane wave state, which is not orthogonal to the deuteron state. BTT correct for the overestimate[2] by an overall normalization factor, determined so as to reproduce the correct integrated total stripping cross section.

We attempt a different correction for the same overestimate, more on the level of the differential cross section, by subtracting from the plane wave state its component parallel to the deuteron state. For computational simplicity this subtraction is only done for the coherent part of the disintegration cross section.

Using a simple Hulthen wavefunction for the deuteron and taking all input parameters for the model from other experimental data, we obtain the curves in Figs. 1 and 2, compared with the data of J. Papp.[3] The thickness of the curves indicates the numerical uncertainty in the calculation. The disagreement with the data at 1.05 GeV/n just above the peak could be due to energy dependences of nucleon-nucleon parameters that are not included in the calculation. The deviation from the data in the high-p region at both energies has at least these two possible causes: a) The Hulthen function does not represent the near-relativistic Fermi-momenta, and b) off-shell effects in the deuteron, which are not correctly taken into account in Glauber theory, become increasingly important.

In order to extract reliable information about the short distance part of the deuteron wave function, the off-shell effects at large Fermi

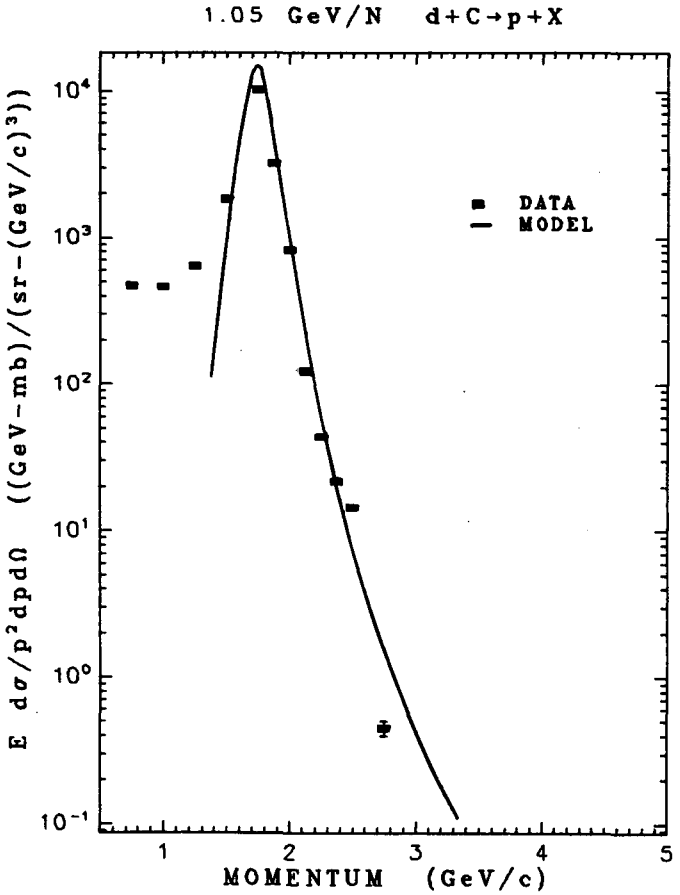


Fig. 1. Comparison of the model prediction (i.e., no fitted parameters) with data from 1.05 GeV/n deuterons on carbon target, taken from Ref. 3. (XBL 778-1647)

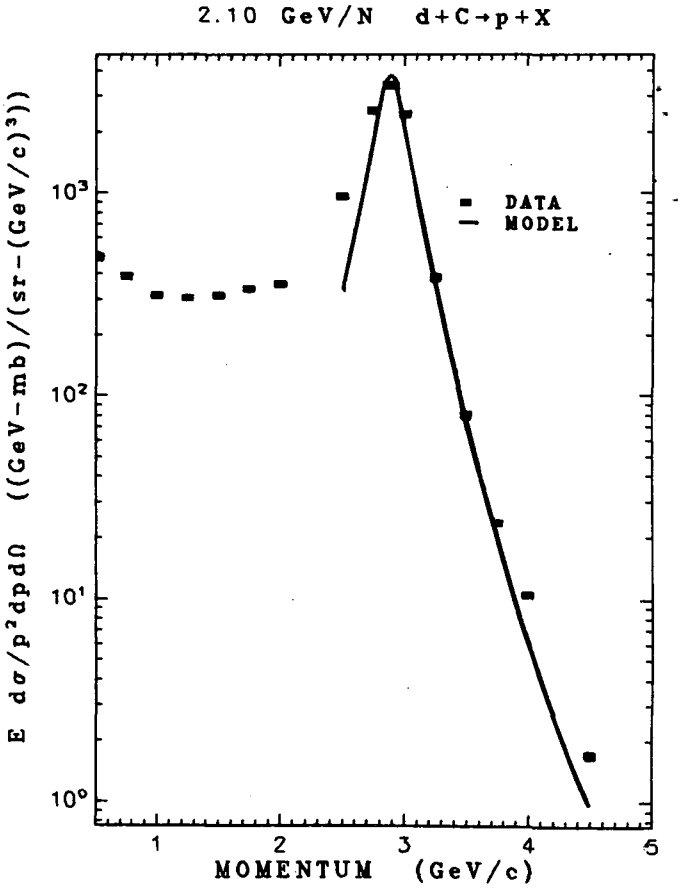


Fig. 2. Same as Fig. 1, at 2.1 GeV/n. (XBL 778-1648)

momenta need a better understanding than in the conventional Glauber theory treatment.

References


1. L. Bertocchi, and A. Tekou, Nuovo Cimento 21A, 223 (1974).
2. L. Bertocchi, and D. Treleani, Preprint, Ref. TH. 2203-CERN, (Aug. 1976).
3. J. Papp, Thesis, University of California, Berkeley, LBL-3633, (May 1975).


# K-VACANCY PRODUCTION BY RELATIVISTIC HEAVY IONS

J. G. Ioannou and J. O. Rasmussen

The electromagnetic interaction between a fast-moving charge particle and an atomic electron can be subdivided into two terms:[1] the unretarded static Coulomb interaction or longitudinal term and the interaction between the currents of the two particles or transverse term. Both interactions are responsible for the transfer of momentum from the projectile to the electron, the longitudinal one along the direction of Coulomb interaction of projectile-electron while the transverse one perpendicular to it. Both interactions then are contributing to the K-vacancy formation. The total (longitudinal + transverse) differential cross section of K-vacancy production using the PWBA method is given by the general formula:[2]

$$d^2G_{\varepsilon K} = 8\pi Z_1^2\left(\frac{e^2}{\hbar v}\right)^2\left[\frac{|F_{\varepsilon K}(q)|^2}{q^4} + \frac{|\beta_t\cdot\bar{G}_{\varepsilon K}(q)|^2}{\left[q^2-\left(\frac{w}{\hbar c}\right)^2\right]^2}\right]2qdqdw \qquad (1)$$

where in Eq. (1) $\hbar\bar{q} = \bar{p}-\bar{p}'$ is the momentum transfer to the electron, $\bar{p}$, $\bar{p}'$, being the initial, final momentum of the projectile with atomic number $Z_1$, v its velocity which is assumed to be constant and

$$w = \varepsilon + E_K = \frac{\hbar^2K^2}{2me} + Z_2^2R_\infty \qquad (2)$$

with w, $\varepsilon$, $E_K$ the total energy transfer to, kinetic energy of, binding energy of the K-shell electron, respectively. Furthermore in Eq. (1), $\bar{\beta}$ -- the transverse component of $\bar{\beta} = \bar{v}/c$ -- is given by

$$\bar{\beta}_t = \bar{\beta} - (\bar{\beta}\cdot\hat{q})\hat{q} \qquad (3)$$

and $F_{\varepsilon K}(9)$, $\bar{G}_{\varepsilon K}(9)$ are the matrix elements corresponding to the lognitudinal and transverse interactions of the K-shell electrons ejected with a kinetic energy $\varepsilon$, and are given by the formulae:[1]

$$F_K(9) = \sum_{j_K}\langle\varepsilon|e^{+i\bar{q}\cdot\bar{r}_{jK}}|0\rangle \qquad (4)$$

$$\bar{G}_{\varepsilon K}(9) = \sum_{jK}^{jK}\langle\varepsilon|\bar{a}_{jK}e^{i\bar{q}\cdot\bar{r}_{jK}}|0\rangle \qquad (5)$$

with $|0\rangle$, $|\varepsilon\rangle$ initial, final state of the system respectively, $j_K$'s referring to the K-shell electrons with position vectors $\bar{r}_{jK}$, and $a_{j_K}$'s being in terms of the electron Dirac $\gamma$ matrices.

Upon integration of (1) over q and w, one obtains the total cross section of $V_1$-vacancy production

$$6_K = 6_K^{\ell} + 6_K^{t}\ . \qquad (6)$$

The longitudinal term $6_K^{\ell}$ has already been studied extensively[2] and its values have been tabulated.[3] Here, we study in detail the transverse term. Since the K-electrons are ejected into the continuum, $\bar{G}_{\varepsilon K}(q)$ can be recognized as the matrix element for the photoelectric absorption of high energy photons. In the spirit of the evaluation of $F_{\varepsilon K}(q)$, nonrelativistic one-electron 1s and continuum wavefunctions are used, and $\bar{q}_{jK}$ is equated with $\bar{v}_{jK}/c = iw/\hbar c\ \bar{r}_{jK}$. In addition since $q/p_2 \ll 1$, we can approximate[1] $|\bar{\beta}_t\cdot\bar{G}_\varepsilon(q)|$ with $\beta_t^2|\bar{G}_{\varepsilon K}(q)|^2$. Furthermore under the previous assumptions for the calculation of $\bar{G}_{\varepsilon K}(q)$, we obtain:[4]

$$|\bar{G}_{\epsilon K}(q)| = \left(\frac{w}{\hbar c}\right)^2 \frac{2}{3}^6 \frac{(Z_2 a)^6 \exp\left\{2 \frac{Z_2 a}{K} \arctan\left[2Z_2 aK/(k^2 - (Z_2 a)^2 - q^2)\right]\right\}}{\left[(q^2+(Z_2 a)^2 + K^2) - 2q^2 k^2\right]^2 \left[1-\exp(-2\pi Z_2 q/k)\right]\left[K^2+(Z_2 a)^2\right]} \quad (7)$$

with $Z_2$ the atomic number of target element and $a = 1/a_o$ = inverse hydrogen Bohr radius. The limits of integration of Eq. (1) are[2] for q, $q_{min} = 2/\hbar v$ to $q_{max} = |\bar{p}| \simeq \infty$ and for w, $w_{min} = E_K$ to $w_{max} \simeq \infty$. We thus obtain for the transverse component $6_u{}^t$ of the K-vacancy production cross section:

$$\sigma_K{}^t = 8\pi \left(\frac{Z_1}{Z_2}\right) \beta^2 \left(\frac{e^2}{\hbar c}\right)^2 \frac{2}{3}^6 a_o{}^2 g(n_K, \beta^2)$$

$$= 8 \times 10^5 \beta^2 \left(\frac{Z_1}{Z_2}\right)^2 g(n_K, \beta^2) \quad , \quad (8)$$

where in Eq. (8)

$$g(n_K, \beta^2) = \int_1^\infty dy \int_0^1 dx \frac{(1-x)\cdot\exp[2/\sqrt{y} \arctan}{(1-\beta^2 x)^2 \cdot [1-\exp(-2\pi/\sqrt{y})]}$$

$$\times \frac{(2\sqrt{y}/(y-1-Q)]}{[(Q+1+y)^2 - 2yQ]^2} \quad (9)$$

and

$$x \equiv q^2 min/q^2, \quad y = K^2/(Z_2 a)^2, \quad Q = \frac{(1+y)^2}{4n_K x}, \quad n_K = \frac{\beta^2}{2(\gamma_K - 1)},$$

$\gamma_K$ being that of the bound K-electron. For non-relativistic bound electron velocities, that is light nuclei or

$$Z_2 < 40 \; n_K \rightarrow \frac{\beta^2}{\beta_K{}^2} = \left(\frac{v}{v_K}\right)^2 .$$

The typical variations of $\sigma_K$, $\sigma_K{}^\ell$, $\sigma_K{}^t$ with projectile energy E are depicted in Fig. 1.

Since $\sigma_K{}^\ell$ has a maximum for $n_K = 1$, where $\sigma_K = \sigma_K{}^\ell$ ($\sigma_K{}^t \lll \sigma_K{}^\ell$), the $\sigma_K{}^t$ component becomes significant for high energies and for heavier elements ($Z_2 > 70$) too. There $\sigma_K{}^t$ is several times

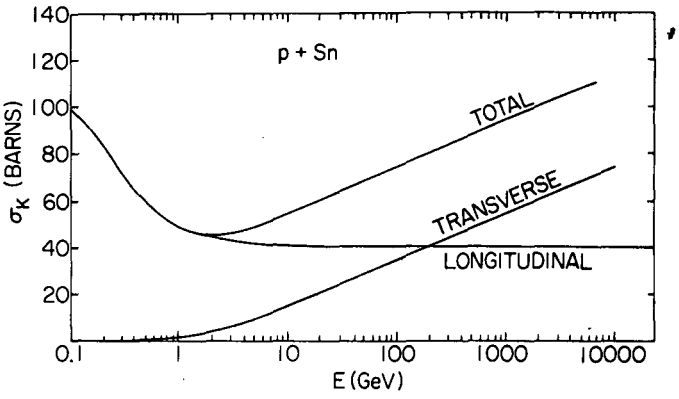


Fig. 1. Very high energy behavior of p + Sn cross section calculated by using the PWBA. (XBL 766-8139)

the corresponding $\sigma_K{}^\ell$ for the same energy, and for heavier elements even the maximum $\sigma_K{}^\ell$ at $n_K = 1$. To illustrate the point consider protons on Mo($Z_2 = 42$) for which at 35 MeV ($n_K = 1$) $\sigma_K = (\sigma_K{}^\ell max) = 186.65$ barns but at 5 GeV $\sigma_K{}^\ell = 55.69b + \sigma_K{}^t = 41.1b) = 96.8$ barns and on Pb ($Z_2 = 82$) for which at 147 MeV ($n_K = 1$) $\sigma_K(\simeq \sigma_K{}^\ell max) = 10.1$ barns but at 5 GeV $\sigma_K = (\sigma_K{}^\ell = 2.11b + \sigma_u{}^t = 13.82b) = 15.93$ barns.

Numerical calculation of (g) over a wide range of $n_K$'s and $\beta$'s is under way.

The problem of the transverse term for x-ray yields at relativistic energies was earlier treated by Anholt et al. The present work gives a somewhat smaller contribution of the transverse term than he derived. The difference mainly arises from the difference in integration limits of Eq. (9).

## References


1. V. Fano, Ann. Rev. Nucl. Sci. 13, 1 (1963).
2. E. Merzbacher and H. Lewis, Encyclopedia of Physics 34, 166 (1958).
3. G. S. Khandelwal, B. H. Choi and E. Merzbacher, At. Data 1, 103 (1969).
4. J. Fischer, Ann. Phys. 8, 821 (1931).
5. R. Anholt et al., Phys. Rev. A 14, 2103 (1976).

# B. NUCLEAR STRUCTURE

## MICROSCOPIC CALCULATIONS OF HIGH-SPIN ROTATIONAL STATES*

Chin W. Ma† and John O. Rasmussen

The high-spin rotational states of $^{162}Er$, $^{168}Yb$, $^{174}Hf$, and $^{238}U$ are calculated microscopically by diagonalizing the cranking Hamiltonian $H-\omega J_x$ using both BCS and fully particle-number projected wavefunctions. The computational effort in the latter case is greatly reduced due to a newly derived compact formula for the residuum integral. The results show that pairing collapse does not occur in all four nuclei up to spin 20. The moderate increase of the moment of inertia at low spin is due to both higher-order cranking and Coriolis antipairing effects. The crossing of the decoupled two quasi-particle band with the ground band is responsible for the rapid increase of the moment of inertia at high spin. The present calculations are able to produce the rotational energies fairly well in general, but the Nilsson single-particle levels have to be adjusted in order to reproduce the backbending behavior in $^{162}Er$. Six figures from the original paper are presented here to illustrate the kind of results obtained.

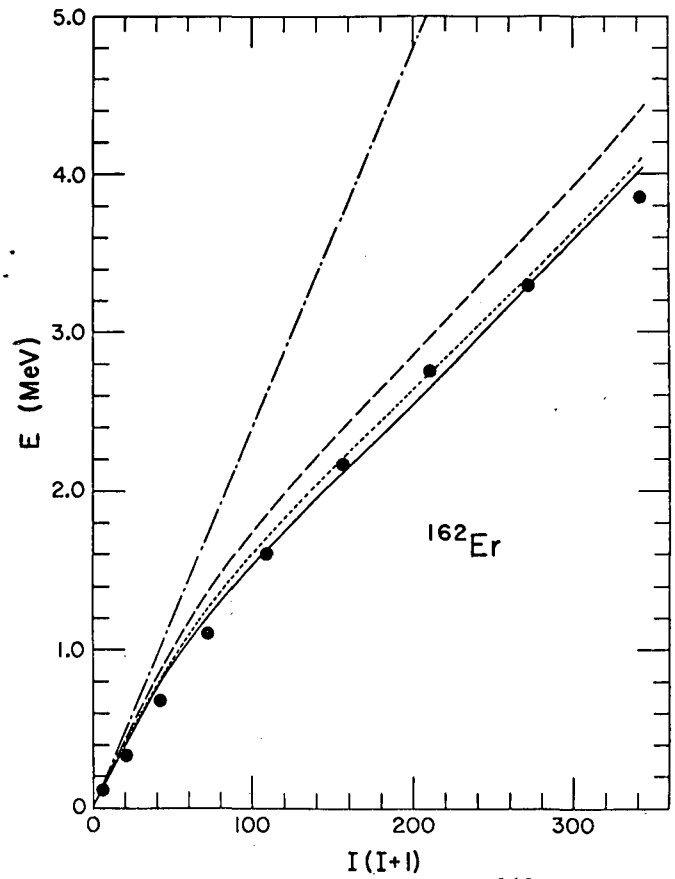


Fig. 1. Energy E vs spin I(I+1) for $^{162}Er$. The dashed curve represents the BCS calculation without Coriolis-antipairing effect; the dotted curve represents the same calculation with CAP effect; the solid curve is the fixed-particle-number-projection (FBCS) calculation also with CAP effect, and the dash-dot curve is the regular cranking result. The experimental data are indicated by dots.
(XBL 778-1763)

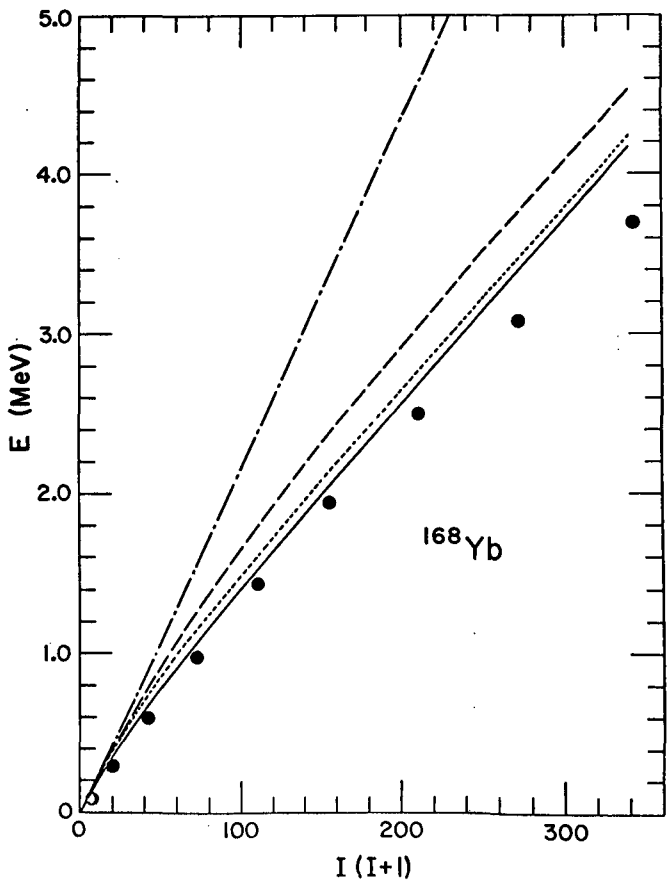


Fig. 2. Energy E vs spin I(I+1) for $^{168}Yb$, see Fig. 1 for detailed explanation.
(XBL 778-1764)

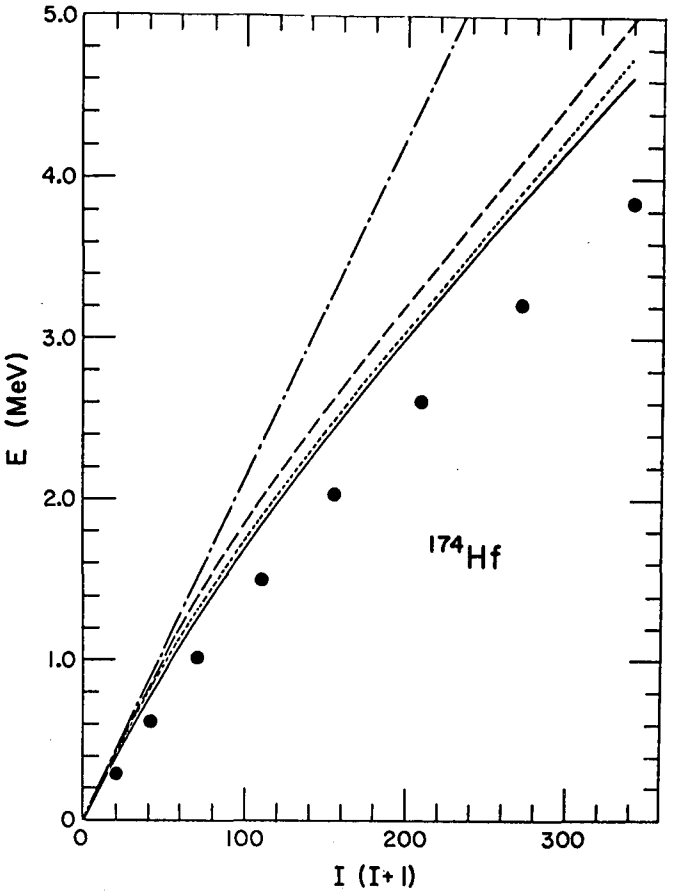


Fig. 3. Energy E vs spin I(I+1) for $^{174}$Hf, see Fig. 1 for detailed explanation.
(XBL 778-1765)

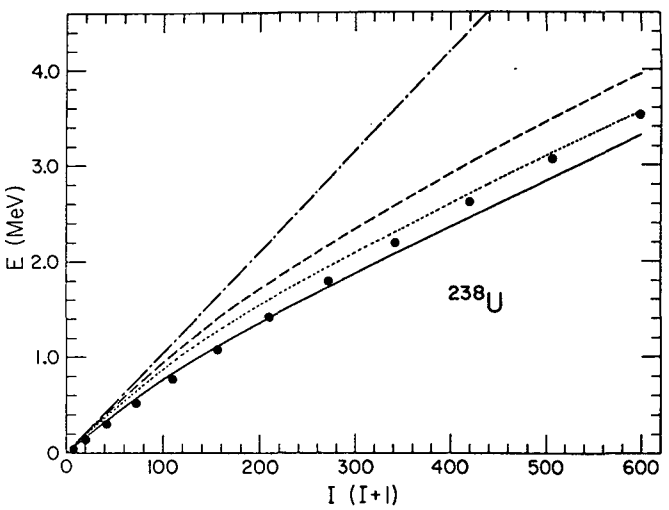


Fig. 4. Energy E vs spin I(I+1) for $^{238}$U, see Fig. 1 for detailed explanation.
(XBL 778-1766)

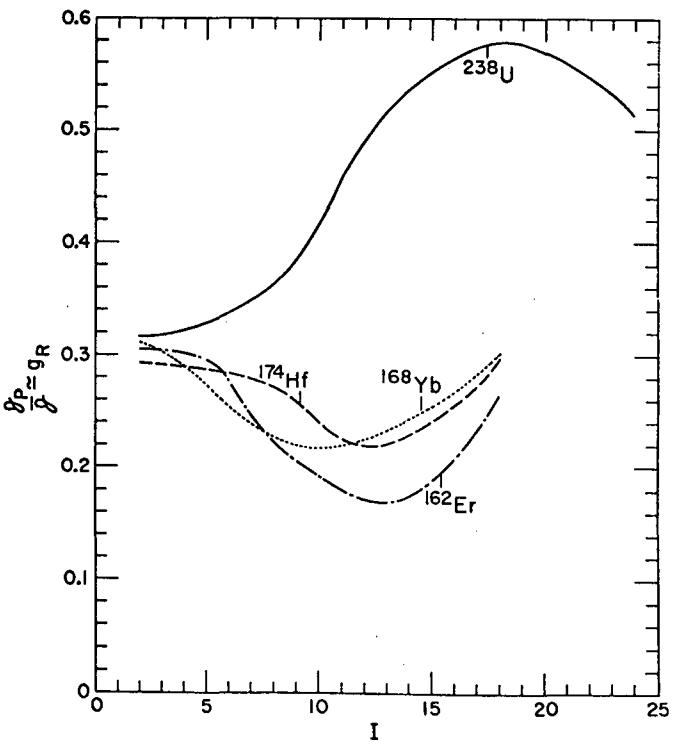


Fig. 5. The collective gyromagnetic ratio $g_R$ vs spin I.
(XBL 778-1767)

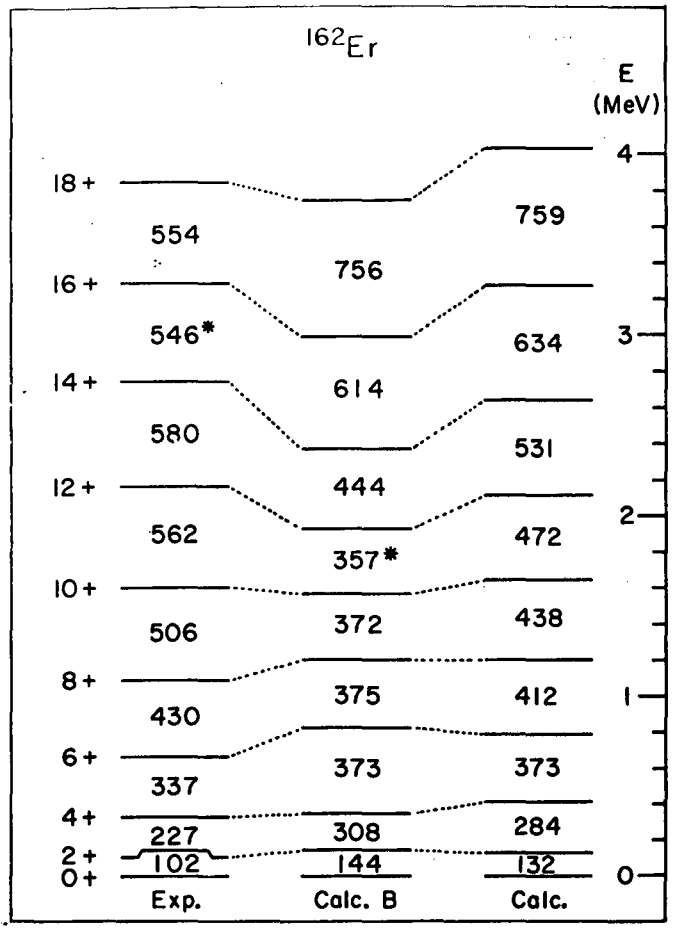


Footnotes

*Condensed from LBL-6521; Phys. Rev. C16, 1179 (1977).

†Cyclotron Institute and Physics Department, Texas A&M University, College State, Texas 77843

Fig. 6. Comparison between the experimental and calculated rotational energies of $^{162}$Er. The second column represents calculations in which the neutron level 3/2[651] is shifted while the third column represents calculations using the 1969 Nilsson energy levels. The numbers between levels are their energy differences in keV. The symbol * has been used to indicate a backbending transition. (XBL 778-1768)

## THE DYNAMIC DROPLET MODEL I. THE GIANT DIPOLE RESONANCE*

W. D. Myers, W. J. Swiatecki, T. Kodama,† L. J. El-Jaick,† and E. R. Hilf‡

The giant electric dipole resonance (GDR) is a beautiful example, among the vast variety of possible nuclear excitations, of a manifestly collective mode that can be understood, to a large extent, in terms of a macroscopic approach. It corresponds to the absorption of electric dipole radiation by the vibration of the neutrons against the protons and the subsequent damping of this motion into intrinsic excitation.

The work that is described here contains two new features. First, all the restoring forces are calculated in terms of the Droplet Model. Second, the motion is considered to be a superposition of Goldhaber-Teller (GT)[1] and Steinwedel-Jensen (SJ)[2] modes with the relative magnitudes of the two modes determined by the coupling between them and the associated forces and inertias. We find that the GDR is mainly a GT mode, but with an essential admixture of the SJ mode which increases for heavier nuclei. We also find a A-dependence for the resonance energy that is intermediate between that of the GT and SJ modes, in excellent agreement with the measured trends.

Since we last reported on this work[3] we have discovered that the theory presented here, according to which the oscillating system is allowed to decide for itself the relative amounts of the GT and SJ modes, leads indeed to a situation where neither mode is expected to be dominant. (See Ref. 4 for a microscopic treatment leading to similar conclusions). On the contrary, the mixture appears to be close to a special combination, the Droplet Mode which, for any value of A, is just such as to make the local neutron excess at any point on the surface and at any instant follow the local neutron skin thickness according to the Droplet Rule. This rule states that, for the static ground state density distributions of neutrons and protons for nuclei throughout the periodic table, the ratio of the neutron skin thickness t to the local neutron excess at the surface $\delta_s$ is given by the universal expression,

$$\frac{t}{\delta_s} = \frac{3}{2}\frac{J}{Q} r_o \ , \qquad (1)$$

where J, Q and $r_o$ are Droplet Model coefficients.[5]

In order to illustrate the nature of the actual density oscillations we show in Fig. 1 the appearance of the density distributions at the instant of maximum displacement (the classical turning point of the quantized oscillation) for $^{208}$Pb. The centers of the neutron and proton spheres are seen displaced by about 0.27 fm, and there is a considerable difference in the values of the local neutron excess at the left and right hand tips of the nucleus.

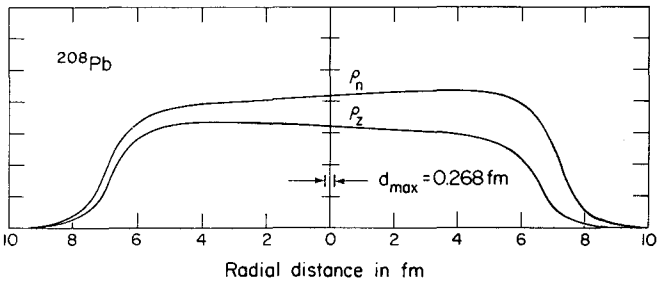


Fig. 1. The neutron and proton density profiles along the GDR symmetry axis are plotted against distance from the center of mass for the case of $^{208}$Pb. The centers of the effective sharp spherical boundaries of the two density distributions (GT mode) are shown displaced from each by the maximum distance that is expected to occur during the vibration (0.268 fm). The corresponding compressional pile up (SJ mode) of neutrons on one side and protons on the other is also indicated. (XBL 7610-4034)

What is the physical significance of the choice by the oscillating system of the Droplet Mode? Mathematically this is the result of the near-vanishing of the determinant of the inertia matrix. As is readily verified the kinematic meaning of this near-vanishing is the similarity of the flow patterns in the GT and SJ modes of oscillation. In general, if two modes of motion have essentially the same flow patterns (and are regarded as separate modes only because the potential energy is different for them) then the off-diagonal (cross) term in the kinetic energy, involving the product of the time derivatives of the two modes, is no different (apart from normalization) from the diagonal terms which involve the squares of the time derivatives of each mode separately. The inertia matrix can then be brought to the form

$$\begin{pmatrix} 1 & 1 \\ 1 & 1 \end{pmatrix}$$

for which the determinant is clearly zero. It is apparently because the GT and SJ flow patterns are (somewhat surprisingly) quite similar, at least in an integral sense, that it is left largely for the potential energy to decide on the optimum mixture of the two modes, with the result that the mixture conforms closely to the static Droplet Rule.

With the relative strengths of the GT and SJ modes determined by Eq. (1) the trend of the GDR energies with A is well reproduced but the calculated values are about 15% less than the measured ones. This apparent discrepancy could be an indication that the effective inertia involved in the oscillations of the neutrons against the protons was somewhat smaller than the inertia of the bodily motions of the neutron masses against the proton masses. The reason might be that part of the time the neutrons and protons exchange character (in virtue of the exchange component of the nucleon-nucleon force) without actually undergoing the associated displacements in space. An effective mass could also serve to absorb any velocity dependence in the nucleon-nucleon interactions that would make the stiffnesses J and Q, relevant for the dynamical oscillations, different from their static values. Evidence for an effective mass m* somewhat less that m is contained in the integrated cross sections for the Giant Dipole resonance, which appear to exceed the dipole sum rule by something of the order of 20%.

Figure 2 shows that once an effective mass $m^*$ equal to 0.7 m is assumed there is perfect agreement with the Droplet Model prediction for the trend of $\hbar\omega$, based on the standard coefficients J = 36.8 MeV, Q = 17 MeV and $r_o$ = 1.18 fm.[6]

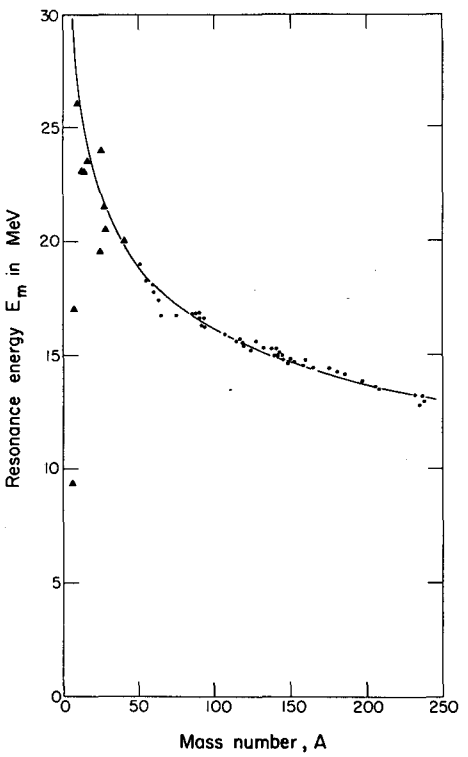


Fig. 2. The measured values of the resonance energy $E_m$ are plotted against mass number A. The curve passing through the points corresponds to predictions based on Eq. (1). (XBL 7610-4309)

Footnotes and References

*Based on Phys. Rev. C 15, 2032 (1977).

†Centro Brasileiro de Pesquisas Físicas
Av. Wenceslau Braz, 71-zc-82, Rio de Janeiro,
RJ 20,000, Brazil.

‡Institut für Kernphysik, Technische Hochschule
Darmstadt, Schlossgartenstrasse 9, 6100 Darmstadt,
Germany

1. M. Goldhaber and E. Teller, Phys. Rev. 74, 1046 (1948).

2. H. Steinwedel and J. H. Jensen, Z. Naturforsch. 52, 413 (1950).

3. Lawrence Berkeley Laboratory, Nuclear Science Division Annual Report, 1975, LBL-5075.

4. G. Bertsch and K. Stricker, Phys. Rev. C 13, 1312 (1976).

5. W. D. Myers and W. J. Swiatecki, Ann. Phys. (NY) 55, 395 (1969).

6. W. D. Myers, LBL-3428.

## A RELATION BETWEEN ADIABATIC INERTIAL PARAMETERS AND SUM RULES*

D. Vautherin†

Recent steps in adiabatic time-dependent Hartree-Fock theory have made it possible to derive from a microscopic point of view the parameters of Bohr's collective Hamiltonian. Indeed numerical calculations have already been performed in light nuclei for quadrupole vibrations.[1] It is clearly desirable to find out what kind of information can be obtained from calculations about the validity of phenomenological models, such as hydrodynamic or cranking-type models.

Some progress in this direction has been obtained by looking at the relation between inertial parameters and sum rules, which have proved to be very useful in the study of giant resonances in recent years.[2] In the case of a collective path generated by a constrained Hartree-Fock calculation ($\delta \langle \Phi(\lambda)|H-\lambda\hat{Q}|\Phi(\lambda)\rangle = 0$), we have been able to derive a simple expression for the adiabatic inertial parameter $M(\lambda)$. This parameter is given by the cubic inverse energy-weighted sum rule calculated in the random-phase approximation (RPA) around each point of the path. Explicitly

$$M(\lambda) = 2\hbar^2 \, m_{-3}(\hat{Q}) \, , \qquad (1)$$

where $m_k$ is the usual notation for the RPA moment of the distribution of multipole strength:

$$m_k(Q) = \sum_{n>o} (E_n - E_o)^k \, |\langle \psi_n | \hat{Q} | \psi_o \rangle|^2 \, . \qquad (2)$$

In this expression $\psi_n$ and $E_n$ denote RPA eigenstates and energies corresponding to the Hamiltonian $H-\lambda\hat{Q}$ and the sum runs over positive energy states only. By using as a collective variable the expectation value $Q = \langle \Phi(\lambda)| \hat{Q} |\Phi(\lambda)\rangle$ the mass parameter is found to be $M(Q) = \hbar^2 \, m_{-3}/2(m_{-1})^2$. As a result of the inequalities satisfied by the moments $m_k$, this expression can be shown to be greater or equal to the irrational mass $B(Q) = \hbar^2/2m_1$ (Ref. 3). Equality occurs in the only case where the distribution of strength is concentrated into one single state. In the numerical calculations of Ref. 1 it was found that $M(Q)$ and $B(Q)$ are rather close for quadrupole vibrations in $^{16}O$, while significant differences occur in $^{12}C$. From the above discussion we see that this result is related to fact that the RPA quadrupole strength is more concentrated in $^{16}O$ than $^{12}C$.

Footnotes and References

*Condensed from LBL-6503.

†Permanent address: Institut de Physique Nucleaire, BP1, 91406 Orsay, France.

1. M. J. Giannoni, F. Moreau, P. Quentin, D. Vautherin, M. Veneroni and D. M. Brink, Phys. Lett. 65B, 305 (1976).

2. J. Martorell, O. Bohigas, S. Fallieros and A. M. Lane, Phys. Lett. 60B, 313 (1976).

3. A. M. Lane, Nuclear Theory (Benjamin, New York, p. 91 (1964).

# VARIATIONAL CALCULATIONS CONCERNING THE POSSIBLE EXISTENCE OF BOUND NEUTRAL NUCLEI

D. Vautherin*

Results of high energy fragmentation experiments performed recently at CERN by Detraz have been interpreted as a tentative evidence for the production of bound neutral nuclei, with an unknown mass of possibly 5 to 9.[1] From a theoretical point of view all calculations predict the neutron gas to be strongly unbound and the neutron-neutron force is known to be very weak.[2] The conclusions of Detraz therefore appear quite challenging in view of what we know about the neutron-neutron force.

Hartree-Fock calculations have been performed for systems of 6 and 8 neutrons using interaction Skyrme-III.[3] This force reproduces reasonably well the binding energies of helium-4 (26.4 MeV vs 28.3 experimentally) and helium-8 (26.8 MeV vs 31.4 experimentally). It also predicts helium-10 to be unbound, in agreement with experimental data. We have found no bound states for N=6 or 8.

We have also investigated the effect of adding a triplet-odd tensor force--which would not alter Hartree-Fock results--but would favor exotic configurations such as cubic configurations. For this purpose we have considered a schematic triplet-odd tensor force of the form

$$V_T \frac{r^2}{\mu^2} \exp(-r^2/\mu^2) \qquad (1)$$

where $V_T$ = 42 MeV and $\mu$ = 0.7 fm. Crystalline configurations have been described by slater determinants of single-particle neutron wave functions centered at various points $\vec{R}$;

$$\phi_i(\vec{r},\sigma) = (b\sqrt{\pi})^{-3} \exp(-(\vec{r}-\vec{R}_i)^2/2b^2)\ \chi_i(\sigma) \quad . \qquad (2)$$

In this formula $\sigma$ is the spin variable and b a variational parameter specifying the degree of localization of each neutron around the point $\vec{R}$. The single-particle orbits[2] are not orthonormal. However the energy of the corresponding determinant can be calculated by standard techniques.[4]

Calculations have been made for cubic configurations of 8 neutrons (with spins up for the upper neutrons, down for the lower neutrons), and prismatic configurations of 6 neutrons. We have explored the energy surface as a function of the parameters b and R, where $R = |R_1 - R_2|$ characterizes the size of the configuration. No bound states or resonances have been found.

## Footnote and References

*Permanent address: Institut de Physique Nucléaire BP1, 91406, Orsay, France.

1. Claude Detraz, Phys. Lett. 66B, 333 (1977).

2. H. A. Bethe, Ann. Rev. of Nucl. Sci. 21, 93 (1971).

3. M. Beiner, H. Flocard, Nguyen van Giai and P. Quentin, Nucl. Phys. A238, 29 (1975).

4. D. M. Brink, Varenna Lectures, Vol. 36 (Academic, New York, 1966).

# III.

# APPARATUS

# A. ACCELERATOR OPERATIONS AND DEVELOPMENT

## 88-INCH CYCLOTRON OPERATION, DEVELOPMENT AND STUDIES

J. Bowen, D. J. Clark, L. Glasgow, R. A. Gough, and D. L. Hendrie

From July 1976 through June 1977, the cyclotron was scheduled for 20 eight-hour shifts per week for experiments in nuclear science, isotope production, and beam development. There were also two maintenance-intensive, three-week shutdowns during this period. Dispensation of accelerator time is shown in Table 1. The indicated unscheduled downtime of 1% represents failures of machine components which resulted in significant time loss to the experimental program. Table 2 lists the total external beam intensities of ions accelerated through June 1977 with the energy range available for each ion and Fig. 1 shows the operating distribution of these beams over the past 8 years. New beams include $^{10}B^{4+}$, $^{19}F^{3+}$, and $^{37}Cl^{7+}$. Several low energy heavy metal beams such as $^{197}Au^{13,14+}$ were developed for specific experiments discussed in other contributions to this Annual Report.

The aluminum cables for the main magnet current have been replaced with copper cables. This permits operation of the main magnet at higher field levels with a concomitant increase in available beam energies. The new cables run cooler reducing both power losses and fire hazards in the building.

A thorough study of the final amplifier tube (FPA) operating characteristics has led to realistic limitations on rf operating parameters, such as voltage vs frequency. This coupled with increased flow of the cooling water should extend the average lifetime of this tube. Extensive modification on the FPA mounting and filament supply has been done. This reduces the time required for changing the tube from 16 hours to a few hours. It also improves the rf grounding and slightly increases the filament power supply efficiency.

A new dee voltage regulator and trimmer control unit has been designed, built, and partially tested. Also a new regulated screen power supply for the rf final amplifier has been built. These units will be installed in the rf system as soon as opportunity is available.

Additional data channels have been added to the existing cyclotron parameter monitoring system. The low level channels have been increased from 40 to 80, while the high level channels from 16 to 48. With these added channels, the computer will be able to monitor the main magnet current, 5 Valley coil currents and angles, rf resonance frequency, most of the rf parameters and most of the vacuum gauge readings. It is expected that these new capabilities will soon be implemented.

Two oil diffusion pumps were substituted for a mechanical pumping system on the polarized ion source, with a large increase in pumping speed. As a result, polarized beam levels have increased and the noise level throughout the building is much lower. With the availability of higher intensities of polarized beams, the scatter chamber

Table 1. 88-inch cyclotron operation time distribution (7/76 through 6/77).

| | Hours | % |
|---|---|---|
| Operating | | |
| Experimental program | | 80.1 |
| Beam development | | 3.5 |
| sub total | 7014 | 83.6% |
| Maintenance | | |
| Routine | | 3.8 |
| Scheduled Shutdown | | 11.7 |
| Unscheduled shutdown | | 0.9 |
| sub total | 1375 | 16.4% |
| TOTAL | 8389 | 100% |

Table 2. 88-inch cyclotron beams, to July 1977.

| Ion | Energy[a] (MeV) | External beam (eμA[b]) | Ion | Energy[a] (MeV) | External beam (eμA[b]) |
|---|---|---|---|---|---|
| p | 0.2-55 | 100-20 | $^{20}Ne^{4+}$ | 63-112 | 10 |
| p(polarized) | 6-55 | 0.3 | $^{20}Ne^{5+}$ | 112-175 | 5 |
| d | 0.5-65 | 100-20 | $^{20}Ne^{6+}$ | 175-252 | 1 |
| | - | - | $^{20}Ne^{7+}$ | 252-343 | 0.014 |
| d(polarized) | 10-65 | 0.3 | $^{22}Ne^{5+}$ | 100-159 | 5 |
| $^{3}He^{2+}$ | 1-140 | 100-10 | - | - | - |
| $^{4}He^{2+}$ | 3-130 | 100-10 | $^{24}Mg^{4+}$ | 50-93 | 2 |
| $^{6}Li^{1+}$ | 2-23 | 10 | $^{24}Mg^{5+}$ | 93-146 | 0.2 |
| $^{6}Li^{2+}$ | 23-93 | 5 | $^{25}Mg^{4+}$ | 50-90 | 2 |
| $^{6}Li^{3+}$ | 93-195 | 0.5 | $^{26}Mg^{4+}$ | 48-86 | 2 |
| $^{7}Li^{2+}$ | 20-80 | 5 | - | - | - |
| | | | $^{28}Si^{5+}$ | 80-125 | 1 |
| $^{9}Be^{2+}$ | 15-62 | 5 | $^{28}Si^{6+}$ | 125-180 | 0.2 |
| $^{9}Be^{3+}$ | 62-140 | 2 | $^{28}Si^{7+}$ | 180-245 | 0.05 |
| | | | $^{32}S^{6+}$ | 100-158 | 2 |
| $^{10}B^{2+}$ | 14-56 | 10 | $^{32}S^{7+}$ | 158-214 | 0.2 |
| $^{10}B^{3+}$ | 56-126 | 50 | $^{37}Cl^{7+}$ | 136-185 | .08 |
| $^{10}B^{4+}$ | 126-224 | 0.2 | $^{40}Ar^{2+}$ | 35-14 | 0.4[c] |
| $^{11}B^{2+}$ | 12-51 | 10 | $^{40}Ar^{6+}$ | 3.5-126 | 4 |
| $^{11}B^{3+}$ | 51-115 | 50 | $^{40}Ar^{7+}$ | 126-172 | 2 |
| $^{11}B^{4+}$ | 115-204 | 0.3 | $^{40}Ar^{8+}$ | 172-224 | 0.5 |
| $^{12}C^{3+}$ | 45-105 | 30 | $^{40}Ar^{10+}$ | 280-350 | $10^3$ particle/sec |
| $^{12}C^{4+}$ | 105-187 | 5 | - | - | - |
| $^{12}C^{5+}$ | 187-292 | 0.05 | $^{40}Ca^{6+}$ | 85-126 | 1 |
| | | | $^{40}Ca^{7+}$ | 126-172 | 0.2 |
| $^{14}N^{2+}$ | 10-40 | 20 | - | - | - |
| $^{14}N^{3+}$ | 40-90 | 15 | $^{56}Fe^{10+}$ | 180-250 | 1 particle/sec |
| $^{14}N^{4+}$ | 90-160 | 15 | $^{84}Kr^{2+}$ | 5-19 | .001[d] |
| $^{14}N^{5+}$ | 160-250 | 2 | $^{84}Kr^{12+}$ | 200-240 | 1 particle/sec |
| $^{14}N^{6+}$ | 250-360 | $10^3$ particle/sec | $^{197}Au^{13+}$ | 102-120 | 112 particle/min |
| $^{15}N^{4+}$ | 130-150 | 15 | $^{197}Au^{14+}$ | 120-140 | 4 particle/min |
| $^{16}O^{3+}$ | 35-79 | 20 | - | - | - |
| $^{16}O^{4+}$ | 79-140 | 20 | - | - | - |
| $^{16}O^{5+}$ | 140-219 | 2 | - | - | - |
| $^{16}O^{6+}$ | 219-315 | 1 | - | - | - |
| $^{16}O^{7+}$ | 315-429 | ~50 epA | - | - | - |
| $^{18}O^{4+}$ | 70-124 | 10 | - | - | - |
| $^{19}F^{3+}$ | 30-66 | 5 | - | - | - |
| $^{19}F^{4+}$ | 66-118 | 10 | - | - | - |
| $^{19}F^{5+}$ | 118-184 | 2 | - | - | - |

[a] Energy range for heavy ions indicates nominal maximum energy for the particular charge state down to the energy which can be reached from the next lower charge state. Beams can also be run with lower charge than shown at energies below 1 MeV/n.

[b] Electrical microamperes except as noted.

[c] 9th harmonic.

[d] 15th harmonic.

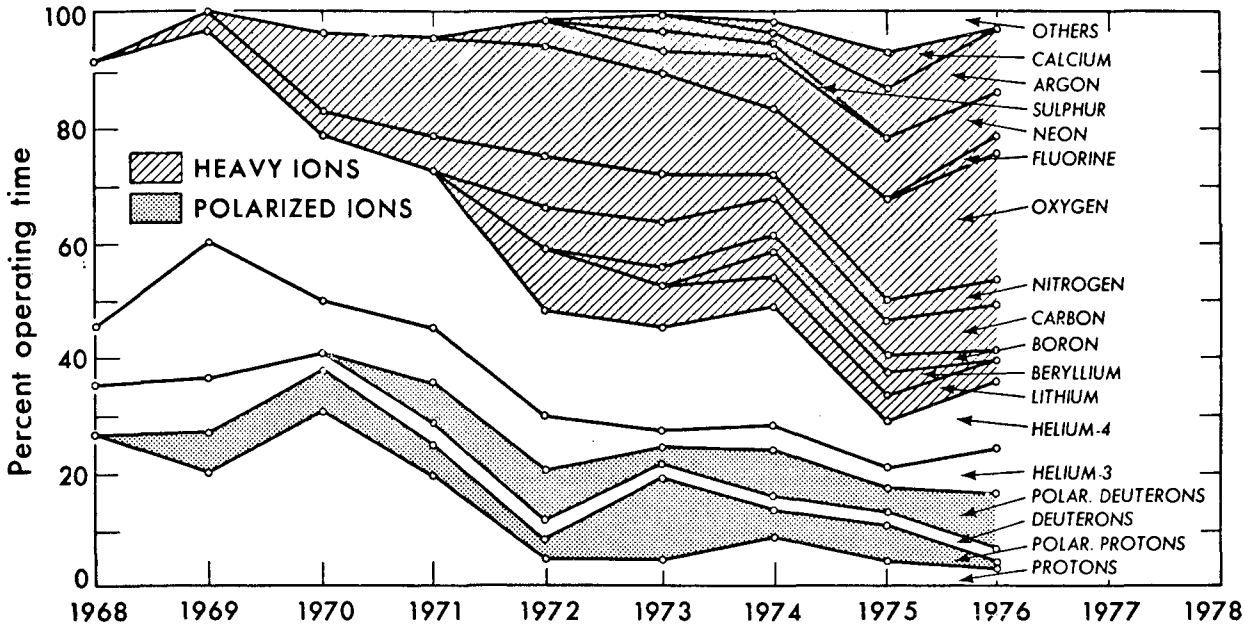


Fig. 1. The 88-inch cyclotron particle distribution history. (XBL 772-402)

for polarization studies, the polarimeter and associated pumping, focusing, and steering magnets have been relocated in a high resolution beam line in cave 4B. A new counting area has been equipped for these experiments.

The area vacated by the polarization group (cave 5) has been equipped to handle three new experimental programs and to provide quick access to external beams for beam development purposes. The new programs include an isotope production facility for $^{11}C$ and a time-of-flight spectrometer used presently by outside users. Additional flammable gas vents have been installed in this cave and in other areas to accommodate the increased use of hazardous gases in experimental equipment.

Other mechanical effort in experimental areas includes a major redesign, fabrication, and installation of new detector arms in the 36 in. scatter chamber in cave 4A. A more powerful quadrupole-sextupole magnet system has been designed for the magnet spectrometer and is awaiting fabrication. The new magnets will accommodate particles of higher magnetic rigidity (matching the capabilities of the spectrometer) and should substantially improve the radial acceptance to the focal plane.

Expansion of transuranic studies at the 88-inch cyclotron has required installation of a PDP-15 computer, and establishing two new counting areas: one in the computer/counting area and the other in a specially, constructed dust-proof room near the target area in cave 0.

Considerable effort has been directed toward cyclotron maintenance and reliability. For example, improvement to the tank vacuum has resulted in a base vacuum of 1 Torr (with cryopanels on) and further improvements seem possible. Improvements to ion source base insulators have made them more reliable and three new ion source anodes have been fabricated and are being used in place of older, worn-out units. The gas valve system has been improved to increase reliability and serviceability. An additional plug-in unit is being fabricated so it can be installed quickly and permit a faulty unit to be repaired and bench tested with minimum cyclotron downtime. Automatic blowdown valves have been installed at various places in the building to improve compressed air quality. Ion source arc interlock gates have been installed permitting safe entry to the pit area without shutting off the ion source arc. Various water circuits have been flushed with citric acid to improve flow and heat transfer characteristics. This flushing technique, which was originally developed for the FPA tube anode cooling water circuit, has been refined and is now in general use around the building. It has proven quite useful.

The exit valve on the cyclotron has been revised to improve accessibility and serviceability. Prior to this modification there was a seal leak that could not conveniently be repaired because it would take about 3 shifts of work to do it. Now the same job should not take more than an hour or two and can conveniently be done during a routine maintenance day.

Design work has been completed on an internal PIG source with filament heated cathodes. This feature has been successfully employed at other laboratories to provide more flexibility in controlling cathode temperature and arc parameters. Adaptation of the technique to the internal PIG source of the cyclotron was facilitated by experiments on the test stand. The base insulator for this new ion source has been tested in the

cyclotron under operating conditions and used in a new series of experiments to develop a sputter electrode for feeding solid materials into the arc discharge. Initial experiments with a graphite electrode and 200 watts of sputter power have produced $^{12}C^{3+}$ beams with intensities (up to 30 A) comparable to those obtained using $CO_2$ gas.

# HEAVY ELEMENT MASS SPECTROSCOPY WITH THE BERKELEY 88-INCH CYCLOTRON

E. J. Stephenson, D. J. Clark, R. A. Gough, W. R. Holley, and A. Jain*

While cyclotrons have been used extensively to produce beams for experiments in nuclear and atomic physics, on very few occasions have they been employed as mass separators for trace element detection.[1-3] We wish to investigate whether the cyclotron could be used to separate and accelerate any atomic mass and identify it unambiguously. We present here the results of several experiments with the cyclotron to demonstrate that mass analysis is possible for all atomic masses, and to illustrate the present levels of sensitivity, accuracy, and mass resolution for the Berkeley 88-inch cyclotron.

In a mass analysis, a sample to be examined is placed in the ion source discharge, where its constituent atoms are ionized and extracted as a beam into the dee for acceleration. Then, the cyclotron is tuned to accelerate those atoms with a specific charge-to-mass ratio and the amount of accelerated beam measured. A large intensity range may be covered by measuring beam currents with either a Faraday cup or a charged particle counter placed directly in the beam line.

The mass analysis of an unknown sample is conducted by varying the cyclotron dee frequency while keeping the main magnetic field constant. With one setting of the radial trim coils, the range over which the frequency may be varied is given in Ref. 4. The expectation that the cyclotron remain in tune during such scans has been confirmed by the observation that intense beams at either end of the scan are efficiently accelerated.[2]

During a mass scan, the magnetic rigidity of each emerging beam is the same. To the extent that beam steering and focusing are governed by magnetic fields, no changes in beam optics are needed. However, the deflector voltage must be continuously adjusted to remain proportional to frequency. During the scan, the dee voltage was kept at its maximum value to minimize charge exchange losses in the beam near the ion source.

Beams can be detected and their intensity measured with the use of either a Faraday cup or charged particle counters. Counters offer the additional advantage of a beam energy measurement which can be related to the charge state of the ions in the beam. The mass and charge of an unknown beam can be determined from the beam energy and the parameters of the cyclotron when the beam is in resonance through the use of equations that describe the particle orbits and beam energy. A circular orbit inside the cyclotron requires that the centripetal force $mv^2/r$ be equal to the magnetic force qvB. In a scan, all beams are related through the equation:

$$B = \frac{mv}{qr} = \frac{m}{q}\omega = 2\pi\frac{mf}{qh} \quad , \qquad (1)$$

where the particle angular velocity $\omega$ is given by $2\pi$ times the ratio of the cyclotron dee frequency f to the harmonic number h. (In this discussion, the harmonic h is the ratio of the cyclotron dee frequency to the particle revolution frequency.)

The harmonic on which an unknown beam is accelerating can be determined from the electrostatic deflector voltage that maximizes the beam current, since that voltage is proportional to the beam velocity. Additional information is provided by an independent measurement of the beam energy in the charged particle counters through the equation (non relativistic)

$$E = K\frac{q^2}{m} \quad . \qquad (2)$$

The cyclotron constant K is equal to $B^2r^2/2$ where r is the radius of the beam at extraction.

To test this scheme, a short scan was run using a PIG source[5] doped with heavy elements. A sample containing rare earth silicates was pulverized, mixed with tantalum powder, compressed into a pellet, and placed in a PIG source at the edge of the discharge, opposite the anode aperture. The discharge was supported with argon gas. A scan was made from f = 6.4 to 7.2 MHz with a heavy ion silicon surface barrier detector[6] placed in the beam line. The frequency was changed continuously with several seconds required to cross the width of one beam. Beams were detected by observing the individual pulses from the detector on an oscilloscope, so beams with rates much below 1 particle/sec may have been missed. Twenty-six beams were extracted and identified. During the scan the electrostatic deflector voltage was set for seventh harmonic, and most of the detected ions were accelerated on that harmonic.

For each beam, the harmonic was determined from the effective deflector voltage V. This effective voltage was taken as $\Sigma\, V_i\ell_i/\bar{s}_i$, where the sum covers each of the two segments of the deflector with $V_i$ the segment voltage, $\ell_i$ the

segment length, and $\bar{s}_i$ the mean plate separation for that segment. The voltages which maximized the beam current for each harmonic were well separated.

The ion charge q was determined from the energy of the beam measured by the silicon surface barrier detector. The locations of the 22 seventh harmonic beams are shown in Fig. 1 as a function of apparent energy and cyclotron frequency. The lines are calculations of the apparent energy using the pulse height defect formula of Kaufman, et al.[7] The separation of charge states is excellent.

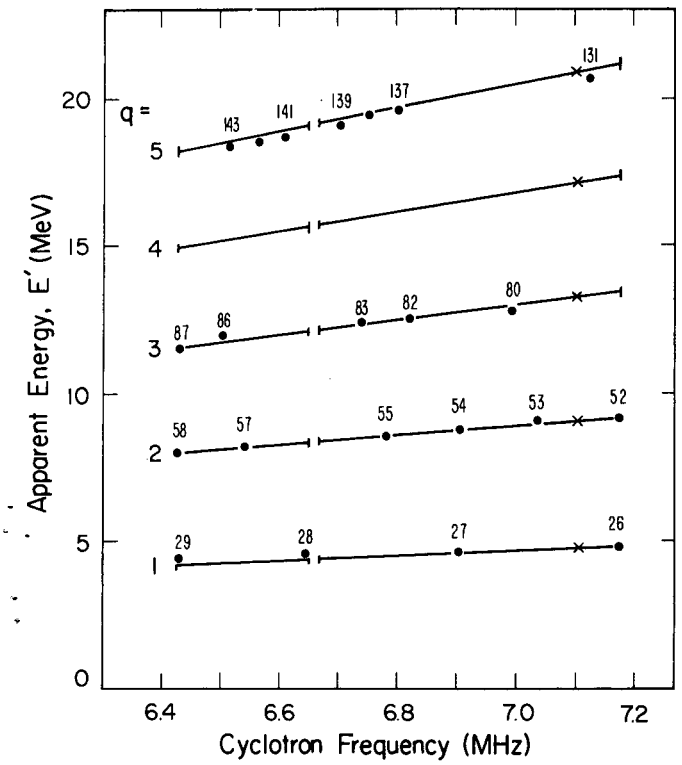


Fig. 1. Location of 7th harmonic beams as a function of apparent energy (pulse height) in the silicon detector and cyclotron frequency. Lines of constant charge were calculated from the formulas of Ref. 7. Breaks in the lines indicate areas not covered in the scan. The cross denotes a change of ion source. Atomic mass numbers are noted by most points.
(XBL 778-1616)

Once the charge and harmonic for an unknown beam were measured, the mass of the ions in the beam was calculated from Eq. (1). To obtain atomic masses, corrections were made for missing electrons and the relativistic mass increase of the beam. The resulting atomic masses were very close to the accepted masses for stable isotopes,[8] and no ambiguity resulted in the assignment of mass number (shown as the points in Fig. 1). The rms deviation of our measured masses from the accepted values was $\Delta m/m = 6.1 \times 10^{-5}$. The mass numbers and beam intensities observed in this scan were compared with the known isotopic abundances[9] to form a self-consistent list of the elements observed.

The sensitivity of an analysis for a particular mass may be defined as the fraction of that mass contained in the source feed which would give one count/sec in the detector. This sensitivity is given by the reciprocal of the product of dwell time (seconds) and beam current (particles/sec) for that mass if it were to constitute 100% of the source feed material or sample. The general trend of sensitivity with mass can be obtained from typical cyclotron beam currents.[10] This sensitivity is plotted in Fig. 2 for a dwell time of 1 sec.

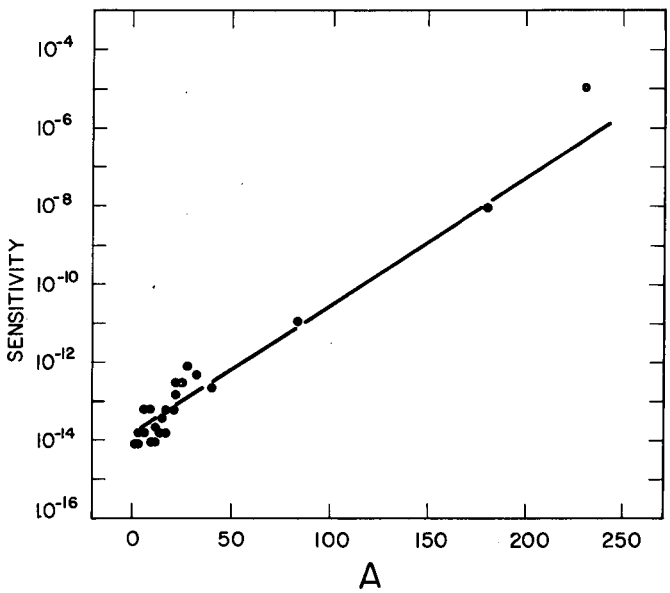


Fig. 2. Sensitivity of the cyclotron for mass analysis as a function of mass. Trace elements present at these concentrations could be accelerated into a 1 particle/sec beam. The straight line is a guide to the eye. (XBL 778-1617)

The principal advantage of the cyclotron for mass spectrometry lies in its sensitivity. By using charged particle detectors to count individual ions, light trace elements can be detected at levels as low as 1 part in $10^{14}$ with only a few seconds of integration time. Because the sensitivity is not limited by background radiation, individual trace elements at levels at least $10^3$ lower may be detected by using longer integration times. Thus this system is particularly well adapted to finding a few, low-level, exotic species.

This sensitivity is achieved because of the absence of background radiation from the cyclotron. The requirement of isochronous acceleration removes ions created by charge exchange or collisions in

the residual gas inside the machine. The production of molecular ions is discouraged by the use of high ion source arc power. Any remaining background radiation can usually be distinguished from beam by its signature in the charged particle counters.

Footnote and References

*On leave from Bhabha Atomic Research Centre, Calcutta, India.


1. L. Alvarez and R. Cornog, Phys. Rev. 56, 379, (1939); Phys. Rev. 56, 613 (1939).
2. R. A. Muller, L. W. Alvarez, W. R. Holley, and E. J. Stephenson, Science 196, 521 (1977).
3. R. A. Muller, Science 196, 489 (1977).
4. D. J. Clark, R. A. Gough, W. R. Holley, and A. Jain, LBL-6502, submitted to Nucl. Instrum. and Methods for publication.
5. D. J. Clark, J. Steyaert, A. Carneiro, and D. Morris, IEEE Transactions on Nuclear Science NS-19 (2) 114 (1972).
6. Fabricated by ORTEC, Oak Ridge, Tennessee.
7. S. B. Kaufman, E. P. Steinberg, B. D. Wilkins, J. Unik, A. J. Gorski, and M. J. Fluss, Nucl. Instrum. and Meth. 115, 47 (1974).
8. A. H. Wapstra and N. B. Gove, Nucl. Data Tables 9, 267 (1971).
9. G. E. Chart of the Nuclides, distributed by U. S. Government Printing Office, Washington, D.C. (1968).
10. 88-Inch Cyclotron Available Beam List (1977), distributed by the Nuclear Science Division of Lawrence Berkeley Laboratory.


## SYSTEMATICS IN THE CONTROL SETTINGS OF THE BERKELEY 88-INCH CYCLOTRON

D. J. Clark, R. A. Gough, W. R. Holley, and A. Jain*

A modern isochronous cyclotron requires a large number of control settings to produce a wide variety of beams and energies. During 15 years of operating experience with the Berkeley 88-inch cyclotron we have developed a system for predicting the approximately 50 parameters which need adjusting for the acceleration of any particular beam particle and energy. The questions we wish to discuss in this article are how the sets of parameters are obtained, how they can be treated systematically, and how they can be extended from existing optimized beams to new beams. Operating parameters for a typical beam are shown in Table 1.

The original control settings were based on magnetic field measurements,[1] electrostatic field maps,[2] equilibrium orbit calculations,[3] calculated sets of trim coil currents to produce approximately isochronous magnetic fields,[4] and ray tracing deflector calculations.[5] Currently a computer code, CYDE, is used to calculate trim and main coil settings to produce the required magnetic field radial profiles for isochronous acceleration of any given beam. Center region settings used now are based on a computer code PINMOD, a modification to the PINWHEEL code of Reiser.[6] Many of the remaining parameters were adjusted during operation to optimize intensity and quality of various beams.

There are a number of useful scaling laws which help in systematizing control settings and extending them to new beams. The simplest example of parameter scaling is illustrated by the resonance condition:

$$f_{rf} = \frac{hBq}{2\pi m} \quad , \qquad (1)$$

which relates the radio frequency $f_{rf}$ to the magnetic field B required to accelerate an ion of charge-to-mass ratio q/m on harmonic number $h = f_{rf}/f_{particle}$. From Eq. (1) it is apparent that tuning out a difficult ion such as $^{40}Ar^{8+}$ can be facilitated using the settings for an existing simple beam such as $^{20}Ne^{4+}$. In this case the two beams can be separated by the small frequency difference (< 0.1%) arising from binding energy effects on the q/m ratio. It can be shown that the energies of the two beams are in proportion to their mass.

The center region settings of the 88-inch cyclotron depend upon the number of turns,

$$N \propto E/(qV_D) \quad , \qquad (2)$$

where E is the beam energy and $V_D$ the peak dee voltage. Since the source radius parameter, $r_s$, is proportional to $N^{-1/2}$, the source and puller are left fixed for beams with a constant number of turns. In order to reduce charge-exchange losses during heavy-ion operation, the dee voltage is normally run near its maximum value. It is seen from Eq. (2) that for constant $V_D$, the condition for a fixed turn number is E/q = const. Other parameters for beams of constant E/q are also easily scaled. For example, the settings for the electrostatic deflector are governed by the approximate relation $V_{def}/g \propto E/q$ where $V_{def}$ is

Table 1. Control settings for typical 88-inch cyclotron beam [element O, mass 16, charge +4, energy (MeV) 104.0].[a]

| Item | | | |
|---|---|---|---|
| 1. | Main Coil (Amps) | | 1661.04 |
| 2. | Frequency (MHz) | | 5.7164 |
| 3. | Dee Volts (kV) | | 65.6 |
| | Trim Coils | | (Amps) |
| 4. | 1 | | 703.0 |
| 5. | 2 | | -591.0 |
| 6. | 3 | | -253.0 |
| 7. | 4 | | -30.3 |
| 8. | 5 | | 0.0 |
| 9. | 6 | | 76.0 |
| 10. | 7 | | 0.0 |
| 11. | 8 | | 111.0 |
| 12. | 9 | | 0.0 |
| 13. | 10 | | 62.0 |
| 14. | 11 | | 0.0 |
| 15. | 12 | | -239.0 |
| 16. | 13 | | 0.0 |
| 17. | 14A<br>14B | | 62.0 |
| 18. | 15 | | -1079.0 |
| 19. | 16 | | -1701.0 |
| 20. | 17 | | 0.0 |
| | Center Region | | |
| 21. | Radius | | 45.2 |
| 22. | Azimuth (Deg) | | 23.8 |
| 23. | Rotation (Deg) | | 21.3 |
| 24. | Puller E/W | | 31.0 |
| 25. | Puller N/S | | 51.7 |
| | Deflector Positions | | (Inches) |
| 26. | 1 | | 39.4 |
| 27. | 2 | | 0.392 |
| 28. | 3 | | 40.382 |
| 29. | 4 | | 0.402 |
| 30. | 5 | | 40.423 |
| 31. | 6 | | 0.451 |
| 32. | 7 | | 42.887 |
| 33. | 8 | | 0.636 |
| 34. | 9 | | 43.571 |
| 35. | 10 | | 1.25 |
| 36. | 11 | | 48.492 |
| 37. | 12 | | 1.745 |
| 38. | JACK | | 0.08 |
| | Deflector Voltages | | (kV) |
| 39. | Ent Volts | | 72.4 |
| 40. | Mid Volts | | 72.0 |
| | Valley Coils | (Deg) | (Amps) |
| 41,42 | 1 | 110 | 200 |
| 43,44 | 2 | 0 | 49 |
| 45,46 | 3 | 0 | 0 |
| 47,48 | 4 | 0 | 0 |
| 49,50 | 5 | 138 | 18.6 |

[a]Reference date 5.22.75, time 2200.

the voltage applied across a gap g. Also, the harmonic (valley) coils have constant azimuths for beams with constant E/q while the currents would scale approximately with main coil current.

It is useful to plot the operating beams on a log-log graph of B vs f forming a resonance chart as shown in Fig. 1. Ions with a given q/m appear on lines of slope = + 1.0, since from Eq. (1) we have log B = log f + const. Assuming fixed dee voltage, ions with a given number of turns (E/q = const.) lie on lines with a slope = -1.0. These are lines of fixed center region, valley coil azimuths and approximately constant deflector strength. Figure 1 shows the entire operating regime of the 88-inch cyclotron including beams which have been run on higher harmonics to h = 15.

The number of model beams needed to cover the operating range of the cyclotron depends on how far a trim coil solution can be "stretched" either in q/m (fixed magnetic field) or in energy E (fixed q/m). Quantitative predictions for stretching trim coil solutions can be made by placing limits on "acceptable" phase errors. For stretching from one ion ($q/m = \varepsilon_a$) to another ($q/m = \varepsilon_b$) at fixed magnetic field, it can be shown[7] using the phase excursion limits illustrated in Fig. 2b that:

$$\left| \frac{\pi h K^2}{931\, V_D}\, \varepsilon_b \left(\varepsilon_b^2 - \varepsilon_a^2\right) \right| \leq 4, \qquad (3)$$

where the energy constant $K = Em/q^2$. Stretching the energy of a given particle, i.e., varying B and $f_{rf}$ with fixed q/m, is difficult to treat analytically because of possibly large variations in field radial profile due to saturation. Above ~10 MeV/n, relativistic effects dominate and the stretching from energy $E_0$ to $E_1$ is limited by:

$$\left| \frac{\pi h\, E_1}{931\, mV_D q} \left(E_1 - E_0 \sqrt{\frac{E_0}{E_1}}\right) \right| \leq 4 \qquad (4)$$

using again the phase slip limitations described in Fig. 2b. Below ~ 10 MeV/n, detailed CYDE runs have been done to determine stretching limits.

The points in the first and third harmonic regions of Fig. 1 are spaced on a grid consistent with calculated stretching limits such that virtually any h = 1 or h = 3 beam can be accelerated from solutions represented by at least one of the points. The quantitative stretching predictions and the scaling laws described above have permitted

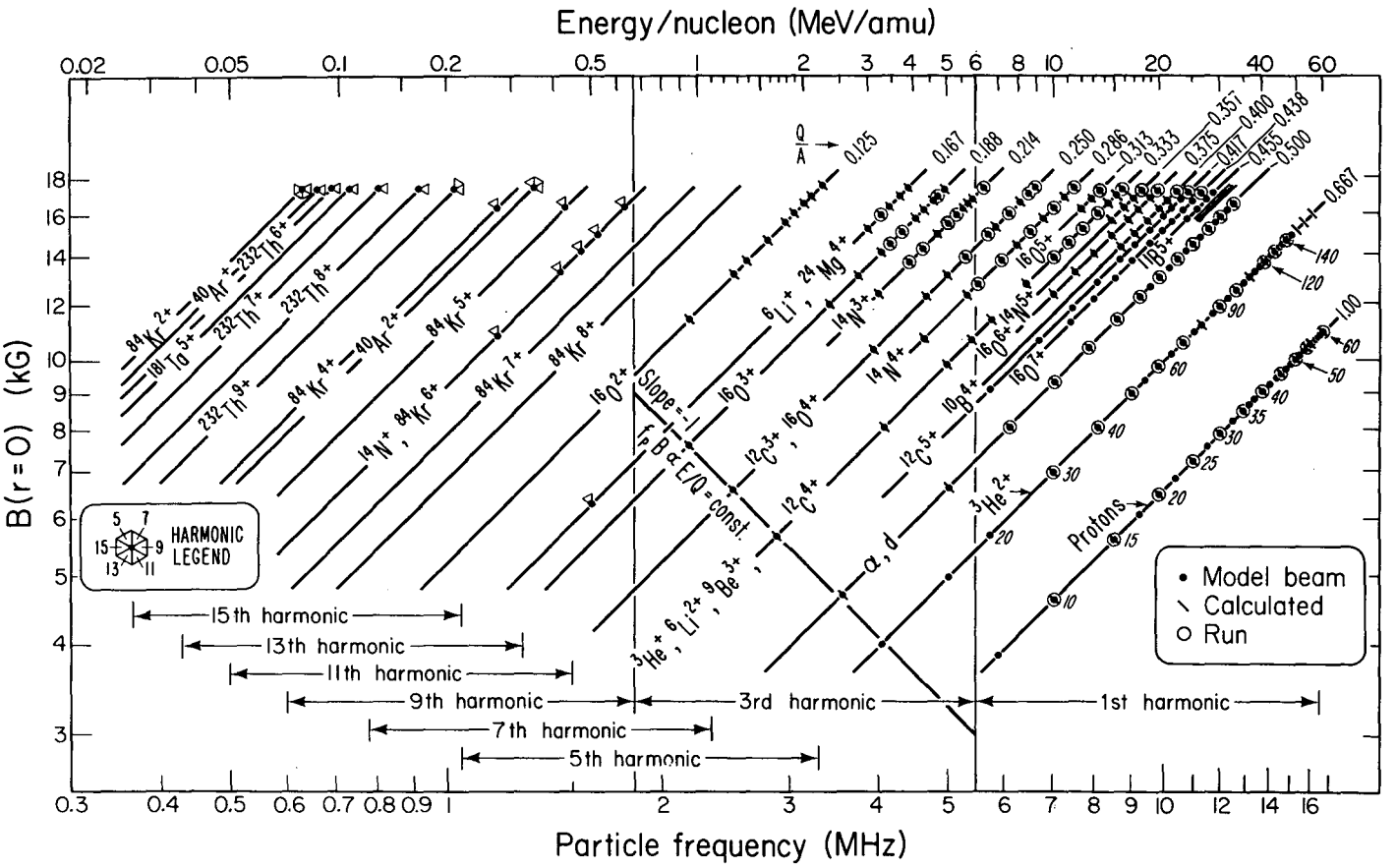


Fig. 1. Resonance chart for the Berkeley 88-inch cyclotron. (XBL 774-839A)

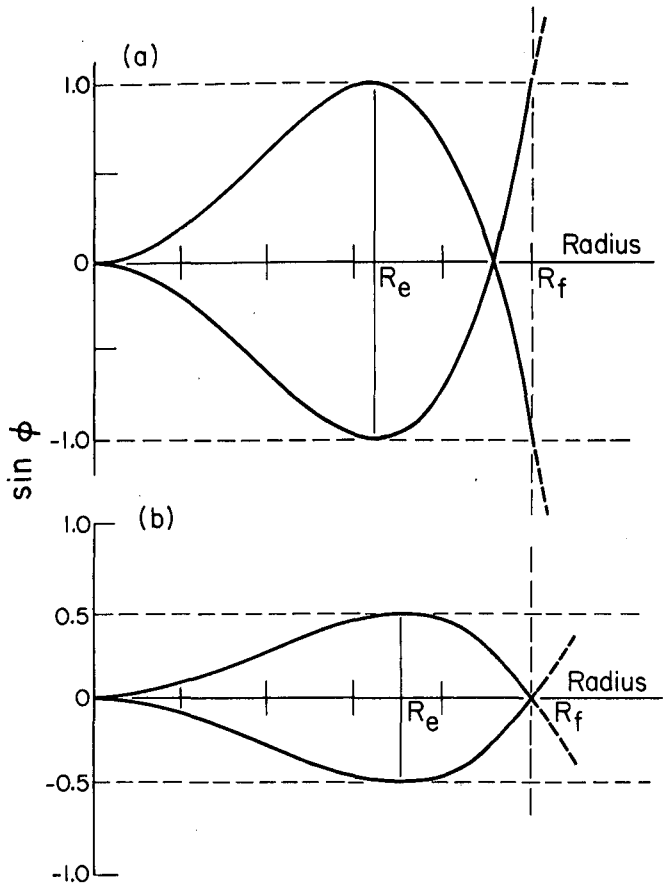


reliable tune out of new beams without advance scheduling of accelerator time for testing, with a net improvement in operational efficiency.

Footnote and References

*Bhabha Atomic Research Centre, Vec, Calcutta-700 064, India.

1. J. H. Dorst, Nucl. Instrum. Meth. 18-19, 135 (1962).

2. H. A. Willax and A. A. Garren, Nucl. Instrum. Meth. 18-19, 347 (1962).

3. J. D. Young et al., Nucl. Instrum. Meth. 18-19, 347 (1962).

4. A. A. Garren Nucl. Instrum. Meth. 18-19, 309 (1962).

5. A. A. Garren et al., Nucl. Instrum. Meth. 18-19, 525 (1962).

6. M. Reiser, Private communication.

7. W. R. Holley, to be published.

Fig. 2. Simplified phase histories illustrating (a) extreme and (b) more conservative phase error limits. (XBL 774-837)

## RECENT PROGRESS IN HEAVY-ION SOURCES*

David J. Clark

The ideal ion source for a modern heavy-ion accelerator should provide beams of all atomic species, of high intensity, good emittance and long lifetime. The source should be easily accessible for maintenance. For cyclotrons and linear accelerators, which require positive ions from the source, high charge states are desirable because the cyclotron energy is proportional to charge squared, and linac length can be reduced by using ions with higher charge states. For tandem electrostatic accelerators the charge state is normally -1.

High charge state ion beams for positive-ion accelerators can be produced by electron bombardment of atoms and ions in a plasma or by stripping of fast ions in a foil or gas. For electron bombardment sources the product of the flux density $j_e$ and ion confinement time $T_i$ must be sufficient to produce the desired charge state q. Also the electron energy distribution should include the region of peak ionization cross section, which occurs at several times the ionization potential. So electron energies should be 10's of eV up to hundreds or several thousand eV. Figure 1 shows the operating ranges of several types of heavy-ion sources. The sources with higher $nT_i$ produce higher charge states. The principal types of heavy ion sources will be described below.

The traditional heavy-ion source for cyclotrons and linacs is the PIG (Penning or Philips Ion Gauge). In the PIG source an arc is struck in an anode along a magnetic field, between two cathodes. The beam is extracted either half way along the anode, perpendicular to the field, or through one cathode, parallel to the field. Solid materials can be fed into the source by placing them in a cathode, in a block tangent to the bore in the anode or by use of an oven. The PIG source gives usable beams of charge states up to $N^{5+}$, $Ne^{7+}$ and $Ar^{8+}$. Performance is briefly summarized in Table 1. The lifetime between source changes is a few hours up to a day, at high duty factor operation. Future developments of the PIG source include operational use of mirror magnetic fields as developed by Makov[1] and investigating possible higher charge state performance in the 40 to 50 kg fields of future superconducting cyclotron magnets.[2]

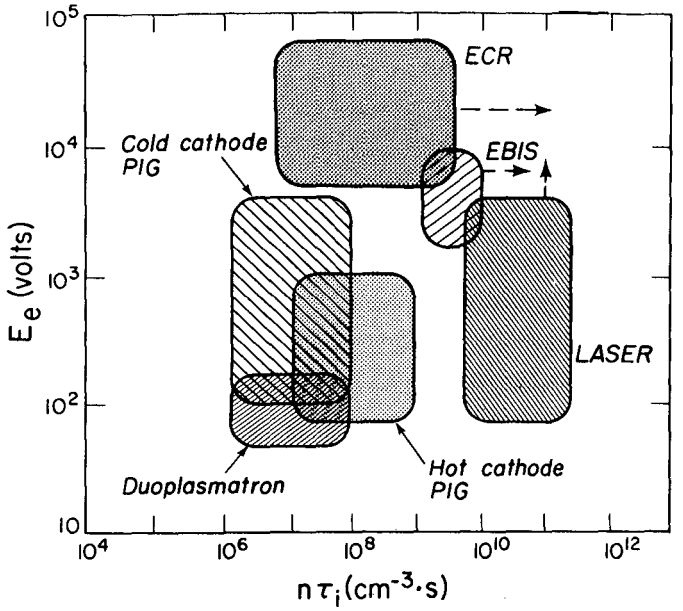


Fig. 1. Plasma parameters of high charge state ion sources. $E_e$ is electron temperature, n is electron density, $T_i$ is ion confinement time. (XBL 7512-9583A)

In the duoplasmatron an arc is formed along a convergent magnetic field between a filament and an anode, through an intermediate electrode. Recent progress has been made by Keller and Muller,[3] who found that the output of $Xe^{5+..11+}$ was greatly increased by placing the position of the maximum magnetic field at the anode aperture instead of between anode and intermediate electrode. Reducing the diameter of the intermediate electrode aperture increases the voltage, which gives higher charge states. Recently Richter and Zajec have developed a duoplasmatron with 20 mA of neon (2% $Ne^{3+}$)[4] and 17 mA of xenon.[5] As shown in Table 1, the duoplasmatron has as high intensity as the PIG, but lower average charge states.

Another type of source which is under development for high charge states is the electron cyclotron resonance source. Here the high energy electrons are produced by feeding in microwave energy at the cyclotron resonance frequency of the electrons in the magnetic field which confines the plasma. The ECR source has been developed at Oak Ridge, Marburg, and Grenoble. The group at Grenoble under R. Geller has made great improvements[6] in the ECR source in the last several years. Table 1 shows two ECR sources. The first is one stage only, referred to as "MAFIOS" by Geller. This gives output currents and charge states similar to those of the PIG. The lifetime is weeks or months. The 3-stage source in Table 1, TRIPLEMAFIOS, shows an average charge state about twice that of the PIG for neon and xenon, but at 100 times lower intensity. A superconducting coil is proposed to reduce the power from its present megawatt level, and to increase the rf frequency and thus the plasma density. Also experiments have been done on uranium beams. One stage has been used to produce 100 μA total uranium beam, including 50 μA of $U^{3+}$.

The electron beam ion source has been pioneered by Donets at Dubna[7] and also developed at Orsay, Frankfurt, Texas A&M, and Giessen. In the Donets source a superconducting solenoid of 1 m length confines an electron beam from a gun placed inside the solenoid at one end. The magnetic field keeps the beam collimated to a radius of several millimeters as it drifts down the solenoid axis to the collector at the other

Table 1. Ions and intensities

| Source | $\bar{q}$* Neon | $\bar{q}$* Xenon | Peak output all q's Particle/Sec | Duty Factor | Ref. |
|---|---|---|---|---|---|
| PIG | 2 | 4 | $10^{15}$-$10^{17}$ | .02-1.0 | 8 |
| Duoplasmatron | 1 | 3 | $10^{15}$-$10^{17}$ | .03-1 | 20,21 |
| ECR--1 Stage | 2 | 4 | $10^{16}$ | .3-1.0 | 24 |
| 3 Stages | 5 | 8 | $10^{14}$ | .3-1.0 | 24 |
| EBIS | 8-9 | 24 | a $10^{10}$-$10^{11}$[a] | $10^{-4}$ | 25,26 |
| | | | b $10^{13}$-$10^{14}$[b] | | |

*$\bar{q}$ weighted by particle/sec.

[a]Average output over long times, assuming 10 pulses/sec.

[b]Output during 100 μsec, $10^{9}$-$10^{10}$ particle/pulse.

end. Gas is ionized and confined electrostatically by the electron beam. A potential well formed by the drift tubes confines the ions longitudinally for typically 10 to 100 milliseconds, until the desired charge state is reached. Then the potential barrier is lowered at the solenoid exit, providing beam extraction. Beams observed include xenon with average charge state of $Xe^{24+}$, and neon with 20% $Ne^{10+}$.[8]

High currents of low charge state ions are produced by the multi-aperture sources developed for ion propulsion and for injection of multi-ampere beams of hydrogen into thermonuclear fusion reactors. A summary of ion sources for ion propulsion of space systems is given by Stuhlinger.[9] The ions used are Cs, Hg or colloid particles. The types of sources include contact ionization sources for Cs, electron bombardment sources for Cs and Hg, rf ionization sources for Hg and a hollow needle spray nozzle for colloidal particles. Accel-decel extraction systems are used. The beam is neutralized just after extraction. Many sources have been designed, with diameters of 5 to 150 cm, beam dc currents of 0.3 to 25 amperes, and beam energies of 1 to 6 keV.

Several types of sources produce high charge state ions such as $Fe^{25+}$ and $W^{55+}$ by dumping large pulses of energy into a solid in short time periods. They are the laser, the vacuum spark and the exploding wire. These sources are being used for studies such as spectroscopy of high charge state ions, usually without extraction of the ions to form a beam.

Negative heavy-ion sources are used mostly for injection into tandem electrostatic accelerators. Negative ions normally have a charge of -1 electron charge, but a few ions such as oxygen, fluorine and chlorine have been observed with a charge of -2 with intensities of about a nanoamp. Negative heavy ions have been produced by several methods: charge exchange using incident or recoil ions, direct extraction, and by special sources such as the triplasmatron and the duodehcatron. The most important recent advance in negative heavy-ion sources has been the development of sputter sources using cesium for bombardment or as surface coating. One of the most sucessful of the sputtering sources is the UNIS source of Middleton.[10] In this source a cesium beam from a tungsten surface ionizer is accelerated to 20-30 keV. It strikes a hollow cone of the feed material, sputtering off negative ions which go through the hole in the cone and are accelerated. A wheel of 18 cones of different material can rotate any desired material to the axis quickly.

## Footnote and References

*Condensed from LBL-6500, IEEE Trans. Nucl. Sci. NS-24(3), 1064 (1977).


1. B. N. Makov, IEEE Trans. Nucl. Sci. NS-23(2), 1035 (1976).
2. H. G. Blosser et al., Proc. 7th Int. Conf. on Cyclotrons and Their Applications, p. 584, Birkhauser (1975).
3. R. Keller and M. Muller, IEEE Trans. Nucl. Sci. NS-23(2), 1049 (1976); GSI-PB-2-75 (1975) Darmstadt.
4. R. M. Richter and E. Zajec, IEEE Trans. Nucl. Sci. NS-23(2), 1073 (1976).
5. E. Zajec, LBL-5543 (1976) p.50.
6. R. Geller, IEEE Trans. Nucl. Sci. NS-23(2), 904 (1976); private communication.
7. E. D. Donets, IEEE Trans. Nucl. Sci. NS-23(2) 897 (1976).
8. E. D. Donets and V. P. Ovsyannikov, JINR Report P7-9799, Dubna, USSR.
9. E. Stuhlinger, Proc. Symp. on Ion Sources and Formation of Ion Beams, BNL-50310 (1971), p.47, (1971).
10. Roy Middleton, IEEE Trans. Nucl. Sci. NS-23(2), 1098 (1976).

# B. NUCLEAR INSTRUMENTATION

## PION RANGE TELESCOPE FOR HIGH-ENERGY HEAVY-ION EXPERIMENTS

J. Chiba,* K. Nakai,* H. R. Bowman, J. Ioannou, and J. O. Rasmussen

For the study of low-energy pion production we have built a pion range telescope. A fundamental difficulty in detecting pions in high-energy heavy-ion reactions is due to the fact that pion production rates are smaller than production rates of nuclear particles; p, n, d, t, $^3$He, $\alpha$, etc. so that pion detectors suffer strong backgrounds. Although the range telescope is by no means a new method, by combination of the conventional method with the current sophisticated CAMAC-computer data-taking system, we were able to improve its performance so as to make it particularly useful for high-energy heavy-ion experiments.

### Principle and Design of the Pion Range Telescope

The principle of the telescope is shown schematically in Fig. 1. To identify the stopped $\pi^+$ we have used the $\pi^+ \rightarrow \mu^+$ decay ($\tau \sim 26$ nsec).

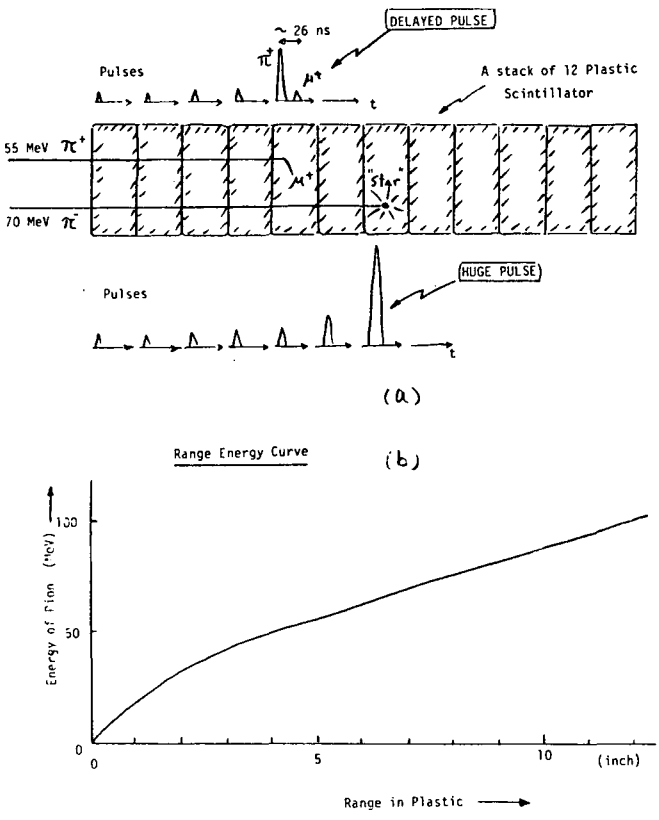


Fig. 1. (a) Schematic drawing of pion range telescope. (b) Range-energy relation for pion whose energy is less than 100 MeV. (XBL 778-9956)

The plastic scintillator, in which the $\pi^+$ stopped, should generate a double pulse -- one due to the $\pi^+$ followed by a second pulse due to the $\mu^+$. A difficulty in this method is that the energy of $\mu^+$ is only 4.7 MeV. The energy deposited by the $\pi^+$ should not be too large in order to separate the second pulse (the $\mu^+$ pulse) from the $\pi^+$ pulse. We chose the thickness of each plastic to be 1 in. in consideration of this fact. The energy deposited in the plastic by the $\pi^+$ would be at most 25 MeV. In Fig. 1(b) the range of the pion is shown in inches. With a stack of 12 plastic scintillators we can cover an energy range of pions up to 100 MeV. When a pion traverses the 1 in. plastic scintillator with an energy in the miniumum ionization range, it generates a pulse of about 5 MeV. Since almost all stopped $\pi^-$ are captured and disintegrate in a carbon nucleus instead of decaying into $\mu^-$, the method mentioned above is only sensitive to the $\pi^+$.

For detection and identification of a stopped $\pi^-$, we have used the large pulse due to the large energy release in the plastic scintillator by the $\pi^-$ nuclear disintegration process (the "star"). In Fig. 2 we compare the energy deposits of a pion and a proton with the same range vs thickness of plastic. We measure pulse heights of all plastic scintillators so that we can identify the $\pi^-$ more clearly by checking the energy deposition along its path.

### Practical Application

We have used an eight-element telescope for measurements of doubly differential cross sections for $\pi^+$ production in bombardment of 800 MeV/n $^{20}$Ne on NaF, Cu and Pb targets. Figures 3 and 4 are schematic drawings of the telescope and electronics used in the experiment. Using the six elements to detect the stopped pions, we measured energy distribution from 10 to 100 MeV. Those were 1 in. thick and names as $R_1$, $R_2$, ... $R_6$. Besides them we prepared 2 in. thick elements $S_3$ and $S_4$ to test a possibility of using thicker elements. The $R_0$ is a solid-angle-defining counter. Putting an absorber in front of the telescope we were able to shift the sensitive energy range of each element.

Time spectra of the delayed pulses and spectra of pulse height that is proportional to the energy deposit in each element were taken with CAMAC-TDC and ADC. Those were stored event-by-event on a magnetic tape with event-pattern information. The event pattern showed which elements were triggered, which element generated the de-

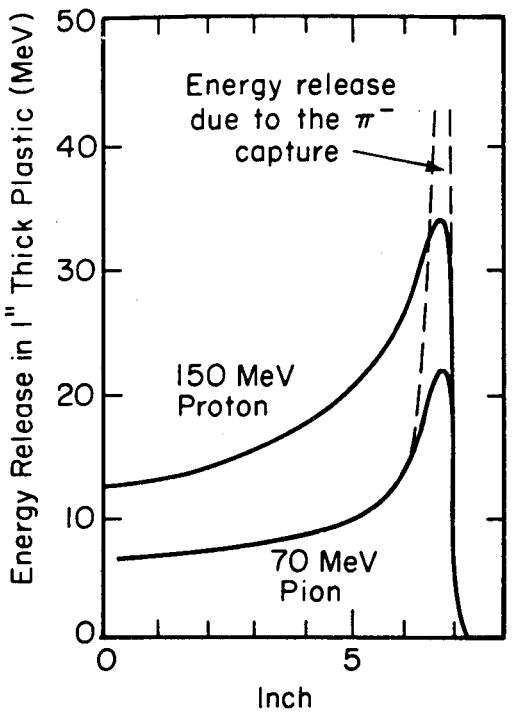


Fig. 2. Energy deposition of 70 MeV pion and 150 MeV proton; these have the same range in the plastic. (XBL 778-9950)

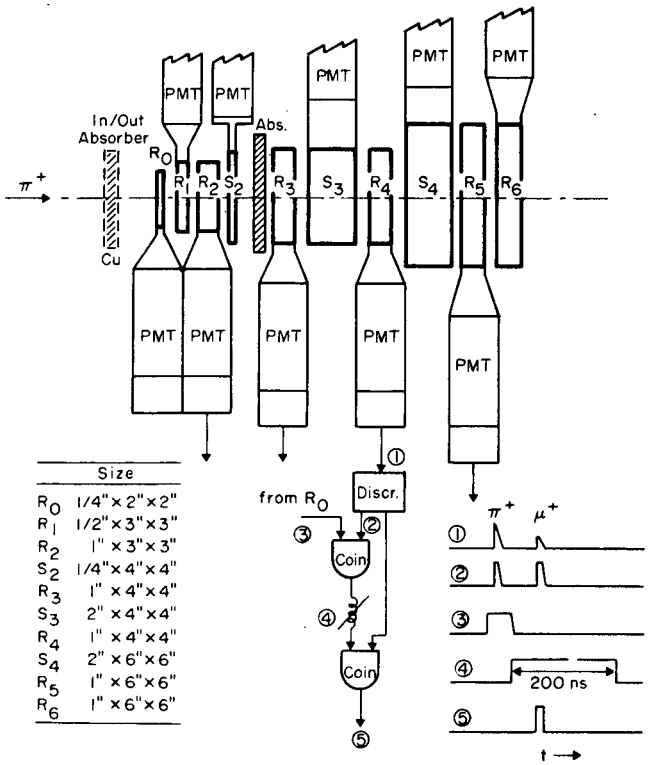


Fig. 3. The plastic scintillators set-up for pion range telescope. (XBL 778-9952)

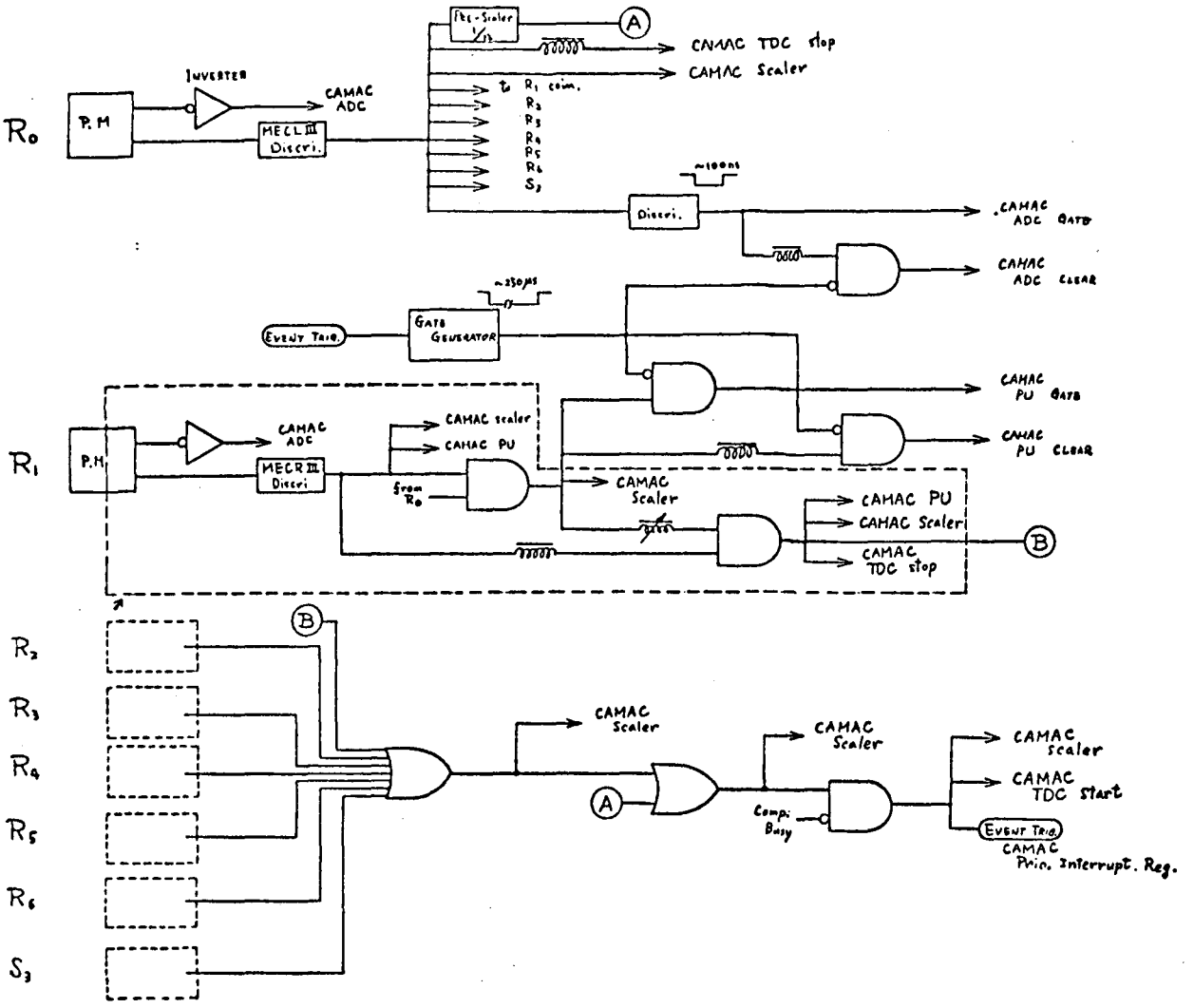


Fig. 4. The electronics set-up. Insides of the dotted-line squares for $R_2$, $R_3$, $R_4$, $R_5$, $R_6$ and $S_3$ are abbreviated. Those are same as that for $R_1$. (XBL 778-9953)

layed pulse, etc. The events were stored only when 1) at least one of the elements generates a delayed pulse (pion events) or 2) once in every hundred events (scaled-down single events). The latter was taken to measure nuclear particles to compare with the pion production.

Figure 5 shows examples of time spectra. Figure 5(a-c) are raw time spectra at 30°, 60° and 120°, respectively. At backward angles we were able to see clean pion decay curves, while at forward angles accidental coincidence due to a large number of particles adds the constant background. Figure 5(d) and (e) are results of a simple sorting of time spectra using event-pattern information to identify events stopped in the element at which we are looking. The background was reduced very effectively. Dramatic improvements were seen in the data at 30°.

We are sure that we can improve discrimination further by sorting data more severely using additional information. The constant background is due to events in which two particles (primarily protons) pass the telescope successively so that the second particle generates a "delayed" pulse. This event can be eliminated if we take events which give a delayed pulse only in the element where the particle stopped, by looking at the event pattern. The accidental event mentioned above generates delayed pulses in more than one element.

We can also look at the pulse height to identify pion events. Taking TDC, ADC and event-pattern information we have redundancy in identifying pions even though the pions to total particles ratio is very small.

It should be mentioned, too, that since the telescope has many elements, it is possible to detect multiple pions in the same telescope. So far, we have had no time to look for such events, but will try to investigate such a possibility.

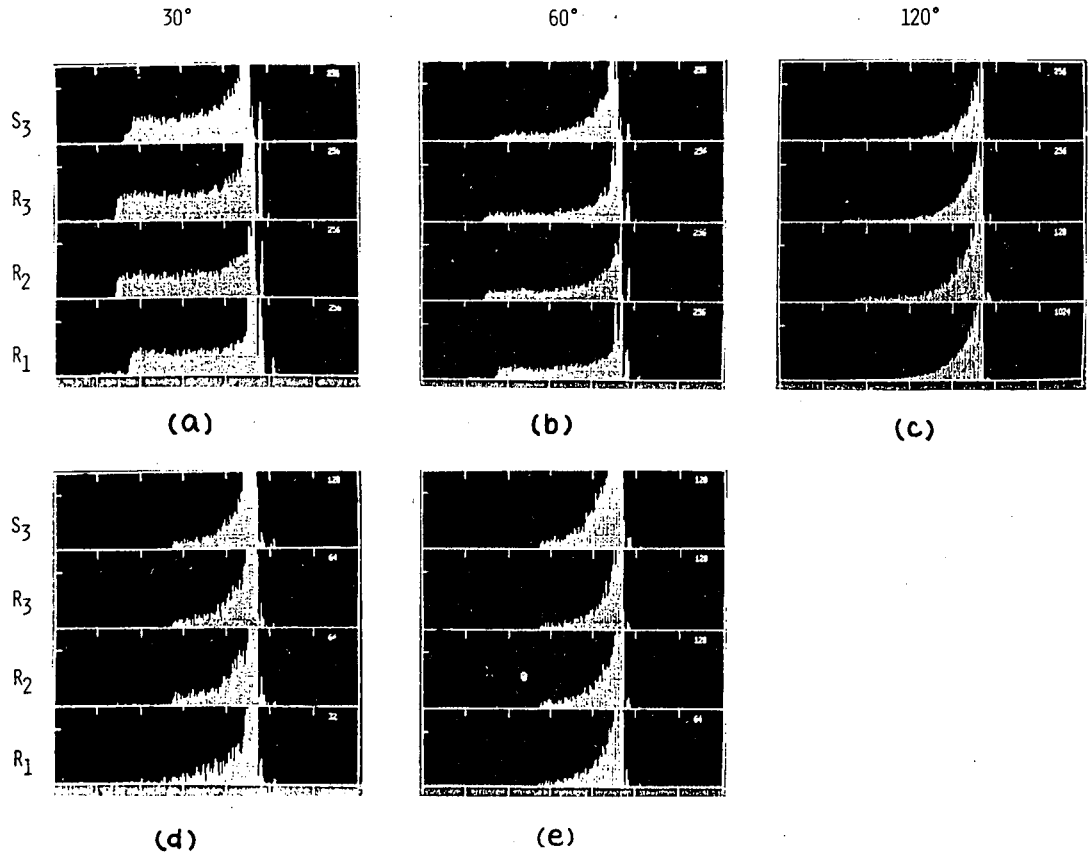


Fig. 5. Typical time spectra. The tick marks are drawn every 32 nsec. The number shown on upper left corner of each spectrum is the full-scale. (a) and (d) are 30-degree data, (b) and (e) 60 degree, and (c) 120 degree. (a), (b) and (c) are the time spectra without anti-coincidence with next positioned plastic counter. (d) and (e) are with anti-coincidence. (XBL 778-7524)

Since we have to separate a delayed $\mu^+$ pulse from a pulse due to a $\pi^+$ that could be five times larger, we cannot avoid some dead region in time spectra near t=0. In cases of data shown in Fig. 5, it was between 10 and 20 nsec. As long as a good portion of a decay curve is observed, this dead time does not matter for inclusive measurements, since we can extrapolate the decay curve to t=0. However, when we want to detect multiplicity of pions by measuring coincidence rates between two or more telescopes it is very important to reduce the dead time.

The dead time is determined by: 1) character of phototube, 2) pulse clipping, 3) discriminator level setting, etc. We are testing a phototube, RCA C31024, which has good timing characteristics. It is clear that this tube is much better, but also it is more expensive. Since we need so many elements, we are using the less expensive XP2230. Even with the XP2230, we are able to make the deal time shorter by adjusting the pulse-clipping time constant and the discriminator-level setting. When we tried to make it shorter, we observe bumps or peaks in the decay curve due to ringing of the pulses. A large pulse generates a second pulse that exceeds the discriminator level. This bump, however, disappears when we sort the time spectrum with a window setting on ADC pulse-height spectra.

In order to minimize the number of elements, we need to know a maximum tolerable thickness for each element. As mentioned we chose the thickness of each element to be 1 in. However, we tried to test the possibility of using thicker elements. The thickness of the element $S_3$ was 2 in. As seen in Fig. 5, it was as good as other elements that were 1 in. thick.

Footnote

* Department of Physics, University of Tokyo, Bunkyo-ku, Tokyo.

# INITIAL EXPERIMENTS WITH THE RAMA SYSTEM

D. M. Moltz, D. J. Vieira, M. S. Zisman, R. A. Gough, R. F. Parry, J. M. Wouters, and Joseph Cerny

At last report the RAMA system was physically in place and aligned. Since that time numerous internal calibrations and in-beam experiments have been performed to test the system. Figure 1 is provided as a general reference schematic; its general characteristics have been described elsewhere.[1-3]

After initially obtaining beam on the focal plane from the RAMA hollow-cathode ion source in June 1976, a scanning wire arrangement was used to measure beam currents of 1-10 μA directly. Initial calibrations were performed using $^{40}Ar^{+1}$ and $^{20}Ne^{+1}$ ions to determine the effect of various optics. The effects of this QSDS system (quadrupole, sextupole, dipole, sextupole) are shown in $^{40}Ar^{+1}$ scans in Fig. 2. These scans were obtained on the center-line of the focal plane and thus the rotation effect of the second sextupole is unobservable (the natural focal plane without the second sextupole is 60° from the normal). Dramatic improvements in the resolution are realized with the addition of the first sextupole, yielding values of m/Δm from 170 to 210 for various masses under different conditions. The resolution was calculated from the equation R = D/2w where D is the measured dispersion of 1.64 m and w is the measured peak width of 0.1 max. Figure 3 shows the mass spectrum of the Xe isotopes after the aforementioned optics parameters were optimized.

After these internal beam calibrations were complete, test experiments were begun. The initial tests involved checking the various optics parameters with $^{20}Na$ activity, produced via the $^{24}Mg$ (p,αn) reaction. The $^{20}Na$ was used because

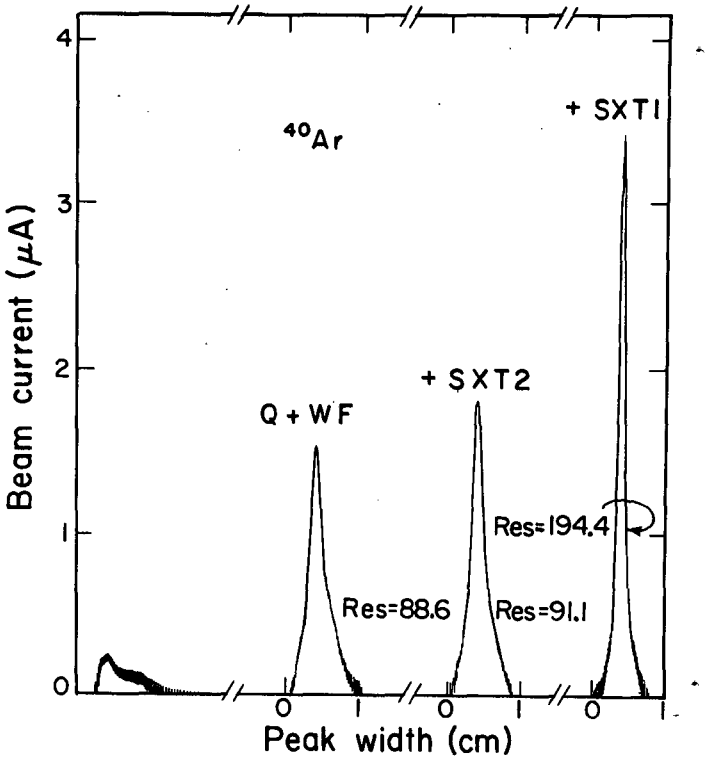


Fig. 2. Effects of various RAMA ion optical devices upon a 10.5 keV $^{40}Ar^{+1}$ beam. (Q = quadrupole, Sxt = sextupole, WF = Wien filter). (XBL 7612-4594)

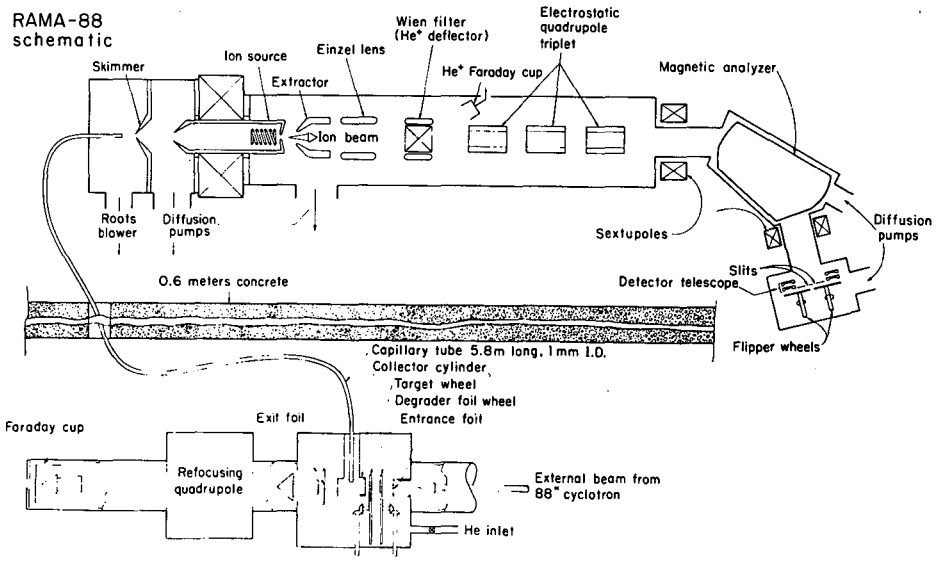


Fig. 1. General RAMA schematic. (XBL 758-3797A).

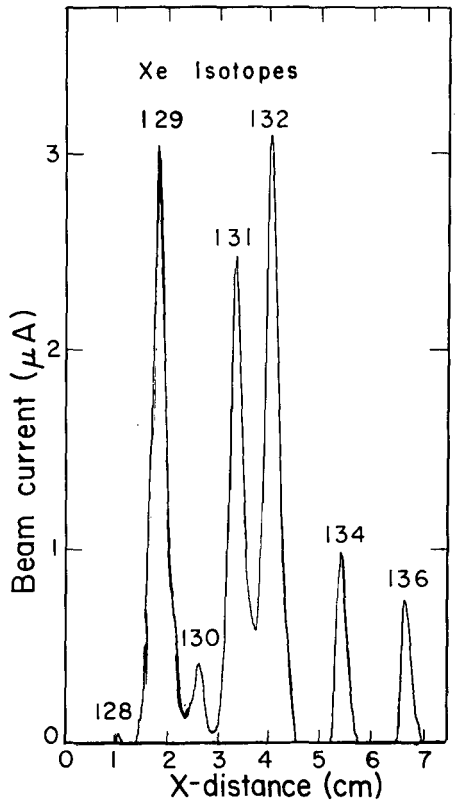


Fig. 3. Xe isotope scan after optimizing the optics parameters. (XBL 7612-4595)

of its short half-life (450 msec) and its easily identifiable alpha-groups at 2.16 and 4.44 MeV. The helium-jet transport efficiency was improved to ∿ 20% by introducing air and ethylene glycol impurities. This, coupled with a 70% skimmer efficiency and ion source-optics efficiency of 0.15%, yields an overall efficiency of 0.03%.

In order to provide an additional test of the ion source operation, calibration experiments were performed using $^{211}$At produced via the $^{209}$Bi(α, 2n) reaction and many rare earth α emitters produced by (HI, xn) reactions on appropriate targets. Of the latter, the initial reaction studied was $^{142}$Nd($^{12}$C, xn)$^{154-x}$Dy ($\sigma \geq 500$ mb), which produced the α emitters $^{150}$Dy($t_{1/2}$ = 7.2m) and $^{151}$Dy ($t_{1/2}$ = 17.7 m). Similar studies of the N = 84, 85 α emitters $^{149}$Tbg, $^{151}$Hohs, $^{152}$Hohs, $^{152}$Er, $^{153}$Er, $^{154}$Tm, $^{154}$Yb, and $^{155}$Yb (with half-lives ranging from 4.1 hr to 400 msec) were also done.

One of the major problems experienced in this work was that the operation of the ion source seemed to vary greatly between the 1600° C used for the Na and At experiments and the 2000° C necessary to observe any appreciable yield of the rare earth α-emitters. This behavior seems directly related to the change in arc conditions at the two different temperatures.

On the basis of this experience, several design changes are planned. First the entire ion source-extractor region will be geometrically improved to allow for greater ion source efficiencies and easier access for ion source changes and maintenance. To improve calibration capabilities and monitor stability during lower yield experiments and to facilitate off-line testing, a channeltron electron multiplier (CEM) is being incorporated into the detector system.

While these improvements are being implemented on the RAMA system, we will begin the next generation of experiments, involving studies of $^{27}$P produced by the $^{28}$Si (p, 2n) reaction and various β-delayed proton emitters near the Z=50 closed-shell region.

References

1. Nuclear Science Division Annual Report for 1975, LBL-5075, p. 351.

2. Nuclear Chemistry Division Annual Report for 1972, LBL-1666, p. 361.

3. Nuclear Chemistry Division Annual Report for 1973, LBL-2366, p. 443.

## A TECHNIQUE FOR THE ACCURATE DETERMINATION OF THE PULSE HEIGHT DEFECT IN SOLID-STATE DETECTORS

J. B. Moulton, E. J. Stephenson, G. J. Wozniak, R. P. Schmitt, and L. G. Moretto

The pulse height defect in Si surface barrier counters has been measured at the 88 in. cyclotron and at the SuperHILAC. At the cyclotron the ion source was fed with a mixed gas containing Ne, Ar, Kr, and Xe. In addition Au pellets were placed on a back insert of the source in one experiment, pellets containing a mixture of rare earths and transitions metals were inserted in another, and Ta was provided by the cathode buttons. A large range of charge states (at very low intensities) of all the ions were selectively brought out of the machine by rf frequency and extractor voltage tuning. Ions up to charge state 14+ for Au, 13+ for Ta, 11+ for Xe, and 8+ for Kr as well as lower charge states of other ions, were produced and accelerated directly (no target scattering) into the Si counters. The pulse height registered by each counter was ampli-

fied and stored electronically on magnetic tape. Because the precise frequency and field of the cyclotron was known for each ion, and because no intermediate scattering of the beam on a target was necessary, the "true" energy of each beam was known quite well (< 1%). Thus the pulse height defect could be determined quite accurately. This pulse height defect is defined as the difference of the true cyclotron energy from the alpha particle energy required to produce the observed pulse height, after correcting for the energy loss in the detector window (typically 40 $\mu g/cm^2$ of Au). The pulse height defect of Au ions at high energies (175 to 230 MeV) was determined at the SuperHILAC by the scattering of $^{86}Kr$ off a thin Au target.

The pulse height defect of solid-state counters has been investigated previously by Kaufman et al.[1] By including the energy loss in the detector window as part of the pulse height defect, they were able to fit the energy dependence of the pulse height defect for a large range of elements with an empirical one-parameter formula. (This parameter varies somewhat from one detector to another and must be determined by calibration for each detector.) The measured pulse height defect vs the true energy for one of our detectors is plotted in Fig. 1 according to Kaufman's definition. LSS[2] units are used in accordance with Kaufman's treatment. One sees that the data fail to cluster on a universal line. In fact a trend is evident. All points of the same element cluster together and the locus is higher for the higher Z's (e.g., Au above Ta, Ta above Xe, etc.). This disagreement with Kaufman may not be too surprising in that a larger range of elements and energies has been investigated in this study.

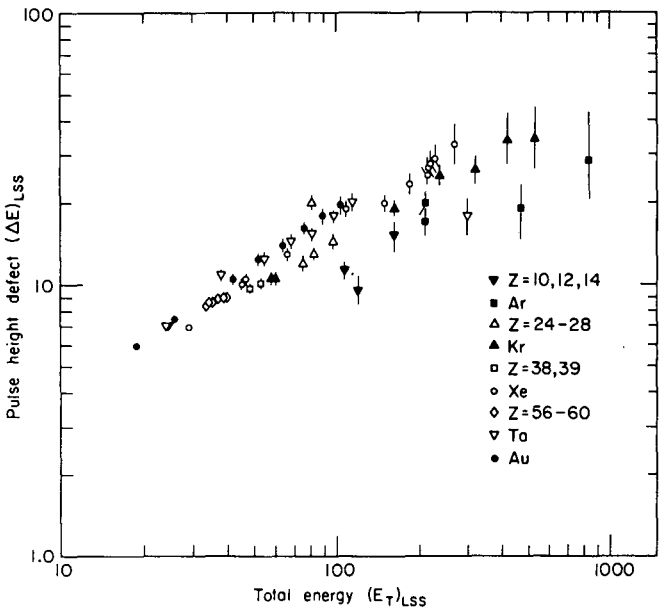


Fig. 1. Pulse height defect vs total energy. ΔE defined according to Kaufman.
(XBL 778-1671)

Since we were unsuccessful in reproducing our data using Kaufman's definition of the pulse height defect and his empirical formula, and since in fact Kaufman does not meet with universal success in representing his own data (especially for light ions such as Ni), we have developed our own method of determining the pulse height defect of any ion from previously measured calibration lines. In our investigation, we discovered that our data fell on a series of straight lines when plotted in MeV units on a log-log plot. Such a plot of our data is shown again in Fig. 2, in MeV units, with the pulse height defect defined as described in paragraph 1 (note the correction for the Au window on the front surface of the detector that was neglected in Kaufman's treatment). The four solid lines represent linear least squared fits to the Au, Ta, Xe, Kr data. The dashed lines are extrapolated from the measured lines to other elements for which the pulse height defect has been measured. The agreement between the extrapolated lines and the data is quite good, even for very light elements like Ar, Si, Mg for which the defects are very small (200 keV to 1 MeV).

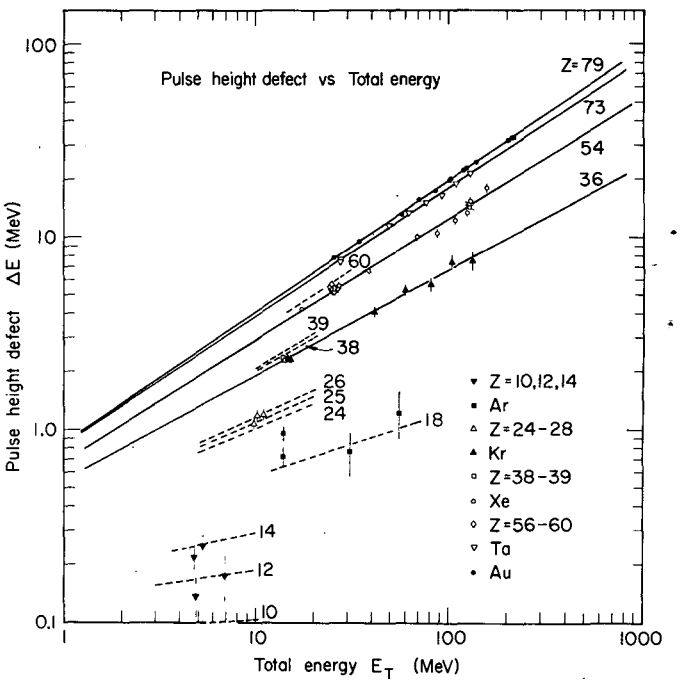


Fig. 2. Pulse height defect vs total energy. ΔE defined in paragraph 1. Solid lines represent fits to data, dashed lines are extrapolated according to procedure in text. (XBL 778-1672)

The extrapolation technique used is as follows. Let $Z_1$ and $Z_3$ be atomic numbers of two elements whose defect vs true energy lines are known. $Z_2$ is the atomic number of the element whose defect line is to be determined. Let $A_i$ and $B_i$ be the slopes and intercepts respectively of these three elements (i = 1,2,3).

Let

$$V = \frac{Z_1 - Z_2}{Z_2 - Z_3}\left(\frac{1 + Z_3^2}{1 + Z_1^2}\right)^{1/2} .$$

Then $A_2$ is determined from $A_1$, $A_3$ and V as follows:

$$A_2 = \frac{A_1\sqrt{1 + A_3^2} + A_3 V\sqrt{1 + A_1^2}}{\sqrt{1 + A_3^2} + V\sqrt{1 + A_1^2}} .$$

Once $A_2$ is calculated, find $C = (A_1 - A_2)(A_2 - A_3)$. Then $B_2$ is found from C, $B_1$ and $B_3$ as follows:

$$B_2 = (CB_3 + B_1)/(C + 1) .$$

In this manner, the defect vs true energy line for any element can be determined from the measured lines for two elements.

Having determined the pulse height defect lines, one needs a technique for deducing the true energy in a real experimental situation, where one knows the identity of the element and the uncorrected ("defective") energy. This is done iteratively by successively approximating the true total energy as the initial defective energy plus the defect that would arise had the true energy actually been the previously calculated energy. Thus: $\log \Delta E^{(i)} = \text{slope} \times \log E^{(i)} + \text{intercept}$; $i = 0,1,2,\ldots$; $E^{(i+1)} = E^{(0)} + \Delta E^{(i)}$. Convergence to 0.1% of $E^{(i)}$ is usually attained in 2 to 3 iterations.

Our data, for which the "true" total energy and the defective energy are both known, have been used as a test of this procedure. Starting with the defective energy, the true energy is approximated iteratively. The percentage deviation of the iteratively calculated energy from the true energy is generally better than 0.5%.

References

1. S. B. Kaufman et al., Nucl. Instrum. and Meth. 115, 47 (1974).

2. J. Linkhard et al., Mat. Fys. Medd. Dan. Vid. Selsk. 33 no. 10 (1963) and 33 no. 14 (1963).

## IDENTIFICATION OF ATOMIC NUMBERS UP TO Z = 60 BY MEANS OF ΔE-E TELESCOPES AND A COMPUTERIZED METHOD*

P. Glässel,† R. C. Jared, and L. G. Moretto

The ΔE-E telescopes[1] have become quite popular for studying heavy-ion reactions because they are so simple to use. In experiments with solid-state ΔE and E counters, the nonuniformities of the ΔE detector thickness limit the Z resolution to fairly low atomic numbers. Range-energy tables, normalized to some experimental values, are often used to define Z-bins, i.e., areas in the two-dimensional ΔE-E spectra that are supposed to contain the events of the same atomic number. However, this method gives questionable results since the commonly used range-energy tables[2] are extrapolations which lead to sizable errors in the region of interest for heavy ions. A more accurate and reliable method is to determine the Z-bins from the reaction data themselves, provided that identification of individual atomic numbers can be achieved.

We present a simple computerized method to determine the Z-bins from the data. It works on marginal statistics and for the highest Z's where the resolution approaches 1 Z-unit (FWHM). The first step is to search the data for Z-ridges. The data are assembled into two-dimensional ΔE-E-arrays (100 E-channels, 960 ΔE-channels). In such an array fragments of the same Z but different energies fall along a ridge line. For a range of Z's as well as energies, a pattern of ridges is produced. The computer program scans E-columns (E = const) for peaks to locate the ridges. In order to improve statistics, a number of columns (odd, so the center will coincide with an original column) is compressed into one. Adjacent columns are added vertically displaced according to the slope of the Z-lines.

A most efficient method for detecting these peaks in the E-columns involves the use of a triangle-shaped "test-function." A normalized convolution of the column with the test-function is carried out. As the test-function is moved along the column, a maximum in the convolution sum results wherever a peak is matched; a minimum is obtained, when a valley is matched. The base-width 2ω+1 of the test triangle

$$t(i) = \omega - |i| \qquad i = -\omega,\ldots, +\omega$$

is chosen to correspond to the average spacing of the Z-lines. The normalized convolution is defined as

$$c(n) = \sum_{i=-w}^{w} f(n - i)\, t(i) \Big/ \sum_{i=-w}^{w} t(i) \sum_{j=-w}^{w} \left(\frac{f(n - j)}{(2w + 1)}\right) ,$$

where f(i) is the data in the compressed column. A flat background would yield c(n) ≡ 1. The resulting vector c(n) is smoothed, then scanned for peaks. Figure 1 shows the result of a convolution on real data.

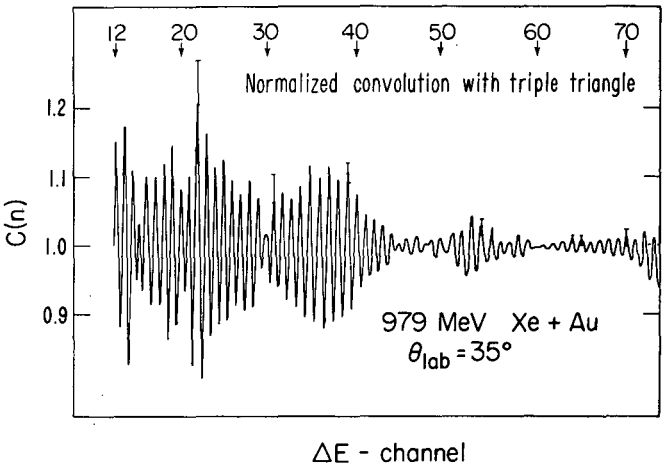


Fig. 1. Normalized convolution sum for the reaction of 980 MeV Xe on $^{197}$Au.
(XBL 768-3864)

The first set of ridge points is improved in a second pass with a three-fold triangular test-function which exploits the experimentally observed periodicity of the structures and increases statistical accuracy. The spacing of the triple triangle test-function is varied according to a fit of spacings obtained in the first pass. The normalized convolution with the triple triangle is checked for significant peaks in the same way as above. The two-pass search procedure is carried out over the whole range of E-columns containing data. The result is a grid of ridge points and of their significance values. It should be emphasized, that up to here, the program works completely automatically, using only three input parameters: the spacing guess 2ω+1, the average slope of the Z-lines and the number of columns to compress into one. Figure 2 shows an example of the grid of ridge points obtained with the single and triple convolution.

The part of the program which defines the Z-lines is interactive and uses a CRT-display for control. From the matrix of ridge points previously found, sets of points are selected that belong to the same Z-ridge. These are fitted with a 4th order polynomial.

The method of Z-identification described above has shown its power in the successful treatment of a large amount of data for various deep inelastic heavy-ion reactions, ranging from Ne+Ag to Xe+Au. It has enabled us to identify Z's up to 60 and given us confidence in our results. Our version of the code is tailored for the use on a POP-9 computer with 32k memory and custom display.

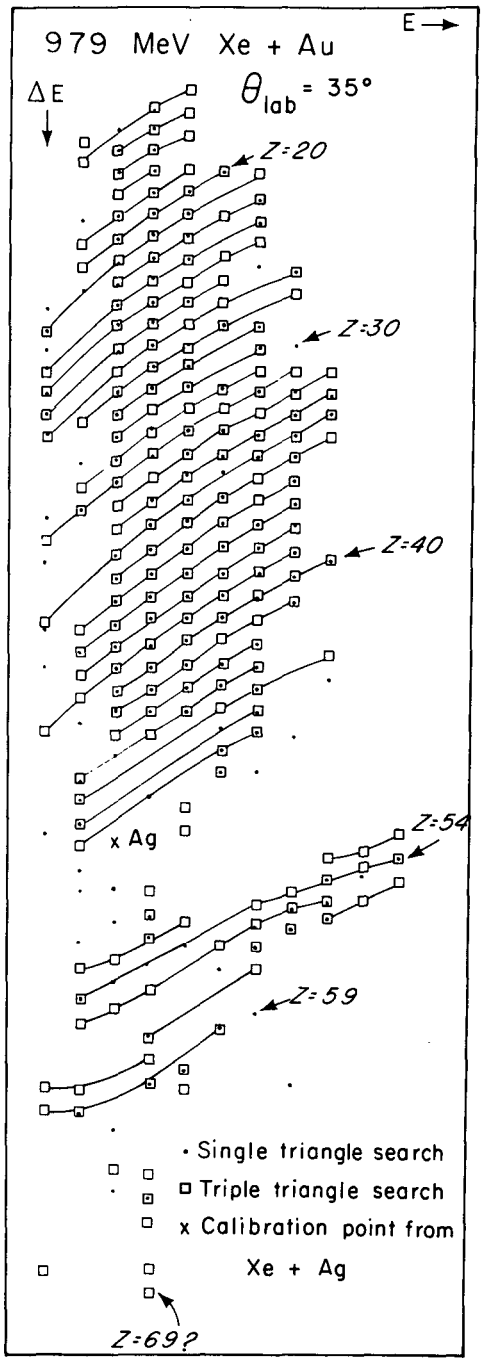


Fig. 2: Ridge points found with the single and triple triangle test-function for data from the reaction of 980 on $^{197}$Au. The lines connecting Z-lines are eye-guides. Shown are all points with a significance value p ≥ 1.0. (XBL 7611-4482)

## Footnotes and References

*Condensed from LBL-5064 and Nucl. Inst. and Meth. 124, 341 (1975).

†Present address: Physikalisches Institut der Universität Heidelberg Philosophenweg Z2, 0-69, Heidelberg, W. Germany.

1. M. M. Fowler, R. C. Jared, Nucl. Inst. Meth. 124, 341 (1975).

2. L. C. Northcliffe and R. F. Schilling, Nucl. Data Tables A7 (1970).

# A SIMPLE POSITION-SENSITIVE PARALLEL-PLATE AVALANCHE COUNTER WITH TWO-DIMENSIONAL READOUT

R. C. Jared, P. Glässel,* J. B. Hunter, and L. G. Moretto

We designed a counter for coincidence measurements of the two fragments from deep-inelastic heavy-ion processes. One fragment is detected in a ΔE-E telescope with small (~1 msr) solid angle. The other partner is then expected at a correlated angle within a finite width distribution, the width stemming from light particle evaporation and other effects. These widths range from ~4° to 20° for various systems. A counter spanning such a range of angles is completely adequate for coincidence measurements of deep-inelastic reactions, by giving close to unity efficiency for the detection of the correlated fragment.

The basic idea of the counter is a combination of the parallel plate avalanche counter (PPAC) with charge division readout in 2 dimensions.[1] The active gas volume of the counter is confined between 3 foils, spaced 2 mm apart. The foils are ~40 μg/cm$^2$ thick and made from polypropylene using a stretching technique. We consider these thin polypropylene foils an important improvement first because of their exceptional strength, which exceeds that of mylar; second because of their ability to maintain tension that is critical for PPAC application. They were also the only foils that could be successfully coated with a suitable resistive metal layer without losing tension. (We tested Formvar, VYNS, Nitrocellulose). The total thickness of the PPAC, including a grid-supported vacuum window is 160 to 200 μg/cm$^2$, thin enough to allow good energy information from a solid-state detector behind it (size 900 mm$^2$).

The center foil (Fig. 1) is coated on both sides with a Ni-Cr layer of ~ 100 Ω/sq, at high voltage. The outer foils are coated with a resistive layer of ~ 1 to 5 kΩ/sq. They have silver-paint strip contacts on opposite sides, one foil being contacted on top and bottom, the other at the left and right-hand side. They give information about the y and x coordinate, respectively. The four contacts are read out by charge-sensitive preamplifiers (for simplicity, other preamplifiers would do as well or better). Since two preamplifier inputs are connected via the foil resistance, there is an increase in preamplifier noise, each preamplifier seeing the effective capacity of the other input. To minimize noise, one would like to maximize the foil resistivity. On the other hand, foils with higher resistance tend to be more non-uniform. A good compromise is seen in the region of ~ 2 to 3 kΩ/sq. The evaporation of Ni-Cr onto the foils is done while monitoring the resistance with an ohm meter. This allows one to obtain any desired resistivity if the oxide layer is taken into account, which develops later in air and which reduces conductivity by ~ .001 Ω$^{-1}$/sq. The principle of operation is similar to that of a Borkowski-Kopp-type counter: A particle passing the counter about perpendicular to the foils initiates avalanches in both the x and y section. The current induced by the avalanche in each section will be divided according to the ratio of the resistances between the position of the avalanche and the two contacts connected to the preamplifier inputs.

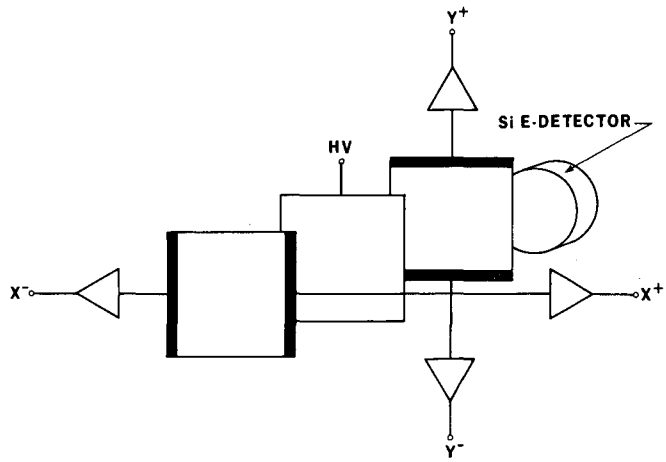


Fig. 1. Expanded view of the position sensitive detector. (XBL 778-2862)

The choice of three electrodes rather than two allows both outer electrodes to be operated near ground potential, thus eliminating problems with charge collection in the neighboring gas volumes, i.e., between the vacuum window and the front foil, or between the back foil and the solid-state detector behind the PPAC. Also, if desired, adequate timing can be derived from the low resistivity high voltage electrode.

The PPAC is operated at ~ 10 Torr hexane, with a high voltage of ~ 500 V for heavy ions. To test the uniformity of the resistive foils, a mask with a grid of holes is placed in front of the counter and illuminated with a $^{252}$Cf-fission source. Figure 2 shows an example of the position spectra obtained with the mask. The four signals $x^+$, $x^-$, $y^+$, $y^-$ are digitized and recorded event by event. The position for each event is calculate

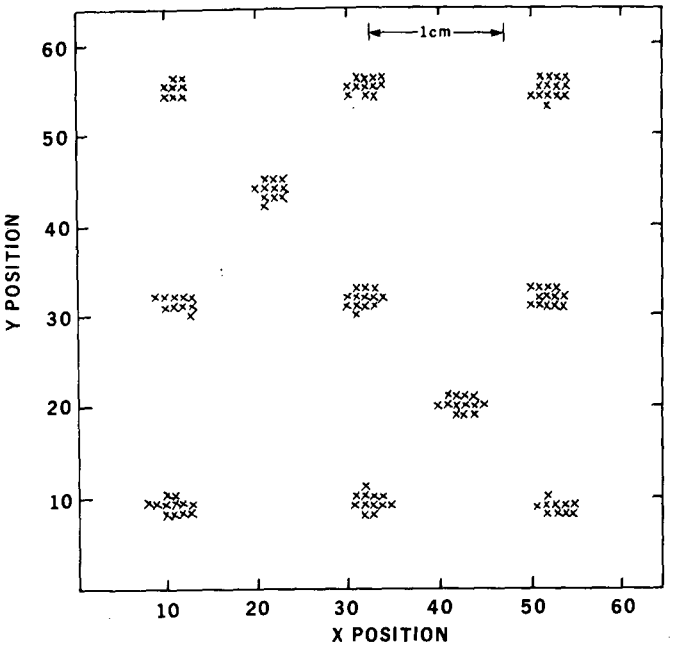


Fig. 2. Contour map made with the detector and an 11-hole mark. The holes form a square with a diagonal. The square is 3 cm on a side. (XBL 778-2861).

according to

$$x = \frac{x^+}{x^+ + ax^-} \qquad y = \frac{y^+}{y^+ + by^-}$$

The constants a and b are used to equalize the gains of the signals $x^+$, $x^-$ and $y^+$, $y^-$, respectively. They are adjusted such, that the center hole of the mask appears at the center position. It is not obvious, that the ratio of the resistances from an arbitrary point on a resistive square sheet to the two opposite contacts should vary as the ratio of the distances of this point to the contacts. The exact solution of this problem is fairly tedious, so we chose to make some simple tests on resistive carbon paper. Within the accuracy of this method, no nonlinearities were found. The nonlinearities in the observed position spectra are due to nonuniformity of the coating.

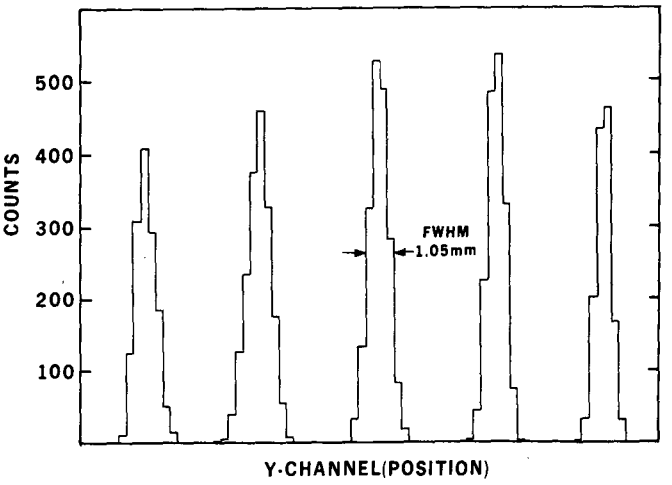


Fig. 3. y position spectrum of 4-80 MeV $^{86}Kr$ with a mask of 5 holes. (The holes are 1-mm diameter, spaced 5 mm apart.) (XBL 779-1669)

The position resolution was determined using a mask with 5 holes of 1 mm diametric, spaced 5 mm apart (Fig. 3). The FWHM is 1.05 mm both for x and y coordinate. It should be mentioned, that no efforts were taken to optimize the position, e.g., by using other kinds of preamplifiers, since the initial results were quite satisfactory for our purposes.

In conclusion, it may be said that the position-sensing principle presented here may be superior to more complex designs for a variety of applications, where an angular acceptance of 10 to 30° is sufficient. Also, the absence of a large number of wires is advantageous in some cases where scattering from the wires is a problem.

Footnote and Reference

*Present Address: Physikalisches Institut du Universität Heidelberg, Philosophenweg Z2, 0-69, Heidelberg, West Germany

1. R. B. Owen and M. L. Awcock, IEEE Trans. NS-15, 290 (1968).

## FROM NANOSECONDS TO HOURS: PHYSICAL TECHNIQUES IN THE SEARCH FOR SUPERHEAVY ELEMENTS

A. Ghiorso, J. M. Nitschke, M. J. Nurmia, R. E. Leber, L. P. Somerville, and S. Yashita

The search for superheavy elements (SHE) has been characterized by its diversity and breadth. Researchers in biology, geology, chemistry, and physics have worked to find evidence for these nuclides, which would be removed from the known elements to a so-called "island of stability" established from shell effects. Exceptional nuclear properties have been predicted for the SHE (see, for example, Refs. 1-3). Long fission half lives and high-energy alpha decay would be attributed to the influence of the closed shell(s). And the shape, size, and neutron number of these nuclei could give rise to relatively high fission energy, high neutron

multiplicity, and a large component of ternary fission. Furthermore, relativistic effects may influence the chemistry of the SHE.[4,5] Counterparts of the chemical investigations undertaken at this and other laboratories,[6,7] physical experiments designed to search for and detect behavior peculiar to the SHE have been executed.

In order to provide details about the decay mode, half-life, excitation function, and genetic relationship of a radioactivity, time-dependent alpha and fission spectroscopy has been emphasized in this work. Accordingly, the search for radionuclides with half-lives in excess of 500 msec has been undertaken with the vertical-wheel system (VW), described more fully in Ref. 8.

The drum-mica system as described in Ref. 9 has been used in the SHE search because it has a particularly high efficiency (∿ 90%) for detecting fission activity over a range of half-lives between milliseconds and hours.

The search for fission activities with half-lives in the approximate 5-ns to 100-ms range (the time of flight of the recoil nucleus to the first baffle and the emptying time of the stopping chamber, respectively, determine these half-life limits ) has been undertaken simultaneously with other experiments through use of the decay-in-flight (DIF) apparatus shown in Fig. 1. In this assembly, which is placed in the same reaction chamber used by the VW system, a series of aluminum-coated stainless steel baffles shield mica detectors from direct beam scatter in order that fission fragments may be registered in the dielectrics with an efficiency of approximately 20%. The angular acceptance of the DIF system is such that forward-peaked products are preferentially detected, hence improving the relative probability of observing compound-nucleus events.

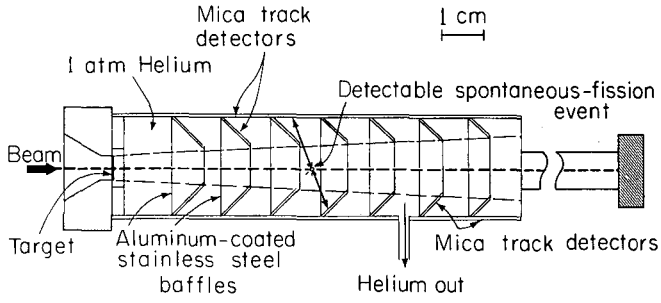


Fig. 1. The assembly for detecting decay-in-flight fission events. (XBL 774-881)

There have been predictions that SHE may be chemically inert and relatively volatile due to relativistic effects on the ordering and spatial distribution of electron orbitals.[4,5] Consequently, the chemistry of SHE may show important differences from that of lighter homologs. Splitting of atomic orbitals into the $\ell + 1/2$ and $\ell - 1/2$ subshells may stabilize, say, E114 (eka-lead) to the extent that its $7p^2_{1/2}$ configuration represents shell closure. The valence-electron binding energy here is such that chemical bonding is -- for the most part -- energetically unfavorable. Hence, only weak dispersion forces are available to maintain this SHE (and likely 112 and 118) in a condensed phase. We have therefore devised a (gas analysis) apparatus to handle and count volatile radioactivities with half-lives greater than 30 min. (See Ref. 10 for a more detailed discussion.)

Insofar as none of the above experiments yielded any evidence for the production of SHE, the detection limits for spontaneous-fission activities are presented in Table 1. Though the various techniques employed in this study differ in their sensitivity, this search represents at least partial coverage of the nanosecond-to-hours half-life range.

The reaction of $^{136}Xe$ with $^{124}Sn$ -- though inappropriate for the production of SHE -- was studied in the context of systems with small mass asymmetry. Experiments at 650 ± 20 MeV (30 MeV above the interaction barrier in the center of mass) showed no evidence for compound-nucleus formation above detection limits of 3 and 2 nanobarns for the VW and drum, respectively. These observations differ significantly from predictions[11] of a compound-nucleus cross section approaching 10 mb at the same energy for the strictly symmetric case of $^{124}Sn + ^{124}Sn$.

While superheavy elements have yet to be found (much further work is anticipated in this area), important discoveries have been made in their pursuit. (See Nitschke et al., Ref. 12 and Baisden et al., Ref. 13.)

## References

1. G. T. Seaborg, Ann. Rev. Nuc. Sci. 18, 53 (1968).

2. J. R. Nix, Conf. on Properties of Nuclei Far from the Region of Beta-Stability, Leysin, Switzerland (September 1960).

3. C. F. Tsang and S. G. Nilsson, Nucl. Phys. A 140, 289 (1970).

4. K. S. Pitzer, J. Chem. Phys. 63, 1032 (1975).

5. B. Fricke and J. T. Waber, Actinides Rev. 1, 433 (1971).

6. E. K. Hulet et al., Phys. Rev. Lett. preprint.

7. R. J. Otto et al., LBL-6509.

8. A. Ghiorso et al., Phys. Rev. Lett. 33, 1490 (1974).

9. A. Ghiorso, Proc. of the Robert A. Welch Foundation Conf. of Chem. Research XIII, The Transuranium Elements (W. O. Milligan, ed.) p. 107 ff (Houston, 1970).

10. S. Yashita and R. E. Leber, LBL-6547; Searching for Volatile Superheavy Elements, in this Annual Report.

Table 1. Experimental limits for SHE spontaneous-fission activity produced by physical techniques.

| REACTION | ENERGY (MeV)* | $\sigma^{SF}_{lim}$(nb) | TECHNIQUE |
|---|---|---|---|
| $^{40}Ar + ^{238}U$ | 200 ± 4 | 1 | VW |
| | | 20 | DIF |
| | 209 ± 4 | 1 | VW |
| | 220 ± 4 | 1 | VW |
| | 249 ± 4 | 3 | VW |
| | 260 - 340 | 0.5 | GAS ANALYSIS |
| $^{40}Ar + ^{244}Pu$ | 245 ± 3 | 5 | VW |
| $^{48}Ca + ^{238}U$ | 300 - 380 | 1.4 | GAS ANALYSIS |
| $^{48}Ca + ^{244}Pu$ | 250 ± 10 | 2 | VW |
| $^{48}Ca + ^{248}Cm$ | 265 ± 6 | 1 | VW |
| | | 40 | DIF |
| $^{86}Kr + ^{208}Pb$ | 475 ± 20 | 5 | VW |
| | | 0.1 | DRUM |
| | | 20 | DIF |
| $^{86}Kr + ^{238}U$ | 560 ± 10 | 7.0 | GAS ANALYSIS |
| $^{136}Xe + ^{238}U$ | 1155 ± 10 | 0.4 | GAS ANALYSIS |

* Projectile laboratory energy at target center.

11. J. R. Nix and A. J. Sierk, Phys. Rev. C 15, 2072 (1977).

12. J. M. Nitschke, R. E. Leber, M. J. Nurmia and A. Ghiorso, LBL-6534; Observations in the Reaction of Two Doubly-Magic Nuclei: $^{208}Pb$ and $^{48}Ca$, in this Annual Report.

13. P. A. Baisden, R. E. Leber, J. M. Nitschke, A. Ghiorso, M. Nurmia, and A. Ghiorso, New Isomers in Bismuth, in this Annual Report.

## MASS RESOLUTION OF A PARTICLE IDENTIFIER TO BE FLOWN ON ISEE-C

D. E. Greiner, F. S. Bieser,* H. J. Crawford,* H. H. Heckman, and P. J. Lindstrom

### Introduction

Measurements of the masses of the cosmic ray particles (when performed without use of a magnetic field) generally involve observations of small effects. When measuring a small effect we must either have high accuracy instruments or many observations with a less ingenious instrument. Many times a compromise is made and we settle for a few observations from a semi-high accuracy

instrument. Then the identification depends on making the best use of the several parameters measured. Mathematically this is achieved by the formulations of a likelihood function which allows assignment of probabilities to each possible particle mass for a given set of observed parameters. But likelihood functions are difficult to formulate and more tractable $\chi^2$ functions provide the same information content, provided the errors in the problem have Gaussian distributions.

Using this multi-parameter approach we have predicted instrument resolutions.[1] Application to a solid-state-detector telescope consisting of ten 5 mm thick Si(Li) detectors predicts mass resolutions better than 0.2 amu through mass 56 if the following requirements can be met:

1. Detectors flat ($\sigma_t \leq 12\mu$),
2. Pulse resolution = 0.1% of the maximum pulse expected for a given particle,
3. Particle direction relative to the Silicon is measured to an average accuracy of 0.3°.

Let us now look at the sensors we have developed to achieve this resolution.

## Method

The Si(Li) detectors were made of Topsil silicon at the Lawrence Berkeley Laboratory. Some average characteristics are:

| | |
|---|---|
| Active diameter | 44 mm |
| Thickness | 4700 μ |
| Noise | 140 keV (rms @ 700 V) |
| Leakage | 6μA (@ 25° C) |

The lithium "dead layer" side of each detector was lapped completely off and a 10μ layer of lithium was re-deposited creating a very thin window. Generally, $^{241}$Am in this side of a detector gives a pulse height of 4.55 MeV. A special planer etch process was used when preparing the surfaces in order to reduce mechanical nonuniformity. All detectors were subjected to a two weeks thermal vacuum test where their noise and leakage were monitored while in vacuum at 25°C for 4 days and 35°C for 10 days. The failure rate in this test was less than 10%.

The thickness variations of the detectors were measured optically and also by passing a beam of heavy ions through the detector. The optical measurements were done using a 3 axis digitized microscope that was calibrated using gage blocks. The thickness of the detectors was measured on a 3-mm grid over the entire surface. Each individual measurement has an accuracy of 5μ. The detectors selected for further testing had maximum variations less than 20μ from the average and a standard deviation of less than 10μ.

The uniformity of signal when particles are passed through at normal incidence was our most important criterion for detector selection. A total of 22 detectors that had passed all the previous tests were exposed to a 400 MeV/n $^{40}$Ar beam at the Bevalac.[2] Enough particles were observed to allow at least 0.1% accuracy in the pulse-height average over each of 80 annular segments of a detector. The results of the particle mapping were in agreement with the optical measurements, indicating the detectors' electronic properties are also quite uniform. Final detector selection was somewhat subjective with emphasis put on the uniformity and the history of noise and leakage. Fortunately, there was an abundance of good detectors.

The size of the silicon detectors and the desire to have a large solid angle lead us to consider either multiwire proportional chambers or drift chambers as the trajectory measuring device. There were several points in favor of drift chambers:

1. Fewer wires, i.e., less to break,
2. One amplifier vs either a delay line or many amplifiers,
3. Sufficient gain without exotic gas mixtures.

For these reasons we chose to precede the silicon stack with 6 drift chambers.

Monte Carlo calculations of the 6 drift chamber array response to heavy ions and the associated δ rays allowed design of a discrimination scheme that reduced the effect of the δ rays to an acceptable level.

The ISEE-C instrument consists then of 6 drift chambers followed by 10 Si(Li) detectors with the detectors surrounded by a scintillator shield. In order to limit telemetry requirements and to be sure of getting important events (i.e., stopping in the silicon), the following five event types were identified:

1. Stopping, $z \geq 3$, no shield
2. Stopping, $z \leq 2$, no shield
3. Through, $z \geq 3$, no shield
4. Through, $z \leq 2$, no shield
5. Through, $z > 2$, shield

The priority scheme requires that type one events always be telemetered, while a subset of types 2 to 5 is sent. The thresholds that are used to determine the event type are set by ground command to allow for precise selection and long term drifts. It is also possible to reconfigure the instrument trigger to require any combination of wire chambers and any two silicon detectors. The detector what determines the stopping and through conditions may also be changed. Lastly, it is possible to command the instrument to not

send any of the event types. The completed instrument weighs 8.5 kg, uses 6.2 watts and transmits 32 bits/sec.

## Results

A carbon beam at 250 MeV/n was used to begin calibration of the instrument in late March 1977. Three types of data were taken:

1. Drift chamber calibration data that consisted of exposing the instrument to the unfragmented beam at 49 different orientations covering the entire acceptance solid angle.

2. Silicon detector beam calibration data which consisted of varying the beam energy with absorbers so that the particles stop in several positions of each detector of the telescope.

3. Mass and charge calibration data where the beam is fragmented and all isotopes below the beam mass are stopping throughout the telescope.

Essentially the same data set was taken using a $^{40}Ar$ beam two weeks later. We have available at the time of this writing the diagnostic checks of the $^{12}C$ data made between the two runs. The drift chamber resolution was the first quantity checked. Fig. 1 shows the tangent of the angle of incidence of the beam as determined by two of the six drift chambers. The standard deviation is $\sim 0.026$. This predicts a path length uncertainty of 50μ in each silicon detector. Monte Carlo calculations for $^{12}C$ predict a 30μ uncertainty in path length assuming chamber resolution is 300μ and all six chambers are used to determine the slope. Thus we feel that when we make use of the information from the other chambers we will achieve the predicted resolution.

The diagnostic tests of the isotopic resolution for fragments of the $^{12}C$ beam consisted of ΔE vs E plots for all choices of stopping detector. A representative sample is shown in Fig. 2 for particles stopping in the third detector. Even without using the greater resolution of the multi-parameter fit we see quite clear separation of isotopes through $^{11}B$. Comparison of these results to the predicted resolution indicates we have achieved our design goals.

Preliminary results with an Fe beam indicate resolution of 0.35 amu with only two detectors used. This resolution includes no information of particle position on the detector and no correction for detector thickness. A histogram of the preliminary Fe resolution result is shown in Fig. 3.

## Footnote and References

* Space Sciences Laboratory, University of California, Berkeley, CA 94720.

1. Nucl. Instrum. and Meth. 103, 291 (1972).

2. Nucl. Instrum. and Metho. 116, 21 (1974).

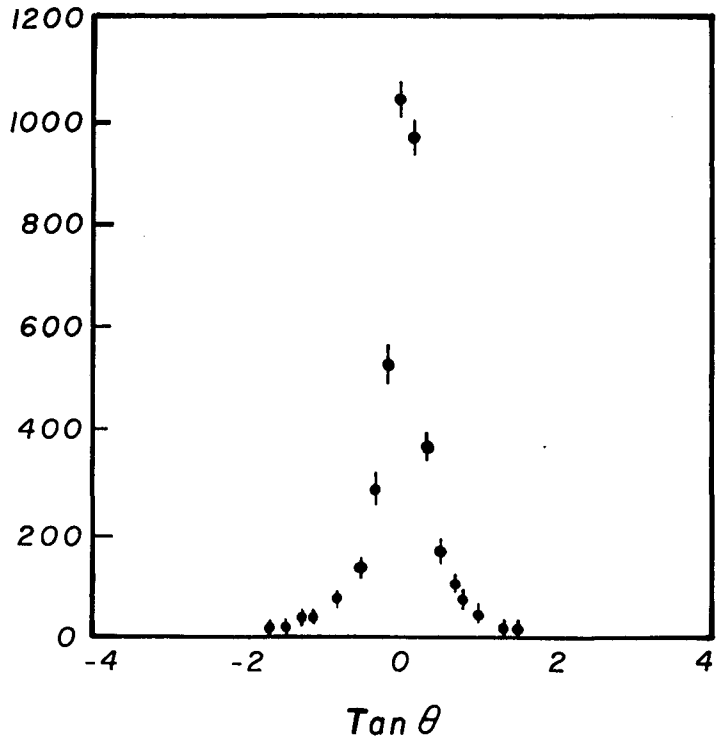


Fig. 1. (XBL 778-1643)

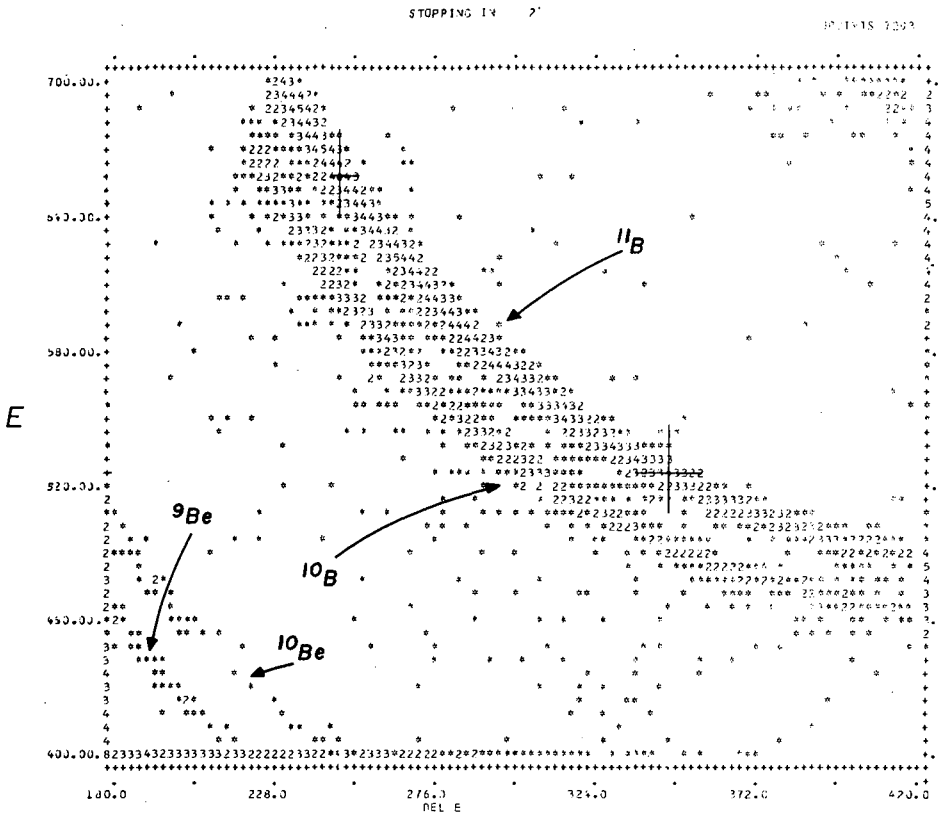


Fig. 2. (XBL 778-1644)

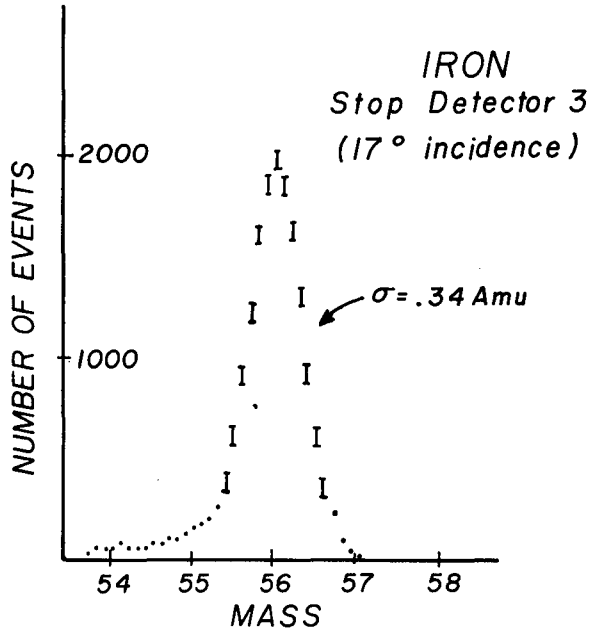


Fig. 3. (XBL 779-1836)

# A PROPORTIONAL DRIFT CHAMBER ARRAY FOR COSMIC-RAY INSTRUMENTS

F. S. Bieser,* D. E. Greiner, E. Beleal,* and D. D. Aalami

## Introduction

Our cosmic-ray instrument on NASA/ESA's ISEE-C satellite has a 45° half-angle field of view to allow the maximum possible count rate.[1] To prevent degradation of isotopic resolution in the silicon detector telescope, each particles's angle of incidence must be known to an accuracy (dependent on Z and angle) ranging from 3° (S.D.) for protons, etc. to 0.2° (S.D.) for Fe isotopes at wide angles. The apparatus for determining these angles must be very reliable to survive the rigors of a rocket launch and continue working for at least 3 years. It must also require very little power, be relatively compact and lightweight, and present a uniformly low mass to the incident cosmic rays.

The six element array of single wire proportional drift chambers (SWPDC) described here can provide this angular resolution. A replenishment gas system allows a minimum 3 year life. The total weight including all power supplies and processing electronics is 3.5 kg and draws a scant 1.5 w.

## Chambers

In general, trajectory measuring detectors can trade-off spatial resolution for increased length provided there is sufficient room in all three axes to maintain the required geometric factor. In our case, there was only 15 cm x 15 cm available in the plane perpendicular to the telescope axis, so with $\theta/2 = 45°$, the array must be $< 1/2 \times 15$ cm/tan 45 = 7.5 cm in thickness and have a spatial resolution $< 7.5$ cm $\Delta\tan\theta = 330$ microns (for an average $\theta=27°$, $\Delta\theta=0.2°$).

The high spatial resolution, low density and low total weight requirements rule out the use of hodoscopes of solid detectors, so we considered gas-filled chambers. The choice here was between multiwire and single wire systems. The overwhelming number of arguments in favor of single wire chambers include: (1) increased reliability -- fewer wires to break; (2) less power and weight in electronics needed to process signals -- only one amplifier per plane; (3) a more readily compressed gas mixture for in-flight sustenance -- multiwire chambers use "magic gas", one constituent of which liquefies at < 3 atm; (4) the unique ability to overcome the ruinous spray of delta-rays signals produced by relativistic heavy ions.[2]

At the C.E.N. Laboratoire de Physique at Saclay, single wire drift chambers have been built with drift paths in excess of 1/2 meter.[3] The challenge of this experiment was to squeeze six chambers (3 x-y pairs) into 7-1/2 cm total thickness. This required a reduction in the thickness of each chamber and a redesign of the drift electrode metallization to completely shield one drift space from the disturbing electric fields of its neighbors. Double-sided, gold-plated Kapton (8μ thick) was etched to form 1-mm wide lines on 2-mm centers with the patterns staggered to provide 100% electrostatic shielding. This material was folded over thin epoxy-fiberglass frames as shown in Fig. 1. A uniform high voltage gradient of 300 V/m was created (on both sides of the Kapton) by a thick-film resistor network with gold contact pads for every line on the Kapton.

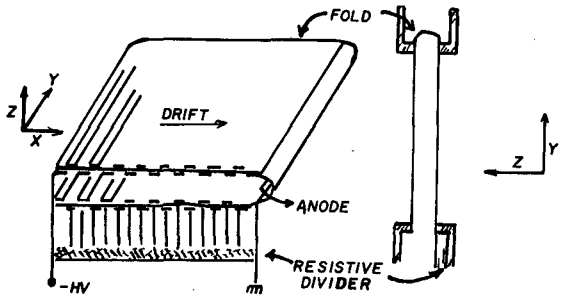


Fig. 1. Construction of a single wire proportional drift chamber. (LBL 778-1639)

The negative end of the drift region is terminated with a metallic strip tied to the high voltage end of the resistor network. The opposite end is closed by a half-cylinder cathode at ground potential and a 20μ anode wire stretched along the axis of the cylinder. A positive 1400 V bias is multiplexed through the amplifier to the anode.

Each chamber is 6-mm thick and a 6-mm space between adjacent chambers is sufficient to stand off the 5 kV worst case potential difference. Chambers 1 and 2 have an active area of 15 cm x 15 cm, 3 and 4 are 12 cm and 5 and 6 are 9 cm. Each chamber is rotated 90° from the previous one. All six chambers are mounted in one machined aluminum housing with 0.005-in. Be-Cu windows front and rear. Since each x-y pair of chambers is a different size, three high voltage feedthrough connectors are required to bias the drift fields. Six anode connections plus a floating ground lead make a total of 10 vacuum feedthroughs. These connectors plus the O-ring seals for the removable front and rear windows of the chamber housing exhibit a combined lead rate of $<10^{-5}$ cc per second. Over the three year expected life of this mission, approximately 900 cc of gas (we use 90% Argon, 10% methane) must be supplied to maintain a fixed chamber pressure (nominally 1.1 atm). A simple two-valve regulator system with an 80 cc x 500 psi reservoir tank should serve for $\sim$ 10 days.

## Electronics

The downfall of multiwire chambers in heavy-ion work is delta-rays. If the discriminators are sensitive enough to detect the lower Z cosmic rays, they are also able to trigger on the multitude of low energy electrons produced in the window and gas by heavier particles. By having only one anode wire in a chamber, it is possible to preview the entire frame of signals from one event and, in real time, set the discriminator to just the right level to pick off the core ionization and not the surrounding delta-rays. The anode avalanche gain must be low enough to keep even the largest heavy-ion signals from saturating.

The amplifier, discriminator chain shown in Fig. 2 has a minimum threshold of 0.02 picocoulombs. By operating with very low gas gain ($\sim 10^4$) minimum ionizing charge 1's produce 0.04 pc while slow iron ions can produce as much as 80 pc. The second stage in Fig. 2 compresses this dynamic range to a more reasonable 200:1. The pulse is then fed to a peak detecting integrator (A4) and through a 4 microsecond delay line (the longest drift time is 3.5μS). The outputs of the integrating amplifier and the delay line are compared by A5 whose output is a logic pulse used to stop a time-to-digital converter. The decay time constant of the peak detector is chosen such that after 4μS, the comparator sees a threshold (at the - input) of 50% of the fast pulse height arriving from the delay line (+ input). Due to the log-compression, this corresponds to a 50% constant fraction discrimination for small pulses while for large pulses, the threshold is closer to 20% of the total charge.

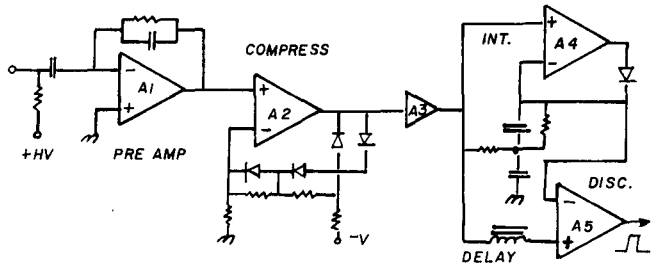


Fig. 2. Signal processing electronics.
(LBL 778-1640)

The time-digitizer is a standard ramp-down-gated clock-ripple counter type with nine bits to cover the range of drift times (0 to 4μS for the largest chamber, 0 to 2μS for the smallest). Since the discriminators introduce less than one channel of jitter for all but the smallest pulses, the electronic resolution is, therefore, 15 cm/512 = 300 μ for the large chambers, 230 μ for the medium size, and 170 μ for the small ones.

## Test Results

Monte Carlo calculations have been performed to aid in the design of the electronics and predict the ultimate performance of the entire system. The 1000 events of several particle species from protons through iron have been Monte Carlo's looking at the energy deposited by the primary ion and all secondary electrons in each quantum of drift path length (defined by the time-digitizing electronics). The effect of the compressor circuit and the peak detecting integrator were folded in to allow an absolute resolution calculation.

These calculations predict:

1. Very low charge particles can occasionally produce delta-rays whose signal is greater than that of the primary ion.

2. The worst case will occur around Z=6 where the angular resolution will be 0.22° using all 6 chambers to find the best straight line fit.

3. For heavy ions (Z > 10), the core ionization will be very large while the maximum delta-ray signals have already plateaued, providing improved resolution, typically 0.1°.

Bench tests of the chambers using a collimated β-source and a scintillator confirm that the chambers have uniform efficiency and constant drift velocity over the entire active area.

The complete flight instrument was tested in March 1977 using a carbon beam from the Bevalac. Preliminary analysis of the data from that run confirms the chamber's uniformity of response and the observed angular resolution is consistent with that anticipated by the Monte Carlo calculations.

Remembering that the six chambers are oriented to measure +x, +y, -x, -y, +x, +y, Fig. 3 is a scatter plot of Tanθ vs x where Tanθ is calculated from chambers 2 and 6 only and x is taken from chamber 5. Clearly the crossed electric fields from adjacent chambers are well isolated. Fig. 4 also uses chambers 2 and 6 only, this time demonstrating the angular resolution's independence on incident angle. Improved accuracy can be expected when all six measurements are combined to determine the angle.

## Footnote and References

* Space Sciences Laboratory, University of California, Berkeley, CA 94620.

1. D. Greiner et al., Mass Resolution of a Particle Identifier to be Flown on ISEE-C, 15th International Cosmic Ray Conference, Plovdiv, Bulgaria.

2. S. H. Morgan et al., Secondary Electron Background Produced by Heavy Nuclei in a Multiwire Proportional Counter Hodoscope, NASA Report, TN D-7591.

3. J. Saudinos et al., Nucl. Instrum. and Meth., 77 (1973).

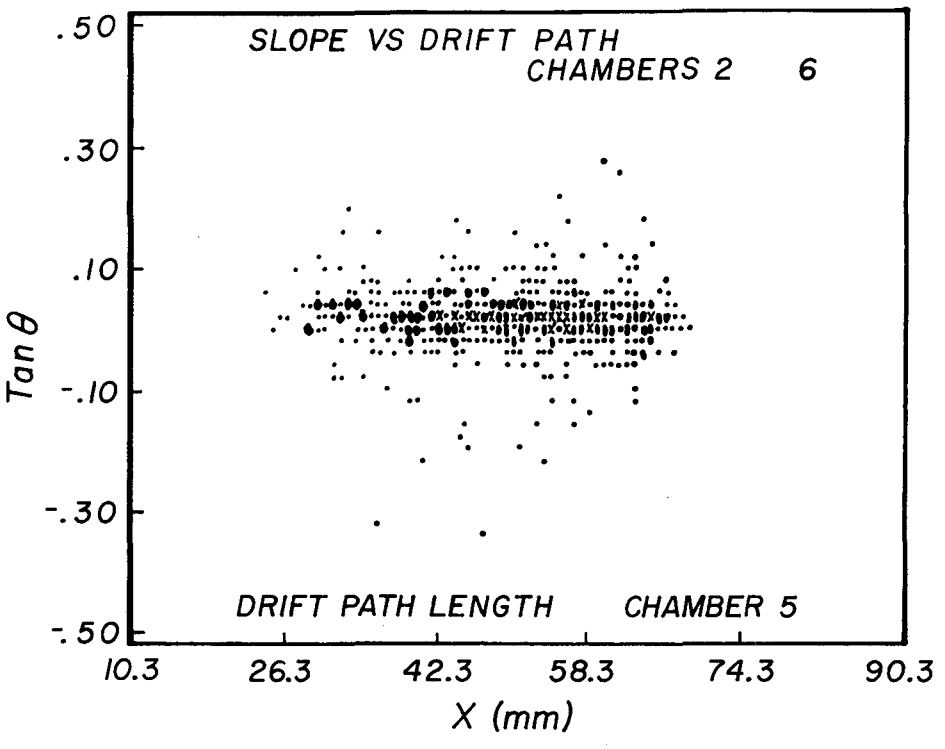


Fig. 3. Tan θ vs x for carbon beam at 0°.
(LBL 778-1641)

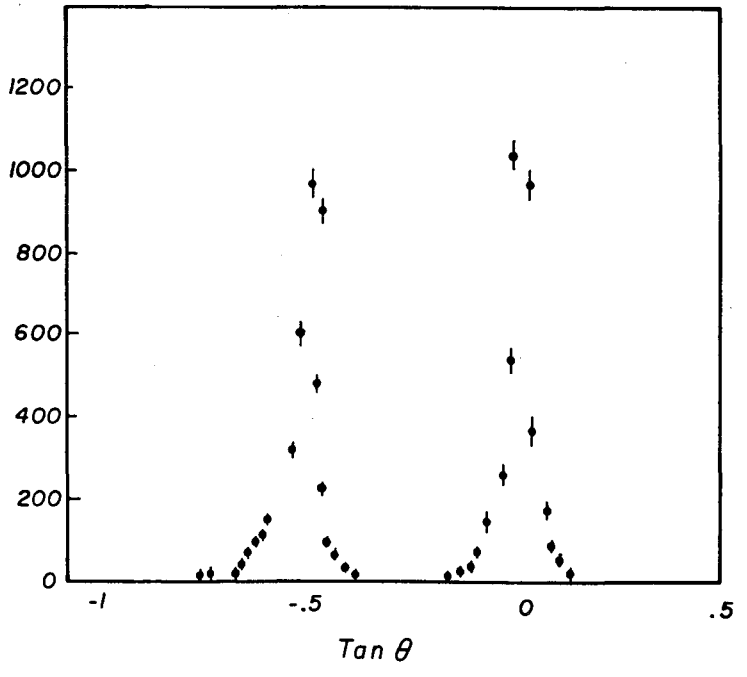


Fig. 4. Histograms of Tan θ for carbon beams at 0° and 30°. (LBL 778-1642)

# A CHEMIST'S GAMMA-RAY TABLE*

I. Binder,† R. Kraus,‡ R. Klein,§ D. Lee, and M. M. Fowler†

A gamma-ray energy and intensity table has been prepared for use in the identification and yield determination of nuclides contained in samples obtained in radiochemical and nuclear chemical experiments. The primary use for this table has been the role it plays in the computer-aided analysis of gamma-ray spectra.[1,2]

Because of the practical limitations inherent in the experiments for which the list was originally intended, the following three criteria were applied for the acceptance of an entry:

1. The half life of the nuclide must be at least five minutes, or else it must be the daughter of such a qualifying parent;
2. The abundance of the gamma ray must be at least one half of one per cent;
3. The energy of the gamma ray must be greater than 90 keV.

X-rays were normally not included because a sample will usually contain a mixture of isotopes for any one element. The above conditions greatly trimmed the list which leads to easing the identification process, increasing the chances of a proper identification, decreasing the amount of computer storage necessary to contain the data and lessening of computer expenses. These are accomplished with very little loss in capability. In some cases, gamma rays with intensities greater than one-half per cent were not included when numerous additional gamma rays with greater abundance existed for the same nuclide and the half life was such that it would be unlikely that an overwhelming amount of that nuclide would be observed in a sample. In cases where a parent nuclide has a half life significantly longer than that of the daughter, the gamma rays of the daughter are often included as also originating from the parent.

The energy table includes for each entry the element symbol, mass number, atomic number, half life and information about which chemical sample should contain the element when a particular chemical separation scheme is used.[3] If only the relative gamma-ray abundance is known, that is so indicated by an asterisk following the abundance value. An unknown abundance is given the value -0. Additional information is contained concerning the nuclide's parents (a maximum of three). Again, such data are included if the parental half life is adequately long and the feeding from the parent is significantly large.

The sources for this material were primarily compilations of similar data.[4-12]. Constant updating from the current literature has contributed to the list. More meaningful experimental results require knowledge of the absolute abundances of gamma rays. Appropriate calculations and/or judgements based on published data often enabled making such determinations or estimations.

The information has been encoded for computer use and storage. Computer programs have been written to permit editing the energy-sorted list and to produce from the energy source list a table of gamma rays sorted by nuclide.

The energy table contains 9299 energy entries.

## Footnotes and References

*Based on LBL-6515.

†Current address: Los Alamos Scientific Laboratory, Los Alamos, NM 87545.

‡Current address: Oregon State University, Corvallis, OR 97331.

§Current address: University of California-San Francisco, San Francisco, CA 94143

1. I. Binder et al., LBL-2366, 451 (1974).

2. M. M. Fowler et al., LBL-4000, 395 (1975).

3. J. V. Kratz, J. O. Liljenzin, G. T. Seaborg, Inorg. Nucl. Chem. Lett. 10, 951 (1974).

4. Nuclear Data, B1-B2 (1966-68).

5. Nuclear Data Sheets, B3-B8 and 9-19 (1969-76).

6. J. Blachot, R. deTourreil, J. Radioanal. Chem. 11, 351 (1972).

7. W. W. Bowman, K. W. MacMurdo, Atomic Data and Nuclear Data Tables 13, 89 (1974).

8. P. M. Endt, C. van derLeun, Nucl. Phys. A 214, 1 (1973).

9. G. Erdtmann, W. Soyka, J. Radioanal. Chem. 26, 375 (1975); J. Radioanal. Chem. 27, 137 (1975).

10. C. M. Lederer, J. M. Hollander, I. Perlman, Table of Isotopes, sixth ed. Wiley (New York, 1967).

11. N. E. Holden, F. W. Walker, Chart of the Nuclides, eleventh ed., General Electric Co. (1972).

12. Unpublished data from LBL Table of Isotopes group.

# DIVACANCY-HYDROGEN COMPLEXES IN DISLOCATION-FREE HIGH-PURITY GERMANIUM*

E. E. Haller, G. S. Hubbard, W. L. Hansen, and A. Seeger†

A defect center with a single acceptor level at $E_V$ + 0.08 eV (Ref. 1) appears in $H_2$-grown dislocation-free high-purity germanium (Figs. 1 and 2). Its concentration changes reversibly upon annealing up to 650° K (Fig. 3). By means of Hall-effect and conductivity measurements over a large temperature range the temperature dependence of the steady-state concentration between 450°K and 720°K as well as the transients following changes in temperature have been determined. The observed acceptor level is attributed to the divacancy-hydrogen complex $V_2H$. The complex reacts with hydrogen, dissolved in the Ge lattice or stored in traps, according to: $V_2H + H \rightleftarrows V_2H_2$. An energy level associated with the divacancy-dihydrogen complex was not observed. These results are in good agreement with the idea that hydrogen in germanium forms a "very deep donor" (i.e., the energy level lies inside the valence band).[2]

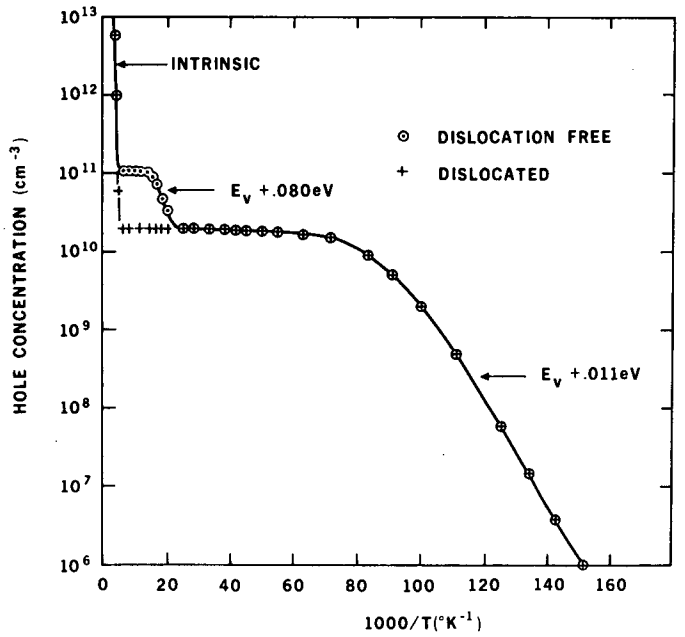


Fig. 1. Hole concentration vs reciprocal temperature 1/T of a dislocated and an undislocated Ge sample cut from the same crystal slice. The net-impurity concentration of shallow acceptors and donors is equal for both samples. The $E_V$ + 0.08 eV acceptor only appears in the dislocation-free piece; its concentration depends on the annealing temperature. (XBL 759-8019)

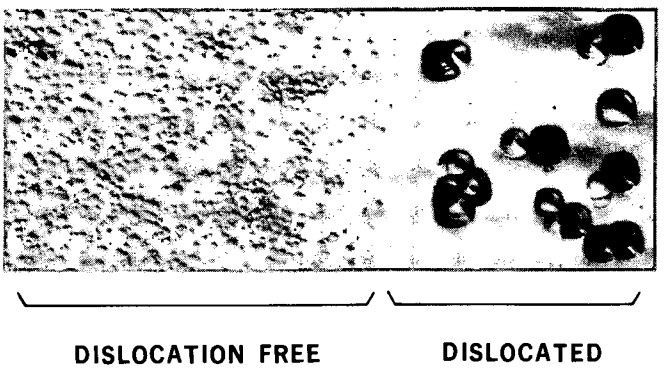


Fig. 2. Photograph of a partially dislocated <100> surface of a hydrogen-grown Ge crystal. The large etch pits with four-fold symmetry in the right half of the picture are due to dislocations. The hemispherical pits in the left half of the picture are attributed to vacancy and hydrogen complexes. (XBL 758-6503)

Our main findings may be summarized as follows:

1. The single acceptor at $E_V$ + 0.08 eV can only and always be found in hydrogen-grown dislocation-free high-purity germanium. This strongly suggests that this acceptor is related to a complex consisting of vacancies (V) and hydrogen (H). The divacancy-hydrogen complex ($V_2H$) is the most probably candidate.

2. The concentration of the acceptor is sensitive to annealing. A model based on the reaction $V_2H+H \rightleftarrows V_2H_2$ and on hydrogen trapping and detrapping at larger traps describes both the stationary concentration of the acceptor centre as well as the response to sudden temperature changes.

3. The model is supported further by (a) excellent correspondence between the energy levels of divacancy-donor complexes and the $V_2H$-centre and (b) the recently discovered complexes of hydrogen with multivalent acceptors (similar to multivalent acceptor-lithium complex formation).

Footnotes and References

*Condensed from LBL-4274.

†Max-Planck Institut für Metallforschung, Stuttgart, Germany.

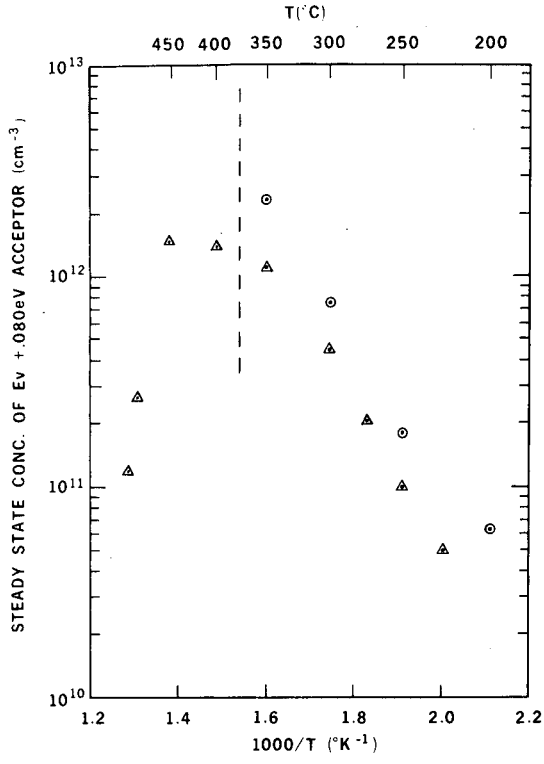


1. W. L. Hansen and E. E. Haller, IEEE Trans. Nucl. Sci. NS-21, 251 (1974).

2. J. Shy-Yih Wang and C. Kittel, Phys. Rev. B7, 713 (1973).

Fig. 3. Steady-state concentration of the $E_V$ + 0.08 eV acceptor of two dislocation-free samples. △ sample cut from center of a crystal (crystal ∅ = 35 mm). ⊙ sample cut near crystal surface. The error for each measurement point is of the order of 5 to 10% for the concentration and less than 2% for the temperature. The dashed line corresponds to $1.04 \cdot 10^{18} \exp(-0.71 \text{ eV}/kT)$ cm$^{-3}$. (XBL 767-8912)

## ION IMPLANTED N-TYPE CONTACT FOR HIGH-PURITY GERMANIUM RADIATION DETECTORS*

G. Scott Hubbard, Eugene E. Haller, and William L. Hansen

It is well known that non-injecting contacts on large-volume high-purity Ge radiation detectors can be reliably produced by using an evaporated metal Schottky barrier and a lithium diffused n+ contact.[1] The metal barrier is inherently thin (< 1000 Å), but in practice the lithium diffused contact cannot be made thinner than approximately 25 μm. When such a detector is radiation damaged[2] and requires annealing, the lithium diffuses even further into the Ge bulk, increasing the dead layer thickness.

For most applications, the lithium diffused contact is thin enough that alternatives have not been vigorously pursued, although some investigations have been published.[3] However, high-energy charged particle experiments utilizing Ge detector telescopes require n+ contacts which are thin (< 1 μm) and remain so upon annealing at moderate (< 420 K) temperatures.

Following the lines of earlier work[4] we have implanted phosphorous ions into high-purity Ge (both n and p type) at 25 keV. Beam current was held to approximately 1 μA/cm$^2$ to reduce sample heating and samples were implanted 8° off the crystal growth axis [100] to avoid channeling. Implant dose as well as pre- and post-implant treatment were varied. To minimize the end of range damage and prevent premature regrowth most samples were maintained at liquid nitrogen temperature (77 K) during implantation. A few implants were made with the samples hot (570 K) and at room temperature (300 K). The higher temperature implants resulted in diodes with excessive leakage for our application and were not investigated further.

The samples were annealed in an argon atmosphere with the temperature programmed to increase 10°/10 min from room temperature to 620 K. Recently we have also introduced a "pre-annealing" stage of 1 to 2 hr at 420 K before continuing to 620 K. In samples with high dose ($10^{16}$ cm$^{-2}$) it was necessary to anneal to 670 K to remove the "bluish" tinge apparently associated with an amorphous surface layer. After annealing, the samples were allowed to cool slowly (∿2°/min) to room temperature. The samples were then prepared and tested as radiation detectors.

$^{241}$Am alpha spectra (Fig. 1) show the influence of the "pre-annealing" stage and confirm that the contact is quite thin. Using the FWHM and equations given elsewhere one can calculate that 57 keV represents a layer of only 0.3 - 0.4 μm.

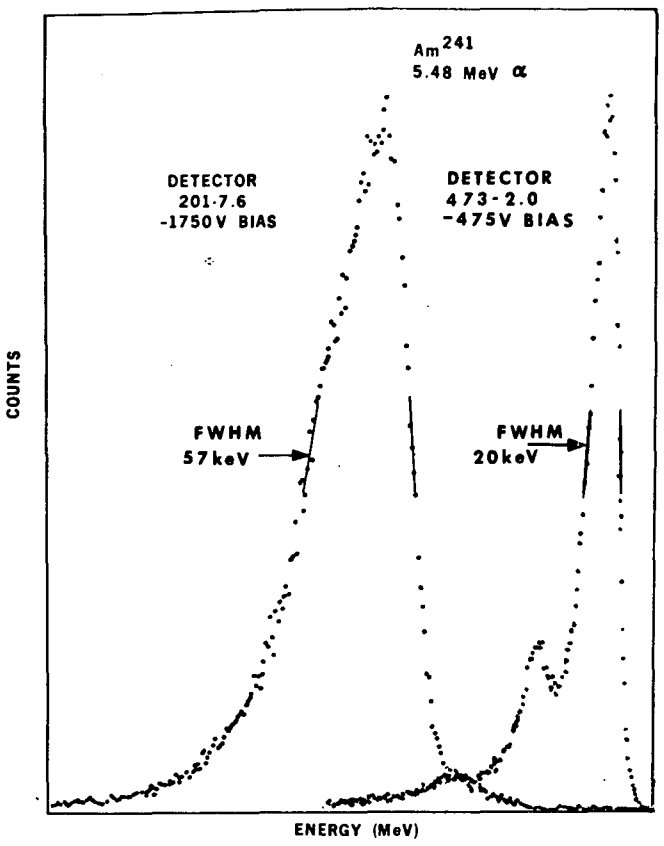


Fig. 1. 5.48 MeV alpha particles are passed through n+ contact. Detector 473-2.0 has been given an additional "pre-annealing" stage of 1-1/2 hours at 420 K. The shift in peak position is due to the difference in dead layer thickness. 20 keV represents a window of 0.3 to 0.4 μm.
(XBL 769-10494)

The latter result is in good agreement with published work on the depth vs concentration profile of phosphorous in Ge,[4] again suggesting that the "pre-annealing" has removed a substantial dead layer of additional damage.

We have demonstrated that phosphorous implantation is a usable technique for producing a thin, stable n+ contact on high-purity Ge radiation detectors. Present contacts appear to be limited by excess current injection at electric fields above ∿ 2000 V/cm but several possibilities for improved detector performance include: 1) lower temperature during implantation, 2) sputter etching before implantation, and 3) varied dose.

Footnote and References

*Condensed from LBL-5563.

1. R. H. Pehl, R. C. Cordi and F. S. Goulding, IEEE Trans. Nucl. Sci. NS-19, no. 1, 265 (1972).

2. H. W. Kraner, R. H. Pehl and E. E. Haller, IEEE Trans. Nucl. Sci. NS-22, No. 1, 149 (1975).

3. R. D. Baertsch and R. N. Hall, IEEE Trans. Nucl. Sci. NS-17, No. 3, 235 (1970).

4. J. P. Ponpon, J. J. Grob, R. Stuck, P. Burger and P. Siffert, Proc. of the II Int. Conf. on Ion Implantation-Semiconductors, Springer-Verlag, New York (1971).

## PHOTOELECTRIC SPECTROSCOPY OF RESIDUAL IMPURITIES IN ULTRA-PURE GERMANIUM AND SILICON*

Eugene E. Haller

Using photoelectric spectroscopy the residual impurities in a large number of ultra-pure germanium and some silicon single crystals were investigated.[1] Our Far Infrared Spectrometer consists of a Michelson Interferometer with an on-line computer and a helium cryostat with constant temperature option. The instrumental resolution is limited to ~ 0.15 $cm^{-1}$ (= 0.02 meV). With samples of ~ 1/10 $cm^3$ volume and net impurity concentrations of ~ $10^9$ $cm^{-3}$, high resolution spectra with signal-to-noise ratios > 100 can be obtained in minutes (Fig. 1).

Special attention was devoted to the formation of good electrical contacts to the samples since they strongly influence the signal-to-noise ratios. Various techniques using liquid and solid phase epitaxy, ion implantation and metal evaporation were investigated. Using IR spectroscopy together with Hall effect measurements, a systematic investigation of the group III and V impurities and their sources was possible. The dominant impurities in ultra-pure germanium are B, Al and P. The acceptors B and Al do not follow simple segregation behavior in germanium. This may be caused by these elements forming complexes with oxygen and possibly silicon. A number of hitherto undiscovered, hydrogenic acceptors and donors were found; several are due to impurity-impurity complexes (Table 1).

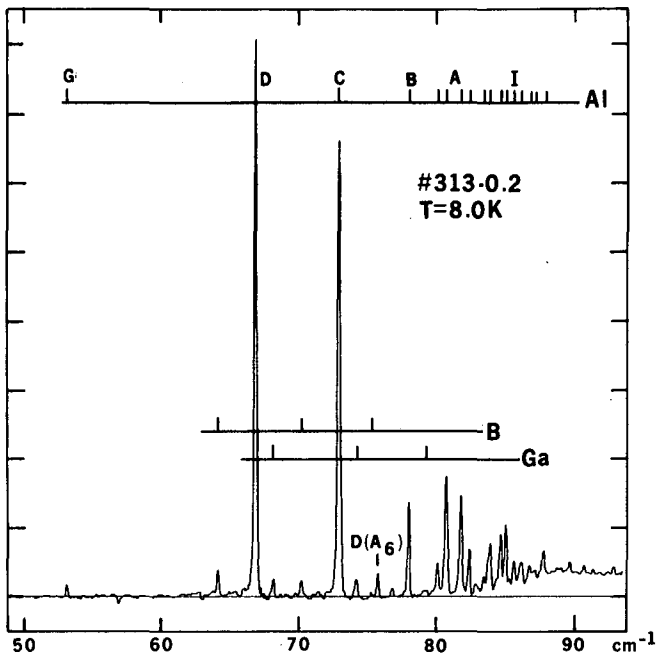


Fig. 1. Photoelectric spectrum obtained with a typical high purity Ge sample (#313-0,2), contact areas $B^+$-implanted = 8 x 8 $mm^2$, thickness = 8 mm; $N_A$-$N_D$ = $10^{10}$ $cm^{-3}$, instrumental resolution = 0.15 $cm^{-1}$.
(XBL 774-8313)

Table 1

| | | Ground state energy in meV | Line positions in $cm^{-1}$ ($\pm$0.01 $cm^{-1}$) | | | | | | |
|---|---|---|---|---|---|---|---|---|---|
| | | $E_{g.s.}$ (meV) | D | C | B | A | | | |
| "Quenched-in", hydrogen related acceptors | $A_1$ | 10.24 | 62.16±.03 | 68.03±.03 | | | | | |
| | $A_2$ | 11.31 | 70.85 | 76.89 | 82.00 | 83.99 | 84.71 | 85.78 | 86.38 |
| Nitrogen atmosphere, pyrolitic-graphite related acceptors | $A_3$ | 9.87 | 59.22 | 65.29 | - | - | - | - | - |
| | $A_4$ | 10.42 | 63.44 | 69.67 | 74.79 | 76.91 | 77.47 | 78.50 | 79.20 |
| | $A_5$ | 10.97 | 68.03 | 74.10 | 79.20 | 81.40 | 81.86 | - | - |
| Unknown acceptors | $A_6$ | 11.93 | 75.79 | 81.85 | 87.02 | 98.67 | 90.89 | 91.28 | |
| | $A_7$ | 10.66 | 65.57 | 71.68 | 76.82 | - | - | - | - |

Footnote and Reference

*Condensed from LBL-6431.

1. E. E. Haller and W. L. Hansen, Sol. State Comm. 158, 687 (1974).

# IMPURITY COMPLEX FORMATION IN ULTRA-PURE GERMANIUM*

E. E. Haller and G. S. Hubbard

Several unknown, hydrogenic acceptors and donors were recently discovered in ultra-pure germanium by photoelectric spectroscopy. These centers are not created by elemental impurities. Comparative analysis of a large number of crystals grown under various conditions lead to the conclusion that copper, a fast diffusing multivalent acceptor, together with lithium and/or hydrogen, is responsible for several of the unknown centers.[1] This is the first time that hydrogen has been recognized as playing the role of a donor pairing with an acceptor. Hall effect measurements complementing the photoelectric spectroscopy results lead to a tentative assignment of the following energy levels:

(Cu,Li) complexes: $E_V$ + 20.5 meV,*
$E_V$ + 25.0 meV,*
$E_V$ + 275 meV.

(Cu,H) complexes: $E_V$ + 17.0 meV,*
$E_V$ + 17.5 meV,
$E_V$ + 175 meV.

*Hydrogenic acceptor.

Photoelectric spectra are shown in Figs. 1 and 2.

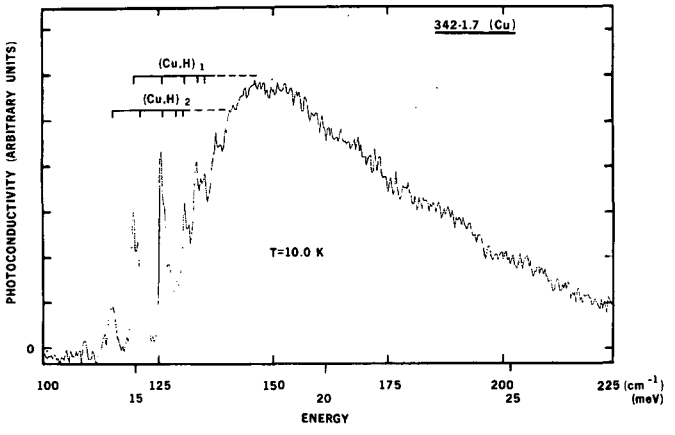


Fig. 1. Photoelectric spectrum of the hydrogen-grown Ge-sample 342 - 1.7 (Cu). Sample size: 7 x 7 x 1.5 mm$^3$. The hydrogenic series belong to acceptors at $E_V$ + 17.0 meV and $E_V$ + 17.5 meV that are due to complexes between Cu and H. (XBL 774-8314)

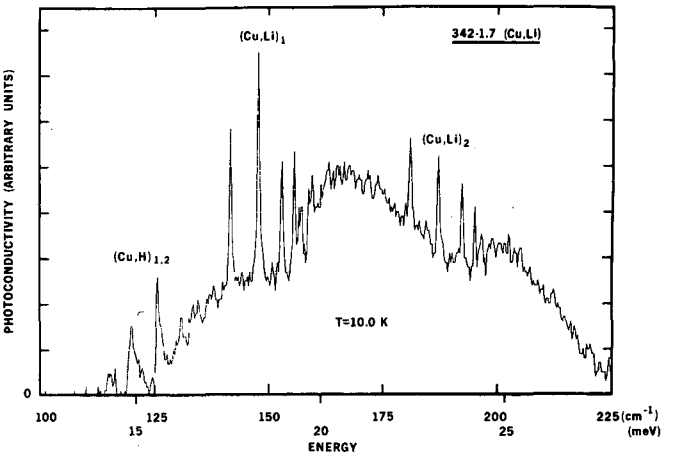


Fig. 2. Photoelectric spectrum of the same sample as in Fig. 1, but with a limited amount of lithium added. The hydrogenic (Cu, $Li_1$) series is created by an acceptor at $E_V$ + 20.5 meV and is believed to be due to a complex involving Cu, H and Li. The hydrogenic (Cu, $Li)_2$ series is due to an acceptor at $E_V$ + 25.0 meV and only involves Cu and Li. (XBL 774-8315)

## Footnote and Reference

*Condensed from LBL-6432.

1. P. LoVecchio, Lithium-Multivalent Acceptor Interaction in Germanium, Thesis, Syracuse University, University Microfilms No. 72-20, 352 (1972).

# CONFIGURATION-MIXED-SHELL-MODEL RELATIVE-ALPHA-DECAY-RATE CALCULATIONS FOR SPHERICAL DOUBLY ODD NUCLEI ($^{212}$At AND $^{212}$At$^{m}$)*

Hafez M. A. Radi,† A. A. Shihab-Eldin,† and J. O. Rasmussen

There has been but little theoretical α-decay rate work on odd-odd nuclei. It is generally recognized that the decay may be grouped into three categories: favored, in which the orbitals and coupling of odd protons and odd neutrons remain unchanged; once hindered, in which the orbitals of one odd nucleon remain unchanged and the other changes; and twice hindered, in which the orbitals of both odd nucleons change.

Favored decay should proceed at a rate comparable to ground decay of even-even neighbors. Twice-hindered α decay will not be considered in this paper; finite-size α theoretical calculations of the twice-hindered α decay of the $^{210}$Bi isomers have been made by Tuggle.[1] We are concerned here with once-hindered decay of odd-odd nuclei. With the extensive configuration mixing and with the substantial angular momentum algebra the finite-size α theory involves rather formidable calculations. Thus, we have chosen to explore the problem first with zero-size α theory. Eventually, Fliessbach's renormalized theory should be applied.

Recently, Shihab-Eldin, Jardine and Rasmussen,[2] (hereafter denoted SJR) have extended the zero-size approximation method to calculate α-decay rates for odd-odd nuclei using graphical presentation techniques. Relative $^{210}$At decay rates were found to be in qualitative agreement with experimentally measured values. The discrepancies were ascribed to mixing in daughter and parent wavefunctions, but shell-model theoretical $^{206}$Bi wavefunctions were not available to test the approach in more detail. We apply the same techniques to the α decay of $^{212}$At and $^{212}$At$^{m}$ to levels in $^{208}$Bi using mixed wave functions which have been calculated by shell-model theory. The structure of the low-lying states of $^{208}$Bi has been calculated in terms of mixed 1p-1h shell-model configurations by different authors.[3-5] The structure of $^{212}$At has not been calculated yet, but we assume as a first approximation that the structure of $^{212}$At is the same as $^{210}$Bi plus two protons in the $h_{9/2}$ orbital coupled to zero.[4-7]

By definition of the reduced width $\gamma_L^2$, the Lth partial decay rates are given by:[8]

$$\lambda_L = \frac{2\gamma_L^2}{\hbar} P_L \quad , \tag{1}$$

where the penetration factor, $P_L$, is given by

$$P_L = \left. \frac{\rho}{G_L^2 + F_L^2} \right|_{r=R_o} ,$$

and where $G_L$ and $F_L$ are the irregular and regular Coulomb functions, respectively; $\rho = kr$, where k denotes the wavenumber of the α particle in the asymptotic region. For mixed parent and daughter wavefunctions, the Lth partial decay rate could be written as

$$\lambda_L = \frac{2}{\hbar} \left( \sum_{\mu\nu} \alpha_\mu \beta_\nu \gamma_L^{\mu\nu} \right)^2 P_L \quad , \tag{2}$$

where $\alpha_\mu$ and $\beta_\nu$ are the amplitudes of the different configurations of the parent and daughter nuclei. The important parent and daughter shell-model configurations for states of interest (low lying) will be briefly discussed in this section. In general, the transitions between $^{212}$At and $^{208}$Bi configurations can be classified into three groups. Symbolically, using SJR notation, the first group

$$[\pi(1h_{9/2})^3_{9/2}\ \nu(\rho_3)^1_{j_3} \rightarrow [\pi(1h_{9/2})^1_{9/2}\ \nu(\rho_4)^2_{j_4}]^{j_4} + \alpha$$

can be written as (after using similar techniques to SJR and substituted into $\gamma_L$)

$$\gamma_L = C \left[ \binom{3}{2}\binom{1}{1}\binom{2j_4+1}{1} \right]^{1/2} \sum_{\substack{J_P=0 \\ \text{(even)}}}^{9} \sum_{\substack{J_N = |j_3-j_4| \\ \text{(odd)}}}^{j_3+j_4} (-1)^{j_3+j_4+j_N} b_{9/2\ 9/2\ J_P^3} R_1 R_2 R_3 R_4 (\hat{J}_P^i \hat{J}_N^i \hat{J}_d \hat{J}_\alpha \hat{J}_N)^{1/2} \begin{Bmatrix} j_4 & j_3 & J_N \\ J_N^i & j_4 & 0 \end{Bmatrix}$$

$$\times \begin{Bmatrix} J_p^d = \frac{9}{2} & J_P & J_P^i = \frac{9}{2} \\ J_N^d = j_4 & J_N & J_N^i = j_3 \\ J_d & J_\alpha & J_i \end{Bmatrix} G(J_P, J_N, J_\alpha) \tag{3}$$

$$\times F[\ell_1(=5), \ell_2(=5), j_1(=\tfrac{9}{2}), j_2(=\tfrac{9}{2}), J_P] F(\ell_3, \ell_4, j_3, j_4, J_N) \quad ,$$

where

$$C = \left(\frac{\hbar R_0}{2M}\right)^{1/2} \left(\frac{4\pi S_\alpha}{3}\right)^{3/2} ,$$

$$G(J_P,J_N,J_\alpha) = (2J_P + 1)^{1/2}(J_\alpha J_P 00|J_N 0),$$

$$F(\ell_1,\ell_2,j_1,j_2,J) = (-1)^{\ell_1} [1 - 0.013\ell_1(\ell_1 + 1)] \times [1 - 0.013\ell_2(\ell_2 + 1)]^{1/2}(2j_1 + 1)^{1/2} \times (Jj_i 0 - \tfrac{1}{2}|j_2 - \tfrac{1}{2}) ,$$

and where $R_i$ is the value of the nucleon radial wavefunction evaluated at $R_0$ for nucleon i. Proceeding as before, we find the second group

$$[\pi(1h_{9/2})_0^2\ \pi(\rho_1)^1_{j_1}\ \nu(\rho_3)^1_3] \rightarrow [\pi(\rho_1)^1_{j_1}\ \nu(\rho_4)^{2j_4}_{j_4}] + \alpha ,$$

can be written as

$$\gamma_L = C\left[\binom{2}{2}\binom{1}{1}\binom{2j_4+1}{1}\right]^{1/2} \sum_{\substack{J_N=|j_3-j_4| \\ \text{(odd)}}}^{j_3+j_4} (-1)^{j_3+j_4+J_N} R_1R_2R_3R_4(\hat{J}_P^i\hat{J}_N^i\hat{J}_d\hat{J}_\alpha\hat{J}_N)^{1/2} \begin{Bmatrix} j_4 & j_3 & J_N \\ J_N^i(=j_3) & j_4 & 0 \end{Bmatrix} \times \begin{Bmatrix} J_P^d(=j_1) & 0 & J_P^i(=j_1) \\ J_N^d(=j_4) & J_N & J_N^i(=j_3) \\ J_d & J_\alpha & J_i \end{Bmatrix} G(0,J_N,J_\alpha) \times F[\ell_1,\ell_2(=5),j_1,j_2(=\tfrac{9}{2})0]F(\ell_3,\ell_4,j_3,j_4,J_N). \quad (4)$$

Finally, the third group,

$$[\pi(\rho_2)_0^2\ \pi(\rho_1)^1_{j_1}\ \nu(\rho_3)^1_{j_3}] \rightarrow [\pi(\rho)^1_{j_2}\ \nu(\rho_4)^{2j_4}_{j_4}] + \alpha ,$$

(doubly hindered) is

$$\gamma_L = C\left[\binom{2}{2}\binom{1}{1}\binom{2j_4+1}{1}\right]^{1/2} \times \sum_{\substack{J_P=|j_1-j_2| \\ \text{(even)} \\ \text{(odd)}}}^{j_1+j_2} \sum_{\substack{J_N=|j_3-j_4| \\ \text{(odd)} \\ \text{(even)}}}^{j_3+j_4} (-1)^{j_1+j_2+j_3+j_4+J_P+J_N} R_1R_2R_3R_4(\hat{J}_P^i\hat{J}_N^i\hat{J}_d\hat{J}_\alpha\hat{J}_P\hat{J}_N)^{1/2} \begin{Bmatrix} j_2 & j_1 & J_P \\ J_P^i(=j_1) & j_2 & 0 \end{Bmatrix} \times \begin{Bmatrix} j_4 & j_3 & J_N \\ J_N^i(=j_3) & j_4 & 0 \end{Bmatrix} \begin{Bmatrix} J_P^d(=j_2) & J_P & J_P^i(=j_1) \\ J_N^d(=j_4) & J_N & J_N^i(=j_3) \\ J_d & J_\alpha & J_i \end{Bmatrix} G(J_P,J_N,J_\alpha) \times F(\ell_1,\ell_2,j_1,j_2,J_P)F(\ell_3,\ell_4,j_3,j_4,J_N). \quad (5)$$

We used the formulation given in the previous section to calculate the relative α-decay rates from $^{212}$At and $^{212}$At$^m$ ($J^\pi = 1^-$ and $9^-$, respectively) to the $5^+_1$, $4^+_1$, $6^+_1$, $4^+_2$, $5^+_2$, $3^+_1$, $7^+_1$, $5^+_3$, $2^+_1$, $3^+_2$, $4^+_3$, $4^+_4$, $3^+_3$, and $6^+_2$ states of $^{208}$Bi. The radial nucleon wave functions were taken from Blomqvist and Wahlborn.[9] The eigenfunctions obtained by Kim and Rasmussen (KR),[3,8] Ma and True (MT),[5] and Kuo and Herling (KH)[4] were used for these states.

In Tables 1 and 2 are given the calculated α-decay rates of the two isomeric states of $^{212}$At to the first 14 states of $^{208}$Bi. The last column gives the experimental percentages of α branching as measured by Reeder.[10] The theoretical relative intensities are normalized to the most intense α group in each case.

For all sets of wavefunctions the radii were varied from 7.0 to 9.5 fm to search for the best fits between the experimental and the calculated values. However, we only tabulate results for $R_0$ equal to 8.0 fm for all cases, except for KR and KH wavefunctions for the $1^-$ where we give the results for $R_0$ = 7.5 fm. Figure 1 plots some theoretical relative intensities for various assumed channel radii $R_0$, and some idea of the general fit and the dependence of results on the assumed channel radius can be gained. The dramatic disagreement for $4^+_4$ and $3^+_2$ decay, for which no set of wavefunctions gives agreement, is evident.

On the basis of α-decay calculations it is not possible to point to clear superiority of one or another of the shell-model wavefunctions tested. The KR wavefunctions work the best for $1^-$ decay, but the MT are best for $9^-$ decay. With this uncertainty it is worth reviewing what other tests can be made of the wavefunctions. Kim and Rasmussen tested their $1^-$ wavefunction for β decay of $^{210}$Bi and were able to explain the anomalous features. They argued that the off-diagonal elements of the tensor force were essential to give the correct sign of configuration mixing of $h_{9/2}i_{11/2}$ into the dominant $h_{9/2}g_{9/2}$. Indeed, the KR wavefunction differs in this phase from MT, who used no tensor force, and from Kuo, who used core polarization as well as tensor. Perhaps this sign difference is significant in α decay as well as β decay, though the poorer agreement of KR for the $9^-$ decay precludes singling out this phase factor as significant.

Table 1. Comparison between the calculated relative α-decay intensities of $^{212}$At and the experimental results.

| Parent Spin = $1^-$ | | | | | | |
|---|---|---|---|---|---|---|
| | | Theoretical Relative Intensities for Various Wave Functions | | | | |
| Daughter States $J^\pi$ | Main Configuration | Pure Parent and Daughter | Kim and Rasmussen[a] | Ma and True[b] | Kuo and Herling[c] | Exp. (%)[d] Reeder |
| $5_1^+$ | $h_{9/2}p_{1/2}^{-1}$ | 80.9 | 80.9 | 80.9 | 80.9 | 80.900±0.80 |
| $4_1^+$ | $h_{9/2}p_{1/2}^{-1}$ | 242.4 | 16.8 | 333.4 | 32.3 | 17.00±0.50 |
| $6_1^+$ | $h_{9/2}f_{5/2}^{-1}$ | 1.31 | 0.23 | 0.24 | 0.15 | 0.26±0.06 |
| $4_2^+$ | $h_{9/2}f_{5/2}^{-1}$ | 3.11 | 0.62 | 3.03 | 0.86 | 0.63±0.06 |
| $5_2^+$ | $h_{9/2}f_{5/2}^{-1}$ | 0.02 | 0.55 | 1.2 | 0.34 | <0.4 |
| $3_1^+$ | $h_{9/2}f_{5/2}^{-1}$ | 0.26 | 1.00 | 1.4 | 0.01 | 0.50±0.08 |
| $7_1^+$ | $h_{9/2}f_{5/2}^{-1}$ | 0.09 | 0.10 | 0.15 | 0.13 | <0.1 |
| $5_3^+$ | $h_{9/2}p_{3/2}^{-1}$ | 0.13 | 0.03 | 0.07 | 0.09 | 0.26±0.03 |
| $2_1^+$ | $h_{9/2}f_{5/2}^{-1}$ | 0.70 | 0.14 | 0.59 | 0.59 | 0.04±0.03 |
| $3_2^+$ | $f_{7/2}p_{1/2}^{-1}$ | 0.0 | 0.6E-5 | 0.004 | 0.013 | 0.12±0.03 |
| $4_3^+$ | $h_{9/2}p_{3/2}^{-1}$ | 0.005 | 0.03 | 0.80 | 0.12 | 0.06±0.02 |
| $4_4^+$ | $f_{7/2}p_{1/2}^{-1}$ | 0.0 | 0.6E-4 | 0.001 | 0.0003 | 0.05±0.02 |
| $3_3^+$ | $h_{9/2}p_{3/2}^{-1}$ | 0.18 | 0.10 | 0.17 | 0.15 | 0.15±0.01 |
| $6_2^+$ | $h_{9/2}p_{3/2}^{-1}$ | 0.014 | 0.001 | 0.08 | 0.006 | <0.02 |

[a]References 3 and 6 [b]Reference 5 [c]Reference 4 [d]Reference 10

Table 2. Comparison between the calculated relative α-decay intensities of $^{212m}$At and the experimental results.

| Parent Spin = $9^-$ | | | | | | |
|---|---|---|---|---|---|---|
| | | Theoretical Relative Intensities for Various Wave Functions | | | | |
| Daughter States $J^\pi$ | Main Configuration | Pure Parent and Daughter | Kim and Rasmussen[a] | Ma and True[b] | Kuo and Herling[c] | Exp. (%)[d] Reeder |
| $5_1^+$ | $h_{9/2}p_{1/2}^{-1}$ | 39.4 | 19.3 | 31.6 | 42.2 | 29.00±0.30 |
| $4_1^+$ | $h_{9/2}p_{1/2}^{-1}$ | 67.3 | 67.3 | 67.3 | 67.3 | 67.30±1.00 |
| $6_1^+$ | $h_{9/2}f_{5/2}^{-1}$ | 0.85 | 1.65 | 0.97 | 0.99 | 0.65±0.07 |
| $4_2^+$ | $h_{9/2}f_{5/2}^{-1}$ | 0.07 | 0.16 | 0.18 | 0.15 | 0.11±0.03 |
| $5_2^+$ | $h_{9/2}f_{5/2}^{-1}$ | 0.34 | 0.12 | 0.83 | 0.47 | 0.53±0.04 |
| $3_1^+$ | $h_{9/2}f_{5/2}^{-1}$ | 0.11 | 0.07 | 0.12 | 0.12 | <0.40 |
| $7_1^+$ | $h_{9/2}f_{5/2}^{-1}$ | 0.77 | 0.62 | 0.78 | 0.67 | 0.61±0.11 |

Table 2 (continued).

| Parent Spin = $9^-$ | | | | | | |
|---|---|---|---|---|---|---|
| | | Theoretical Relative Intensities for Various Wave Functions | | | | |
| Daughter States $J^\pi$ | Main Configuration | Pure Parent and Daughter | Kim and Rasmussen | Ma and True | Kuo and Herling | Exp. (%) Reeder |
| $2_1^+$ | $h_{9/2}^{-1} f_{5/2}$ | 0.003 | 0.003 | 0.001 | 0.004 | <0.02 |
| $3_2^+$ | $f_{7/2}^{-1} p_{1/2}$ | 0.0 | 0.6E-5 | 0.4E-4 | 0.3E-4 | <0.02 |
| $4_3^+$ | $h_{9/2}^{-1} p_{3/2}$ | 0.02 | 0.01 | 0.04 | 0.05 | 0.16±0.1 |
| $4_4^+$ | $f_{1/2}^{-1} p_{1/2}$ | 0.0 | 0.3E-4 | 0.3E-3 | 0.1E-3 | <0.1 |
| $3_3^+$ | $h_{9/2}^{-1} p_{3/2}$ | 0.0002 | 0.7E-3 | 0.1E-3 | 0.1E-3 | <0.03 |
| $6_2^+$ | $h_{9/2}^{-1} p_{3/2}$ | 0.22 | 0.20 | 0.27 | 0.28 | 0.19±0.12 |

[a]References 3 and 6 [b]Reference 5 [c]Reference 4 [d]Reference 10

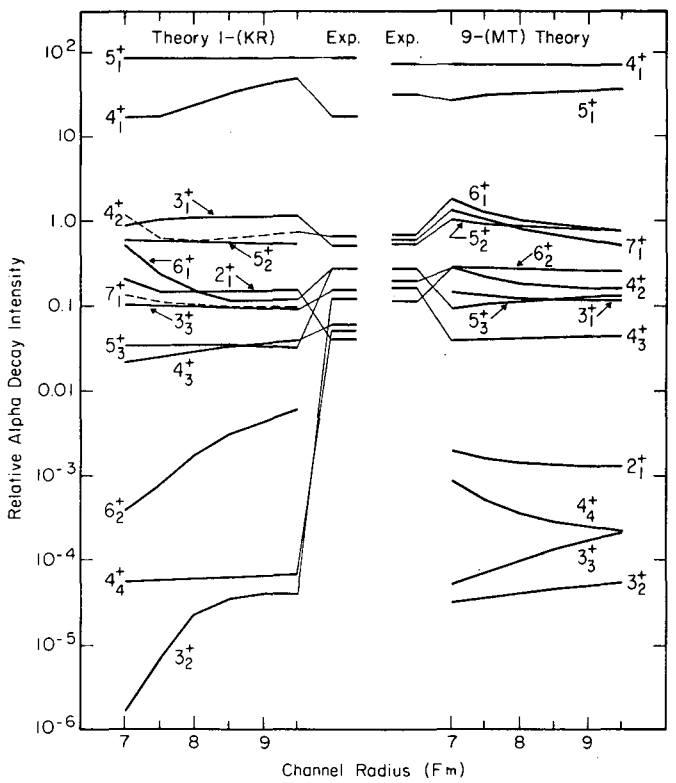


Fig. 1. Comparison of theoretical and experimental α-decay ratios as a function of assumed channel radius. On the left are results for the $^{212}$At ground-state decay with Kim-Rasmussen wavefunctions. On the right are results for the $^{212}$At$^m$ isomeric state decay with Ma-True wavefunctions.
(XBL 769-10549)

## Footnotes and References

*Condensed from Phys. Rev. C 15, 1917 (1977).

†Physics Department, Kuwait University, Kuwait and Nuclear Science Division, Lawrence Berkeley Laboratory, University of California, Berkeley, California 94720.

1. D. Tuggle, Ph.D. thesis, Univ. of Calif., Berkeley, 1976 (unpublished).

2. A. A. Shihab-Eldin, L. J. Jardine, and J. O. Rasmussen, Nucl. Phys. A 244, 435 (1975).

3. Y. E. Kim and J. O. Rasmussen, Phys. Rev. 135, B44 (1974).

4. T. T. S. Kuo, Nucl. Phys. A 122, 325 (1968); T. T. S. Kuo and G. M. Herling, Naval Research Laboratory Memorandum Report No. 2258 (Washington, D. C.) March 1971 (unpublished).

5. C. W. Ma and W. W. True, Phys. Rev. C 8, 2313 (1973), and private communication.

6. Y. E. Kim and J. O. Rasmussen, Nucl. Phys. 47, 184 (1963); Errata 61, 173 (1965).

7. G. H. Herling and T. T. S. Kuo, Nucl. Phys. A 181, 113 (1972).

8. J. O. Rasmussen, Nucl. Phys. 44, 93 (1963).

9. J. Blomqvist and S. Wahlborn, Ark. Fys. 16, 545 (1960).

10. P. L. Reeder, Phys. Rev. C 1, 721 (1970).

# IV.

# THESIS ABSTRACTS

## A RADIOCHEMICAL STUDY OF THE REACTIONS OF HEAVY IONS WITH GOLD

Irwin Binder

(LBL-6526)

Thick gold foils have been bombarded with heavy-ion projectiles at energies above the Coulomb barrier. The radioactive products were identified and their yields measured using gamma-ray spectrometry and an extensive series of computer programs developed for the data analysis. The total mass-yield distribution was extracted from the data using charge-dispersion curves inferred from the experimental results.

One observes a change in the mass-yield distributions corresponding to primarily fusion-fission tractions occurring with the lighter projectiles Ne-20 and Ar-40 and deep-inelastic transfer reactions predominating with heavier Kr-84, Kr-86 and Xe-136 projectiles.

For the deep-inelastic transfer reaction, more mass transfer is seen to occur for a higher incident projectile energy, and the Gaussian distribution of products shows exponential tailing. The preferred direction for mass transfer is from gold to the projectile nucleus. Sequential fission is a likely fate for nuclides beyond the lead shell closure. The "gold finger" is explained as a combination of mass transfer, nucleon evaporation and sequential fission.

The yields of gold nuclides indicate a superposition of two reaction mechanisms, quasi-elastic and deep-inelastic. The angular momentum involved with each mechanism determines which of two isomeric states is the end product of the nuclear reaction.

Suggestions are offered regarding the possibility of synthesizing super-heavy elements by use of heavy-ion nuclear reactions.

## THE CLASSICAL-LIMIT S-MATRIX FOR HEAVY ION SCATTERING

Raul Jose Donangelo

(LBL-5825)

An integral representation for the classical limit of the quantum mechanical S-matrix is developed and applied to heavy-ion Coulomb excitation and Coulomb-nuclear interference.

The method combines the quantum principle of superposition with exact classical dynamics to describe the projectile-target system. A detailed consideration of the classical trajectories and of the dimensionless parameters that characterize the system is carried out.

The results are compared, where possible, to exact quantum mechanical calculations and to conventional semiclassical calculations. We find that in the case of backscattering the classical limit S-matrix method is able to almost exactly reproduce the quantum-mechanical S-matrix elements, and therefore the transition probabilities, even for projectiles as light as protons. The results also suggest that this approach should be a better approximation for heavy-ion multiple Coulomb excitation than earlier semi-classical methods, due to a more accurate description of the classical orbits in the electromagnetic field of the target nucleus.

Calculations using this method indicate that the rotational excitation probabilities in the Coulomb-nuclear interference region should be very sensitive to the details of the potential at the surface of

the nucleus, suggesting that heavy-ion rotational excitation could constitute a sensitive probe of the nuclear potential in this region.

The application to other problems as well as the present limits of applicability of the formalism are also discussed.

## TWO-PROTON PICKUP STUDIES WITH THE ($^{6}$Li,$^{8}$B) REACTION

Robert Benjamin Weisenmiller

(LBL-5077)

The ($^{6}$Li,$^{8}$B) reaction has been investigated on targets of $^{26}$Mg, $^{24}$Mg, $^{16}$O, $^{13}$C, $^{12}$C, $^{11}$B, $^{10}$B, and $^{9}$Be at a bombarding energy of 80.0 MeV, and on targets of $^{16}$O, $^{12}$C, $^{9}$Be, $^{7}$Li, and $^{6}$Li at a bombarding energy of 93.3 MeV. Only levels consistent with a direct, single-step two-proton pickup reaction mechanisms were observed to be strongly populated. On $T_z = 0$ targets, the spectroscopic selectivity of this reaction resembles that of the analogous (p,t) reaction. Additionally, these data demonstrate the dominance of spatially symmetric transfer of the two protons. On $T_z > 0$ targets the ($^{6}$Li,$^{8}$B) reaction was employed to locate two previously unreported levels (at 7.47 ± 0.05 MeV and 8.86 ± 0.07 MeV) in the $T_z = 2$ nuclide $^{24}$Ne and to establish the low-lying 1p-shell states in the $T_z = 3/2$ nuclei $^{11}$Be, $^{9}$Li, and $^{7}$He. However, no evidence was seen for any narrow levels in the $T_z = 3/2$ nuclide $^{5}$H nor for any narrow excited states in $^{7}$He.

The angular distributions reported here are rather featureless and decrease monotonically with increasing angle. This behavior can be shown by a semi-classical reaction theory to be a consequence of the reaction kinematics. A semi-classical approach also suggests that the kinematic term in the transition matrix element is only weakly dependent upon the angular momentum transfer (which is consistent with simple Distorted Wave Born Approximation calculations). However, only qualitative agreement was obtained between the observed relative transition yields and semi-classical predictions, using the two-nucleon coefficients of fractional parentage of Cohen and Kurath, probably due to the limitations of the semi-classical reaction theory.

# V.

# PUBLICATIONS

# PAPERS PUBLISHED AND LBL REPORTS ISSUED
## 1976-1977

ABRAHAM, M. M. (See KOLBE, W. LBL-4034)

AJZENBERG-SELOVE, F. (See KEKELIS, G. J., LBL-6557)

ALEONARD, M. M. (See BUTLER, P. A., LBL-5854)

ALEONARD, M. M. (See LEE, I. Y. LBL-6559)

ALEONARD, M. M. (See NEWTON, J. O., LBL-5830)

ANHOLT, R., J. Ioannou-Yannou, H. Bowman, E. Rauscher, S. Nagamiya, J. O. Rasmussen, T. Shibata, and H. Ejiri
Atomic K Vacancy Production with 3 GeB Carbon Ions
LBL-4359, January 1976
Phys. Letters 59A, 429 (1977)

ARTZY, Michal, I. Perlman, and F. Asaro
Imported and Local Bichrome Ware in Megiddo
LBL-4088, August 1975
Journal Levant

ASARO, F. (See ARTZY, Michal, LBL-4088)

ASPREY, L. B. (See SEABORG, G. T., LBL-4366)

BABINET, R. (See SCHMITT, LBL-5042)

BACHER, A. D. (See de SWINIARSKI, LBL-2322) REV

BALTZ, A. J., S. K. Kauffmann, N. K. Glendenning, and P. Pruess
Long Range Absorption in the Heavy-Ion Optical Potential
LBL-6581, August 1977

BALTZ, A. J., S. K. Kauffmann, N. K. Glendenning, and K. Pruess
A Long Range Imaginary Optical Potential in Elastic Scattering
LBL-6588, September 30, 1977
Presented at the Symposium on Nuclear Direct Reaction Mechanism, Hosei University, Tokyo, Japan, September 5-10, 1977

BANASCHIK, M. V. (See SIMON, R. S., LBL-5827)

BARANOWSKI, F. P. (See SEABORG, G. T., LBL-4366)

BECCHETTI, F. D., B. G. Harvey, D. Kovar, J. Mahoney, C. Maguire, and D. K. Scott
$^{208}Pb(^{16}O,^{15}O)^{208}Pb$ Reaction
No No., September 1975
Phys. Rev. C12, 894 (1975)

BENDER, Charles F. (See BREWINGTON, R., LBL-4318)

BERTSCH, G. F.
Threshold Pion Production in Heavy-Ion Collisions
LBL-5070, August 1976
Phys. Rev. C15, 713 (1976)

BIESER, F. S. (See GREINER, D., LBL-3651)

BINDER, I., R. Kraus, R. Klein, D. Lee, and M. M. Fowler
A Chemist's Gamma-Ray Table
LBL-6515, June 1977

BINI, M. (See GELBKE, C. K., LBL-6551)

BLANK, H. (See MÜLLER, W., LBL-4369)

BŁOCKI, J., Y. Boneh, J. R. Nix, J. Randrup, M. Robel, A. J. Sieri, and W. J. Swiatecki
One-Body Dissipation and the Super-Viscidity of Nuclei
LBL-6536, August 10, 1977
Annals of Phys.

BOISSON, J. P., J. G. Ioannou, T. Shibata, and J. O. Rasmussen
Shell Model Theory for Peripheral Collisions
LBL-5814, November 1976

BOISSON, J. P. (See GUIDRY, M. W., LBL-4363)

BONEH, Y. (See BŁOCKI, J., LBL-6536)

BORYSOWICZ, J. (See PETROVICH, F., LBL-1951)

BOWMAN, H. (See ANHOLT, R., LBL-4359)

BOWMAN, H. R. (See RAICH, D. G., LBL-5049)

BOWMAN, Harry R. (See NOBLE, Donald, LBL-4324)

BREWINGTON, Robert B., C. F. Bender, and H. F. Schaefer III
TETRAHEDRAL $Be_4$
LBL-4318, September 1975
J. Chem Phys. 64, (1976).

BROWNE, E. (See MEYER, R. A., LBL-5816)

BUENERD, M., C. K. Gelbke, B. G. Harvey, D. L. Hendrie, J. Mahoney, A. Menchaca-Roca, C. Olmer, and D. K. Scott
Similarity of Cross Sections for Peripheral Collisions at 20 MeV/A and 2.1 GeV/A
LBL-5067, August 1976

BUENERD, M. (See GELBKE, C. K., LBL-5094)

BUENERD, M. (See GELBKE, C. K., LBL-5826)

BUENERD, M. (See OLMER, C., LBL-5805)

BUTLER, P. A., I. Y. Lee, J. O. Newton, Y. El-Masri, M. M. Aleonard, P. Colombani, R. M. Diamond, F. S. Stephens, R. W. Lougheed, and E. K. Hulet
Fission of $^{232}Th$, $^{238}U$ $^{244}Pu$, $^{248}Cm$ Induced by Xe and Kr Ions at Coulomb Barrier Energies
LBL-5854, March 1977
Phys. Rev. Lett. 38, 1454, (1977)

BUTLER, P. A. (See COLOMBANI, P., LBL-5027)

BUTLER, P. A. (See GUIDRY, M. W., LBL-4038)

BUTLER, P. A. (See LEE, I. Y., LBL-5031)

BUTLER, P. A. (See LEE, I. Y., LBL-6512)

BUTLER, P. A. (See WARD, D., LBL-4375)

CARNALL, W. R. (See SEABORG, G. T., LBL-4366)

CAUVIN, B., R. P. Schmitt, G. J. Wozniak, P. Glässel, P. Russo, R. C. Jared, J. B. Moulton, and L. G. Moretto
Transitional Features Observed in the Charge and Angular Distribution of Deeply Inelastic Fragments Produced in the Reaction $^{181}$Ta + 620 MeV $^{86}$Kr
LBL-6506, April 1977

CAUVIN, B. (See RUSSO, P., LBL-5050)

CAUVIN, B. (See RUSSO, P., LBL-5810)

CERNY, J. (See GEESAMAN, D. F., LBL-4361)

CERNY, J. (See ZISMAN, M. S., LBL-5098)

CERNY, Joseph, and J. C. Hardy
Delayed Proton Radioactivities
LBL-5852, March 1977

CERNY, Joseph (See HICKEY, G. T.
Phys Rev. Lett. 37, 130 (1976)

CERNY, Joseph (See JAHN, R., LBL-5038)

CERNY, Joseph (See JAHN, R., LBL-5079)

CERNY, Joseph (See KEKELIS, G. J., LBL-6557)

CERNY, Joseph (See ZISMAN, M. S., LBL-5078)

CHARLTON, L. A., G. Delic, N. K. Glendenning, K. Pruess
Polarizability of Nuclear Wave Functions in Heavy Ion Reactions
LBL-6592, August 1977

CHARLTON, L. A.
Finite Range Evaluation of (p-d, d-t) with Momentum Space Techniques
LBL-4356, January 1976
Phys. Rev. C14, 506 (1976).

CHARLTON, L. A. (See DELIC, G., LBL-5074)

CHEIFETZ, E. (See STROUGHTON, R. W., LBL-5053)

CLARK, David J.
Recent Progress in Heavy Ion Sources
LBL-6500, June 1977
IEE Trans. on Nucl. Sci. NS-24, 1064 (1977)

CLARK, D. J. (See STEPHENSON, E. J., LBL-6591)

CLINE, D. (See COLOMBANI, P., LBL-5027)

CLINE, D. (See LEE, I. Y., LBL-5031)

CLINE, D. (See LEE, I. Y., LBL-6512)

COLOMBANI, P., P. A. Butler, I. Y. Lee, D. Cline, R. M. Diamond, F. S. Stephens, and D. Ward
Subcoulomb Fission Induced by Xe and Kr Ions
LBL-5027, May 1976
Phys. Letters 65B, 39 (1976)

COLOMBANI, P. (See BUTLER, P. A., LBL-5854)

COLOMBANI, P. (See GUIDRY, M. W., LBL-4038)

COLOMBANI, P. (See LEE, I. Y., LBL-5031)

COLOMBANI, P. (See WARD, D., LBL-4375)

CONWAY, J. G. (See SEABORG, G. T., LBL-4366)

CONZETT, H. E. and F. Seiler
Extreme Values of Spin-Polarization Analyzing Powers in Nuclear Reactions: M-Matrix Conditions
LBL-5850, February 1977

CONZETT, H. E. (See KING, N. S. P., LBL-5849)

CORK, Bruce (See GREINER, D., LBL-3651)

CRAMER, J. G., R. M. Devries, D. A. Goldberg, M. S. Zisman, and C. F. Maguire
"Unique" Energy - Independent Woods - Saxon Optical Potential For $^{16}$O + $^{28}$Si Elastic Scattering
LBL-5813, June 1976
Phys. Rev. C14, 2158 (1976)

CRANDALL, J. L. (See SEABORG, G. T., LBL-4366)

CRAWFORD,H. J. (See HECKMAN, H. H., LBL-6561)

CRAWFORD, H. J. (See HECKMAN, H. H., LBL-6562)

CRAWFORD, H. J. (See LINDSTROM, P. J., LBL-6568)

CRAWLEY, G. M. (See HICKEY, G. T.)
Phys. Rev. Lett. 37, 130 (1976)

DE SWINIARSKI, R., P. G. Resmini, D. L. Hendrie, and A. D. Bacher
Study of $^{16}$O, $^{20}$Ne, $^{22}$Ne, $^{28}$Si, and $^{32}$S by Inelastic Scattering of Polarized Protons
LBL-2322 Rev., August 1975
Nucl. Phys. A 261, 111-129, (1976)

DELEPLANQUE, M. A. (See LEE, I. Y., LBL-6559)

DELIC, G., K. Pruess, L. A. Charlton, and N. K. Glendenning
Effect of Polarization of Shell-Model States in Reaction Calculations for $^{40}$Ca($^{16}$O, $^{15}$N) $^{41}$Sc$_{if_{7/2}}$
LBL-5074, October 1976
Phys. Lett.

DELIC, George and Dieter Kurath
Finite Range Distorted Waves Born Approximation Calculations for $^{13}$C($^{3}$He,$^{6}$He)$^{10}$C
LBL-4364, January 1976
Phys. Rev. C14, 619 (1976)

DELIC, G. (See CHARLTON, L. A., LBL-6592)

DEVRIES, R. M. (See CRAMER, J. G., LBL-5813)

DIAMOND, R. M. (See BUTLER, P. A., LBL-5854)

DIAMOND, R. M. (See COLOMBANI, P., LBL-5027)

DIAMOND, R. M. (See GLÄSSEL, P., LBL-5086)

DIAMOND, R. M. (See GUIDRY, M. W., LBL-4038)

DIAMOND, R. M. (See KLEINHEINZ, P., LBL-4352)

DIAMOND, R. M. (See LEE, I. Y., LBL-5031)

DIAMOND, R. M. (See LEE, I. Y., LBL-6512)

DIAMOND, R. M. (See LEE, I. Y., LBL-6559)

DIAMOND, R. M. (See NEWTON, J. O., LBL-5830)

DIAMOND, R. M. (See SIMON, R. S., LBL-5827)

DIAMOND, R. M. (See WARD, D., LBL-4375

DIAMOND, Richard M.
Very High-Spin States in Nuclei
LBL-6505, April 18, 1977
Presented at the Physics Summer School Meeting, Jindabyne, Australia
February 7-11, 1977

DIETRICH, Klaus, and Christiane Leclercq-Willian
On the General Form of the Cross-Section of Deep Inelastic Collisions
LBL-5815, December 1976
Annals of Physics

DONANGELO, R. (See GUIDRY, M. W., LBL-4357)

DONANGELO, R. (See GUIDRY, M. W., LBL-4363)

DONANGELO, R. (See KAWAKAMI, H., LBL-4303)

DONANGELO, Raul Jose
The Classical-Limit S-Matrix for Heavy Ion Scattering
LBL-5825, January 1977

DONANGELO, Raul (See RASMUSSEN, John, LBL-6580)

DRURY, J. S. (See STROUGHTON, R. W., LBL-5053)

DYSTRA, Clifford E., Henry F. Schaefer III
Electronic Structure of Dicarbonyls: The Ground State of Glyoxal
LBL-3470, March 1975
J. Am. Chem. Soc. 97, 7210 (1975)

ECKROAD, S. W., R. E. Leber, and A. Ghiorso
A Simple Sputtering System for Nuclear-Science Applications
LBL-5085, September 1976
Nucl. Inst. & Meth.

EDELSTEIN, N. (See KOLBE, W., LBL-4034)

EDELSTEIN, N. (See SEABORG, G. T., LBL-4366)

EICHLER, E. (See GUIDRY, M. W., LBL-4038)

EICHLER, E, (See LEE, I. Y., LBL-5031)

EJIRI, H. (See ANHOLT, R., LBL-4359)

EL-JAICK, L. J. (See MYERS, W. D., LBL-4390)

EL-MASRI, Y. (See BUTLER, P. A., LBL-5854)

EL-MASRI, Y. (See LEE, I. Y., LBL-6559)

EL MASRI, Y. (See NEWTON, J. O., LBL-5830)

EPPLEY, R. E. (See RAICH, D. G., LBL-5049)

FABBI, B. P. (See NOBLE, Donald C., LBL-4324)

FENG, D. H. (See YAGI, LBL-4382)

FIELDS, P. R. (See SEABORG, G. T., LBL-4366)

FINCH, C. B. (See KOLBE, W., LBL-4034)

FLIESSBACH, T. (See RASMUSSEN, J. O., LBL-5048)

FOWLER, M. M. (See OTTO, R. J., LBL-6509)

GABOR, G. (See ZEBELMAN, A. M., LBL-5095)

GARRISON, Barbara, Jr., William A. Lester, Jr., Per Siegbahn, and Henry F. Schaefer, III.
Effect of Electron Correlation on the $H_2CO$-He Interaction Potential
LBL-4328, June 1975
J. Chem. Phys. 63, 4167 (1975)

GARRISON, W. M. (See JAYKO, M. E., LBL-4098)

GEESAMAN, D. F., R. Malmin, R. L. McGrath, J. W. Noe, and J. Cerny
$^{52}$Fe (6.8 MeV) β-Decaying Isomeric State
LBL-4361, August 1974
Physics Rev. Lett. 34, 326 (1975)

GELBKE, C. K., M. Buenerd, D. L. Hendrie, J. Mahoney, M. C. Mermaz, C. Olmer and D. K. Scott
Trends of Isotope Yields Observed in Reactions Induced by $^{16}$O Ions of 140, 315 and 33600 MeV
LBL-5094, October 1976
Phys. Letters 65, 227 (1976).

GELBKE, C. K., C. Olmer, M. Buenerd, D. L. Hendrie, J. Mahoney, M. C. Mermaz and D. K. Scott
Energy Dependence of Peripheral Reactions Induced by Heavy Ions
LBL-5826, June 1977

GELBKE, C. K., C. Olmer, D. L. Hendrie, J. L. Lavillee, J. Mahoney, M. C. Mermaz and D. K. Scott
Particle-Particle Angular Correlations for Quasi-Elastic and Deeply-Inelastic Scattering in the Reaction $^{208}$Pb($^{16}$O, Cα) at 20 MeV/A
LBL-5821, December 1976
Phys. Rev. Lett.

GELBKE, C. K., D. K. Scott, M. Bini, D. L. Hendrie, J. L. Laville, J. Mahoney, M. C. Mermaz, and C. Olmer
Influence of Intrinsic Nucleon Motion on Energy Spectra and Angular Distributions for $^{16}O$-Induced Reactions at 20 MeV/A.
LBL-6551, July 1977

GELBKE, C. K. (See BUENERD, M. LBL-5067)

GELBKE, C. K. (See OLMER, C., LBL-5805)

GHIORSO, A. (See ECKROAD, S. W., LBL-5085)

GHIORSO, A. (See NITSCHKE, J. M., LBL-6534)

GHIORSO, A. (See OTTO, R. J., LBL-6509)

GHIORSO, A. (See SEABORG, G. T., LBL-4366)

GHIORSO, A.
Final Resolution of the Element 104 Questions
LBL-5037, May 1976
Presented at the 3rd International Conference on Nuclei Far From Stability
Cargese, Corsica, France, May 19-26, 1976

GIUSTI, E. R. (See STROUGHTON, R. W., LBL-5053)

GLÄSSEL, P., R. C. Jared and L. G. Moretto
Identification of Atomic Numbers up to Z=60 Means of ΔE-E Telescopes and a Computerized Method
LBL-5064, August 1976
Nucl. Inst. of Meth. 142, 569-572 (1977)

GLÄSSEL, P., R. S. Simon, R. M. Diamond, R. C. Jared, I. Y. Lee, L. G. Moretto, J. O. Newton, R. Schmitt, and F. S. Stephens
Angular Momentum Transfer in Deep Inelastic Processes
LBL-5086, September 1976
Phys. Rev. Letters 38, 331 (1976)

GLÄSSEL, P. (See CAUVIN, B., LBL-6506)

GLÄSSEL, P. (See RUSSO, P., LBL-5050)

GLÄSSEL, P. (See RUSSO, P., LBL-5810)

GLÄSSEL, P. (See WOZNIAK, G. J., LBL-6532)

GLENDENNING, N. K. and Georg Wolschin
Indirect Transition in Two-Nucleon Transfer Reactions Between Heavy Ions
LBL-5052, July 1976

GLENDENNING, N. K. (See BALTZ, A. J., LBL-6581)

GLENDENNING, N. K. (See BALTZ, A. J., LBL-6588)

GLENDENNING, N. K. (See CHARLTON, L. A., LBL-6592)

GLENDENNING, N. K. (See DELIC, G., LBL-5074)

GLENDENNING, Norman
One- and Two-Nucleon Transfer Reactions
LBL-4358, 1975
Nucl. Spect. & Reac., Part D, 319 (1975)

GLENDENNING, N. K. and G. Wolschin
Indirect Transitions in Two-Nucleon Transfer Reactions Between Heavy Ions
LBL-5052, July 1976
Nucl. Phys. A281, 486-508, (1977)

GLENDENNING, N. K. and Y. Karant
Can the Hadronic Mass Spectrum Be Discovered Through High Energy Nuclear Collisions
LBL-6590, August 8, 1977

GOLDBERG, D. A. (See CRAMER, J. G., LBL-5813)

GOSSET, J., H. H. Gutbrod, W. G. Meyer, A. M. Poskanzer, A. Sandoval, R. Stock, and G. D. Westfall
Central Collisions of Relativistic Heavy Ions
LBL-5820, May 10, 1977
Phys. Rev. C 16, 629 (1977)

GOSSET, J. (See GUTBROD, H. H., LBL-5039)

GOSSET, J. (See WESTFALL, G. D., LBL-5072)

GOUGH, R. A. (See STEPHENSON, E. J., LBL-6591)

GUIDRY, M. W., P. A. Butler, P. Colombani, I. Y. Lee, D. Ward, R. M. Diamond, F. S. Stephens, E. Eichler, N. R. Johnson and R. Sturm
Reduced Transition Probabilities for High Spin States in $^{232}Th$
LBL-4038
Nucl. Phys. A 266, 228-252 (1976)

GUIDRY, M. W., R. Donangelo, J. O. Rasmussen, and J.-P. Boisson
The Classical-Limit S-Matrix and Orbital Dynamics in Semiclassical Coulomb Excitation Theory
LBL-4363, July 13, 1977

GUIDRY, M. W., H. Massmann, R. Donangelo and J. O. Rasmussen
Theory of Coulomb-Nuclear Interference for Heavy-Ion Excitation of Rotational States
LBL-4357, January 1976
Nucl. Phys. A 274, 183-201 (1976)

GUIDRY, M. W. (See LEE, I. Y., LBL-5031)

GUNNINK, R., (See MEYER, R. A., LBL-5816)

GREINER, D. E., P. J. Lindstrom, H. Heckman, Bruce Cork, and F. S. Bieser
Momentum Distributions of Isotopes Produced By Fragmentation of Relativistic $^{12}C$ and $^{16}O$ Projectiles
LBL-3651, March 1975
Phys. Rev. Letters 35, 152 (1976)

GREINER, D. E. (See HECKMAN, H. H., LBL-3656)

GREINER, D. E. (See HECKMAN, H. H., LBL-6561)

GREINER, D. E. (See HECKMAN, H., LBL-6562)

GREINER, D. E. (See LINDSTROM, P. J., LBL-6568)

GUIDRY, M. W., P. A. Butler, P. Colombani, I. Y. Lee, D. Ward, R. M. Diamond, F. S. Stephens, E. Eichler, N. R. Johnson and R. Sturm
Reduced Transition Probabilities for High Spin States in $^{232}$Th
LBL-4038, January 1976
Nucl. Phys. A266, 228-252 (1976)

GUTBROD, H. H. (See GOSSET, J., LBL-5820)

GUTBROD, H. H. (See WESTFALL, G. D., LBL-5072)

GUTBROD, H. H., A. Sandoval, P. J. Johansen, A. M. Poskanzer, J. Gosset, W. G. Meyer, G. D. Westfall and R. Stock
Final State Interactions in the Production of Hydrogen and Helium Isotopes by Relativistic Heavy Ions on Uranium
LBL-5039, July 1976
Phys. Rev. Letters 37, 667 (1976)

GYULASSY, Miklos
Pionic Instabilities in High-Energy Heavy Ion Collisions
LBL-6525, June 1977
Presented at the Proceedings, Falls Creek Falls Meeting on Heavy Ion Collisions, June 13-17, 1977, Falls Creek Falls, Tennessee

HAGSTROM, R. (See LINDSTROM, P. J., LBL-6568)

HALBACH, K. (See ZEBELMAN, A. M., LBL-5095)

HALPERIN, J. (See STROUGHTON, R. W., LBL-5053)

HAMMERSTEIN, G. R. (See PETROVICH, F., LBL-1951)

HARDY, J. C. (See CERNY, J., LBL-5852)

HARVEY, B.G. (See BECCHETTI, F. D., No No. 1975)

HARVEY, B. G. (See BUENERD, M., LBL-5067)

HARVEY, B. G. (See OERTZEN, W. von, LBL-5848)

HARVEY, B. G., G. Herrmann, R. W. Hoff, D. C. Hoffman, E. K. Hyde, J. J. Katz, O. Lewin Keller, Jr., M. Lefort and G. T. Seaborg
Criteria for the Discovery of Chemical Elements
Science 193, 1271-1272, (1976)

HEBBARD, D. F. [See HICKEY, G. T., Phys. Rev. Lett. 37, 130 (1976)]

HEBERT, A. J. (See NOBLE, D. C., LBL-4324)

HECKMAN, H. H., H. J. Crawford, D. E. Greiner, P. J. Lindstrom, and L. W. Wilson
Study of Central Collisions Produced by Relativistic Heavy Ions in Nuclear Emulsion
LBL-6561, July 1977

HECKMAN, H. H. and P. J. Lindstrom
Coulomb Dissociation of Relativistic $^{12}$C and $^{16}$O Nuclei
LBL-4380, March 1976
Phys. Rev. Letters

HECKMAN, H. H., H. J. Crawford, D. E. Greiner, P. J. Lindstrom, and L. W. Wilson
Non-Peripheral Collisions of Heavy Ions in Nuclear Emulsion
LBL-6562, July 1977
Proceedings of Meeting on Heavy Ion Collisions Falls Creek Falls State Park, Tenn. June 13-17, 1977

HECKMAN, H. H., D. E. Greiner, P. J. Lindstrom, and H. Shwe
Fragmentation of $^{4}$He, $^{12}$C, $^{14}$N, and $^{16}$O Nuclei in Nuclear Emulsion at 2.1 GeV/Nucleon
LBL-3656, July 1977

HECKMAN, H. (See GREINER, D., LBL-3651)

HECKMAN, H. H. (See LINDSTROM, P. J., LBL-6568)

HEDGE, C. E. (See NOBLE, D. C., LBL-4324)

HENDRIE, D. L. (See Buenerd, M., LBL-5067)

HENDRIE, D. L. (See GELBKE, C. K., LBL-5094)

HENDRIE, D. L. (See GELBKE, C. K., LBL-5821)

HENDRIE, D. L. (See GELBKE, C. K., LBL-5826)

HENDRIE, D. L. (See GELBKE, C. K., LBL-6551)

HENDRIE, D. L. (See Olmer, C., LBL-5805)

HENDRIE, D. L. (See OERTZEN, W. von., LBL-5848)

HENDRIE, D. L. (See SHERMAN, J. D., LBL-4379)

HENDRIE, D. L. (See de SWINIARSKI, LBL-2322 Rev.)

HENDRIE, D. L. (See YAGI, K., LBL-4382)

HEROPOULOS, C. E. (See NOBLE, D. C., LBL-4324)

HERRMANN, G. (See HARVEY, LBL- No No.)

HICKEY, G. T., D. C. Weisser, J. Cerny, G. M. Crawley, A. F. Zeller, T. R. Ophel and D. F. Hebbard
Use of the Four-Neutron Transfer Reaction $^{18}$O($^{18}$O,$^{14}$O)$^{22}$O
Phys. Rev. Lett. 37, 130 (1976)

HILF, E. R., (See MYERS, W. D., LBL-4390)

HOFF, R. W. (See HARVEY, B., LBL-No No.)

HOFFMAN, D. C. (See HARVEY, B., LBL-No No.)

HOLLEY, W. R. (See STEPHENSON, E. J., LBL-6591)

HOMEYER, H. (See OERTZEN, W. von, LBL-5848)

HULET, E. K. (See BUTLER, P. A., LBL-5854)

HULET, K. (See SEABORG, G. T., LBL-4366)

HYDE, E. K. (See HARVEY, B., LBL-No No.)

IMMELE, J. D. (See MATHEWS, G. J., LBL-5076)

IOANNOU, J. G. (See BOISSON, J. P., LBL-5814)

IOANNOU-YANNOU, J. (See ANHOLT, R., LBL-4359)

JAHN, R., D. P. Stahel, G. J. Wozniak, J. Cerny, and H. P Morsch
Monopole Excitation of $^{4}He$ in α - Particle Scattering From $^{12}C$, $^{13}C$, and $^{16}O$
LBL-5079, October 1976
Phys. Letters 65B, 339 (1976)

JAHN, R., G. J. Wozniak, D. P. Stahel and J. Cerny
The (α,$^{2}He$) Reaction as a Spectroscopic Tool for Investigating High Spin States
LBL-5038, June 1976
Phys. Rev. Lett. 37, 812 (1976)

JAHN, R. (See KEKELIS, G. J., LBL-6557)

JAHNKE, U. (See YAGI, K. LBL-4382)

JAIN, A. (See STEPHENSON, E. J., LBL-6591)

JARED, R. C. (See CAUVIN, B., LBL-6506)

JARED, R. C. (See GLÄSSEL, P., LBL-5064)

JARED, R. C. (See GLÄSSEL, P., LBL-5086)

JARED, R. C. (See RUSSO, P., LBL-5050)

JARED, R. C. (See RUSSO, P., LBL-5810)

JARED, R. C. (See SCHMITT, R. P., LBL-5042)

JARED, R. C. (See STROUGHTON, R. W., LBL-5053)

JAYKO, M. E., T.-L. Tung, G. P. Welch and W. M. Garrison
Methodology in the Radiolysis of Biochemical Compounds with Cyclotron Beams at Low Flux Densities
LBL-4098, August 1975
Bio. Chem. & Bio. Phys. Research Comm. 68, 307 (1976)

JOHANSEN, P. J. (See GUTBROD, H. H., LBL-5039)

JOHANSEN, P. J. (See WESTFALL, G. D., LBL-5072)

JOHNS, Oliver
An Extension of the S. I. Unit System for Use in Physics
LBL-4099, August 1976

JOHNSON, N. R. (See GUIDRY, M. W., LBL-4038)

JOHNSON, N. R. (See LEE, I.Y., LBL-5031)

KAPUSTA, J. I.
Bremsstrahlung in the Nuclear Fireball Model
LBL-5056, October 1976
Phys. Rev. C 15, 1580 (1976)

KAPUSTA, J. I.
Particle Production in the Nuclear Fireball Model
LBL-6504, April 1977

KARANT, Yasha (See GLENDENNING, N. K., LBL-6590)

KATZ, J. J. (See HARVEY, B., LBL- No No.).

KAUFFMANN, S.K. (See BALTZ, A. J., LBL-6581)

KAUFFMANN, S.K. (See BALTZ, A. J., LBL-6588)

KAWAKAMI, H., M. Koike, K. Komura, M. Sakai, N. Yoshikawa, R. Donangelo and J. O. Rasmussen
Cross Section and Reaction Mechanisms of (p,pxn) Reactions on $^{208}Pb$ in the 24-52 MeV Range
LBL-4303, August 1975
Nuclear Physics A 262, 52-60, 1976

KEKELIS, G., (See ZISMAN, M.S., LBL-5098)

KEKELIS, G. J., M. S. Zisman, D. K. Scott, R. Jahn, D. J. Vieira, J. Cerny, and F. Ajzenberg-Selove
Measurement of the Masses of the Unbound Nuclei $^{16}Ne$, $^{15}F$ and $^{12}O$
LBL-6557, September 1977

KELLER, L. O. (See HARVEY, B., LBL-No No.)

KING, N. S. P., J. L. Romero, J. Ullmann, H. E. Conzett, R. M. Larimer, and R. Roy
Polarization in Proton-Deuteron Scattering at 50 MeV
LBL-5849, February 17, 1977

KLEIN, R. (See BINDER, I., LBL-6515)

KLEINHEINZ, P., M. R. Maier, R. J. Diamond, F. S. Stephens, and R. K. Sheline
Revised Single-Particle Energies in N=83 Nuclei
LBL-4352, January 1975
Phys. Lett. 53B, 442-444 (1975)

KODAMA, T. (See MYERS, W. D., LBL-4390)

KOIKE, M. (See KAWAKAMI, H., LBL-4303)

KOLBE, W. and N. Edelstein, C. B. Finch and M. M. Abraham
Electron Paramagnetic Resonance of $^{239}Pu^{3+}$ and $^{243}Am^{4}$ in $CeO_2$ and of $^{241}Pu^{3+}$ in $ThO_2$
LBL-4034, June 1975
J. Chem. Phys., 60, 607 (1974)

KOMURA, K. (See KAWAKAMI, H., LBL-4303)

KOONIN, S. E. (See FLOCARD, H., LBL-6546)

KOVAR, D. (See BECCHETTI, F. D., No No. 1975)

KOVAR, D. (See OERTZEN, W. von., LBL-5848)

KRAUS, R. (See BINDER, I., LBL-6515)

KRIEN, K., R. A. Naumann, J. O. Rasmussen, and I. Rezanka
High Spin States in $^{155}Dy$ and $^{154}Dy$ from ($^{12}C$,xn, γ) Studies
LBL-1652, March 1973
Nucl. Phys. A 209, 572-588 (1973)

KURATH, D. (See DELIC, G., LBL-4364)

LANDIS, D. A. (See ZEBELMAN, A. M., LBL-5095)

LARIMER, R. M. (See KING, N. S. P., LBL-5849)

LAVILLEE, J. L. (See GELBKE, C. K., LBL-5821)

LAVILLEE, J. L. (See GELBKE, C. K., LBL-6551)

LEBER, R. E. (See ECKROAD, S. W., LBL-5085)

LEBER, R. E. (See NITSCHKE, J. M., LBL-6534)

LECLERCQ-WILLIAN, C. (See DIETRICH, K., LBL-5815)

LEDERER, C. M. (See MEYER, R. A., LBL-5816)

LEE, D. (See BINDER, I., LBL-6515)

LEE, D. (See Otto, R. J., LBL-6509)

LEE, I. Y., M. M. Aleonard, M. A. Deleplanque, Y. El-Masri, J. O. Newton, R. S. Simon, R. M. Diamond, and F. S. Stephens
Second Discontinuity in the Yrast Levels of $^{158}Kr$
LBL-6559, July 18, 1977
Phys. Rev. Lett. 38, 1454 (1977)

LEE, I. Y., D. Cline, P. A. Butler, R. M. Diamond, J. O. Newton, R. S. Simon and F. S. Stephens
Coulomb Excitation of $^{192,194,196}Pt$ with $^{136}Xe$ Projectiles
LBL-6512, June 1977

LEE, I.Y., D. Cline, R. S. Simon, P. A. Butler, P. Colombani, M. W. Guidry, F. S. Stephens, R. M. Diamond, N. R. Johnson and E. Eichler
Coulomb Excitation into the Backbend Region of $^{164}Er$
LBL-5031, May 1976
Phys. Rev. Lett. 37, 420 (1976)

LEE, I. Y. (See BUTLER, P. A., LBL-5854)

LEE, I. Y. (See COLOMBANI, P., LBL-5027)

LEE, I. Y. (See GLÄSSEL, P., LBL-5086)

LEE, I. Y. (See GUIDRY, M. W., LBL-4038)

LEE, I. Y. (See NEWTON, J. O., LBL-5830)

LEE, I. Y. (See WARD, D., LBL-4375)

LEFORT, M. (See HARVEY, B., LBL-No No.)

LESTER, W. A. (See GARRISON, B. J., LBL-4328)

LICHTNER, P. (See PRUESS, K., LBL-4381)

LICHTNER, P. (See PRUESS, K., LBL-6524)

LIETZE, M. H. (See STROUGHTON, R. W., LBL-5053)

LINDSTROM, P. J.
Coulomb Dissociation of Relativistic $^{12}C$ and $^{16}O$ Nuclei
LBL-4380, March 1976
Phys. Rev. Lett.

LINDSTROM, P. J., H. J. Crawford, D. E. Greiner, R. Hagstrom, and H. H. Heckman
Evidence Against Copious Threshold Pion Production in Heavy Ion Collisions
LBL-6568, July 1977

LINDSTROM, P. L. (See Greiner, D., LBL-3651)

LINDSTROM, P. J. (See HECKMAN, H. H., LBL-3656)

LINDSTROM, P. J. (See HECKMAN, H. H., LBL-6561)

LINDSTROM, P. J. (See HECKMAN, H. H., LBL-6562)

LOUGHEED, R. W. (See BUTLER, P. A., LBL-5854)

LOVELAND, W., R. J. Otto, D. J. Morrissey, and G. T. Seaborg
Further Studies of Large Collision Residues in Relativistic Heavy Ion Reactions with Heavy Nuclei
LBL-6522, May 1977

LOVELAND, W., R. J. Otto, D. J. Morrissey, and G. T. Seaborg
Large Collision Residues and Nuclear Fission in Relativistic Heavy Ion Reactions
LBL-6513, April 1977
Phys. Rev. Lett.

LOVELAND, W. (See D. J. Morrissey, LBL-6539)

LOW, K. S. (See YAGI, K., LBL-4382)

LUCCHESE, R. R., and H. F. Schaefer III
Charge-Transfer Complexes. $NH_3$-$F_2$, $NH_3$-$Cl_2$, $NH_3$-ClF, $N(CH_3)_3$-$F_2$, $N(CH_3)_3$-$Cl_2$, and $N(CH_3)_3$-ClF
LBL-3471, March 1975
J. Am. Chem. Soc. 97, 7205 (1975)

MA, C. W., and J. O. Rasmussen
Microscopic Calculations of High-Spin Rotational States
LBL-6521, May 1977

MACFARLANE, M. H. (See OLMER, C., LBL-5805)

MAGUIRE, C. (See BECCHETTI, F. D., No No. 1975)

MAGUIRE, C. F. (See CRAMER, J. G., LBL-5813)

MAGUIRE, C. F. (See YAGI, K., LBL-4382)

MAHONEY, J. (See BECCHETTI, F. D., No No. 1975)

MAHONEY, J. (See Buenerd, M., LBL-5067)

MAHONEY, J. (See GELBKE, C. K., LBL-5094)

MAHONEY, J. (See GELBKE, C. K., LBL-5821)

MAHONEY, J. (See GELBKE, C. K., LBL-5826)

MAHONEY, J. (See GELBKE, C. K., LBL-6551)

MAHONEY, J. (See OLMER, C., LBL-5805)

MAHONEY, J. (See YAGI, K., LBL-4382)

MAIER, M. R. (See KLEINHEINZ, P., LBL-4352)

MALMIN, R. (See GEESAMAN, D. F., LBL-4361)

MANG, H. J., B. Samadi, and P. Ring
On the Solution of Constrained Hartree-Fock-Bogolyubov Equations
LBL-5015, April 1976
Z. Physik

MANG, H. J. (See RASMUSSEN, J. O., LBL-5048)

MARKOWITZ, S. S. (See RAPE, A. J., LBL-3485)

MARQUEZ, L. (See RASMUSSEN, J. O., LBL-5048)

MASSMANN, H. (See GUIDRY, M. W., LBL-4357)

MASSMANN, H. (See RING, P., LBL-6538)

MATHEWS, G. J., G. J. Wozniak, R. P. Schmitt, and L. G. Moretto
Evidence for the Characterization of Heavy-Ion Reactions by the Ratio E/B
LBL-5812, November 1976

MATHEWS, G. J. and J. D. IMMELE
Generalized Particle-Core Coupling
LBL-5076, August 1976
Phys. Lett.

McCRATH, R. L. (See GEESAMAN, D. F., LBL-4361)

McMANUS, H. (See PETROVICH, F., LBL-1951)

MEKJIAN, A.
Explosive Nucleosynthesis, Equilibrium Thermodynamics and Relativistic Heavy Ion Collisions
LBL-6545, June 1977

MEKJIAN, A.
A Thermodynamic Model for Composite-Particle Emission in Relativistic Heavy-Ion Collisions
LBL-5819,
Phys. Rev. Lett. 38, 640 (1977)

MENCHACA-ROCHA, A. (See BUENERD, M., LBL-5067)

MENCHACA-ROCHA, A. (See OLMER, C., LBL-5805)

MERMAZ, M. C. (See GELBKE, C. K., LBL-5094)

MERMAZ, M. C. (See GELBKE, C. K., LBL-5821)

MERMAZ, M. C. (See GELBKE, C. K., LBL-5826)

MERMAZ, M. C. (See GELBKE, C. K., LBL-6551)

MERMAZ, M. C. (See OLMER, C., LBL-5805)

MEYER, R. A., R. Gunnink, C. M. Lederer, and E. Browne
Level Structure of $^{155}$Gd and the Electron-Capture Decay of $^{155}$Tb
LBL-5816, June 1976
Phys. Rev. C 13, 2466 (1976)

MEYER, W. G., (See GUTBROD, H. H., LBL-5039)

MEYER, W. G., (See ZEBELMAN, A. M., LBL-5095)

MEYER, W. G. (See Gosset, J., LBL-5820)

MEYER, W. G. (See WESTFALL, G. D., LBL-5072)

MEYER, W. G. (See ZEBELMAN, A. M., LBL-5095)

MITRA, Gautam (See WILKE, C. R., LBL-2334)

MORETTO, L. G.
Diffusion Model Predictions for Kinetic Energy, Mass Angular Distributions and $\gamma$ ray Multiplicities in Heavy Ion Induced Reactions
LBL-6572, August 1977

MORETTO, L. G., and R. Schmitt
Experimental Evidence and Physical Implications of the Time Evolution Along the Mass Asymmetry Mode in Heavy Ion Reactions
LBL-5057, September 1976
Presented at the European Conference on Nuclear Physics with Heavy Ions, Caen, France, September 6-10, 1976

MORETTO, L. G. (See CAUVIN, B., LBL-6506)

MORETTO, L. G. (See GLÄSSEL, P., LBL-5064)

MORETTO, L. G. (See GLÄSSEL, P., LBL-5086)

MORETTO, L. G. (See MATHEWS, G. J., LBL-5812)

MORETTO, L. G. (See RUSSO, P., LBL-5050)

MORETTO, L. G. (See RUSSO, P., LBL-5810)

MORETTO, L. G. (See SCHMITT, R. P., LBL-5042)

MORETTO, L. G. (See SVENTEK, J., LBL-5012)

MORETTO, L. G. (See WOZNIAK, G. J., LBL-6532)

MORRISSEY, D. J., W. Loveland, R. J. Otto, and G. T. Seaborg
Lowered Fusion Cross Section in the Quadruply Magic Heavy Ion Systems
LBL-6539, June 1977

MORRISSEY, D. J. (See LOVELAND, W., LBL-6513)

MORRISSEY, D. J. (See LOVELAND, W., LBL-6522)

MORRISSEY, D. J. (See OTTO, R. J., LBL-6509)

MORSCH, H. P. (See JAHN, R., LBL-5079)

MOULTON, J. B. (See CAUVIN, B., LBL-6506)

MÜLLER, W., and H. Blank
Heavy Element Properties
4th International Transplutonium Element Symposium
5th International Conference on Plutonium and Other Actinides 1975
LBL-4369, September 13, 1975
Proceedings of the Joint Session of the Baden Baden Meetings, September 13, 1975, Heavy Element Properties (1976), North-Holland Publ. Co., Amsterdam

MYERS, W. D., W. J. Swiatecki, T. Kodama, L. J. El-Jaick and E. R. Hilf
The Droplet Model of the Giant Dipole Resonance
LBL-4390, September 1976
Phys. Rev. C 15, 2032 (1977)

MYERS, W. D.
Droplet Model Description of Nuclear Masses, Fission Barriers and Radii
LBL-3428, November 1974
Nucl. Phys. A

MYERS, W. D.
Geometrical Properties of Nuclei
LBL-5829, 1976
Nukleonike 21, 3 (1976)

MYERS, W. D.
A Model for High Energy Heavy Ion Collisions
LBL-6569, August 1977

NAGAMIYA, S. (See ANHOLT, R., LBL-4359)

NAUMANN, R. A. (See KRIEN, K., LBL-1652)

NEWTON, J. O., I. Y. Lee, R. S. Simon, M. M. Aleonard, Y. El Masri, R. S. Stephens, and R. M. Diamond
Energy-Dependent Multiplicities of Continuum Gamma Rays
LBL-5830, January 1977
Phys. Rev. Lett. 38, 810 (1977)

NEWTON, J. O. (See BUTLER, P. A., LBL-5854)

NEWTON, J. O. (See GLÄSSEL, P., LBL-5086)

NEWTON, J. O. (See LEE, I. Y., LBL-6512)

NEWTON, J. O. (See LEE, I. Y., LBL-6559)

NEWTON, J. O. (See SIMON, R. S., LBL-5827)

NITSCHKE, J. M., R. E. Leber, M. J. Nurmia, and A. Ghiorso
Observations in the Reaction of Two Doubly-Magic Nuclei: $^{208}Pb$ and $^{48}Ca$
LBL-6534, June 10, 1977

NITSCHKE, J. M. (See OTTO, R. J., LBL-6509)

NIX, J. R. (See BLOCKI, J., LBL-6536).

NOBLE, D. C., H. R. Bowman, A. J. Hebert, M. L. Silberman, C. E. Heropoulos, B. P. Fabbi, and C. E. Hedge
Chemical and Isotopic Constraints on the Origin of Low-Silica Latite and Andesite from the Andes of Central Peru
LBL-4324, 1975
Geology (1975), p. 501

NOE, J. W. (See GEESAMAN, D. F., LBL-4361)

NURMIA, M. J. (See NITSCHKE, J. M., LBL-6534)

OERTZEN, W. Von, H. Homeyer, B. G. Harvey, D. Hendrie, and D. Kovar
Two Proton Transfer Reactions Between Pairing Rotational States with 104 $^{16}O$ on $^{142}Nd$, $^{144}Sm$, $^{148}Sm$ and $^{152}Sm$
LBL-5848, June 24, 1976
Z. Physik A 279, 357-366 (1976)

OLIVEIRA, L. (See RASMUSSEN, J., LBL-6580)

OLMER, C., M. C. Mermaz, M. Buenerd, C. K. Gelbke, D. L. Hendrie, J. Mahoney, A. Menchaca-Rocha, D. K. Scott, M. H. Macfarlane, and S, C. Pieper
Energy Dependence of the Reaction $^{208}Pb(^{16}O,^{15}N)^{209}Bi$
LBL-5805, November 1976
Phys. Rev. Lett. 38, 476 (1976)

OLMER, C. (See BUENERD, M., LBL-5067)

OLMER, C. (See GELBKE, C. K., LBL-5094)

OLMER, C. (See GELBKE, C. K., LBL-5821)

OLMER, C. (See GELBKE, C. K., LBL-5826)

OLMER, C. (See GELBKE, C. K., LBL-6551)

OPHEL, T. R. [See HICKEY, G. T., Phys. Rev. Lett. 37, 130 (1976)]

OTTO, R. J., D. J. Morrissey, D. Lee, A. Ghiorso, J. M. Nitschke, G. T. Seaborg, M. M. Fowler, and R. J. Silva
A Search for Superheavy Elements with Half-Lives Between a Few Minutes and Several Hundred Days, Produced in the $^{48}Ca$ + $^{248}Cm$ Reaction
LBL-6509, April 1977
Presented at the 173rd ACS National Meeting, New Orleans, LA, March 21-25, 1977; also submitted to Journal of Inorganic and Nuclear Chemistry

OTTO, R. J. (See LOVELAND, W., LBL-6513)

OTTO, R. J. (See LOVELAND, W., LBL-6522)

OTTO, R. J. (See MORRISSEY, D. J., LBL-6539)

PERLMAN, I. (See ARTZY, M., LBL-4088)

PETERSON, J. R. (See SEABORG, G. T., (LBL-4366)

PETROVICH, F., H. McManus, J. Borysowicz, and G. R. Hammerstein
Core Polarization in Inelastic Scattering
LBL-1951, May 1976
Phys. Rev. C 16, 839 (1977)

PIEPER, S. C. (See OLMER, C., LBL-5805)

POSKANZER, A. M. (See WESTFALL, G. D., LBL-5072)

POSKANZER, A. M. (See STOCK, R., LBL-5055)

POSKANZER, A. M. (See ZEBELMAN, A. M., LBL-5095)

POSKANZER, A. M. (See GUTBROD, H. H., LBL-5039)

POSKANZER, A. M.
Relativistic Heavy Ion Reactions
LBL-6586, August 1977

POSKANZER, A. M. (See GOSSET, J., LBL-5820)

PRUESS, K. (See BALTZ, A. J., LBL-6581)

PRUESS, K. (See BALTZ, A. J., LBL-6588)

PRUESS, K. and P. Lichtner
A New Approach to Antisymmetrization and Rearrangement in Nucleus-Nucleus Collisions
LBL-4381, March 1976
Nucl. Phys. A 269, 252-268 (1976)

PRUESS, K.
Polarization of Single Particle States in Heavy Ion Induced Nuclear Reactions within the Two Center Shell Model
LBL-5066, August 1976
Nucl. Phys. A 278, 124-148 (1976)

PRUESS, K. and P. Lichtner
Calculations of Single Particle Polarization Using a Realistic Two-Center Shell Model
LBL-6524, May 1977

PRUESS, K. (See CHARLTON, L. A., LBL-6592)

PRUESS, K. (See DELIC, G., LBL-5074)

RADI, Hafez M. A., A. A. Shihab-Eldin, J. O. Rasmussen
Configuration Mixed Shell Model Relative Alpha Decay Rate Calculations for Spherical Doubly Odd Nuclei ($^{212}$At and $^{212m}$At)
LBL-5071, October 1976
Phys. Rev.

RAICH, D. G., H. R. Bowman, R. E. Eppley, J. O. Rasmussen and I. Rezanka
Gamma and Alpha Decay from the 2.1 -msec Isomer $^{213m}$Ra
LBL-5049, July 1976
Z. Physik, A 279, 301-311 (1976)

RAICH, D. G. (See Rasmussen, J. O., LBL-5048)

RAICH, G. G. (See SOINSKI, A. J., LBL-6516)

RANDRUP, J.
Nuclear One-Body Proximity Friction
LBL-5847, December 1976

RANDRUP, J. (See BLOCKI, J., LBL-6536)

RAPE, A. J. and S. S. Markowitz
Radiochemical Study of the $^{12}$C($^{3}$He,$^{7}$Be) Reaction Mechanism at 30 MeV.
LBL-3485, April 1975
Phys. Rev. C 13, 2116 (1975)

RASMUSSEN, J. O., D. G. Raich, H. J. Mang, T. Fliessbach and L. Marquez
Alpha Decay Theoretical Calculations for 125-Neutron Nuclei
LBL-5048, July 1976
Z. Physik, A 279, 313-317 (1976)

RASMUSSEN, J. O. (See ANHOLT, R., LBL-4359)

RASMUSSEN, J. O. (See BOISSON, J. P., LBL-5814)

RASMUSSEN, J. O. (See GUIDRY, M. W., LBL-4357)

RASMUSSEN, J. O. (See GUIDRY, M. W., LBL-4363)

RASMUSSEN, J. O. (See KAWAKAMI, H., LBL-4303)

RASMUSSEN, J. O. (See KRIEN, K., LBL-1652)

RASMUSSEN, J. O., (See RADI, Hafez, M. A., LBL-5071)

RASMUSSEN, J. O. (See RAICH, D. G., LBL-5049)

RASMUSSEN, J. O. (See RING, P., LBL-6538)

RASMUSSEN, J. O. (See SOINSKI, A. J., LBL-6516)

RASMUSSEN, J. O.
Microscopic Calculations of High-Spin Rotational States
LBL-6521, May 1977

RASMUSSEN, J. O., R. Donangelo, and L. Oliveira
Theoretical Calculations of Peripheral Reaction Yields from Relativistic Heavy Ions
LBL-6580, August 1977

RAUSCHER, E. A. (See SOINSKI, A. J., LBL-6516)

RESMINI, P. G. (See DE SWINIARSKI, R., LBL-2322) Rev.

REZANKA, I. (See KRIEN, K., LBL-1652)

REZANKA, I. (See RAICH, D. G., LBL-5049)

RING, P., H. Massmann, and J. O. Rasmussen
On the Treatment of a Two-Dimensional Fission Model with Complex Trajectories
LBL-6538, June 1977

RING, P. (See MANG, H. J., LBL-5015)

ROBEL, M. (See BLOCKI, J., LBL-6536)

ROMERO, J. L. (See KING, N. S. P., LBL-5849)

ROY, R. (See KING, N. S. P., LBL-5849)

RUSSO, P., B. Cauvin, P. Glässel, R. C. Jared, R. P. Schmitt, G. J. Wozniak and L. G. Moretto
Charge and Angular DISTRIBUTIONS and Secondary Fission of Deep Inelastic Productions from the Reaction $^{197}$Au + 979 MeV $^{136}$Xe
LBL-5050, August 1976
Phys. Lett. 67B, 155 (1977)

RUSSO, P., R. P. Schmitt, G. J. Wozniak, R. C. Jared, P. Glässel, B. Cauvin, J. S. Sventek, and L. G. Moretto
Evidence for Diffusive Relaxation Along the Mass Asymmetry Coordinate in the Reaction $^{197}$Au + 620 MeV $^{86}$Kr
LBL-5810, November 1976

RUSSO, P. (See CAUVIN, B., LBL-6506)

RUSSO, P. (See SCHMITT, LBL-5042)

SAKAI, M. (See KAWAKAMI, H., LBL-4303)

SAMADI, B. (See MANG, H. J., LBL-5015)

SANDOVAL, A. (See GOSSET, J., LBL-5820)

SANDOVAL, A. (See GUTBROD, H. H., LBL-5039)

SANDOVAL, A. (See WESTFALL, G. D., LBL-5072)

SCHMITT, R. P., P. Russo, R. Babinet, R. Jared, and L. G. Moretto
Nuclear Relaxation Phenomena, Diffusion and Orbiting in the Reaction $^{107,109}Ag + ^{84,86}Kr$ at 7.2 MeV/Nucleon
LBL-5042, June 1976
Nucl. Phys. A 279, 141-158 (1977)

SCHMITT, R. P. (See CAUVIN, B., LBL-6506)

SCHMITT, R. P. (See GLASSEL, P., LBL-5086)

SCHMITT, R. P. (See MATHEWS, G. J., LBL-5812)

SCHMITT, R. P. (See MORETTO, L. G., LBL-5057)

SCHMITT, R. P. (See RUSSO, P., LBL-5050)

SCHMITT, R. P. (See RUSSO, P., LBL-5810)

SCHMITT, R. P. (See WOZNIAK, G. J., LBL-6532)

SCHROEDER, L. S.
High Energy Nucleus-Nucleus Studies at the Berkeley Bevalac
LBL-5082, September 1976
Presented at the XVI School of Theoretical Physics, Zakopane, Poland, May 25- June 7, 1976; Also to be published in Acta Physica Polonica

SCHROEDER, L. S.
Particle Production in High Energy Nucleus-Nucleus Experiments at Berkeley
LBL-5083, September 1976
Proceedings of the Topical Meeting on Multiparticle Production on Nuclei at Very High Energy, International Centre for Theoretical Physics, Trieste, Italy, June 10-15, 1976

SCOTT, D. K. (See BECCHETTI, F. D., No No. 1975)

SCOTT, D. K. (See BUENERD, M., LBL-5067)

SCOTT, D. K. (See GELBKE, C. K., LBL-5094)

SCOTT, D. K. (See GELBKE, C. K., LBL-5821)

SCOTT, D. K. (See GELBKE, C. K., LBL-5826)

SCOTT, D. K. (See GELBKE, C. K., LBL-6551)

SCOTT, D. K. (See KEKELIS, G. J., LBL-6557)

SCOTT, D. K. (See OLMER, C., LBL-5805)

SCOTT, D. K. (See YAGI, K., LBL-4382)

SCOTT, D. K. (See ZISMAN, M. S., LBL-5098)

SEABORG, G. T.
Actinides and Transactinides
LBL-5097
Prepared for publication in the Third Edition of Kirk/Othmer, "Encyclopedia of Chemical Technology," John Wiley and Sons, Inc.

SEABORG, G. T. [See HARVEY, B., Science 193, 1271 (1976)]

SEABORG, G. T., S. G. Thompson, A. Ghiorso, K. Street, P. R. Fields, J. L. Crandall, F. P. Baranowski, J. R. Peterson, L. B. Asprey, K. Hulet, W. R. Carnall, J. G. Conway, and N. Edelstein
Proceedings of the Symposium Commemorating the 25th Anniversary of Elements 97 and 98 held on January 20, 1975
LBL-4366, July 1976

SEABORG, G. T. (See LOVELAND, W., LBL-6513)

SEABORG, G. T. (See LOVELAND, W., LBL-6522)

SEABORG, G. T. (See MORRISSEY, D. J., LBL-6539)

SEABORG, G. T. (See OTTO, R. J., LBL-6509)

SEILER, F. (See CONZETT, H. E., LBL-5850)

SEXTRO, R. G. (See ZEBELMAN, A. M., LBL-5095)

SHELINE, R. K. (See KLEINHEINZ, P., LBL-4352)

SHERMAN, J. D., D. L. Hendrie, and M. S. Zisman
Spectroscopy of $^{140}Ce$ and $^{138}Ce$ Via the $^{140}Ce(p,p')$, $^{142}Ce(p,t)$, and $^{140}Ce(p,t)$ Reactions at $E_p = 30$ MeV
LBL-4379, October 1976
Phys. Rev. C 15, 903 (1976)

SHIBATA, T. (See ANHOLT, R., LBL-4359)

SHIBATA, T. (See BOISSON, J. P., LBL-5814)

SHWE, H. (See HECKMAN, H. H., LBL-3656)

SIEGBAHN, Per (See GARRISON, B., Jr., LBL-4328)

SHIHAB-ELDIN, A. A. (See RADI, Hafez M. A., LBL-5071)

SIERI, A. J. (See BŁOCKI, J., LBL-6536)

SILBERMAN, MILES L. (See NOBLE, D. C., LBL-4324)

SILVA, R. J. (See OTTO, R. J., LBL-6509)

SILVA, R. J. (See STROUGHTON, R. W., LBL-5053)

SIMON, R. S., M. V. Banaschik, R. M. Diamond, J. O. Newton, and F. S. Stephens
Experimental Study of Yb Nuclei at High Angular Momentum
LBL-5827, January 1977

SIMON, R. S. (See LEE, I. Y., LBL-5031)

SIMON, R. S. (See GLÄSSEL, P., LBL-5086)

SIMON, R. S. (See LEE, I. Y., LBL-6512)

SIMON, R. S. (See LEE, I. Y., LBL-6559)

SIMON, R. S. (See NEWTON, J. O., LBL-5830)

SIMON, R. S. (See WARD, D., LBL-4375)

WESTFALL, G. D. (See GOSSET, J., LBL-5820)

WESTFALL, G. D. (See GUTBROD, H. H., LBL-5039)

WILKE, C. R. and G. Mitra
Enzymatic Utilization of Waste Cellulosics
LBL-2334, January 1974
Biotechnol. & Bioeng. Symp. No. 5, 253 (1975)

WILSON, LANCE W. (See HECKMAN, H. H., LBL-6561)

WILSON, LANCE W. (See HECKMAN, H. H., LBL-6562)

WINSBERG, Lester
The Analysis of Thick-Target Thick-Catcher Nuclear Recoil Experiments
LBL-6583, August 11, 1977

WOLSCHIN, Georg (See GLENDENNING, N. K., LBL-5052)

WOZNIAK, G. J., R. P. Schmitt, P. Glässel, and L. G. Moretto
A Study of Diffusion Phenomena in the Rare Earth Region: The Reaction $^{159}Tb$ + 620 MeV $^{86}Kr$
LBL-6532, September 1977

WOZNIAK, G. J. (See JAHN, R., LBL-5038)

WOZNIAK, G. J. (See JAHN, R., LBL-5079)

WOZNIAK, G. J. (See MATHEWS, G. J., LBL-5812)

WOZNIAK, G. J. (See RUSSO, P., LBL-5050)

WOZNIAK, G. J. (See RUSSO, P., LBL-5810)

WOZNIAK, G. J. (See SCHMITT, R. P., LBL-6506)

YAGI, K., D. L. Hendrie, U. Jahnke, C. F. Maguire, J. Mahoney, D. K. Scott, D. H. Feng, T. Udagawa K. S. Low and T. Tamura
$^{142}Nd(^{18}O,^{16}O)^{144}Nd$ Reaction and Its Contrast to $^{144}Nd(^{12}C,^{14}C)^{142}Nd$ Reaction
LBL-4382, March 1976
Phys. Rev. C 14, 351 (1976)

YOSHIKAWA, N. (See KAWAKAMI, H., LBL-4303)

ZEBELMAN, A. M., W. G. Meyer, K. Halbach, A. M. Poskanzer, R. G. Sextro, G. Gabor, and D. A. Landis
A Time-Zero Detector Utilizing Isochronous Transport of Secondary Electrons
LBL-5095, October 14, 1976
Nucl. Inst. & Meth. 141, 439-447 (1977)

ZELLER, A. F. [See HICKEY, G. T., Phys. Rev. Lett. 37, 130 (1976)]

ZISMAN, M. S., G. Kekelis, D. K. Scott, and J. Cerny
Exotic Nuclear Reactions in the Light Elements
LBL-5098, October 1976
Invited talk presented at the San Francisco Meeting of the American Chemical Society San Francisco, Ca., August 30 - September 3, 1976

ZISMAN, M. S. and J. Cerny
Very Light Neutron-Rich Nuclei Studies via the ($^{6}Li$, $^{8}B$) Reaction
LBL-5078, December 1976
Nucl. Phys. A 280, 217-227 (1977)

ZISMAN, M. S. (See CRAMER, J. G., LBL-5813)

ZISMAN, M. S. (See KEKELIS, G. J., LBL-6557)

ZISMAN, M. S. (See SHERMAN, J. D., LBL-4379)

# VI.

# AUTHOR INDEX

## AUTHOR INDEX

U.S.GOVERNMENT PRINTING OFFICE:1978-793-670/157